

Analytical Use of Fluorescent Probes in Oncology

Edited by
Elli Kohen and
Joseph G. Hirschberg

NATO ASI Series

Series A: Life Sciences Vol. 286

Analytical Use of Fluorescent Probes in Oncology

NATO ASI Series

Advanced Science Institutes Series

A series presenting the results of activities sponsored by the NATO Science Committee, which aims at the dissemination of advanced scientific and technological knowledge, with a view to strengthening links between scientific communities.

The series is published by an international board of publishers in conjunction with the NATO Scientific Affairs Division

A Life Sciences	Plenum Publishing Corporation
B Physics	New York and London
C Mathematical and Physical Sciences	Kluwer Academic Publishers Dordrecht, Boston, and London
D Behavioral and Social Sciences	
E Applied Sciences	
F Computer and Systems Sciences	Springer-Verlag
G Ecological Sciences	Berlin, Heidelberg, New York, London,
H Cell Biology	Paris, Tokyo, Hong Kong, and Barcelona
I Global Environmental Change	

PARTNERSHIP SUB-SERIES

1. Disarmament Technologies	Kluwer Academic Publishers
2. Environment	Springer-Verlag
3. High Technology	Kluwer Academic Publishers
4. Science and Technology Policy	Kluwer Academic Publishers
5. Computer Networking	Kluwer Academic Publishers

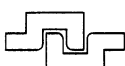
The Partnership Sub-Series incorporates activities undertaken in collaboration with NATO's Cooperation Partners, the countries of the CIS and Central and Eastern Europe, in Priority Areas of concern to those countries.

Recent Volumes in this Series:

Volume 284 — Advances in Morphometrics
edited by Leslie F. Marcus, Marco Corti, Anna Loy, Gavin J. P. Naylor,
and Dennis E. Slice

Volume 285 — Molecular, Cellular, and Clinical Aspects of Angiogenesis
edited by Michael E. Maragoudakis

Volume 286 — Analytical Use of Fluorescent Probes in Oncology
edited by Elli Kohen and Joseph G. Hirschberg



Series A: Life Sciences

Analytical Use of Fluorescent Probes in Oncology

Edited by

Elli Kohen and
Joseph G. Hirschberg

University of Miami
Coral Gables, Florida

Proceedings of the NATO Advanced Research Workshop on
Analytical Use of Fluorescent Probes in Oncology,
held October 14–18, 1995,
in Miami, Florida

NATO-PCO-DATA BASE

The electronic index to the NATO ASI Series provides full bibliographical references (with keywords and/or abstracts) to about 50,000 contributions from international scientists published in all sections of the NATO ASI Series. Access to the NATO-PCO-DATA BASE is possible in two ways:

—via online FILE 128 (NATO-PCO-DATA BASE) hosted by ESRIN, Via Galileo Galilei, I-00044 Frascati, Italy

Library of Congress Cataloging-in-Publication Data

Analytical use of fluorescent probes in oncology / edited by Eliel Kohen and Joseph G. Hirschberg.
p. cm. -- (NATO ASI series. Series A. Life sciences : v.
286)
"Published in cooperation with NATO Scientific Affairs Division."
"Proceedings of the NATO Advanced Research Workshop on Analytical Use of Fluorescent Probes in Oncology, held October 14–18, 1995, in Miami, Florida"--T.p. verso.
Includes bibliographical references and index.
ISBN 978-1-4613-7679-8 ISBN 978-1-4615-5845-3 (eBook)
DOI 10.1007/978-1-4615-5845-3
1. Fluorescent probes--Diagnostic use--Congresses. 2. Cancer-Diagnosis--Congresses. I. Hirschberg, Joseph G. II. North Atlantic Treaty Organization. Scientific Affairs Division. III. NATO Advanced Research Workshop on Analytical Use of Fluorescent Probes in Oncology (1995 : Miami, Fla.) IV. Series.
[DNLM: 1. Neoplasms--diagnosis--congresses. 2. Fluorescent Dyes-diagnostic use--congresses. 3. Microscopy, Fluorescence--congresses. 4. Flow Cytometry--congresses. QZ 241 A532 1996]
RC270.3.F58A53 1996
616.99'4075--dc20
DNLM/DLC
For Library of Congress

96-31495
CIP

Additional material to this book can be downloaded from <http://extras.springer.com>
ISBN 978-1-4613-7679-8

© 1996 Springer Science+Business Media New York
Originally published by Plenum Press, New York in 1996
Softcover reprint of the hardcover 1st edition 1996

10 9 8 7 6 5 4 3 2 1

All rights reserved

No part of this book may be reproduced, stored in a retrieval system, or transmitted in any form or by any means, electronic, mechanical, photocopying, microfilming, recording, or otherwise, without written permission from the Publisher

PREFACE

Fluorescence is a very powerful tool for work at the frontier of cell biology, photobiology and bioinstrumentation. The stated aim of the workshop was to highlight the significance of fluorescence work for the understanding of cell and tissue physiology, physiopathology and pharmacology, particularly in terms of the analytical use of fluorescent probes in oncology. In the organization of the workshop a multidisciplinary approach was selected. The purpose of the Advanced Research Workshop (ARW) was to bring together researchers in the various disciplines of tissue optics, imaging, microspectrofluorometry and state of the art probes, in order to explore the full benefits that can be derived in biomedicine through the convergence of these approaches.

When applied to *in vivo* and *in situ* studies, fluorescence and related optical methods enable us to explore within tissues, cells and organelles photon effects previously understood only in solution photochemistry. Processes which can be studied at the molecular level by photophysics, photochemistry and physical chemistry can be evaluated in living tissue by fluorescence spectroscopy and imaging at the intracellular level in terms of structure and function. Thus, fluorescence adds a new dimension to cell biology and physiology. This approach is now supported by a full and versatile, rapidly growing armamentarium of new selective probes for organelles, enzymes, cations, cytoskeleton and metabolic control. Furthermore, an updating of the development of appropriate fluorescence probes for enhancing the quality and extending the nature of the *in vivo* and *in situ* responses was also expected as an important part of the workshop. Despite the tremendous progress in the acquisition of new probes, there was a certain lagging in the development of dynamic probes in the crucial area of nucleic acids, where we remained limited to the classical compounds used in flow cytometry and imaging. There are now strong indications from contributions at the workshop that this gap is rapidly being filled.

At the workshop we have seen that *in vivo* spectroscopy and imaging offers possibilities analogous to CT and MRI scans in diagnostics through the absorption and fluorescence of photodiffusive waves. Imaging of breast and neck tumors is realized using a carbocyanine dye with determination of scattering and absorption coefficients. Fluorescence and Raman spectroscopy is used for diagnosis of gynecologic, digestive and respiratory tumors. Frequency domain tomography allows in-depth scanning of tissues.

Signal transduction in living cells is studied by fluorescence resonance energy transfer. Modulated and pulsed photoacoustic spectroscopy are used to acquire depth profile spectra of chromophores, lifetimes of intermediates in photosynthesis and time-resolved spectra of visual pigments. Two- and three-photon fluorescence excitation minimizes photodamage and provides greater depth of penetration of tissue. Light quenching by a second pulse to control excited state population is advantageous for exploration of usually inaccessible processes, including small changes in intensity, anisotropy and lifetime of fluorescence.

Highlights included three-dimensional imaging of calcium-loaded myocytes, NADH videofluorometry and quenching of Pd-porphyrin fluorescence to measure tissue oxygenation, study of cellular pH, Ca^{++} , membrane potential components pixel by pixel with msec time resolution, estrogen and progesterone imaging, detection of microscopic breast tumor recurrences and urothelial tumors, determination of microvascular wall adhesion thresholds of tumor cells with high and low metastatic potential, *in vivo* three-dimensional confocal microscopy of skin and immunofluorescence probing of cytoskeleton. New methods and probes included integration of scanning probe microscopy with classical optical techniques, a proposal for dual interferometry to study metabolic control by fluorescence excitation spectroscopy, time-resolved fluorescent lanthanide-substituted nucleotides, state of the art nucleic acid probes, metal-ligand probes with considerable fluorescence lifetime, immuno-photodetection and fluorogenic probes to study gene expression in transfected cells.

In conclusion, the workshop has emphasized the considerable advantages to be derived in cell and tissue physiopathology and pharmacology as well as diagnostics, prognostics and therapeutics from the analytical use of fluorescent probes.

A natural consequence of the workshop was the generation of conviviality between participants belonging to all these various disciplines. This created a demand to maintain the intellectual exchange generated, and perhaps to formalize it through a series of future newsletters.

We embarked on this workshop with the question: “*Quo Vadis Analytical Use of Fluorescent Probes in Oncology?*” As the interest grew and intensified, could it be that we are all on the verge of embarking, with all the potentials of fluorescence and future promises, on a trip a little alike to that of the Argonauts in search of the Golden Fleece?

CONTENTS

1. Overview: Workshop on Analytical Use of Fluorescent Probes	1
Elli Kohen	
2. Detection of Breast Tumors by Absorption and Fluorescence of Photon Diffusive Waves	25
Britton Chance	
3. Fluorescence-Lifetime Based Sensing in Tissues and Other Random Media with Measurements of Photon Migration	31
Eva M. Sevick-Muraca, Christina L. Hutchinson, and Tamara L. Troy	
4. Spectroscopy and Tomography of Tissues in the Frequency-Domain	41
Enrico Gratton, Sergio Fantini, Maria Angela Franceschini, Scott Walker, and John Maier	
5. Fret Microscopy in Cellular Signal Transduction	53
Philippe I. H. Bastiaens and Thomas M. Jovin	
6. Photoacoustic Spectroscopy Applied to Biological Materials	59
Roger M. Leblanc and Germain Puccetti	
7. Recent Developments in Fluorescence Spectroscopy: Long-Lived Metal-Ligand Probes, Multi-Photon Excitation, and Control of the Excited State	65
Joseph R. Lakowicz, Ewald Terpetschnig, Henryk Szmacinski, Henryk Malak, Józef Kuśba, and Ignacy Gryczynski	
8. Photonic Pathology: Fluorescence and Raman Spectroscopy for Tissue Diagnosis and Characterization	81
R. R. Alfano and A. Katz	
9. <i>In Vivo</i> Application PD-Porphine for Measurement of Oxygen Concentrations in the Gut	91
M. Sinaasappel, M. van Iterson, and C. Ince	
10. Laser Scanning Confocal Fluorescence Microscopy of Cell Function	97
John J. Lemasters	

11. Sub-Cellular Localization of Second Generation PDT Photosensitizers Studied by Microspectrofluorometry 113
Marc Gèze, Jean-Michel Gaullier, Marc Bazin, and René Santus
12. Photofrin Uptake as a Function of Tumor Size and the Detection of Microscopic Nests of Tumor Cells by Photofrin Fluorescence: Mechanistic Implications for PDT 123
W. R. Potter and D. A. Bellnier
13. The Detection of Apoptotic Cells and Their Quantification by Flow Cytometry . 129
Michael G. Ormerod
14. Adhesion Stabilization of Blood Borne Cancer Cells in the Microcirculation . . 137
David G. Menter, Thomas W. Smith, Zhong Yun, John Patton,
Larry V. McIntire, and Garth L. Nicolson
15. Probing of Connexin Channels: Evidence for Involvement of Junctional Coupling in Pancreatic Secretion 149
Paolo Meda
16. The Analysis of Drug-Induced Cell Cycle Perturbations by Flow Cytometry 157
Anne T. O'Meara, Bernd-Uwe Sevin, and James Perras
17. The Effects of Tumor Heterogeneity on the Flow Cytometric Analysis of Clinical Specimens 173
Wade E. Bolton and Melissa O'Brien
18. Videomicrofluorometry of Progesterone Receptors and Their Genes in Breast Cancer Cells 181
Sylvie Cassanelli, Agnès Mialhe, Josette Louis, and Daniel Seigneurin
19. Immunophotodetection of Cancer by Antibody-Indocyanin Conjugates: Experimental and Preliminary Clinical Results 189
S. Folli, P. Westermann, D. Braichotte, A. Pèlegrin, J. Mizeret,
G. Wagnières, H. van den Bergh, J-F. Savary, P. Monnier, J-P. Cerottini,
J-C. Givel, and J-P. Mach
20. Three-Dimensional Optical Functional Imaging of Tissue with Two-Photon Excitation Laser Scanning Microscopy 205
Barry R. Masters
21. Estrogen Receptor Imaging Using Intrinsically Fluorescent Ligands 213
Richard J. Miksicek and John A. Katzenellenbogen
22. Videomicrofluorometry and Intracellular Ionic Concentration in Single Living Cells: From Toy to Tool 221
P. Viallet, J. M. Salmon, M. Yassine, and J. Vigo
23. Multiwavelength Microfluorometry to Investigate Cytotoxic Processes on Sensitive and Resistant Human Lymphoblastoid CCRF-Cem Lines 231
Jean-Marie Salmon, Emmanuelle Rocchi, Jean Vigo, and Pierre Viallet

24. Laser-Induced Auto Fluorescence of Normal and Tumor Bladder Cells and Tissues: <i>In Vitro</i> and <i>in Vivo</i> Studies	241
Maurice Anidjar, Olivier Cussenot, Jocelyne Blais, Olivier Bourdon, Sigrid Avrillier, Dominique Ettori, Jean-Marie Villette, Pierre Teillac, and Alain Le Duc	
25. Fluorescent Imaging of Membrane Potential Components	249
Eitan Gross, Richard S. Bedlack, Jr., and Leslie M. Loew	
26. Probing of Microtubule Structures with Monoclonal Antibodies and Immunofluorescence Microscopy	257
Pavel Dráber, Eduarda Dráberová, and Vladimír Viklický	
27. Immunofluorescence Detection of Cytoskeletal Structures	265
Eduarda Dráberová and Pavel Dráber	
28. Cell Expression System in V79 Cells Transfected with Cytochrome P450 and Its Performance in Metabolism Studies	273
Johannes Doebrer, Wolfgang A. Schmalix, and Helmut Greim	
29. Direct Transfer of Control and Multidrug Resistance	283
Hans V. Westerhoff, Johann M. Rohwer, Marc Heijn, Sipko Mülder, Rick I. Ghauharali, Peter Wielinga, Boris N. Kholodenko, Ellen C. Spoelstra, and Jan Lankelma	
30. Instrumentation Design for Study of Metabolic Control in Living Cells	293
Joseph G. Hirschberg and Elli Kohen	
31. Use of Fluorescent Derivatives for Labeling Cells: Diagnosing, Preventing, and Correcting Genetic Diseases; Photosynthesizing and Killing of Tumors, Parasites, and Viruses	299
Shimon Gatt, Tama Dinur, Sara Cerbu-Carabat, Vered Agmon, and Arie Dagan	
32. Ca ²⁺ Signaling and Cytoskeleton Reorganization in Endothelial Cells Stimulated by Bradykinin	309
Lilly Y. W. Bourguignon, Leya Matheu, Lucia Sobrin, and Gerard J. Bourguignon	
33. Integration of Optical Techniques in Scanning Probe Microscopes: The Scanning Near-Field Optical Microscope (SNOM)	317
Achim Kirsch, Christoph Meyer, and Thomas M. Jovin	
34. Perfusion, Temperature, and PO ₂ Control in a Leiden Culture Bath for Single Cell Measurements and Manipulations	325
C. Ince, A. de Vos, G. Verschragen, M. Sinaasappel, and B. Van Duijn	
35. Immunofluorescence Study of Intermediate Filament Protein Expression under Normal and Pathological Conditions	331
Vladimír Viklický, Zdeněk Lukás, and Pavel Dráber	

36. The Use of Fluorescent Probes in Characterizing Drug Resistance in Cultured Cells	339
Anna-Marija Helt, Gary D. Kruh, and Kenneth D. Tew	
37. A High Resolution Multimode Digital Imaging System for Fluorescence Studies of Mitosis	349
E. D. Salmon and J. C. Waters	
38. Use of Photodiode Array Fluorescence Spectroscopy in Biochemistry, Pharmacology, and Oncology	357
Roy Pottier and James C. Kennedy	
39. Hydrophobic Photosensitizers Delivery to Tumor Tissues by an Amphiphilic Peptide: <i>In Vitro</i> and <i>in Vivo</i> Fluorimetric Studies	363
O. Bourdon, J. Blais, J. Bolard, V. Vonarx, L. Morlet, T. Patrice, C. Bedel, N. Cempel, and D. Guillochon	
40. Merocyanine 540—A Fluorescent Dye and a Biological Probe	371
Cyril Párkányi, Alain Adenier, and Jean-Jacques Aaron	
41. High Pressure Infrared Spectroscopy in Biological and Biomedical Studies	383
Adnan Taymaz, Ghaith Breiki, Ipek Kanat, Ali Karaman, and Patrick T. T. Wong	
42. Fluorescence Spectroscopy for Diagnosis of Cancerous Tissues	393
T. Rézio, M. L. Fraser Monteiro, William H. Clode, and J. M. G. Martinho	
43. Solvent-Dependent Excited State Properties of Psoralens: A Model to Their Antiproliferative Action	405
T. Sa e Melo and C. Sousa	
44. Fluorescent Probes in Breast Tumor	411
Ayse Zehra Aroguz and Nezih Hekim	
45. Use of Fluorescence <i>in Situ</i> Hybridization for Mapping and Ordering YAC Clones from Chromosomal Regions with Suspected Tumor-Suppressor Activity	419
V. Macheraki, V. Orphanos, S. Kamakari, M. Kokkinaki, G. Stephanou, N. Demopoulos, G. M. Maniatis, N. Moschonas, and D. H. Spathas	
46. Photochemical and Photophysical Studies of an Anthocyanin: Fast Excited-State Proton Transfer from 4-Methyl 7-Hydroxyflavylium Chloride to Water	423
Isabel Abreu, J. C. Lima, M. Helena Santos, Raymond Brouillard, and António L. Maçanita	
47. Selectivity and Localization of Anthracyclines in Cardiac-Muscle and Non-Muscle Cells Relevance to Multidrug Resistance	425
T. J. Lampidis, D. Kolonias, N. Savaraj, M. Israel, and W. Priebe	
Index	427

OVERVIEW

Workshop on Analytical Use of Fluorescent Probes

Elli Kohen

Department of Biology
University of Miami
Coral Gables, Florida

IN VIVO SPECTROSCOPY AND IMAGING

Detection of Breast Tumors by Absorption and Fluorescence of Photon Diffusive Waves

The introductory paper (Chance) on “Detection of breast tumors by absorption and fluorescence of photon diffusive waves,” presented evidence on natural tissue fluorescence (*i.e.* NADH) and probe fluorescence (indocyanine green). It was found that in the sequence, nitrogen breathing - reoxygenation, NADH becomes oxidized prior to the recovery of electrical activity due to the time required to build up the phosphate potential necessary for such activity.

For three-dimensional scan of the redox state in tissue, a system has been used which includes a liquid nitrogen microtome for grinding away the surface of freeze-trapped tissue, in order to sequentially study planes in the tissue at any depth. This instrument has perhaps been the most versatile and effective one for observing the NADH/llavin fluorescence ratio. In a tumor grown on the flank of a rat and studied by freeze trapping and redox scanning, the highly reduced generally normoxic state becomes highly heterogenous and more oxidized with the animal breathing a CO₂/O₂ mixture (carbogen). Highly reduced, presumably hypoxic regions persist which are radiation-insensitive.

For fluorescence signals from deep within the breast tissue, probes such as indocyanin green with excitation at 780 nm and emission at 830 nm are definitely superior to probes with excitation in the UV. The fact that one is able to detect and to image important biological processes by Near Infra-Red (NIR) spectroscopy provides a pathway by which the bulk of knowledge acquired on single cells and isolated tissues can now be applied to important clinical studies.

Photon migration through a breast tumor in a patient injected with indocyanin green, excites probe fluorescence in the vascular bed. In a breast tumor for example, the magnitude of the optical fluorescent signal due to probe accumulation in the vascular bed of the tumor is larger than the signal from the corresponding position in the contralateral breast. This

indicates a greater content of blood vessels (*i.e.* angiogenesis) in the breast tumor as compared with the non-tumoral breast tissue. Thus, tumors are characterized by the rapidity and the magnitude of the occupancy of the vascular volume in the probe. In the original studies the signal was not imaged. Much greater contrast would be obtained if those voxels originating only from the tumor tissue were observed. One can foresee that the development of the fluorescent probes in the NIR window near 800 nm may allow tissue images of calcium uptake, membrane potential and antigen/antibody reactions deep within the human tumor bearing breast and also the brain.

Fluorescence–Lifetime Based Sensing in Tissues and Other Random Media with Measurement of Photon Migration

For activated fluorescent probes undergoing collisional quenching, the measured lifetime, τ , can be used to determine the non-reemitting probe-metabolite or quencher concentration from the empirical Stern–Volmer relationship:

$$\tau_o/\tau = 1 + K_{SV}\tau_o[Q]$$

where τ_o is the probe lifetime in the absence of metabolite and K_{SV} is the (known) Stern–Volmer coefficient (Sevick-Muraca *et al*). The increased time-of-flight due to the multiple scattering of light in tissues may be comparable to or even exceed fluorophore lifetimes. As a consequence, in the frequency domain method of lifetime determination phase-shifts may exceed 360 degrees and amplitude demodulation may be increased significantly.

Frequency-domain measurements were conducted on micromolar solutions of 3,3'-Diethyltricarbocyanine iodide (DTTCI) with determinations of phase-shift and amplitude demodulation of *re-emitted* fluorescence and *excitation* light (789 nm from an argon ion pumped Ti:sapphire laser). Since the isotropic scattering coefficient increases in the transillumination geometry, the fluorescence phase-shift delay, θ_m , increases and the modulation ratio, $M_{m(\omega)}/M_{m(0)}$ decreases.

Frequency–Domain Spectroscopy and Tomography of Tissues

For spectroscopy and tomography of tissues in the frequency domain, measurements can be made at a single modulation frequency, thereby sacrificing some of the information, but with the advantage of speed, accuracy and excellent signal-to-noise ratio (Gratton). A measurement at a single frequency provides three independent quantities: phase and AC and DC components of demodulation. From any pair of these quantities the reduced scattering and absorption coefficients may be obtained.

In heterogenous tissues an object at a given location can influence the light distribution at another location. This effect decreases at least exponentially as the distance from the object increases. The diffraction pattern obtained in an experiment with two totally absorbing spheres immersed in an Intralipid solution is approximately the sum of the diffraction patterns of each individual object.

In a model for reconstruction of the tissue interior, the object under study is divided into voxels and every voxel produces an independent effect at the detector point. Strictly speaking, the photon density waves scatter from every object in the medium. In the linear approximation, if a number, N , of objects scatter the photon density wave, the effect on the detector is given by the sum of the contributions from each object.

An alternative way to describe the propagation of light in tissues is to consider the set of all possible trajectories that photons can follow from source to detector. Along the

light trajectory, the intensity decreases exponentially due to absorption. The particular position of an object moving along the light bundle from source to detector should not matter, since the extinction due to light absorption should be the same along the photon trajectory.

The reconstruction of absorbing objects is achieved, similarly in principle to the method used in x-ray computed tomography. The value of the absorption and scattering coefficients is measured at a number of source-detector positions using a frequency domain scanner. The operation is repeated for different sample orientations. In a model experiment, two glass spheres of 1 cm diameter, separated by 2 cm (center to center) and filled with the same intralipid suspension as that of the background, are inserted into the scattering medium. In the reconstructed 3-D image, weakly scattering objects can be easily distinguished and the general shape of the object (two spheres) can be recognized. Each image is displayed essentially in real time. The total acquisition time for a 3-D image of a 4x4x4 cm sample is about 10 minutes.

The Study of Signal Transduction in Living Cells by Fluorescence Resonance Energy Transfer Microscopy

The interactions and structural states of relevant signalling molecules responsible for the pleiotropic responses of the cell after stimulation are studied by the transfer of excitation energy between fluorescent markers through the Forster mechanism over the limited range of 1-10 nm (FRET microscopy) in cellular signal transduction (Bastiaens and Jovin). One approach is the measurement of the increase in the donor quantum yield (release of quenching by acceptor) following the local photochemical destruction of the energy acceptor.

Sulfoindocyanine succinimide ester Cy3 (fluorescent label of the serine/threonine protein kinase regulatory domain) and *sulfoindocyanine succinimide ester Cy5* (label of the polyclonal antibody directed against the catalytic domain) constitute an excellent donor-acceptor pair. In T3 fibroblasts, as the incubation with the phorbol ester PMA (which cleaves the protein into regulatory and catalytic domains) proceeded, Cy3 fluorescence (λ_{ex} : 543nm; λ_{em} : 590 nm) became predominantly nuclear, while Cy5 fluorescence (λ_{ex} : 633 nm; λ_{em} : 699 nm) was increasingly perinuclear. This is confirmed by the decreased FRET efficiency in the nuclear region after photodestruction of Cy5 by 633 nm illumination, suggesting that the protein has been fragmented into catalytic and regulatory domains, with the latter retained in the nucleus.

Photoacoustic Spectroscopy Applied to Biological Systems

Photoacoustic spectroscopy (PAS) has been applied to study complex biological media like leaves (photosynthesis), retina (vision) or human skin (membrane permeability) (Leblanc). PAS is carried out in a modulated (MPAS) or pulsed (PPAS) form. In MPAS, a high-power light source (usually a xenon lamp), filtered in wavelength by a monochromator, provides a continuously tunable source of light. Detection will be performed at the same frequency as the modulation of the excitation light beam, which eliminates any noise from the surrounding environment. The detected signal comes from a limited layer of the sample from which heat emission has the time to diffuse towards the surface and contribute to the gas temperature increase, e.g. within the 50 msec (half period) signal detection period at the 10 Hz modulation frequency. The thickness of the layer, at a given modulation frequency, f , is related to the heat diffusion length of the specific sample.

For PPAS a continuously tunable source of light pulses is required. MPAS gives a time-averaged value of the heat response at a single frequency. In PPAS, by Fourier transform analysis, the response is decomposed into its components *at all acoustic frequencies* between

1 Hz and several kHz. These frequencies in PPAS are the *direct equivalent to the modulation frequencies in MPAS*. In PPAS, the signal arises first from the surface layers, at short times t , corresponding to high acoustic frequencies, and then progressively from deeper layers of the sample at longer times of observation, *i.e.* low acoustic frequencies. In the diffusion of sunscreens, τ is the time necessary for half of the product to penetrate into the deep layers of the skin, *i.e.* beyond the detection level. A depth profile of different sunscreen chromophores into the layers of the skin can be inferred from the Fourier transform of the PPAS response. In addition to pigment/chromophore penetration studies, PPAS has broad applications in the study of the time evolution of the different phases of the two photosystems (*e.g.* intermediate state lifetimes and their discrimination, as well as delay of charge transfers) or time-resolved spectroscopy of deexcitation phenomena (charge transfer in vision).

Metal Ligand Complexes as the New Class of Probes for the Biophysical and Biomedical Applications of Fluorescence

Probes with long decay times allow intensity and anisotropy decay measurements with relatively simple instrumentation (Lakowicz). A series of metal-ligand complex (MLC) probes display decay times up to 400 ns, and other molecules in this class can have decay times as long as 100 μ s. The presence of a suitable non-identical ligand [*i.e.* 2,2'-bipyridyl (dcbpy)] on the parent compound [Ru(bpy)₃]²⁺ results in high fundamental anisotropy.

The FLIM requirements of a light source modulated near the 100 MHz and of a high-speed gain-modulated image intensifier can be eliminated using long-lived MLC probes. The capabilities of FLIM may then become a routine part of fluorescence microscopy. With a series of MLC probes for analysis of pH, Ca²⁺, and Mg²⁺, MLC probes and FLIM may find widespread uses in clinical chemistry, analytical chemistry and cellular imaging.

Two-Photon Excitation

In two-photon excitation (TPE) the intensity of the emission depends on the square of the incident light intensity (Lakowicz). The observed intensities of the calcium-free and calcium-bound forms of Indo-1 are proportional to the cube of the laser power (three-photon excitation). The emission spectra of the calcium probe Indo-1 appear to be essentially identical for 295 nm (one-photon excitation) and 895 nm (three-photon excitation). Three-photon excitation has a number of potential advantages in time-resolved fluorescence and fluorescence microscopy: (1) the fundamental output of Ti:sapphire lasers is more intense from 800-900 nm, which is suitable for three-photon excitation of UV-absorbing proteins; (2) the Ti-sapphire fundamental wavelengths are above the absorption bands of most biological chromophores, which minimizes autofluorescence; (3) photomultiplier tubes without significant sensitivity over 600 nm are readily available, thus avoiding problems due to stray or scattered excitation radiation.

Light Quenching

In the control of excited state population by light quenching (LQ) the sample is excited by one pulse, and the excited state population is modified by a subsequent pulse which overlaps the emission spectrum (Lakowicz). *The second pulse causes stimulated emission.* Since the emitted photon is directed along the path of the quenching beam, it is not observed with right-angle detection, resulting in a decrease (quenching) of the observed emission.

If the quenching beam is delayed in time relative to the excitation pulse, the intensity and anisotropy display instantaneous changes upon arrival of the quenching pulse. LQ can be achieved without addition of quenchers, *i.e.* without changes in chemical composition which can alter the conformation of sensitive biomolecules and the effect is rapidly reversible by blocking illumination. Hence, even small changes in intensity, anisotropy, lifetime, phase or modulation can be detected, and little photochemical damage is expected because the quenching light is not absorbed by the fluorophores. The ability to decrease the lifetime by LQ may increase our ability to resolve complex phenomena in rigid and/or hard to access environments. In a mixture of fluorophores one can expect those which most closely match the quenching wavelength to be preferentially quenched. The ability to measure time-dependent LQ and multi-pulse experiments may find use in studies of the rotational diffusion of asymmetrical biomolecules and may be informative in studies of macroscopically oriented specimens.

Photonic Pathology: Optical Fluorescence and Raman Spectroscopy for Tissue Diagnosis and Characterization

There are several natural fluorophores that exist in tissue and cells which, when excited with ultraviolet light, fluoresce in the ultraviolet and visible region of the spectrum, *i.e.* tryptophan, elastin, collagen, nicotinamide adenine dinucleotide, lipids, flavin and porphyrin (Alfano). The complex structure of tissue, variation in blood concentration, and the large site-to-site differences in elastic scattering have complicated the spectral analysis. The mathematical tools employed to improve diagnostic accuracy include intensity ratios, Fourier analysis, least squares, curve differentiation and integration at defined wavelengths.

With UV excitation at 300 nm, the ratio of fluorescence intensity at 340 nm and 440 nm (blood absorption and scattering coefficients are about the same at these two wavelengths) was consistently greater than 9 for malignant breast tissue and less than 9 for benign and normal breast tissue. This tissue is a complex system made up of ducts, lobes, lobules and fibrous tissue. Correcting for fat (emission peak around 340 nm; almost no emission at 449 nm) and the variation in blood content of the tissue, and using pathology as a standard, this analysis produced a sensitivity of 91% for malignant and 95% for benign tissue specimens. Similar studies were carried out in normal *vs.* malignant colon and gynecological tissue, in N-nitrosamine benzyl amine (NMBA)-induced premalignant and malignant aerodigestive tumors (in rat) *vs.* normal tissue, as well as retinoid-treated *vs.* untreated Multicellular Spheroids (MSC).

Near Infrared Fourier Transform (NIR-FT) Raman spectroscopy and conventional Near IR CCD systems yield spectra with sharp well-defined lines which can locate tumors with submillimeter accuracy, using endoscopes or needle tipped fiber optic probes. The Raman spectra from benign breast tumors showed three vibrational frequencies at 1240, 1445 and 1659 cm⁻¹, while malignant spectra showed only the last two frequencies. The 1657/1445 ratio was greater than 1 in normal cervical tissue, smaller than 1 in cancerous tissue. The results show that Raman spectroscopy of tissues can be used both to diagnose malignancy and to improve our understanding of the differences between normal and cancerous tissue.

NADH Videofluorometry and Quenching of Pd-Porphyrin Phosphorescence for Measurement of the Oxygenation of Tissue *in vivo*

Microcirculatory tissue oxygen concentration is measured *in vivo* via oxygen-dependent quenching of fluorescent and phosphorescent dyes (Sinaasappel, Van Iterson and

Ince), such as Pd-Porphine, *i.e.* Pd *meso*-tetra carboxyphenyl porphine, as described by the Stern–Volmer relation. Use of a fiber optic system combined with an intravital microscope provides measurements of the oxygen concentration in individual blood vessels.

Confocal Fluorescence Microscopy of Living Cells

Operating the confocal microscope with stable fluorophores, at lower laser power, high detector sensitivity, and maximum objective numerical aperture, hundreds of images can be collected with little adverse effect, stored in computer memory and then displayed (Lemasters). Coverslips are treated with polylysine, Type I collagen or laminin to improve cell adherence. Probes of cell viability and electrical potential, markers of specific intracellular compartments, of specific chemical species (*e.g.* ions, oxygen radicals and thiols) are used. Cationic dyes such as propidium iodide penetrate after the onset of cell death and bind to nuclear DNA.

At equilibrium, accumulation of lipophilic cationic fluorophores (F) like rhodamine 123 and tetramethylrhodamine methylester (TMRM) across a charged membrane is related to the negative membrane potential ($\Delta\Psi$) by the Nernst equation:

$$\Delta\Psi = -60 \log F_{\text{in}}/F_{\text{out}}$$

where F_{in} and F_{out} are fluorophore concentrations inside and outside the membrane respectively. Thus, a 10 to 1 uptake ratio signifies a -60 mV gradient and a 100 to 1 ratio a -120 mV gradient. For excitable cells, a plasma membrane $\Delta\Psi$ of -90 and a mitochondrial $\Delta\Psi$ of -150 mV are typical values. Since these $\Delta\Psi$'s are additive, mitochondria can be as much as 240 mV more negative than the extracellular space, which corresponds to a fluorophore concentration ratio of 19,000 to 1 inside to outside of the cell.

Under conditions allowing equilibrium distribution in response to the intracellular gradients, confocal images are collected, including fluorescence (F) in the extracellular space. The ratio of F_{in} over average F_{out} is determined on a pixel-to-pixel basis.

Green-fluorescing calcein accumulates virtually exclusively into the cytosol and nucleus; it is excluded from within membranous cytoplasmic organelles which appear as dark voids. Co-loading with red-fluorescing TMRM labels mitochondria. At the onset of depolarization, mitochondria release TMRM and fill with calcein.

The computer-generated reconstruction of serial confocal images collected from a single lining cell labeled with calcein yields a display of three-dimensional structure and surface topography with results rivaling scanning electron micrographs. Reconstruction of a myocyte shows a branched cylindrical structure, with rib-like surface corrugations that represent mitochondria aligned along the sarcomeres. Ratio images are converted to maps of intracellular ion distribution using a pseudo-color display. Confocal microscopy of SNARF-1 shows a pH gradient of 0.8 across the mitochondrial membrane, as predicted by Mitchell's hypothesis.

Sub-Cellular Localization of Second Generation PDT-Photosensitizers Studied by Microspectrofluorometry

Second generation photosensitizers with strong molar absorbance in the 650-800 nm range, rapid body clearance and higher tumor specificity (*e.g.* purpurins, chlorins, pheophorbides and phtalocyanins) have proved more effective than Photofrin II™ (P2) *in vivo* in the treatment of many animal tumor models (Santus). The main PDT targets in tumors are the vasculature and the cancer cells themselves.

Information from microspectrofluorometry regarding the microenvironment of pheophorbides and ALA-induced protoporphyrin (PP) can contribute to the mapping of the targets of photosensitization. The photons received by the bidimensional detector produce a “spectropotographic image.” This image can be interpreted either as a succession, along the *x* axis (wavelengths), of monochromatic images or as a succession of spectra along the *y* axis.

Molecules bound to LDL and VLDL may be internalized by endocytosis via the apolipoprotein B/E cell surface receptor. In HT29-18 colonic adenocarcinoma cells or normal fibroblasts, localized fluorescence spots corresponding to lysosomes stained with a methyl pheophorbide derivative (delivered as LDL-bound) are observed. The pheophorbide ring of the probably lysosomotropic photosensitizer must lie in the non-acidic compartment of the lysosomes, as suggested by the fluorescence maximum at 668 nm. Relocalization of pheophorbide within the cytoplasm and extensive blebbing of the plasma membrane is seen after a small irradiation dose (5 J/cm^2).

In fibroblasts where intralysosomal co-localization of pheophorbide (MPH) and Lucifer Yellow (LY) has been obtained, a 10-fold increase of lysosomal fluorescence follows unstacking of MPH upon addition of the lysosomotropic detergent N-dodecylimidazole.

As confirmed by fluorescence spectra, PP accumulates in the plasma membrane and perinuclear spots of NCTC keratinocytes incubated with 5-aminolevulinic acid (ALA) up to 42 hours.

Co-localization with Rh123, LY or NR demonstrates that at least some of the fluorescent spots are lysosomes.

Fluorescence Detection of Microscopic Tumors Using Fluorescent Photosensitizers

In situ Photofrin fluorescence has been used in the detection of microscopic disease, *e.g.* in one-year or more postmastectomy patients with a recurrent lump (Potter). 24 hours after injection of Photofrin the chest wall was scanned with a fiber optic probe attached to a fluorescence photometer. Tissue background fluorescence was excited at 612 nm, Photofrin plus background fluorescence was excited with 532.8 nm light. The contributions of each exciting wavelength to 690 nm emission were separated by chopping the two excitation wavelengths at different frequencies. The tumor detection threshold (*i.e.* a positive signal equal to the average tissue background signal plus three times the square root) resulted in the detection of 30 suspicious points in 9 patients. Punch biopsies of each point of high fluorescence demonstrated some abnormalities and 50% showed small nests of malignant cells ranging from about one hundred to one thousand cells. Nothing was found in a control group of 12 random biopsies. Extrapolation of results for tumors made of 100 cells falls about 30 fold short of the amount of Photofrin necessary to give the fluorescence signal found clinically. However, the reported clinical detection of 100 isolated tumor cells becomes plausible, with tight binding of Photofrin, if for the same volume the geometry of cells is more sheet like than spherical.

APOPTOSIS

The Detection of Apoptotic Cells and Their Quantification by Flow Cytometry

Apoptosis can be considered as the “natural” mode of cell death, as opposed to death by necrosis which occurs during, for example, tissue injury. Any untoward change in the

environment of the cell (*e.g.* a failure to establish correct cell-to-cell contacts) or toxic insults will trigger the *apoptotic program* (Ormerod).

Apoptotic cells can be quantified in DNA histograms as a hypodiploid or “sub-G1” peak. After scission of the chromatin at the sites of nucleosomal linkage, using terminal deoxynucleotidyl transferase (Tdt), the ends of DNA can be labelled directly with fluorescein-deoxyuridine triphosphate (duTP) [*In Situ* End Labelling (ISEL)]. The cells are counter-stained with propidium iodide (PI) so that the position in the cell cycle from which the cells underwent apoptosis can be observed.

Unfixed cells with a damaged plasma membrane can be excluded either by gating on light scatter or by adding PI which penetrates only cells with damaged membrane, and gating for negative red fluorescence. In the Hoechst/PI method the apoptotic cells take the Hoechst dye faster and fluoresce bright blue.

CELL ADHESION

Adhesion Stabilization of Blood–Borne Cancer Cells in the Microcirculation

Selectins, cadherins, integrins and receptors of the immunoglobulin-supergene family may contribute to adhesion stabilization (Nicholson). In addition, signaling events that cause receptor recruitment, clustering, patching and enzyme activation may occur immediately after the arrest phase of attachment. Cell stabilization is a *necessary* step that precedes cell spreading, invasion and migration. Computerized imaging techniques, using fluorescent vital dyes such as calcein-EM, enable one to examine: (a) the wall shear adhesion threshold (WSAT), a measure of the dynamic adhesive potential of tumor cells; (b) the adhesion stabilization lag time (ASLT) or length of time required for tumor cells to stabilize adhesive contacts capable of withstanding wall shear forces up to 100 dynes/cm₂.

Human malignant melanoma cells immediately arrested and bound to ECM protein or endothelial cells and remained adherent even at high levels of wall shear stress (WSS). The melanoma cells adhered to fibronectin (FN) or vitronectin (VN) coated surfaces at higher WSAT levels (lower ASLT) compared to most lymphoma cells. In ASLT, measurements obtained by imaging high pixel values correspond to post-stabilization adherent phase bright cells and low pixel values to dark background, where the cells could not withstand the shear force. ASLT's of both melanoma and lymphoma cells are considerably lower with hepatic sinusoidal endothelial (HSE) cells as the substratum.

Fluorescence Probing of Connexin Channels: Evidence for Involvement of Junctional Coupling in Pancreatic Secretion

Direct cell-to-cell communication is mediated by connexins, the non-glycosylated proteins which form the gap junctions (Meda), *i.e.* clusters of highly permeable channels for a diffusional cell-to-cell exchange of cytoplasmic ions and small molecules. The functioning of the main secretory cells of both endocrine and exocrine pancreas is coordinated by hormones, neuromediators, and cell-to-cell contacts, including intercellular exchanges of ions and molecules via gap junctions.

In a resting β cell, there are 800-2000 gap junctions which occupy less than 1 μm^2 of the plasma membrane and allow β -to- β cell exchange of current-carrying ions (electrical coupling), synchronization of free Ca^{2+} oscillations and exchange of exogenous fluorescent probes, nucleotides and glycolytic intermediates (metabolic coupling). The 10-3,000 β cells

that comprise a pancreatic islet appear to be functionally grouped in multiple communication territories. *In vivo* as well as *in vitro* sustained stimulation of insulin release was found associated with an increased expression of gap junctions and Cx43. Changes in coupling coefficient, as well as enhanced synchronization in the electrical activity and Ca²⁺ oscillations suggest that β-cell coupling may acutely increase during glucose stimulation.

Most tumoral and transformed insulin-producing cell lines, which show abnormal glucose sensitivity, do not express connexins and are essentially uncoupled. INS tumor cells that have been stably transfected with the gene coding for Cx43 express gap junctions and coupling and display a qualitatively but not quantitatively normal glucose responsiveness.

The enzyme-producing 10-50 cells that form an acinus of the exocrine pancreas are electrically and mechanically coupled by numerous gap junctions, which are made of 32 kDa (Cx32) and 26 kDa (Cx26) proteins. Hence they represent a truly syncytial unit. Junctional coupling could ensue, as experimentally verified. In both the β- and acinar cell populations, the functional recruiting of cells heterogenous in their ability to biosynthesize their secretion products, balances the disparities, thus permitting a synchronised coordinated function.

CELL CYCLE

Chemotherapy-Induced Cell Cycle Perturbations: A New Method to Analyze and Present Results

A refined method of two-parameter flow cytometry is adopted in order to define the cell cycle: propidium iodide (PI) stains DNA and fluorescein isothiocyanate (FITC) stains protein (O'Meara and Sevin). Synthesis of chromosomal protein occurs prior to DNA synthesis and may be critical to the advancement through the cell cycle. PI and FITC staining resolves the cell cycle into six compartments (G1A, G1B, S, G2A, G2B and M).

Flow cytometry has been used to pinpoint the stage of the cell cycle most sensitive to the application of specific agents. In nude mouse xenografts prepared from primary and recurrent ovarian cancers, cisplatin caused the primary tumor to show a significant decrease of G1 with accumulation of S, allowing only a small proportion of cells to progress to G2M. In the recurrent tumors, however, cells were able to overcome the block in S phase and a large proportion continued into G2M followed by reentry into G1.

Using the antibrromodeoxyuridine fluorescein conjugate cells were seen to recover from arrest after cisplatin alone, and not to recover after cisplatin plus the chemotherapy modulator pentoxyfilline.

Analysis with three subgroups of nine chemotherapeutic agents showed a positive correlation between the magnitude of cell cycle perturbations and chemosensitivity. The flow cytometric method has been successfully extended to cells treated with X-irradiation, as well as taxol, a first-line agent in many gynecologic malignancies.

The Effects of Tumor Heterogeneity on the Flow Cytometric Analysis of Clinical Specimens

A combination of accelerated mutation rates and the presence of numerous different cell types in solid tumors creates a degree of stemline and cellular heterogeneity that constitutes a considerable challenge to the flow cytometric analysis of prognostic parameters (Bolton). The presence of up to dozens of different cell types, primarily of stromal and reactive origin, in addition to apoptotic and necrotic cells, can significantly reduce analytical

sensitivity to tumor cells (*i.e.* dilution effect). A panel of probes, consisting of the DNA dye DAPI and antibodies to cytokeratin (CK), epithelial mucin antigen (MC5), tubulin, and proliferating cell nuclear antigen (PCNA) was optimized using a breast tumor model. The model consists of an equal mixture of live and dead breast tumor cells of the MDA-MB-175-VII cell line, live lymphoblastic cells of the CM line, and liver peripheral blood mononuclear cells (PBMCs). Non-epithelial, non-tumor and dead cells were excluded by CK, MC5 and tubulin, respectively.

A series of electronic gates was cumulatively applied to the cell mixture's DAPI, tubulin, CK and MC5 distributions to exclude, respectively, doublets and dead, non-epithelial, and non-breast tumor cells.

A major object is the accurate assessment of cell proliferation in solid tumors, utilizing flow cytometry and an array of monoclonal antibodies directed against proliferation-associated antigens (PAA), such as PCNA, Ki67, etc. Using cumulative gating to refine the accurate assessment of tumor cells will help to better understand both the biology and clinical presentation of tumors in general.

FLUORESCENCE IMAGING AND IMMUNOFLUORESCENCE

Video–Microfluorometry of Progesterone Receptors and Gene Probes in Breast Cancer Cells

Quantification by videomicrofluorometry of progesterone receptors (PR, a good prognostic parameter in breast cancer), has shown heterogeneity in immunocytochemical staining of MCF-7 breast cancer cells (Cassanelli, Mialhe, Louis and Seigneurin), with a rat monoclonal anti-PR antibody (PgR-ICA) followed by tetramethyl rhodamine isothiocyanate (TRITC) conjugated goat antirat IgG fragment. The murine monoclonal antibody Ki-67 binds to a nuclear antigen expressed at all stages of the cell cycle except G₀.

A triple quantification of PR, Ki-67 antigen and DNA (staining with Hoechst-Behring 33342) in a representative number of cell nuclei, showed that strongly Ki-67 labeled cells had a high PR level as opposed to Ki-67 negative cells.

Immunofluorescent staining of PR allowed the characterization of 20 PR negative and 10 PR positive MCF-7 clones. Proliferative features and the percentage of Ki-67 positive cells were lower in PR negative clones compared to PR positive. A majority of MCF-7 cells contain four to six copies of the centromere of chromosome 11, but generally there is no correlation with the number of copies of the PR gene; this may be due to deletions or translocation of PR genes to chromosomes other than 11.

Fluorescence *in situ* hybridization (FISH) on interphase cells, associated with immunofluorescence of PR expression, may give useful insight into the relation at the cell level between the number of copies of PR gene and the amount of expressed PR.

Immunophotodetection of Cancer by Fluorescent Molecules Coupled to Monoclonal Antibodies, Experimental and Clinical Preliminary Results

Indopentamethinecyanin N-hydroxysuccinimidyl ester (indocyanin) with absorption and emission respectively at 652 and 667 nm, a very high extinction coefficient and a favourable quantum yield, is a more suitable fluorochrome than fluorescein for use in immunophotodetection (Folli). This is primarily due to better penetration of longer excitation light and emission signal (relative to fluorescein) through the tissue.

The human colon carcinoma T380 and the human squamous cell carcinoma (SCC) A431 serially transplanted subcutaneously into Swiss nude mice were used as target for the indocyanin-labeled anti-CEA Mab 35 antibody. Sequential fluorescence spectra were recorded *in vivo* with excitation at 633 nm. In the first reported case of *ex vivo* demonstration of post-surgery immunophotodetection of colon carcinoma, the red signal (emission at 667 nm) was homogenously distributed through the tumor and a very precise delineation between the tumor and normal adjacent tissue was observed.

In Vivo Three-Dimensional Confocal Fluorescence Microscopic Visualization of the Living Human Skin

Non-invasive optical monitoring of cellular metabolism, using the intrinsic fluorescent mitochondrial and cytosolic pyridine nucleotides (λ_{exc} 365 nm, λ_{em} 400-500 nm) and the mitochondrial flavoproteins (λ_{exc} 450 nm, λ_{em} 500-600 nm) has been applied to measurements in individual cellular layers of the normoxic and anoxic eye (Masters). Optical sections of μm thickness can be combined to visualize the full three-dimensional images of thick tissue.

The principle of two-photon excitation microscopy, in three-dimensional laser scanning fluorescence microscopy of the cornea and skin, is *the simultaneous absorption of two photons in the near infrared region with summation of their energy to produce an electronic transition to the excited state of the chromophore equivalent to that produced by a single ultraviolet photon*. Because of the longer wavelength excitation light the two-photon method is used to overcome the problems of photobleaching and insufficient deep tissue penetration. The diffraction-limited focusing of the laser beam and the temporal concentration of the 150-fsec pulses result in two-photon excitation processes only in the region of focus. Thus *optical sectioning* is obtained, as in confocal microscopy, yielding one μm sections across the full thickness of the cornea. Imaging is possible of the 4-6 μm thick corneal endothelial cells across 400 μm of cornea. Developments in progress involve the application of the method to *in vivo* imaging of thicker and more highly scattering tissues such as normal and pathological skin.

Estrogen Receptor Imaging with the Use of Inherently Fluorescent Light

Reversibly binding fluorescent ligands are considerably more advantageous than chemically conjugated antibodies for the analysis of receptor expression and distribution because of better optical resolution of the target protein and effective immobilization at the target binding site (Mikcisek). Intrinsically fluorescent ligands of estrogen receptors (ER) are used in fluorescence video cinematography to study the dynamics of real-time motion of ER within the cell nucleus and to quantitatively assess the level and heterogeneity of ER expression in tumor samples.

The probe *coumestrol*, a phytoestrogen found in many legumes, is excited by near UV light (340-380 nm). The emission spectrum is shifted towards longer wavelengths when these probes become protein bound. Extensive overlap exists between its excitation spectrum and the emission spectrum of tryptophanyl residues, enabling fluorescence energy transfer techniques to be applied to an analysis of the coumestrol/ER complex. The specificity of ER staining is documented by the occurrence of the staining reaction at concentrations of probe close to the equilibrium binding constant (K_d) for ER high-affinity binding sites, and its sensitivity to competition by non-fluorescent estrogens.

Intense coumestrol binding is limited to Cos7 cultures transfected with an ER expression plasmid pCMV-ER.

Videomicrofluorometry and Intracellular Ionic Concentration in Single Living Cells: From Toy to Tool

A data processing method has been proposed that allows us to extract from fluorescence spectral shifts information on any unexpected chemical interaction of the calcium probes Indo-1 and Fura-2 with other intracellular chemicals, as well as potential modifications of the probe microenvironment (Viallet). An aliquot of CCRF-CEM human leukemia line cells was incubated with C-SNARF1/AM. When the complex fluorescence spectrum from a pixel results from N chemicals, its intensity at each wavelength can be described as *a linear combination of the intensities of each component at the same wavelength*. Using a set of N convenient filters, each being defined by a transfer function $\Phi_j(\lambda)$, allows one to generate the set of N equations to resolve the system.

The fluorescence emission spectra of C-SNARF1/AM treated cells were resolved using a combination of the respective characteristic fluorescence spectra obtained from water solutions of protonated and deprotonated C-SNARF1. The fit between the experimental fluorescence spectrum and the calculated spectrum indicates that only these two species are necessary to account for the intracellular fluorescence.

Multi-Wavelength Microfluorometry to Investigate Cytotoxic Processes in Sensitive and Resistant Lymphoblastoid CCRF-CEM Lines

The failure of combination cancer chemotherapy can usually be associated with the development of drug resistance (Salmon) resulting from the genetic instability of malignant cell populations and the acquisition under selection pressure of the Multidrug Resistance (MDR) phenotype. Multiwavelength multiparameter microfluorometry combined with numerical image analysis is used to monitor the MDR phenotype via simultaneous intracellular labelling with: i) the nuclear probe Hoechst 33342 (Ho 342), ii) the mitochondrial probe Rhodamine 123 (R123), iii) the membrane probe Nile Red (NR).

Using fluorescence digital imaging microscopy a mask for each cell was generated from NR images to delineate the cell contour which was then superimposed to the R123 fluorescence image.

The human lymphoblastoid line CCRF-CEM was compared to the resistant derivative lines obtained after selection with vinblastine (VLB), *i.e.* (CEM-VLB100) or teniposide (VM1), *i.e.* (CEM-VM1). Vinblastin appears to affect, in both control and resistant cells, the cycle by arrest at G2 + M, which could result from the binding of the drug to tubulin.

In CEM-VT controls, adriamycin (ADR) treatment induces large shifts of cell distribution towards higher values of both Ho342 and R123 fluorescence intensities and a larger heterogeneity of the cell population. The strong increase of nuclear DNA content beyond G2 + M phase levels seems to rule out an inhibition of DNA replication. This effect is less obvious for CEM-VLB and CEM-VM1, which may be G2 + M arrested. While CEM-VLB exhibits an increase in the mitochondria energy level, the opposite is seen in ADR-treated CEM-VM1. ADR may have different modes of action depending on the cell type and the doses used for treatment. The modification of cell sizes points to the necessity of complementing the set of evaluated parameters by determinations of intracellular ionic concentrations, pH, Na⁺, Mg⁺⁺, ..., that could influence cell volume depending on osmotic pressure related to ion transport.

Argon Laser Induced Autofluorescence of Normal and Tumoral Bladder Cells; *in Vitro* and *in Vivo* Spectrofluorometric Studies

Laser-induced autofluorescence spectroscopy (LIAFS) has demonstrated its ability for demarcating lung, colonic and cerebral tumors from normal surrounding tissues (Blais, Anidjar *et al.*).

The autofluorescence of single living urothelial cells including normal (NU) and tumor cells of different stage and grade were studied, exciting with the 488 nm line of an ionized argon laser. The argon laser induced autofluorescence appeared as a broad structureless band with a maximum in the 550-600 nm range, corresponding most likely to oxidized flavoproteins. Autofluorescence was more intense by a factor of 10 in the normal urothelial cell, compared to the tumor cells studied. Since the fluorescence yield of flavins is quenched in aerobic conditions, the decrease of fluorescence observed for all tumor cells suggests a "deficient" aerobic oxidation system.

Using an optical fiber fluorimeter with excimer laser excitation at 308 nm the intensity of emission at 360 (tryptophan or collagen) over the intensity of emission at 440 nm (NADH)=R was 0.87 ± 0.19 in normal bladder mucosa, 1.28 ± 0.40 in non-specific inflammatory mucosa and 3.04 ± 0.64 in bladder tumors (suggestive of low coenzyme concentration in the latter).

A prototype for autofluorescence ratio imaging for detection of 360-380/440-460 nm emission should become in the near future a useful adjunct for precise mapping of urothelial CIS in the bladder.

Fluorescent Imaging of Membrane Potential Components

The response of the membrane-soluble potential-sensitive fluorescent dye *di-8-ANEPPS* can be understood in terms of an *electrochromic* mechanism, in which its absorbance and fluorescence spectra are shifted in the presence of an electric field (Gross). Dual-wavelength ratiometric measurements are used for mapping regional variations in the intramembrane electric field. Along the surface of the NIE-115 mouse neuroblastoma cells, the mean intramembrane potential associated with the *neurites* was found to be 9.5 ± 2.0 mV/angstrom more positive than that at the *somata*.

Intramembrane electric fields have three components: (1) transmembrane potentials arising from the differences in ion concentration between the extracellular and intracellular fields; (2) surface potentials arising from the differences in charge density along the surface of the outer and inner faces of the membrane (3) dipole potentials arising from the aligned molecular dipoles of lipid ester groups or the water molecules adjacent to them.

Addition of valinomycin, a potassium ionophore, should set the transmembrane potential equal to the potassium equilibrium potential over all regions of the cell membrane, thereby overwhelming any intrinsic heterogeneities in ion channel distribution. However in NIE-115 cells the *regional variation in intramembrane electric field* remained, in the presence of valinomycin.

Increasing the concentration of calcium in the extracellular fluid should have screened surface charge along the outer surface of the neuron, but elevation of calcium did not cancel the neurite to soma difference in electric field.

Increasing the mole fraction of 6-ketocholestanol (6-KC) causes a 2.5-fold increase in the dual wavelength ratio of di-ANEPPS (R), while a 3-fold decrease was obtained by 15% phlorenin. These effects suggest that R is sensitive to changes in the intrinsic dipole potential.

N-115 cells increase their cholesterol/phospholipid ratio concomitant with developing neurites. An increased cholesterol content would affect the intramembrane electric field within the outer leaflet of the bilayer in the same direction as depolarization. This could perhaps initiate the cascade that culminates in enhanced neurite growth. Thus, the distribution of lipids within the plasmalemma may influence the process of differentiation and the ability of the cell to sustain spatially distinct structures and functions.

FLUORESCENCE PROBING OF CYTOSKELETON

Probing of Microtubule Structures with Monoclonal Antibodies and Immunofluorescence Microscopy

Microtubules were probed with domain-specific antibodies to study the expression of neuron-specific class-III β -tubulin and the localization of γ -tubulin in taxol-treated cells (Draber). The TU-04 antibody against α -tubulin was directly conjugated with rhodamine B sulphonylchloride.

A panel of monoclonal antibodies against the phylogenetically preserved c-peptide of γ -tubulin was prepared in order to answer the question whether γ -tubulin is the substrate for post-translational modifications. The antibody TU-30 selected from the panel decorated all typical γ -tubulin-containing structures, *i.e.* centrosomes, spindle poles and the two half-spindles within metaphase, microtubule bundles forming midbodies within telophase. TU-30 reacted with centrosomes in all tested lines from evolutionary distant species including avian cells and cultured cells from *Nicotiana tabacum*.

3T3 cells treated with taxol were characterized by multiple nuclei and the rearrangement of interphase microtubules into bundles, disruption of the mitotic spindle and assembly of new microtubule asters. Triple-label staining with TU-4 (against α -tubulin), TU-30 and HOECHST33258 (for DNA) showed that in cells that had entered mitosis, γ -tubulin was sometimes located in the area where induced aster-like aggregates of short microtubules were found. 4 to 20 microtubule asters were found in a single cell. The localization of Tu-30, was, however, limited to only a few asters in one mitotic cell. These data indicate that in taxol-treated mitotic cells, microtubule asters are nucleated independently of γ -tubulin, and other nucleators are probably necessary for generation of taxol-induced asters in cultured cells.

Immunofluorescence Detection of Cytoskeletal Structures

The cytoskeleton of eukaryotic cells is a highly dynamic structure involved in the segregation of chromosomes in mitosis, signal transduction and cell motility (Draberova). According to their sequence homologies and tissue distribution, intermediate filaments can be divided into five types. A combination of blue, green and red fluorescence with the proper filter sets is most often used for triple labelling of cytoskeletal structures according to the following sequence: (1) a mixture of rabbit antitubulin and mouse-antivimentin VI-01 antibodies; (2) a mixture of 7-amino-4-methylcoumarin-3-acetic acid (AMCA)-conjugated anti rabbit antibody and FITC-conjugated anti-mouse antibody; (3) rhodamine-phalloidin (for actin labeling). Quadruple fluorescence labelling of microtubules, vimentin filaments, mitochondria and endoplasmic reticulum has been reported.

The *microtubule-associated MA-01 antigen* was found distributed diffusely in the cytoplasm. Subsequently the immunofluorescence was accumulated around the nucleus and after 3 hours a perinuclear cap was formed. Double immunofluorescence with *anti-tubulin*

antibody showed that the microtubule network remained unchanged. Double immunofluorescence with *anti-vimentin* antibody revealed that injection of antibody gradually induced complete disruption of the vimentin network. Staining with rhodamine-phalloidin showed that the stress fibers of microfilaments remained intact. The collapse of the vimentin network was reversible, and returned to normal within 20 hours. The MA-01 seems to be a microtubule-interacting protein that mediates directly or indirectly an interaction between microtubules and vimentin-type intermediate filaments.

Immunofluorescen Study of Intermediate Filament Protein Expression Under Normal and Pathological Conditions

In 6-8 week human embryos vimentin was found by immunofluorescence microscopy with monoclonal antibodies in radial fibers located very close to the nuclei, predominantly in the vicinity of the central canal (Viklicky). At 10 weeks glial fiber-associated protein (GFAP) positive cells were noted in the radial processes of the marginal layer, but in smaller number than vimentin-positive cells. At 23 weeks the fibers of glial cells gave a positive reaction with both antibodies.

GFAP is a suitable marker for neoplasms derived from neuroglial differentiation. Some glioblastomas and anaplastic astrocytomas stained positive for vimentin only. Co-expression of vimentin and GFAP was found in well-differentiated astrocytomas and anaplastic glioblastomas as well as in undifferentiated tumors.

The Use of Fluorescent Probes in Characterizing Drug Resistance in Cultured Cells

Confocal microscopy in conjunction with fluorescence probes has been useful in drug efflux studies aimed at uncovering how cancer cells develop resistance to the drug Eramustine (EM) (Helt, Kruh and Tew). This agent with efficacy in combination treatment of hormone-dependent prostate cancer, consists of estradiol linked to nor-nitrogen mustard through a carbamate bond. Exposure to EM results in depolymerization of microtubules starting at the distal ends. Absence of up-regulated p-glycoprotein mRNA and glutathione S-transferase activity, plus the lack of cross-resistance to doxorubicin, taxol and vinblastine indicate that a multidrug resistance (MDR) type mechanism is not involved. The fluorochrome Dansyl chloride was attached to EM. Colony-forming assays demonstrated that the toxicities of EM and DnsEM were similar.

A secondary peak of DnsEM emission was detected using a 515 nm long pass filter. Superimposing phase images with corresponding fluorescence images, revealed that bright, punctate fluorescence was concentrated around the nucleus in wild-type cells. In resistant cells, individual spots could be seen migrating towards the periphery of resistant prostatic carcinoma E4 cells where a dramatic drop in fluorescence of dnsEM occurred within 10 minutes.

Confocal imaging and three-dimensional volume rendering software was used in conjunction with calcein which fills the entire cell with a bright green fluorescence upon excitation with blue light. In EM-resistant cells immunofluorescently-labeled for β -tubulin and propidium iodide, mitotic spindles were about 25% smaller than in parental cells. It is possible that the smaller spindles of EM-resistant cells are an adaptation that aids in surviving insult by the drug, while the wild type cells are blocked in G2/M. Another adaptation may be the expresion of different tubulin isotypes in the resistant cells.

High Resolution Multimode Imaging of Mitosis *in Vivo* and *in Vitro*

Spindle organization in living cells and in *in vitro* systems can be quantitatively determined by adding X-labeled tubulin subunits to the cellular tubulin pool to selectively label microtubule polymers. (ED Salmon and C Waters). Fluorescence techniques are often used in combination with differential interference contrast (DIC) to record the movements of chromosomes and centrosomes in transparent cells. Polarization methods provide a quantitative measure of microtubule assembly and orientation. The development of 4-D (3-D with 200-1000 nm optical sectioning in the z dimension, and time lapse) image acquisition and analysis will have a major impact on our understanding of mitotic mechanisms.

The digital imaging system has programs and drivers to control for either time-lapse or z-axis stepping. A time-lapse journal controls the timing and sequence of image acquisition, to take phase contrast, DAPI and rhodamine images of the same spindle.

For high-resolution real-time images of yeast nuclear motion in the cell division cycle, with Green Fluorescent Protein (GFP, photoactivated using a several sec pulse of 360 nm) histones are expressed to visualize the nucleus and cellular structural detail is recorded by DIC. DAPI fluorescence image stacks record chromosome movements while X-rhodamine labeled tubulin fluorescence shows spindle microtubule assembly dynamics. 3-D images derived from a single time-point stack of optical sections are very useful for determining the behavior of all chromosomes and their kinetochore region within the spindle. A metaphase newt lung epithelial cell is microinjected with X-rhodamine labeled tubulin (excitation at 450-600 nm) to label all the spindle microtubules and caged-fluorescein labeled tubulin (excitation at 360 nm) for photoactivation of tubulins within the spindle fiber microtubules through a 25 μm slit. The photoactivated marks on the kinetochore fibers flux poleward, demonstrating that at metaphase the kinetochore microtubules which connect the chromosomes to the poles have a net addition of tubulin subunits at their kinetochore ends and a net disassembly of subunits at their polar ends.

FLUORESCENCE AND GENE EXPRESSION

Cell Expression System in V79 Cells Transfected with cyt P450 and Its Performance in Metabolism of Drugs

More than 300 different cytochrome P450 isoforms across all species are known, either as cloned cDNA and/or purified enzyme (Doehmer). Both the large number and overlapping specificities are reason for the plasticity of this enzyme system, which is sufficiently wide to handle all sorts of chemicals. Cytochrome P450 genes are believed to originate from an ancestral P450 gene. Based on their sequence homologies, cytochrome P450s have been grouped in families and subfamilies. Expression of cytochrome P450 genes depend on developmental stage, sex, tissue type or the presence of inducing chemicals.

V79 cells of Chinese hamster lung fibroblast maintain an intact karyotype with no variation in their chromosome number and *do not metabolically activate chemicals*. Because of zero cytochrome P450 background in the parental V79 line, these cells are very well suited for genetic engineering with cytochrome P450 expressing vectors.

V79 cells were constructed for expression of rat and human cytochrome P450 1A1, which is considered to be the most potent cytochrome P450 in the metabolic activation of benzo[a]pyrene into its ultimate carcinogenic form of 7,8-diol-9,10-epoxid.

The use of chromophore-carrying substrates combined with video imaging systems would allow metabolism studies on a single cell in *real time*. This would establish a new

technology in toxicology and pharmacology with new insights into metabolic activation of chemicals and drugs together with cellular consequences. The monitoring of metabolites, *e.g.* for DNA binding or organelle sorting in a cell would improve our knowledge of the mechanisms on when, how and where toxic chemicals work in a cell.

METABOLIC CONTROL MECHANISMS IN LIVING CELLS

Direct Transfer of Control and Multidrug Resistance

Fluorescence methods have been important in the elucidation of the biochemistry of P-glycoprotein and the multidrug resistance pump, *i.e.* MRP (Westerhof). When daunorubicin, one of the anti-tumor drugs that is pumped by P-glycoprotein, binds to DNA its fluorescence decreases. The association and dissociation of this drug to DNA can be assumed to be at equilibrium within minutes if not seconds. The rate at which daunorubicin fluorescence decreases when it is added to the cell culture medium reports the rate of net influx. After a while steady state is reached. When the cells are washed and placed in a medium without daunorubicin, the total fluorescence increases due to drug efflux. The rate of this increase is smaller in cells lacking P-glycoprotein or treated with efflux-blocker verapamil. The rate of pumping out should be a function of the intracellular free daunorubicin.

At steady state there is no net flux of drug into the cell and the drug concentration in the effluent equals that in the influent. When any drug pump is inactivated, drug concentration in the effluent is temporarily lowered and drug flows transiently into the cells until a new steady state at higher intracellular drug concentration is attained.

An arithmetic model for the drug-efflux pump in a cell has been constructed. A passive plasma membrane permeability of the pump is assumed. For fluxes through metabolic pathways, Metabolic Control Analysis (MCA) has shown that there need not be a single rate-limiting step. For the concentration, x , of a drug inside a cell the control coefficient of the drug efflux pump on the intracellular drug concentration approaches -0.5 at high pump activities. Because of the summation theorem for concentration control coefficients, the control by the drug permeability of the plasma membrane on the intracellular drug concentration must be the opposite of this control by the pump.

Efflux pumping should arise if the drug binding site of the pump equilibrates more readily with the membrane phase than with the aqueous cytoplasm and if the membrane phase and the cytoplasm did not equilibrate at the time scale of drug pumping. This behaviour has been called the “vacuum cleaning” effect. The “vacuum cleaner” model should be regarded as a three compartment system: outside, membrane phase, cytoplasm. The transfer of drug between pump and membrane should be quicker than the transfer of drug between pump and cytosol, and the transfer of drug between the membrane phase and the cytoplasm should be slow at the time scale of drug pump operation.

An arithmetic model for a symmetrical membrane with “vacuum cleaner” showed that in the absence of pumping the drug concentration in the membrane should quickly increase upon administration of the drug to the cells. This quick phase should be followed by a slower but equally extensive increase, witnessing equilibration of the drug with the cytoplasm. A vacuum cleaner should reduce the extent of the first phase, whereas a protein pumping from the cytoplasm should only reduce the extent of the second phase. Using the membrane soluble fluorescent compound TMA-DPH and its fluorescence energy transfer to daunorubicin in the plasma membrane, vacuum cleaner behaviour was observed in one cell line, whereas in a different cell line there was no or less vacuum cleaning. Thus it may be useful to implement a vacuum cleaning index (VCI). In the case of a symmetrical pure vacuum cleaner, at the initial moment half of the entering drug will be rapidly effluxed while

at the steady state influx will equal efflux ($VCI = 1$). A pump that communicates only with the cytoplasm will lead to a VCI of 0.

Biomathematical modelling and quantitative experimentation (*e.g.* by fluorescence methods) appear to be essential for the understanding of these processes *in vivo*.

UPDATE ON FLUORESCENT PROBES

Use of Fluorescent Derivatives for Diagnosis of Genetic Diseases and Selection of Their Gene-Corrected Cells as Well as Photosensitization and Selective Killing of Cancer Cells, Solid Tumors, Parasites, and Viruses

Fluorescent probes including lissamine-rhodamine (LR) or sulforhodamine (Texas Red, SR or TR) derivatives with dodecanoic acid (LR12 or SR12) linked to various glycoprophospholipids and the corresponding phospholipid sphingomyelin were synthesized, to be used as substrates for determining the activities of hydrolases such as glycosidases and sphingomyelinases in intact cells (Gatt). These studies were done using normal cells and those derived from patients with sphingolipid storage disorders, such as Gaucher, Krabbe, Fabry, Schindler, Tay-Sachs, GM1-gangliosidosis and Niemann-Pick diseases.

Adding Apolipoprotein E (ApoE), fluorescent sphingolipid loaded phosphatidyl-choline liposomes were administered into living cells by receptor-mediated endocytosis via the LDL receptor and trafficked to the cell lysosomes. The cells were subjected to a "pulse and chase", *i.e.* they were first incubated in the presence of the fluorescent compound (pulse); incubation was then continued from 1 day up to a week in fresh medium devoid of fluorescent substrate. The intracellular fluorescence due to probe persistence was quantitated by confocal computerized fluorescence microscopy, which also provided an image of the fluorescence distribution in the subcellular components. In cells capable of hydrolyzing, the substrate fluorescence gradually decreased due to probe cleavage and extrusion (chase). Thus, *a higher fluorescence relative to the intact normal cells indicates an enzymatic disorder related to the specific genetic disorder (lipidosis)*.

Fibroblasts from a patient with Niemann-Pick disease (NPD) type B were transduced with retroviral vectors expressing the normal lysosomal sphingomyelinase (ASM). The entire cell population was labelled with LR-dodecanoylsphingosylphosphocholine (LR-SPM). The metabolically corrected cells which degraded LR-SPM, and consequently had a reduced fluorescence, were sorted and collected under sterile conditions and regrown; they were enriched in vector sequences and proved to be *stably transduced in the normal ASM*. When the gene-corrected cells and NPD cells are grown together, the NPD cells also function as corrected, most probably by transfer of sphingomyelinase.

Analysis of Calcium Channel-Cytoskeleton Interactions by Fluorescence Probe Spectroscopy

Because the cytoskeletal network can potentially form a physical link between the plasma membrane, organelle membranes and the nuclear membrane, it has been suggested that it may be directly involved in signal transduction. The effects of bradykinin (BK) on Ca^{2+} mobilization, cytoskeleton rearrangement and DNA synthesis has been studied in Fura-2 pretreated bovine endothelial cells (Bourguignon). For calcium determinations R is the ratio of Fura-2 fluorescence excited at 340 nm over the fluorescence excited at 380 nm.

The level of Ca^{2+} begins to increase within seconds after addition of BK and reaches a maximum within 20 sec, then decreases to a constant lower level within about 3 min. Intracellular Ca^{2+} mobilization appears as one of the early signalling events, followed by reorganization of the cytoskeletal protein ankyrin and DNA synthesis. The close association between ankyrin and perinuclear structures following BK stimulation may be required for the onset of DNA synthesis. Ca^{2+} may be needed for the ankyrin rearrangement process.

NEW METHODS

Integration of Scanning Probe Microscopy with Optical Techniques

The scanning near-field optical microscope (SNOM) combines a force or tunneling current sensor and a detection scheme for optical signals in a multifunctional probe (Jovin). In conventional microscopy the resolution is diffraction limited. In the SNOM the distance between probe and sample is *smaller* than the wavelength and the resolution is of the order of the probe tip diameter. The sample is illuminated through the tip with for example 633 nm, the emission of a He-Ne laser. The same tip collects light reflected and emitted from the sample surface. The fluorescence is focused on a single-photon counting avalanche photodiode and the bright-field reflection is directed through a dichroic filter and beam splitter to a standard photodiode. The sample to probe distance is kept constant by a feedback mechanism which varies the z -position of the sample so as to maintain constant amplitude of a piezo-driven vibration imposed on the tip (which is itself determined via motion of a laser-diode produced diffraction pattern oriented parallel to the sample surface). In SNOM images of 3T3 fibroblasts, the smallest structures revealed in the optical signal were 100 nm in width.

It is possible, using SNOM, to simultaneously record topographic and fluorescence data with very satisfactory contrast and spatial resolution. In topography/fluorescence images of rat basophilic leukemia cells (RBL-2H3) the fluorescence label Cy5 (a reagent directed against all moieties bearing a free amino group, *i.e.* glycolipids, glycoproteins) showed an homogenous distribution. Images of cells labeled with Cy5-IgE, a ligand specific for the Fc_{ϵ} receptors mediating the immediate allergic response of mast cells, revealed that the receptors were distributed in more discrete arrangements, compared to the diffuse fluorescence of Cy5-labelled cells.

Creating Physiological Conditions for Single Cell Investigation on the Stage of a Microscope

Techniques which can be applied to single living cells during their functional activity include video-time lapse and confocal observations, use of vital fluorescent or phosphorescent indicator dyes, ion channel measurements, intracellular injections of DNA, manipulations of cell functions with caged compounds, etc (Ince). The Leiden Culture Chamber (LCC) allows temperature and gas pressure control on the microscope stage with free access for microelectrodes on the stage of an inverted microscope in conjunction with single cell fluorescence studies with optimal control of the cell environment. Argon gas (relatively heavy) was passed through the heating ducts and directed over the surface of a mineral oil layer covering the cell medium containing the Pd-porphine compound. As can be seen very low O_2 levels can be achieved. At the end of the experiment the lid covering the culture dish is lifted and a rise in pO_2 is seen.

Double Interferometry (Fabry–Perot and Michelson) for Fluorescence Excitation Spectra in Living Cells

An ideal microfluorometry apparatus for the study of metabolic control in single living cells should include Real-Time Parameter Interactive Experimental Control (RIPEC) (Hirschberg and Kohen). RIPEC, might, among others, comprise provisions for excitation and emission fluorescence spectra, scanning near-field microscopy (SNOM), total internal reflection microscopy (TIRM), confocal fluorescence optics, and modulated laser excitation for fluorescence lifetime measurements. The fluorescence excitation spectrum is the dependence of the intensity of the fluorescent light on the wavelength of the exciting radiation. Because the shape of excitation spectra often reflect the vibrational levels of higher excited electronic states than those of emission spectra, the former can be more indicative of the microenvironment of fluorophores. In combination with emission spectra, excitation spectra may also help to identify the sources of fluorescence arising from a mixture of fluorophores. The cell tolerance to exciting light is often the limiting factor in the amount of excitation light that can be used. In excitation spectra the wavelength selector element, whether a prism, a grating, an interferometer or an interference filter, is placed in the optical train before the cell instead of after, as is the case with emission spectra. Since the primary source of light loss is the wavelength selector it is advantageous to place it before the cell where excitation intensity has often to be reduced to match cell tolerance, than after the cell where an acceptable signal-to-ratio requires as much as possible of the emission intensity to be recuperated at the detector.

Simultaneous spectral encoding (SSE) has the advantage that the whole spectrum is observed at once (leading to more efficient use of the light), and that time-dependent changes will not result in a distortion of the spectrum. Among the SSE methods suggested, is one in which a Fabry-Perot and a Michelson interferometer are used in combination. Interferometer patterns have circular symmetry which matches the aperture of the microscope, and the use of an interferometer yields a luminosity advantage up to a factor of ten, compared to a monochromator.

Light from a continuous source falls on a Fabry-Perot with $\Delta\lambda = \lambda^2/nh$, where $\Delta\lambda$, the free spectral range is about 10 nm, n is the inter-mirror refractive index and h is the geometrical distance between the two mirrors. This will result in a “comb spectrum” with peaks 10 nm apart, e.g. 10 peaks between 350 and 450nm. This light will then fall on a collimated Michelson interferometer, constructed so that one of its mirrors can be accurately translated perpendicularly to its surface. The collimated Michelson fringe maxima occur according to $n\lambda = 2x$. Differentiating: $dn/dt \lambda = 2 dx/dt$, from which one obtains $f = 2v/\lambda$ where f is the frequency of the light variations and v is the speed of the moving mirror. Each wavelength will be then modulated at a different frequency.

The fluorescence microscope with combined Fabry-Perot and Michelson interferometry for excitation will be used for metabolic studies in living cells.

MORE ON FLUORESCENCE SPECTROSCOPY AND IMAGING

Use of Photodiode Array Fluorescence Spectroscopy in Biochemistry, Pharmacology, and Oncology

A typical photodiode array spectrofluorometer with a bifurcated optical fiber bundle, one branch for excitation light delivery, the other for delivery to the emission polychromator is adapted for *in vivo* use (Pottier).

The administration of 5-aminolevulinic acid (ALA) into a rodent leads to the observation of protoporphyrin IX (PP) fluorescence with emission peaks at 635 and 700 nm and rapid clearance by conversion into heme, a non-fluorescent metalloporphyrin.

The development of a *quantitative optical biopsy system* has to take into account the severely limited penetration of visible light, the many complexities in the optical properties of tissue, including light scattering). While it is relatively straightforward to obtain fluorescence spectral data *in vivo* from both normal and malignant tissue, and the region of tumor tissue can be easily delineated at the surface, depth profiling of the tumor is still in the experimental stage.

Hydrophobic Photosensitizer Delivery to Tumor Cells by Peptides: A Microspectrofluorometric Study

Recently, an amphiphilic peptide isolated from bovine hemoglobin has been shown to highly improve the solubility of hydrophobic compounds, forming a non-covalent association (Blais). The penetration of the protoporphyrin IX (PPIX)-peptide complex in human colorectal carcinoma (HT29) cells has been studied by microspectrofluorometry, using for excitation the 488 nm line of an ionized argon laser. In HT29 cells incubated with PPIX-peptide the intense emission was characterized by a well resolved maximum at 636 nm and a lower peak at 700 nm. In cells incubated with the endogenous PPIX precursor 5-aminolevulinic acid the emission at 632 nm at 700 nm was quite comparable. The dissociation of PPIX-peptide with release of PPIX has been shown to occur at the cellular level.

Merocyanine 540, a Fluorescent Dye and Biological Probe

Merocyanine 540 (MC-540), a sodium salt of sulfonic acid, with a chain of four conjugated methine groups is an anionic, lipophilic fluorescent dye (Parkanyi) used as an optical probe for transmembrane potentials. It is also used for characterization of the multidrug resistance phenotype, for photoinduced toxicity in the photodynamic purging of neoplastic cells in bone marrow explants, in the treatment of lymphomas, metastatic neuroblastoma, malaria, *Herpes simplex* and HIV. MC-540 is also a selective stain for leukemic and immature hemopoietic cells.

MC-540 is *electrochromic*; it shows changes in electronic absorption and emission spectra in the presence of an external electric field. Because MC-540 is *amphiphilic*, many of its optical and chemical properties depend on the polarity of the solvent.

Membrane-Associated MC-540 Becomes More Monomeric with Decreasing Dielectric Constant of the Solvent or Microenvironment

The absorption wavelengths of MC-540 are located between 555-571 nm for the entire solvent range (dielectric constant 4.8 to 32.7).

For all solvents under study, an identical fluorescence emission spectrum is obtained when exciting in any part of the MC-540 absorption spectrum, which confirms the existence of only one emitting species. *Negative solvatochromism* (*i.e.* blue shift with increasing solvent polarity) occur when the ground state dipole moment is higher than the first excited state dipole moment.

Among the mechanisms proposed for the phototherapeutic activity of MC-540, the possible involvement of singlet oxygen has been related to the monomeric form of MC-540 bound to membranes. In aqueous solution, an increase in the concentration leads to a gradual

decrease of the intensity at 534 nm, explainable by self-stacking of the monomeric species leading to formation of dimers, trimers, tetramers, etc. The curve of the surface tension σ plotted against $\log (MC-540)$ is typical of the behavior of classical surfactants above and below the critical micelle concentration (CMC). Comparable self-stacking dimerization and micellization has been reported with biomedically important oxalopyridocarbazoles and with the cytostatic ellipticine chromophore.

Fourier-Transform Infrared and Raman Spectroscopy

In the structure of biological systems or their models at the molecular level, the effect of pressure on the lipid volume permits one to study the variation in intermolecular distances (Taymaz), using computerized Fourier-transform infrared spectroscopy and Raman spectroscopy. In biomedical applications, the changes in the frequency region $1000-1350\text{ cm}^{-1}$ are compared in normal *vs.* malignant colon, stomach, skin and breast tissues Such comparisons cannot be interpreted unless the exact cell population in these tissues is mapped.

Fluorescence Spectroscopy for Diagnosis of Cancerous Tissues

The *in vitro* autofluorescence of normal and cancerous human stomach tissues, as well as that of tissues obtained from mice inoculated with breast cancer cells or mice developing tumors after exposure to ionizing radiation, was studied (Monteiro).

With excitation at 340 nm the emission band for cancerous tissue is centered at 400 nm, and for both tissues there is also an emission centered at 470 nm. In human stomach tissue the results are similar, but the band centered at 400 nm in rat tissue is at 380 nm. The fluorescence observed in these tissues seems to be related to tryptophan, which dominates the near ultraviolet absorption and fluorescence. The tryptophan metabolite hydroxytryptamine (a product of paracrine APUD cells) could account for the 400 nm band. In general, the interpretation of the recorded spectra should be postponed until the exact cell population of the tumor and normal tissues is determined, since the validity of comparisons rests on a similar origin of normal and tumor tissue.

PHOTOCHEMOTHERAPY

Solvent Dependent Excited State Properties of Psoralens: A Clue to Their Antiproliferative Activities

Dioxan-water mixtures with solvent composition properties which are the best-known models of the intracellular microenvironment have been used to determine the triplet reactive state of psoralens and thus the photoreactions occurring at cell membranes or proteins (Sa e Melo). At long emission wavelengths and high solvent polarity, the singlet-triplet energy gap decreases, and intersystem crossing is promoted.

The photophysical parameters, fluorescence quantum yield, Φ_f , fluorescence lifetime, τ_f , and triplet quantum yield, Φ_{2T} , in dioxan/water mixtures can be used to model psoralen triplet reactivity in biological model systems. The importance of the hydrophobic environment is underlined by the kinetic results in the presence of micelles, liposomes and LDL. Thus, PSO and 8MOP are able to photoreact at the interface of cell membranes by an oxygen-dependent photodynamic mechanism (Types I and II). With lower $\Phi_T = 0.04$, 8MOP must photoreact at the cell membrane by oxidized products (Type I) and PSO with higher $\Phi_T = 0.4$ is able to produce singlet oxygen (Type II) at cell membranes. Both 8MOP and

PSO are erythemogenic. In contrast, 5MOP, TMP and TMA, are able to induce oxygen-independent photoreactions producing photoadducts inside the cytoplasmic organelles of the cell, as observed *in vivo*.

FLUORESCENCE *IN SITU* HYBRIDIZATION

Use of Fluorescence *in Situ* Hybridization for Mapping and Ordering YAC Clones from Chromosomal Regions with Suspected Tumor-Suppressor Activity

Deletions or loss of heterozygosity in certain regions of the long arms of human chromosomes have been reported in acute lymphoblastic leukemia, non-Hodgkins lymphoma, prostate cancer and glioblastoma multiforme (Macheraki, 48). Single or double color fluorescence *in situ* hybridization (FISH) have been employed to map tumor suppressor genes in these regions, aiming at their identification and subsequent isolation. The sequences for visualization of single color FISH signals were probe-biotinylated goat anti-avidin-avidin FITC, biotinylated probe-avidin-FITC or digoxigenated probe-anti-digoxigenin (in mouse)-anti mouse IgG-FITC (in rabbit)-anti rabbit FITC (in goat). For double color FISH, biotinylated or digoxigenated probes were visualized as described above with the addition of Texas Red as an alternative fluorochrome. Chromosomes were stained with DAPI that gives a Q banding pattern and propidium iodide as a counterstain for FITC detection.

These methods make possible the construction of an integrated physical and genetic map of chromosomal domains as a framework for the isolation, characterization and mapping of novel transcripts of genes in order to investigate their role in malignancy and tumor progression.

DETECTION OF BREAST TUMORS BY ABSORPTION AND FLUORESCENCE OF PHOTON DIFFUSIVE WAVES

Britton Chance

Department of Biochemistry and Biophysics
Johnson Foundation
University of Pennsylvania
Philadelphia, Pennsylvania

HISTORICAL INTRODUCTION

It is a privilege to be able to give an introductory lecture to this workshop, and it is an honor to pay a tribute to those who have been my colleagues over the years, Elli and Cahide Kohen, for their remarkable development of the NADH fluorescence technology. The initiation of my work on NADH fluorescence was a result of a chance experiment at Stockholm with Herrick Baltscheffsky where Hugo Theorell's sensitive fluorometer was available and Herrick was glad to prepare a suspension of mitochondria (1). We found not only a marked fluorescence signal of mitochondrial matrix NADH, but what turned out to be more important, a variation of its intensity with metabolic state as reproduced in Fig. 1 in which the intensity is inversely related to the metabolic intensity and the biochemical nature of the metabolic states, labeled 5, 4, 3, 2. These metabolic states have enabled the interpretation of the nature of the metabolic state in a variety of tissues, including brain, liver, heart, kidney and skeletal muscle (2,3,4).

The location of the origin of the NADH signal in cells, cytosolic or mitochondrial, had not been demonstrated in tissues *in vivo*. Thus, the clustering of mitochondria into a single organelle or *nebenkern* in the insect spermatid afforded an anatomical distinction to compare the NADH fluorescence of the *nebenkern* with the cytosol fluorescence in an *in vivo* experiment together with the late Bo Theorell (5). We constructed an appropriate vibrating aperture microscope, which enabled us to observe in a 6 μm spot the fluorescence intensity of the *nebenkern* and to compare it with that in the cytosol. Furthermore, we were able to observe the time course of exhaustion of oxygen under the cover slip by mitochondrial respiration in the sample and to observe the State 3/State 5 transition (Fig. 2 (6)), i.e. aerobic to anaerobic transition in the *nebenkern*. This is compared with that of the neighboring cytosol, and establishes that the redox states of the two cell compartments are different. The mitochondrial compartment is the oxygen-sensitive compartment. It is noteworthy that the redox state of the cytosol was largely unchanged even though the cell was undergoing the

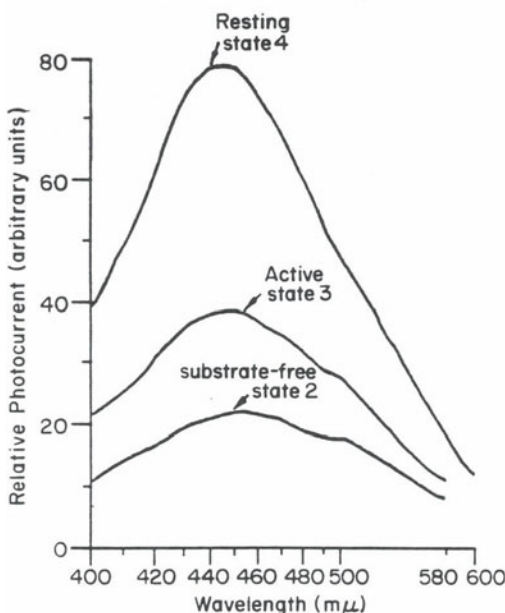


Figure 1. The fluorescence emission of mitochondrial NADH reprinted from Chance and H. Baltscheffsky (1958) (1). The intensity of the fluorescence of the NADH of the mitochondrial matrix space is shown to be related to the metabolic state of the mitochondria and is inversely related to the intensity of the metabolic activity. In anaerobic state 5 (not shown but higher than state 4), there is no metabolic activity, and in aerobiosis state 4, the metabolic activity is limited by the supply of adenosine diphosphate and phosphate. In state 3, the metabolic activity is limited by substrate oxygen delivery and electron transport. By using these fluorescent signals in cells and tissues as is illustrated in Figs. 2 and 3, it has been possible to identify intracellular metabolic states.

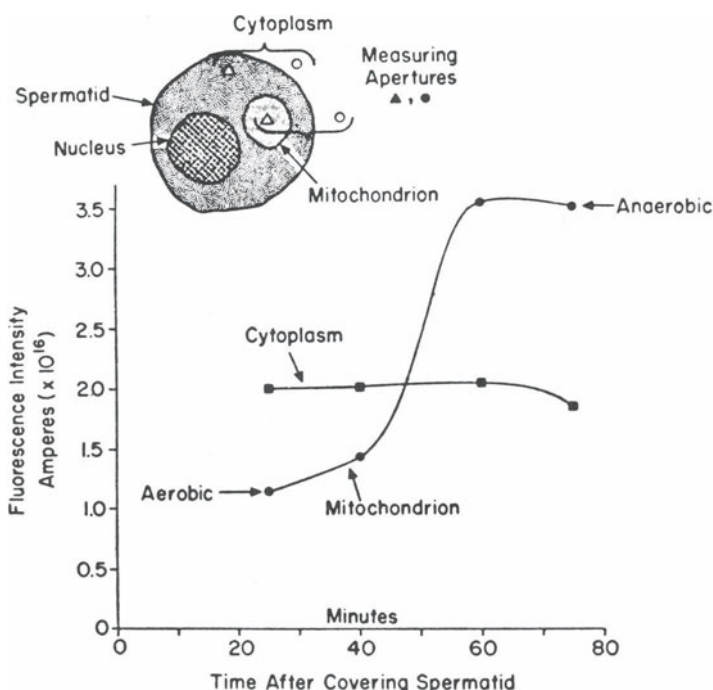


Figure 2. An experiment for distinguishing the contribution of mitochondrial and cytosolic fluorescence signals to a functional state, initially aerobic state 3 (see Fig. 1) and after a lapse of 20 min, the anaerobic state 5 (see note in Fig. 1). Here fluorescence microscopy permits the distinction of signals from the mitochondrial aggregate (nebukern) i.e. open triangular symbol, and from the cytosol (closed triangular symbol) with respect to the extracellular space (open circle).

transition from aerobic to anaerobic metabolism in the particular spermatid because substrate equilibrium applies in the cytosol while O_2 governs the redox state of the mitochondrial matrix.

The observation of NADH fluorescence in tissue was studied in detail with my good colleague Schoener and an example of a localized fluorescence change in the aerobic/anaerobic transition of the exposed cortex of the rat brain is shown in Fig. 3 (4). In this case a 10 μm spot of light excites the fluorescence in a region in the cortex between major blood vessels and the time-course of intensity changes in an aerobic/anaerobic transition is compared with those of electrical activity of the cortex (EEG) as the inspired oxygen is diminished to zero by breathing nitrogen. The NADH intensity increases in the brain as indeed it did in the nebenkern in the aerobic/anaerobic transition, and concurrently the electrical activity falls to zero. In recovery, the redox state of NADH becomes oxidized prior to the recovery of electrical activity due to the time required to build up the phosphate potential necessary for electrical activity.

These two experiments, one demonstrating the localization of NADH in the mitochondrial space as opposed to the cytosolic space, on the one hand, and on the other showing the time relationship between mitochondrial redox state and physiological function, have made it possible to initiate a number of studies at the single cell level and at the tissue level and to afford a basis for some of the discussions to be presented today.

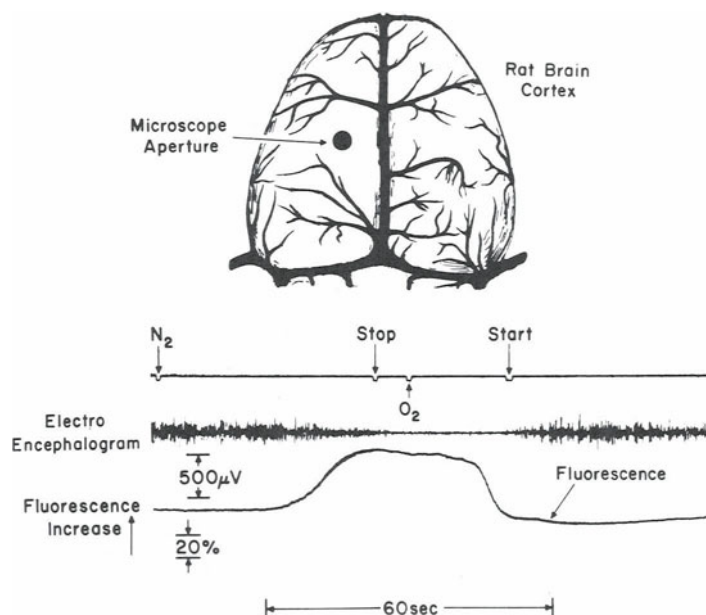


Figure 3. Illustrating the use of NADH fluorescence in identifying metabolic changes in rat brain from aerobiosis initially to anerobiosis (caused by nitrogen breathing) using a fluorometer similar to that used in Fig. 2. For comparison, functional activities are indicated by the electroencephalogram trace which diminishes to 0 as energy metabolism fails in anoxia.

FUTURE STUDIES

So much for the past. For the future, we look for fluorescence signals from deep within the tissue as, for example, from a tumor 5 cm deep in a 12 cm diameter human breast. In order to achieve adequate sensitivity, we must obtain signals from the photons that have diffused from the light source (laser diode) to a detector (photomultiplier sensitive in the region of 800 nm) and have appropriate source and detector positions to be able not only to receive the signal from the fluorescent labeled tumor but also to locate it by triangulation for fluorescence emission and by more sophisticated algorithms if the incident and emitted radiation are distinguished. Current activity on this topic is represented by Fig. 4 in which a subject with a tumor-bearing breast is injected (i.u.) with 0.5 mg/kg of the fluorescent tricarbocyanine probe indocyanin green (7). Here, the greater magnitude of the optical fluorescent signal as compared with the signal from the corresponding position on the contralateral breast gives indication of the greater content of blood vessels in the breast tumor as compared with the tumor bearing tissue. This signal was not imaged and much greater contrast would be obtained if those voxels originating only from the tumor tissue were to be observed.

We foresee that translation of many of the fluorescent probes to be discussed in this workshop into the NIR window near 800 nm would afford tissue images of calcium uptake, membrane potential, antigen/antibody reactions deep within the human tumor bearing breast or, indeed, brain. Thus, we foresee a great interest in the studies of *in situ* tumors in human organs by the optical imaging method using photon diffusion.

While the localization of NADH obtainable in *in vivo* experiments was adequate, no in depth study could be obtained since the excitation at 366 nm penetrates the tissue less than 1 mm. To this point, Quistorff and I have worked together to develop a freeze trapped redox state system which includes a liquid nitrogen microtome for grinding away the surface of a freeze trapped tissue to give both two dimensional scans of the surface of the tissue, and subsequent

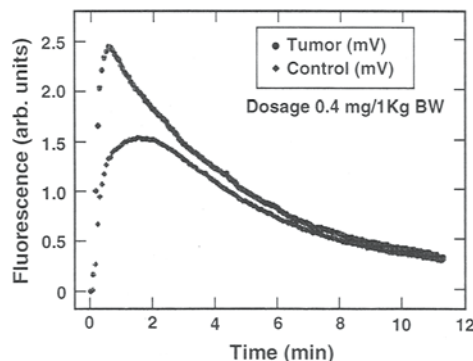


Figure 4. Illustrating the use of a fluorescence probe in detecting the relatively larger vascular volume of a human breast tumor as compared with the similar volume on the contralateral breast. A fluorometer with excitation at 780 nm illuminates the patient's breast in the region of the suspected tumor. The fluorescence emission, maximal around 830 nm, is selected with a "tight" secondary filter (around 10^{-4} attenuation), thus, the sensor is placed approximately 4 cm away from the detector. Photon migration through the tumor excites the fluorescence in the tumor vascular bed which is emitted as a higher peak as shown with the dosage marked 0.4 milligram/kilo body weight. The lower curve is taken from the same source-detector separation on the mirror image portion of the contralateral breast and shows a slower and smaller uptake of the contrast agent. Tumors are characteristically identified by the rapidity and the magnitude of the occupancy of the vascular volume by contrast agents using NMR, as is verified for the optical technique by the single example of a human breast tumor. Patient M84. data (941011) (courtesy of Xingde Li, et. al. (7)).

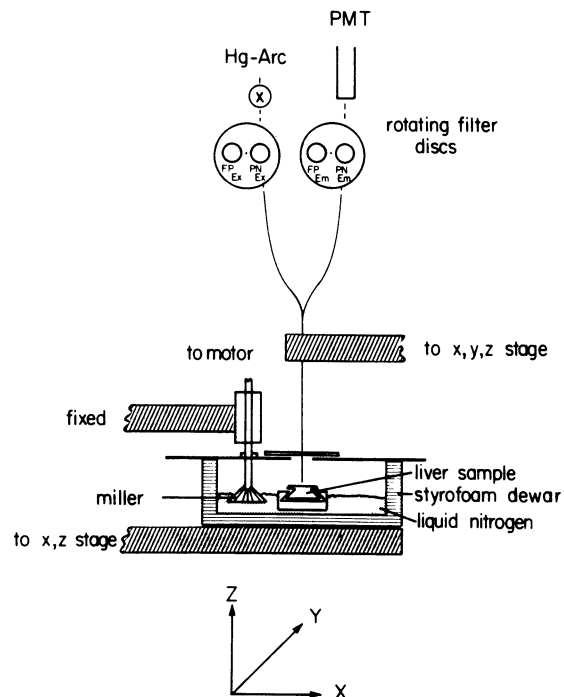


Figure 5. The principle of the redox scanner where tissue samples are prepared by freeze trapping in isopentane and mounted in a chuck under liquid nitrogen. The mill wheel grinds the surface smooth to a few microns under nitrogen and the fiber optic light pen ($50\mu\text{m}$ diameter) scans the surface in X and Y to produce an image of the metabolic state of the tissue, noted in this example to be liver, but in the following Fig. 6 to be the rat 9L tumor. Excitation and emission wavelengths appropriate to flavoprotein (436/560 nm) and NADH (366/450 nm) are used in order that signals from the metabolic state could be obtained according to Fig. 1 but with additional information from flavoprotein which is fluorescent in the oxidized form and non-fluorescent in the reduced form.

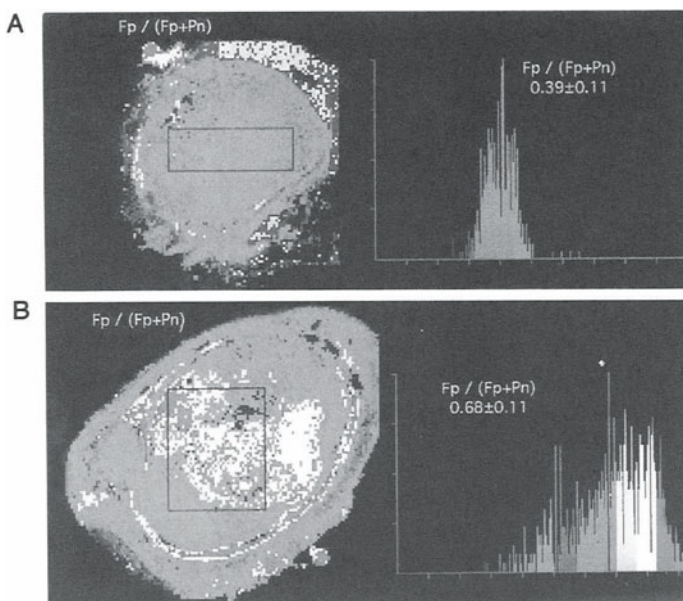


Figure 6. Illustrating a transformation from a highly hypoxic state, near state 5 of Fig. 1 for a rat 9L tumor grown on the flank of a rat to a normoxic state. This is studied by freeze trapping and redox scanning (Fig. A). Figure B, the effect of breathing 95% oxygen, 5% carbon dioxide (carbogen) to increase the oxygen delivery to a 9L tumor and increase the oxidation of flavoprotein in diminishing the reduction of NADH, as best depicted by the ratio of the flavoprotein to the pyridine nucleotide signal. A color representation of this figure can be found following p. 214.

planes in the tissue at any lower depth (8). This instrument has perhaps been one of the most versatile and effective ones for observing NADH fluorescence. The detail of the scanner is shown in Fig. 5, the sample being maintained in contact with liquid nitrogen throughout the whole procedure of scanning and grinding the surfaces (9). This method has been of great advantage in interpreting the aerobic-anaerobic transition in the 9L tumor (see Fig. 6), where the flavoprotein and NADH fluorescence maps are displayed as are their ratios ($Fp/Fp+PN$). The highly reduced relatively homogeneous normoxic state becomes highly heterogeneous and more oxidized with the animal breathing a CO_2/O_2 mixture (carbogen), yet highly reduced presumably hypoxic regions persist with consequent radiation insensitivity.

SUMMARY

The fact that we are able to detect and to image important biological processes by NIR spectroscopy of light absorption and light scattering through the skin, skull and brain, is a pathway by which the bulk of knowledge obtained on single cells and isolated tissues can now be applied to important clinical studies. Furthermore, the development of appropriate fluorescent probes for enhancing the quality and extending the nature of the *in vivo* responses is also expected to be an important part of this workshop.

Many thanks to my collaborators, the organizers and to the supporters of the organizers are appropriate.

SUPPORT

Supported in part by National Institutes of Health Grants CA-60182, CA-56679, CA-50766.

REFERENCES

1. Chance, B. and Baltscheffsky, H. Respiratory Enzymes in Oxidative Phosphorylation. VII. Binding of Intramitochondrial Reduced Pyridine Nucleotide. *J. Biol. Chem.* 233:73336-739 (1958).
2. Chance, B., Williamson, J.R., Jamieson, D. and Schoener, B. Properties and Kinetics of Reduced Pyridine Nucleotide Fluorescence of the Isolated Rat Heart. *Biochem. Zeit.* 341:357-377 (1965).
3. Chance, B. and Schoener, B. A Correlation of Absorption and Fluorescence Changes in Ischemia of the Rat Liver, *in vivo*. *Biochem. Zeit.* 341:340-345 (1965).
4. Chance, B., Schoener, B., and Ferguson, J.J. *In vivo* Induced Oxidation by Adrenocorticotropic Hormone of Reduced Pyridine Nucleotide in the Adrenal Cortex of Hypophysectomized Rats. *Nature* 195:776-778 (1962).
5. Perry, R.P., Thorell, B., Akerman, L. and Chance, B. Localization and Assay of Respiratory Enzymes in Single Living Cells, Absorbancy Measurements on the Nebenkern. *Nature* 184:929-935 (1959).
6. Chance, B. The Recording of Enzyme Reactions within Single Cells and in Tissues of Living Animals. *J. Franklin Inst.* 282:349-356 (1966).
7. Li, X., White, R., Beauvoit, B., Chance, B. and Yodh, A.G. Tumor Localization by using Fluorescence of Indocyanine green (ICG). Proc. of Optical Tomography, Photon Migration, and Spectroscopy of Tissue and Model Media: Theory, Human Studies, and Instrumentation (Britton Chance and Robert R. Alfano, eds.) SPIE, Bellingham, WA, USA 2389:789-797 (1995).
8. Quistorff, B. and Chance, B. Simple Techniques for Freeze Clamping and for Cutting and Milling of Frozen Tissue at Low Temperature for the Purpose of Two- or Three-Dimensional Metabolic Studies *in vivo*. *Anal. Biochem.* 108:237-248 (1980).
9. Quistorff, B., Chance, B. and Hunding, A. Experimental Model of the Krogh Tissue Cylinder: Two-Dimensional Quantitation of the Oxygen Gradient. In *Oxygen Transport to Tissue III* (Silver, I.E. and Bicher, H.I., eds.) Plenum Publ. New York, NY, USA pp. 127-133 (1978).

FLUORESCENCE-LIFETIME BASED SENSING IN TISSUES AND OTHER RANDOM MEDIA WITH MEASUREMENTS OF PHOTON MIGRATION

Eva M. Sevick-Muraca, Christina L. Hutchinson, and Tamara L. Troy

School of Chemical Engineering
Purdue University
West Lafayette, Indiana 47907

INTRODUCTION

The development of fluorescent and phosphorescent dyes which excite and re-emit in the near-infrared wavelength region now promises the capacity for non-invasive biochemical sensing in tissues. Fluorescence intensity and fluorescence lifetime spectroscopies are established methods by which fluorophores can provide sensing in dilute, non-scattering samples. However, fluorescence intensity or fluorescence lifetime spectroscopy in tissues or other scattering media is a complex problem. In order to extract the intrinsic fluorescence intensity for identification of the fluorophore concentration and yield, *a priori* information about tissue absorption and scattering must be obtained. Richards-Kortum¹ developed a simple model which relates the fluorescence of a homogeneous scattering medium to the concentrations of chromophores which can generate emission light and attenuate both excitation and emission light. This model corrects fluorescence spectra using the attenuation spectra collected at the excitation wavelength in order to empirically account for attenuation due to scattering and non-remitting chromophores. Sinaasappel and Sterenborg² developed a dual-wavelength approach for determining the uniform concentration of a photodynamic agent in tissues which eliminates the contribution of scatter and chromophore absorption in a homogeneous medium. While these and other CW (continuous wave) measurements³⁻⁵ provide concentration and yield information, they nonetheless may not describe the local environment which influences the intrinsic fluorescence. Exogenous ratiometric probes offer the potential for non-invasive fluorescence intensity spectroscopy independent of probe concentration only if differences in tissue optical properties do not differ at the dual wavelengths employed. Thus ratiometric probes with maximum sensitivity to the metabolite of interest must be designed for a small wavelength window in which tissue absorption and scattering spectra are featureless. Since endo-

ogenous probes rarely exhibit ratiometric or isosbestic qualities, re-emitted fluorescence must be deconvolved from tissue scattering and absorption effects.

In contrast to fluorescence intensity spectroscopy using dual wavelength ratiometric probes, fluorescence-*lifetime* tissue spectroscopy offers the ability to directly determine metabolite concentration independently of the concentration of fluorophore. Instead of monitoring the fluorescent intensity due to the re-emission process, the “lifetime” or stability of the photon-activated fluorophore is measured. The lifetime of the activated state is defined as the mean time between absorption of the excitation photon and re-emission of a fluorescent photon. Typically, endogenous fluorophores have lifetimes on the order of nanoseconds while exogenous compounds have lifetimes ranging from sub-nanosecond to milliseconds. For an activated probe experiencing collisional quenching, the measured lifetime, τ or τ^s , can be used to determine the metabolite or quencher concentration [Q], from the empirical Stern–Volmer relationship:

$$\frac{\tau_0}{\tau} = 1 + K_{SV}\tau_0[Q] \quad (1)$$

where τ_0 is the probe lifetime in the absence of metabolite and K_{SV} is the known Stern–Volmer coefficient. Wilson and others⁶ have used long-lived phosphorescence lifetimes of palladium porphyrin compounds in order determine the concentration of oxygen which quenches the activated state. However, using probabilistic arguments we have shown that when the fluorophore lifetime exceeds the typical “time-of-flights” associated with photon scatter, the origin of the fluorescent signals is confined to the surface or sub-surface volumes.⁷ On the other hand, when lifetimes are comparable to photon “time-of-flights,” then the kinetics of re-emission are convoluted and disable the determination of lifetime from re-emitted fluorescent signals.

Figure 1 shows the traditional measurement of fluorophore lifetimes using frequency-domain approaches. Typically the dilute fluorophore in non-scattering solvent is excited with light whose intensity is sinusoidally modulated at the angular frequency ω . The generated fluorescent light is also modulated, but is phase-shifted, θ_m , and amplitude demodulated, M_m , with respect to the incident excitation light. The phase-shift and amplitude demodulation provides a measure of the fluorophore lifetime, τ , using simple relationships described below. The values of fluorescent θ_m and M_m can be described by a complex number obtained from the Fourier transform of the exponential decay due to radiative decay from a single activated state:

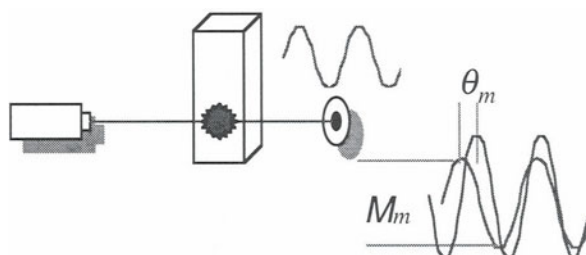


Figure 1. Measurement of fluorescent phase-shift and amplitude demodulation for determination of fluorophore lifetime in dilute, non-scattering media.

$$P(\omega) = \int_0^{\infty} \frac{\varepsilon\alpha [C(r)]L}{\tau} \exp(-\frac{t}{\tau}) \exp(i\omega t) dt = \frac{\alpha\beta [C(r)]}{1 - i\omega\tau} \quad (2)$$

where α is the quantum yield; $[C]$, the concentration of fluorophore; L is the pathlength over which the excitation occurs; ε is the molar extinction coefficient; and β is the product of the latter two quantities. The phase-shift of fluorescent light is reported relative to the incident excitation light, $\theta_x(\omega)$, and is independent of fluorophore concentration and quantum yield: $\theta_m(\omega) = \tan^{-1}(\omega\tau)$. Usually, commercial lifetime measurement devices require a reference measurement to account for phase-delays associated with instrumentation.⁸ In this case, the lifetime of the “sampling” fluorophore, τ^s , can be determined from a relative measurement employing a “reference” fluorophore of known and constant lifetime, τ^r , and from the analogous relationship:

$$\theta_m^s(\omega) - \theta_m^r(\omega) = \tan^{-1}(\omega\tau^s) - \tan^{-1}(\omega\tau^r) \quad (3)$$

The reference fluorophore usually consists of a laser dye with known, reported lifetime at the wavelength of interest. The lifetime of the reference fluorophore is frequently unknown at the wavelength at which the lifetime of the “sampling” fluorophore, τ^s , is desired. This requires independent measurement of lifetime using time-domain techniques.⁸

The amplitude demodulation of re-emitted fluorescence is dependent upon the quantum yield and fluorophore concentration when reported relative to the amplitude modulation of the source excitation light. However, when referenced to the value obtained under CW or constant illumination ($\omega=0$) conditions, the demodulation is dependent only upon probe lifetime:

$$\frac{M_m^s(\omega)}{M_m^s(0)} = \frac{1}{\sqrt{1 + (\omega\tau^s)^2}} \quad (4)$$

Usually, commercial lifetime measurement devices require a reference measurement to account for the modulation losses associated with the instrument frequency response.⁸ In this case, the measurement of the lifetime of a sampling fluorophore lifetime, τ^s , can be determined from a relative measurement made with a reference fluorophore with a known and constant lifetime, τ^r :

$$\left[\frac{M_m^s(\omega)}{M_m^s(0)} \right] / \left[\frac{M_m^r(\omega)}{M_m^r(0)} \right] = \frac{\sqrt{1 + (\omega\tau^r)^2}}{\sqrt{1 + (\omega\tau^s)^2}} \quad (5)$$

However, when the fluorophore is contained in a scattering medium such as tissues, there is an additional phase delay and amplitude demodulation associated with the propagation of excitation and fluorescent photons. The increased photon “time-of-flight” arises due to the multiple scattering of light in tissues and may be comparable and even exceed fluorophore lifetimes. As a consequence of tissue scatter, phase-shifts may exceed 360 degrees and amplitude demodulations may be significant. The subject of this work is to discover a method for lifetime determination in tissues from non-invasive measurements of θ and M . For the purposes of this paper, we restrict our discussions to fluorophores which exhibit a single lifetime.

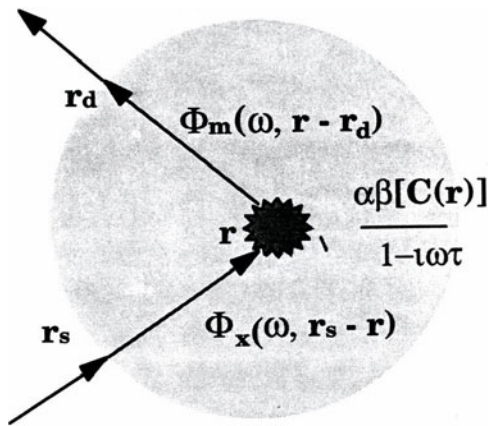


Figure 2. Schematic illustrating the probability for detecting a fluorescent photon at position r_d that is generated at position r in response to an excitation source modulated at frequency, ω at r_s .

THEORY

In the case of a single activated state, the detected signal can be represented by the probabilities for excitation and emission light propagation as illustrated in Figure 2. The probability for finding an excitation photon density wave modulated at frequency, ω , at position r is given by $\Phi_x(r_s - r, \omega)$. The probability for fluorescent photon generation by a fluorophore located at position r is given by Eq. (2). Finally, the probability that the fluorescent photon density wave modulated at frequency, ω , generated at position r , and detected at r_d is given by $\Phi_m(r - r_d, \omega)$. The probabilities $\Phi_x(r - r_s, \omega)$ and $\Phi_m(r - r_d, \omega)$ are given by the Green's function to the AC component of the diffusion equation when multiple light scattering occurs.⁹ Otherwise, $\Phi_x(r_s - r, \omega)$ and $\Phi_m(r - r_d, \omega)$ can be computed from the radiative transfer equation or Monte Carlo analysis. Nonetheless, the fluorescent photon density wave modulated at frequency ω and originating from the source-detector pair at (r_s, r_d) can be obtained upon integrating over the entire volume. For the current discussion, we assume the lifetime is independent of position, only to relax that restriction in the next section. Under these conditions, the detected signal can be written as:

$$P(\omega) = \int_V \Phi_x(r_s - r, \omega) \Phi_m(r - r_d, \omega) \frac{\alpha [c(r)] L}{1 - i\omega\tau} d^3 r \quad (6)$$

Previously, Hutchinson *et al.*¹⁰ have shown through numerical approaches that lifetime-based spectroscopy in scattering media depends upon referencing the detected signal to one generated by a integrated reference fluorophore with a known and constant lifetime. However when the Stoke's shift is small and the fluorophore concentration dilute, the Green's functions for excitation and emission may be considered equal (i.e., $\Phi_x = \Phi_m$). The error in such an assumption may be small owing to the broad absorption and scattering spectra of tissue. Upon referencing the re-emitted fluorescence signal, $P_m(\omega)$, to the re-emitted excitation signal, $P_x(\omega)$, the contribution of photon migration could be accounted for without the use of a reference fluorophore. The re-emitted excitation signal, $P_x(\omega)$, can be analogously derived for the excitation light propagation from r_d to r and the excitation light

propagating from r to r_s . The re-emitted fluorescent signal referenced to the re-emitted excitation signal can be written:¹¹

$$\frac{P_m(\omega)}{P_x(\omega)} = \frac{\frac{1}{1-i\omega\tau} \int_V \Phi_x(\omega, r_s - r) \Phi_m(\omega, r - r_d) d^3r}{\frac{\int_V \Phi_x(\omega, r_s - r) \Phi_x(\omega, r - r_d) d^3r}{\int_V \Phi_x(\omega, r_s - r) \Phi_x(\omega, r - r_d) d^3r}} \approx \frac{\frac{1}{1-i\omega\tau_s} \int_V \Phi_x(\omega, r_s - r) \Phi_x(\omega, r - r_d) d^3r}{\int_V \Phi_x(\omega, r_s - r) \Phi_x(\omega, r - r_d) d^3r} \quad (7)$$

Here, we assume only that excitation and emission light propagations are identical and that the lifetime throughout the medium is constant. In other work,¹² we solve the inverse problem of non-invasively determining lifetimes for heterogeneous distribution of lifetimes and the heterogeneities in optical properties which would invalidate the assumption of equal excitation and emission light propagation.

From Eq. (7), one can see that the phase-shift relative to the re-emitted excitation light is given by:

$$\theta_m(\omega) - \theta_x(\omega) = \tan^{-1}(\omega\tau) \quad (8)$$

$$\left[\frac{M_m(\omega)}{M_m(0)} \right] / \left[\frac{M_x(\omega)}{M_x(0)} \right] = \frac{1}{\sqrt{1 + (\omega\tau)^2}} \quad (9)$$

Since there is no “reference” lifetime required, this measurement is the simplest to accomplish.

EXPERIMENTAL APPROACH

In order to validate Eqs. (7) through (9), frequency-domain measurements were conducted on micromolar solutions of 3,3'-Diethylthiatricarbocyanine iodide (DTTCI) and IR-125 (Fisher Scientific, Pittsburgh, PA USA) in ethanol and monodisperse polystyrene microspheres (Polysciences, Warrington, PA). Experimental measurements of phase-shift and amplitude demodulation of re-emitted fluorescence and excitation light were conducted at modulation frequencies between 40 and 240 MHz. The excitation source consisted of an argon ion pumped, pulsed Ti:Sapphire laser with a pulse repetition rate of 4 MHz and a pulse FWHM of 2 psec. The wavelength of excitation light was 780 nm. Average powers were approximately 50 mW. A glass microscope slide served as a beamsplitter providing <1% reflection which was collected into a 1000 mm fiber (HCP-M1000T-08, Spectron Specialty Optics Co., Avon, CT USA) and passed to a referencing photomultiplier tube (PMT) (Hamamatsu, R928). The unreflected optical pulse train was focused onto another fiber and delivered to the sample which was held in a 10x10x40 mm glass cuvette. The re-emitted light was collected at a 90 degree angle from the incident source using a third optical fiber. The collected light was then transmitted to a sampling PMT. Neutral density filters (CVI Laser Corp., Albuquerque, NM) and an 830 interference filter (830 nm, bandwidth: ± 10 nm, model 10-830-4-1.00, CVI) were used to make frequency-domain measurements at the excitation and emission wavelengths, respectively. The PMTs were heterodyned at a

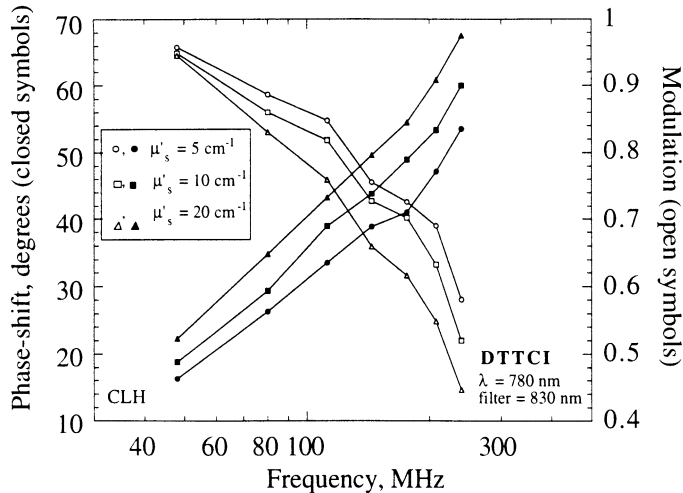


Figure 3. Phase-shift, $\theta_m(\omega)$, and amplitude demodulation ratio, $M_m(\omega)/M_x(0)$, as a function of frequency for re-emitted fluorescence light which is generated by the excitation of DTTCI in ethanol. The symbols denote measurements for isotropic scattering coefficients varying between 5 and 20 cm^{-1} . Measurements are reported relative to the incident excitation light and include contributions from the instrument.

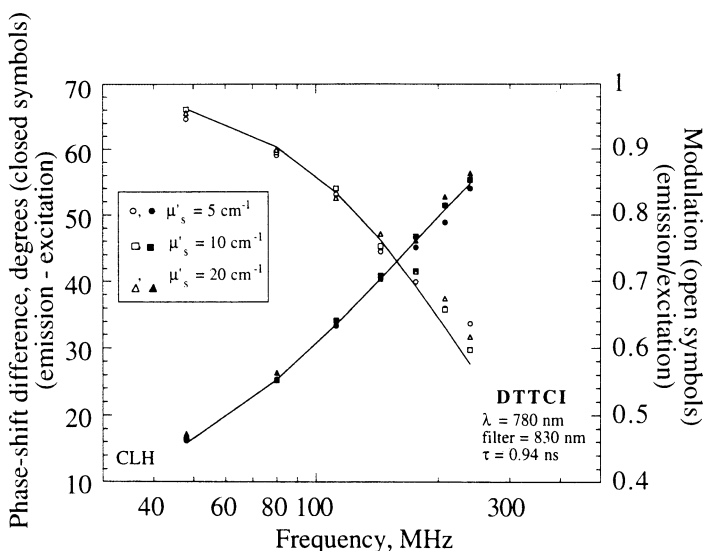


Figure 4. Phase-shift difference, $\theta_m(\omega) - \theta_x(\omega)$, and amplitude demodulation ratio, $[M_m(\omega)/M_m(0)]/[M_x(\omega)/M_x(0)]$, as a function of frequency for re-emitted fluorescence light which is generated by the excitation of DTTCI in ethanol and varying concentrations of polystyrene beads. Measurements are reported relative to the detected excitation light. The symbols denote actual measurements while the solid line represents the least squares fit to Eq 7 ($\tau=0.94 \text{ ns}$).

cross correlation frequency of 100 Hz using a commercial electronics package and data acquisition modules (ISS, Champaign, IL USA).

RESULTS AND DISCUSSION

The contribution of scattering to measurements of fluorescent phase-shift and amplitude demodulation are illustrated in Figure 3. As the isotropic scattering coefficient increases from 5, 10, to 20 cm^{-1} in the transillumination geometry, the measurement of fluorescent phase-shift delay, θ_m , increases and the modulation ratio, $M_{m(\omega)}/M_m(0)$, decreases due to the increased delays and increased volumes associated with a greater contribution from photon migration. Measurements are made relative to the incident excitation source and since they are not referenced, they contain a contribution from the instrument function. Increased scattering was achieved through the addition of an aqueous 2.5% by volume, 0.528 μm diameter polystyrene microspheres and isotropic scattering coefficients were computed from Mie scattering theory.¹³ When frequency-domain values are reported relative to the detected excitation light as $\theta_m - \theta_x$ and $[M_{m(\omega)}M_m(0)]/[M_{x(\omega)}M_x(0)]$, the dependence upon scattering disappears as illustrated in Figure 4 and suggested by Eqs. (8) and (9). The solid lines denote the values predicted from Eqs. (8) and (9) using the parameter estimate of τ obtained from the least squares fit of phase-shift data. The least squares fit yields a lifetime of 0.94 ns, which compares well with that computed from phase-shift measurements made in non-scattering ethanol. Reported literature values for DTTCI are 1.33 ± 0.016 ns for excitation at 790 nm and emission at 820 nm¹⁴ and 1.12 ns for excitation at 780 nm and emission at >780 nm¹⁵. The slight difference in lifetimes may be due to the varying amounts of water in the polystyrene samples.¹⁵

In addition, we have monitored the kinetics of the fluorescent re-emission of two fluorescing laser dyes, DTTCI and IR-125 located in compartmentalized volumes in an Intralipid solution. IR-125 has a single exponential lifetime of approximately 0.58 ns. Since fluorescence generation occurred in a smaller volume than excitation light propagation (i.e., the integration limits in Eq. (7) in the denominator and numerator

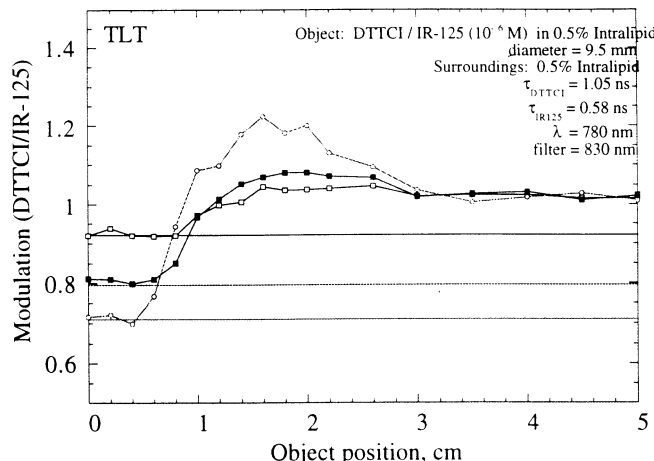


Figure 5. Modulation ratio of signals obtained from DTTCI and IR-125 as a function of heterogeneity position. At positions < 1 cm, lifetime values can be determined from a Green's function analysis¹¹.

were different), the referencing to re-emitted excitation light would lead to erroneous results. For this reason, we referenced the fluorescence signal generated from DTTCI to the signal generated in a separate measurement using IR-125. From a Green's function analysis, it is predicted that the ratio of the re-emitted fluorescent modulation of the two dyes should be a known function of their lifetimes and independent of the position of the dyes, provided that the quantum yields were similar.¹⁰ In order to test the analysis, DTTCI and IR-125 scattering solutions (of approximately the same absorption and scattering cross sectional areas) were separately moved radially towards a source/detector pair in the tissue phantom while measurements of fluorescent modulation at modulation frequencies of 80, 160, and 240 MHz were acquired.

Figure 5 shows the ratio of fluorescent amplitude modulation of the two dyes as a function of position for the modulation frequencies measured. In addition, the solid straight lines predict the values from the Green's function analysis. As one can see from the Figure, the experimental ratio matches the ratio predicted by the Green's functions and the lifetimes of the two dyes. Unfortunately, the quantum efficiency of IR-125 is smaller than that of DTTCI and the relationship falls apart at distances greater than 1 cm from the periphery of the phantom. Nonetheless, our Green's function analysis and experimental measurements show that lifetime information can be readily extracted from frequency-domain measurements of fluorescent re-emission.

CONCLUSIONS

We have shown the capacity for determining lifetime in scattering media using properly referenced frequency-domain measurements of re-emitted fluorescent and excitation light. It is important to note that in traditional frequency-domain lifetime spectroscopy in dilute non scattering samples, phase-shift and amplitude demodulation values relative to the *incident* excitation source are employed. We have shown that when excitation and fluorescent photons migrate similarly (i.e., they experience similar optical properties upon transit to and from position, r), the phase-shift and amplitude demodulation values relative to the *re-emitted* excitation light provide direct information for lifetime-based spectroscopy independent of tissue optical properties. On the other

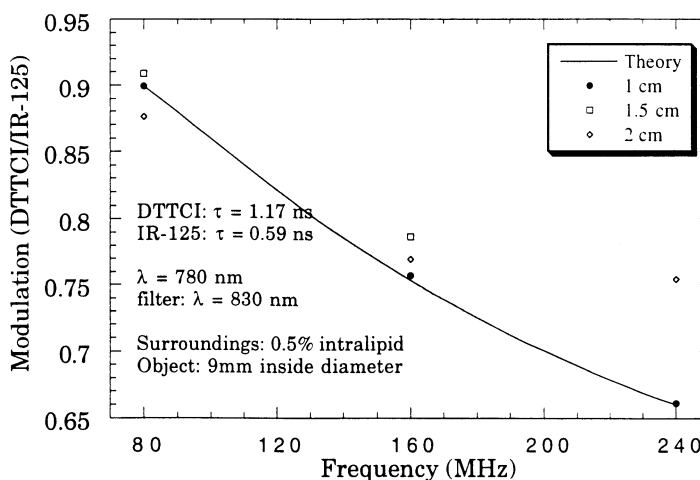


Figure 6. Values of modulation predicted from Green's theory and dye lifetimes (solid line).

hand, when this assumption cannot be made, “referencing” on the basis of a second fluorophore must be accomplished to determine lifetime as shown in Figure 6. When fluorophore concentrations exceed the micromolar concentrations used herein, we see deviations suggesting that our assumptions become invalid (Sevick and Hutchinson, unpublished results). This is an area of continuing research.

Finally, it is important to note that upon introducing frequency-domain measurements of fluorescent light relative to the re-emitted excitation light, the need for finding a “reference” dye with the same excitation and emission spectra as the sample of interest no longer exists. Since the instrument function exists similarly with the excitation as with the emission light, the phase-shift difference $\theta_m(\omega) - \theta_x(\omega)$ and amplitude demodulation ratio, $[M_m(\omega)/M_m(0)]/[M_x(\omega)/M_x(0)]$ provide cancellation of any instrument function. It is also noteworthy that the problems of photobleaching and quenching of dyes are minimized when lifetime measurements are conducted in *scattering* as opposed to *non-scattering* solutions. Since scattering reduces photon densities, the probability for quenching is reduced.

ACKNOWLEDGMENTS

This work was supported in part by the Whitaker Foundation and the National Science Foundation Young Investigator Award (BES-9496239). The authors acknowledge Dilip Paithankar for his creative ideas and critical thoughts and Enrico Gratton for his challenging discussions and insights.

REFERENCES

1. R. Richards-Kortum, R.P. Rava, R. Cothren, A. Mehta, M. Fitzmaurice, N.B. Ratliff, J.R. Kramer, C. Kitrell, and M.S. Feld, A model for extraction of diagnostic information for laser induced fluorescence spectra of human artery wall, *Spectrochimica Acta* 45A: 87-93 (1989).
2. H.J. Sinaasappel and C.M. Sterenborg, Quantification of the hematoporphyrin derivative by fluorescence measurement using dual-wavelength excitation and dual wavelength detection, *Applied Optics* 32: 542-548 (1993).
3. J. Wu., M.S. Feld, and R.P. Rava, Analytical model for extracting intrinsic fluorescence in turbid media, *Applied Optics* 32: 3585-3595 (1993).
4. A.J. Durkin, S. Jaikumar, N. Ramanujam, and R. Richards-Kortum, Relation between fluorescence spectra of dilute and turbid samples, *Applied Optics* 33: 414-423 (1993).
5. S.A. Ahmed, K.W. Zhang, K.M. Yoo, M.A. Ali, and R.R. Alfano, Effect of multiple scattering and self absorption on the fluorescence and excitation spectra of dyes in random media, *Applied Optics* 33: 2746-2750 (1994).
6. D.F. Wilson, Measuring oxygen using oxygen dependent quenching of phosphorescence: a status report in E. Dirmagl, et al. eds., “Optical Imaging of Brain Function and Metabolism,” Plenum Press, New York, NY(1993).
7. E.M. Sevick-Muraca and C.L. Burch, Origin of phosphorescence signals re-emitted in tissues, *Opt. Lett.* 19: 1928-1930 (1994).
8. J.R. Lakowicz, “Principles of Fluorescence Spectroscopy”, Plenum Press, New York (1985).
9. D.A. Boas, M.A. O’Leary, B. Chance, and A.G. Yodh. Scattering of diffuse photon density waves by spherical inhomogeneities within turbid media: analytical solution and applications, *Proc. Natl. Acad. Sci. USA* 91: 4887-4891 (1994).
10. C.L. Hutchinson and J.R. Lakowicz, and E.M. Sevick-Muraca, Fluorescence lifetime based sensing in tissues: a computational study, *Biophys. J.* 68: 1574-1582 (1995).

11. C.L. Hutchinson, T.L. Troy, and E.M. Sevick-Muraca, Fluorescence-lifetime determination in tissues and other scattering media from measurement of excitation and emission kinetics, *Applied Optics*, 35: 2325-2332, 1996..
12. E.M. Sevick-Muraca, C.L. Hutchinson, and D.Y. Paithankar, Optical Tissue Biodiagnostics Using Fluorescence Lifetime, *Optics and Photonics News* 7: 24-28 (1996).
13. C.F. Bohren and D.R. Huffman, "Absorption and Scattering of Light by Small Particles," John Wiley and Sons, New York, NY(1983).
14. R.B. Thompson, J.R. Frisoli, and J.R. Lakowicz Phase fluorometry using a continuously modulated laser diode, *Anal. Chem.* 64:2075-2078 (1992).
15. S.A. Soper and B.I. Legendre, Error analysis of simple algorithms for determining fluorescence lifetimes in ultradilute dye solutions, *Appl. Spectr.* 48: 400- 405 (1994).

SPECTROSCOPY AND TOMOGRAPHY OF TISSUES IN THE FREQUENCY-DOMAIN

Enrico Gratton, Sergio Fantini, Maria Angela Franceschini, Scott Walker,
and John Maier

Laboratory for Fluorescence Dynamics
University of Illinois at Urbana Champaign
Urbana, Illinois 61801

1. FREQUENCY DOMAIN METHODS IN TISSUE SPECTROSCOPY AND IMAGING

Substantial progress in the field of light spectroscopy and imaging of tissues was achieved when the group of Chance, Patterson and Wilson showed that the optical parameters of a turbid medium can be obtained from time resolved measurements of short light pulses propagating in the medium (Patterson et al, 1991a). Essentially, a fit of the intensity as a function of time, measured at some distance from the source, can provide separately the values of the absorption and of the reduced scattering coefficients. This demonstration was important because the focus was shifted from attempts to separate the scattering from absorption, using empirical corrections to the Beer-Lambert law, to a rigorous application of a physical model. During the same period, our lab proposed employing the Fourier transform equivalent concept using an intensity modulated light source (Gratton et al, 1990). Since frequency domain methods have better resolution and sensitivity and are much faster than the time domain methods, our proposal was followed by many others including Chance, Patterson and Wilson (Boas et al, 1993,1994; Cui and Ostrander, 1993; Duncan et al, 1993; Kaltenbach and Kaschke, 1993; O'Leary et al, 1992; Patterson et al, 1991b; Tromberg et al, 1993). It is well known that time domain and frequency domain measurements are mathematically equivalent, when the frequency domain measurement is carried out using a wide range of modulation frequencies (Gratton et al, 1983; Alcala et al, 1984). However, frequency domain measurements can be made at a single modulation frequency, thereby sacrificing some of the information. The advantage of measurements at a single frequency is that they can be very fast, accurate and have an excellent signal-to-noise ratio. The question is whether the information that is lost by measuring the values of the phase shift, DC and AC at a single frequency, instead of using a frequency range, is essential or not. In the diffusive regime in a homogeneous medium, only two parameters are required to fully define the properties of the medium; namely the reduced scattering and the absorption coefficient. A measurement at a single frequency provides three independent quantities: phase, AC and DC. In the

diffusive regime, from any combination of two of them, it is possible to obtain the reduced scattering and the absorption coefficient. Which pair of quantities is used depends only on signal-to-noise considerations. This approach provides the technical basis for the development of instruments capable of measuring the reduced scattering and absorption coefficients.

2. FREQUENCY-DOMAIN DESCRIPTION OF LIGHT PROPAGATION IN HOMOGENEOUS STRONGLY SCATTERING MEDIA

In the range of source-detector distances used in our experiments and for relatively small values of the absorption coefficient (compared to the scattering coefficient), the physical model based on the diffusion approximation to the Boltzmann transport equation is adequate to describe the propagation of light in highly scattering materials, such as tissues. The theory of light propagation in tissue has been extensively described in the context of the transport theory (Case and Zweifel, 1967; Ishimaru ,1978). The diffusion approximation of the transport equation is shown below

$$v\mu_a U(r,t) + \frac{\partial U(r,t)}{\partial t} - vD\nabla^2 U(r,t) = vS(r,t) \quad (1)$$

where $U(r,t)$ represents the photon density in units of photons /cm³, $vD=v/(3\mu_a+3\mu'_s)$ is the diffusion coefficient in units of cm²/s, μ'_s is the reduced scattering coefficient in cm⁻¹, μ_a is the absorption coefficient in cm⁻¹, v the velocity of light in the medium in cm/s and r the distance between the source and the detector in cm . The source term $S(r,t)$ on the right side of the equation is a sinusoidally intensity modulated source at an angular frequency ω . The solution of this equation in an infinite homogeneous medium has been reported by us (Fishkin and Gratton, 1993) and by others. The expressions for the phase, DC and AC parts are repeated below for convenience.

$$\phi = r \left[\frac{v^2 \mu_a^2 + \omega^2}{v^2 D^2} \right]^{\frac{1}{4}} \sin \left[\frac{1}{2} \arctan \left(\frac{\omega}{v\mu_a} \right) \right] + \epsilon \quad (2)$$

$$\ln(rU_{DC}) = -r \sqrt{\frac{\mu_a}{D}} + \ln\left(\frac{S_o}{4\pi v D}\right) \quad (3)$$

$$\ln(rU_{AC}) = -r \left[\frac{v^2 \mu_a^2 + \omega^2}{v^2 D^2} \right]^{\frac{1}{4}} \cos \left[\frac{1}{2} \arctan \left(\frac{\omega}{v\mu_a} \right) \right] + \ln\left(\frac{S_o A}{4\pi v D}\right) \quad (4)$$

Note that expressions 2-4 contain the reduced scattering and absorption coefficients, but also some other unknowns; S_o , A and ϵ , representing the strength, the modulation and the phase of the light source, respectively. Unless the source constants are precisely known, they need to be measured. In our work, after analysis of several possibilities, we have found it more convenient to measure the values of the phase, DC and AC at several source-detector separations from the source (Fantini et al, 1994). We then used only the slope of the plots of phase, $\ln(rDC)$ and $\ln(rAC)$ as a function of the distance to obtain the values of the reduced

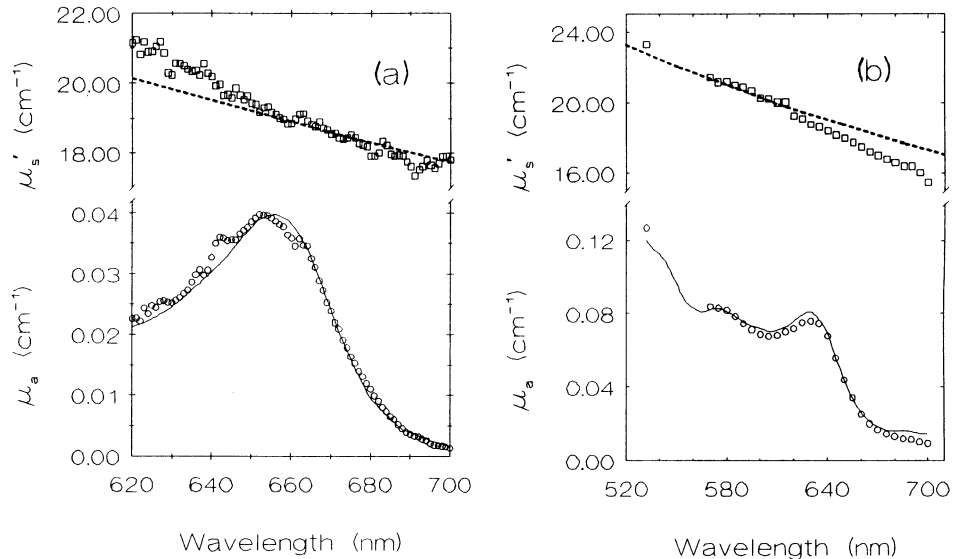


Figure 1. a) Absorption and scattering spectrum of methylene blue in Intralipid. The upper curve is the scattering spectrum. The dashed line is the predicted scattering spectrum based on the average Intralipid size particles. The lower solid curve is the spectrum of the same solution of methylene blue before the addition of Intralipid. b) Absorption and scattering spectrum of a suspension of methemoglobin in Intralipid. The solid line represents the spectrum measured with a normal spectrophotometer before the addition of the Intralipid.

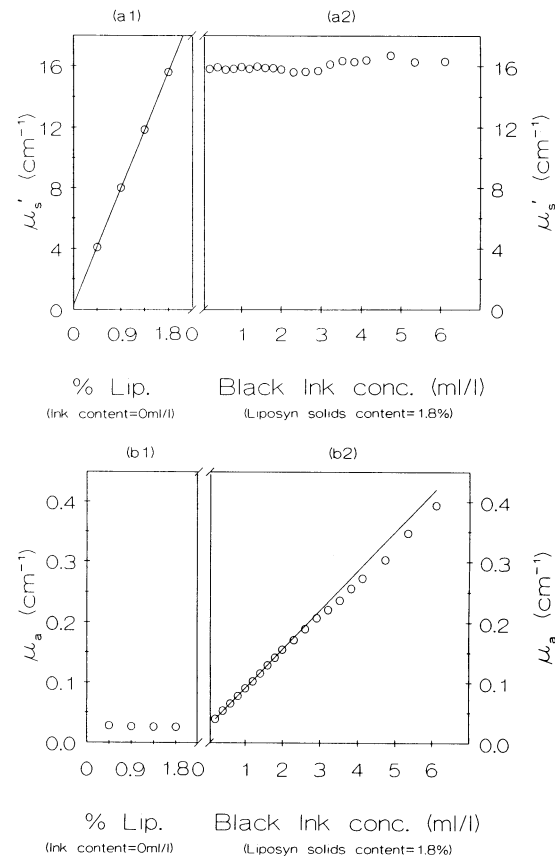


Figure 2. Independence of the measurement of the scattering from the absorption coefficient. In part 1 (left) the addition of scatterers does not affect the absorption value. In part 2 (right), the addition of absorbers does not affect the value of the scattering coefficient. The scatterer is Intralipid and the absorber is black India ink.

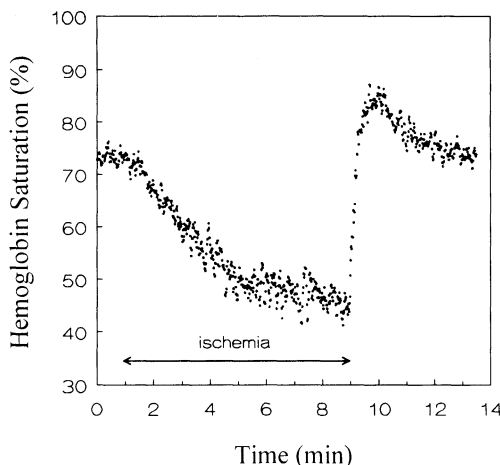


Figure 3. Continuous monitoring of muscle oxygenation. After about 1 minute, the blood flow was stopped by an external pneumatic cuff. The circulation was allowed again after about 6 minutes. Note the overshoot of the muscle oxygenation and the recovery of the normal oxygenation value.

scattering and absorption coefficients. The details of the method have been described in Fantini et al, 1995. The key point is that the method is based on a physical model rather than on empirical corrections or prior separate estimation of the scattering contribution or path length. The measurement is fast, e.g., each determination of the scattering and of the absorption coefficient can be obtained in few milliseconds with high precision and accuracy. The separation of the scattering from the absorption is complete. Cross talk between the two measurements is minimal for the entire range of scattering and absorption values of normal tissues. An example of simultaneous measurement of the scattering and of the absorption coefficients of a strongly scattering suspension is shown in Figures 1 and 2.

On the basis of this idea and using the solution of the diffusion equation taking into account the boundary between air and tissue, an instrument was built that operates simultaneously at two wavelengths, 715 nm and 850 nm. At these wavelengths, the major contributions to absorption in tissues are due to deoxyhemoglobin and oxyhemoglobin, respectively. Since absorption can be measured free of the scattering contribution, an absolute estimation of hemoglobin saturation can easily be obtained. An example of the operation of this instrument is shown in Figure 3. It reports an experiment in which the hemoglobin saturation in a muscle was changed by constricting the circulation with an externally applied pressure cuff. A more detailed description of measurements on a number of subjects is reported in De Blasi et al (1995)

3. HETEROGENEOUS MEDIA

One of the assumptions of the multiple distance method for the measurement of the reduced scattering and absorption coefficients in turbid media is that the medium is homogeneous. By contrast, tissues are heterogeneous. In practice, for measurements of tissue masses such as large muscles, the effect of the skin layer is very small using the multidistance method. The reason is that the photon trajectories spend very little time in the skin and the effect on the measured parameters, using the multiple distance method, is very small. Also, the contact of the optical elements with the skin, which is very important for intensity

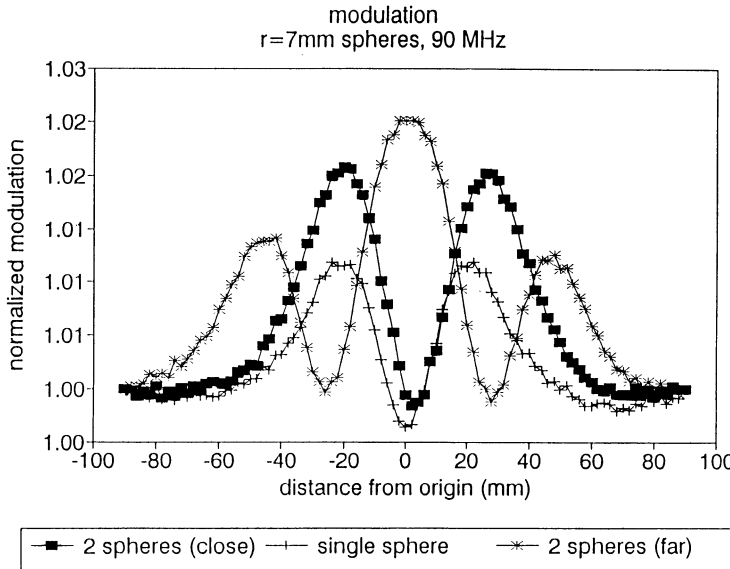


Figure 4. Photon density wave diffraction due to totally absorbing spheres. The diffraction pattern due to two spheres is very close to the sum of the diffraction patterns of each sphere when they are close and when they are far apart.

measurements, produces no appreciable effect, using the multiple distance measurement protocol.

We are interested in detecting and quantifying macroscopic regions of different optical properties in tissues. In general, the problem of reconstructing the optical properties of tissues is referred to as the inverse problem. From measurements at a large number of locations at the surface of the tissue one wishes to reconstruct the map of the optical parameters at every volume element inside the tissue. Since the diffusion of light in tissues is a non-linear process, the solution of the inverse problem presents a formidable challenge. Several groups have proposed reconstruction algorithms, some of which seem to be quite successful, but invariably all are computationally intensive and require relatively long times on large computers (Arridge et al, 1991; Arridge, 1993; Barbour et al, 1993; Gruber et al, 1993; Singer et al, 1990). The problem is complicated by the non-linear nature of the light propagation process. An object at a given location can influence the light distribution at another location. However, the diffusion model shows that the effect of one object decreases at least exponentially as the distance from the object increases.

As a consequence, the influence of an object on distant objects is not very large, as shown in Figure 4, which reports the measurement of the diffraction pattern due to the presence of one and two absorbing spheres.

Note that the diffraction pattern obtained in the two-sphere experiments is approximately the sum of the diffraction patterns of each individual object. The objects used for the experiments of Figure 4 are totally absorbing spheres immersed in an Intralipid® suspension. In practice, tissue regions are not totally absorbing and the effect of one object on the other should be even smaller than that shown in the measurements of Figure 4. On the basis of these and other considerations, we used a simple linear superposition algorithm as a model for reconstruction of the tissue interior. Several ingredients are necessary for this approach to be valid and some preliminary tests have been performed as discussed below. Other labs have proposed a similar approach based on the perturbation method (O'Leary et al. 1995).

4. LINEAR SUPERPOSITION IN A LIGHT BUNDLE

We have used a perturbation approach for reconstructing the map of the scattering and absorption coefficients of tissues based on the linear superposition of light bundles. Our approach does not use iterations. The method is a simple weighted back-projection scheme intended for rapid display. The basic idea is that we can divide the object under study in voxels and that every voxel produces an independent effect at the detector point. Strictly speaking, this assumption should not be valid. The photon density waves scatter out of every object in the medium. The scattered density wave can then be scattered again from the other objects present in the medium giving rise to higher order scattered waves. In the perturbation approach, we only consider the first scattering events. We should distinguish the scattering of the photon density wave due to the macroscopic objects of the medium from the multiple scattering of the light from the microscopic particles of the medium. This latter effect gives rise to propagation of light by diffusion. Using the concept of photon density waves and light bundles, we have used a mathematical theory that is linear in the local variations of the scattering and absorption coefficient due to the macroscopic inhomogeneities. Schematically, we describe the photon density wave from a source using the following representation

$$w(r, t) \propto W_o(r, t) \frac{e^{-kr}}{r} \quad (5)$$

$$k^2 = \frac{\nu\mu_a - i\omega}{\nu D} \quad (6)$$

This expression describes the photon density wave, k is the complex wave vector and contains the scattering and absorption parameters of the uniform medium. When the wave reaches an inhomogeneity of the medium at a location r_i , either absorbing or scattering, a new wave propagates from this location. In the first order perturbation, the scattered wave W_s has the same mathematical form as the incoming wave, but a different amplitude that depends on the optical properties of the inhomogeneity. For example, for an absorbing inhomogeneity of absorption coefficient $\Delta\mu_a$ different from the surrounding medium, the scattered wave gives the following contribution at the detector located at r_d

$$w_{sd}(r, t) \propto \Delta\mu_{ai} \frac{e^{-kr_{si}}}{r_{si}} \frac{e^{-kr_{id}}}{r_{id}} \quad (7)$$

Equation 7 is mathematically identical to the equation describing the light bundle (Feng et al, 1994), where $\Delta\mu_{ai}$ represents the perturbation of the light bundle.

Although equations 5-7 are valid for an infinite medium, expressions for the light bundle for a semiinfinite medium, with both source and detector at the medium surface, are also available (Kaltenbach and Kaschke, 1993). The same reference by Kaschke's group also reports the expression for different boundary conditions such as the slab geometry. The expressions for a scattering inhomogeneity have a more complex form, because a scattering inhomogeneity contributes to the intensity at the detector with a dipole term rather than with the monopole term described by equation 7. In the linear approximation, if a number, N , of objects scatter the photon density wave, the effect at the detector is given by the sum of the contributions from each object:

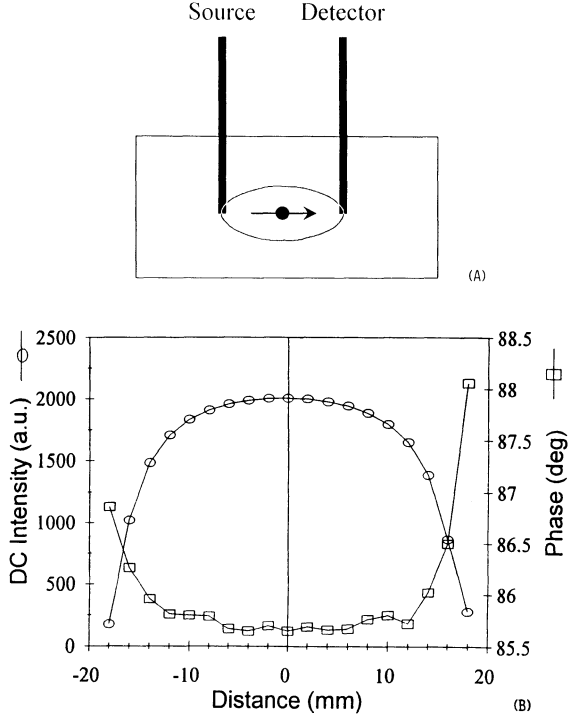


Figure 5. Tests for the applicability of the back projection scheme. In panel A a fully absorbing object is moved along the light bundle from the source to the detector. In panel B the measured values of the DC and phase are approximately independent on the absorber position for the central part of the movement.

$$w_{sd}(r, t) = \sum_{i=1, N} \Delta\mu_{ai} \frac{e^{-kr_{si}}}{r_{si}} \frac{e^{-kr_{id}}}{r_{id}} \quad (8)$$

Equation 8 can be rewritten for every source-detector pair. If the number of those pairs is equal or larger than the number of voxels, then the inversion of the linear system of equations represented by equation 8 can, in principle, provides the value of the absorption and scattering coefficient at every voxel. An important issue is the inversion of the system of equations represented by expression 8, given the ill-posed character of this problem. There are also a number of questions related to signal-to-noise ratio concerning the effect of the scattered photon density wave at the detector. Is this wave of sufficient amplitude to be detected as a variation of the unscattered photon density wave? How accurate can be the recovered scattering and absorption parameters? Are the semiinfinite medium and the slab geometry equivalent in regard to the sensitivity of the perturbing object?

An alternative way to describe the propagation of light in tissue is to consider the set of all possible trajectories that photons can follow from the source to the detector. This concept has been recently discussed (Maier and Gratton, 1993; Feng et al., 1994) and an analytical expression for the bundle of photon trajectories in a homogeneous medium, both infinite and semi-infinite, has been presented. Along the light trajectory, the intensity decreases exponentially due to absorption and we can apply the Beer-Lambert law. We have performed some tests to better understand if this concept can be applied to real situations. The test was performed in the simplest possible situation, i.e., in a uniform, infinite, scattering and absorbing medium. An absorbing object was moved along the line from the source to the detector as shown in Figure 5a. In the infinite medium this path is, of course, the most probable photon trajectory.

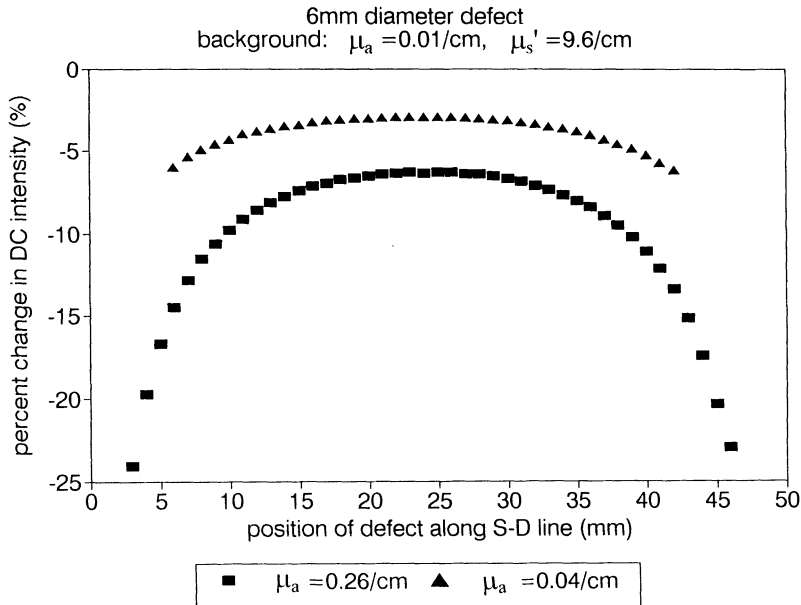


Figure 6. DC value of an absorbing object as it moves from the source to the detector for two different values of the absorption coefficient of the object. The scattering coefficient of the object is the same as that of the background.

One condition for the linear approximation to be valid is that the particular position of the object along the source-detector line should not matter, since the extinction due to absorption should be the same along the photon trajectory. Figure 5b shows the values of the phase and DC measured at different positions along the source-detector line. Clearly, at least for this particular case, the values of phase and DC are not strongly dependent upon the position of the object and consequently neither are the absorption nor the reduced scattering coefficients. Also note that this experiment was performed using a totally absorbing object of about 5 mm in size. Figure 6 shows a similar experiment, but now the object has an absorption coefficient a factor of four larger than the background and the same scattering as the background. For this experiment the deviations from linearity are even smaller than for the measurements using a fully absorbing object. For these experiments the medium is a suspension of 1.5% dry weight of Intralipid and the absorption was increased by ink additions. The background scattering and absorption were measured using the multidistance method and resulted in 6.3 cm^{-1} and 0.2 cm^{-1} for the scattering and absorption coefficients, respectively.

A second condition for the linear superposition idea to be valid is that two equal objects along the line should cause twice the effect. We have confirmed this prediction using phantom studies. Finally, we repeated the experiments with an object that is twice as absorbing as the first object, and the effect approximately doubled. We know that the superposition method should fail when the objects are very absorbing or very scattering as compared with the surrounding medium. We have shown that deviations from linearity are observed for totally absorbing objects (Figure 6), but the effect is not very large.

The important question concerns measuring values of the scattering and absorption coefficients in real tissue inhomogeneities. Our experiments only show, that under some controlled conditions, the idea of superposition can be safely applied. These results were

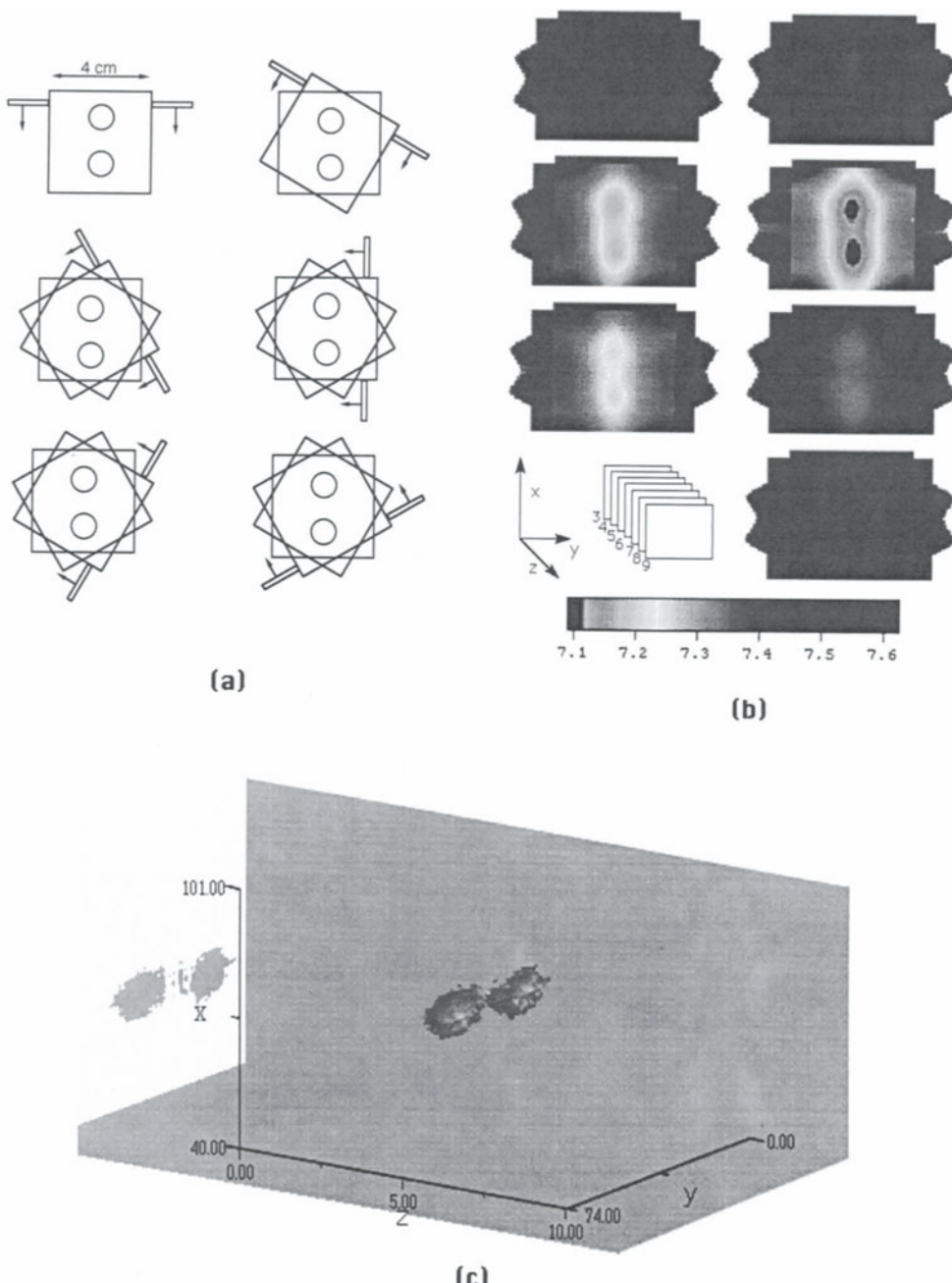


Figure 7. Back projection reconstruction of two glass spheres. a). The circles indicate the positions of the two glass spheres. The larger squares indicate the scan area. Six scans at 30 degrees interval were collected for the back projection. b) The gray scale indicates the scattering coefficient levels in cm^{-1} . The panels from #3 to #9 show the back projection reconstruction at seven different planes. c) 3D reconstruction of the two spheres using the SLICER program. This program is designed to interpolate different z-planes and to draw a particular isosurface at a selected value of the scattering coefficient. The shadow at the border of the reconstruction area is an artifact of the back projection process. This region, which is outside of the reconstruction region was left to better visualize the size of the glass particles with respect to the reconstruction region. The medium is a suspension of 1.5% solid content of Intralipid.

obtained in the infinite medium. However, we have analytical expressions and experimental measurements of the light bundle in the semi-infinite geometry. Finally, we show in Figure 7 the reconstruction of absorbing objects using the linear superposition principle and a back projection algorithm (in the infinite geometry) similar in principle to the one used in x-ray computed tomography.

To obtain this reconstruction, we have measured the value of the absorption and scattering coefficients at a number of source-detector positions using our frequency domain scanner. To calculate the value of the absorption and scattering coefficient we used the reference method described in Walker et al (1995). We weighted the measured value of the absorption and reduced scattering values in the line joining source-detector using the light bundle density along that line. This operation was repeated for different sample orientations. Finally, the back projected image was low-pass filtered to obtain the reconstructed images of Figure 7. The 3-D reconstruction region has a size of about 4x4x4 cm. The panel to the right #3 shows the map at one plane of the scattering coefficient in the reconstruction region well above the objects. The gray scale below indicates the scattering coefficient levels in cm^{-1} . The background scattering is very uniform. The sample consisted of a suspension of 1.5% Intralipid solid content. When two glass spheres of 1 cm diameter separated by 2 cm (center to center) filled with the same intralipid suspension as that of the background were inserted into the scattering medium as shown in Figure 7a, the maps of the absorption coefficient shown in Figure 7b were obtained for each particular z-plane. To obtain this figure, the source and detector optical fibers where scanned simultaneously and the data were collected at 0.4 mm intervals in the x-y plane. Then the two spheres were moved by an angle of 30 degrees and a new scan was acquired. Six scans were acquired at 30 degrees rotation intervals. To obtain a new plane for the 3-D reconstruction, the object was moved in the z direction by 4 mm steps. A total of 11 planes were acquired (only planes from 3 to 9 are shown; the other planes are very uniform). The back projection algorithm was applied for each plane to obtain the images of panel b. Finally, the back projections obtained at the different planes were processed by the SLICER software by SPYGLASS to interpolate the 3-D image shown in the Figure 7c. The important point is that the weakly scattering objects can be easily distinguished and the general shape of the object (two spheres) can be recognized.

Although we only show the scattering coefficient map, the absorption coefficient map is equally well resolved. The processing time per plane is less than a second on the 486DX66 PC computer. The acquisition time per plane (6 rotations) is about 60 seconds. Each plane image is displayed essentially in real time. The total acquisition time for the 3-D image was about 10 minutes. Although this time is still relatively long for clinical applications, we have obtained equally sharp images scanning the objects using a 1 millimeter step in the x, y plane.

ABSTRACT

Frequency-domain methods provide a simple approach to spectroscopy and tomography of tissues. Non-invasive tissue spectroscopy can be achieved with complete separation of the scattering from the absorption contribution. A non-invasive monitor of tissue oxygenation based on a dual-wavelength multidistance method is presented. The effect of tissue inhomogeneities is analyzed using a perturbative approach and a backprojection reconstruction algorithm. The backprojection algorithm directly produces maps of the scattering and absorption coefficients.

REFERENCES

- Alcala, R., E. Gratton, and D. M. Jameson, "A multifrequency phase fluorometer using the harmonic content of a mode-locked laser," *Analytical Inst.* 14, 225-250 (1985).
- Arridge, S. R., van der Zee, P., Cope, M. and Delpy, D. T. "Reconstruction methods for infrared absorption imaging". *Time resolved spectroscopy and imaging of tissues*, B. Chance Editor, Proc SPIE 1431, 204-217 (1991).
- Arridge, S. "Forward and inverse problems in time-resolved infrared imaging." In *Medical Optical Tomography: Functional Imaging and Monitoring*, Müller et al eds. SPIE Vol. IS 11, 35-64 (1993).
- Barbour, R. L., Gruber, H. L., Wang, Y., Chang, J. and R. Aronson, "Perturbation approach for optical diffusion tomography using continuous-wave and time resolved data." In *Medical Optical Tomography: Functional Imaging and Monitoring*, Müller et al eds. SPIE Vol. IS 11, 87-120 (1993).
- Boas, D. A., M. A. O'Leary, B. Chance, A. G. Yodh, "Scattering and wavelength transduction of diffuse photon density waves," *Phys. Rev. E* 47, R2999-R3002 (1993).
- Boas, D. A., M. A. O'Leary, B. Chance, A. G. Yodh, "Scattering of diffuse photon density waves by spherical inhomogeneities within turbid media: analytic solution and applications," *Proc. Nat. Acad. Sci.* 91, 487-491 (1994).
- Case, K. M. and Zweifel, P. F. *Linear transport theory*, Addison-Wesley Publishing Co., Inc., Reading, MA, Palo Alto, London, Don Mills, Ontario, 1967.
- Cui, W. and L. E. Ostrander. "Effect of local changes on phase shift measurement using phase modulation spectroscopy," in *Photon Migration and Imaging in Random Media and Tissues*, B. Chance and R. R. Alfano, eds., Proc. SPIE 1888, 289-296 (1993).
- De Blasi, R. A., S. Fantini, M. A. Franceschini, M. Ferrari and E. Gratton. "Cerebral and muscle oxygen saturation measurement by a novel frequency-domain near-infrared spectrometer." *Medical & Biological Engineering & Computing*, 33, 228-230 (1995).
- Duncan, T. L. Whitlock, M. Cope, and D. T. Delpy, "A multi-wavelength, wideband, intensity modulated optical spectrometer for near infrared spectroscopy and imaging." in *Photon Migration and Imaging in Random Media and Tissues*, B. Chance and R. R. Alfano, eds., SPIE 1888, 248-257 (1993).
- Fantini, S., M. A. Franceschini, J. B. Fishkin, B. Barbieri and E. Gratton. "Quantitative determination of the absorption spectra of chromophores in strongly scattering media: a novel LED based technique". *Applied Optics*. 33, 5204-5212 (1994).
- Fantini, S., M. A. Franceschini, J. S. Maier, S. A. Walker, B. Barbieri and E. Gratton. "Frequency-domain multichannel optical detector for non-invasive tissue spectroscopy and oximetry". *Opt. Engr.* 34, 32-42 (1995).
- Feng, S., Zeng, F. and Chance B. "Perturbation theory of photon migration in the presence of a single defect" in *Advances in Optical Imaging and Photon Migration*, R.R. Alfano, ed. *Optical Soc. of Amer. WB1-1*, (1994).
- Fishkin, J. B. and Gratton, E. "Propagation of photon density waves in strongly scattering media containing an absorbing "semi-infinite" plane bounded by a straight edge". *J. Opt. Soc. Amer. A* 10, 127-140 (1993).
- Graber, H. L., Chang, J. Aronson, R. and Barbour R. L., "Perturbation model for imaging in dense scattering media: derivation and evaluation of imaging operators". In *Medical Optical Tomography: Functional Imaging and Monitoring*, Müller et al eds. SPIE Vol. IS 11, 121-146 (1993).
- Gratton, E. and Limkeman, M. "A continuously variable frequency cross-correlation phase fluorometer with picosecond resolution". *Biophys. J.* 44, 315-324 (1983).
- Gratton, E. Jameson, D. M., Rosato, N. and Weber, G. "Multifrequency cross-correlation phase fluorometer using synchrotron radiation". *Rev. Sci. Instrum.* 55, 486-493 (1984).
- Gratton, W. W. Mantulin, M. J. vandeVen, J. B. Fishkin, M. B. Maris, and B. Chance, "The possibility of a near-infrared optical imaging system using frequency-domain methods," Proc. Third Intl. Conf.: Peace through Mind/Brain Science, 183-189, Hamamatsu City, Japan (1990).
- Ishimaru, A., *Wave propagation and scattering in random media*, Academic Press, New York, 1978, Vol. 1.
- Kaltenbach, J., and Kaschke, M., "Frequency- and time-domain modeling of light transport in random media", in *Medical Optical Tomography: Functional Imaging and Monitoring*, Müller et al. eds. SPIE Vol. IS 11, 65-86 (1993).
- Maier, J. S. and Gratton, E. "Frequency-domain methods in optical tomography: detection of localized absorbers and a backscattering reconstruction scheme." *SPIE 1888*, 440-451 (1993).
- O'Leary, M.A., D. A. Boas, B. Chance, and A. G. Yodh, "Refraction of diffuse photon density waves," *Phys. Rev. Lett.* 69, 2658-2661 (1992).

- O'Leary, M.A., D. A. Boas, B. Chance, and A. G. Yodh, "Experimental images of heterogeneous turbid media by frequency-domain diffusive-photon tomography" *Opt. Lett.* **20**, 426-428 (1995).
- Patterson, M. S., Chance, B. and Wilson, B. C., "Time resolved reflectance and transmittance for the non-invasive measurement of tissue optical properties". *Appl. Opt.* **28**, 2231-2236 (1991a).
- Patterson, J. D. Moulton, B. C. Wilson, K. W. Berndt, and J. R. Lakowicz, "Frequency-domain reflectance for the determination of the scattering and absorption properties of tissues", *Appl. Opt.* **30**, 4474-4476 (1991b).
- Singer, J. R., Grunbaum, F. A., Kohn, P. and Zubelli, J. P. "Image reconstruction of the interior of human bodies that diffuse radiation". *Science* **248**, 990 993 (1990).
- Tromberg, L. O. Svaasand, T. Tsay, R. C. Haskell, "Properties of photon density waves in multiple-scattering media". *Appl Opt.* **32**, 607-616 (1993).
- Walker, S. A., A. E. Cerussi, and E. Gratton. "Back-projection image reconstruction using photon density waves in tissues." *SPIE Proc.* **2389**, 350-357 (1995).

FRET MICROSCOPY IN CELLULAR SIGNAL TRANSDUCTION

Philippe I. H. Bastiaens and Thomas M. Jovin

Department of Molecular Biology
Max Planck Institute for Biophysical Chemistry
P.O. Box 2841, D-37018 Göttingen, Germany

1. INTRODUCTION

The study of cellular signal transduction is a rapidly expanding discipline. However, an integrated approach for assessing the behavior of signaling proteins on and in intact cells is lacking. Myriad factors determine the pleiotropic responses of a cell after stimulation. They are mediated to a large extent by interactions of the signaling proteins: binding to cofactors, subcellular (re)localization, covalent processing, and specific binary and higher order complexation with downstream components of the signal transduction cascade. Thus, the elucidation of cellular responses to the (biochemical) environment requires knowledge about the interactions, and the structural states of relevant signaling molecules *in situ*, that is within the complex architecture of the living cell. In order to measure these molecular events we have adopted an experimental strategy based on the labeling of proteins with fluorescent markers (donors) that transfer excitation energy through the Förster mechanism over the limited range of 1-10 nm. The fluorescently labeled proteins are reintroduced into a cell by microinjection. Alternatively, fluorescently labeled antibodies, peptides or ligands can be used as carriers of the fluorescent probes, thereby bypassing the requirement for microinjection in measurements performed on fixed cells. The combination of a labeled protein and a labeled antibody is also feasible, providing the means for assessing which (protein) partners interact with a given labeled target protein. The advantage of this method is that the antibody need not be absolutely specific for its target protein, inasmuch as one can detect and quantitate molecular proximity by measuring the spectral properties of the donor exclusively (see below). The spatially resolved detection of fluorescence resonance energy transfer (FRET) between tagged biomolecules is carried out in the microscope so as to determine the subcellular distribution and interactions of the fluorescently labeled biomolecules in response to external stimuli such as growth factors and xenobiotics.

Fluorescence lifetime imaging microscopy (FLIM) and photobleaching digital imaging microscopy (pbDIM) are techniques for measuring FRET between tagged biomolecules in single cells¹⁻⁶. The spatially resolved nanosecond lifetimes of fluorophores in a microscopic sample can be determined by FLIM, providing a direct measure of FRET

efficiency since excited state reactions such as FRET shorten the fluorescence lifetime of the (energy) donor fluorophore²⁻⁴. pbDIM is a complementary technique for FRET microscopy based on the inverse relation between the fluorescence lifetime and the photobleaching time constant of a fluorophore^{1,4,6}. Still another approach featured here is the measurement of the increase in the donor quantum yield (release of the quenching by acceptor) following the local photochemical destruction of the energy acceptor⁶. Data acquired in this fashion are presented on the intracellular proteolytic processing of protein kinase C β I in response to tumor promotor phorbol myristate acetate (PMA).

2. FLUORESCENT PROTEIN KINASE C

The 80 kDa serine/threonine protein kinase C β I (PKC β I) consists of two major domains. The 35 kDa regulatory domain binds the phosphatidylserine (PS) and diacyl-glycerol (DG) lipid cofactors and Ca^{2+} . The 45 kDa catalytic domain contains the ATP and substrate binding sites⁷⁻¹⁰. Tumor promoting phorbol esters such as PMA bind to the DG binding site and activate the protein^{7, 11-13}. The hinge region between the domains then becomes exposed to proteases that cleave the protein into a regulatory and a constitutively activated catalytic domain^{9, 10}. We have labeled protein kinase C β I (Cy3PKC β I) on the regulatory domain (predominantly) with the fluorescent sulfoindocyanine succinimide ester Cy3⁶. By using a polyclonal antibody (C16, Santa Cruz Biotechnology) directed against the catalytic domain, an assay was developed for detecting the proteolytic processing of PKC β I in cells after exposure to PMA. The antibody was labeled with the fluorescent acceptor, the sulfoindocyanine succinimide ester Cy5 (Cy5C16). By using reaction conditions leading to a high labeling ratio on the antibody (11 labels per antibody) the effective extinction coefficient of the acceptor and thus the efficiency of FRET could be increased dramatically. The Cy3 and Cy5 labels constitute an excellent donor-acceptor pair with a critical transfer distance (R_0) of 5 nm⁶. The integrity of PKC β I can be monitored by FRET between Cy3 on the regulatory domain and Cy5 on the antibody against the catalytic domain.

3. FRET MEASURED IN THE MICROSCOPE BY ACCEPTOR PHOTODESTRUCTION

FRET can be measured by photodestruction of the acceptor molecule in a region of interest (i.e. a portion of the cell¹⁴). Donor fluorophores engaged in FRET exhibit an increase in quantum yield after acceptor photodestruction, reflected as an increase of fluorescence ΔF_i at pixel i . The efficiency of energy transfer E_i is given by

$$E_i = 1 - \frac{F_i^0}{F_i^1} = \frac{\Delta F_i}{F_i^1} \quad (1)$$

where F_i^0 is the intensity of donor fluorescence in pixel i prior to bleaching and F_i^1 is the intensity after photodestruction of the acceptor. One can thus obtain FRET efficiencies by bleaching the acceptor molecule in a region of interest and taking the ratio of two images. In practice, the experiment can be performed on a confocal microscope equipped with a multiple laser system providing lines corresponding to the absorption maxima of both donor and acceptor. A scheme of the measurement is given in Fig. 1. Cy3PKC β I was microinjected in Balb/c 3T3 mouse fibroblast cells. In order to follow the redistribution and molecular state of Cy3PKC β I after a stimulus, the cells were incubated for variable times with the tumor

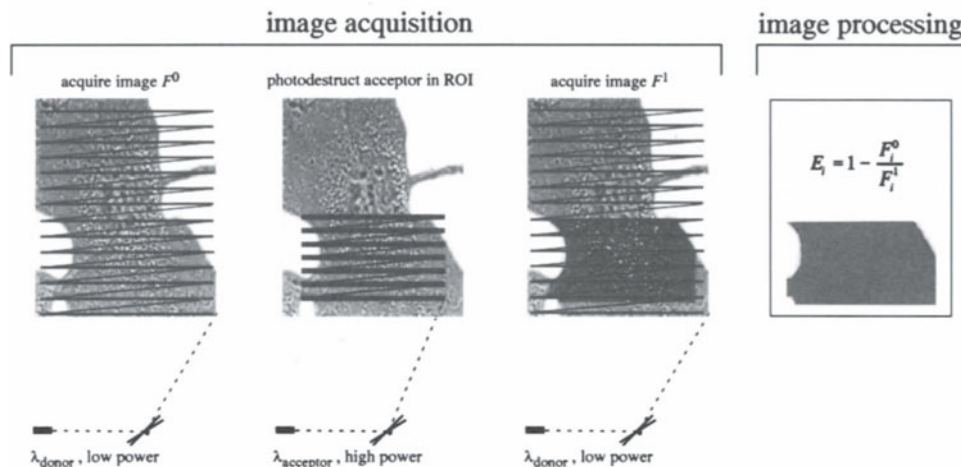


Figure 1. Principle of acceptor photobleaching FRET microscopy. A donor fluorescence image (F^0) is taken with low power excitation at an excitation wavelength (λ_{donor}) corresponding to the first electronic transition of the donor. The acceptor probe is subsequently photod destructed in a region of interest (ROI) by high power irradiation at an excitation wavelength ($\lambda_{\text{acceptor}}$) in the absorption peak of the acceptor. A donor fluorescence image (F^1) is obtained after acceptor photodestruction. The increase in signal intensity in the ROI indicates a release from the quenching effect of the acceptor on the donor, i.e. denotes the presence of FRET. The pixel-by-pixel FRET efficiencies in the ROI are calculated from the image arithmetic operation of Eq. 1. In this example, a uniform FRET efficiency was simulated.

promotor PMA. After fixation and incubation with the Cy5C16 antibody the time dependent redistribution of Cy3PKC β I and Cy5C16 in response to PMA was determined by confocal laser scanning microscopy. In unstimulated cells the Cy3PKC β I fluorescence was predominantly cytoplasmic, whereas in PMA stimulated cells nuclear translocation as well as some membrane association were evident within 5 min after exposure to PMA. As the incubation proceeded, Cy3PKC β I yielded a predominant nuclear signal, in contrast to the Cy5C16 fluorescence which was increasingly perinuclear. The differential localization of the corresponding signals indicated that the protein was fragmented and that the regulatory but not the catalytic domain was retained in the nucleus.

The spatially resolved FRET efficiencies were calculated from the ratio of the donor fluorescence images according to Eq. 1. In resting cells or shortly after addition of PMA, Cy3PKC β I was intact throughout the cell, as indicated by the high FRET efficiency measured at pixel positions in the acceptor bleached regions. However, at longer incubation times the FRET efficiencies decreased throughout the cell, including the nucleus, indicating that the protein had been fragmented into its catalytic and regulatory fragments. The FRET efficiency remained substantial in the perinuclear region throughout the PMA incubation, from which we conclude that intact protein persisted in this region of the cell.

4. CONCLUSIONS

The acceptor photobleaching method described in this report is easily implemented on confocal microscopes. Data analysis does not require complex image processing algorithms. Thus, the technique permits the exploitation of FRET in the study of the processing and interactions of biomolecules in cells, leading to detailed information about the multiple pathways of signal transduction in particular. We have applied FRET microscopy in studies

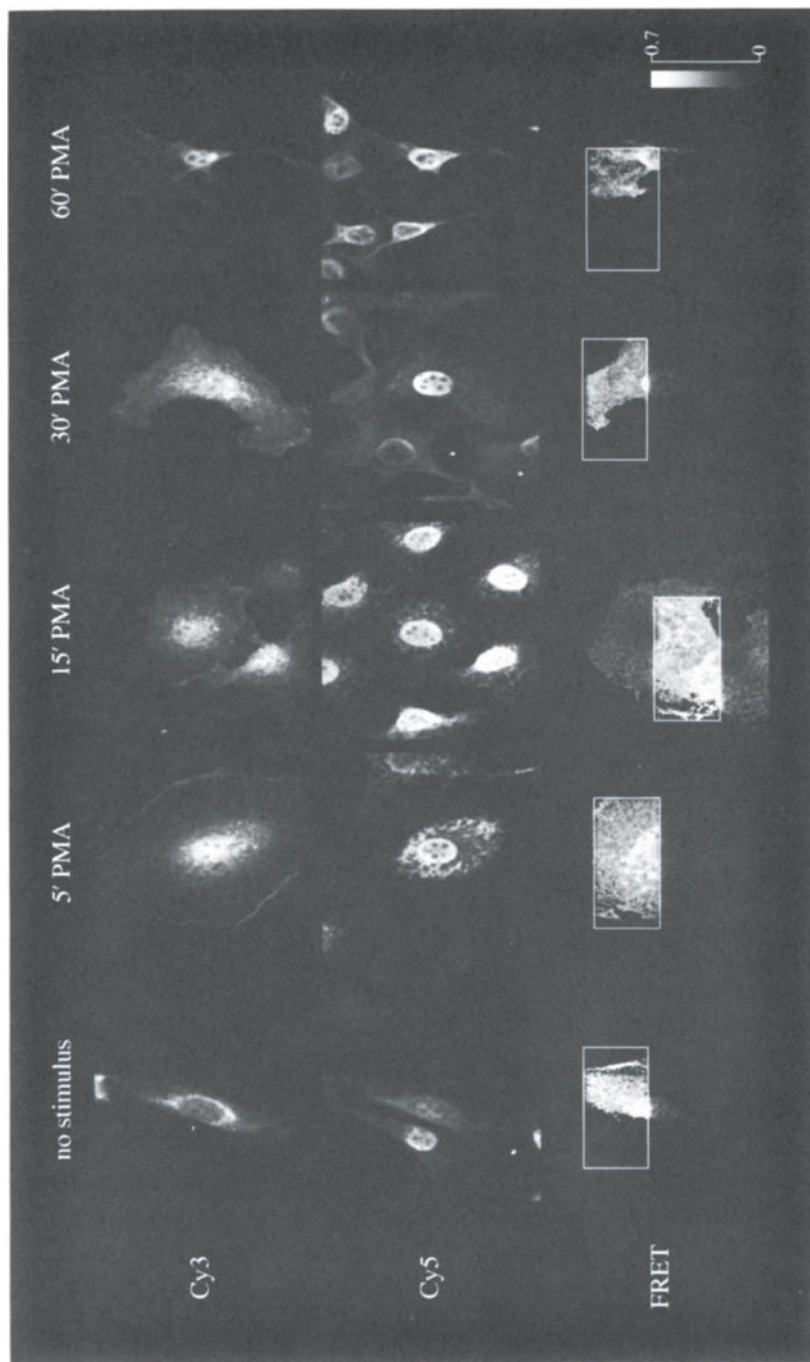


Figure 2. Confocal images demonstrating localization and proteolytic processing of PKC β I in Balb/c 3T3 cells. Top row: regulatory domain of PKC β I detected by Cy3 fluorescence ($\lambda_{\text{ex}}: 543 \text{ nm}$, $\lambda_{\text{em}}: 590 \text{ nm}$), middle row: catalytic domain detected by Cy5 fluorescence ($\lambda_{\text{ex}}: 633 \text{ nm}$, $\lambda_{\text{em}} > 690 \text{ nm}$), bottom row: calculated FRET efficiency maps. The ROIs in which Cy5 was photodestructed by 633 nm illumination are enclosed by rectangles bounded by white. The different incubations of the cells are indicated above the image. A color representation of this figure can be found following p. 214.

of tyrosine kinase receptors⁴, PKC isozymes^{6,15}, various lipid transfer proteins, and cholera toxin¹⁶.

5. REFERENCES

1. Jovin, T. M., and D. J. Arndt-Jovin. 1989. FRET microscopy: digital imaging of fluorescence resonance energy transfer. Application in cell biology. In *Cell structure and function by microspectrofluorimetry* (eds. Kohen, E., Ploem, J.S. & Hirschberg, J.G.). Academic Press, Orlando, FL, pp. 99-117.
2. Gadella, T. W. J. Jr., T. M. Jovin, and R. M. Clegg. 1993. Fluorescence lifetime imaging microscopy (FLIM): spatial resolution of microstructures on the nanosecond time scale. *Biophys. Chem.* 48:221-239.
3. Gadella, T. W. J. Jr., R. M. Clegg, and T. M. Jovin. 1994. Fluorescence lifetime imaging microscopy: pixel-by-pixel analysis of phase-modulation data. *Bioimaging*. 2:139-159.
4. Gadella, T. W. J. Jr., and T. M. Jovin. 1995. Oligomerization of epidermal growth factor receptors (EGFR) on A431 cells studied by time-resolved fluorescence imaging microscopy. A stereochemical model for tyrosine kinase receptor activation. *J. Cell Biol.* 129:1543-1558.
5. Clegg, R. M. 1996. Fluorescence resonance energy transfer. In *Fluorescence imaging spectroscopy and microscopy* (eds. Wang, X.F. & Herman, B.). John Wiley & Sons, New York. pp. 179-252.
6. Bastiaens, P.I.H., and T.M. Jovin (1996) Microscopic imaging tracks the intracellular processing of a signal transduction protein: Fluorescent-labeled protein kinase Cbl. *Proc. Natl. Acad. Sci. USA* (in press).
7. Takai, Y., A. Kishimoto, M. Inoue, and Y. Nishizuka. 1977. Studies on cyclic nucleotide-independent protein kinase and its proenzyme in mammalian tissue. *J. Biol. Chem.* 252:7603-7609.
8. Kishimoto, A., N. Kajikawa, M. Shiota, and Y. Nishizuka. 1983. Proteolytic activation of calcium-activated phospholipid-dependent protein kinase by calcium-dependent neutral protease. *J. Biol. Chem.* 258:1156-1164.
9. Lee, M. H., and R. M. Bell. 1986. The lipid binding, regulatory domain of protein kinase C. *J. Biol. Chem.* 261:14867-14870.
10. Huang, F. L., Y. Yoshida, J. R. Cunha-Melo, M. A. Beaven, and K. P. Huang. 1989. Differential down-regulation of protein kinase C isozymes. *J. Biol. Chem.* 264:4238-4243.
11. Takai, Y., A. Kishimoto, U. Kikkawa, T. Mori, and Y. Nishizuka. 1979. Unsaturated diacylglycerol as a possible messenger for the activation of calcium-activated, phospholipid-dependent protein kinase system. *Biochem. Biophys. Res. Comm.* 91:1218-1224.
12. Takai, Y., A. Kishimoto, Y. Iwasa, Y. Kawahara, T. Mori, and Y. Nishizuka. 1979. calcium-dependent activation of a multifunctional protein kinase by membrane phospholipids. *J. Biol. Chem.* 254:3692-3695.
13. Castagna, M., Y. Takai, K. Kaibuchi, K. Sano, U. Kikkawa, and Y. Nishizuka. 1982. Direct activation of calcium-activated, phospholipid-dependent protein kinase by tumor-promoting phorbol esters. *J. Biol. Chem.* 257:7847-7851.
14. Bastiaens, P. I. H., F. S. Wouters, and T. M. Jovin. 1995. Imaging the molecular state of proteins in cells by fluorescence resonance energy transfer (FRET). Sequential photobleaching of Förster donor-acceptor pairs. *Proc. of the second Hamamatsu International Symposium on Biomolecular Mechanisms and Photonics: Cell - Cell Communication.* in press.
15. Bastiaens, P. I. H., J. W. Borst, and T. M. Jovin. 1995. The localization and processing of fluorescent labeled rat brain protein kinase C in single cells. submitted.
16. Bastiaens, P. I. H., I. V. Majoul, H. D. Söling, and T. M. Jovin. 1995. Imaging the intracellular trafficking and state of the AB5 quaternary structure of cholera toxin. submitted.

PHOTOACOUSTIC SPECTROSCOPY APPLIED TO BIOLOGICAL MATERIALS

Roger M. Leblanc and Germain Puccetti

Department of Chemistry
University of Miami
Miami, Florida 33124-0431

INTRODUCTION

The conventional method of analysis used to investigate properties of molecules inside a medium consists of measuring the transmission and reflection coefficients of the material in order to determine the absorption of a given chromophore in the medium. However, this classical technique only gives access to an average value over the thickness of the material being investigated. It does not allow for the establishment of a depth profile of the density of chromophores in the material, i.e. their local concentration. In addition, this technique necessitates good optical quality of the medium in the range of the optical wavelengths used which makes it less suited to amorphous biological tissues because these are often subject to strong light diffusion, diffraction or a too high absorption. In contrast to this technique, photoacoustic spectroscopy (PAS) allows for the in-depth characterization of either homogenous or heterogenous non-transparent materials.¹⁻⁴ This spectroscopy has already been applied to study complex biological media like leaves (photosynthesis)⁵⁻⁷, eye retina (vision)⁸⁻⁹ or human skin (membrane permeability).¹⁰⁻¹²

The basic principles of PAS consist of irradiating the sample with light and measuring the heat response induced in the material by this light.¹³⁻¹⁶ By using physical parameters of the heat response signal, this technique allows for a spatial scanning inside the material. The depth of this scan depends, first, on the optical absorption coefficient and, second, on the thermal properties of the medium. Two types of photoacoustic spectroscopy are well-known and distinguished by the mode of light irradiation: either in a modulated (MPAS) or pulsed (PPAS) form. Both techniques have been widely applied to many domains and proven to be reliable and quantitative.^{1,2,16} The theoretical development has first been done by Rosencwaig and Gersho¹⁶ in the case of MPAS and extended to the case of pulsed excitation light (PPAS) by Mandelis and Royce.¹⁴ The acoustic response depends on several properties of the sample, i.e., the optical absorption, β , the thermal conductivity, k , the specific capacity, C , and the density, ρ . Typical light pulse durations, as used in this technique, are about 100 μ s down to several hundredths of femtoseconds. This wide range of possibilities of the pulsed technique has given rise to

an important number of derived spectroscopies, e.g. multiphoton, high resolution in time, pump and probe nonlinear.

Two typical examples of biological systems investigated by this technique will be presented that show the potential of photoacoustic spectroscopy through the numerous parameters which can be controlled and the rich information it provides. The two examples have been investigated by both modulated and pulsed photoacoustic spectroscopies so that the major features are demonstrated. The reader can refer to the abundant literature in this field for detailed information.

1. PHOTOACOUSTIC SPECTROSCOPY

The two main photoacoustic techniques are distinguished from each other by their light irradiation mode: a modulated light beam or pulses of light. In the case of MPAS, a high power light source (usually a xenon lamp), filtered in wavelength by a monochromator, provides a continuously tunable source of light. This source can be adapted to a wide variety of biological materials, i.e. through absorption bands associated with the phenomena under study. An additional variable is introduced through modulation, mechanical or otherwise, of this light beam. The modulation serves two purposes: to provide a quantified absorption to the heat response and to vary the depth of scanning inside the medium. The primary purpose is to eliminate any extraneous noise which might affect the signal. This point is even more important in the case of indirect detection. By indirect detection, we mean that the light-induced heat emission is detected through its influence on a buffer material, e.g. gas in a closed cavity. Any heat emission inside the sample can serve to increase the temperature of the gas buffer, increasing the pressure of the gas. These pressure variations can be detected by high sensitivity microphones. Here again, detection will be performed at the same frequency as the modulation of the excitation light beam, which rules out any noise from the surrounding environment of the measurement cell. The response signal is obtained through a lock-in amplifier whose purpose is to be sensitive only to the amplitude and phase of a signal at a chosen frequency. This instrument performs the measurement during the half period following light irradiation. At 10 Hz modulation frequency, the sample is excited by a repetition of 50 ms of light irradiation followed by 50 ms of "darkness". After each 50 ms of irradiation, the lock-in detector will perform a 50 ms signal detection. Averaging all response values over a long time interval, therefore, provides an averaged response signal at the frequency of 50 Hz. However, the detected signal comes only from a limited layer of the sample from which heat emission has time to diffuse towards the surface of the sample and contribute to the gas temperature increase. The thickness of the layer, at a given modulation frequency, f , is related to the heat diffusion length of the specific sample. One will therefore understand that varying the modulation frequency has a direct influence on the depth of scan (Figure 1).^{14,16}

Numerous PPAS studies have shown great advantages of pulsed photoacoustic spectroscopy over the more classical MPAS technique.¹⁷ This new technique has been shown to provide much more information about the heat response of the sample, so that scientists are obtaining insight into the bulk of the samples. Three major advantages can be pointed out: (i) the possibility of obtaining the time evolution of the heat response, (ii) the simultaneous recording of the response at all acoustic frequencies, in contrast to modulated photoacoustic spectroscopy which gives a time averaged value of the heat response at a single frequency and finally (iii) the possibility of adjusting the light pulse duration to the characteristic time(s) of the phenomenon under investigation.^{18,19} However, one major drawback of this latter technique is due to the difficulty to provide a continuously tunable source of light pulses over a large wavelength range. In the temporal domain, i.e. PPAS, the

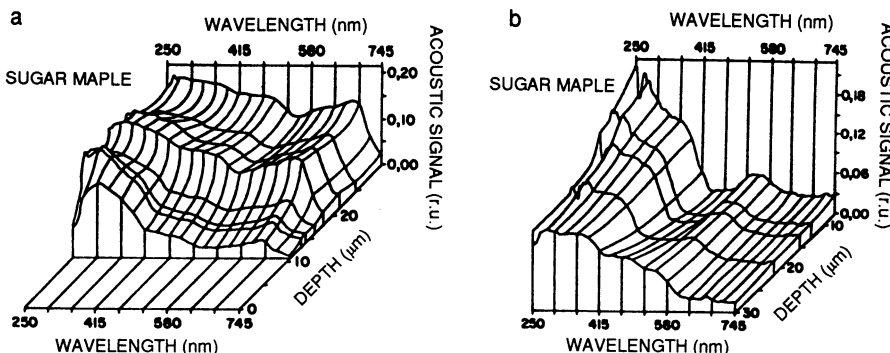


Figure 1. Depth profile spectra (by MPAS) of sugar maple leaves collected during summer (a) and fall (b), showing chlorophyll absorption bands (430 and 670 nm) in the first case and strong carotenoid (470 nm) and anthocyanin (525 nm) bands in the second case, explaining the color changes between seasons.

signal arises first from the surface layers, at short times, t , which correspond to high modulation frequencies in MPAS, and then progressively, from deeper layers of the sample at longer times of observation, t , which correspond to low modulation frequencies in MPAS. This shows that one pulse is sufficient in pulsed photoacoustic spectroscopy (PAS), while a complete scanning procedure is necessary in MPAS to record the acoustic spectrum of heat response of a given sample. The equivalency between modulation frequencies in MPAS and the frequencies obtained through Fourier transform has been demonstrated elsewhere.¹⁴

Photoacoustic measurements are presented for two investigations on biological samples: leaves and human skin.

2. PHOTOSYNTHETIC ACTIVITY OF LEAVES

Among the first biological systems investigated by modulated photoacoustic spectroscopy was the photosynthetic activity in plants. The high efficiency of the photosynthetic energy transduction plays an important role for many applications, applied (efficient energy conversion) as well as fundamental. Two major interests for the intense research in this field can be pointed out: a better understanding of the influence of environmental factors (pollution, intensity at different wavelengths,...) on the efficiency of the photosynthetic cycle and the elaboration of solar organic cells for energy conversion.

MPAS allows scientists to investigate the properties, at different levels of the photosynthetic activity, of photosystems I and II inside plants through a selective excitation of different pigments. This technique allows us to clearly separate the thermal from the oxygen emission, both giving direct information about the efficiency of the photosynthesis process.^{20,21} This discrimination is made possible because heat emission occurs with a delay with respect to gas, e.g. O₂ release. Therefore, pure heat emission is measured at high frequencies while both are detected at low frequencies. Further quantitative parameters can be obtained about the chemical storage energy which accompanies photosynthetic activity. In addition to the information available through MPAS, the access to the time parameter by using PPAS has provided much more information about the time evolution of the different phases of the two photosystems, e.g. intermediate state lifetimes and their discrimination, as well as delay of charge transfers.²²

3. DIFFUSION OF SUNSCREENS INTO HUMAN SKIN

The kinetics of the diffusion of sunscreen derivatives have been investigated through pulsed photoacoustic spectroscopy. A small layer of product was deposited onto samples of human skin and the presence of the chromophores detected versus the time of penetration. The results presented used a UVB radiation source (nitrogen laser, 338 nm) to excite the chromophores of the product. The response signal allows for the establishing of a diffusion pattern, characteristic to each product and whose evolution is quasi-independent of the amount of product deposited. Modeling this evolution by a law derived from diffusion in a semi-infinite medium provides a half lifetime value, τ , which represents the time necessary for half of the product to penetrate into deep layers of skin, i.e. out of detection. The modeling can thus be performed through the temporal response $P(t)$ as a function of chemical composition and skin structure. For all products, the time evolution of the heat response P_{\max} has been characterized by a time constant, τ , and the global amplitude variation. The time parameter provides a quantitative comparison between products, independent of their composition.²³⁻²⁵

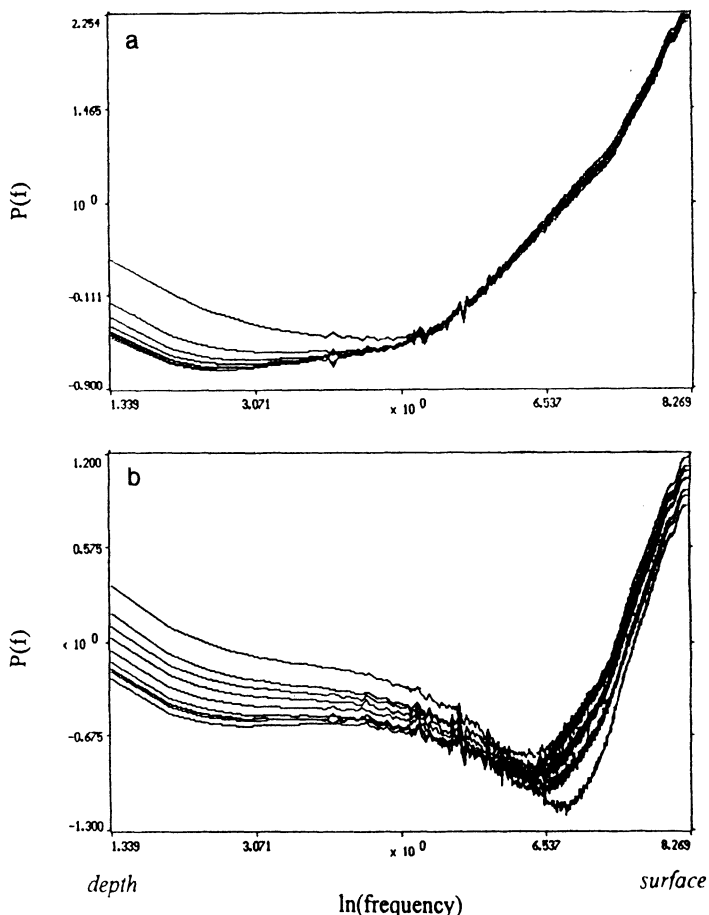


Figure 2. Depth profiles (by PPAS) of two sunscreens diffusing into human skin samples depending on their composition, both containing UV absorbing chromophores but only sunscreen SPF=15 containing titanium dioxide.

In a second step, an equivalent depth profile of the chromophore presence inside the layers of skin can be inferred from the previous time response signals $P(t)$ by using Fourier transform analysis. The response is decomposed into its components at all acoustic frequencies between 1 Hz and several kHz. One will remember that these frequencies are the direct equivalent in pulsed PAS, to the modulation frequencies in modulated PAS. The resulting spectra $P(f)$ directly gives evidence of signal alterations inside the sample such as diffusion processes, discontinuities between layers, photochemical reactions and so on.

CONCLUSION

Photoacoustic spectroscopy provides a powerful tool for scientists to investigate quantitatively properties of materials whose complexity renders other techniques useless. This technique enables the establishment of depth profiles of wavelength-selective particles inside a medium with a high sensitivity in signal detection. This selectivity and the possibility to perform depth scans of opaque complex materials makes the method of very high interest for biologists, as has been proven by the rich literature in the field. This same property makes it adapted for many types of studies like selectively induced activity (photosynthesis), pigment/chromophore penetration and mapping or time resolved spectroscopy of deexcitation phenomena (charge transfer states in vision).

REFERENCES

1. Fournier, D and J.P Roger (Eds) (1994) *Topical meeting on photoacoustic and photothermal phenomena*. Journal De Physique IV. Coll. C7, supp. au Journal de Physique III Vol. 4, n° 7.
2. Commandre, M. and E. Pelletier, (1990) Measurements of absorption losses in TiO₂ films by a collinear photothermal deflection technique, *Appl. Opt.* 29, 4276-4283.
3. Hess, P. and J. Pelzl (Eds) (1987) *Photoacoustic and Photothermal Phenomena V*, Proc. of the 5th International Topical Meeting, Springer Series in Optical Sciences vol. 58, Heidelberg, Germany.
4. Murphy J.C., J.W. Machlachlan Spicer, L.C. Aamodt and B.S.H. Royce (Eds), (1989), *Photoacoustic and Photothermal Phenomena VI*, Proc. of the 6th International Topical Meeting, Springer Series in Optical Sciences vol. 62, Berlin, Germany.
5. Malkin S., (1987) Fast photoacoustic transients from dark-adapted intact leaves: oxygen evolution and uptake pulses during photosynthetic induction, *Planta* 171, 65-72.
6. Mauzerall D.C., (1990) Determination of oxygen emission and uptake in leaves by pulsed, time resolved photoacoustics, *Plant Physiol.* 94, 278-283.
7. Malkin S., M. Charland and R.M. Leblanc, (1992) A photoacoustic study of water infiltrated leaves, *Photosynthetic Res.* 33, 37-50.
8. Peters K.S., T. Watson and K. Marr, (1991) Time-resolved photoacoustic calorimetry: A study of myoglobin and rhodopsin, *Annu. Rev. Biophys. Chem.* 20, 343-362.
9. Sarna T.,(1992) Properties and function of the ocular melanin - A photobiophysical view, *J. Photochem. Photobiol. B: Biol.* 12, 215-258.
10. Campbell S.D., S.S. Yee and M.A. Aframowitz (1979) Application of photoacoustic spectroscopy to problems in dermatology research, *IEEE Trans. Biomed. Eng.*, BME 26, 220-225.
11. Giese K. and K. Kolmel (1983) A photoacoustic hydration study of human stratum corneum, *J. Phys.*, coll. C6, 10, 44-49.
12. Hass, U., J. Franz and F. Nimmerfall (1987) Photoacoustic *in vitro* investigation of human skin. In *Photoacoustic and Photothermal Phenomena* (Hess, P. and J. Pelzl Eds.) Proc. of the 5th International Topical Meeting, Springer-Verlag, Heidelberg, Germany
13. Rosencwaig A. (1980) *Photoacoustics and photoacoustic spectroscopy*, John Wiley & Sons, New York, N.Y., USA.
14. Mandelis A. and B.S.H. Royce (1979) Time-domain photoacoustic spectroscopy of solids, *J. Appl. Phys.* 50 , 4330-4338.

15. Tam A.C., (1983) Photoacoustics: Spectroscopy and other Applications, in *Ultrasensitive Laser Spectroscopy*, ed. D.S. Kliger, Academic Press, New York, N.Y., USA.
16. Rosencwaig A. and A. Gersho (1976) Theory of the photoacoustic effect with solids, *J. Appl. Phys.*, **47**, 64-69.
17. Tam A.C. (1991) Signal enhancement and noise suppression considerations in photothermal spectroscopy. In *Photoacoustic and Photothermal Phenomena*. (Edited by D. Bicanic), pp. 114-145. Proc. of the 7th International Topical Meeting, Doorwerth, the Netherlands.
18. Braslavsky S.E.(1986) Photoacoustic and photothermal methods applied to the study of radiationless deactivation processes in biological systems and in substances of biological interest. *Photochem. Photobiol.* **43**, 667-679.
19. Patel C.K.N. and A.C. Tam (1981) Pulsed optoacoustic spectroscopy of condensed matter, *Rev. Modern Phys.* **53**, 517-550.
20. Carpentier R., R.M. Leblanc and M. Mimeault, (1988) Monitoring electron transfer by photoacoustic spectroscopy in native and immobilized thylakoid membranes, *Biotechnol. Bioeng.* **32**, 64-67.
21. Carpentier R., R.M. Leblanc and M. Mimeault, (1989) Photoacoustic detection of photosynthetic energy storage in photosystem II submembrane fractions, *Biochim. Biophys. Acta* **975**, 370-376.
22. Canaani O., S. Malkin and D. Mauzerall, (1988) Pulsed photoacoustic detection of flash-induced oxygen evolution from intact leaves and its oscillations, *Proc. Natl. Acad. Sci. USA* **85**, 4725-4729.
23. Imhof R.E., C.J. Whitters and D.J.S. Birch (1990) Time-domain Opto-thermal Spectro-radiometry. *Photoacoustic and Photothermal Phenomena II* (editors: J.C. Murphy, J.W. MacLachlan-Spicer, L Aamodt and B.S.H. Royce. Springer-Verlag Berlin, Heidelberg, Germany.
24. Lahjomri F., G. Puccetti, R.M. Leblanc, V. Alard and A. Denis (1995) Photoacoustic study of the diffusion of chromophores in human skin. Submitted for publication to *J. Photochem. Photobiol.*
25. Giese K., A. Nicolaus and B. Sennhennof (1986) Photoacoustic *in vivo* study of the penetration of sunscreen into human skin. *Can. J. Phys.* **64**, 1139-1141.

RECENT DEVELOPMENTS IN FLUORESCENCE SPECTROSCOPY

Long-Lived Metal-Ligand Probes, Multi-Photon Excitation, and Control of the Excited State

Joseph R. Lakowicz, Ewald Terpetschnig, Henryk Szmacinski,
Henryk Malak, Józef Kuśba, and Ignacy Gryczynski

Center for Fluorescence Spectroscopy
Department of Biological Chemistry
University of Maryland School of Medicine
108 North Greene Street
Baltimore, Maryland 21201

ABSTRACT

In recent years there have been significant advances in the instrumentation for time-resolved fluorescence spectroscopy. Development of the frequency-domain method and the availability of suitable laser sources and detectors now provides remarkable resolution of complex intensity and anisotropy decays. At present the applications of fluorescence are more limited by the lack of suitable fluorophores than by instrumentation. In particular, the information content of fluorescence is primarily on the 10 ns timescale, which is comparable to the decay times of most fluorophores.

To circumvent the short lifetime of most available fluorophores, we will describe a new class of fluorophores, ruthenium and osmium metal-ligand complexes, which display decay times ranging from 100 ns to several microseconds. Surprisingly, these complexes display useful anisotropy, and thus can be used to measure protein hydrodynamics on the microsecond timescale. These compounds are highly photostable and should thus be useful in fluorescence microscopy. Importantly, the long decay times of these probes allows off-gating of the prompt autofluorescence and the design of simple instrumentation for lifetime-based sensing and imaging.

The increasing availability of ps and fs lasers has resulted in an interest in two-photon excitation for time-resolved spectroscopy and for intrinsic confocal microscopy. We show that two-photon excitation near 300 nm can be used to excite the intrinsic fluorescence of alkanes, thereby avoiding the usual requirement of vacuum UV excitation. Alkane fluorescence is quenched by water and alcohols, and it is possible that fluorescence from aliphatic groups will be obtained from biological molecules. Additionally, we show that the calcium

probe Indo-1 can be excited by simultaneous absorption of three photons at 885 nm, a wavelength conveniently available from Ti:Sapphire lasers.

And finally, we describe a new type of fluorescence experiment which uses multiple light pulses. The initial pulse is used to create the excited state population, and subsequent longer wavelength pulses are used to modify this population. We refer to this phenomena as light quenching, which allows changes in the excited state orientation and wavelength-selective removal of fluorophores. Light quenching promises to provide an increased information content on the complex intensity and anisotropy decay of biomolecules.

INTRODUCTION

Fluorescence spectroscopy is widely used as a research tool in biochemistry and cell biology [1-2]. Fluorescence methods have been used to study the solution properties of biomolecules, including interactions between macromolecules, rotational and translational diffusion, conformation transitions, and permeability to quenchers. While information can be obtained by stationary or steady state methods, maximal information is available from fluorescence using the time-resolved intensity or anisotropy decays, which often reveal behavior undetectable by steady state methods. Additionally, time-resolved sensing and imaging provide an opportunity to avoid the difficulties of interpreting the local fluorescence intensities in fluorescence microscopy.

In the present lecture we will describe recent advances in time-resolved fluorescence. Three topics will be discussed. First, we will describe a new class of fluorescence probes which extend the timescale of fluorescence from nanoseconds to microseconds. Secondly, we will describe two- and three-photon excitation of alkanes and the calcium probe Indo-1, respectively. And finally, we will describe a new class of multi-pulse fluorescence experiments which promises to increase the information available from the time-resolved data.

LONG-LIFETIME METAL-LIGAND COMPLEXES

In designing a fluorescence experiment one has available thousands of fluorophores with different absorption and emission wavelengths. However, in spite of this diversity, the range of available decay times is rather limited with most decay times being in the range of 1 to 10 ns. While this is a useful timescale for many biochemical experiments, it would be valuable to have longer decay times to allow measurement of slower domain-to-domain motions in proteins, or rotational motions of membrane-bound proteins. Probes with long decay times allow intensity and anisotropy decay measurements with relatively simple instrumentation. The sensitivity of the measurements can be increased by off-gating of the interfering auto-fluorescence. Additionally, the development of long lived probes would allow fluorescence lifetime imaging microscopy (FLIM) with simple solid state instrumentation.

We have developed a series of metal-ligand complex (MLC) probes which display decay times up to 400 ns [3-4], and other molecules in this class can have decay times as long as 100 μ s [5-6]. The first of these MLC probes are shown in Figure 1. The parent compound $[\text{Ru}(\text{bpy})_3]^{2+}$ has been widely studied for use in solar energy conversion. However, such molecules have not been used as anisotropy probes. Apparently, as a result of its symmetric structure it was thought that the anisotropy of $[\text{Ru}(\text{bpy})_3]^{2+}$ would be low, and thus not useful for measuring the hydrodynamics of biomolecules. We have now found that the presence of a suitable non-identical ligand on $[\text{Ru}(\text{bpy})_3]^{2+}$ results in a high fundamental anisotropy. One such ligand is the dicarboxy derivative of 2,2'-bipyridyl (dcbpy) (Figure 1,

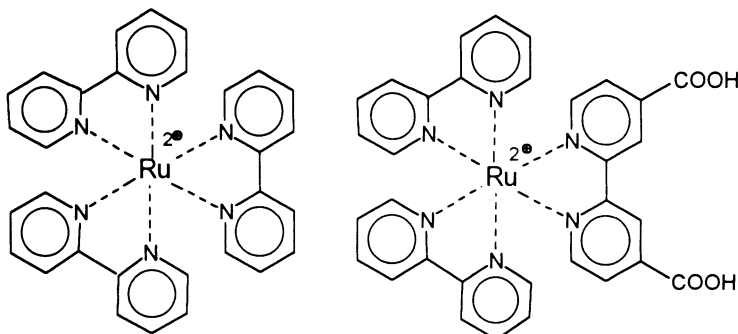


Figure 1. Chemical structure of $[\text{Ru}(\text{bpy})_3]^{2+}$ and of $[\text{Ru}(\text{bpy})_2(\text{dcpby})]$.

right). This ligand allows coupling of $[\text{Ru}(\text{bpy})_2(\text{dcpby})]$ to macromolecules by formation of a reactive N-hydroxy succinimide ester. Importantly, the presence of one dcbpy ligand results in high anisotropy in the absence of rotational diffusion [3-4]. This is seen from the excitation anisotropy spectra measured in frozen solution where rotational diffusion is inhibited (Figure 2). The anisotropy of $[\text{Ru}(\text{bpy})_2\text{dcpby}]$ is substantially higher than that of the parent compound $[\text{Ru}(\text{bpy})_3]^{2+}$, making $[\text{Ru}(\text{bpy})_2(\text{dcpby})]$ a good anisotropy probe.

The lifetime of the Ru complex is considerably longer than that of standard fluorophores. A typical intensity decay, measured by time-correlated single photon counting (TCSPC) is shown in Figure 3. The decay times are as long as 500 ns, and we are presently aware of other metal-ligand complexes capable of conjugation, with decay times as long as 2 μ s.

The main advantage of a long decay time is the ability to measure longer rotational correlation times. This is illustrated in Figure 4, which shows anisotropy decay of the Ru-complex conjugated to concanavalin A (Con-A) and to ferritin. For these measurements we added glycerol and decreased the temperature to slow the rate of rotational diffusion. In the case of Con-A (Figure 4, left) the rotational correlation time was as long as 218 ns. In

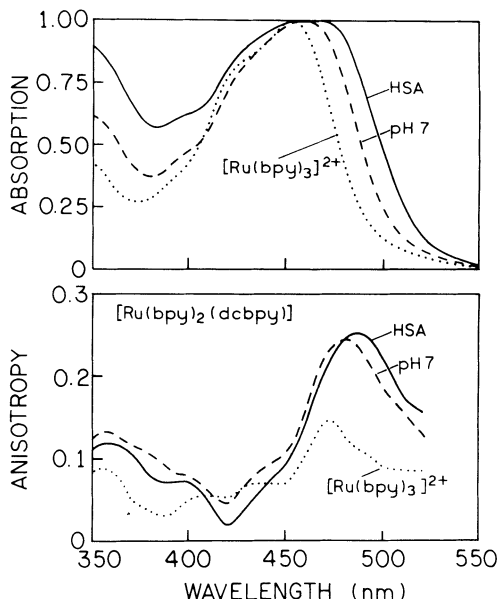


Figure 2. Absorption spectra (top) and excitation anisotropy spectra of $[\text{Ru}(\text{bpy})_2(\text{dcpby})]$, free (—) and when conjugated to HSA (—). The dotted lines (.....) represent the symmetrical $[\text{Ru}(\text{bpy})_3]\text{Cl}_2$. In glycerol-water, (9:1, V/V) at - 55°C.

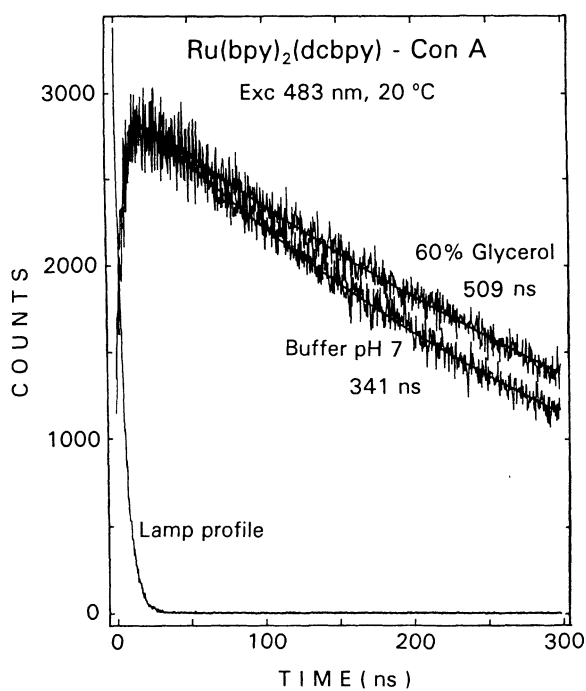


Figure 3. Intensity decays of [Ru(bpy)₂(dcbpy)] conjugated to ConA. Similar intensity decays were obtained for [Ru(bpy)₂(dcbpy)] and conjugated to other proteins.

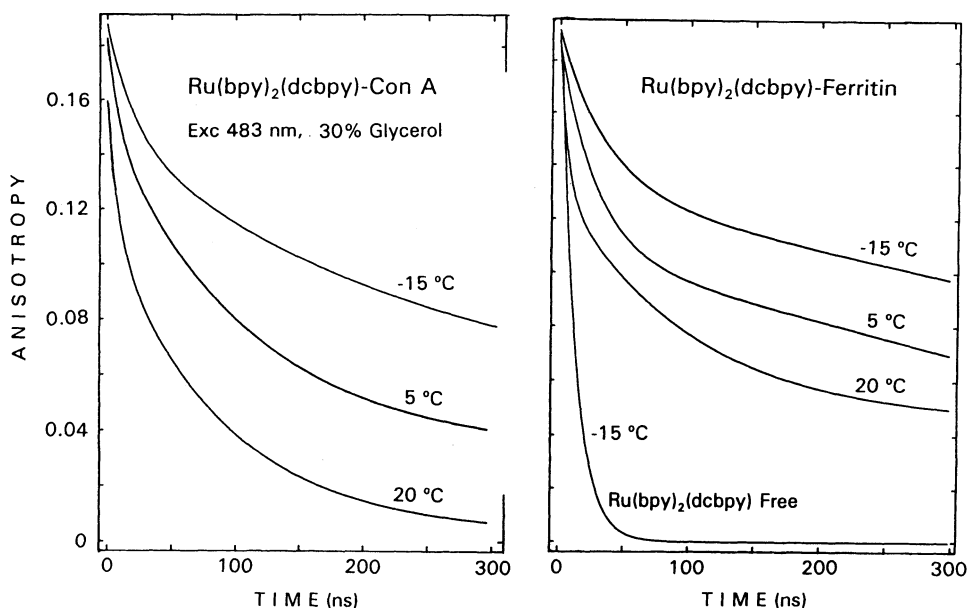


Figure 4. Temperature-dependent anisotropy decays of [Ru(bpy)₂(dcbpy)] conjugated to Con-A (left) and Ferritin (right) in 30% glycerol.

the case of ferritin the correlation time was in excess of 1 μ s. Such correlation times were previously inaccessible using ns decay time fluorophores.

It should also be noted that such long-lived probes can be useful for studies of translational diffusive processes on a timescale presently not accessible by the usual fluorescence probes. For instance, there is considerable interest in the rates and amplitudes of domain-to-domain motions in proteins, and there have been repeated attempts to study such motions by time-resolved fluorescence resonance energy transfer (FRET) [7-9]. These measurements have been mostly unsuccessful because of the 5-10 ns decay times and the limited extent of inter-domain motions on this timescale. The use of longer-lived MLC emission can allow measurements of these motions. We note that such measurements are not the equivalent of diffusion-enhanced energy transfer using the lanthanide donors, in which the rate of diffusion is not determined, and the data reveal only the distance of closest approach of the donor and acceptor.

An important property of the metal-ligand complex is their high photostability. We have had an aqueous solution $[\text{Ru}(\text{bpy})_2(\text{dcbpy})]^{2+}$ exposed to the room light for over two years with no change in its absorption spectrum. This suggests that metal-ligand complexes will be valuable in fluorescence microscopy where the usual fluorophores often photobleach in seconds or minutes.

In the past several years we have demonstrated the possibility of cellular imaging based on the fluorescence lifetime or decay time at each point in the image [10-11]. We refer to this method as fluorescence lifetime imaging microscopy (FLIM). As presently accomplished FLIM requires a light source modulated near 100 MHz and a high-speed gain-modulated image intensifier [10-11]. These requirements can be eliminated using long-lived MLC probes. It is now known that the output of LEDs can be modulated at frequencies up to 50 MHz [12]. The output of blue LEDs is well matched to the absorption spectra of the Ru metal-ligand complexes. Importantly, CCDs are becoming available with gated detection near 50 ns [13]. Such detectors would allow collection of the phase sensitive images for FLIM without an image intensifier (Figure 5). Hence, the instrumentation for FLIM can be rather simple, and the use of a LED light source and photostable MLCs may minimize

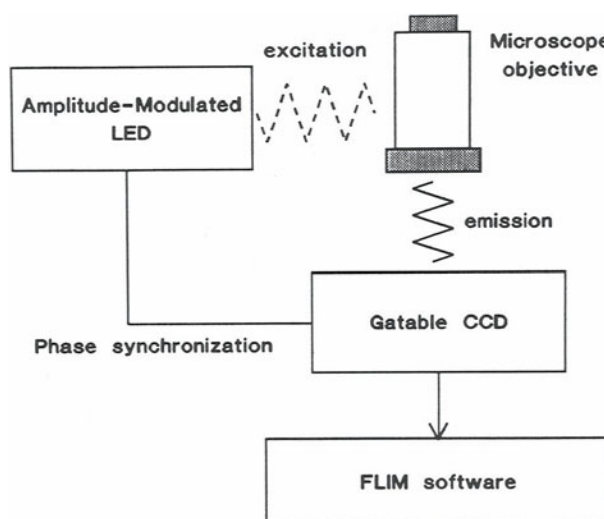


Figure 5. Fluorescence lifetime imaging microscopy (FLIM) with long-lived probes. The excitation can be an amplitude-modulated LED and the emission detected with a gatable CCD.

problems of photobleaching. The capabilities for FLIM may then become a routine part of a fluorescence microscope.

The absorption and emission wavelengths and large Stokes shift displayed by the MLCs are also convenient. The wide absorption near 450 nm allows convenient excitation with a variety of lasers or light-emitting diodes. The large Stokes shift, shifting the emission to over 600 nm, means that it will be moderately easy to separate the MLC emission from scattered excitation. Also, the long emission wavelengths may allow observation of the emission even in whole blood as well as in less absorbing biological samples. The use of MLC probes is presently in its infancy, and one can expect future probes with improved quantum yields and decay times. Additionally, one can imagine a series of MLC probes specific for analytes of interest, such as pH, Ca^{2+} , and Mg^{2+} . MLC probes and FLIM may find widespread uses in clinical chemistry, analytical chemistry and cellular imaging.

TWO-PHOTON INDUCED FLUORESCENCE OF ALKANES

It is well known that aromatic molecules display fluorescence. Less known is the fact that alkanes [14-15] also display significant fluorescence when excited in the vacuum ultraviolet (VUV) region of the spectrum near 140-160 nm [14-15]. The need for VUV excitation has resulted in the limited study of alkane fluorescence because the light sources are weak, it is necessary to exclude oxygen, and quartz optics are not sufficiently transparent at these wavelengths. However, we now show that tetradecane can be excited by two-photon excitation (TPE) near 300 nm, and the emission over 200 nm is readily transmitted by standard quartz optics [16]. The use of TPE circumvents the need for VUV conditions, and suggests the use of the intrinsic fluorescence of saturated hydrocarbons as an intrinsic probe.

The emission spectrum of tetradecane is shown in Figure 6 for excitation at 300 nm. The emission maximum is at 210 nm in this uncorrected spectrum. The intensity depends on the square of the incident light intensity as expected for TPE (insert). The emission of tetradecane is decreased in the presence of n-propanol. The decrease in intensity follows

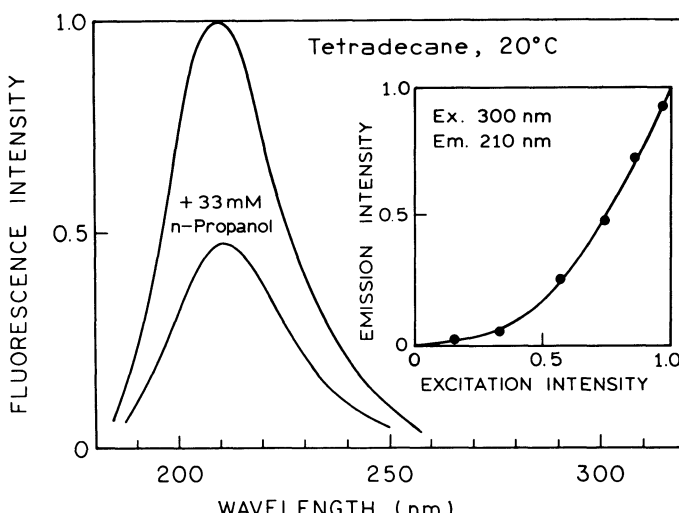


Figure 6. Emission spectra of tetradecane with two-photon excitation at 300 nm. Spectra are shown for neat tetradecane (—) and in the presence of 33 mM n-propanol. The insert shows the quadratic dependence on the emission at 210 nm, with 300 nm excitation.

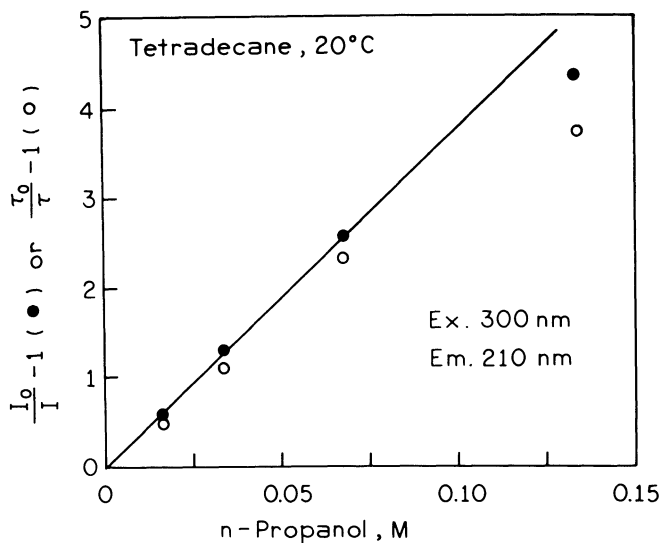


Figure 7. Stern–Volmer intensity (●) and lifetime (○) plot for n-propanol quenching of tetradecane.

Stern–Volmer kinetics, as seen by the linear intensity Stern–Volmer plot (Figure 7, ●). Quenching of tetradecane by n-propanol is most likely collisional in that the Stern–Volmer quenching constant of 37 M^{-1} , and the unquenched lifetime of 4.4 ns (see Figure 8 below), result in a bimolecular quenching constant of $8.4 \times 10^9 \text{ M}^{-1} \text{ s}^{-1}$. This value is near that expected for 100% efficient collisional quenching in a solvent of the viscosity of tetradecane (2.18 cP). Tetradecane and n-propanol do not appear to form observable exciplexes since the emission spectrum is unchanged in the presence of n-propanol.

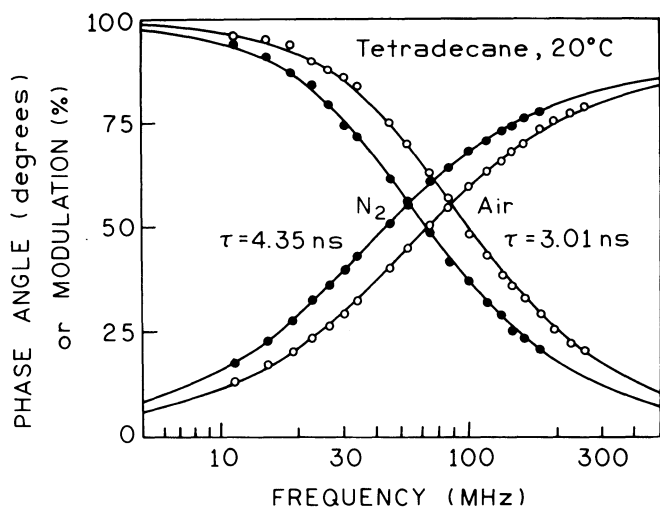


Figure 8. Frequency-domain intensity decay of tetradecane in the absence (●) and presence (○) of dissolved oxygen from equilibration with the air.

Tetradecane fluorescence is readily quenched by dissolved oxygen. Equilibration with air, rather than nitrogen, decreases its decay time from 4.4 to 3.0 ns (Figure 8). Using the known solubility of oxygen in liquid alkanes like dodecane (about 0.009 M/atmosphere of O₂), the bimolecular quenching constant is $4.8 \times 10^{10} \text{ M}^{-1} \text{ sec}^{-1}$, which is slightly above the diffusion controlled limit. Tetradecane also appears to be collisionally quenched by water, as seen by a decrease in the decay time from 3.0 ns to 2.85 when equilibrated with water. The sensitivity of alkane fluorescence to dissolved oxygen and water suggests that alkane fluorescence can provide an intrinsic probe of oxygen transport in membranes. Oxygen quenching of alkanes will be the subject of a separate study.

The fluorescence of linear alkanes can be observed without VUV excitation when excited by a two-photon process. Our experiments demonstrate that the emission of tetradecane is collisionally quenched by water, alcohol and oxygen, which in turn suggests that the emission of aliphatic groups can be a sensitive indicator of exposure of the methylene chains to solvent. These results suggest that intrinsic fluorescence could be observed from the acyl side chain region of cell membranes.

THREE-PHOTON EXCITATION OF THE CALCIUM PROBE INDO-1

During the past several years, there has been an increased use of intense laser pulses as an excitation source for two-photon excitation in time-resolved fluorescence spectroscopy and for fluorescence imaging microscopy. We now describe the unexpected observation of three-photon induced fluorescence of the calcium probe Indo-1 [17]. This probe is widely used for intracellular calcium imaging. Indo-1 is an emission-wavelength ratiometric probe [18-19], and is thus most often used in laser scanning confocal microscopy in which the excitation source is a focused laser beam at a single wavelength. Three-photon excitation has only been observed infrequently, and to date there have been no studies of biochemical fluorophores with three-photon excitation, no time resolved studies, and no reports of potential application of this phenomenon to biophysics.

Absorption and emission spectra of Indo-1 are shown in Figure 9. The one-photon absorption spectra are seen to be dependent on Ca²⁺, with the Ca²⁺ bound form displaying a shorter wavelength absorption (Figure 9, top). The emission spectra are also dependent on Ca²⁺, with the Ca²⁺-bound form of Indo-1 displaying a blue shifted emission (Figure 9, bottom). Emission spectra of Indo-1 for excitation at 885 nm appear to be slightly shifted towards shorter wavelengths (about 5 nm at maxima) compared to the excitation at 295 nm. The minor differences between spectra for one- and three-photon excitation are likely to be within experimental error, so that the emission spectra appear to be essentially identical for 295 and 885 nm excitation.

We were surprised by the observation of Indo-1 emission at this long excitation wavelength. Indo-1 is known to display a significant cross section for two-photon excitation [20]. However, two-photon excitation of Indo-1 at 885 nm seems unlikely because the one-photon absorption spectra do not display significant absorbance above 400 nm (Figure 9, top), and thus one does not expect two-photon excitation at 885 nm. To determine the nature of the long-wavelength excitation we examined the dependence on the emission intensity on the incident laser power. These data show that the observed intensity of the calcium-free and calcium-bound forms of Indo-1 are proportional to the cube of the laser power (Figure 10). Three photon excitation of Indo-1 is only observed for long excitation wavelengths. The intensity of Indo-1 becomes dependent on the square of the laser power for wavelengths below 840 nm (not shown).

Three-photon excitation has a number of potential advantages in time-resolved fluorescence and for fluorescence microscopy. The fundamental output of Ti:Sapphire lasers

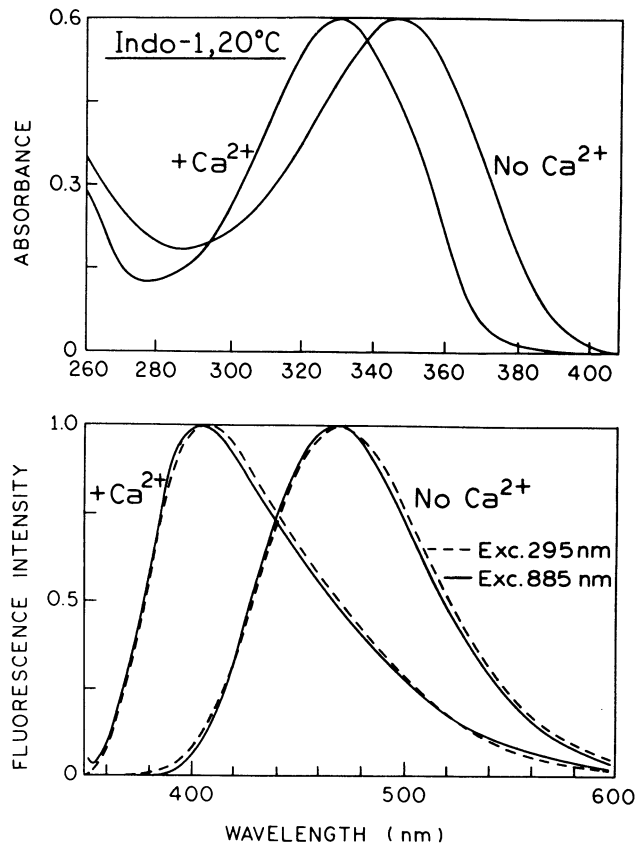


Figure 9. Absorption spectra of Indo-1 (top) and emission spectra (bottom) for one-photon (295 nm, —) and three-photon (885 nm, -) excitation.

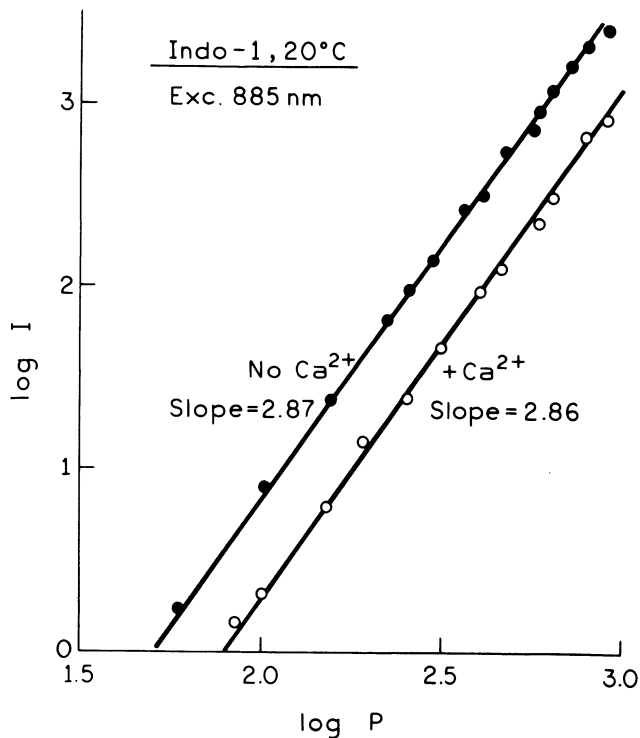


Figure 10. Dependence on the emission intensity of Indo-1 on laser power. The laser power is in mW. [Indo-1] = 15 μ M.

is most intense from 800-900 nm, which is suitable for three-photon excitation of UV-absorbing fluorophores, potentially including the intrinsic fluorescence of proteins. The Ti:Sapphire fundamental wavelengths are above the absorption bands of most biological chromophores, suggesting that the amounts of auto-fluorescence will be minimal for three-photon excitation. Furthermore, these wavelengths are below the absorption bands of water, suggesting that the biological samples will not be excessively heated by 800-900 nm illumination. An additional advantage of these excitation wavelengths is that they are poorly detected by most photomultiplier tubes (PMTs), and PMTs without significant sensitivity above 600 nm are readily available. Hence experimental problems due to stray or scattered excitation should be easily minimized with three-photon excitation.

A further advantage of three-photon excitation is the smaller excited volume. In the case of two-photon excitation the absence of signal from outside the focal region has been used to avoid out-of-focus signal. By visual comparison of the emission from cuvettes containing fluorophores which display two- or three-photon excitation, we have observed that the emission is seen from a smaller area for three-photon excitation. This indicates that higher spatial resolution in laser scanning microscopy can be obtained by three-photon excitation.

In closing we note that the reader may regard simultaneous absorption of three photons to be an exotic process with little practical usefulness. However, the same could have been said about two-photon excitation, which can now be regarded as a promising research tool in biophysics and cell biology.

CONTROL OF EXCITED STATE POPULATION BY LIGHT QUENCHING (LQ)

At present almost all measurements of time-resolved fluorescence follow the same paradigm, which is to excite the sample with a single pulse of light followed by measurement of the time-resolved emission. Frequency-domain measurements follow the same paradigm, except the sample is excited with a single amplitude-modulated light beam.

We are now developing a new type of fluorescence experiment in which the sample is excited by one pulse, and the excited state population is modified by a subsequent light pulse which overlaps the emission spectrum. The second pulse causes stimulated emission. Since the emitted photon is directed along the path of the quenching beam (Figure 11), this photon is not observed with right-angle observation conditions, resulting in a decrease (quenching) of the observed intensity.

One can imagine two classes of LQ experiments. The simplest experimental situation is when the excitation and quenching are provided by the same light pulse (Figure 12, left), in which case the excitation and quenching beams are coincident in time and direction of propagation. In this case, there is cylindrical symmetry of the emission field around the z-axis (Figure 13).

In the second class of LQ experiments the quenching pulse is delayed in time relative to the excitation pulse (Figure 12, middle and right). In such two-beam experiments the intensity and anisotropy display instantaneous changes upon arrival of the quenching pulse. Perhaps the most remarkable and promising aspect of LQ is that it displays the same photoselection rules as does light absorption, that is, the dot-vector product of the electric vector of the polarized excitation (or polarized quenching light) and the orientation of the transition moment. This means that the polarization or anisotropy of the excited state can be modified by the quenching pulse. Depending on the polarization of the quenching pulse one

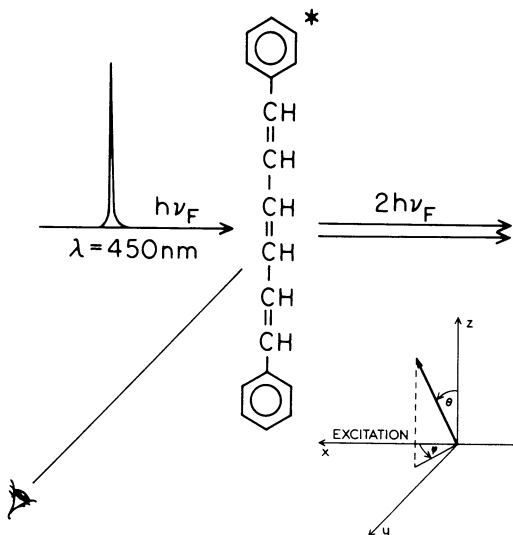


Figure 11. Intuitive description of light quenching.

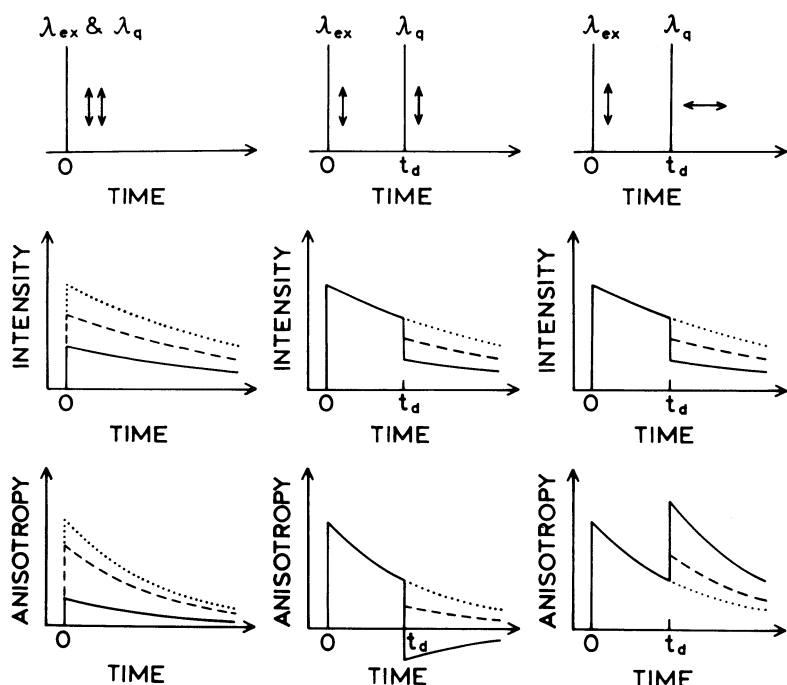


Figure 12. Intuitive description of the effects of LQ on the intensity and anisotropy decays of fluorescence for one-beam (left) and two-beam (center and right) experiments. The effects caused by LQ of different intensity are shown by the solid and dashed lines. The dotted lines show the intensity or anisotropy decays in the absence of LQ.

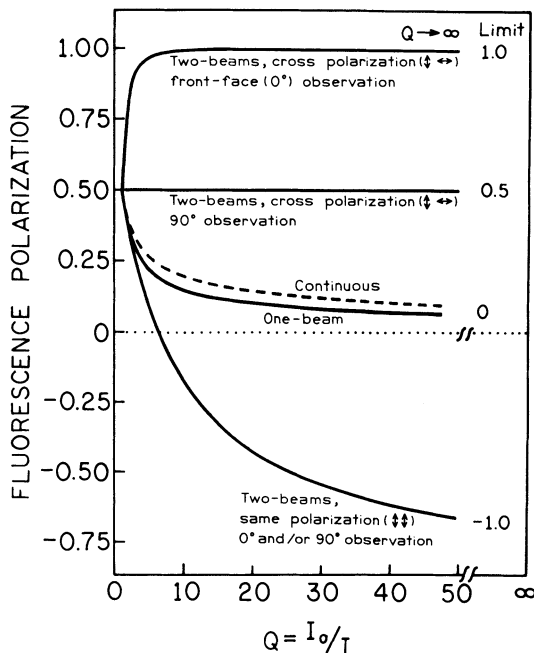


Figure 13. Emission polarization in the presence of LQ.

can increase or decrease the anisotropy (Figure 13). In fact, the polarization can be varied from +1 to -1 by light quenching.

A remarkable aspect of a two-beam experiment is the possibility of breaking the cylindrical symmetry normally pervasive in studies of homogeneous solutions. This is seen in Figure 14 (bottom right), where we show the excited state population following quenching with a horizontally polarized quenching pulse. This pulse results in selective depletion of excited fluorophores with their transition moments oriented along the y-axis. Because of the symmetry of this population with respect to the x-z plane, there is no effect on the population observed along the y-axis. However, if the emission is observed at a small angle from the x-axis, then the population appears to be highly oriented. Since horizontal quenching breaks the z-axis symmetry, it is preferable to use polarization instead of anisotropy, since the use of anisotropy normally assumes z-axis symmetry ($I_x = I_y$). When observed along the x-axis, horizontally polarized quenching results in polarization values as high as 1.0 (Figures 13 and 14). In this case, high polarization values can be achieved for modest amounts of LQ ($Q < 10$).

It is important to recognize that LQ can be accomplished without addition of quenchers, that is without changes in chemical composition, which can potentially alter the conformation of sensitive biomolecules. Additionally, the effect is rapidly reversible by blocking the illumination. Hence, even small changes in intensity, anisotropy, lifetime, phase or modulation can be detected with the use of light choppers and lock-in amplifiers. And finally, little photochemical damage is expected because the quenching light is not absorbed by the fluorophores.

Light quenching can be effective under conditions where collisional quenching is not practical, such as in viscous or vitrified solutions where diffusion is slow. Additionally, fluorophores occasionally are inaccessible to some collisional quenchers, as found for the same tryptophan residues in protein or for dyes intercalated in DNA. For such systems we

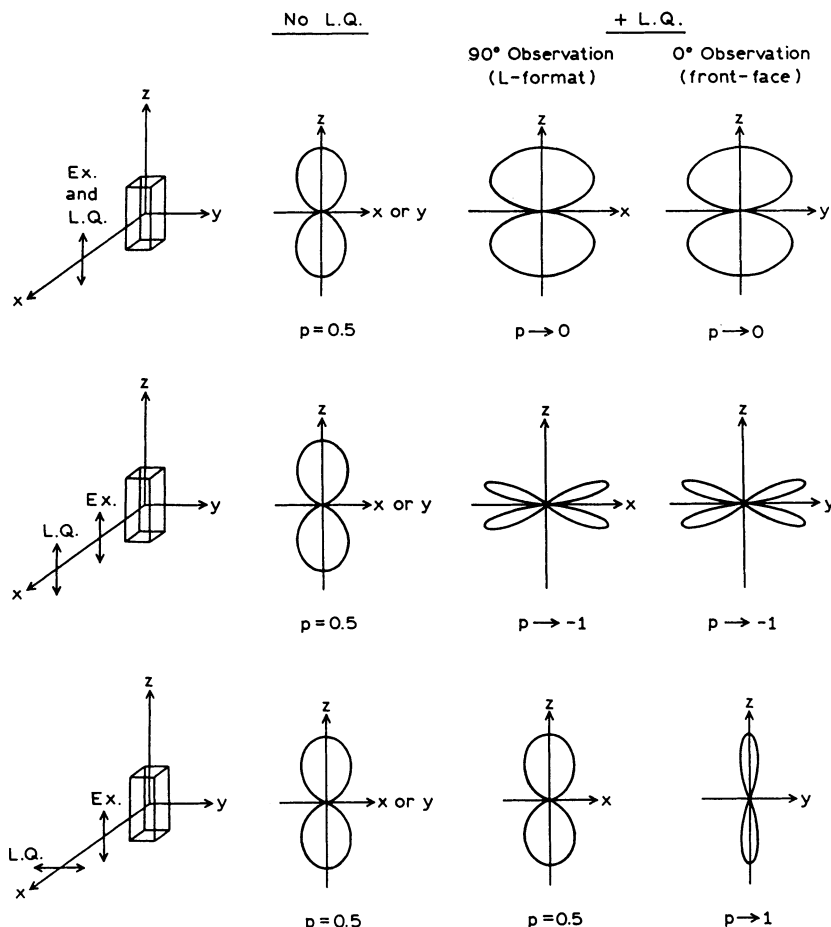


Figure 14. Effects of polarized LQ on the excited state population.

cannot use collisional quenchers. However, LQ will most probably be insensitive to the local environment of the probe and can thus be used to control the decay times of even inaccessible fluorophores. The ability to decrease the lifetime by LQ may increase our ability to resolve complex phenomena in rigid and/or inaccessible environments.

Light quenching can also be expected to be sensitive to the emission spectra of fluorophores or their decay times. For instance, light quenching depends on spectral overlap of the quenching wavelength with the emission spectrum of a fluorophore. In a mixture of fluorophores one can thus expect the fluorophores which most closely match the quenching wavelength to be preferentially quenched. Additionally, the amount of light quenching is expected to be sensitive to the decay time because different decay times suggest different cross sections for light quenching. The amount of light quenching is also expected to be sensitive to the decay time between the pulses because the amount of light quenching depends on the number of excited molecules upon arrival of the quenching pulse.

And finally we note that technological advances in commercially available lasers are resulting in the increasing practicality of the experiments described above. For instance, it is now possible to buy synchronized mode-locked Ti:sapphire lasers, where the time delays

between the pulses are easily adjustable. Additionally, it is possible to obtain Q-switched laser sources with the output centered near 355 nm, the emission maximum of proteins.

In conclusion, the ability to measure time-dependent LQ can result in a new class of fluorescence experiments in which the sample is excited with one pulse, and the excited state population is modified by the quenching pulse(s) prior to measurement. Such multi pulse experiments may find use in studies of the rotational diffusion of asymmetric biomolecules and may be even more informative in studies of macroscopically oriented systems.

ACKNOWLEDGMENTS

This work was supported by grants from the national Science Foundation (MCB-8804931 and BIR-9319032) and the National Institute of Health (RR-08119, RR-10416 and GM-35154).

REFERENCES

1. Wolfbeis, Otto S. (Ed.) *Fluorescence Spectroscopy New Methods and Applications*. Springer-Verlag, New York, pp. 309 (1993).
2. Slavik, J. (Ed.) *Fluorescent Probes in Cellular and Molecular Biology*. CRC Press, Boca Raton, pp. 295 (1994).
3. Terpetschnig, E., H. Szmacinski, and J.R. Lakowicz. Fluorescence Polarization Immunoassay of a High-Molecular-Weight Antigen Based on a Long-Lifetime Ru-Ligand Complex. *Anal. Biochem.*, 227:140-147 (1995).
4. Terpetschnig, E., H. Szmacinski, H. Malak, and J.R. Lakowicz. Metal-Ligand Complexes as a New Class of Long-Lived Fluorophores for Protein Hydrodynamics. *Biophys. J.*, 68:342-350 (1995).
5. Demas, J.N., and B.A. DeGraff. Applications of Highly Luminescent Transition Metal Complexes in Polymer System. *Macromol. Chem. Macromol. Symp.*, 59:35-51 (1992).
6. Sacksteder, L.A., M. Lee, J.N. Demas, and B.A. DeGraff. Long-lived, Highly Luminescent Rhenium(I) Complexes as Molecular Probes: Intra- and Intermolecular Excited-state Interactions. *J. Am. Chem. Soc.*, 115:8230-8238 (1993).
7. Eis, P.S., J. Ku_ba, M.L. Johnson, and J.R. Lakowicz. Distance Distributions and Dynamics of a Zinc Finger Peptide from Fluorescence Resonance Energy Transfer Measurements. *J. Fluoresc.*, 3(1):23-31 (1993).
8. Lakowicz, J.R., I. Gryczynski, J. Ku_ba, W. Wiczk, H. Szmacinski, and M.L. Johnson. Site-to-Site Diffusion in Proteins as Observed by Energy Transfer and Frequency-Domain Fluorometry. *Photochem. and Photobiol.*, 59(1):16-29 (1994).
9. Haran, G., E. Haas, B.K. Szpikowska, and M.T. Mas. Domain Motions in Phosphoglycerate Kinase: Determination of Interdomain Distance Distributions by Site-Specific Level in Time-Resolved Fluorescence Energy Transfer. *Proc. Natl. Acad. Sci. USA*, 89:11764-11768 (1992).
10. Lakowicz, J.R., H. Szmacinski, K. Nowazyk, K. Berndt and M.J. Johnson. Fluorescence Lifetime Imaging. *Anal. Biochem.*, 202:316-330 (1992).
11. Lakowicz, J.R., H. Szmacinski, K. Nowacyk, W.J. Lederer and M.L. Johnson. Fluorescence Lifetime Imaging of Intracellular Calcium in COS Cells Using Quin-2. *Cell Calcium*, 15:7-27 (1994).
12. Fantini, S., M.A. Franceschini, J.B. Fishkin, B. Barbieri and E. Gratton. Quantitative Determination of the Absorption Spectra of Chromophores in Strongly Scattering Media: A Light-Emitting Diode Based Technique. *Appl. Optics*, 33(22):5204-5213 (1994).
13. Reich, K.K., R.W. Mountain, W.H. McGonagle, C.M. Huang, J.C. Twichell, B.B. Kosicki and D. Savoye. An Integrated Electronic Shutter for Back-Illuminated Charge-Coupled Devices. *Proc. IEEE* 91, 721-724 (1991).
14. Hirayama, F., W. Rothman and L. Sanford. Fluorescence of Saturated Hydrocarbons. II. The Effect of Alkyl Substituents. *Chem. Phys. Letts.*, 5(5):296-298 (1970).
15. Rothman, W., F. Hirayama and S. Lipsky. Fluorescence of Saturated Hydrocarbons. III. Effect of Molecular Structure. *J. Chem. Phys.*, 58(4):1300-1317 (1973).

16. Gryczynski, I., A. Razynska and J.R. Lakowicz. Two-Photon Induced Fluorescence of Linear Alkanes: A Possible Intrinsic Lipid Probe. *Biophys. Chem.*, 57: 291-295 (1996).
17. Szmacinski, H., I. Gryczynski and J.R. Lakowicz. Three-Photon Induced Fluorescence of the Calcium Probe Indo-1. *Biophys. J.*, 70: 547-555 (1996).
18. Gryniewicz, G., M. Poenie and R.Y. Tsien. A New Generation of Ca^{2+} Indicators with Greatly Improved Fluorescence Properties. *J. Biol. Chem.*, 260(6):3440-3450 (1985).
19. Luckhoff, A. Measuring Cytosolic Free Calcium Concentration in Endothelial Cells with Indo-1: The Pitfall of Using the Ratio of Two Fluorescence Intensities Recorded at Different Wavelengths. *Cell Calcium*, 7:233-248 (1986).
20. Szmacinski, H., I. Gryczynski and J.R. Lakowicz. Calcium-Dependent Fluorescence Lifetimes of Indo-1 for One- and Two-Photon Excitation of Fluorescence. *Photochem. & Photobiol.*, 58(3):341-345 (1993).

PHOTONIC PATHOLOGY

Fluorescence and Raman Spectroscopy for Tissue Diagnosis and Characterization

R. R. Alfano and A. Katz

New York State Center for Advanced Technology
for Ultrafast Photonic Materials and Applications
The City College of the City University of New York
Convent Ave and 138 St. New York, New York 10031

ABSTRACT

In the future, smart optical spectroscopic non-invasive-based diagnostic instruments will aid in the operating room and doctor's office. The colors of emitted and scattered light from tissues show potential in the medical arena. Optical spectroscopy offers exciting possibilities for novel **Optical Biopsy** diagnostic and therapeutic approaches. The foundation for optical spectroscopy has been evolving since its beginnings over fifty years ago. Fluorescence and Raman spectroscopy have made inroads to identify cancerous from non-cancerous states of a tissue. Fluorescence spectroscopy measures the allowed electronic transitions while Raman spectroscopy measures vibrational transitions from various functional groups in molecules. The underlying physical basis for these optical approaches is that they are strongly influenced by the composition and cellular structure of tissues. Tissues are made up of proteins, nucleic acids, lipids, and other components with many fluorescing and non-fluorescing chromophores in complex structures. The change in the state of tissue, such as from normal to cancerous alters fluorescence and Raman spectra in tissues. This presentation will review the use of fluorescence and Raman spectroscopy to investigate GYN, breast, colon and ADT tissues as a potential photonic pathology tool.

1. INTRODUCTION

Over the past ten years, extensive research has been done on the use of optical spectroscopy for tissue diagnosis and characterization. The use of native tissue fluorescence or Raman spectroscopy allows for the development of a wide range of non-invasive diagnostic tools for *in-vivo* and *in-vitro* tissue examination. The high spatial resolution of optical systems can allow for the detection of very small tumors. Fiber optics allows for investigation inside the body with or without needles. Fluorescence and Raman scattering

both determine the composition of tissues by measuring the optical properties of various molecules in tissue. The change in tissue state from normal to cancerous alters tissue composition. If these changes can be observed in tissue spectra, then optics can be used to distinguish normal or cancerous tissue. Fluorescence spectroscopy measures allowed electronic transitions of various chromophores in the complex tissue structure. These chromophores can be either extrinsic dyes or intrinsic molecules. Fluorescent dyes such as hematoporphyrin derivative (HPD) have been investigated for cancer detection.¹ However, the interaction of some extrinsic dyes with tissue can limit their use for *in-vivo* diagnosis. There are several natural fluorophores that exist in tissue and cells which, when excited with ultraviolet light, fluoresce in the ultraviolet and visible regions of the spectrum. Some of the important ones include tryptophan, elastin, collagen, nicotinamide adenine dinucleotide (NADH), components of adipose tissue, flavin and porphyrin. Some of their absorption and emission spectra are schematically shown in Figs. 1 and 2, respectively. The Flavins and NADH show changes in the spectra between their oxidized and reduced state. The relatively large emission intensity from tissues and the need for broadly tuneable excitation sources in the UV and visible has led researchers to develop lamp-based fluorescence systems instead of lasers.

Significant progress has been made using native fluorescence spectroscopy to detect cancer. Alfano and coworkers first used fluorescence to detect tumors in rat tissue.² This work was later extended to *in vitro* human tissue.³ Fluorescence spectroscopic cancer detection has been applied to human breast^{3,4,5} colon,^{6,7} gynecological (GYN)^{8,9} and aerodigestive tract^{10,11} tissue. The complex structure of tissue, variation in blood concentration, and the large site-to-site differences in elastic scattering, have complicated the spectral analysis. A number of mathematical tools are being employed to assist in tissue analysis and improve the diagnostic accuracy. These tools include intensity ratios, Fourier analysis, least squares fits, curve differentiation, and integration at well defined wavelengths.

In Raman spectroscopy vibrational transitions from various functional groups in tissue are measured. IR Raman spectra are composed of narrow emission lines which are more well defined than the broad emission spectrum from fluorescence measurements. However, the higher spectral resolution, lower signal strength, and complex spectra of Raman spectroscopy require a laser excitation source. Near infrared Fourier Transform (NIR-FT) Raman spectroscopy and conventional Near IR CCD systems have been applied to human GYN, breast and aorta tissue.^{12,13,14,15}

In this paper, we review our research work on the use of fluorescence and Raman spectroscopy to investigate breast, colon, GYN and aerodigestive tract tissue.

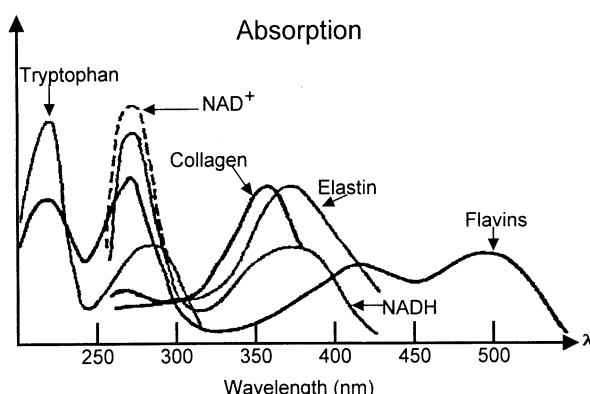


Figure 1. Absorption spectra of tryptophan, elastin, collagen, nicotinamide adenine dinucleotide (NADH), and flavins.

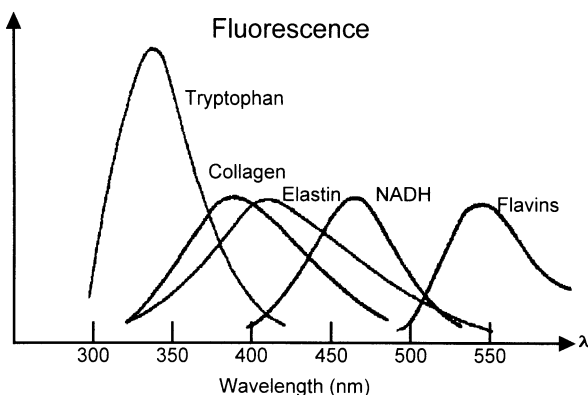


Figure 2. Emission spectra of tryptophan, elastin, collagen, nicotinamide adenine dinucleotide (NADH), and flavins.

2. FLUORESCENCE SPECTROSCOPY OF TISSUE

2.1 Breast Tissue

Initial investigation on emission from breast tissue in the visible was performed by Alfano and coworkers.^{3,4,5} The 488 nm emission from an argon ion laser was used to excite normal, benign and malignant breast tissue. The emission spectra from 500 nm to 700 nm was measured for the different tissue samples. The observed differences in spectra between cancer and normal tissue was attributed to the higher blood concentration in normal tissue. The inability to distinguish benign and malignant tumors later led the use of UV excitation at 300 nm to excite tryptophan, collagen and NADH for the purpose of improving diagnostic methods.

The emission spectra from a large number of fresh normal, benign and malignant tissue samples were taken. All samples were excited with 300 nm excitation and the emission intensity from 320 nm to 580 nm was measured. The ratio of fluorescence intensity at 340 nm to 440 nm was measured for all samples. These two wavelengths were selected because blood absorption at 340 nm and 440 nm is the same, and the scattering cross-section of tissue does not vary significantly in the range of 300 nm to 600 nm. The effects of blood were minimized by comparing these two wavelengths. It was determined that the 340 nm to 440 nm intensity ratio for malignant tissue was consistently greater than 9, while for normal and benign tissue the ratio was less than 9. Emission spectra from normal and malignant breast samples are shown in Figure 3.

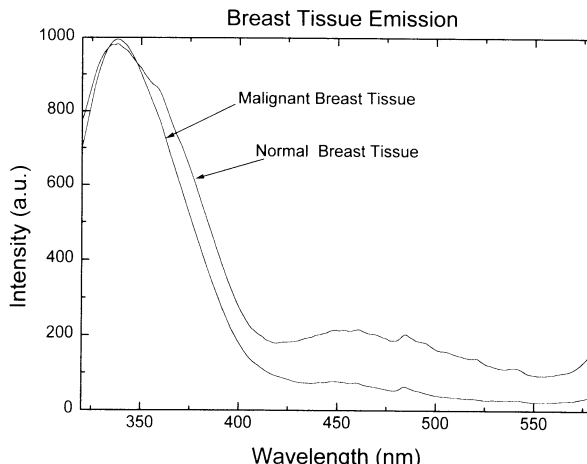


Figure 3. Average of emission spectra from normal and malignant breast tissue. The individual curves were normalized before computing the average.

Breast tissue is a complicated system made up of ducts, lobes, lobules, fibrous tissue and fat with underlying muscle and bone. The presence of fat in breast tissue complicates the analysis by intensity ratio. Fat has an emission band which peaks around 330 nm and almost no emission at 440 nm. The emission and excitation spectra of a large number (~ 100) of benign and malignant tissue samples, also containing fat tissue, were analyzed. A series of analytical tools were developed to aid in tissue diagnosis. These tools involved analyzing both the curve shape and intensity ratios at multiple wavelengths in order to correct for the presence of fat and the variation in blood content of the tissue. Using pathology as a standard, this analysis produced a sensitivity of 91% for malignant specimens and a specificity of 95% for benign tissue specimens.

2.2 Colon Tissue

Recent developments in minimal invasive surgery have provided patients with significant improvements in comfort and recovery time at the expense of reducing the physician's diagnostic capability. Laparoscopy removes a physician's tactile feedback as well as reducing depth perception. However, laparoscopy is very well suited for *in-vivo* spectroscopic measurements of tissue. Fluorescence measurements also have the potential to detect dysplasia or other precancerous conditions which may not be detectable by visual examination. *In-vivo* optical spectroscopy in the UV and blue regions of the spectrum have been used to differentiate normal and cancerous colon tissue. Kapadia *et al.*¹⁶ excited colon tissue at 325 nm using a helium-cadmium laser as an excitation source. They used a multivariate linear regression analysis of the spectra to identify six significant emission wavelengths. A score was determined based on the emission intensity at these six wavelengths and a successful separation between *in-vitro* adenomatous and normal colon tissue was achieved.

The emission and excitation of normal and malignant colon tissue was studied⁶ in order to determine the optimum excitation/emission wavelengths for distinguishing malignant from normal tissue. A lamp based fluorescence spectrophotometer was employed to allow either excitation or emission measurements. In one series of measurements, normal and malignant tissue samples were excited by 325 nm light and the emission was measured in the range of 350 nm to 600 nm. The emission spectra of both types of tissues showed two broad emission bands. One was centered at 470 nm, the other band at 380 nm. However there were considerable differences in the emission intensity profile of the normal and malignant samples, especially in the region from 350 nm to 420 nm. It was found that the ratio of the emission intensity at 360 nm to the intensity at 380 nm was an important indicator of the presence of malignancy, with the malignant samples having an intensity ratio > 0.74, while the normal tissue the ratios were < 0.74. It was also found that the I_{360} / I_{380} ratio depended on excitation wavelength. For excitation wavelengths between 290 and 305 nm, the difference in intensity ratio of normal and malignant tumors was smaller than for excitation wavelengths longer than 305 nm. Spectra of typical normal and malignant samples are shown in Figure 4. Measurements were taken on 39 normal and 35 malignant tissue samples. Using the I_{360} / I_{380} ratio, a specificity of 0.92 and a sensitivity of 0.94 was achieved.

2.3 GYN Tract Tissue

The early detection of neoplasia in the female reproductive tract is a medical priority. The number of newly diagnosed cancers and the number of deaths from ovarian and endometrial cancer is extremely high.^{8,9} The cure rate is directly related to the stage at which the cancer is detected; yet current diagnostic procedures are time consuming, subject to human error, and often result in pain for the patient. The standard methods for early cancer diagnosis require an abnormal pap smear, colposcopy, biopsy and sample preparation by a

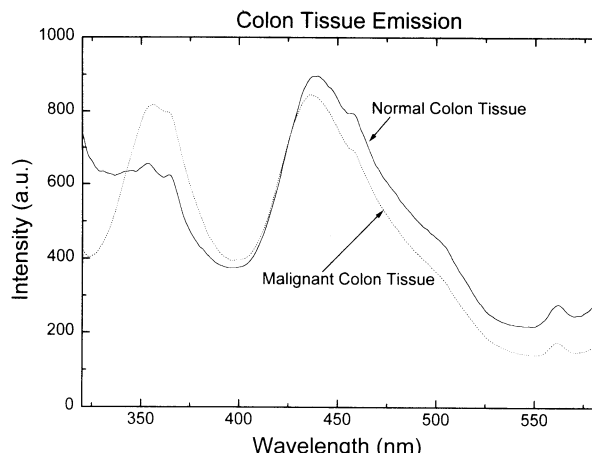


Figure 4. Average of emission spectra from normal and malignant colon tissue. The individual curves were normalized before computing the average.

pathologist for microscopic evaluation. Cytological smears have a false negative error rate of 20–30%.⁹ Future diagnostic techniques based on optical spectroscopy to scan the cervix have the potential to provide a real time, *in-vivo*, diagnostic tool to assist in cervical cancer detection. This would provide a new optical PAP method.

Emission and excitation spectra were taken from a large number of malignant and non-malignant GYN tissue samples. The spectra from three different type of GYN tract tissue (uterus, cervical and ovarian) were measured. Although the spectral intensity and shape varied from tissue sample to sample, consistent differences were found between malignant and non-malignant tissues when excited by light in the 300 to 320 nm region. The excitation wavelength was 300 nm. The fluorescence spectra consists of two broad bands, one centered around 340 nm, the other around 475 nm. For all tissue samples, the ratios of the emission intensity at 340 nm to the intensity at 440 nm (for 300 nm excitation) and the ratio of the emission intensity at 383 nm to 460 nm (for 320 nm excitation) was calculated. The 340/440 nm emission ratio for 21 of the 22 malignant samples was found to be greater than 12 while for all the non-malignant tissues, the ratio was under 11. For the 383/460 nm emission ratio, most (12 of 18) malignant samples had a ratio less than 1, while most (8 of 10) non-malignant samples had ratios greater than 1. Additional studies were performed on 65 cancerous and 24 normal GYN tract tissue samples. Steady state excitation and emission spectral measurements were performed for excitation/emission in the UV and blue regions of the spectrum. Again, the ratio of the 340 nm emission intensity to the 440 nm emission intensity (when excited by 300 nm light) was found to be a consistent indicator of the presence of malignancy in the tissue. Using an intensity ratio of 11.5 as a criteria to characterize the tissue samples, a sensitivity of 0.97 and a specificity of .875 was achieved when compared to the gold standard of pathology.

2.4 Aerodigestive Tract Tissue

The ability of fluorescence spectroscopy to monitor molecular activity can be used to study the effects of therapeutic agents on malignancy. Squamous cell carcinoma of the aerodigestive tract is an ideal system to investigate optically. Retinoic acid has been evaluated as a chemopreventive agent for these neoplasms in the aerodigestive tract. Fluorescence spectroscopy was employed to monitor the antitumor effects of retinoids on Multicellular Tumor Spheroids (MTS).^{10,17} Emission and excitation spectra were measured on retinoid treated and non-treated MTS. Reproducible differences in the treated and non-treated MTS spheroids were observed. Spectroscopic differences were observed in emission spectra with the samples excited at 340 nm and in excitation spectra with the

emission intensity measured at 450 nm. These differences are associated with native fluorophors; NADH, flavins, and tryptophan. The ratio of the emission intensity at 340 nm to the intensity at 440 nm was significantly lower for the retinoid treated group (mean value 10.8) as compared to the untreated group (mean value 13.56).

The ability to identify subclinical neoplastic disease of the aerodigestive tract could significantly contribute to cancer screening. Our recent studies, in collaboration with Memorial Sloan Kettering Cancer Center, have demonstrated the use of fluorescence spectroscopy in monitoring tumor growth. Tissue autofluorescence was used a biomarker for monitoring changes in *N*-nitrosamine benzyl amine (NMBA) induced premalignant and malignant tumors in rats.¹¹ Significant differences between the NMBA exposed and control groups was noted in both excitation and emission scans. The excitation spectra (measuring emission at 380 nm) showed two major peaks at 290 nm and 330 nm. For the control samples, the average ratio of the intensity at 290 nm to the intensity at 330 nm was 1.12 ± 0.04 . The NMBA exposed group showed a significant decrease in the 330 nm emission intensity relative to the 290 nm emission intensity.

3. RAMAN SPECTROSCOPY OF TISSUE

NIR-Raman spectroscopy has potential to provide a new diagnostic technique for monitoring tumor growth in tissue. NIR-Raman spectroscopy has several advantages: (1) it yields spectra with sharp well defined features; (2) it can locate tumors with sub millimeter accuracy; (3) the spectra are independent of the size or shape of tissue sample and; (4) use of endoscopes or needle based fiber optic probes can help to investigate internal organs. The research on near Infrared Fourier Transform (IR FT) Raman spectroscopy as applied to tissue is summarized in the following section.

3.1 Raman Spectroscopy of Breast Tissue

NIR Raman spectroscopy was first applied to cancer diagnosis by Alfano *et al.*¹³ A Nd:YAG laser, with 1 watt of output power at 1064 nm, was used to acquire the Raman spectra of normal breast tissue, benign and malignant tumors. Raman spectra were measured from 700 to 1900 cm⁻¹. Normal, benign and malignant spectra are shown in Figure 5. The Raman spectrum of normal tissue showed four characteristic vibrational frequencies at 1078, 1300, 1445 and 1651 cm⁻¹. The Raman spectrum from benign tumors showed three vibrational frequencies at 1240, 1445 and 1659 cm⁻¹ while the malignant spectra showed only two frequencies at 1445 and 1651 cm⁻¹. Additionally, the relative intensity of the 1445 cm⁻¹ emission was larger compared to the 1651 cm⁻¹ emission intensity for the normal tissue (≈ 1.25) as compared to benign (≈ 0.93) or malignant (≈ 0.87) tumors. The Raman spectra data for breast tissue is summarized in Table I. The assignment of the Raman frequencies is tentative and requires further research.

3.2 Raman Spectroscopy of GYN Tissue

The use of NIR FT Raman spectroscopy as a diagnostic tool for the detection of GYN tract cancer was demonstrated.¹² A Nd:YAG laser emitting 1 watt of power at 1064 nm was used to acquire the Raman spectra from 700 cm⁻¹ to 1900 cm⁻¹ from normal and malignant GYN tissue samples. The samples consisted of cervix, uterus, endometrium or ovary tissues. All samples were divided into two pieces; Raman spectra was acquired from one part, while the other part was sent to pathology for evaluation. The samples were irregularly shaped slices. Each sample was scanned over a 6 mm² area with a spatial resolution less than 1 mm.

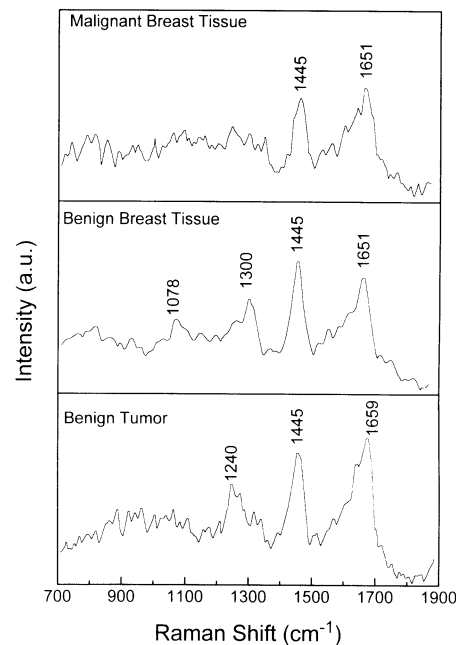


Figure 5. Raman spectra of normal breast tissue, benign tumor and malignant breast tumor.

Differences were found in the Raman spectra of normal and malignant tissues although the nature of the differences depended on the tissue type. The Raman spectra for cervical benign, normal and malignant tissue are shown in Figure 6.

The Raman spectra of normal cervical tissue had peaks at 1657, 1445, 1262 and 934 cm⁻¹. The Raman spectra of the cancerous samples did not show the 934 cm⁻¹ emission, and the 1262 cm⁻¹ consisted of a broad band rather than a distinct peak. For the normal samples the intensity of the 1657 cm⁻¹ was greater than the 1445 cm⁻¹ line ($I_{1657} > I_{1445}$), while for cancerous tissue the 1657 cm⁻¹ was weaker ($I_{1657} < I_{1445}$). The Raman spectra data for GYN tract tissue is summarized in Table II. The assignment of the Raman frequencies is tentative and requires further research.

Table I. Differences in NIR-FT Raman spectra for benign tissue, benign tumor and malignant tumor of breast tissue between 700 cm⁻¹ to 1900 cm⁻¹

Tissue	Benign tissue	Benign tumor	Malignant tissue	Tentative assignment
Raman frequency	1651	1659	1651	Protein: Amide I, Collagen and Lipid, C=O stretching; C=C stretching from hydrocarbon region
	1445	1445	1445	Protein/Lipid, CH ₂ scissoring deformation
	1300-1240	1240		Protein/Lipid, CH ₂ ,CH ₃ , twisting
	1079			Protein: Amide III Lipid: C-C stretch
Relative intensity	$I_{1445} > I_{1651}, I_{1079} < I_{1445} < I_{1659}$	$I_{1445} < I_{1651}$	$I_{1300} < I_{1445} < I_{1651}$	
Intensity ratio	1.25 (0.09)	0.93 (0.03)	0.87 (0.05)	

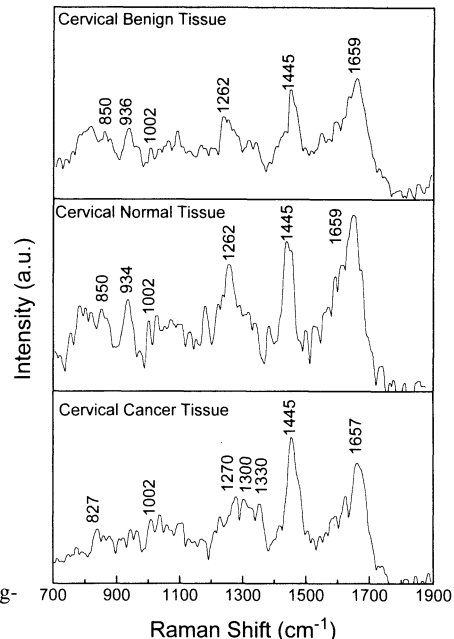


Figure 6. Raman Spectra of benign, normal and malignant cervical tissue.

The results of this work show that Raman spectroscopy of tissues can be used both to diagnose malignancy and to improve our understanding of the differences in normal and cancerous tissues.

This Research was funded by Mediscience Technology Corp. We wish to acknowledge our coworkers who performed the work reviewed in this paper: C.H. Liu, B. Das, W.

Table II. NIR-FT Raman spectra from GYN tract tissues

Tissues	Cancer				Benign /normal				Tentative assignment
	Cervix	Uterus	Endo	Ovary	Cervix	Uterus	Endo	Ovary	
Raman frequency	1657 VS	1659 VS	1655 VS	1651 VS	1659 VS	1659 VS	1656 VS	1659 VS	Protein: Amide I, Collagen and Lipid. C=O stretching; C=C stretching from hydrocarbon region
	1445 VS	1445 VS	1450 VS	1453 VS	1445 VS	1453 VS	1445 VS	1445 VS	Protein/Lipid, CH ₂ scissoring deformation
	1270- 1330 W	1240- 1330 W	1247- 1270 VW		1262- S	1262 VS	1262- S	1262- W	Protein: Amide III mixture Lipid: CH ₂ twisting with =C-H in-plane deformation Monosaccharides (e.g. D-Glucose), C(6)-H ₂ CH ₃ , COH
Relative intensity	I ₁₆₅₇ < I ₁₄₄₅	I ₁₆₅₅ > I ₁₄₄₅	I ₁₆₅₉ > I ₁₄₄₅		I ₁₆₅₉ > I ₁₄₄₅	I ₁₆₅₆ > I ₁₄₄₅	I ₁₆₅₉ > I ₁₄₄₅		

Sha-Glassman, A, Pradhan, Y. Yang, G.C. Tang, S. Lubicz, S.P. Schantz, H.E. Savage and M. Bessler.

REFERENCES

1. A.E. Profio and O. Balchum, Fluorescence diagnosis of cancer. in "Methods in Porphyrin Photosensitization", D. Kessel ed., Plenum, New York (1985).
2. R.R. Alfano, D. Tata, J. Cordero, P. Tomashevsky, F. Longo and M.A. Alfano, Laser induced fluorescence spectroscopy from native cancerous and normal tissue, *IEEE J. Quantum Electron.* 20:1507-1511 (1984).
3. R.R. Alfano, G.C. Tang, A. Pradhan, W. Lam, D.S. Choy and E. Opher, Fluorescence spectra from cancerous and normal human breast and lung tissue, *IEEE J. Quantum Electron.* 23:1806 (1987).
4. G.C. Tang, A. Pradhan and R.R. Alfano, Spectroscopic differences between human cancer and normal lung and breast tissues, *Lasers in Surgery and Medicine* 9: 290-295 (1989).
5. G.C. Tang, Asima Pradhan, Wenling Sha, J. Chen, C.H. Liu, S.J. Wahl and R.R. Alfano, Pulsed and CW laser fluorescence spectra from cancerous, normal and chemically treated human breast and lung tissues, *Applied Optics* 28:2337 (1989).
6. Y. Yang, G.C. Tang, M. Bessler and R.R. Alfano, Fluorescence spectroscopy as a photonic pathology method for detecting colon cancer, *Lasers in the Life Sci.* 6:259-276 (1995).
7. R.E. Petras, R.R. Kortum, L. Tong, M. Fitzmaurice, M. Feld and M. Sivak, Fluorescence spectroscopy of colonic adenomas: implications for an endoscopic laser diagnostic system. *Gastrointest. Endosc.* 35:181 (1989).
8. W. Sha Glassman, C.H. Liu, G.C. Tang, S. Lubicz and R.R. Alfano, Ultraviolet excited fluorescence spectra from non-malignant and malignant tissues of the gynecological tract, *Lasers in the Life Sciences* 5:49 (1992).
9. N. Ramanujam, M.F. Mitchell, A. Mahadevan, S. Thomsen, E. Silva and R. Richards-Kortum, Fluorescence spectroscopy: A diagnostic tool for cervical intraepithelial neoplasia (CIN), *Gynecologic Oncology*, 52:31-38 (1994).
10. G.C. Tang, H.E. Savage, M. Silverberg, P.G. Sacks, V. Ried, S.P. Schantz and R.R. Alfano, Native fluorescence spectroscopic detection of the effects of chemotherapeutic retinoids on a cancer model of the aerodigestive tract, in: "Optics for protection of man and environment against natural and technological disasters", G. von Bally and H. I. Bjelkhagen ed. Elsevier Science Publisher, Amsterdam (1993).
11. R. Glasgold, M. Glasgold, H. Savage, J. Pinto, R.R. Alfano and S. Schantz, Tissue autofluorescence as an intermediate endpoint in NMBA-induced esophageal carcinogenesis, *Cancer Letters*, 82,33 (1994).
12. C.H. Liu, B.B. Das, W.L. Sha Glassman, G.C. Tang, K.M. Yoo, H.R. Zhu, D.L. Akins, S.S. Lubicz, J. Cleary, R. Prudente, E. Celmer, A. Caron and R.R. Alfano, Raman, fluorescence, and time-resolved light scattering as optical diagnostic techniques to separate diseased and normal biomedical media, *J. Photochem. Photobiol. B: Biol.* 16:187-209 (1992).
13. R.R. Alfano, C.H. Liu, W.L. Sha Glassman, H.R. Zhu, D.L. Akins, J. Cleary, R. Prudente, and E. Celmer, Human breast tissue studied by IR-Fourier transform Raman spectroscopy, *Lasers Life Sci.* 4:1-6 (1991).
14. C.H. Liu, B.B. Das, W.L. Sha Glassman, G.C. Tang, H.R. Zhu, D.L. Akins, S.S. Lubitz, J. Cleary, R. Prudente, E. Celmer, E. Caron, and R.R. Alfano, NIR Raman and fluorescence spectroscopies diagnose cancer, *SPICE Proc.* 1887:188-194 (1993).
15. R.P. Rada, J.J. Borage and M.S. Feld, Near infrared Fourier Raman spectroscopy of human artery, *Spectrochim. Acta, Part A*, 47:509 (1991).
16. C.R. Kapadia, F.W. Cutruzzola, K.M. O'Brien, M.L. Stetz, R. Enriquez and L.I. Deckelbaum, Laser induced fluorescence spectroscopy on human colonic mucosa, *Gastroenterology*, 99:150 (1990).
17. M.B. Silverberg, H.E. Savage, G.C. Tang, P.G. Sacks, R.R. Alfano, S.P. Schantz, Detecting retinoic acid - induced biochemical alterations in squamous cell carcinoma using intrinsic fluorescence spectroscopy, *Laryngoscope*, 104:278 (1994).

IN VIVO APPLICATION PD-PORPHINE FOR MEASUREMENT OF OXYGEN CONCENTRATIONS IN THE GUT

M. Sinaasappel, M. van Iterson, and C. Ince

Department of Anaesthesiology Academic Medical Centre
University of Amsterdam, The Netherlands

INTRODUCTION

Adequate measurement of microcirculatory tissue oxygen concentrations *in vivo* is essential for further understanding of determinants of cellular respiration under normal and pathological conditions. Because the oxygenation of tissue primarily takes place in the microcirculation, techniques need to be developed which are applicable in the arterioles, capillaries and venules *in vivo*. Conventionally such types of measurements have been made by use of oxygen electrodes and spectrophotometry of the haemoglobin molecule. Spectrophotometrically measured changes in the absorption spectrum of the haemoglobin molecule determines the ratio of the amount of oxy- and deoxy-hemoglobin. This method gives a qualitative measure of the amount of available oxygen but cannot give quantitative information about the amount of dissolved oxygen in the plasma. Oxygen electrodes on the other hand provide quantitative measurements but are too big to measure at the microcirculatory level and if inserted into the tissue disrupt the microcirculatory environment. These constraints have led to the development of alternative methods. One of the most promising techniques in this respect has been the use of oxygen dependent quenching of fluorescent and phosphorescent dyes (Sanders 1995, Wilson 1991, Sinaasappel and Ince 1996). In such measurements the decay time of either fluorescence or phosphorescence following excitation by a light pulse is oxygen dependent and described by the Stern-Volmer relation. This time resolved technique is very suitable for use *in vivo* because many of the problems encountered with intensity measurements, such as the absorption and scattering of light by tissue components, are eliminated. One such technique has been developed by Wilson and co-workers (Wilson 1991) and makes use of the oxygen dependent quenching of phosphorescence properties of Pd-Porphine compounds. In this technique Pd-Porphine is bound to albumin, making a large molecular complex which confines it to the vascular compartment when injected intravascularly in living animals. Because the technique is optical it can be applied macroscopically as well microscopically. Use of a fibre optic system measures the oxygen concentration over an area of about 1 cm² providing a signal which is an average of the different oxygen concentrations of the arterioles and venules in that area (Pawlowski 1992).

Microscopical application of the technique makes use of an intravital microscope facilitating measurements of the oxygen concentration in individual vessels (Torres de Filho 1993).

In this study we present results from macroscopic measurements in a mechanically ventilated pig undergoing hemorrhagic shock following resuscitation using the phosphorimeter we developed in conjunction with calibration measurements (Sinaasappel 1995) as well as results from microscopical measurements using an intravital microscopical set-up we recently developed.

MATERIALS AND METHODS

Quenching of Phosphorescence

When a molecule excited to its lowest triplet state collides with an oxygen molecule, the excitation energy can be transferred. As a result of this energy transfer the triplet state of the molecule is depopulated. This process called quenching results in a diminishing of the intensity and decay time of the emitted light. The relation between the quenched phosphorescence and the oxygen pressure is described by the Stern-Volmer relation

$$\frac{\tau_0}{\tau} = 1 + \tau_0 k_q [O_2]$$

where τ_0 is the decay time in the absence of oxygen, τ the decay measured in the presence of $[O_2]$ and k_q the quenching constant.

The Setups

The macroscopic phosphorimeter has been described elsewhere (Sinaasappel and Ince 1996).

A schematic drawing of the intravital microscope (BH2-UMA Olympus, Japan) we developed is shown in Figure 1.

The animal is placed on a movable stage. Two types of fluorescence/phosphorescence measurements can be done with this set-up; 1) continuous illumination with an Hg lamp and imaging of the fluorescence or phosphorescence with the ICCD camera or 2) time resolved measurements using the flash lamp and photomultiplier (PMT). To be able to measure the decay time of a single vessel an adjustable slit is positioned in front of the PMT and in the image plane of the microscope. The size of the opening of the slit is visualised by illumination of the slit by a lamp and focusing the image of the slit on the glass which lies on the preparation. Now the slit is visible on the ICCD camera and can be marked on the monitor. Next, the vessel to be measured is focused and visualised on the ICCD. The vessel and the animal are positioned so that the slit and the vessel coincide. The objective used is a 20 X Olympus (Olympus, Japan) objective with a long working distance (1 cm).

200 mg Pd *meso*-tetra [4-carboxyphenyl] porphine is dissolved in 3ml DMSO. This solution is added to a 50 ml saline containing 0.9% NaCl and 40 gr/l bovine serum albumin (BSA) which is brought to a pH of 8 using Trism base. Finally, the solution is buffered to a pH of 7.4 using HCl. In both animals 12 mg/kg body weight Pd-porphine is injected intravenously.

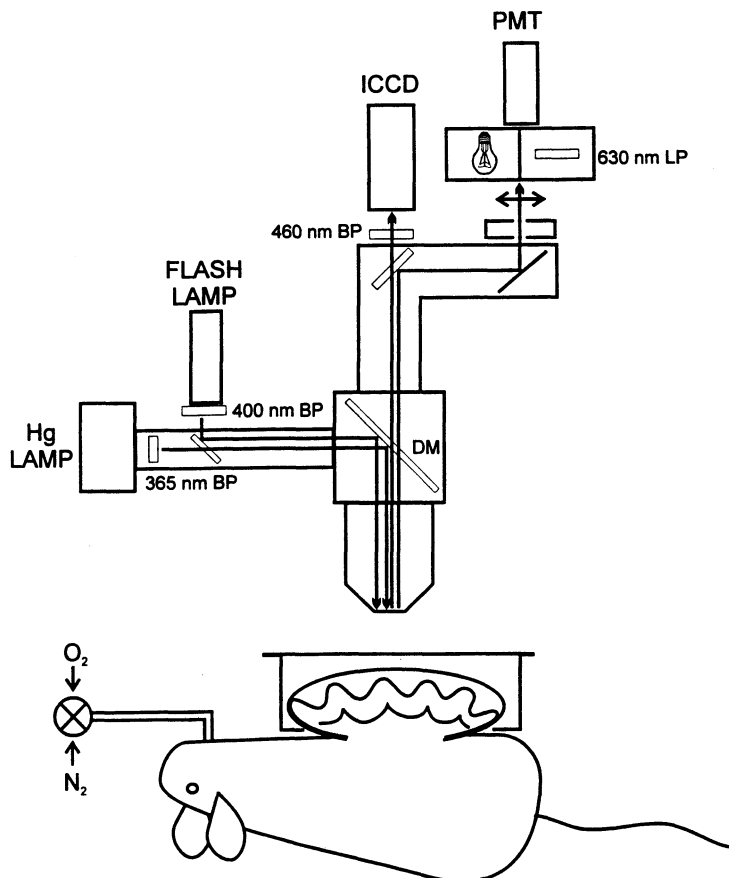


Figure 1. Shows the intravital microscope. The Hg lamp in combination with the ICCD camera is used for imaging of endogenous NADH fluorescence; the flash lamp excites the Pd-porphine. The phosphorescence signal is measured by the PMT after which the signal is amplified and digitized by a 1MHz A/D converter. The decay time is calculated using a least square fitting procedure.

The Animal Models

In this study two animal models are illustrated. In both experiments the quenching of Pd-Porphine phosphorescence was measured in the serosa of the ileum.

In the first application on a pig, macroscopic measurements were performed on a hemorrhagic shock model followed by resuscitation. Shock was induced by withdrawal of 400 ml blood in four steps with 10 min between each step. After a stabilisation period of 30 min the animal was resuscitated by intravenous administration of 1200 ml Hartmann solution. Experiments were performed on 15 kg Yorkshire pigs under complete anaesthesia. The pigs were sedated with ketamine (20mg/kg) and anesthetized with pentobarbital (5mg/kg). A tracheotomy was performed and the pig was connected to a Dräger AV1 ventilator and ventilated with a mixture of 33% O₂ and 67% N₂. A catheter was placed in the ear vein for administering the anesthetics. The anaesthesia was maintained by continuous administration of fentanyl (bolus 15 :g/kg; 15:g/kg/h), dormicum (bolus 0.75 mg/kg; 1.5 mg/kg/h) and vecuroniumbromide (bolus 1 mg/kg; 0.75 mg/kg/h). Catheters were placed in the brachial artery to measure blood pressure and heart rate. A Swan Ganz catheter

was introduced in the right jugular vein for measurement of the cardiac output and central temperature. A catheter in the left jugular vein was used for the blood withdrawal and resuscitation. The oxygen concentration was measured in the gut by use of the quenching of Pd-Porphine phosphorescence. Blood samples were taken from the brachial artery and the right pulmonary artery for determination of respectively the arterial and mixed venous blood gasses. A length of ileum was extracted from the peritoneal cavity via a midline laparotomy. The fibre of the phosphorimeter and a thermocouple were placed on the serosa of the last 10cm of the ileum. The Pd-Porphine measurements were performed every 20 seconds. 25 decay curves were averaged before the decay time was estimated. Blood gasses were determined every 15 min.

In the second application a microscopic measurement was performed on male Wistar rats which were anesthetized by continuous intravenous Nembutal infusion and mechanically ventilated with 33% oxygen and 67% nitrogen. The intestines were placed in a special chamber according to Itoh 1994. This chamber provided control of temperature and humidity by bathing the intestine in saline kept at 38 °C. The serosa of the ileum was chosen for measurement of the oxygen concentration using Pd-Porphine phosphorescence.

RESULTS AND DISCUSSION

Figure 2 shows the time course of the pO_2 and temperature on the ileum of the pig during a hemorrhagic shock and resuscitation. Figure 2 shows that initially the oxygen pressure as measured with the quenching of Pd-Porphine is higher than the mixed venous blood gasses. Withdrawal of blood causes the oxygen pressure in the gut to drop to a level below the mixed venous pO_2 . A thermocouple placed on the surface of the gut shows a clear decrease of the gut temperature during blood withdrawal, indicating that the flow in the gut is reduced. This, combined with the

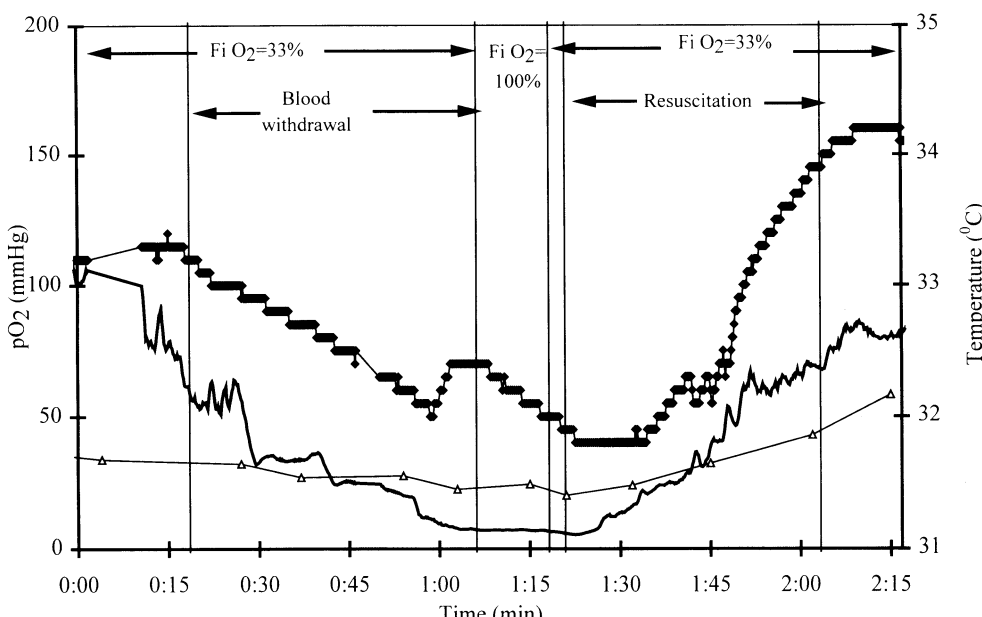


Figure 2. Shows the time course of pO_2 as measured with the Pd-porphine (C), the mixed venous pO_2 (●) and the temperature (—) on the ileum of a mechanically ventilated pig, during hemorrhagic shock and resuscitation.

latter observation suggests that the systemic blood flow is redistributed away from the gut as occurs during compensatory shock. In the shock phase the FiO_2 was increased to 100% to see whether extra oxygen would improve the oxygenation of the gut. Although the rise in the temperature indicates an improvement in the flow neither mixed venous bloodgasses or gut pO_2 showed any improvement. After the shock phase the pig is resuscitated with a crystalloid (75 ml/kg). As Figure 2 shows the oxygen pressure and temperature rise again, the oxygen pressure in the gut is returned to normal and above the level of the mixed venous oxygen pressure indicating a recovery from the hemorrhagic shock.

In a previous study we made macroscopic measurements of the pO_2 in the intestine using the quenching of phosphorescence during shock (Sinaasappel 1995). The measurement of oxygen pressures in single blood vessels, however, should give more detailed insight into the mechanisms surrounding shock and gut ischemia. Therefore we modified an intravital microscope as shown in Figure 1 to determine the oxygen pressure in arterioles and venules of the intestine of a rat using the quenching of Pd-Porphine phosphorescence.

Figure 3 shows the result of two experiments performed on the same rat. The slit was placed over two types of vessels, a vessel with a approximate diameter of 60 μm and a vessel with a diameter of 30 μm . The size of the slit was 200 $\mu\text{m} \times 30\mu\text{m}$. In both experiments shock was induced by exchange of O_2 by N_2 in the ventilation gases. Figure 3 shows that the small vessel has initially a lower pO_2 than the bigger one. Figure 3 also shows that the response of the big vessel is much faster than the small one.

ACKNOWLEDGMENTS

M. Sinaasappel is supported by the Netherlands Science Foundation (grant No. 900-519-110)

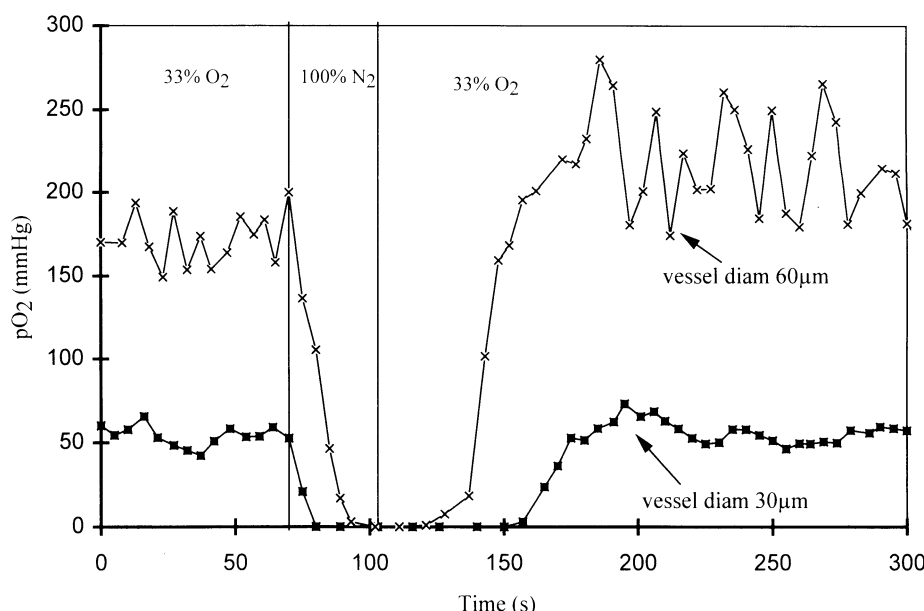


Figure 3. Shows the pO_2 in two single vessels (30 μm -60 μm diameter) of the ileum of a mechanically ventilated rat before during and after 30 s of 100% N_2 ventilation.

REFERENCES

- Green, T. J., D. F. Wilson, J. M. Vanderkooi, and S. P. DeFeo. Phosphorimeters for analysis of decay profiles and real time monitoring of exponential decay and oxygen concentrations. *Anal. Bioch.* 174: 73-79, 1988.
- Itoh, T., K. Yaegashi, T. Kosaka, T. Kinoshita and T. Morimoto. *In vivo* visualisation of oxygen transport in microvascular network. *Am. J. Physiol.* 267 (Heart Circ. Physiol. 36): H2068-H2078, 1994.
- Pawlowski, M. and D. F. Wilson. Monitoring of the oxygen pressure in the blood of live animals using the oxygen dependent quenching of phosphorescence. *Adv. Exp. Med. Biol.* 316: 179-185, 1992.
- Sanderse, R. Imaging of oxygen concentrations in single cells. in: fluorescence lifetime as a contrast mechanism in confocal imaging. Ph.D. Thesis University of Utrecht, ISBN no. 90-393-0648-6, pp. 45-53, 1995
- Sinaasappel, M., C. Ince, J.P. van der Sluijs and H. A. Bruining. New phosphorimeter for measurement of oxygen pressures using Pd-porphine phosphorescence. *Adv. Exp. Med. Biol.* 361: 105-110, 1995.
- Torres Filho, I. P. and M. Intaglietta. Microvessel pO₂ measurements by phosphorescence decay method. *J. Appl. Physiol.* H1434-H1438, 1993.
- Wilson, D. F., A. Pastuszko, J. E. DiGiacomo, M. Pawlowski, R. Schneiderman, and M. Delivoria-Papadopoulos. Effect of hyperventilation on oxygenation of the brain cortex of newborn piglets. *J. Appl. Physiol.* 70: 2691-2696, 1991.

LASER SCANNING CONFOCAL FLUORESCENCE MICROSCOPY OF CELL FUNCTION

John J. Lemasters

Laboratories for Cell Biology
Department of Cell Biology and Anatomy
University of North Carolina at Chapel Hill
Chapel Hill, North Carolina 27599

HETEROGENEITY OF CELLULAR EVENTS

The response of cells to various stimuli may often be quite heterogeneous. Responses may vary both in magnitude and time course. Thus, bulk measurements may not be representative of events in individual cells. For this reason, the study of individual cells as they respond to imposed stresses and stimuli is desirable. Recent advances in microscope optics, video cameras, computer technology and fluorophore chemistry increasingly permit such measurements of single cell physiology.

FORMATION OF HIGHLY RESOLVED OPTICAL SECTIONS BY CONFOCAL MICROSCOPY

Conventional wide-field fluorescence microscopy creates an image with an effective depth of field at high power of 2-3 μm . Since the lateral resolving power of optical microscopy is 0.2 μm , superimposition of detail within this thick plane of focus obscures structures that might otherwise be resolved. Additionally in specimens more than a few μm thick, fluorescence from out-of-focus planes degrades image quality, creating diffuse halos around objects under study. Confocal microscopy eliminates these distortions to the in-focus image and produces images whose depth of field is less than 1 μm while simultaneously rejecting out-of-focus light. Together the rejection of out-of-focus light and the small depth of field combine to produce images that are remarkably detailed. The improvement in useful resolution is akin to that of computerized axial tomography over conventional radiography. Recently, ultraviolet laser scanning confocal microscopes have become commercially available for applications with UV-excited fluorophores.

A laser scanning confocal microscope is a highly complex instrument incorporating sophisticated light optics, electronics, computers and mechanical devices, but the principle

of confocal microscopy as originally described by Minsky (1961) is quite simple (Figure 1). A beam of light reflected off a dichroic mirror is focused to a small spot in the specimen. Typically, spot diameter is diffraction limited, or about $0.2\text{ }\mu\text{m}$ for a high power oil immersion objective lens. Light fluoresced or reflected by the specimen is focused by the objective lens onto a pinhole aperture. In-focus light passes through the aperture to a light detector beyond, but light originating from above and below the focal plane strikes the wall of the aperture and is not transmitted to the photodetector (Figure 1). Thus, the photodetector “sees” light from only a very narrow plane of focus. To generate two-dimensional images, the beam is moved or scanned across the specimen using vibrating mirrors in the light path. The scan generator moves the light path across the specimen and also “descans” the returning light so that it can be focused on a stationary pinhole. In most scanning confocal microscopes, the output of the photodetector is stored in computer memory and then displayed on a monitor as the scanned image (White *et al.*, 1987; Wilson, 1990).

PRECAUTIONS AGAINST PHOTOBLEACHING AND PHOTODAMAGE

Confocal microscopy images light from a thin confocal slice rather than from the entire specimen. Thus to produce equivalent signal intensity, greater excitation energies must be used, compared to conventional wide field fluorescence microscopy. As a result, photobleaching and photodamage are greater concerns in confocal microscopy, especially for studying living cells where serial measurements are usually desired. However, if stable fluorophores are employed while operating the confocal microscope at low laser power, high detector sensitivity, and maximum objective numerical aperture (NA), then literally hundreds of images can be collected with little adverse effect.

A high quality oil or water-immersion lens is essential for high resolution studies. Light transmission through an objective lens varies with the square of the NA. Light transmission also depends on the number of lens elements and type of glass. Thus, empirical measurement of light transmission by various lenses may be necessary for some applications, especially for ultraviolet applications since ordinary glass does not transmit the ultraviolet spectrum. Most laser scanning confocal microscopes have a ‘zoom’ feature that permits magnification to be varied over a 5-fold or greater range. Increasing zoom magnification

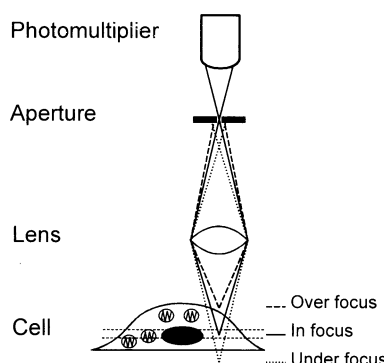


Figure 1. Principle of confocal microscopy. Fluorescence from the specimen is focused by the objective lens through a pinhole aperture to a photomultiplier. Fluorescence from out-of-focus planes above and below the specimen plane strikes the walls of the pinhole aperture and is not transmitted. Thus, only fluorescence arising from the in-focus specimen plane is detected by the photomultiplier.

concentrates laser energy into smaller volumes of the sample and increases the rate of photobleaching and photodamage in the imaged region. Thus, zooming should be the minimum needed consistent with the resolution requirements of the experiment. Empty magnification exceeding the resolving power of the microscope system (maximally about 0.2 μm) should be especially avoided since this serves only to accelerate photobleaching without any improvement of the image. High NA (1.3-1.4) objective lenses that produce initial magnifications of 40 to 60X are especially useful for confocal microscopy since at the same zoom settings these lenses produce as much as 6 times less photodamage than 100X lenses. High NA water immersion objective lenses are now available from several manufacturers for use in confocal microscopy. Water immersion lenses are useful for imaging deep into aqueous samples. Such lenses avoid aberrations and distortions that are otherwise created by oil immersion optics.

For most biological applications, laser power exceeds by orders of magnitude the minimum required for excellent image quality. Thus, laser intensity should be routinely attenuated by 100 to 3000-fold by using neutral density filters and by reducing the power setting of the laser. Even so, fluorophores like fluorescein and acridine orange may still photobleach or cause phototoxicity. If possible, these fluorophores should be avoided, since other fluorophores, such as Texas red and rhodamine dyes, are quite stable under the same conditions.

Confocal microscopy produces thin optical sections through thick specimens. For high NA lenses, the thickness of the confocal sections can achieve a theoretical limit of about 0.5 μm . Section thickness decreases as the diameter of the detector pinhole decreases (Figure 2). Not all applications require the thinnest possible confocal slice. In this instance, sensitivity can be improved by opening the pinhole aperture, since doubling the diameter of the pinhole quadruples sensitivity, but only about doubles the thickness of the optical section (Figure 2). Most laser scanning confocal microscopes are equipped with variable pinholes for this purpose. With light-sensitive specimens, a larger pinhole setting may be used so that greater laser attenuation can be employed. Conversely, to decrease section thickness and optimize resolution in the z-axis, pinhole diameter can be decreased. However, below a minimum pinhole diameter, the thickness of confocal sections no longer decreases as the pinhole becomes smaller, although image intensity continues to decrease (Figure 2). Thus, overly small pinhole diameters reduce sensitivity substantially without increasing resolution.

CELL PREPARATION

For viewing by confocal microscopy, cells should be attached to number 1½ glass coverslips, a designation which means that the slips are 170 μm thick. Since cells usually adhere poorly to glass, coverslips should be treated with a material to improve adherence,

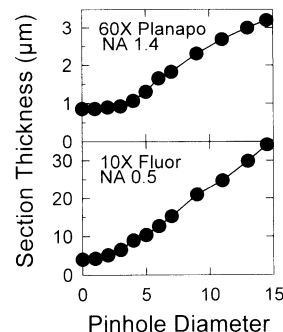


Figure 2. Pinhole size and thickness of confocal sections. The thickness of confocal sections was determined for a 60X NA 1.4 planapochromat objective lens and 10X NA 0.5 Fluor lens as a function of pinhole diameter in a Bio-Rad MRC-600 laser scanning confocal microscope operating in the reflectance mode. Pinhole diameter is given in arbitrary units corresponding roughly to the diameter in millimeters minus 1. After Lemasters *et al.* (1993)

such as polylysine, Type I collagen or laminin. Coverslips are first sterilized by rinsing in ethanol, followed by drying and placement inside plastic Petri dishes. One or two drops (about 100 µl) of poly-D-lysine (100,000 MW, 0.1 mg/ml), Type I collagen (1 mg/ml in 0.1% acetic acid) or laminin (0.1 mg/ml in tris-buffered saline) are spread out across the coverslips. After air-drying overnight, the coverslips are rinsed with buffer and cells are added in the usual fashion. Cells become adherent in 1-2 hours. For viewing, coverslips are mounted in a specimen chamber and placed on the stage of the confocal microscope. Usually, a microscope in an inverted configuration is used to permit easy access from above to the cell medium. Temperature regulation is generally needed using an electric heater or stream of conditioned air.

ENVIRONMENTALLY SENSITIVE FLUOROPHORES TO REPORT EVENTS IN SINGLE CELLS

Conventional bright field microscopy provides useful structural information but little biochemical and physiological data. For the latter, cells can be labeled with fluorophores whose fluorescence responds to a specific cellular characteristic, such as intracellular ion concentration or electrical potential. By loading cells with probes emitting light at different wavelengths, multiple parameters of interest can be measured simultaneously. Such measurements are non-destructive, allowing repeated sampling over time in living cells and tissues.

In laser scanning confocal microscopy, the excitation wavelength is determined by the type of laser used: 488 and 514 nm for argon lasers, 543 nm for helium-neon lasers; 488, 568 and 647 nm for argon-krypton lasers, and 351-365 nm for UV-argon lasers. The argon-krypton laser with three well separated emissions (blue, yellow and red) is perhaps the most useful of these lasers for biological applications. In particular, the 488 and 568 nm lines excite green-fluorescing dyes, like Fluo-3 and rhodamine 123, and red-fluorescing dyes, like tetramethylrhodamine methylester (TMRM) and propidium iodide. Emissions from these fluorophores can then be detected simultaneously using different photomultipliers. Simultaneous detection is a particular advantage for resolving compartmental changes where one probe identifies a compartment and the second measures the parameter of interest.

The number of useful fluorescent probes is large and growing. These fluorophores can be categorized into three broad groups: 1) probes of general cell function, such as cell viability and electrical potential; 2) markers of specific intracellular compartments, such as the mitochondrial and lysosomal compartments; and 3) probes of specific chemical species, such as ions, oxygen radicals and thiols. Table 1 shows a partial list of probes useful in confocal microscopy.

INDICATORS OF CELL VIABILITY

The classic indicator of cell death is nuclear labeling by trypan blue. Viable cells exclude this cationic dye, but after onset of cell death trypan blue enters and binds to nuclear DNA. Other cationic dyes, such as propidium iodide, behave identically to trypan blue in labeling non-viable cells (Jones and Senft, 1985). Since binding to DNA causes a large enhancement of propidium iodide fluorescence, fluorescence microscopy easily identifies non-viable cells. The enhancement of fluorescence is large enough that the progression of cell killing after injurious stresses can be followed by simple filter fluorometry (Nieminne *et al.*, 1992).

Table 1. List of useful fluorophores

Parameter	Fluorophore
<i>Probes of general cell function:</i>	
Cell Viability	Propidium iodide Ethidium homodimer PRO probes Fluorescein diacetate Calcein acetoxymethyl ester Rhodamine 123 Tetramethylrhodamine methylester
<i>Markers of subcellular compartments</i>	
Cell volume/topography	Calcein
Endosomes	Rhodamine microspheres
Lysosomes	Rhodamine-dextran Texas Red-dextran
Golgi	BODIPY-ceramide
Endoplasmic reticulum	Carbocyanine dyes
<i>Probes of specific chemical species:</i>	
Ca ²⁺	Indo-1 Fluo-3 Rhod-2
pH	SNARF-1
Mg ²⁺	Mag-Indo
Na ⁺	SBFI
K ⁺	PBFI
Glutathione	Monochlorobimane
Protein thiols	Monobromobimane
Oxygen radicals	Dichlorofluorescin Dihydrorhodamine 123 Dihydroethidium

Other fluorophores are retained by viable cells only to be released at the onset of cell death (Jones and Senft, 1985; Zahrebelski *et al.*, 1995). These polyanionic fluorophores, such as fluorescein and calcein, are loaded as their ester derivatives, which cross the plasma membrane and enter the cytoplasm. Here, esterase activity releases the free acid forms of the fluorophores, which cannot cross the plasma membrane and remain trapped in the cytoplasm. In theory, cells should retain these fluorophores until the onset of cell death. However, carriers in the plasma membrane can transport these anionic fluorophores out of the cells. Thus, dye retention may not be as reliable as dye exclusion as an indication of cell viability.

LABELING OF NEGATIVELY CHARGED CELLULAR COMPARTMENTS BY CATIONIC DYES

A negative membrane potential ($\Delta\Psi$) is characteristic of the plasma membrane and mitochondria. Lipophilic cationic fluorophores like rhodamine 123 and TMRM accumulate into negatively charged compartments in response to these membrane potentials (Johnson *et al.*, 1981; Emaus *et al.*, 1986; Ehrenberg *et al.*, 1988). At equilibrium, accumulation of monovalent fluorophores across a charged membrane is related to $\Delta\Psi$ by the Nernst equation:

$$\Delta\Psi = -60 \log F_{\text{in}}/F_{\text{out}}$$

where F_{in} and F_{out} are fluorophore concentrations inside and outside the membrane, respectively, and $\Delta\Psi$ is in mV. Thus, a 10 to 1 uptake ratio of a monovalent cationic fluorophore signifies a -60 mV gradient, a 100 to 1 signifies a -120 mV gradient, and so forth. By quantifying the intracellular distribution of fluorophore using confocal microscopy, one can measure the distribution of electrical potential within a cell and, in particular, identify highly negative structures like mitochondria.

For excitable cells, a plasma membrane $\Delta\Psi$ of -90 mV and a mitochondrial $\Delta\Psi$ of up to -150 mV are typical values. Since these $\Delta\Psi$'s are additive, mitochondria can be as much as 240 mV more negative than the extracellular space, which corresponds to a fluorophore concentration ratio of 10,000 to 1 inside mitochondria relative to the outside of the cell. With only a conventional 256 gray levels (8 bits) per pixel of memory, measurement of such large gradients on a linear scale is impossible. Sixteen bit systems or a non-linear (gamma) scale must be used instead (Chacon *et al.*, 1994). Gamma scales are based on a logarithmic transformation of the input signal that condenses a very large signal range into the 256 gray levels of video memory.

To determine the intracellular distribution of electrical potential, several steps are involved. Cells are first loaded with a monovalent cationic fluorophore (100-500 nM). After loading, a small amount of fluorophore (50-150 nM) should be maintained in the experimental buffer throughout to keep extracellular dye concentration constant and to maintain the equilibrium distribution of fluorophore inside the cells. The validity of measurement depends on ideal behavior by the fluorophore used. Some probes do not behave ideally. For example, rhodamine 123 binds non-specifically to the mitochondrial matrix, and its fluorescence is quenched as it accumulates (Emaus *et al.*, 1986). High matrix concentrations of rhodamine 123 also inhibit the oligomycin-sensitive mitochondrial F_1F_0 -ATPase that catalyzes ATP synthesis during oxidative phosphorylation. The methyl and ethyl esters of tetramethylrhodamine seem to lack these undesirable features and are more desirable for confocal imaging of electrical potential (Ehrenberg *et al.*, 1988; Farkas *et al.*, 1989).

In cells loaded with TMRM or other cationic fluorophore under conditions allowing equilibrium distribution in response to intracellular electrical gradients, confocal images are collected of the full range of fluorescence intensities, including fluorescence in the extracellular space. Average extracellular fluorescence intensity is divided into intracellular fluorescence on a pixel-by-pixel basis. The Nernst equation is then applied to each pixel to calculate electrical potential of each point within the cell relative to the extracellular space, and the data are displayed as a pseudocolor map showing intracellular distribution of electrical potential (Chacon *et al.*, 1994).

Figure 3 illustrates intracellular electrical potential measured in a cultured cardiac myocyte. In areas under the sarcolemma and in the nucleus, pseudocoloring shows an electrical potential of about -80 mV. Since the electrical potential of the extracellular medium is zero, sarcolemmal $\Delta\Psi$ is -80 mV, as expected for myocytes. Distributed throughout the cytoplasm are also found electronegative mitochondria. These mitochondria show heterogeneity of electrical potential. Heterogeneity is due to the fact that not all mitochondria extend completely through the confocal slice. Thus, fluorophore uptake for many mitochondria is underestimated. In Figure 3, mitochondrial electrical potential calculated by the Nernst equation was as great as -160 mV. Since cytosolic potential was -80 mV, the difference, -80 mV, represents a minimum estimate of mitochondrial $\Delta\Psi$.

VISUALIZATION OF SPECIFIC ORGANELLES

Many fluorophores label specific intracellular organelles. Because mitochondrial membranes have a high negative $\Delta\Psi$, cationic fluorophores like rhodamine 123 and tetra-

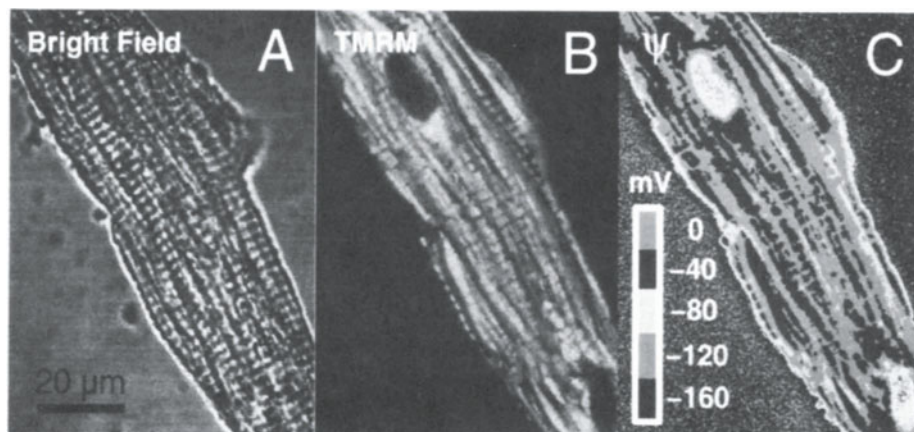


Figure 3. Electrical potential in a cardiac myocyte. The panels show a TMRM-loaded cultured adult rabbit cardiac myocyte. Panel **A** is a non-confocal transmitted light image. Panel **B** is a confocal fluorescence image obtained using gamma circuitry and 568 nm laser excitation. Panel **C** shows a processed image that is pseudocolored to show the intracellular distribution electrical potential. After Chacon *et al.* (1994). A color representation of this figure can be found facing p. 214.

methylrhodamine methylester brightly label mitochondria, as already discussed above. Dextran conjugates of rhodamine and other fluorophores are readily endocytosed and accumulate in lysosomes (Figure 4). Lysosomes do not digest these conjugates, and fluorescence can persist for many days (Gores *et al.*, 1989). Other organelle-specific fluorophores can also be used. For example, carbocyanine dyes label endoplasmic reticulum, and BODIPY-ceramide conjugates label the Golgi apparatus (Lee and Chen, 1988; Pagano *et al.*, 1991). By exciting with multi-line lasers, two or more probes may be imaged at once. Using a transmitted light detector, confocal fluorescence can also be simultaneously compared with conventional non-confocal brightfield images to show, for example, disintegration of lysosomes accompanying cell surface changes just prior to death of hypoxic hepatocytes (Figure 4).

The cytosolic compartment may be specifically labeled by incubating cells with calcein-acetoxyethyl ester at 37°C. After warm ester loading, calcein accumulates virtually exclusively into the cytosol and the nucleus. Membranous cytoplasmic organelles, especially mitochondria, exclude the fluorophore and appear as dark voids in the fluorescence (Figure 5) (Nieminens *et al.*, 1995). Co-loading cells with red-fluorescing TMRM confirms that the voids in the calcein fluorescence are indeed mitochondria. Occasionally, dark voids in the calcein fluorescence do not correspond to TMRM-labeled mitochondria. These structures represent other organelles, most likely lysosomes.

MITOCHONDRIAL PERMEABILITY TRANSITION

Opening of a very high conductance pore in the mitochondrial inner membrane with a molecular weight cut off of about 1500 daltons causes onset of the so-called mitochondrial permeability transition (Gunter and Pfeiffer, 1990). In addition to making the inner membrane permeable to small solutes, pore opening also causes mitochondrial depolarization and uncoupling of oxidative phosphorylation. In intact cells at the onset of the mitochondrial permeability transition, mitochondria release TMRM, which indicates depolarization, and

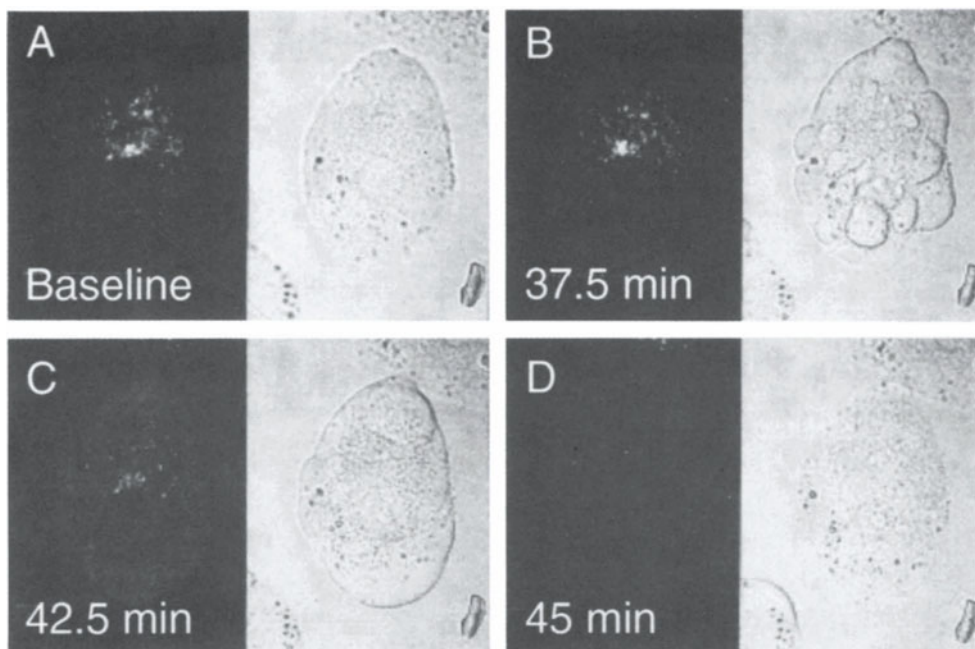


Figure 4. Disintegration of rhodamine-dextran-labeled lysosomes during chemical hypoxia. Transmitted light images (right) and confocal fluorescence images (left) were collected before and after chemical hypoxia with 2.5 mM KCN and 0.5 mM iodoacetate to a rhodamine-dextran-labeled rat hepatocyte. Note lysosomal breakdown in **C** causing diffuse release of rhodamine-dextran into the cytoplasm. In **D**, viability was lost after bleb rupture. After Zahrebelski *et al.* (1995).

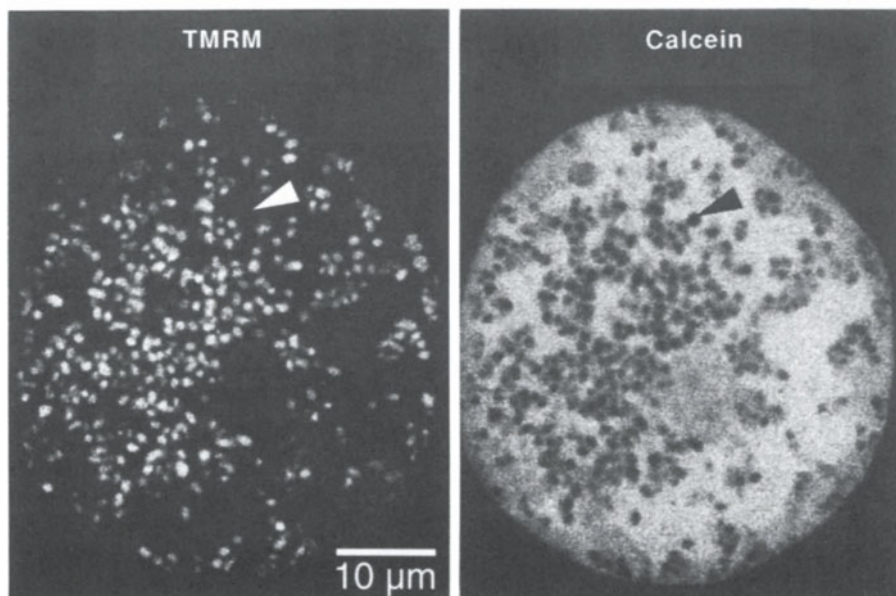


Figure 5. Cytosolic and mitochondrial fluorescence in a double-labeled cultured hepatocyte. A cultured rat hepatocyte was co-loaded with TMRM and calcein. Small dark voids in the green calcein image correspond to mitochondria in the red TMRM image. Occasional voids in the calcein fluorescence (arrowhead) are non-mitochondrial and are probably lysosomes. After Nieminen *et al.* (1995).

fill with calcein, which indicates permeability of the mitochondria to small solutes (Nieminens *et al.*, 1995; Zahrebelski *et al.*, 1995). Onset of the mitochondrial permeability transition may be an important event contributing to cell injury and death in hypoxic, toxic and reperfusion injury.

IMAGING CELL SURFACE TOPOGRAPHY AND VOLUME

Size, shape, and surface topography are basic features of cell structure. Confocal microscopy can provide this basic structural information for single living cells. The experimental strategy is to label cells with a fluorophore and then to collect serial confocal images through the entire thickness of individual cells. Subsequently, the serial images are reconstructed as a computer-generated volume rendering to display 3-dimensional structure. Calcein, whose fluorescence is independent of physiological changes in ion concentration and pH, is a useful probe for this purpose and is ester-loaded into cells, as described above (Chacon *et al.*, 1994; Zahrebelski *et al.*, 1995).

Figure 6 illustrates the reconstructed 3-dimensional image of a calcein-loaded cardiac myocyte after confocal serial sectioning and volume rendering. The reconstruction shows the myocyte as a branched cylindrical structure. Notable are rib-like surface corrugations that represent impressions of underlying mitochondria aligned along the sarcomeres. These structures were not recognized in the individual confocal sections, but only became evident in the 3-dimensional volume rendering. The 3-dimensional reconstructions rival scanning

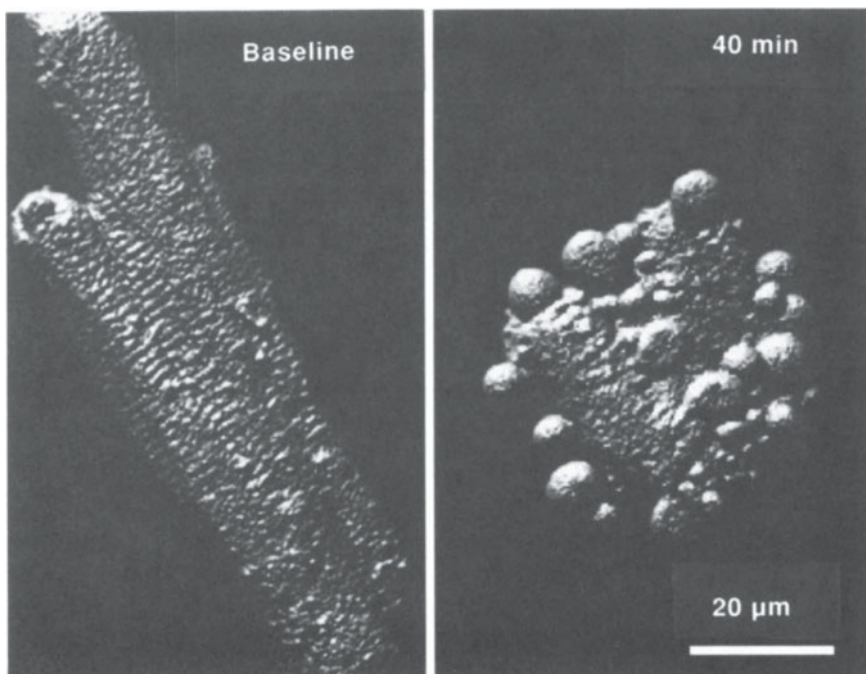


Figure 6. Volume rendering of a calcein-labeled myocyte. Serial confocal images were collected from a calcein-loaded adult rabbit cardiac myocyte before and after 40 minutes of chemical hypoxia. Volume renderings were created from the serial sections using contour-dependent shading to enhance perception of depth and surface detail. After Chacon *et al.* (1994).

electron micrographs in detail and clarity, but unlike scanning electron micrographs, these images can be collected repeatedly over time, as illustrated in Figure 6 for a myocyte subjected to hypoxia. Other information can be obtained from the renderings as well, particularly a quantification of cell volume.

RATIO-IMAGING OF ION-INDICATING PROBES

A number of fluorophores are now available to measure ions in individual living cells (Table 1). Typically these fluorophores are loaded as their membrane-permeant ester derivatives, as described above. Endogenous esterases release and trap the ion-sensitive free acid forms of the fluorophores into the cytosol and often inside organelles, especially mitochondria. Loading at 37°C promotes predominantly cytosolic loading, whereas loading at 4°C favors loading into both mitochondrial and cytosolic compartments (Nieminan *et al.*, 1995). At higher temperatures, cytosolic esterases are apparently so active that fluorophore esters cannot traverse the cytosol to the mitochondria without being hydrolyzed first. Low temperatures reduce esterase activity, permitting some esters to diffuse through the cytosol into mitochondria. Probe loading varies greatly between cell types, and optimal loading conditions must always be determined empirically.

Inside cells, fluorescence of ion-indicating fluorophores also depends on the amount of fluorophore present in the light path. To correct for variations in fluorophore concentration, a ratioing procedure may be used with certain fluorophores. Images are acquired at two different excitation or emission wavelengths, one that is ion-sensitive and one that is not (or whose fluorescence changes in the opposite direction). After background subtraction, the first image is divided by the second image on a pixel-by-pixel basis to form a so-called ratio image. For example, when SNARF-1 is excited at 568 nm, fluorescence emission at 640 nm increases as pH increases but emission at 585 nm remains the same (Chacon *et al.*, 1994). Thus, the ratio of emitted fluorescence at the two wavelengths is proportional to pH. Since fluorescence at both wavelengths is equally dependent on SNARF-1 concentration, the ratio becomes independent of fluorophore concentration. Therefore, such ratioing eliminates variations in the signal due to differences of path length, regional fluorophore concentration, dye leakage over time, photobleaching and accessible volume. Ratio images are then converted to maps of intracellular ion distribution using a standard curve, often using a pseudocolor display. Not all ion-indicating fluorophores can be ratioed, only those having ion-induced spectral shifts, such as Indo-1 for Ca^{2+} and SNARF-1 for pH.

When such probes are imaged by confocal microscopy, mitochondrial and cytosolic ion concentrations can be distinguished. For example, confocal imaging of SNARF-1 demonstrates marked heterogeneity of pH within cells (Figure 7). The pH of cytosolic and nuclear areas is about 7.2, whereas mitochondrial pH is close to 8. Thus, the gradient of pH across the mitochondrial membranes is 0.8 pH units, as predicted by Peter Mitchell's chemiosmotic hypothesis (Mitchell, 1966).

Ca^{2+} IMAGING

Fluo-3 and Rhod-2 are useful visible wavelength fluorophores for confocal imaging of free Ca^{2+} . The K_d of Fluo-3 for Ca^{2+} is about 400 nM, and its fluorescence increases 30-80-fold after binding (Minta *et al.*, 1989). Rhod-2 has a somewhat higher K_d and a smaller range of fluorescence changes. However, Ca^{2+} binding does not produce a spectral shift of Fluo-3 and Rhod-2 fluorescence. Therefore, ratiometric techniques cannot be used. Nonetheless, green-fluorescing Fluo-3 and red-fluorescing Rhod-2 are useful to measure relative

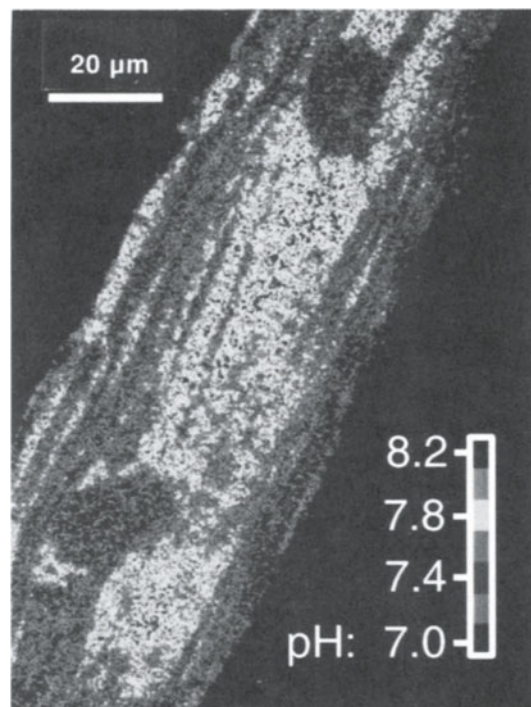


Figure 7. Intracellular pH in a SNARF-1-loaded cardiac myocyte. Fluorescence was imaged simultaneously at 584 nm and >620 nm using 568 nm laser excitation, ratioed and pseudocolored to represent the distribution of pH. After Chacon *et al.* (1994). A color representation of this figure can be found facing p. 214.

changes of free Ca^{2+} and can also be used in combination with other probes. For example, by comparing red and green images from cells co-loaded with Fluo-3 and TMRM, the relative distribution of Ca^{2+} in mitochondrial and cytosolic compartments can be appreciated (Figure 8A) (Chacon *et al.*, 1993, 1994; Ohata *et al.*, 1994; Lemasters *et al.*, 1995).

LINE SCANNING

Ordinarily, acquisition of a confocal image with an acceptable signal to noise ratio requires several seconds of scanning. To improve temporal resolution, a technique called line scanning can be employed. In line scanning, the light beam is scanned in the x-axis but remains stationary in the y-axis. The images generated are x vs. time images, as illustrated in Figure 8B. Here, a cultured cardiac myocyte was loaded with Fluo-3 and TMRM, and red and green fluorescence were imaged simultaneously in the line-scanning mode. The red TMRM image shows vertical striations representing mitochondria. Spaces between the stripes are the cytosol. In contrast, the green Fluo-3 fluorescence is diffuse and nearly equal in the cytosolic and mitochondrial compartments. In this experiment, the myocyte was stimulated electrically as line scans were collected. With each stimulation, Fluo-3 fluorescence increased in both the cytosolic and mitochondrial compartments. TMRM fluorescence was unchanged except for movement artifacts giving the vertical stripes a wavy appearance.

Image processing can quantify the changes of cytosolic and mitochondrial Fluo-3 fluorescence after stimulation. Basically, the TMRM image is used to identify those pixels in the Fluo-3 image that are either mitochondrial or cytosolic. For each time point (line) in the scan, the cytosolic and mitochondrial intensities are averaged and plotted. Such image analysis shows for the first time that mitochondrial free Ca^{2+} rises and falls rapidly during

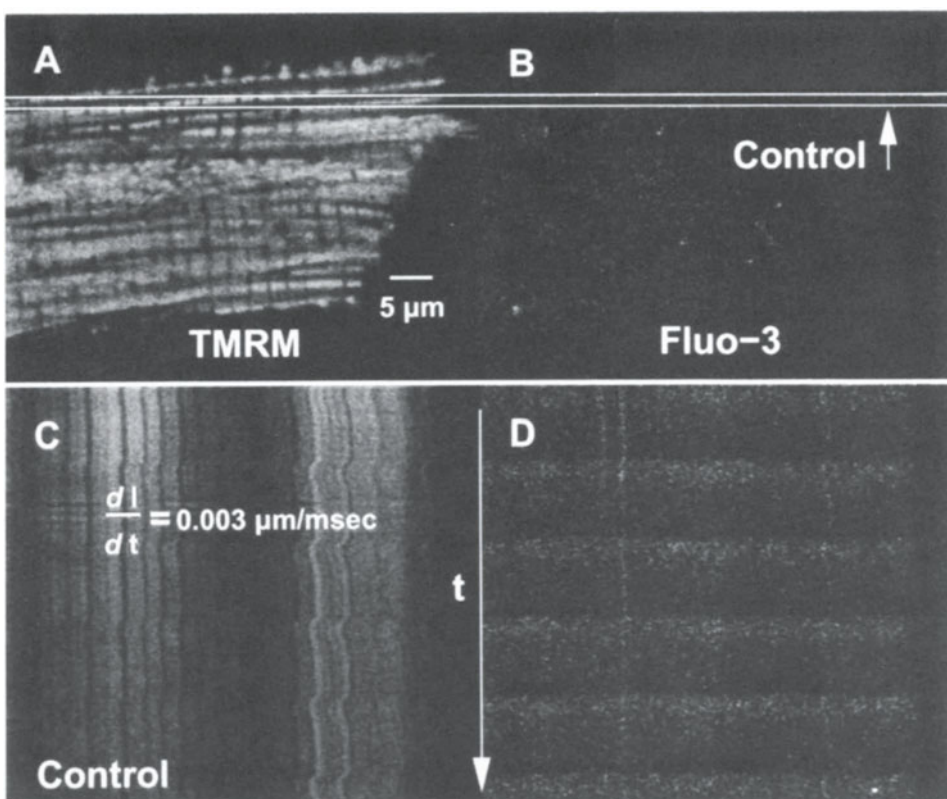


Figure 8. Mitochondrial and cytosolic free Ca^{2+} during the excitation-contraction coupling in a cardiac myocyte. In **A**, red TMRM (left) and green Fluo-3 (right) fluorescence was imaged from a quiescent cardiac myocyte. TMRM fluorescence distributed into mitochondria. Fluo-3 fluorescence was weak and present in both mitochondria and the cytosol. In **B**, an x vs. time line scan was collected during electrical stimulation at 0.75 Hz at the y -axis position indicated by the dashed line in **A**. Note the increase and decrease of Ca^{2+} -dependent Fluo-3 fluorescence after each stimulation in both mitochondrial and cytosolic regions (compare to TMRM image). After Chacon *et al.* (1993)

excitation-contraction coupling (Chacon *et al.*, 1993; Ohata *et al.*, 1994; Lemasters *et al.*, 1995).

RATIO METRIC Ca^{2+} IMAGING

The availability of ultraviolet confocal microscope systems now permits use of Indo-1 for ratiometric measurement of free Ca^{2+} . When Indo-1 is excited with the ultraviolet output of a UV-argon laser, fluorescence emitted at 405 nm increases and fluorescence at 480 nm decreases as free Ca^{2+} increases (Grynkiewicz *et al.*, 1985). This allows the 405/480-nm fluorescence ratio to be used to measure free Ca^{2+} . Indo-1 ratio imaging confirms that mitochondrial Ca^{2+} increases after each electrical excitation (Figure 9) (Ohata *et al.*, 1994; Lemasters *et al.*, 1995).

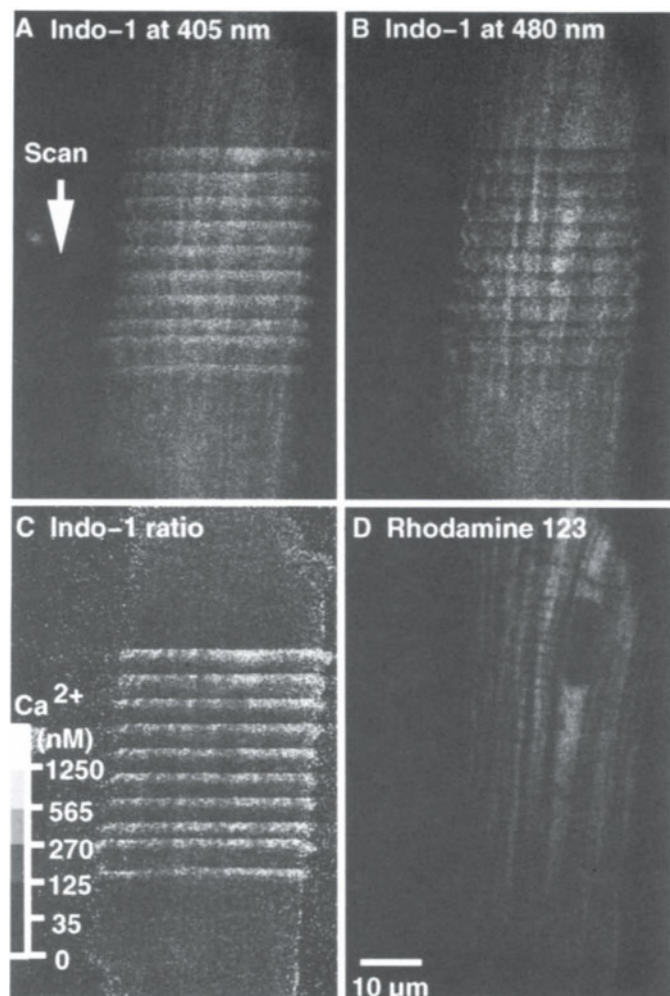


Figure 9. Indo-1 ratio-imaging of a cardiac myocyte during electrical stimulation. Using 351 nm excitation, fluorescence images of an Indo-1-loaded cardiac myocyte were collected at emission wavelengths of 405 nm (**A**) and 480 nm (**B**) during electrical stimulation at 0.5 Hz for 10 sec during the 40 second scan. In panel **C**, the ratio image is scaled to represent free Ca^{2+} concentration. Ca^{2+} transients occurred in both cytosolic and mitochondrial compartments, the latter identified by rhodamine 123 labeling (**D**). After Ohata *et al.* (1994). A color representation of this figure can be found facing p. 214.

SUMMARY

Confocal microscopy creates optical sections that are less than 1 μm in thickness through thick biological specimens, and increasingly confocal microscopy is an essential tool for studying the structure and physiology of living cells. The number of parameter-specific fluorophores useful for confocal microscopy of single living cells is large and increasing. By collecting serial confocal sections, the volume, shape and surface topography of single living cells labeled with calcein can be reconstructed in three-dimensions with results rivaling scanning electron micrographs. Calcein also indicates increases of mitochondrial membrane permeability associated with oxidative stress. Cationic fluorophores like rhodamine 123 and tetramethylrhodamine methylester distribute in response to electrical potentials within single cells, identifying both mitochondrial and plasmalemmal membrane potentials. Ion-indicating fluorophores like SNARF-1, Fluo-3 and Indo-1 measure the subcellular pH and Ca^{2+} with millisecond time resolution when line-scanning techniques are employed. Confocal microscopy is a powerful new technique to probe the physiology of

single cells and organelles. Its impact on experimental physiology may someday rival that of single cell electrical recording.

ACKNOWLEDGMENTS

The author is indebted to numerous former and present colleagues and collaborators for their contributions to the experiments described here: Ms. Kristin Al-Ghoul, Dr. Enrique Chacon, Dr. Ian S. Harper, Dr. Brian Herman, Dr. Anna-Liisa Nieminen, Dr. Hisayuki Ohata, Dr. Ammasi Periasami, Mr. Ting Qian, Mr. Jeffrey M. Reece, Mr. Samuel A. Tesfai, Ms. Donna Trollinger, and Dr. George Zahrebelski. This work was supported, in part, by Grants HL48769, AG07218 and DK37034 from the National Institutes of Health.

REFERENCES

- Chacon, E., Harper, I.S., Reece, J.M., Herman, B., and Lemasters, J.J., 1993, Mitochondrial and cytosolic Ca^{2+} transients during the contractile cycle of cultured cardiac myocytes: a laser scanning confocal microscopic study. *Biophys. J.* 64:A106.
- Chacon, E., Reece, J.M., Nieminen, A.-L., Zahrebelski, G., Herman, B., and Lemasters, J.J., 1994, Distribution of electrical potential, pH, free Ca^{2+} , and cell volume inside cultured adult rabbit cardiac myocytes during chemical hypoxia: a multiparameter digitized confocal microscopic study. *Biophys. J.* 66:942-952.
- Ehrenberg, B., Montana, V., Wei, M.-D., Wuskell, J.P., and Loew, L.M., 1988, Membrane potential can be determined in individual cells from the Nernstian distribution of cationic dyes. *Biophys. J.* 53:785-794.
- Emaus, R.K., Grunwald, R., and Lemasters, J.J., 1986, Rhodamine 123 as a probe of transmembrane potential in isolated rat liver mitochondria: spectral and metabolic properties. *Biochem. Biophys. Acta* 850:436-448.
- Farkas, D.L., Wei, M.-D., Febbroriello, P., Carson, J.H., and Loew, L.M., 1989, Simultaneous imaging of cell and mitochondrial membrane potential. *Biophys. J.* 56:1053-1069.
- Gores, G.J., Nieminen, A.-L., Wray, B.E., Herman, B., and Lemasters, J.J., 1989, Intracellular pH during 'chemical hypoxia' in cultured rat hepatocytes: protection by intracellular acidosis against the onset of cell death. *J. Clin. Invest.* 83:386-396.
- Grynkiewicz, G., Poenie, M., and Tsien, R.Y., 1985, A new generation of Ca^{2+} indicators with greatly improved fluorescence properties. *J. Biol. Chem.* 260:3440-3450.
- Gunter, T.E., and Pfeiffer, D.R., 1990, Mechanisms by which mitochondria transport calcium. *Am. J. Physiol.* 258:C755-C786.
- Johnson, L.V., Walsh, M.L., Bockus, B.J., and Chen, L.B., 1981, Monitoring of relative mitochondrial membrane potential in living cells by fluorescence microscopy. *J. Cell Biol.* 88:526-535.
- Jones, K.H., and Senft, J.A., 1985, An improved method to determine cell viability by simultaneous staining with fluorescein diacetate-propidium iodide. *J. Histochem. Cytochem.* 33:77-79.
- Lee, C., and Chen, L.B., 1988, Dynamic behavior of endoplasmic reticulum in living cells. *Cell* 54:37-46.
- Lemasters, J.J., Chacon, E., Zahrebelski, G., Reece, J.M., and Nieminen, A.-L., 1993, Laser scanning confocal microscopy of living cells, in: "Optical Microscopy: Emerging Methods and Applications," B. Herman and J.J. Lemasters, eds., Academic Press, New York, pp. 339-354.
- Lemasters, J.J., Chacon, E., Ohata, H., Harper, I.S., Nieminen, A.-L., Tesfai, S.A., and Herman, B., 1995, Measurement of electrical potential, pH, and free Ca^{2+} in individual mitochondria of living cells by laser scanning confocal microscopy, in: "Methods in Enzymology, Volume 206, Mitochondrial Genetics and Biogenesis: Part A," G.M. Attardi and A. Chomyn, eds., Academic Press, New York, pp. 428-444.
- Minsky, M., 1961, Microscopy apparatus, United States Patent 3,013,467 Dec. 19, 1961 (Filed Nov. 7, 1957).
- Minta, A., Kao, J.P.Y., and Tsien, R.Y., 1989, Fluorescent indicators for cytosolic calcium based on rhodamine and fluorescein chromophores. *J. Biol. Chem.* 264:8171-8178.
- Mitchell, P. (1966) Chemiosmotic coupling in oxidative and photosynthetic phosphorylation. *Biol. Rev.* 41:445-502.

- Nieminen, A.-L., Gores, G.J., Bond, J.M., Imberti, R., Herman, B., and Lemasters, J.J., 1992, A novel cytotoxicity assay using a multi-well fluorescence scanner. *Toxicol. Appl. Pharmacol.* 115:147-155.
- Nieminen, A.-L., Saylor, A.K., Tesfai, S.A., Herman, B., and Lemasters, J.J., 1995, Contribution of the mitochondrial permeability transition to lethal injury after exposure of hepatocytes to *t*-butylhydroperoxide. *Biochem. J.* 307:99-106.
- Ohata, H., Tesfai, S.A., Chacon, E., Herman, B., and Lemasters, J.J., 1994, Mitochondrial Ca^{2+} transients in adult rabbit cardiac myocytes during excitation-contraction coupling. *Circulation* 90 (Part 2):I-632.
- Pagano, R.E., Martin, O.D., Kang, H.C., and Haugland, R.P., 1991, A novel fluorescent ceramide analogue for studying membrane traffic in animal cells: accumulation at the Golgi apparatus results in altered spectral properties of the sphingolipid precursor. *J. Cell Biol.* 113:1267-1279.
- White, J.G., Amos, W.B., and Fordham, M., 1987, An evaluation of confocal versus conventional imaging of biological structures by fluorescence light microscopy. *J. Cell Biol.* 105:41-48.
- Wilson ,T., 1990, "Confocal Microscopy," Academic Press, London.
- Zahrebelski, G., Nieminen, A.-L., Al-Ghoul, K., Qian, T., Herman, B., and Lemasters, J.J., 1995, Progression of subcellular changes during chemical hypoxia to cultured rat hepatocytes: a laser scanning confocal microscopic study. *Hepatology* 21:1361-1372.

SUB-CELLULAR LOCALIZATION OF SECOND GENERATION PDT PHOTOSENSITIZERS STUDIED BY MICROSPECTROFLUOROMETRY

Marc Gèze, Jean-Michel Gaullier, Marc Bazin, and René Santus

Museum National d'Histoire Naturelle
Laboratoire de Photobiologie
(INSERM U 312), 43 rue Cuvier
75231 Paris Cedex 05, France

1. INTRODUCTION

Encouraging clinical results in the PDT of human tumors have been obtained with Photofrin IITM (P2) in early lung, stomach, bladder and skin cancers¹. However, the low specificity of P2 delivery to tumor tissues and the lack of light absorption of the mixture of porphyrins constituting P2 in the 650 - 800 nm range, where tissues maximally transmit precludes the use of PDT for large tumor masses. In the case of skin tumors, selectivity has been recently improved by the induction of excess protoporphyrin IX (PP) in tumor cells through topical application of 5-aminolevulinic acid (ALA), a precursor of heme biosynthesis².

Within the last four years, PDT research also focused on the synthesis and biological testing of chemically well-defined second generation photosensitizers with strong molar absorbance in the 650 - 800 nm range, rapid body clearance and higher tumor specificity³. Among these, purpurins, chlorins, pheophorbides and phthalocyanins are quite promising photosensitizers since they proved more effective than P2 *in vivo* in the treatment of many animal tumor models.

The most effective photosensitizers used so far are rather lipophilic. Their transport and delivery to the tumor mass implies binding to serum proteins and lipoproteins⁴. Studies of tumor response to PDT *in vivo* demonstrated that not only with P2 but also with members of the second generation photosensitizers, the main PDT targets in tumors are the vasculature and the cancerous cells¹. More and more often, as with other treatment modalities, PDT is used in conjunction with chemotherapeutic agent⁵. It can be expected that chemopotentiation of PDT by antineoplastic drugs could be optimized by using those drugs which specifically act on cell structures and functions which have been fragilized but not irreversibly destroyed by the PDT. A good example is the occurrence of shoulders at low irradiation doses in the

survival curves of cancer cells submitted to PDT *in vitro*. As a consequence, it is of utmost importance to determine the sub-cellular targets of the photodynamic action of effective new photosensitizers undergoing clinical trials. Microspectrofluorometry of single living cells is a valuable tool in the study of the intracellular localization and of the nature of primary photochemical events of photoactive drugs used in PDT of cancers⁶. This technique is used here to specify the subcellular localization of four photosensitizers either undergoing clinical trials, e.g. hexyl ether of pyropheophorbide *a* (HMP) and ALA-induced PP or undergoing animal tumor testing, e.g. N-(4-butanol) pheophorbamide *a* (Ph4-OH) and N-(2-aminoethyl) pheophorbamide *a* (Ph2-NH2). Besides co-localization experiments with vital fluorescent probes of organelles or other cell structures of rat EMT6 cells, human colonic HT29 cells, human normal fibroblasts and keratinocytes, examination of correlated photochemical events induced by a phototoxic drug in cells can give useful information regarding the microenvironment of the photosensitizer within an organelle or in adjacent organelles of the same kind, thus contributing to the mapping of the targets of the cell photosensitization.

2. EXPERIMENTAL

2.1. Chemicals

The HMP was a generous gift by Prof. K.M. Smith (University of California at Davis, CA., USA) whereas Ph4-OH and Ph2-NH2 were kindly provided by Prof. S. Gatt (Hebrew University of Jerusalem). The fluorescent probes of the purest available grade were purchased from Molecular Probes (Eugene, OR, USA). All the other chemicals of analytical grade were purchased from Sigma-Aldrich or Merck.

2.2. Cells

The murine mammary tumor cell line, EMT-6, was a generous gift from Dr J.D. Chapman at the Fox Chase Cancer Center in Philadelphia, PA, USA. They were propagated *in vitro* as monolayers in plastic tissue culture flasks in HAM'S F10 medium supplemented with 10% fetal bovine serum and antibiotics (100 units/ml penicillin and 100 µg/ml streptomycin). The HT29 -18 colonic adenocarcinoma cell line established by Dr D. Louvard (Institut Pasteur, Paris, France) was a generous gift from Dr C. Gespach (INSERM U55). Cells were cultured in Dulbecco's modified minimum essential medium (DMEM) supplemented with 4 g/l glucose, 10% FCS and antibiotics. Normal human skin fibroblasts obtained from plastic surgery were used between the 4th and 8th passage. They were grown as monolayers without antibiotics in Eagle minimum essential medium modified with Earl's salts (EMEM) supplemented with 10% fetal calf serum (FCS), both from GIBCO - France. The rapidly dividing NCTC 2544 human-skin-derived keratinocytes were purchased from Flow - France. They were incubated for 42 hours with 1 mM ALA in complete culture medium to induce excess PP. ALA was removed before experiments by washing with culture medium. For microspectrofluorometric studies, the cells were grown in a 5% CO₂ atmosphere on a 0.14 mm thick coverglass in a region circumscribed by a 35 mm diameter silica ring.

2.3. Labelling Cells with Lysosomal and Mitochondrial Probes

The lysosomal probes used for these experiments were classically Lucifer Yellow (LY) and Neutral Red (NR). In the case of LY, cells are incubated overnight (15 hours) with 50 µM LY in the culture medium. Before experiments performed with 2 ml of EMEM without serum, cells are washed three times with 2 ml of Eagle minimum essential medium modified

with Earl's salt (EMEM) containing 10% FCS, the last washing lasting 15 minutes. In the case of NR, cells are incubated just before experiments during 15 minutes with 50 μ M NR in EMEM. Then, they are washed as described above for LY but the last washing lasted 1h. Staining with rhodamine 123 (Rh 123), a well-established fluorescent mitochondrial probe, was performed as above but NR was replaced by 26 μ M Rh 123.

2.4. Microspectrofluorometry

The instrument is centered around a Leitz "Diavert" inverted microscope equipped with a stage thermostated at $37^{\circ}\text{C} \pm 1^{\circ}\text{C}$. To avoid bleaching of the photosensitizers during the brightfield observation of the cells with phase contrast, suitable band-pass filters are intercalated in the lamp housing. Fluorescence excitation was performed over the whole microscopic field with 435 nm light provided by a 100W super-high pressure mercury lamp. It is of note that the light dose absorbed by cells cultured in monolayers at the maximum incident energy dose; e.g. $I_o = 2.5 \text{ W/cm}^2$ is weak. Indeed, cells grown in monolayers have roughly an optical pathway of, say, $l \sim 20 \mu\text{m}$ (absorbed dose: $I_o A [P] l$; where A is the molar absorbance of photosensitizer, P). Hence, assuming fluence rate I_o and a realistic average $[P] \ll 10 \mu\text{M}$ in monolayers, there will be an extremely low absorbed energy dissipated in monolayers and no significant hyperthermia. A bidimensional adjustable slit in the primary image plane delimits the area in the microscopic field from which the fluorescence is collected. In the topographic mode, the fluorescence is reflected by a mirror to the bidimensional cooled CCD target (1024×1024 pixels) associated to signal recording and processing software (Photometrics, Tucson, Arizona). Usually images of 256×256 superpixels are recorded. In the spectrotopographic mode, a 150 grooves/mm grating replaces the mirror. The slit is reduced to a narrow strip and is used as the entrance slit of the grating, delineating in the object plane a $2 \mu\text{m}$ -width and about $40 \mu\text{m}$ -length strip along the whole field from which fluorescence is collected. Fluorescence photons received by the bidimensional detector produce a "spectrotopographic image". This image can be interpreted either as a succession, along the x axis (wavelengths), of monochromatic images of the $2 \mu\text{m}$ -width strip (in the y direction) or as a succession of spectra along the y axis, each corresponding to a "point" ($0.5 \mu\text{m}^2$) of the strip. In this mode, nearly confocal conditions are obtained⁷.

3. RESULTS AND DISCUSSION

3.1. Lipid Traffic; a Determinant of the Intracellular Localization of Hydrophobic Photosensitizers

To date, the hydrophobic properties of most photosensitizers proposed for PDT applications have an important consequence; they must be bound to serum proteins to reach tumor sites. The main carriers of such photosensitizers are albumin and lipoproteins⁸. The extent to which they partition into serum proteins depends on several factors including substituents and coulombic or Van der Waals interactions. Thus, after i.v. administration and partitioning into albumin, HDL, LDL and VLDL, delivery to cells involves several mechanisms. Molecules of photosensitizer bound to albumin or HDL are readily exchanged upon collisional interaction of the macromolecules with the plasma membrane whereas molecules bound to LDL or VLDL may be internalized by endocytosis via the apo B/E surface cell receptor⁴. The rapid membrane turnover and the subsequent lipid traffic implied by endocytic processes in actively dividing cells and the processing of endocytic vesicles itself by lysosomal hydrolases leads to a more or less general staining of all the cell membranes.

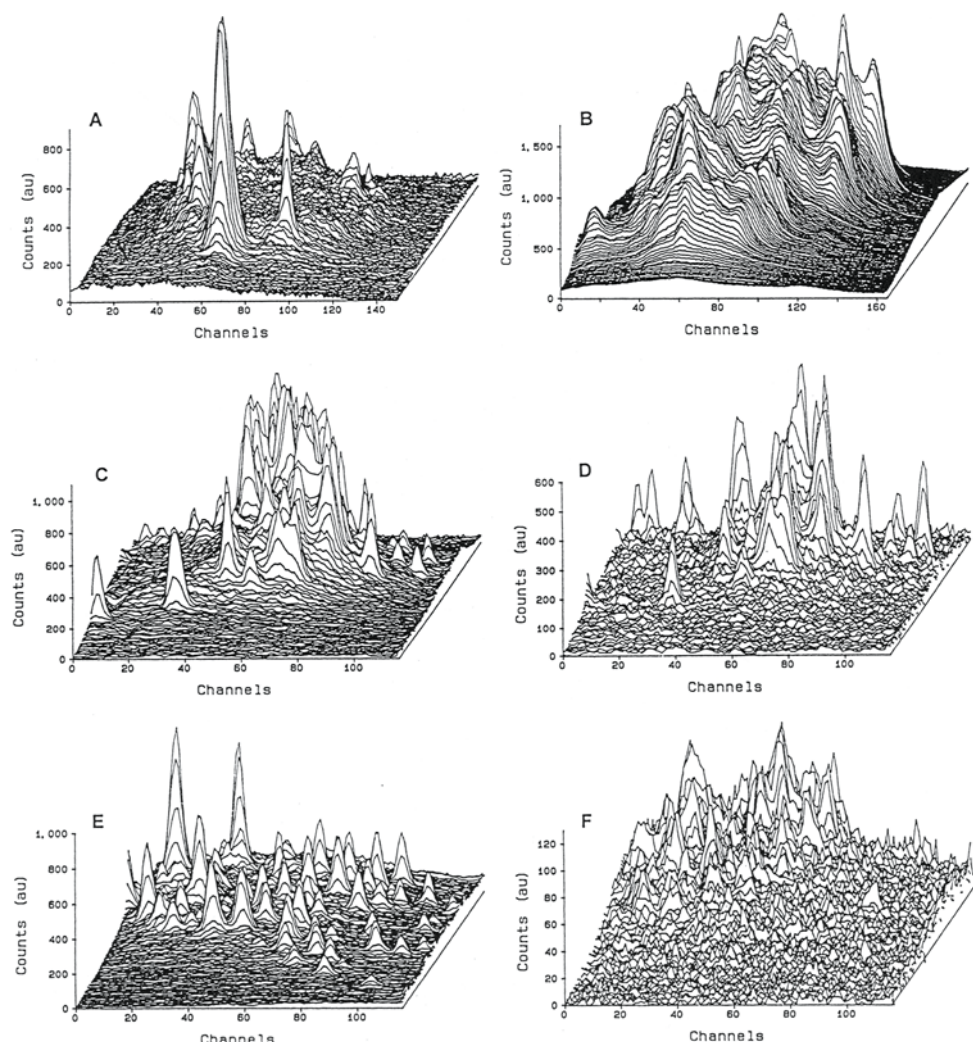


Figure 1. A: Topographic image of HT29-18 cells incubated for 18 h with $5\mu\text{M}$ of MPH in EMEM complemented with 2% of a delipidated serum substitute (DSS) and $60\ \mu\text{g}/\text{ml}$ LDL. $\lambda_{\text{em}} \geq 645\ \text{nm}$, $I_0 \approx 0.63\ \text{W}/\text{cm}^2$. B: Topographic image of HT29-18 cells incubated for 21 h with $5\mu\text{M}$ MPH in serum supplemented culture medium. $I_0 \approx 2.5\ \text{W}/\text{cm}^2$. Note the nuclear region clearly delimited by surrounding fluorescence spikes. C and D: Topographic images of the fluorescence of human skin fibroblasts incubated for 20 h with $5\ \mu\text{M}$ MPH and $25\ \mu\text{g}/\text{ml}$ LY in EMEM complemented with 2% DSS and $60\ \mu\text{g}/\text{ml}$ LDL. $\lambda_{\text{em}} \geq 645\ \text{nm}$ (C), $\lambda_{\text{em}} = 536\ \text{nm}$ (D), $I_0 \approx 0.63\ \text{W}/\text{cm}^2$. Images corresponding to the fluorescence emission of MPH (C) and LY (D) were recorded from the same cell. E and F: Topographic images of the fluorescence of human skin fibroblasts recorded 41 min after addition of $400\ \mu\text{M}$ of N-dodecylimidazole. Images corresponding to fluorescence emissions of MPH (E) and LY (F) were recorded as in C, D but $I_0 \approx 63\ \text{mW}/\text{cm}^2$ e.g. 10 times lower than that in A and B (adapted with permission from Gèze et al., *J. Photochem. Photobiol. B. Biol.* 200: 23 (1993))

Whereas endocytosis of LDL-bound photosensitizer is a prerequisite for incorporation of the latter in lysosomes and subsequent photodamage to this organelle, the cell metabolism contributes to lysosome protection by transferring the photosensitizer to other cell sites.

3.1.1. Illustration of the Effect of Photosensitizer Partitioning on the Cellular Localization. The LDL-bound methyl pheophorbide derivative (MPH) is rather specifically delivered to lysosomes of HT29-18 cells (Fig 1A) or normal fibroblasts. On the other hand, because of the binding to other serum components, in medium supplemented with 10% serum, general staining of the plasma membrane occurs, but localized fluorescent spots, probably corresponding to lysosomes stained with MPH, are also observed (Fig 1B)⁸.

Similarly, after overnight incubation of EMT6 cells with complete medium containing Ph4-OH which mainly binds to HDL and serum albumin and, to a lesser extent, to LDL⁹, no specific intracellular localization of the photosensitizer can be observed (lower micrograph in Fig. 2). In membranes, the Ph4 - OH emission peaks at 674 nm (Fig. 2).

Replacing Ph4 - OH by Ph2-NH2, a more hydrophilic pheophorbamide derivative which binds to VLDL, HDL and LDL¹⁰, leads to strongly fluorescent spots (upper micrograph in Fig 2) and weak staining of the plasma membrane. The Ph2-NH2 fluorescence maximum is at 668 nm either in spots or in the plasma membrane (Fig. 2) while the fluorescence maximum is found at 663 and 668 nm in water at pH 6.5 and 9, respectively. Interestingly, the pKa of Ph2-NH2 is about neutral (~7.3). It follows that Ph2-NH2 is probably a lysosomotropic photosensitizer but the pheophorbine ring must lie in the nonacidic compartment of the lysosomes, as suggested by the fluorescence maximum. In agreement with this hypothesis, incubation of Ph2-NH2-loaded EMT6 cells with NR, a specific fluorescent lysosomotropic substance which normally stains lysosomes under the experimental conditions given in section 2.3, leads to poor localization of NR and Ph2-NH2. Thus, in the region of a highly fluorescent spot (row 39 in the micrograph of Fig. 3) and in row 30 corresponding to a cell area with diffuse fluorescence a weak NR fluorescence is observed at ~ 580 nm in addition to that of Ph2-NH2. Despite its main lysosomal localization, it can be deduced from Fig. 4 that Ph2-NH2 is a remarkable photocytotoxic agent as judged by the extensive blebs formed at the cell boundary after a small irradiation dose (~ 5 J/cm²).

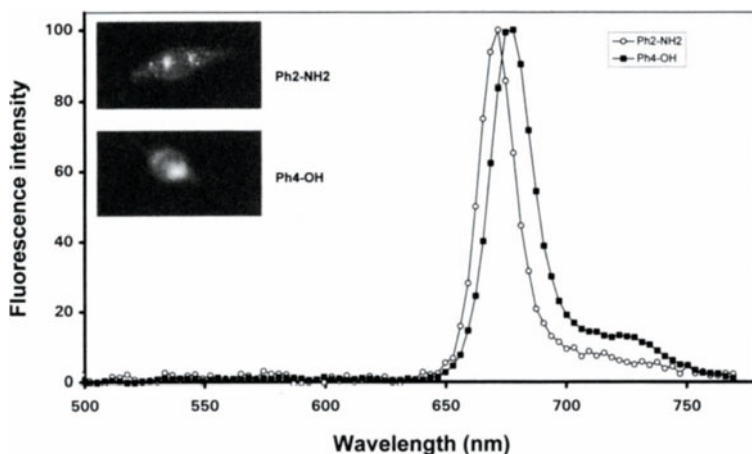


Figure 2. Fluorescence spectra of Ph2-NH2 and Ph4-OH recorded in living EMT 6 cells after overnight incubation with the photosensitizer (5 μ M in complete culture medium). $I_0 \sim 2.5 \text{ W/cm}^2$. Spectra have been recorded from an area of $I_0 \sim 2.5 \sim 0.5 \mu\text{m}^2$: Upper micrograph: EMT 6 cell stained with Ph2NH2 - lower micrograph: EMT 6 stained with Ph4 - OH.

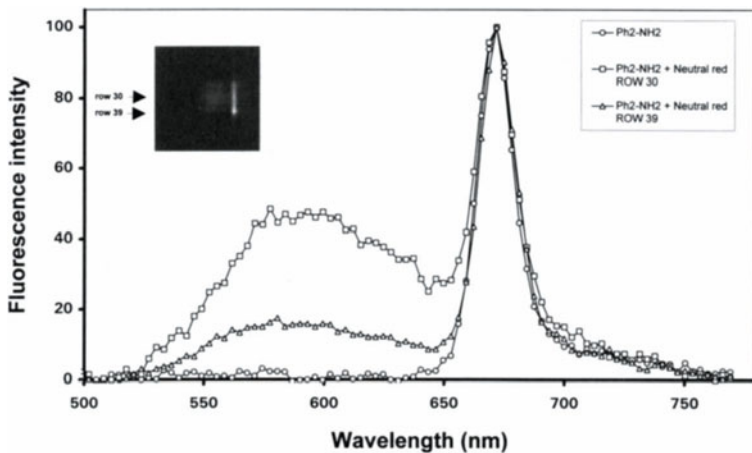


Figure 3. Normalized fluorescence spectra of EMT 6 cells incubated overnight with 5 μ M Ph2-NH2 followed by incubation with NR (see Section 2.3). Excitation and detection conditions are the same as in Fig. 2. Note the different NR fluorescence contributions in row 30 (diffuse fluorescence) and in row 39 (spot of intense fluorescence). Insert shows a spectrophotographic image from which the spectra were obtained.

Figure 4 also shows that relocalisation of Ph2-NH2 within the cytoplasm also takes place, strongly supporting photosensitized lysosomal membrane rupture.

3.1.2 Evidence for Stacking-Induced Fluorescence Quenching in Lysosomes. It should be noted that delivery of photosensitizer-loaded LDL to cells may lead to accumulation and stacking of the photosensitizer in lysosomes. Accumulation largely depends on cell aging, growth and incubation conditions. This can be nicely illustrated with normal human fibroblasts after overnight incubation with LDL-bound MPH. Specific incorporation of MPH in the lysosomes is clearly evidenced by the topographic image of the same fibroblast in Fig. 1 C and D where co-localization of LY and MPH is obvious. Stacking of MPH, leading to apparent quenching of the photosensitizer fluorescence can be demonstrated using lysosomotropic detergents such as N-dodecylimidazole which destabilize the lysosomal membrane and induce swelling of lysosomes and release of acid hydrolases in cells with pinocytotic activity¹¹. Indeed, upon addition of 400 μ M N-dodecylimidazole to the culture medium of fibroblasts whose lysosomes are stained with MPH, the unstacking of MPH by the lysosomotropic detergent induces a ten-fold increase in the fluorescence of the lysosomal area, as compared to cells without N-dodecylimidazole, while LY diffuses in the cytosol because of the inhibition of the lysosomal proton gradient (Fig. 1 E,F). It is possible that this stacking leads to a partial inhibition of the photosensitizing effectiveness of MPH during PDT at least in cultured tumor cells. Moreover, it should be emphasized that the stacking results in an underestimate of the intracellular content of photosensitizers (or other fluorophores) and is a severe limitation to quantitative measurements of tissue fluorescence not only *in vitro*, as shown here, but also *in vivo*, especially for the purpose of pre-treatment dosimetry. Spectral resolution may sometimes partially help to minimize the consequences of stacking by revealing the presence of aggregated species⁷.

3.2. Discriminating Sites of Photosensitization by ALA-Induced PP at the Cytosol-Organelle Interface in Keratinocytes by Time-Resolved Microfluorometry. When NCTC 2544 keratinocytes are incubated with 5-aminolevulinic acid (ALA) for times up to 42 hours,

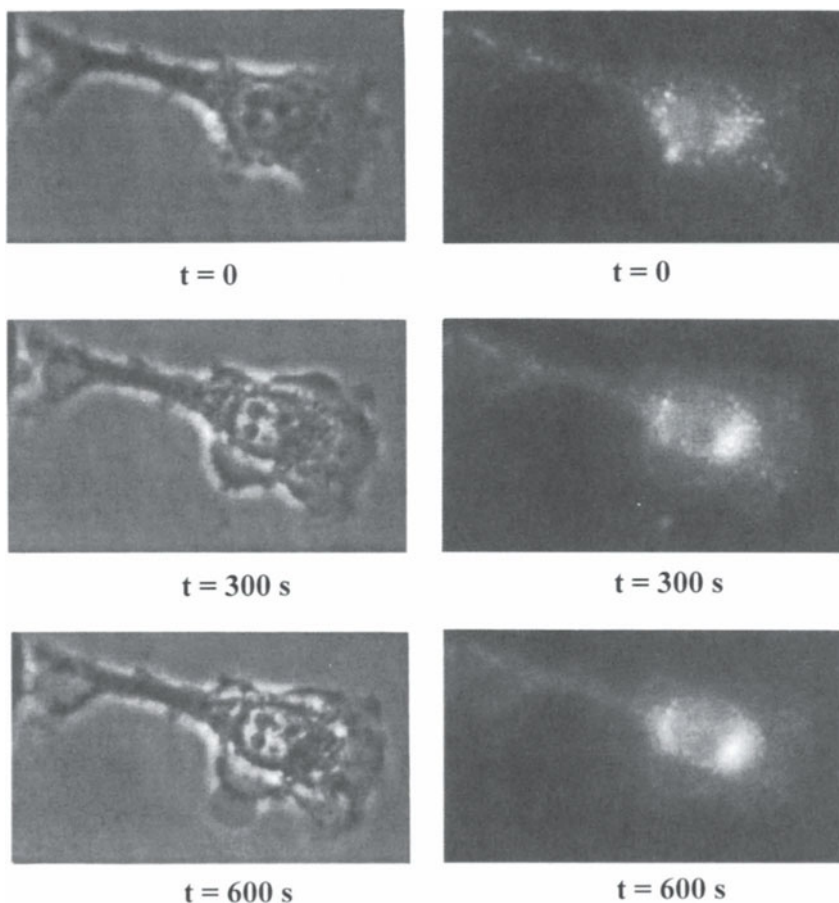


Figure 4. A succession of micrographs of EMT 6 cells recorded at various times after the photosensitization with Ph2-NH₂ showing on the left-hand side the phase contrast images with developing blebs and on the right-hand side the corresponding fluorescence images demonstrating the relocalization of the photosensitizer. Excitation conditions are the same as in Fig. 2.

the plasma membrane shows strong staining and fluorescent spots are observed within the cytoplasm, especially in the perinuclear region. Fluorescence spectra confirm that the fluorophore is PP. Co-localization experiments with Rh123 and LY or NR, demonstrate that some of these spots are lysosomes but internal membranes are also stained⁷. Although PP is synthesized in mitochondria, no PP fluorescence can be detected in the spectrotopographic image after incubation with ALA followed by staining with Rh 123. However, photosensitization of mitochondria by PP occurs under irradiation with visible light since the kinetics of the Rh 123 relocalization under irradiation with 436 nm light is modified in cells previously incubated with ALA as compared to cells without ALA (Fig. 5A). We have previously shown that irreversible mitochondrial damage parallels the photoinduced Rh 123 relocalization in the cytosol¹². It is not known whether mitochondrial damage is induced by traces of mitochondrial PP or by PP bound to cytosolic proteins interacting with mitochondria such as cytoskeleton proteins or transporters required for the transfer of cytosolic substrates

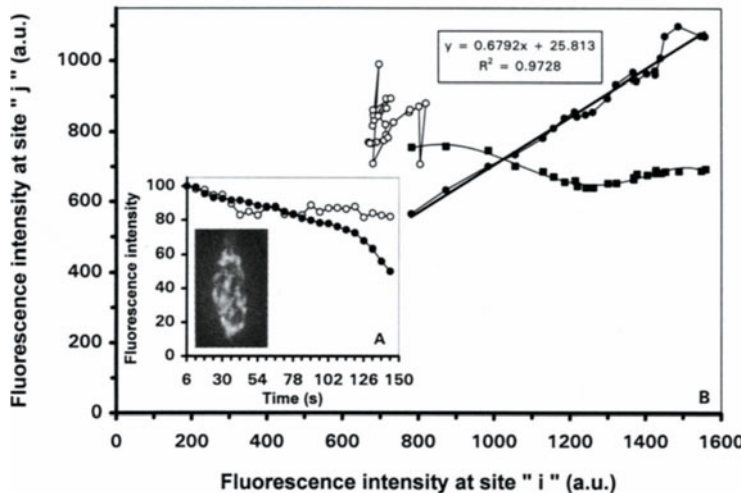


Figure 5. A: Kinetics of Rh 123 leakage from mitochondria of NCTC 2544 keratinocytes incubated for 42 hours with 1 mM ALA (●) under irradiation as described in 2.4. I_0 was 250 mW/cm². Controls (no ALA) are also shown (○). The micrograph represents mitochondria stained with Rh 123; Kinetics are recorded from an area of 2x2 pixels (0.5 μm^2). B: Plots of Rh 123 fluorescence at site "i" versus Rh 123 fluorescence at site "j" measured at the same time "t" on kinetics such as those shown in A. (●) "i" and "j" (2x9 pixels and 1x7 pixels, respectively) are within the same mitochondrion. (■) "i" and "j" (3x3 pixels) corresponds to a site within a mitochondrion and another site at the edge of this mitochondrion. (○) "i" and "j" belong to the same mitochondrion but deals with control cells (no ALA).

to mitochondria. In cells treated with ALA, interesting information can be obtained by the comparison of the relocalization kinetics of Rh123 measured at various sites in single and separate mitochondria and at the edge of mitochondria such as those shown on the micrograph of Fig. 5 A. Figure 5 B shows plots, on rectangular axes, of the Rh 123 fluorescence recorded at the same time at two different locations in the same mitochondrion. It can be seen that the kinetics of the PP-induced Rh 123 leakage from two sites of the same mitochondrion or from separate mitochondria are strongly correlated, whereas the same plot built with fluorescences counted at a site located at the edge of a mitochondrion and at another site within the mitochondrion are quite uncorrelated. Similarly, in the absence of PP, the Rh 123 fluorescence concomitantly measured at two sites in mitochondria is totally uncorrelated. Such plots can be explained considering that, at time (t), the Rh 123 fluorescence ($F_i(t)$) induced by PP photosensitization is proportional to the "overall quantum efficiency (Φ)" of the mitochondrial membrane photosensitized alteration at site (i), e.g. (Φ_i) times the rate of light absorption: e.g. $\Phi_i I_0 A [PP_i] P_i$, where I_0 is the light fluence rate, A, the molar absorbance of PP at concentration $[PP_i]$ and P_i the mean mitochondrial optical path at the site (i) of measurement at time (t). At the same time, at another location (j) within a mitochondrion or outside mitochondria, the Rh 123 fluorescence is now proportional to $\Phi_j I_0 A [PP_j] P_j$. Hence, $F_i(t) = F_j(t) [\Phi_i [PP_i] P_i / \Phi_j [PP_j] P_j]$. A prerequisite for $F_i(t)$ to be proportional to $F_j(t)$ is that the ratio between brackets remains constant during the photoinduced membrane alteration. It is most probable that the endogenously produced PP still present in mitochondria must be located at sites (for example, close to the site of PP synthesis) which share in common quite similar microenvironments conditioning the time-dependent local effectiveness (Φ) of the PP photosensitization. Accordingly, at other unrelated sites, such as the cytosol / mitochond-

drion interface or in the absence of PP, this time-independent constancy does not hold and no correlation can be observed.

4. CONCLUSION

The present study demonstrates that microspectrofluorometry on single living cells can bring unique information regarding the sites of localization of photosensitizers of therapeutic interest in relation to their chemical structure or their biosynthesis not only via topo- and spectrotopographic analyses but also by investigating photobiological reactions in real time, in localized area of living cells.

REFERENCES

1. B.W. Henderson and T.J. Dougherty, How does photodynamic therapy work ? *Photochem. Photobiol.*, 55 : 145 (1992).
2. J.C. Kennedy and R.H. Pottier, Endogenous protoporphyrin IX, a clinical useful photosensitizer for photodynamic therapy, *J. Photochem. Photobiol. B : Biol.*, 14: 275 (1992).
3. E. Ben-Hur, Second generation photosensitizers for photodynamic therapy of cancer, in "Radiation Research : A Twentieth Century Perspective" W.C. Dewey, M. Edington, R.J.M. Fry, E.J. Hall and G.F. Whitmore (eds.), *Radiation Research*, Academic Press, San Diego, CA, USA, pp 664-669 (1992).
4. G. Jori, M. Geltramini, E. Reddi, B. Salvato, A. Ragnan, L. Ziron, L. Tomio and T. Zsanov, Evidence for a major role of plasma lipoproteins as hematoporphyrin carriers *in vivo*, *Cancer Lett.*, 24 : 291 (1984).
5. K. Berg, H.B. Steen, J.W. Winkelman and J. Moan, Synergistic effects of photoactivated tetra(4-sulfonatophenyl)porphyrine and nocodazole on microtubule assembly, accumulation of cells in mitosis and cell survival *J. Photochem. Photobiol.*, 13: 59 (1992).
6. R. Santus, P. Morlière and E. Kohen, The photobiology of the living cell as studied by microspectrofluorometric techniques *Photochem. Photobiol.*, 54 : 1071 (1991).
7. J.M. Gaullier, M. Gèze, R. Santus, T. Sa e Melo, J.C. Mazière, M. Bazin, P. Morlière and L. Dubertret, Subcellular targets of ALA-induced endogenous porphyrins in cultured human keratinocytes and fibroblasts : a microspectrofluorometric study, *Photochem. Photobiol.*, 62 : 114 (1995).
8. M. Gèze, P. Morlière, J.C. Mazière, K.M. Smith and R. Santus, Lysosomes, a key target of hydrophobic photosensitizers proposed for photochemotherapeutic applications, *J. Photochem. Photobiol. B : Biol.*, 20 (1993) 23-25.
9. P. Grellier, V. Agmon, P. Palud, J.C. Mazière, D. Rigommier, A. Dagan, R. Santus, S. Gatt and J. Schrevel, Photosensitized inactivation of Plasmodium Falciparum and Babesia Divergens infected erythrocytes in whole blood by pheophorbide derivatives Vox Sanguinis (1997).
10. A. Dagan, S. Gatt, S. Cerbu-Karabat, J.C. Mazière, C. Mazière, R. Santus, E.L. Engelhardt, K.A. Yeh, C. C. Stobbe, M.C. Fenning and J. D. Chapman, Uptake by cells and photosensitizing effectiveness of novel pheophorbide derivatives *in vitro* *Int. J. Cancer* 63: 831-839 (1995).
11. D.K. Miller, E. Griffiths, J. Lenard and R.A. Firestone, Cell killing by lysosomotropic detergents, *J. Cell. Biol.*, 97: 1841 (1983).
12. P. Morlière, R. Santus, M. Bazin, E. Kohen, V. Carillet, F. Bon, J. Rainasse and L. Dubertret, Is Rhodamine 123 a photosensitizer ? *Photochem. Photobiol.*, 52: 703 (1990).

PHOTOFRIN UPTAKE AS A FUNCTION OF TUMOR SIZE AND THE DETECTION OF MICROSCOPIC NESTS OF TUMOR CELLS BY PHOTOFRIN FLUORESCENCE

Mechanistic Implications for PDT

W. R. Potter and D. A. Bellnier

Roswell Park Cancer Institute
Department of Radiation Biology
Buffalo, New York 14263

ABSTRACT

Detection of subcutaneous microscopic nests of tumor cells by the fluorescence of the photosensitizer Photofrin has been reported in breast cancer patients. The detection sensitivity problem posed by these results will be discussed and a solution examined in light of the published data on Photofrin uptake as a function of tumor size. The uptake data as a function of tumor mass offers an interesting insight into the unexpected detection sensitivity of the fluorescence method and the mechanism of action of photodynamic therapy.

INTRODUCTION

Photodynamic therapy (PDT) is a new mode of cancer treatment that has been under clinical development since the mid-1970's. PDT which employs the photosensitizing drug Photofrin, has been approved for a variety of solid tumors in Canada, the Netherlands, and Japan. Photofrin (formerly known as Photofrin II) is a mixture of porphyrin polyethers produced by QLT Phototherapeutics in Vancouver, Canada.

The treatment involves the intravenous injection of a tumor localizing photosensitizer (Photofrin). Twenty-four to 72 hours are allowed for the drug to clear from the blood and normal tissues. Then the tumors are exposed to red (630 nm) light. The light penetrates the tissue at therapeutic levels to a depth of 3 to 9 mm. The light dose rates are 100 - 200 milliwatts per square centimeter and produce only a small temperature rise of 3-4 °C. The tumor toxic effect is the result of the generation of singlet oxygen. The optical energy absorbed by the photosensitizer is passed to molecular oxygen by a non-radiative transfer,

producing singlet oxygen. As the ground state of molecular oxygen is a triplet, the transition between the singlet and ground state by emitting or absorbing a photon is forbidden. The singlet excited state of molecular oxygen can only be produced by non radiative means. The non radiative transfer of energy can be thought of as a collision that transfers the energy of an excited state from one molecule to another. The singlet excited state of molecular oxygen has a lifetime of seconds in the proper environment (e.g., octanol). In a cell, singlet oxygen has a lifetime of approximately 0.1 microseconds or less. In a cell membrane, singlet oxygen has a diffusion range of about 7 nanometers (about the thickness of a cell membrane). Within this distance it either oxidizes a target molecule or is quenched by a non-radiative transfer. The band near 1200 nm in the OH vibration spectrum of a liquid water molecule is efficient in such physical quenching of singlet oxygen. The physical quenching of singlet oxygen by water makes singlet oxygen chemistry most effective in a non-aqueous or lipid environment. Photofrin is (like most effective photosensitizers) lipophilic. The targets of Photofrin PDT are believed to lie in the various membranes of the cell. Mitochondrial membranes are thought to be the most important targets of PDT.

Efficient production of singlet oxygen requires that, upon absorption of light, the excited photosensitizer molecule has a high probability of inter system crossing (ISC) to a forbidden excited state. The state is forbidden because it cannot emit a photon without a change in the spin quantum number. That is, all lower states have a different spin quantum number. Spin quantum numbers are invariant in all transitions involving the absorption or emission of a photon. In a lipid environment this forbidden state lasts long enough to allow for the non-radiative transfer of energy by collision with an oxygen molecule. The sensitizer molecules that do not undergo ISC or lose energy by some other non radiative mechanism can return to the ground state by fluorescence. In the case of Photofrin the fluorescence quantum efficiency is about 1% and the ISC efficiency is about 90%. Because Photofrin shows some selectivity for tumors, the fluorescence properties are of interest independent of therapy.

Historically, detection of tumors by porphyrin fluorescence predates the use of porphyrin derivatives in cancer therapy by at least 50 years. In 1924 Policard [1] observed that tumors occasionally fluoresced because they accumulated endogenous porphyrins.

By 1963 Lipson [2] and his colleagues at the Mayo Clinic, had developed hematoporphyrin derivative (HpD) for the express purpose of finding occult superficial tumors in the bronchus by rigid endoscopy. They used a chopped filtered mercury arc lamp to provide the exciting light at 406 nm and detected the fluorescence at 630 nm with a filtered photomultiplier tube. They were successful in locating tumors that could not be localized by other means.

During the 1970's Dougherty and his collaborators developed PDT and the drug Photofrin which was made from HpD. By the late 1970's the interest in tumor localizing porphyrins had shifted to therapy. Nevertheless, work has continued on the development of various methods of fluorescence detection.

The principal reason that tumor localizing porphyrins have not been more widely used for detection is photosensitivity. The injection of Photofrin causes skin photosensitivity that requires the patient to stay out of strong outdoor light for four to six weeks. The photosensitivity is less severe with lower doses of Photofrin and the reactions are quite mild for doses of 0.5 mg per kg or less.

Thus Photofrin is used on patients with proven disease. The fluorescence is used to localize the disease in much the same way as the early workers at the Mayo Clinic [2] used it. The Mayo study used fluorescence on patients with a positive cytology and with disease that was not evident on x-ray or white light bronchoscopy.

Photofrin fluorescence could prove useful for examining nodes during head and neck surgery for the removal of a primary tumor. *In situ* fluorescence may also prove useful in establishing tumor free surgical margins.

DETECTION OF MICROSCOPIC DISEASE

One of the more interesting recent efforts in fluorescence detection is a report by Mang and his collaborators [3]. They reported the clinical finding of small isolated nests of 100 to 1000 tumor cells. The results were biopsy proven on the chests of patients post mastectomy. The patients in the study were women who had received a mastectomy for breast cancer. Subsequently (typically one year or more post surgery) their disease had recurred as a lump just below the skin on the chest. The lump was surgically removed and the pathology confirmed. The patients had no clinical evidence of disease but were undergoing a prophylactic course of chemotherapy at the time they were studied by Mang et al.

This group received an intravenous injection of 0.5 mg Photofrin per kg body weight followed at 24 hours by scanning of the chest wall with a fiber optic probe attached to a fluorescence photometer. The photometer used a dual excitation wavelength to excite fluorescence at 690 nm. Tissue background fluorescence (also at 690 nm) was excited with 612 nm light and Photofrin plus background fluorescence was excited with 632.8 nm light. The contributions of each exciting wavelength to the 690 nm fluorescence were separated by chopping the two excitation wavelengths at different frequencies. Tuned amplifiers and phase locked detection allowed the separation of the background fluorescence from the Photofrin plus background. The resulting signals were subtracted. The difference signal was then evaluated.

The average difference signal was the result of normal tissue uptake of Photofrin. The square root of this signal represented the random point-to-point fluctuations in normal tissue Photofrin uptake. The detection threshold was a positive signal equal to the average tissue background signal plus three times the square root of the average tissue background. This algorithm resulted in the detection of 30 suspicious points in 9 patients. Punch biopsies of each point of high fluorescence were exhaustively sectioned and examined. The pathology of all demonstrated some abnormalities and 50% showed small nests of malignant cells ranging from about one hundred to one thousand cells.

The possibility that any random biopsy might produce a similar result in this group of patients was ruled out by a small control group of 12 random biopsies that found nothing.

The detection of these small nests of cells would not have occurred had the samples been examined in the conventional manner by taking a few sections through each. Only the complete sectioning of each sample and the inspection of the hundreds of sections resulting allowed the pathologist to detect the microscopic nests of cells that produced the fluorescence signals. The cell nests showed no evidence of inflammation or other host response that might have accounted for the extraordinary result. The size of the fluorescence signal required for detection implies a remarkably high uptake by the tumor cells.

PHOTOFRIN UPTAKE AS A FUNCTION OF TUMOR SIZE: ANALYSIS OF THE PUBLISHED DATA

To appreciate the dilemma posed by these results it is necessary to examine the literature on the uptake of Photofrin by tumors. Most of the data are in studies of transplantable mouse tumors. These results demonstrate a tumor level at 24 hours post intravenous

injection approximately equal to the whole body injected concentration. Typical tumors studied are a few millimeters in diameter.

A few studies have resulted in published data on the uptake of Photofrin as a function of tumor size. Notable is the study of Bellnier et al [4]. These workers employed C¹⁴ labeled Photofrin and published a table of uptake for tumors ranging in size from 400 mg to 20 mg. Seven different sizes were measured.

In addition are the data of West [5] on the uptake of cells grown as micro spheres with masses of 1.6 to 63 micrograms.

We plot the tumor drug concentration data tabulated in the papers of West and Bellnier in Figure 1 and note that it fits very well the solid line through the points. This line is the graph of equation 1.

$$C_{\text{tumor}} = C_{\text{inj}} \left[\frac{16.8}{M^{\frac{1}{3}}} + 0.199 \right] \quad (1)$$

Where: C_{tumor} is the tumor Photofrin concentration in micrograms per gram tumor. C_{inj} is the injected dose in mg Photofrin per kg body weight and M is the tumor mass in grams.

Equation (1) was fitted to the seven data points published by Bellnier [4] with the uptake doubled at every point. Doubling the uptake is equivalent to doubling the injected dose used in the Bellnier experiment. The uptake was doubled to improve the fit of the back extrapolated curve to the data of West [5]. Equation (1) models the uptake through the surface of the tumor plus uptake through the tumor volume due to circulating blood. The tumor is assumed to have a uniform spherical or elliptical shape. The first term in the bracket on the right side of the equation (1.) is proportional to the surface area divided by the volume. The surface area is proportional to the square of the cube root of the tumor mass. The tumor volume is proportional to the tumor mass. Thus the surface area to volume ratio is proportional to the reciprocal of the cube root of the tumor mass. The second, or volume uptake, term is a constant that represents an uptake proportional to the injected dose. For large tumors clearly the second term is dominant. In the case of very small tumors the first term dominates as the tumor mass approaches zero. In the case of West's data the volume term can be attributed to the diffusion of the culture media into the spheroid.

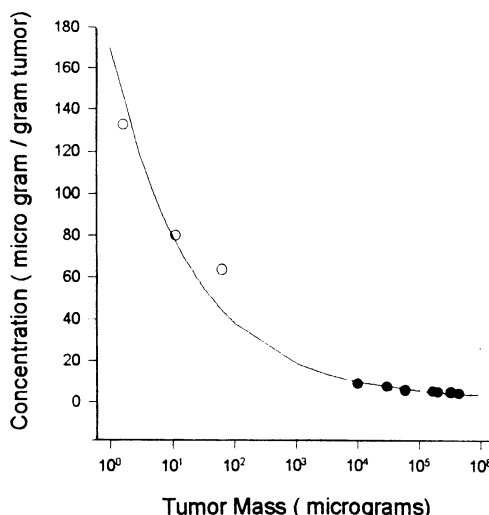


Figure 1. The solid points are the data of Bellnier with the uptake figures doubled. This is equivalent to an injection of 10 mg per kg rather than the 5 mg Photofrin per kg body weight dose that was used by Bellnier et al . The open circles are the data table values published by West. The solid line is equation (1) with C_{inj} equal to 10. A precise fit to the data of West is possible if the constants of equation (1) are adjusted.

A single cell weighs about one nanogram. Extrapolation of the results of measuring tumors in the gram to milligram range to single cells is flawed. The result is an uptake per cell which when multiplied by 100 cells falls about 30 fold short of the amount of Photofrin necessary to give the fluorescence signal found clinically.

A sphere encloses a given volume with the least possible surface area. Treating individual cells as spheres is clearly not correct. The geometry of the cells is more sheet-like than spherical. The total surface area of a single cell is many times that of a smooth sphere enclosing the same volume. Thus the reported clinical detection of 100 isolated tumor cells becomes plausible in light of what is known about Photofrin uptake.

THERAPEUTIC IMPLICATION OF THE UPTAKE RESULTS

The uptake results point in another interesting direction. They show that the tumor cells bind Photofrin irreversibly. The property of tight binding is required for the high concentrations found in very small tumors. Such concentrations are far above the levels that exist in blood immediately following intravenous injection. Without tight binding small nests of tumor cells would never greatly exceed the surrounding Photofrin concentration since they would rapidly come into equilibrium with the extracellular drug levels. The levels in cells found in small nests (100-1000 cells) far exceed any external drug levels that they have encountered. The bound Photofrin levels are many orders of magnitude greater than the circulating drug levels at 24 hours post injection.

This irreversible binding also appears to occur in the skin and is probably responsible for the long term photosensitivity. Strong binding of Photofrin in tumor cells may be in part responsible for the clinical efficacy of this photosensitizer.

A typical transplantable mouse tumor is encapsulated with well-defined borders. Henderson and Fingar [7] have shown that such tumors respond to PDT mainly through vascular damage rather than direct tumor cell kill. A real spontaneous malignancy lacks a well-defined capsule and typically exhibits local satellite deposits of tumor cells.

The local control of a real spontaneous malignancy requires the destruction of small nests of tumor cells that may not even have a distinctive tumor vasculature. As PDT with the correct dosimetry spares normal tissue, such isolated small groups of tumor cells can only be destroyed by direct damage to the cells.

The data on Photofrin uptake as a function of tumor size can be extrapolated as we have shown above. The high tumor cell levels of Photofrin predicted by extrapolation are required for the detection results reported by Mang et al. [3]. They are more than adequate to kill the cells in these small nests by direct damage to the cells. Thus direct cell kill could account for the excellent long term clinical results reported by Okunaka and coworkers [7] and by Furuse et al. [8] in the PDT treatment of early stage bronchogenic lung cancer .

ACKNOWLEDGMENT

This investigation was supported by PHS grant number Ca 55791 awarded by the National Cancer Institute, DHHS.

REFERENCES

1. Poliard A (1924) Experimental tumors studied by Wood's light. Comp Rend Soc. Biol. **91**: 1423-1424

2. Cortese DA, Kinsey JH, Woolner LB, Payne WS, Sanderson DR, and Fontana RS (1979). Clinical application of a new endoscopic technique for detection of *in situ* bronchial carcinoma. Mayo Clinic Proceed. **54**, 635-641.
3. Mang TS, McGinnis C, Crean DH, Khan, S and Leibow C (1992) Fluorescence detection of tumors: studies on the early diagnosis of microscopic lesions in pre-clinical and clinical studies. J Cell Pharmacology. **3** : 132-140
4. Bellnier DA, Ho Y-K, Pandey RK, Misset JR, and Dougherty TJ (1989) Distribution and elimination of Photofrin II in Mice. Photo Chem Photobiol. **50** (2), 221-228.
5. West CLM (1989) Size dependent resistance of human tumor spheroids to photodynamic treatment. Br. J. Cancer **59**, 510-514.
6. Henderson BW and Fingar VH (1987) Relationship of tumor hypoxia and response to photodynamic treatment in an experimental mouse tumor. Cancer Research **47**, 3110-3114
7. Okunaka T, Kato H, Konaka C, Kawate N, Bonaminio A, Yamamoto H, Ikeda N, Tolentino M, Eckhauser ML and Hayata Y (1991) Photodynamic therapy for multiple bronchogenic carcinoma. Cancer **68** (2) , 253-258
8. Furuse K, Funuoka M, Kato H, Horai T, Kubota K, Kodama N, Kusunoki Y, Takifumi N, Okunaka T, Konaka C. et al . (1993)A prospective phase II study on photodynamic therapy with Photofrin II for centrally located early stage lung cancer. The Japan Lung Cancer Photodynamic Therapy Study Group. Journal of Clinical Oncology 11 (10) 1852-1857

THE DETECTION OF APOPTOTIC CELLS AND THEIR QUANTIFICATION BY FLOW CYTOMETRY

Michael G. Ormerod

34 Wray Park Road
Reigate, RH2 0DE
United Kingdom

INTRODUCTION

Apoptosis is an important mode of cell death in natural development. Unwanted cells are eliminated from an organism through a built-in program and cell death, as part of the developmental process. It is often referred to as programmed cell death. Apoptosis can be considered as the 'natural' mode of cell death, as opposed to death by necrosis which occurs during, for example, tissue injury. The importance of apoptosis in the development and maintenance of an animal is attested to by its conservation through evolution - it has been recognised in organisms as diverse as nematode and man. Indeed, some of the genes involved which have been identified in a nematode, *Caenorhabditis elegans*, have their counterpart in mammals (Stellner, 1995).

It has been postulated that all cells contain the apoptotic program which is blocked by the presence of appropriate growth factors (Raff, 1992). Any untoward change in the environment of the cell, possibly a failure to establish the correct cell-to-cell contacts, could result in an initiation of the apoptotic program. Apart from its key role in tissue maintenance and development, a variety of toxic insults will trigger apoptosis and many drugs used in the chemotherapy of cancer can cause apoptotic death (Hickman, 1992).

This short paper deals entirely with apoptosis induced in cultured cells. A brief outline of methods for identifying such cells is given and several flow cytometric methods for quantifying apoptotic cells are described. Reviews on apoptosis have been written by Wyllie et al. (1980), Arends and Wyllie, (1991), Cohen, (1991), and Wyllie (1994). Experimental details of methods for quantifying apoptotic cells are given by Darzynkiewicz et al. (1994), Ormerod (1994), Fraker et al. (1995) and Sherwood and Schimke (1995). The latter two references are in a volume which deals entirely with methods for studying cell death (Schwartz and Osborne, 1995).

Table 1. Changes in apoptotic and necrotic cells

Apoptotic	Necrotic
Cells shrink	Cells swell
Characteristic changes in chromatin	Chromatin loses structure
Plasma membrane retains integrity	Plasma membrane loses integrity
Degradation of DNA at linkers between chromatin domains (30-50 kbp)	Non-specific degradation of DNA
Further degradation at internucleosomal linkers	

IDENTIFICATION OF APOPTOTIC CELLS

Apoptotic cells need to be distinguished from normal cells and from cells dying by necrosis. Some of the more important changes are summarised in Table 1.

Apoptotic cells are distinguished by characteristic changes in the nuclear chromatin and, in the initial stage of any study, these cells should be identified morphologically by light or electron microscopy (see Figure 1). In some cells, apoptosis is accompanied by internucleosomal degradation of DNA giving rise to a distinctive 'ladder' pattern on DNA

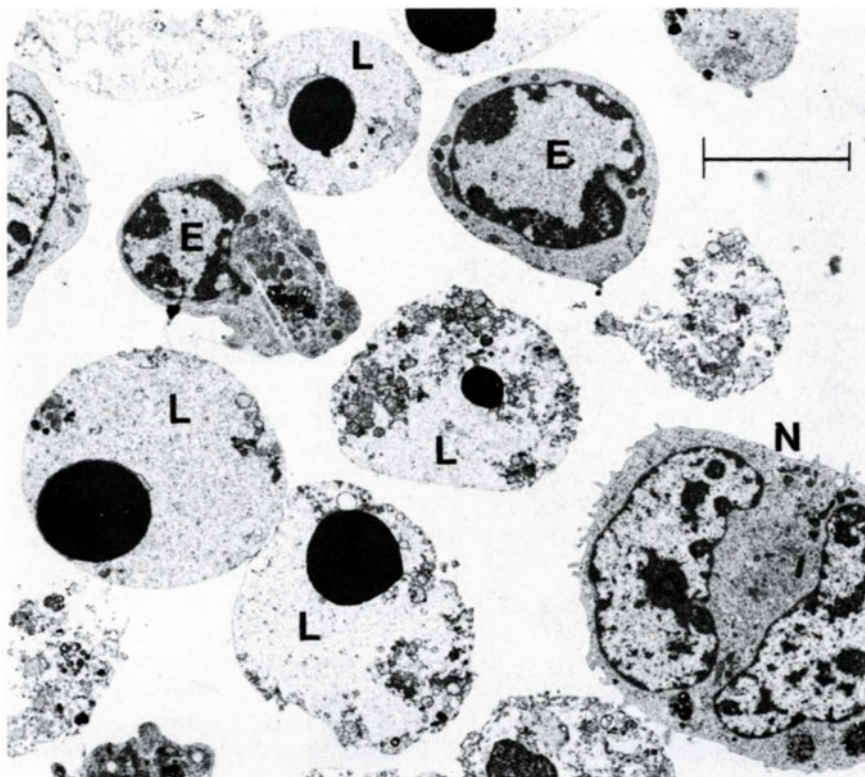


Figure 1. Electron micrograph of cells from a murine haemopoietic cell line, BAF3, undergoing apoptosis induced by withdrawal of the essential growth factor, interleukin-3. The photograph shows normal cells (N) and cells in the early (E) and late (L) stages of apoptosis. Note the condensation of the chromatin on the nuclear membrane (E) followed by fragmentation of the nucleus into highly condensed, osmophilic particles (L). Bar = 5 μ m. Micrograph supplied by Mr. David Robertson, Institute of Cancer Research, Sutton, England.

gel electrophoresis (Wyllie, 1980). When it is known that this change occurs, gel electrophoresis is a useful method for detecting the presence of apoptotic cells. However, it should be noted that not all cells proceed to this end stage of the apoptotic process (Oberhammer et al., 1993; Ormerod et al., 1994). The introduction of double strand breaks at intervals of 30 - 50 kbp (possibly corresponding to the size of chromatin loops) is an earlier change in the DNA which can be observed by pulse field gel electrophoresis (Walker et al., 1992).

Apoptotic cells were originally identified by their unusual morphology (Kerr et al., 1972). It must be stressed that morphology is still the only way of unequivocally identifying an apoptotic cell.

QUANTIFICATION OF APOPTOTIC CELLS

Gel electrophoresis cannot be used to count the number of cells undergoing apoptosis. Cells which grow in culture attached to the surface of the culture dish detach on undergoing apoptosis. After treatment, microscopical examination of the detached cells will often reveal that over 90% of them are apoptotic (for example, see Ormerod et al., 1994). The apoptotic cells can be quantified by counting them. In suspension cultures, counting apoptotic cells under a microscope can be time consuming and inaccurate. They can be quantified by flow cytometry and several methods for counting apoptotic cells have been developed. Most methods fall into two broad categories: those which detect degradation of DNA and those which rely on changes in the plasma membrane of apoptotic cells.

Measuring a 'Sub-G₁' Peak' in the DNA Histogram

Frequently, at a late stage in the apoptotic process, the DNA is cut at the linker regions between the nucleosomes. During fixation and subsequent rehydration of the cells, some of the lower molecular weight DNA leaches out, lowering the DNA content. These cells can be observed as a hypodiploid or 'sub-G₁' peak (Figure 2).

The amount of DNA extracted - and hence the position of the sub-G₁ peak - depends on the type of cell being studied and the buffer in which the cells are resuspended. Figure 3 shows data from a sub-line of the human lymphoblastoid cells, W1L2, incubated with KCN. This treatment triggers apoptosis in these cells but there is no 'sub-G₁' peak. The cells were fixed in 70% ethanol and resuspended in PBS. Inspection of a cytogram of DNA-peak versus

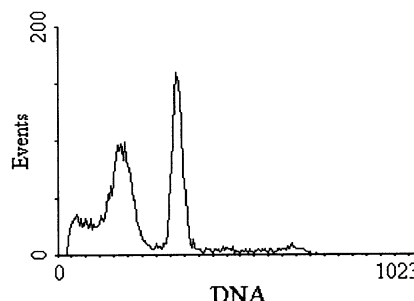


Figure 2. A murine haemopoietic cell line, BAF3, incubated for 16 h without the essential growth factor, interleukin-3. Cells were fixed in 70% ethanol, resuspended in PBS and then stained with PI. Note that the cells are mainly in G₁ of the cell cycle and that there is a greatly enhanced 'sub-G₁' peak in the DNA histogram due to apoptotic cells. Argon-ion laser giving 200 mW at 488 nm.

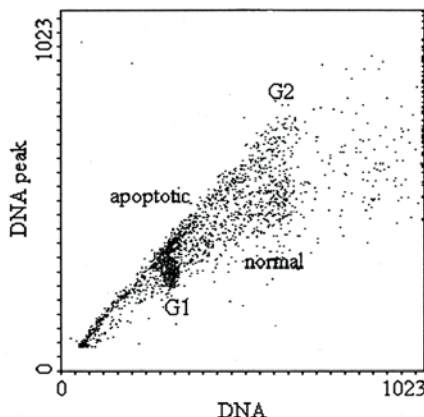


Figure 3. A sub-line of W1L2 incubated for 18 h with 2 mM KCN. Cells were fixed in 70% ethanol, resuspended in PBS and stained with 20 µg/ml PI. Argon-ion laser giving 200 mW at 488 nm.

DNA-area revealed two populations of the same DNA content but one had smaller nuclei (higher DNA-peak for the same DNA-area). Cell sorting revealed that these cells were apoptotic (Ormerod, M.G., Titley, J.C. and Kimbell, R., unpublished work).

If, after ethanol fixation, the cells are resuspended in a phosphate-citrate buffer (0.2 M Na₂HPO₄, 4 mM citric acid, pH 7.8), more DNA is extracted from the apoptotic cells (Gong et al., 1994). With BAF3 cells, the sub-G1 peak may disappear of the end of the cytogram - the DNA can be over-extracted (Figure 4A). In the W1L2 cells, a sub G1 peak is formed, albeit rather smeared out (Figure 4B).

***In Situ* End Labelling (ISEL) of Strand Breaks**

Scission of the chromatin at the sites of nucleosomal linkage creates a large number of strand breaks in the DNA of apoptotic cells. The broken ends can be labelled enzymatically *in situ* (*In Situ* End Labelling - ISEL). The enzyme used is either the Klenow fragment of *Escherichia coli* polymerase or terminal deoxynucleotidyl transferase (Tdt), the latter now being favored. The ends of DNA can be labelled directly using fluorescein-dexoyuridine triphosphate (dUTP) or biotin-dUTP followed by fluorescein-streptavidin or digoxygenin-dUTP followed by fluorescein-anti-digoxygenin. The last two methods are more sensitive. The cells are fixed in ice cold 1% paraformaldehyde followed by 70% ethanol. The

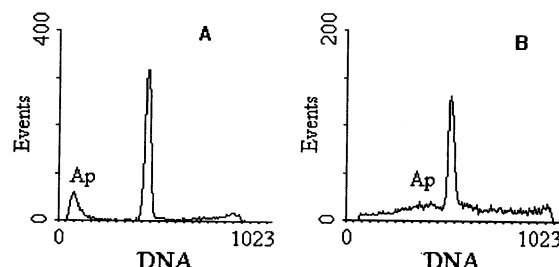


Figure 4. Cells fixed in 70% ethanol and rehydrated into a citrate buffer. A. BAF3 cells (see Figure 2). B. W1L2 cells (sub-line) (see Figure 3). Argon-ion laser giving 200 mW at 488 nm.

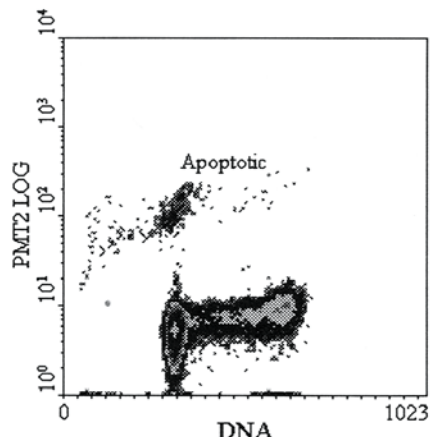


Figure 5. A murine haemopoietic cell line, BAF3, incubated in full growth medium. Cells were labelled by the Tdt assay using biotin-dUTP followed by fluorescein streptavidin; counter-stained with PI. 6% of the cells were apoptotic. Argon-ion laser giving 200 mW at 488 nm.

paraformaldehyde fixation crosslinks the DNA into the cell and prevents the low molecular weight DNA from being extracted. The cells are counter-stained with PI so that the position in cell cycle from which the cells underwent apoptosis can be observed (Figure 5).

Methods Relying on a Change in Membrane Permeability

The plasma membrane shows a variety of changes during apoptosis. One such change is an increase in the permeability of the membrane. Two methods are described below which exploit this change to quantify apoptotic cells. These methods will work with some cells but not others; the reason for this is not understood.

The advantage of these methods is that they are applied to unfixed cells. Cells with a damaged plasma membrane can be excluded by either gating on light scatter or by adding PI and gating for negative red fluorescence. Apoptotic and pre-apoptotic cells can be sorted for further study.

In the Hoechst/PI method, cells are incubated at 37°C with 1 µg/ml Hoechst 33342 for 5-10 min depending on the type of cell under study (Ormerod et al., 1992; Sun et al., 1992). The apoptotic cells take up the dye faster and fluoresce bright blue compared to the dim blue fluorescence of the pre-apoptotic cells. Figure 5 shows an example of a murine haemopoietic cell line, BAF3, incubated for 16 h without IL3. A histogram of blue fluorescence gated on blue positive, red negative fluorescence (R2 in the Figure) showed that about

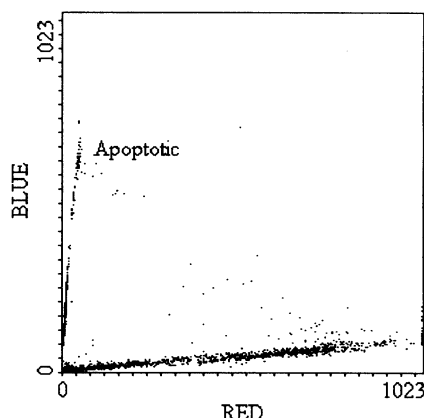


Figure 6. A murine haemopoietic cell line, BAF3, incubated for 16 h without IL3 labelled for 10 min at 37°C with 1 µg/ml Hoechst 33342. 5 µg/ml PI added just before analysis. Display of blue (Hoechst) versus red (PI) fluorescence. Argon-ion laser tuned to give 100 mW uv.

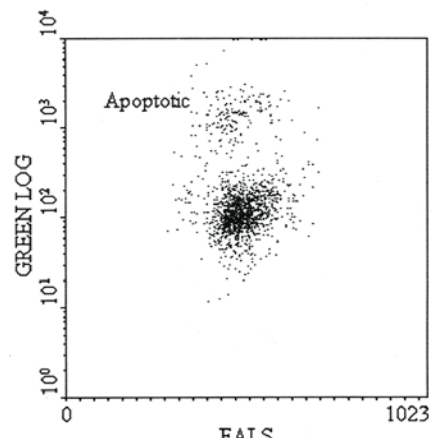


Figure 7. A murine haemopoietic cell line, BAF3, incubated for 16 h without IL3. Labelled for 10 min at 37°C with 10 µM YOPRO-1. Argon-ion laser giving 200 mW at 488 nm.

10% of the 'viable' cells were apoptotic (viable in this context is referring to cells with an intact plasma membrane).

A similar method using the dye, YOPRO-1, has recently been reported (Idziorek et al., 1995). YOPRO-1 (Molecular Probes, Eugene, OR, USA), a cyanine based dye which binds to DNA, is excited by blue light and fluoresces green. Figure 7 shows the method applied to the cell line, BAF3. The green fluorescence of the YOPRO-1 dye was recorded using a logarithmic amplifier. The file was gated on a cytogram of RALS versus FALS to exclude dead cells. The same gating could have been achieved by adding PI and excluding PI +ve cells. The apoptotic cells have clearly taken up more of the dye.

OTHER METHODS

When cells are incubated with Hoechst 33342 and the ratio of red to blue fluorescence is measured, the apoptotic cells show relatively greater red fluorescence (Ormerod et al., 1993; Belloc et al., 1994). This change in the emission spectrum of the dye-DNA complex is probably caused by a greater amount of the Hoechst dye being taken up by the apoptotic cells.

There are considerable changes in the membranes of apoptotic cells and phosphatidyl serine groups may be exposed on the surface. Such groups can be detected by incubating the cells with fluorescein-labelled Annexin V (Homburg et al., 1995). It is not yet known whether this method can be applied universally.

EXPERIMENTAL NOTE

All the experiments described above were performed at the Institute of Cancer Research, Sutton, UK, using a Coulter Elite ESP flow cytometer. I would like to thank Mrs. J.C. Titley for her assistance in the laboratory.

REFERENCES

- Arends, M.J., Wyllie, A.H., 1991, Apoptosis: Mechanisms and role in pathology. *Int. Rev. Exp. Pathol.* 32:223.

- Belloc, F., Dumain, P., Boisseau, M. R., Jalloustre, C., Reiffers, J., Bernard, P. Lacombe, F., 1994, A flow cytometric method using Hoechst 33342 and propidium iodide for simultaneous cell cycle analysis and apoptosis determination in unfixed cells. *Cytometry*. 17:59.
- Cohen, J.J., 1991, Programmed cell death in the immune system. *Adv. in Immunol.* 50:55.
- Darnzynkiewicz, Z., Li, X. and Gong, J., 1994, Assays of cell viability: discrimination of cells dying by apoptosis, in "Flow Cytometry", Darzynkiewicz, Z. Robinson, J.P. and Crissman, H.A. (eds.) Methods in Cell Biology, 41, Academic Press, Inc., San Diego.
- Fraker, P.J., King, L.E., Lill-Elghanian, D. and Telford, W.G., 1995, Quantification of apoptotic events in pure and heterogeneous populations of cells using flow cytometry, in "Cell Death", Schwartz, L.M. and Osborne, B.A. (eds.) (1995). Methods in Cell Biology, 46, Academic Press, San Diego.
- Hickman, J.A., 1992, Apoptosis induced by anticancer drugs. *Cancer and Metastasis Reviews*, 11:121.
- Homburg, C.H., de Haas, M. von dem Borne, A.E. Verhoeven, A.J. Reutelingsperger, C.P. and Roos, D., 1995, Human neutrophils lose their surface Fc gamma RIII and acquire Annexin V binding sites during apoptosis in vitro. *Blood* 85:532.
- Idziorek, T., Estaquier, J., De Bels, F. and Ameisen, J.C., 1995, YOPRO-1 permits cytofluorometric analysis of programmed cell death (apoptosis) without interfering with cell viability. *J. Immun. Meth.* 185:249.
- Kerr, J.F.R., Wyllie, A.H. and Currie, A.R., 1972, Apoptosis: a basic biological phenomenon with wide ranging implications in tissue kinetics. *Brit. J. Cancer* 26:239.
- Oberhammer, F., Wilson, J.W., Dive, C., Morris, I.D., Hickman, J.A., Wakeling, A.E., Walker, P.R., Sikorska, M., 1993, Apoptotic death in epithelial cells, cleavage of DNA to 300 and/or 50 kb fragments prior to or in the absence of internucleosomal fragmentation. *EMBO J.* 12:3679.
- Ormerod, M.G., Collins, M.K.L., Rodriguez-Tarduchy, G. and Robertson, D., 1992, Apoptosis in interleukin-3-dependent haemopoietic cells. Quantification by two flow cytometric methods. *J. Immunol. Meth.* 153:57.
- Ormerod, M.G., 1994, Further applications to cell biology, in "Flow Cytometry. A Practical Approach", Ormerod, M.G. (ed.). 2nd edition. IRL Press at Oxford University Press, Oxford.
- Ormerod, M.G., Sun, X-M., Snowden, R.T., Davies, R., Fearnhead, H. and Cohen, G.M. Increased membrane permeability of apoptotic thymocytes: a flow cytometric study. *Cytometry* 14:595.
- Ormerod, M.G., O'Neill, C.F., Robertson, D., Harrap, K.R., 1994, Cisplatin induces apoptosis in a human ovarian carcinoma cell line without concomitant internucleosomal degradation of DNA. *Exp. Cell Res.* 206: 231.
- Raff, M., 1992, Social controls on cell survival and cell death. *Nature* 356: 97.
- Schwartz, L.M. and Osborne, B.A. (eds.), (1995, "Cell Death". Methods in Cell Biology, 46, Academic Press, San Diego.
- Sherwood, S.W. and Schimke, R.T., 1995, Cell cycle analysis of apoptosis using flow cytometry, in "Cell Death". Schwartz, L.M. and Osborne, B.A. (eds.) Methods in Cell Biology, 46, Academic Press, San Diego.
- Stellner, H., 1995, Mechanisms and genes of cellular suicide, *Science*. 267:1445.
- Walker, P.R., Smith, C., Youdale, T., Leblanc, J., Whitfield, J.F. and Sikorska, M., 1991, Topoisomerase II-reactive chemotherapeutic drugs induce apoptosis in thymocytes. *Cancer Res.* 51:1078.
- Sun, X-M., Snowden, R.T., Skilleter, D.N., Dinsdale, D., Ormerod, M.G. and Cohen, G.M., 1992, A flow cytometric method for the separation and quantitation of normal and apoptotic thymocytes. *Anal. Biochem.* 204:351.
- Wyllie, A.H., 1980, Glucocorticoid-induced thymocyte apoptosis is associated with endonuclease activation. *Nature* 284:555.
- Wyllie, A.H., 1993, Apoptosis. *Br. J. Cancer* 67:205.
- Wyllie, A.H., Kerr, J.F.R., Currie, A.R., 1980, Cell death: the significance of apoptosis. *Int. Rev. Cytology* 68:251.

ADHESION STABILIZATION OF BLOOD BORNE CANCER CELLS IN THE MICROCIRCULATION

David G. Menter,¹ Thomas W. Smith,² Zhong Yun,¹ John Patton,²
Larry V. McIntire,² and Garth L. Nicolson¹

¹ Department of Tumor Biology
The University of Texas M. D. Anderson Cancer Center
Houston, Texas 77030

² Cox Laboratory for Biomedical Engineering and Institute of Biosciences
and Bioengineering
Rice University
Houston, Texas 77251

ABSTRACT

Metastatic tumor cells must form stable adhesive contacts with microvascular elements in target organs. The interactions at the vessel wall are complex and may vary depending on the cells involved. We have developed hydrodynamic assays that mimic conditions in the microcirculation to study metastatic tumor cell interactions with endothelial cells and their underlying extracellular matrix. Acquisition and analysis of data are computerized, enabling us to distinguish the primary events of arrest from secondary events of adhesion stabilization. Using this system we have determined that initial receptor-ligand interactions do not effectively maintain prolonged adhesive contacts unless followed by adhesion stabilization. We have examined tumor cell lines that were derived from different developmental origins and malignant potentials and observed differences in their adhesion stabilization behavior. The adhesion behaviors of human metastatic melanoma cells that originate from the neuroepithelium (MeWo, 3S5, and 70W cells) are quite different from murine large-cell lymphoma cells that arise from mesothelia (RAW117-P, -L17, and -H10). Melanoma cells adhered to many extracellular matrix proteins or RGD peptides but large-cell lymphoma cells responded to a more limited repertoire of components. Melanoma cells express a variety of integrins compared to the more limited integrin profiles expressed by large-cell lymphoma cells, and melanoma cells were more highly responsive and spread more fully under laminar flow than the limited spreading and slow adhesion stabilization of large-cell lymphoma cells. The adhesion stabilization properties of these tumor cells correlated with their metastatic properties; melanoma cells typically metastasize to a variety of organ sites compared to the organ preferential targeting of large-cell lymphoma cells. These

methods measure dynamic responses of tumor cells and we conclude that these hydrodynamic analysis methods are highly sensitive and reflective of metastatic behavior.

INTRODUCTION

Cell-cell and cell-substrate interactions in the microcirculation are important during the formation of blood-borne metastases. An important step in cancer metastasis involves tumor cell adherence to microvessel endothelial cell surfaces and underlying extracellular matrix (ECM) under the influence of fluid shear stress. In the circulating blood, fluid shear constraints dynamically influence cellular interactions and may add a mechanical force component to the adhesion process. Laminar flow can produce more than one force component in circulation, (a) a spin induced shear component due to the rapid rotation of cells and (b) an elongated shear component as the cell begins to adhere to the vascular intima or exposed ECM (Figure 1). In many instances cells of lymphocytic origin exhibit rolling properties as part of their behavioral response¹. In this case, the rolling cells may experience a combination of spin and elongated shear (Figure 1). To remain lodged in the presence of fluid shear, circulating cells must rapidly respond and stabilize adhesion contacts after encountering the blood vessel wall^{2,3}. We have focused on rapid stabilization as an important component of tumor cells' resistance to fluid detachment forces.

Certain cell surface receptors are known to initiate specific adhesive responses and may contribute to adhesion stabilization, such as: selectins, cadherins, integrins, or those receptors of the immunoglobulin-supergene family⁴. Simple engagement of receptors may not suffice for immobilizing circulating cells to the endothelial wall in the presence of hemodynamic shear. Signaling events that cause receptor recruitment, clustering and patching, and enzyme activation may occur immediately after the arrest phase of attachment^{5,6}. While many of the later cell adhesion events have been studied, such as cell spreading and focal adhesion plaque formation, we chose to focus on the initial events of cell arrest and stabilization. We believe that such stabilization of adhesive contacts following initial cell contact in the microcirculation is an important process. Furthermore, cell stabilization is a

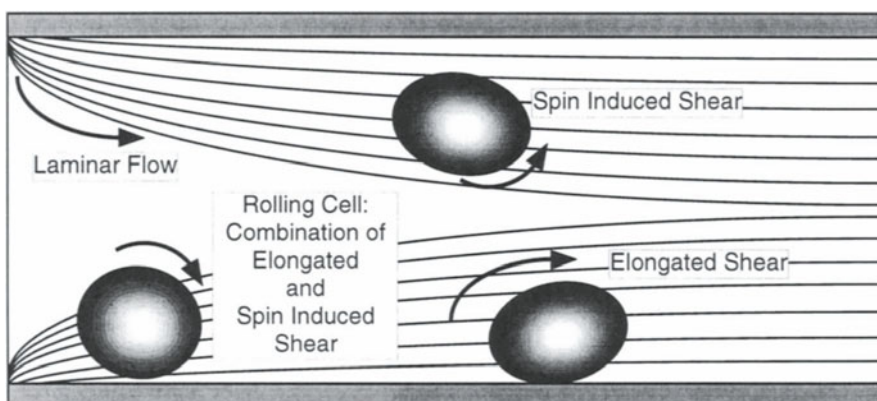


Figure 1. In the blood vessel fields of laminar flow, represented by parallel lines, can exert more than one force component on circulating tumor cells. (a) A spin induced shear component is exerted on rapidly rotating cells and (b) an elongated shear component arises as cells begin to adhere to the blood vessel wall, the cell projects into the center of the blood vessel, and flow fields must pass over the cell surface. Rolling cells experience both spin induced shear and elongated shear.

necessary step that precedes cell spreading, invasion and migration. As such, it was necessary to develop computerized imaging methods to analyze very early adhesion events because they are difficult to quantitate, particularly under fluid shear conditions^{2, 3}. In our early experiments we used fluorescent vital dyes such as calcein-EM to examine adhesion but they tend to raise intracellular pH and alter adhesion results. The minimization computer subroutines used in our current studies track phase bright cells and do not require special treatments or probes to visualize and maintain normal behavior.

Certain germ cell line characteristics that arise as part of tissue development may be important to the progression and behavior of metastatic cells. For example we have used cell lines that were derived from different germ layers to examine adhesion characteristics in relation to blood-borne metastatic properties. Melanoma cells that arise from neuroectodermal origins were studied and compared to large-cell lymphoma cells that originate from the mesoderm. The melanoma cells studied included the moderately metastatic MeWo parental cell line and WGA-selected (3S5) subline that was poorly metastatic and a highly metastatic (70W) subline. The large-cell lymphoma variants that were used consisted of RAW117 poorly metastatic parental (P) cells and two highly metastatic variant sublines that were sequentially selected for metastasis to lung (L17) or liver (H10).

An important adhesion system in many types of tumor cells is mediated by heterodimeric integrin molecules. Many tumor cell types have been shown to express integrins that recognize ECM components that make up the basement membrane matrix⁷⁻⁹. Certain sites in the body may synthesize ECM proteins that circulating tumor cells can potentially interact with such as the Space of Disse located in the liver sinusoids. Similarly, tumor cells and certain cancer therapeutics can cause endothelial cell retraction exposing subendothelial ECM proteins. The purpose of our studies was two-fold; first, to document the cell adhesion stabilization process for certain proteins found in the ECM, and second, to discover the surface receptors involved in the arrest and stabilization of various tumor cells. These studies may help identify conditions that favor a determining role for adhesion during the formation of organ metastases.

MATERIALS AND METHODS

Tumor and endothelial cell culture: Human melanoma MeWo parental cells were used to select sublines for resistance to wheat germ agglutinin (WGA)¹⁰ and were provided by Dr. R. S. Kerbel (Sunnybrook Health Science Centre, Toronto, Ontario, Canada). Two variants were selected by increasing amounts of WGA; the 3S5 variant that was selected had reduced sialylation on its cell surface and showed very poor experimental metastatic potential in nude mice. The MeWo and 70W lines showed similar levels of surface sialic acid but the 70W line had a much higher experimental metastatic potential than the MeWo and 3S5 lines. Cells were cultured on 100-mm tissue culture plates (Corning, Houston, TX) in a humidified 5% CO₂ atmosphere in Dulbecco's modified Eagles medium (DMEM)/F12 (1:1) containing 5% fetal bovine serum (FBS) without antibiotics.

Three sublines of murine RAW117 large-cell lymphoma cells with varying metastatic potentials and specificities were used: the poorly metastatic parental P cells, the highly liver-metastatic H10 cells and the highly lung- and liver-colonizing L17 cells. The RAW117 cells were maintained as suspension cultures in Petri dishes in the DMEM/F12 medium described above. Hepatic sinusoidal endothelial (HSE) cells were isolated from syngeneic Balb/c mice and characterized as described previously¹¹. The endothelial cells were cultured in gelatin-coated tissue-culture dishes (Corning, Corning, NY) in (DMEM)/F12 (1:1) containing 5% FBS and 50 µg/ml endothelial mitogen (Biomedical Technologies, Stoughton, MA, USA).

Reagents. Peptides (GRGDS_4) or D₄, GRGDNPKY or R1, GQQIVGRGDNPKY or QR1 were synthesized according to the standard solid-phase synthesis method by the Peptide Synthesis Facility, M. D. Anderson Cancer Center, Houston, TX, USA. GRGDSPK was purchased from Sigma Chemical (St. Louis, MO) and PepTite 2000 containing a monomeric RGD coupled to a hydrophobic tail was purchased from Telios Pharmaceuticals (LaJolla, CA, USA). Fibronectin (FN) was purchased from Boehringer Mannheim (Indianapolis, IN) and vitronectin (VN) from Collaborative Biomedical (Bedford, MA, USA).

Immobilization of peptides and proteins: The peptides were immobilized in the Corning 6-well plates (Corning, Corning, NY, USA) pretreated with a surface coating reactive to primary amine groups. Peptide solutions were prepared in 10 mM phosphate buffer, pH 8.0, containing 20 mM freshly dissolved sodium cyanoborohydride (Aldrich Chemical, Milwaukee, WI, USA). A solution (100 μl) was applied to an area 6 mm in diameter, and the reaction was carried out overnight at 25°C. The plates were washed with Delbucco's phosphate buffered saline DPBS and finally treated with adhesion medium containing 0.1% BSA. PepTite-2000, FN and VN were immobilized at 25°C for about 1 h by hydrophobic adsorption to 35 mm nontissue culture dishes (Corning, Corning, NY) at about 7.5 $\mu\text{g}/\text{cm}^2$.

Flow experiments and image analysis: The hydrodynamic adhesion system, image acquisition and data analysis have been extensively discussed ^{3, 12}. Briefly, the cells were harvested at log growth phase shortly before each experiment, washed with CMFH [Ca²⁺, Mg²⁺-free N-2-hydroxyethylpiperazine-N'-2-ethane-sulfonic acid (HEPES) buffered saline (CMFH: 129 mM NaCl, 5 mM KCl, 0.3 mM Na₂HPO₄·7 H₂O, 1 mM NaHCO₃, 5 mM Glc, 25 mM HEPES, pH 7.4)] to remove serum components, and resuspended at 1.5 $\times 10^5$ cells/ml in serum-free DMEM containing 12 mM HEPES, pH 7.4 and 0.1% BSA. Cell adhesion was initiated by flowing the cell suspension through the chamber at about 1.0 dynes/cm², followed by a stepwise decrease in wall shear stress (WSS) until cell adhesion occurred. The WSS value for initial cell adhesion was called the wall shear adhesion threshold (WSAT). Flow of the cell suspension continued for 3-10 min, allowing cells time to stabilize their adhesion. Microscope images were digitized using a pixel minimization function over a 15 digital frame sequence (0.5 sec). A higher pixel value corresponds to the phase bright tumor cells compared to the low pixel values registered by the phase dark background. A phase bright image must remain in a given region for a minimum of 15 frames to be recorded or the background pixel value is registered. This protocol does not record moving cells and only adherent cells are saved in digital images. Cell-free medium is used at a high flow rate to dislodge cells that fail to stabilize their adhesion. The computer defines regions of interest around the center of phase bright cells and the data are segmented from the start of the experiment to the point at which the flow rate was increased to detach nonstabilized cells. The segmented data are then stepped though by the computer to determine if each cell detaches or remains adherent and the length of time each cell remains as a definable image. The elapsed time required for 50% of a given cell population to establish stabilized cell adhesion was defined as the mean adhesion stabilization lag time or ASLT. Statistical data analysis was performed using the UNIX Version 6.07 of SAS (SAS Institute, Cary, NC, USA).

Immunoprecipitation of Radioiodinated or Surface-Biotinylated Tumor Cell Lysates

Cell surface radioiodination: We used a vectorial cell surface-labeling procedure that retains biological activity in whole cells ¹³. Briefly, subconfluent cell cultures were washed and removed with buffer containing 2 mM EDTA. After resuspension, 2 $\times 10^7$ tumor cells

were radioiodinated with ^{125}I -sulfosuccinimidyl-3(4-hydroxyphenyl)propionate (Pierce, Rockford, IL, USA). Radiolabeled cells were solubilized in solubilization buffer at five times the packed cell volume.

Cell surface biotinylation of cells: Cells were harvested in the log phase of growth and washed with cold CMFH. Cells were then resuspended and incubated for 30 min in ice-cold CMFH containing 10 mM sulfo-NHS-LC-biotin (Pierce). After washing 3 times by centrifugation and resuspension in cold CMFH, the labeled cells were solubilized at a concentration of 2×10^7 cells.

Immunoprecipitation of cell lysates: Surface-labeled cell lysates (100 μl each) were precleared by incubation for 1 -2 h at 4° C with 2-10 μg of control IgG and protein A/G agarose beads (Pierce). The precleared lysates were incubated with 2 -10 μg of primary antibody for 2 h at 4° C. The immune complexes were adsorbed to protein A/G-agarose beads by incubation for at least 2 h at 4° C. After washing, the agarose beads were treated with sodium dodecyl sulfate (SDS) sample buffer and electrophoretically resolved on a 6-16 % moving boundary velocity gradient-SDS-polyacrylamide gradient gel electrophoresis. Gels were either fixed and vacuum dried or processed for chemoluminescence and exposed to Kodak XAR 5 film.

RESULTS

Adhesion Stabilization to Ecm Proteins, Peptides, and Endothelial Cells

Computerized imaging methods enabled us to examine various substrates for: (a) the wall shear adhesion threshold (WSAT), a measure of the dynamic adhesive potential of tumor cells; and (b) the adhesion stabilization lag time (ASLT) or length of time required for tumor cells to stabilize adhesive contacts capable of withstanding wall shear forces up to 100 dynes/cm². These adhesion parameters take into account a force component as a distinguishing property of the dynamic adhesion potential of cells subjected to fluid shear. The WSAT measurement helps to describe a given population of cells as they overcome the forces generated by laminar flow and arrest from circulating fluids while the ASLT measures, in a given population of cells, the resistance to detachment forces generated by dramatic increases laminar flow that might be experienced in the microcirculation.

We observed that unlike, blood granulocytes, human malignant melanoma cells immediately arrested and bound to ECM protein or endothelial cell monolayers without rolling ¹⁻³. Following arrest, melanoma cells stabilized their adhesive interactions and remained adherent even at high levels of wall shear stress ($\text{WSS} \geq 100$ dynes/cm²). Although melanoma cells could spread in less than 15 min on immobilized FN under fluid shear, spreading was not necessary to withstand high WSS levels. Stabilization of rounded cells under flow occurred while cells had a minimal contact area and presented a high shear profile under flow.

Large-cell lymphoma lines were expected to exhibit rolling properties similar to blood granulocytes. We were surprised, however, to discover that RAW117 large-cell lymphoma cells exhibited arrest and stabilization properties similar to melanoma cells. Cell rolling behavior was not observed on ECM protein or endothelial cell monolayers, and stabilization occurred with rounded cells exhibiting a high wall shear profile.

Large-cell lymphoma cells differed from melanoma cells in their secondary response characteristics and the strength of their adhesive contacts. The L17 and parental cells never spread and the H10 cells spread on VN but H10 cells never flattened to the same extent as melanoma cells on this ECM surface. Large-cell lymphoma lines did not form strong adhesive contacts, compared to melanoma cells. Large-cell lymphoma cells all detached

from FN at high WSS ($\text{WSS} \geq 100 \text{ dynes/cm}^2$). Therefore, the WSS had to be adjusted down to 20 dynes/cm 2 to perform the stabilization experiments.

We examined the WSAT adhesion dynamics of MeWo, 3S5 and 70W melanoma cells on FN and VN ECM proteins. As a group, melanoma cells adhered to FN or VN at shear levels approaching 0.3 dynes/cm 2 . The 70W cells were able to adhere to VN at a WSAT of nearly 0.5 dynes/cm 2 (Fig. 2A), which was significantly higher than the MeWo and 3S5 cells or large-cell lymphoma cells (Fig. 2A). The P and H10 cells only adhered to FN at low WSAT, and on VN the WSAT approached 0.3 dynes/cm 2 (Fig. 2A). The L17 cells did not stabilize at high shear forces on either FN or VN (Fig. 2A). The ability to adhere at high WSAT (Fig. 2A) corresponded to very short stabilization times (ASLT, Fig. 3A). Interestingly, the H10

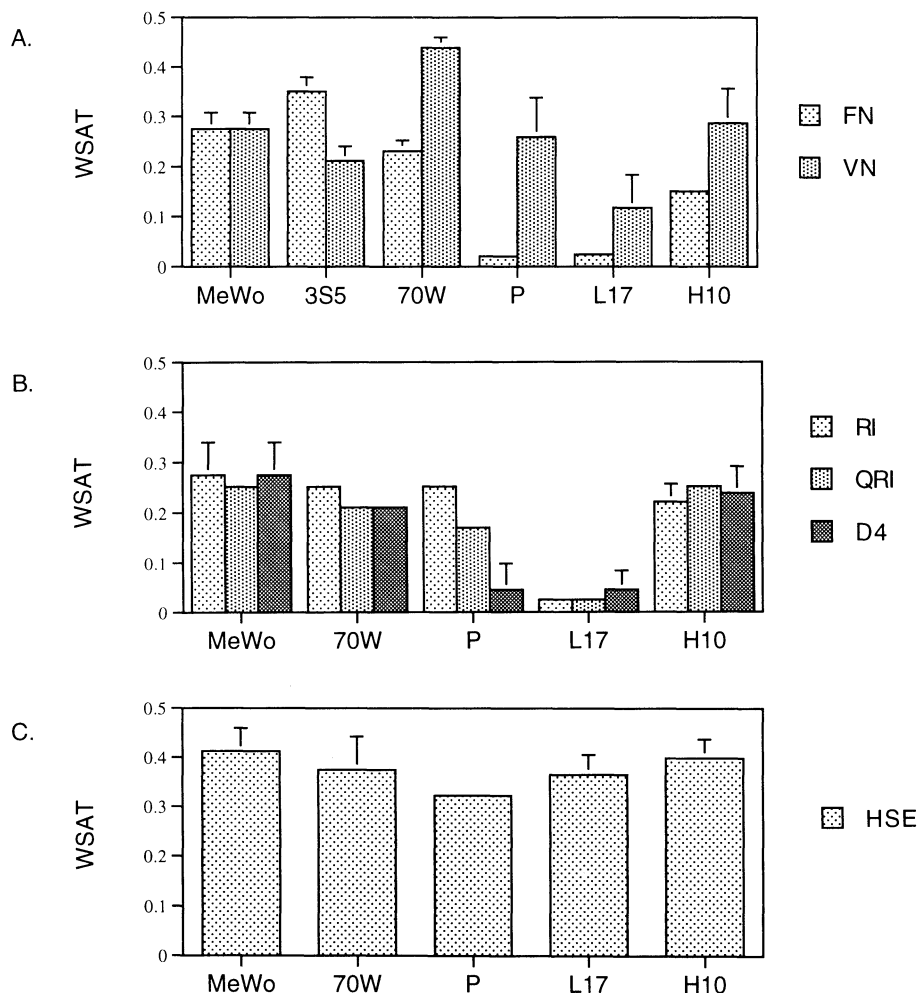


Figure 2. The flow of a tumor cell suspension is started at a flow rate or wall shear stress (WSS) level that prohibits adhesion ($\sim 1.0 \text{ dyne/cm}^2$). The flow rate is incrementally decreased until at least 5 cells adhere in the optical field and the WSS recorded as the the wall shear adhesion threshold (WSAT). The WSAT is considered a measure of the dynamic adhesive potential of a tumor cell population and describes their arrest from circulating fluids as they overcome the forces generated by laminar flow. Data are presented as the mean and standard error values from a series of experiments. For additional information refer to our other references 2, 3, 12, 26.

cells adhered to FN or VN at brief ASLT similarly to the melanoma cells (Fig. 3A). The L17 cells were all detached from FN or VN when WSS was increased.

The RGD adhesion consensus sequence was incorporated into a series of peptides that were used as substrates to understand the contribution of RGD to adhesion stabilization. The R1 peptide (GRGDNPKY) represented an RGD containing monomer, the QR1 peptide (GQQIVGRGDNPKY) contained 5 nonspecific N-terminal flanking sequences and the D4 peptide [(GRGDS)₄] polymeric RGD containing peptide. The adhesion stabilization pattern

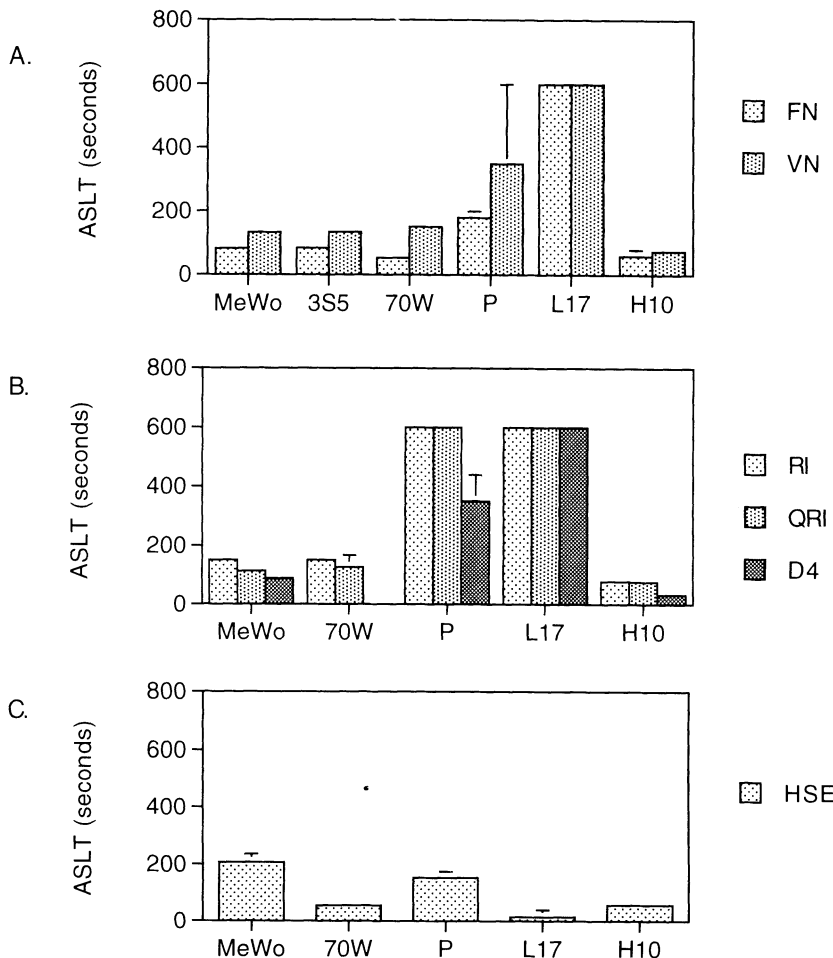


Figure 3. The adhesion stabilization lag time (ASLT) measures the length of time required for tumor cells to stabilize adhesive contacts capable of withstanding wall shear forces up to 100 dynes/cm². To determine the ASLT flow of the cell, suspension is performed for 3–10 min, allowing cells time to stabilize their adhesion. The flow rate is increased to detach cells that have not stabilized their adhesion. Over the course of each experiment, digital microscope images were recorded using a pixel minimization function. High and low pixel values correspond to phase bright tumor cells or phase dark background, respectively. Minimization refers to a phase bright pixel image remaining in a given region for a minimum of 15 frames to be recorded otherwise the computer records the background pixel value. This program segmentally records only adherent phase bright cells within computer defined regions of interest. The segmented data are then stepped through by the computer to determine if each cell detaches or remains adherent and the length of time each cell remains as a definable image. Data are presented as the mean elapsed time and upper 95% confidence values required for 50% of a given cell population to stabilize adhesion. For additional information refer to our other references^{2, 3, 12, 26}.

observed for FN or VN was similar to that observed for these synthetic peptides (Fig. 2B & 3B). The MeWo and 70W melanoma cells and the H10 large-cell lymphoma cells adhered at WSAT of nearly 0.3 dynes/cm² and stabilized in under 150 sec on all RGD-peptides (Fig. 2B). The P and L17 large-cell lymphoma cells required very low WSAT to arrest, and for the most part never stabilized to this series of RGD-peptides (Fig. 2B).

Melanoma and large-cell lymphoma tumor cell adhesion was examined using HSE cells as a substrate. All tumor cells adhered at high WSAT (Fig. 2C) and stabilized in less than ~200 sec (Fig. 3C). These results suggest that tumor cells can stabilize at higher shear rates and in less time to HSE cells than to ECM components. The less metastatic MeWo melanoma cells did stabilize as rapidly to HSE as the highly metastatic 70W melanoma cells (Fig. 3C). Surprisingly, the variation between large-cell lymphoma cells was not as profound during adhesion to HSE as there was for adhesion to ECM. The poorly metastatic P cell WSAT levels were not significantly different from those of the L17 and H10 cells; the poorly metastatic P cells did take longer to stabilize than either the L17 and H10 cells. Since endothelial cells can contribute to adhesion by initiating behavioral responses in the tumor cells this adds some of complexity to the interpretation of these data.

Adhesion Receptor Profiles

Melanoma Cells. Tumor cells most commonly adhere to ECM proteins by using integrins. We previously examined melanoma cells for integrin expression using a battery of PCR primers¹⁴. Semiquantitative PCR was used both to determine the presence of a given receptor mRNA and provide an estimate of the relative levels of message expression. The $\beta 1$ and $\beta 3$ integrin subclasses have been associated most frequently with ECM protein binding. Several of the α subunits that have been reported to associate with $\beta 1$ showed greater expression in the highly metastatic 70W cells than in the less metastatic 3S5 and MeWo cells, including $\alpha 1$, $\alpha 3$, $\alpha 4$, $\alpha 5$, and $\alpha 6$ ¹⁴. Interestingly, the levels of $\beta 1$, $\beta 3$, and αv mRNA did not vary significantly between the three metastatic variants¹⁴. These progression-related differences in integrin expression to a large degree are similar to those previously described for melanoma cell lines^{7, 9, 15} as well as melanoma tissues^{7, 9}. For example, some of the differences reported were: slight increases in αv expression, no significant change in $\beta 1$ or $\beta 3$ expression, or no detectable expression of $\alpha 2$ or αIIb . The association of melanoma cell αv integrin subunits with β subunits other than $\beta 3$ has not been reported⁹. Highly metastatic 70W cells expressed 1.80-times the $\beta 5$ mRNA levels of poorly metastatic 3S5 cells and nearly 1.65-times that of MeWo cells.

We also examined melanoma cells for expression of certain other cell adhesion molecules using semiquantitative RT-PCR. We found a 2-4 fold increase in ICAM-1 expression in the highly metastatic 70W cells compared to the MeWo and nonmetastatic 3S5 melanoma cells. PCR products for αIIb , $\alpha 2$, CD36, or ICAM-2 were not detected. The 70W cells also had higher levels of αx and $\beta 2$ (CD11/CD18 and p150 leukocyte antigen) expression than either the MeWo or 3S5 cells¹⁴.

Surface radioiodinated melanoma cell lysates were immunoprecipitated using polyclonal antibodies against FN receptor (FNR) and VN receptor (VNR). The FNR antibody differentially precipitated components that correlated with their stabilization profile on FN. The precipitate density was the lowest for the poorly metastatic 3S5 cells and there was a considerable shift in the Rf for both the α and β subunits (Fig. 4). This decrease in Mr probably represents the reduced glycosidation that occurs on the 3S5 cells as a result of WGA selection¹⁰. The FNR heterodimer profile of both the moderately metastatic MeWo parental cells and highly metastatic 70W cells demonstrated a density consistent with the stabilization profile, and it occurred at the appropriate Mr (Fig. 4). The VNR antibody precipitated a more

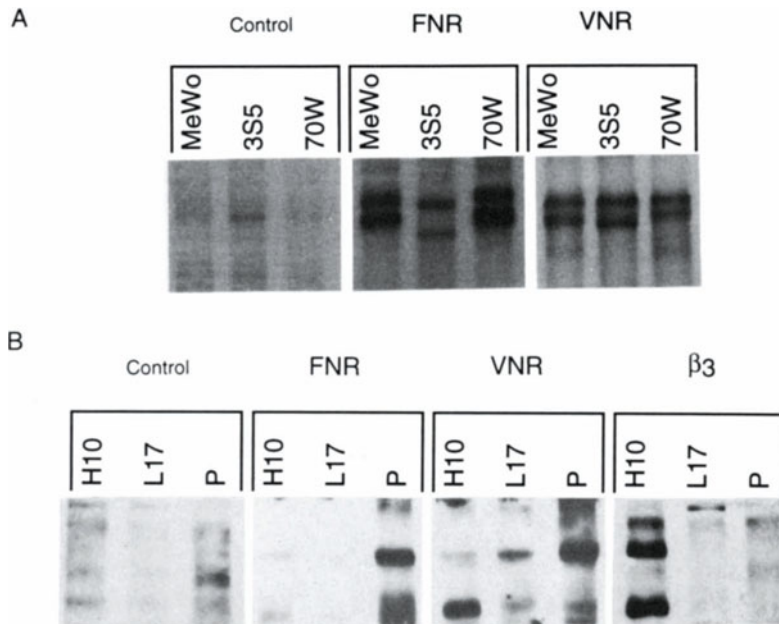


Figure 4. Surface labeled cell lysates were immunoprecipitated using polyclonal antibodies against FN receptor (FNR) and VN receptor (VNR). The FNR and VNR heterodimer profiles of MeWo parental cells and highly metastatic 70W cells occurred at the appropriate Mr. There was a slight shift in the FNR and VNR β subunits of the 3S5 cells probably, owing to a decrease in glycosidation¹⁰. Surface labeled protein was immunoprecipitated using anti-FNR only from P cell lysates and anti-VNR was immunoprecipitated from both the H10 and P cells. The presence of β 3 integrin on H10 cells was verified using a specific hamster anti-mouse β 3 antibody.

uniformly dense profile for all three cell lines (Fig. 4). The VNR antibody demonstrated a slight shift in the β subunits of the 3S5 cells, probably owing to a similar decrease in glycosidation observed with the FNR¹⁰.

Large-Cell Lymphoma Cells. When we used the PCR primers that were used to study melanoma cell integrin expression, there was very little amplification product produced using these primers to analyze RAW117 large-cell lymphoma cell RNA. The most significant product observed was the β 3 subunit. Since the complete sequences of the mouse integrins are not completely defined, a certain level of mismatch can occur and may account for the lack of amplification product.

Polyclonal antibodies against FNR and VNR were also used to immunoprecipitate large-cell lymphoma cell lysates. The FNR antibody precipitated significant amounts of cell surface biotinylated protein from P cell lysates but little to none from the H10 or L17 lysates (Fig. 4). The VNR antibody precipitated significant amounts of surface biotinylated protein from both the H10 and P cells but very little from the L17 cells (Fig. 4). Using a specific hamster anti-mouse β 3 antibody we found that the H10 cells expressed the β 3 integrin and an associated α subunit that was most likely α v but the P and L17 did not express these integrin subunits (Fig. 4).

These results emphasize the differences in integrin expression between tumor cells that arise from different germ layers. In addition to other integrins, the melanoma cells all expressed significant amounts of both the FNR and VNR receptor complexes although they

did exhibit some differences in molecular weight. The various large-cell lymphoma cell sublines predominantly expressed a single integrin class. For example, the H10 cells primarily expressed VNR, the parental cells expressed FNR and the L17 cells did not express either receptor.

Cell Spreading and Cytoskeletal Elements. The growth patterns of tumor cells in tissue culture may be reflective of how they behave during cell adhesion. For example, the melanoma cells spread extensively in tissue culture and establish a well organized cytoskeletal network that contains prominent stress fibers. The large-cell lymphoma cells grow as suspension cultures and only the H10 cells are capable of spreading on some substrates but not to the same extent as melanoma cells. The cytoskeletal elements of the large-cell lymphoma cells are less well developed than those found in melanoma cells. In addition to the type of integrin receptors these cells express, the differences in spreading behavior and cytoskeletal organization probably contribute to the cell stabilization properties which are reflected in their metastatic organ colonization patterns to certain organs.

DISCUSSION

Adhesion is one of the determining factors during the formation of distant organ metastases. Our data suggest that tumor cell arrest and stabilization properties may be important for tumor cells to differentially target to certain organs. For example, RAW117 cells generally do not exhibit strong arrest and stabilization properties except under certain conditions. The L17 and P cells that express limited levels of $\alpha v\beta 3$ receptors do not effectively stabilize on FN or VN. H10 cells expressed high levels of $\alpha v\beta 3$ receptors, readily stabilized on VN and resisted detachment at WSS of 20 dynes/cm². We hypothesize that the series of RAW117 large-cell lymphoma cells examined exhibited a more narrow set of organ colonization targets as a result of their low stabilization potential compared to the melanoma cells. H10 cells, for example, specifically target to the liver, the primary source of VN synthesis in the body. H10 cells were the only RAW117 subline to express significant levels of $\alpha v\beta 3$, and this may be important in adhering to VN in the liver sinusoids. In general, however, the detachment WSS observed for the RAW117 sublines (20 dynes/cm²) was significantly lower than that found for melanoma cells, which resisted very high WSS (≥ 100 dynes/cm²). Melanoma cells express greater numbers of different integrin receptors, including both $\alpha v\beta 3$ and $\alpha 5\beta 1$ receptors¹⁴. The melanoma cells that we examined metastasize widely to a large number of organs, including the brain and heart. Thus the arrest and stabilization properties of melanoma cells may assist them to metastasize to a wider range of organ sites. Since the basal adhesion potential of melanoma cells is so high, there may be another set of factors other than adhesion components that contributes to the organ specificity. Other factors that are important include responses to organ derived motility factors, survival factors and growth factors^{16, 17}.

In particular, cytokines, paracrine growth factors and trophic factors may have profound effects on the adhesive potentials of tumor cells and endothelial cells. Cytokines are known to elevate the expression of cell adhesion molecules at the surface of endothelial cells. For example, exposure to IL-1 or TNF causes endothelial cells to increase synthesis of E-selectin, ICAM-1 and VCAM-1¹⁸⁻²⁰ which can lead to increased tumor cell adhesion^{21, 22}. Tumor cells also respond to cytokines by increasing their expression of certain integrins, a process that is dependent on the types of tumor cells and cytokines^{7, 23}. In the brain, we have found that the expression of neurotrophin receptors on malignant cells may contribute to the survival of brain-colonizing melanoma cells^{24, 25}.

Tumor cells may also respond to hydrodynamic shear by upregulating their level of integrin expression, altering their cell surface integrin distribution, initiating integrin signaling events or changing the conformation of integrin cell surface molecules. We have found that integrin $\alpha_v\beta_3$ supports adhesion of H10 cells to monomeric RGD peptides only in the presence of hydrodynamic shear when compared to static adhesion conditions. H10 cells responded to hydrodynamic shear stress by some intracellular response or cell surface change that enables integrin $\alpha_v\beta_3$ to recognize the monomeric RGD peptides under shear conditions²⁶. Others have also reported that hydrodynamic shear alters the adhesiveness of cells. For example, differing ligand recognition capabilities of E-selectin on HL60 cells were observed by varying the hydrodynamic conditions²⁷. Fluid shear stress also induces potassium²⁸ and calcium²⁹ currents in endothelial cells, activates protein kinase C³⁰ and phosphorylation by protein tyrosine kinases³¹ in platelets. Fluid shear can also alter the expression of adhesion receptors. Shear also induces changes in ICAM-1 and VCAM-1 expression on the surface of endothelial cells³²⁻³⁴. The mechanisms for the possible regulation of integrin function by hydrodynamic shear stress remain to be determined.

The adhesion stabilization assays that we developed enabled us to examine a component few other adhesion assays can examine. We are able to determine (a) a force resistance component and (b) a rate of stabilization that measures the dynamic aspects of cell adhesion during their early phase. This provides us with a more realistic picture of the adhesion process and is more predictive of the true contribution of adhesive potential to metastatic cell behavior.

REFERENCES

1. M. B. Lawrence, C. W. Smith, S. G. Eskin and L. V. McIntire, Effect of Venous Shear Stress on CD18-mediated neutrophil adhesion to cultured endothelium, *Blood*. 75; 227 (1990).
2. D. G. Menter, J. T. Patton, T. V. Updyke, R. S. Kerbel, M. Maamer, L. V. McIntire and G. L. Nicolson, Transglutaminase stabilizes melanoma adhesion under laminar flow, *Cell Biophys.* 18; 123 (1992).
3. J. T. Patton, D. G. Menter, D. M. Benson, G. L. Nicolson and L. V. McIntire, Computerized analysis of tumor cells flowing in a parallel plate chamber to determine their adhesion stabilization lag time, *Cell Motil. Cyto.* 26; 88 (1993).
4. A. Sonnenberg, Integrins and their ligands, in Current Topics in Microbiology and Immunology: Adhesion in leukocyte homing and differentiation, D. Dunon, C. R. Mackay and B. A. Imhof, ed., Springer-Verlag, Heidelberg (1993).
5. G. L. Nicolson, Tumor and host molecules important in the organ preference of metastasis, *Semin. Cancer Biol.* 2; 143 (1991).
6. S. S. Smyth, C. C. Jonekis and L. V. Parise, Regulation of vascular integrins, *Blood*. 81; 2827 (1993).
7. M. Weterman A. J., G. N. P. Vanmuijen, H. P. J. Bloemers and D. J. Ruiter, Molecular markers of melanocytic progression, *Laboratory Invest.* 70; 593 (1994).
8. M. Pignatelli and G. Stamp, Integrins in tumour development and spread, in Cancer surveys: Cell adhesion and Cancer, E. Sidebottom. Cold Spring Harbor Laboratory Press, Plainview, NY, 113 (1995).
9. M. Edward, Integrins and other adhesion molecules involved in melanocytic tumor progression, *Current Opinion in Oncology*. 7; 185 (1995).
10. M. Ishikawa, J. W. Dennis, S. Man and R. S. Kerbel, Isolation and characterization of spontaneous wheat germ agglutinin-resistant human melanoma mutants displaying remarkably different metastatic profiles in nude mice, *Cancer Res.* 48; 665 (1988).
11. P. N. Belloni and G. L. Nicolson, Differential expression of cell surface glycoproteins on various organ-derived microvesicular endothelia and endothelial cells cultures., *J. Cell. Physiol.* 136; 398 (1988).
12. T. W. Smith, Yun Z, D. G. Menter, L. V. McIntire and G. L. Nicolson, Computer analysis of tumor cell interaction with extracellular matrix proteins and endothelial cells under laminar flow., *Biotechnol. Bioeng.*, In press.; (1995).
13. J. L. Herrmann, D. G. Menter, J. Hamada, D. Marchetti, M. Nakajima and G. L. Nicolson, Mediation of NGF-stimulated extracellular matrix invasion by the human melanoma low-affinity p75 neurotrophin receptor: melanoma p75 functions independently of trkA, *Mol Biol Cell*. 4; 1205 (1993).

14. D. G. Menter, L. F. Fitzgerald, J. T. Patton, L. V. McIntire and G. L. Nicolson, Human melanoma integrins contribute to arrest and stabilization potential while flowing over extracellular matrix, *Immunol. Cell Biol.* in press; (1995).
15. R. Montarini, A. Arichini and G. Parmiani, Heterogeneity for integrin expression and cytokine-mediated VLA modulation can influence the adhesion of human melanoma cells to extracellular matrix proteins, *Int. J. Cancer.* 47; 551 (1991).
16. G. L. Nicolson, Cancer progression and growth: Relationship of paracrine and autocrine growth mechanisms to organ preference of metastasis, *Exp Cell Res.* 204; 171 (1993).
17. G. L. Nicolson, D. G. Menter, J. L. Herrmann, P. Cavanaugh, L. Jia, J. Hamada, Z. Yun, M. Nakajima and D. Marchetti, Tumor metastasis to brain: role of endothelial cells, neurotrophins and paracrine growth factors., *Crit. Rev. Oncogenesis.* (1994).
18. M. L. Dustin, R. Rothelein, A. K. Bhan, C. A. Dinarello and T. A. Springer, Induction by IL-1 and interferon- γ tissue distribution, biochemistry, function of natural adherence molecule (ICAM-1),, *J. Immunol.* 137; 245 (1986).
19. M. P. Bevilacqua, S. Stengelin, M. A. Gimbrone and B. Seed, Endothelial leukocyte adhesion molecule 1: an inducible receptor for neutrophils related to competent regulator proteins and lectins., *Science.* 243; 1160 (1989).
20. G. E. Rice, J. M. Munro and M. P. Bevilacqua, Inducible cell adhesion molecule (INCAM-110) is an endothelial cell receptor for lymphocytes. A CD11/CD18-independent adhesion mechanism., *J. Exp. Med.* 171; 1369 (1990).
21. M. Bertomeu, S. Gallo, D. Lauri, T. Haas, F. Orr, E. Bastida and M. Buchanan, Interleukin 1-induced cancer cell/endothelial cell adhesion *in vitro* and its relationship to metastasis *in vivo*: role of vessel wall 13-HODE synthesis and integrin expression., *Clin. Exper. Metastasis.* 11; 243 (1993).
22. A. Tozeren, H. Kleinman, D. Grant, D. Morales, A. Mercurio and S. Byers, E-selectin-mediated dynamic interactions of breast- and colon-cancer cells with endothelial-cell monolayers., *Int. J. Cancer.* 60; 426 (1995).
23. R. Mortarini, A. Anichini and G. Parmiani, Heterogeneity for integrin expression and cytokine-mediated VLA modulation can influence the adhesion of human melanoma cells to extracellular matrix proteins., *Int. J. Cancer.* 47; 551 (1991).
24. D. G. Menter, J. L. Herrmann and G. L. Nicolson, The role of trophic factors and autocrine/paracrine growth factors in brain metastasis, *Clin. Exp. Metastasis.* 13; 67 (1995).
25. D. G. Menter, J. L. Herrmann, D. Marchetti and G. L. Nicolson, Involvement of neurotrophins and growth factors in brain metastasis formation, *Invas. and Metastasis.* in press; (1995).
26. Z. Yun, T. W. Smith, D. G. Menter, L. V. McIntire and G. L. Nicolson, Static and hydrodynamic adhesion to Arg-Gly-Asp peptides of metastatic RAW117 large-Cell lymphoma: role of the $\alpha v \beta 3$ integrin, *in preparation.* (1995).
27. N. Kojima, K. Handa, W. Newman and S. Hakamori, Multi-recognition capability of E-selectin in a dynamic flow system, as evidenced by differential effects of sialidase and anti-carbohydrate antibodies on selectin-mediated cell adhesion at low vs. high shear stress., *Biochem. Biophys. Res. Commun.* 189; 1686 (1992).
28. S. P. Olesen, D. E. Clapham and L. V. McIntire, Haemodynamic shear stress activates a K^+ current in vascular endothelial cells., *Nature.* 331; 168 (1983).
29. R. V. Geiger, B. C. Berk, R. W. Alexander and R. M. Nerem, Flow-induced calcium transients in single endothelial cells: spatial and temporal analysis., *Am. J. Physiol.* (1992).
30. M. H. Kroll, J. D. Hellums, Z. Guo, W. Durante, K. Razdan, J. K. Hrbolich and A. Schaffer, Protein kinase C is activated in platelets subjected to pathological shear stress., *J. Biol. Chem.* 256; 3520 (1993).
31. K. Razdan, J. D. Hellums and M. H. Kroll, Shear-stress-induced von Willebrand factor binding to platelets causes the activation of tyrosine kinases., *Biochem. J.* 302; 681 (1994).
32. R. Sampath, G. L. Kukielka, C. W. Smith, S. G. Eskin and L. V. McIntire, Shear stress-mediated changes in the expression of leukocyte adhesion receptors on human umbilical vein endothelial cells *in vitro*., *Annals Biomed. Engineer.* 23; 247 (1995).
33. M. Morigi, C. Zoja, M. Figliuzzi, M. Foppolo, G. Micheletti, M. Bontempelli, M. Sarponi, G. Remuzzi and A. Remuzzi, Fluid shear stress modulates surface expression of adhesion molecules by endothelial cells., *Blood.* 85; 1696 (1995).
34. J. Ando, H. Tsuboi, R. Korenaga, Y. Takada, N. Toyama-Sorimachi, M. Miyasaka and A. Kamiya, Down-regulation of vascular adhesion molecule-1 by fluid shear stress in cultured mouse endothelial cells., *Ann. N. Y. Acad. Sci.* 748; 148 (1995).

PROBING OF CONNEXIN CHANNELS

Evidence for Involvement of Junctional Coupling in Pancreatic Secretion

Paolo Meda

Department of Morphology
University of Geneva Medical School
1211 Genève 4, Switzerland

INTRODUCTION

Normal functions of multicellular systems depend on a network for cell-to-cell communication. Via such a network, individual cells sense the state of activity of their neighbors and thereby regulate their own level of functioning. Vertebrate cells may communicate in a variety of ways. A widespread mechanism for intercellular communication is via the diffusion in the extracellular space of hormones and neuromediators that are simultaneously sensed by cells bearing cognate receptors. A second form of cell-to-cell communication is provided by the diffusion in the extracellular space of ions and molecules which enter cells by free diffusion through the lipid membrane bilayer or by way of specific channels and transporters. Coordination is then achieved by the simultaneous activation of specific metabolic and effector steps in several cells. In spite of the diversity of the structures and signals used to establish cellular cross-talk, all these mechanisms require the passage of signals through extracellular spaces, and are referred to as "indirect" forms of cell-to-cell communication. Most cells also communicate in a "direct" way, i.e. by mechanisms which do not involve the passage of signals in the extracellular space and which obligatorily require cell-to-cell contact. One way of establishing such communication is via cell adhesion molecules, the surface glycoproteins which associate with the cytoskeletal elements that act as information transducers at both cytoplasm and nucleus level. Direct cell-to-cell communication also is mediated by connexins, the non glycosylated proteins which form gap junctions. These structures are clusters of highly permeable channels that cross the membranes of adjacent cells and bridge the intervening extracellular space, thus allowing for a diffusional cell-to-cell exchange of cytoplasmic ions and small molecules (Bennett et al., 1991; Kumar and Gilula, 1992).

The main secretory cells of both endocrine and exocrine pancreas communicate with companion cells by all the mechanisms listed above. Hence, it has long been known that their functioning is coordinated by hormones, neuromediators and other signals, which reach the pancreas from outside or which are generated within the gland itself (Singer, 1986;

Stagner, 1991). More recently, it has been recognized that the hormone and enzyme secretion of the functional subunits of pancreas is still a regulated event under *in vitro* conditions which perturb the native blood supply, innervation and flux of intercellular fluid, indicating that other communication mechanisms should also be operative. The finding that single β - and acinar cells of pancreas show an altered secretion, which rapidly improves with cell aggregation (Salomon and Meda, 1986; Bosco et al., 1989; 1994), suggests that these mechanisms depend on proper cell-to-cell contacts. Several lines of evidence indicate that one of such mechanisms could be the intercellular exchange of ions and molecules via gap junction channels (Meda, 1995; Chanson and Meda, 1993).

JUNCTIONAL COUPLING AND INSULIN SECRETION

Within the islets of Langerhans, the insulin-producing β -cells are connected to each other by numerous and minute gap junctions (Orci et al., 1973), made of a 43 kDa connexin protein, referred to as Cx43 (Meda et al., 1991). In a resting β -cell, there are 800-2000 gap junction channels which altogether occupy less than 1 μm^2 of the plasma membrane (Meda et al., 1979). These channels allow for the β -to- β -cell exchange of current-carrying ions (electrical coupling), as shown by the intercellular spread of electrotonic potential changes (Meissner, 1976; Eddlestone et al., 1984), by the detection of junctional conductances at individual β -to- β -cell interfaces (Meda et al., 1991) and by the synchronization of free Ca^{2+} oscillations (Valdeolmillos et al., 1993) and membrane potentials across the islets (Meda et al., 1984). Gap junction channels also mediate the exchange between β -cells of molecules which do not permeate the cell membrane (metabolic coupling), such as exogenous fluorescent probes, nucleotides and glycolytic intermediates (Kohen et al., 1979; Meda et al., 1981, 1983, 1991). Electrical and metabolic coupling, as well as gap junctions, are not observed between all β -cells. Hence, the 10-3,000 β -cells that comprise a pancreatic islet appear to be functionally grouped in multiple communication territories rather than in a single syncytial unit (Meda, 1995).

Several lines of evidence indicate a contribution of β -cell coupling to the control of insulin secretion. First, single β -cells show perturbed functioning, as indicated by increased basal release of insulin, poor responsiveness to secretagogues, decreased protein biosynthesis, decreased basal expression of the insulin gene and loss of its normal, cAMP-dependent control, whereas restoration of β -to- β -cell contacts is paralleled by a rapid improvement in these defects (Salomon and Meda, 1986; Bosco et al., 1989; Pipeleers, 1984; Bosco and Meda, 1992; Philippe et al., 1992). The finding that a drug which blocks gap junction channels prevents the increase in insulin secretion that normally occurs under the latter conditions (Meda et al., 1990), indicates that coupling may play a major role in these changes.

Second, *in vivo* as well as *in vitro*, sustained stimulation of insulin release was found associated with an increase in β -cell coupling due, at least in some cases, to increased expression of gap junctions and Cx43 (Kohen et al., 1979; Meda et al., 1979, 1983, 1991). Other experiments have further suggested that β -cell coupling may also acutely increase during glucose stimulation, as judged by changes in coupling coefficient, as well as by enhanced synchronization in the electrical activity and Ca^{2+} oscillations of islet cells (Valdeolmillos et al., 1993; Eddlestone et al., 1984). However, it remains to be determined to what extent these changes are actually due to improved junctional communication.

Third, conditions that inhibit insulin release decrease or abolish β -to- β -cell coupling (Meda et al., 1983; Kohen et al., 1983). *In vivo*, however, such conditions result in hyperglycemia and increased β -cell-coupling (Meda et al., 1983), suggesting that the level of circulating glucose and the ability of β -cells to properly recognize the sugar, may independently influence junctional channels.

Fourth, the acute pharmacological blockade of gap junction channels markedly alters β -cell function, as indicated by increased basal insulin release and loss of stimulated insulin secretion from both isolated islets of Langerhans and intact pancreas (Meda et al., 1990). These alterations, which could not be accounted for by concomitant changes in the main second messengers controlling insulin secretion, were rapidly and fully reversible after wash out of the uncoupling drugs and were not observed with single β -cells (Meda et al., 1990), indicating that they may well be a specific result of cell uncoupling. This view is further supported by preliminary observations showing that antisense oligonucleotides which block the transcription of Cx43 mRNA, also decrease in a similar way the secretory response of clustered, but not of single β -cells (unpublished data).

Fifth, a number of tumoral and transformed insulin-producing cell lines (RIN, HIT, INS, AtT20ins, CGT5, GT6) which show abnormal glucose sensitivity, do not express connexins and gap junctions and are essentially uncoupled (Vozzi et al., 1995). These defects cannot be explained simply by the *in vitro* downregulation of gap junctional channels since primary β -cells in monolayer culture consistently express Cx43, gap junctions and coupling (Kohen et al., 1979; Meda et al., 1981; Kohen et al., 1983; Vozzi et al., 1995). Nor can these defects be ascribed solely to the proliferation capacity of the cell lines, since the glucose-sensitive cells of a rat insulinoma, from which at least two of the communication-deficient lines were derived, still express Cx43, gap junctions and coupling *in vivo* (Meda et al., 1991). Hence, coupling defects appear to be a shared attribute of cell lines showing abnormal sensitivity to glucose, whatever their origin and metabolic characteristics. Two sets of recent data support this view. First, another tumoral line (MIN6) which also produces insulin, and has retained at least some glucose sensitivity, show small gap junctions made of Cx43 (unpublished data). Second, INS cells that have been stably transfected with the gene coding for Cx43, and express gap junctions and coupling like primary β -cells, display a qualitatively normal glucose-responsiveness, a markedly increased insulin content and an enhanced expression of the insulin gene (Vozzi et al., in press). *In vivo*, these cells grow less and secrete more insulin than wild type, non communicating INS cells (unpublished data).

JUNCTIONAL COUPLING AND AMYLASE SECRETION

The enzyme-producing acinar cells of the exocrine pancreas are also coupled by numerous gap junctions, which are made of two proteins of 32 kDa and 26 kDa, referred to as Cx32 and Cx26 (Meda et al., 1991, 1993). In a resting acinar cell, there are 60,000-138,000 gap junction channels occupying about 5 μm^2 of the cell membrane (Meda et al., 1983). The ionic and molecular exchanges which occur through this large number of junctional channels are quite extensive, as judged by a high junctional conductance (Chanson et al., 1989) and a large spread of both electrotonic potentials (Iwatsuki and Petersen, 1977) and low molecular weight gap junction tracers (Iwatsuki and Petersen, 1979; Meda et al., 1986). As a result, the 10-50 cells that form a pancreatic acinus are electrically and metabolically coupled to each other, and, hence, represent a truly syncytial unit.

Several lines of evidence indicate that coupling is involved in the control of amylase secretion by acinar cells. First, dispersed acinar cells secrete poorly under basal and stimulatory conditions, and markedly increase their response to secretagogues after reestablishment of junctional contacts (Bosco et al., 1994). The pattern of junctional coupling which is observed under such conditions is analogous to that observed in the intact pancreas (Bosco et al., 1994).

Second, the most efficient secretagogues of the exocrine pancreas rapidly uncouple acinar cells *in vitro* (Chanson et al., 1989; Iwatsuki and Petersen, 1977, 1979; Meda et al., 1986, 1987). At least for cholinergic agonists, we know that this effect is due to the activation

of muscarinic receptors and is mediated by a Ca^{2+} -, pH- and PKC-independent gating of gap junction channels (Chanson et al., 1989; Iwatsuki and Petersen, 1977, 1979; Meda et al., 1986, 1987). The observation that an identical uncoupling is elicited *in vivo*, by the endogenous cholinergic neuromediators that are focally released within the pancreas during vagal nerve stimulation (Chanson et al., 1991), provides direct evidence that this coupling modulation may be of physiological relevance.

Third, the acute pharmacological blockade of gap junction channels increases amylase release within seconds in the absence of other stimuli, *in vitro* as well as *in vivo* (Chanson et al., 1989; Meda et al., 1986, 1987). This stimulation is not associated with detectable alterations in non-junctional conductances and in the major second messengers which control acinar cell secretion. Furthermore, it is prevented under conditions inhibiting exocytosis of pancreatic enzymes, and is rapidly reversed after wash out of the uncoupling drugs and restoration of normal junctional communication (Chanson et al., 1989; Meda et al., 1986, 1987). Together, these data suggest that the uncoupling drugs act specifically on gap junctions, an interpretation further supported by the lack of effect of these drugs on acinar cells that are already uncoupled after physical dispersion or maximal stimulation by cholinergic secretagogues (Chanson et al., 1989; Meda et al., 1986; Bosco et al., 1994). In contrast, during stimulation by secretagogues which do not perturb acinar cell coupling, drugs blocking gap junctions potentiate amylase secretion up to the maximal levels observed during cholinergic stimulation (Meda et al., 1987). Since this stimulation was independent of the intracellular mechanism used by these secretagogues to activate acinar cells, uncoupling probably results in the activation of a distal step in the normal chain of events which leads to exocytosis of pancreatic enzymes.

Fourth, prolonged exposure to dexamethasone of cells of the AR4-2J line, which are derived from a pancreatic acinar cell carcinoma, increases amylase production and secretion as well as junctional coupling, and differentially modifies the expression of Cx32 and Cx26 (Meda et al., 1995). Thus, hormonal conditions favoring differentiation of specific acinar cell markers, also selectively modulate junctional communication and the expression of distinct connexins.

HOW JUNCTIONAL COUPLING MAY AFFECT PANCREATIC SECRETION

The set of observations summarized above provides compelling evidence that changes in junctional coupling parallel changes in secretion, in both endocrine and exocrine pancreas. Coupling appears to be implicated both in the moment-to-moment regulation of the release of secretory products, as well as in the more long term regulation of their cell specific expression. However, whether and how coupling and secretion are causally linked, remains to be shown. Also, it remains to be established why modulation of junctional coupling may affect secretion.

Compared to all other forms of cell-to-cell communication, gap junctional coupling is unique in that it provides a direct mechanism for equilibrating ionic and molecular gradients between nearby cells (Bennett et al., 1991; Kumar and Gilula, 1992). In such a system, the increase in cytoplasmic ions or molecules less than 900 Da in one cell, is followed by their diffusion-driven passage into nearby cells. In the steady state, this passage leads to the equilibration of electrochemical concentrations on the two sides of the channels. If the resulting concentration reaches the threshold level for activation of an effector mechanism, functioning will be simultaneously modified in all coupled cells. In this way, junctional coupling could ensure the functional recruitment of many cells that, otherwise, would not

be directly activated. Such a recruiting role has been experimentally verified in both the β - and acinar cell populations (Salomon and Meda, 1986; Bosco et al., 1989, 1994; Bosco and Meda, 1992). Since insulin and amylase secretion of coupled cells is larger than that of uncoupled cells (Bosco et al., 1989, 1994), the coupling-induced equilibration is also likely to optimize the concentration of factors controlling secretion. This view is consistent with the observation that the threshold level for activation of insulin secretion and biosynthesis is lowered under conditions promoting β -cell coupling (Sorenson and Parsons, 1985). Eventually, coupling would also be expected to synchronize cell functions which are modulated by factors exchanged through gap junctions. This expectation has been verified, at least for Ca^{2+} , in both endocrine and exocrine pancreatic cells (Valdeolmillos et al., 1993; Petersen and Petersen, 1991).

This model implies that junctional coupling may be particularly advantageous in systems comprising functionally different cells. Increasing evidence shows that this is the case in the pancreas, since individual β - and acinar cells are substantially different in their ability to release secretory products, *in vitro* and *in vivo* (Salomon and Meda, 1986; Bosco et al., 1989, 1994; Stefan et al., 1987). Furthermore, β -cells are also heterogeneous in their ability to biosynthesize proteins, including insulin, and in a number of metabolic features which are critical for proper processing of glucose stimulation (Bosco and Meda, 1992; Heimberg et al., 1993; Schuit et al., 1988). Conceivably, these disparities could explain the asynchronous functioning of individual cells. By equilibrating ionic and molecular gradients, junctional coupling could balance and coordinate these disparities, thus permitting the coordinated functioning of intrinsically different cells.

The identification of an intrinsic heterogeneity of both β - and acinar cells permits to conceptualize why and how junctional coupling could modulate the endocrine and exocrine secretion of the pancreas. What is not determined is the molecular mechanism underlying this modulation. A first possibility is that coupling enhances the secretagogue-induced changes in free intracellular Ca^{2+} . Indeed, the levels and oscillations of this cation, which plays a critical role in the control of both insulin and amylase secretion, are differentially affected by the establishment of contacts between both β - and acinar cells (Valdeolmillos et al., 1993; Petersen and Petersen, 1991).

Second, coupling may modulate electrophysiological characteristics of secretory cells. Resting membrane potentials and individual conductances become larger and more stable after establishment of cell-to-cell contacts, presumably because individual β - and acinar cells are equipped with such limited numbers of K^+ and Ca^{2+} channels that they cannot ensure stable ionic fluxes as these channels fluctuate between the open and the closed state (Atwater et al., 1983; Petersen and Findlay, 1987). By mediating the intercellular equilibration of current-carrying ions, junctional coupling may result in the functional sharing of these channels, that could then be always available in sufficient numbers to all coupled cells. Such a channel sharing may markedly promote the responsiveness of β - and acinar cells, since the activation of the distal steps of their secretory machinery depends on proper control of membrane potentials and ionic fluxes.

Third, intercellular exchanges of both Ca^{2+} and K^+ could account for the electrical synchronization of β - and acinar cells which has been observed in intact islets of Langerhans and acinar cell assemblies (Meissner, 1976; Valdeolmillos et al., 1993; Petersen and Petersen, 1991).

Fourth, coupling could ensure the spreading of signals controlling secretion across large cell populations. Secretagogue-induced Ca^{2+} waves, indicating a temporally and spatially coordinated change in the levels of this ion, have been observed throughout intact islets and acini (Valdeolmillos et al., 1993; Petersen and Petersen, 1991). These waves may result from the intercellular exchange of Ca^{2+} via gap junctions, and may mediate the rapid recruitment of secreting cells at a distance from the site of signaling. An analogous

mechanism has been shown to ensure the hormonal stimulation of cells devoid of cognate receptors, provided these cells were coupled to neighbors that are able to recognize the signal (Lawrence et al., 1978; Murray and Fletcher, 1984). This effect, which is probably due to a gap junction-mediated transfer of second messengers, may operate in the pancreas to functionally recruit cells deficient in factors which rate-limit secretion. Some acinar cells lack receptors for gut hormones and neuromediators (Bosco et al., 1994). By sharing gap junctions with cells equipped with these receptors, defective cells may acquire the ability to exhibit an adequate secretory response.

CONCLUSIONS

Secretion of both endocrine and exocrine pancreas is the result of the activity of numerous and functionally heterogeneous cells, whose integration obligatorily depends on proper communication. Full control of β - and acinar cell function cannot be ascribed to a sole regulatory mechanism, but rather to the interaction between multiple mechanisms that involve cell-to-cell signaling by nutrients, intrinsic and extrinsic neural inputs, local and circulating hormones, as well as direct interactions between adjacent cells. A major problem in unravelling the regulation of pancreatic secretion stems from the complex interactions between these signals, which converge at the islet and acinar level. The multiplicity of mechanisms for intercellular coordination permits the pancreas to properly adapt its hormonal and enzymatic secretion to the needs of the organism, which continuously change throughout the day, depending on the physiological condition. It also provides pancreatic cells with a regulatory system that, even though redundant and costly for the cells, allows for preservation of a normal secretory function under most conditions.

The precise contribution of different communication mechanisms to the net response of the pancreas remains to be fully understood, as does the hierarchic organization of pancreatic controls. In this respect, the finding of a gap junction-mediated modulation of pancreatic functions under conditions abolishing indirect cell-to-cell communication, indicates a fundamental, hitherto disregarded role of cell-to-cell coupling. In view of the now well established functional heterogeneity of both β -cells and acinar cells, it is probable that this mechanism has become an obligatory feature in evolution since it provides the most direct way for compensating intrinsic metabolic and effector differences of secretory cells. Hence, this equilibrating mechanism may be essential for building an appropriate output of hormones and enzymes, starting from the highly heterogeneous β - and acinar cell populations.

At this time, however, the molecular mechanism underlying the relationship between the control of coupling and pancreatic secretion remains to be unravelled, and our understanding of whether such a relationship is causal is limited by several unknowns. It remains also to be assessed whether and how coupling defects participate in the early and still obscure pathogenesis of pancreatic dysfunctions of major relevance to human medicine. As yet, such a possibility has not been investigated. The recent availability of novel cell and molecular biology tools, and of strategies with which to interfere with specific steps of junctional coupling and secretion, offers now the exciting perspective of directly addressing these questions, *in vitro* as well as *in vivo*.

ACKNOWLEDGMENTS

Supported by grants from the Swiss National Science Foundation (32-43086.95), the Juvenile Diabetes Foundation International (195077), and the European Union (BMH4-CT96-1427).

REFERENCES

- Atwater, I., Rosario, L. and Rojas, E. (1983) Properties of the Ca-activated K⁺ channel in pancreatic B-cells. *Cell calcium*, 4, 451-461.
- Bennett, M. V. L., Barrio, L. C., Bargiello, T. A., Spray, D. C., Hertzberg, E. and Saez, J. C. (1991) Gap junctions: New tools, new answers, new questions. *Neuron* 6, 305-320.
- Bosco, D. and Meda, P. (1992) Actively synthetizing B-cells secrete preferentially during glucose stimulation. *Endocrinology*, 129, 3157-3166.
- Bosco, D., Orci, L. and Meda, P. (1989) Homologous but not heterologous contact increases the insulin secretion of individual pancreatic B-cells. *Exp. Cell Res.*, 184, 72-80.
- Bosco, D., Soriano, J.V., Chanson, M. and Meda, P. (1994) Heterogeneity and contact-dependent regulation of amylase release by individual acinar cells. *J. Cell Physiol.*, 60, 378-388.
- Chanson, M. and Meda, P. (1993) Rat pancreatic acinar cell coupling: comparison of extent and modulation in vitro and in vivo. *Prog. Cell. Res.*, 3, 199-205.
- Chanson, M., Bruzzone, R., Bosco, D. and Meda, P. (1989) Effects of n-alcohols on junctional coupling and amylase secretion of pancreatic acinar cells. *J. Cell Physiol.*, 139, 147-156.
- Chanson, M., Orci, L. and Meda, P. (1991) Extent and modulation of junctional communication between pancreatic acinar cells *in vivo*. *Am. J. Physiol.* 261, G28-G36.
- Eddlestone, G. T., Gonçalves, A., Bangham, J. A. and Rojas, E. (1984) Electrical coupling between cells in islets of Langerhans from mouse. *J. Membr. Biol.*, 77, 1-14.
- Heimberg, H., De Vos, A., Vandercammen, A., Van Schaftingen, E., Pipeleers, D. and Schuit, F. (1993) Heterogeneity in glucose sensitivity among pancreatic β-cells is correlated to differences in glucose phosphorylation rather than glucose transport. *EMBO J.*, 12, 2873-2879.
- Iwatsuki, N. and Petersen, O. H. (1977) Acetylcholine-like effects of intracellular calcium application in pancreatic acinar cells. *Nature*, 268, 147-149.
- Iwatsuki, N. and Petersen, O. H. (1979) Direct visualization of cell to cell coupling: transfer of fluorescent probes in living mammalian pancreatic acini. *Pflügers Arch. Eur. J. Physiol.*, 380, 277-281.
- Kohen, E., Kohen, C. and Rabinovitch, A. (1983) Cell-to-cell communication in rat pancreatic islet monolayer cultures is modulated by agents affecting islet cell secretory activity. *Diabetes*, 32, 95-98.
- Kohen, E., Kohen, C., Thorell, B., Mintz, D. H. and Rabinovitch, A. (1979) Intercellular communication in pancreatic islet monolayer cultures: a microfluorometric study. *Science*, 204, 862-865.
- Kumar, N. M. and Gilula, N. B. (1992) Molecular biology and genetics of gap junction channels. *Sem. Cell. Biol.* 3, 3-16.
- Lawrence, T. S., Beers, W. H. and Gilula, N. B. (1978) Transmission of hormonal stimulation by cell-to-cell communication. *Nature* 272, 501-506.
- Meda, P. (1995) Junctional coupling of pancreatic β-cells. In: *Pacemaker activity and intercellular communication*. (Ed J. D. Huizinga), p. 275-290. CRC Press, Boca Raton, Florida.
- Meda, P., Amherdt, M., Perrelet, A. and Orci, L. (1981) Metabolic coupling between cultured pancreatic B-cells. *Exp. Cell Res.* 133, 421-430.
- Meda, P., Atwater, I., Gonçalves, A., Bangham, A., Orci, L. and Rojas, E. (1984) The topography of electrical synchrony among B-cells in the mouse islets of Langerhans. *Quart. J. Exp. Physiol.*, 69, 719-735.
- Meda, P., Bosco, D., Chanson, M., Giordano, E., Vallar, L., Wollheim, C. and Orci, L. (1990) Rapid and reversible secretion changes during uncoupling of rat insulin-producing cells. *J. Clin. Invest.*, 86, 759-768.
- Meda, P., Bruzzone, R., Chanson, M., Bosco, D. and Orci, L. (1987) Gap junctional coupling modulates secretion of exocrine pancreas. *Proc. Natl. Acad. Sci. USA*, 84, 4901-4904.
- Meda, P., Bruzzone, R., Knodel, S. and Orci, L. (1986) Blockage of cell-to-cell communication within pancreatic acini is associated with increased basal release of amylase. *J. Cell Biol.*, 103, 475-483.
- Meda, P., Chanson, M., Pepper, M., Giordano, E., Bosco, D., Traub, O., Willecke, K., El Aoumari, A., Gros, D., Beyer, E., Orci, L. and Spray, D. C. (1991) *In vivo* modulation of connexin 43 gene expression and junctional coupling of pancreatic B-cells. *Exp. Cell Res.*, 192, 469-480.
- Meda, P., Michaels, R. L., Halban, P. A., Orci, L. and Sheridan, J. D. (1983) *In vivo* modulation of gap junctions and dye coupling between B-cells of the intact pancreatic islet. *Diabetes*, 32, 858-868.
- Meda, P., Pepper, M., Traub, O., Willecke, K., Gros, D., Beyer, E., Nicholson, B., Paul, D. and Orci, L. (1993) Differential expression of gap junction connexins in endocrine and exocrine glands. *Endocrinology*, 133, 2371-2378.
- Meda, P., Perrelet, A. and Orci, L. (1979) Increase of gap junctions between pancreatic B-cells during stimulation of insulin secretion. *J. Cell Biol.*, 82, 441-448.

- Meda, P., Vozzi, C., Ullrich, S., Dupont, E., Charollais, A., Sutter, E. and Bosco, D. (1995) Gland cell connexins. *Prog. Cell Res.*, 4, 281-287.
- Meissner, H. P. (1976) Electrophysiological evidence for coupling between pancreatic β cells of pancreatic islets. *Nature*, 262, 502-504.
- Murray, S. A. and Fletcher, W. H. (1984) Hormone-induced intercellular signal transfer dissociates cyclic AMP-dependent protein kinase. *J. Cell Biol.*, 98, 1710-1719.
- Orci, L., Unger, R. H. and Renold, A. E. (1973) Structural coupling between pancreatic islet cells. *Experientia*, 29, 1015-1018.
- Petersen, C. C. and Petersen, O. H. (1991) Receptor-activated cytoplasmic Ca^{2+} spikes in communicating clusters of pancreatic acinar cells. *FEBS Lett.*, 284, 113-116.
- Petersen, O. H. and Findlay, I. (1987) Electrophysiology of the pancreas. *Physiol. Rev.* 67, 1054-1116.
- Philippe, J., Giordano, E., Cjinovci, A. and Meda, P. (1992) cAMP prevents the glucocorticoid-mediated inhibition of insulin gene expression in rodent islet cells. *J. Clin. Invest.*, 90, 2228-2233.
- Pipeleers, D. (1984) Islet cell interactions with pancreatic B-cells. *Experientia*, 40, 1114-1126.
- Salomon, D. and Meda, P. (1986) Heterogeneity and contact-dependent regulation of hormone secretion by individual B cells. *Exp. Cell Res.* 162, 507-520.
- Schuit, F. C., In't Veld, P. A., and Pipeleers, D. G. (1988) Glucose stimulates proinsulin biosynthesis by a dose-dependent recruitment of pancreatic beta cells. *Proc. Natl. Acad. Sci. USA*, 85, 3865-3869.
- Singer, M. V. (1986) Neurohormonal control of pancreatic enzyme secretion in animals. In: *The Exocrine Pancreas Biology, Pathology, and Diseases* (Eds V. L. W. Go, F. P. Brooks, E. Lebenthal, E. P. DiMagno, G. A. Scheele), p. 315-331. Raven Press, New York.
- Sorenson, R. L. and Parsons, J. A. (1985) Insulin secretion in mammosomatotropic tumor-bearing and pregnant rats. A role for lactogens. *Diabetes* 34, 338-341.
- Stagner, J. I. (1991) Pulsatile secretion from the endocrine pancreas: metabolic, hormonal, and neural modulation. In: *The Endocrine Pancreas* (Ed E. Samols), p. 283-302. Raven Press, New York.
- Stefan, Y., Meda, P., Neufeld, M. and Orci, L. (1987) Stimulation of insulin secretion reveals heterogeneity of pancreatic B cells *in vivo*. *J. Clin. Invest.*, 80, 175-183.
- Valdeolmillos, M., Nadal, A., Soria, B. and Garcia-Sancho, J. (1993) Fluorescence digital image analysis of glucose-induced $[\text{Ca}^{2+}]_i$ oscillations in mouse pancreatic islets of Langerhans. *Diabetes*, 42, 1210-1214.
- Vozzi, C., Ullrich, S., Charollais, A., Philippe, J., Orci, L. and Meda, P. Adequate connexin mediated coupling is required for proper insulin production. *J. Cell Biol.*, 131, 1561-1572.

THE ANALYSIS OF DRUG-INDUCED CELL CYCLE PERTURBATIONS BY FLOW CYTOMETRY

Anne T. O'Meara, Bernd-Uwe Sevin, and James Perras

Department of Gynecologic Oncology
University of Miami
Miami, Florida

1. INTRODUCTION

The understanding of cell cycle kinetics in both normal and malignant cells is becoming increasingly important for both the laboratory scientist and the clinician. Techniques of flow cytometry, which have developed in the last 30 years, have allowed for the rapid assessment of the cell cycle kinetics of large numbers of individual cells. These techniques can provide information on cell volume, DNA and protein content as well as more sophisticated measures of biochemical activity. The obvious application to oncology is the ability to begin to explore the genetic differences between normal and malignant cells. Transformation of normal cells to malignant cells involves changes in cellular DNA and kinetics. With flow cytometry, one can exploit these changes in order to study tumor behavior.

Pioneers in flow cytometry, including van Dilla et al.¹, Fulwyler², and Kamentsky et al.³ helped to develop the technology in use in today's flow cytometry chambers. Fluorescent dyes which are able to bind directly to DNA, single stranded nucleic acids, nuclear protein, and mitochondria produce a labelled cell particle suspension which, when introduced into the flow chamber as a constant flow of single particles past a focused laser beam, produce fluorescence at specific wavelengths which can be measured by photoelectric sensors. These sensors produce pulse-like electric currents of variable duration and height. The flow cytometer can correlate the pulse height directly to fluorescent staining intensity, and can then convert this information to digital units and produce a single parameter histogram. More than 15 different fluorescent dyes, with various excitation and emission wavelengths, are available.⁴ Dyes such as ethidium bromide (EB) and propidium iodide (PI) bind selectively to double stranded nucleic acid by intercalation in direct proportion to the total amount of DNA.^{5,6} Traganos et al. demonstrated the use of Acridine orange (AO) to bind double stranded as well as single stranded nucleic acids, thus making it possible to measure simultaneously DNA and RNA.⁷ The AO bound to DNA produces green fluorescence at 530 nm while AO bound to RNA produces red fluorescence at >600 nm. Using optic

filters and separate photoelectrodes, the flow cytometry chamber can simultaneously measure both specified wavelengths.

In our laboratory we have adopted a refined method of two-parameter flow cytometry in order to better define the cell cycle. Roti Roti et al. and Pollack et al. originally described this technique which allows for simultaneous measurement of nuclear DNA and protein.^{8,9} Propidium iodide (PI) stains nuclear DNA and Fluorescein isothiocyanate (FITC) stains protein. Gerner and Humphrey had demonstrated previously that synthesis of chromosomal protein occurs prior to DNA synthesis and may be critical in the process of advancement through the cell cycle.¹⁰ This technique of staining both nuclear DNA and protein with PI and FITC respectively, resolves the cell cycle into six components (G1A, G1B, S, G2A, G2B, and M) rather than the three compartments which had been definable previously (G1, S, and G2/M).

In this chapter, we will review briefly how several investigators have capitalized on these techniques of cell cycle analysis to study *in vitro* the effects of chemotherapeutic agents and the perturbations they cause in the cell cycle of malignant cells. We will specifically review the data which we have collected in our laboratory relating to gynecologic tumors, and then we will comment on the available data on correlation of these flow cytometric data with clinical outcome.

2. DRUG INDUCED CELL CYCLE PERTURBATIONS

Even before the development of flow cytometry, investigators were interested in the effects of chemotherapeutic agents on cell kinetics. For example in 1970, Averette et al. studied normal human genital tissues by examining the labelling index with autoradiography.¹¹ They later utilized the same method to measure labelling index and mitotic index in order to assess the effects of methotrexate and vincristine, two "cell cycle specific" agents.¹² They showed that continuous methotrexate exposure blocks cells in the S phase (increases the labelling index) and that vincristine blocks cells in mitosis (increases the mitotic index).

Since the techniques of flow cytometry made it possible to analyze a much larger number of cells much more rapidly, cell cycle perturbations could be quantitated much more easily on serial samples.¹³ Not only could the cell cycle information provide data on the behavior of individual tumors in response to chemotherapeutic agents, but the techniques also provide powerful methods to study the mechanisms of action of specific agents. For example, by observing arrested murine leukemia cells (L1210/0) in the G2 phase of the cell cycle by flow cytometry and correlating that with visible DNA double strand breaks induced by cisplatin, Sorensen and Eastman proposed that cells affected by cisplatin are unable to transcribe damaged DNA and make the mRNA necessary for subsequent mitosis.¹⁴ They noted that at lower doses of cisplatin, cells were able to overcome the G2 arrest, suggesting that they were able to repair their DNA. Those cells that suffered cell death were unable to repair their DNA and recover their transcription ability. The same group in a later study, again on L1210/0 cells treated with various concentrations of cisplatin, observed that even after cells are lethally damaged, transcription, RNA synthesis, and protein synthesis can continue for a period of time.¹⁵ They observed the previously noted DNA double strand breaks more clearly as fragmentation in the nucleosome spacer region of chromatin. They felt that these data could be consistent with apoptosis as a mechanism of cell death due to cisplatin.

Further study by Ormerod et al. again used the L1210 murine leukemia cells to analyze the effects of both a standard dose of cisplatin and a supralethal dose.¹⁶ Their data showed that 10 hours after a supralethal dose (100 micromoles) of cisplatin, apoptosis was induced. At a dose of 1-10 micromoles, cells showed a slowing in transit through S phase

followed by a block in G2. Their flow cytometry data showed that these cells either overcame the G2 block and continued to cycle or died. They revised Sorensen's hypothesis to accommodate their data by proposing a dual mechanism of cell death due to cisplatin: apoptosis at high doses and failure to overcome G2 block at lower doses. Studies like these have exploited the techniques of flow cytometry in order to learn more about the mechanisms of action of various drugs.

Many investigators have obtained data on specific chemotherapy-induced cell cycle perturbations in various malignancies. Since the techniques of flow cytometry require a cell suspension, it is apparent that some of the most readily applicable tumors to this technology include the hematologic malignancies. In 1976, Barlogie et al. studied the effect of bleomycin on a human lymphoma cell line.¹⁷ They discovered that bleomycin causes lymphoma cells to accumulate in G2M phase without affecting their transit time through S. The extent to which cells were delayed in G2M depended on bleomycin concentration, exposure time, and the stage of the cell cycle at which bleomycin was administered. Investigators have also studied leukemia cells, as in the studies mentioned by Sorensen et al. and Ormerod et al^{14,15,16}.

Engelholm et al. used *in vitro* cell cycle perturbations to study the reaction of three previously characterized Ehrlich ascites tumors to adriamycin.¹⁸ These tumors also lend themselves easily to flow cytometric analysis since they are naturally in suspension. The adriamycin sensitive tumor showed G2M phase accumulation, whereas the two resistant tumors manifested no effect except at very high doses. This accumulation of cells in G2M at high doses in the resistant group fell back to control levels by day 4 of the experiment. The investigators suggested that the continuous incubation of tumor cells with chemotherapeutic agent followed by flow cytometry could be useful as a clinical drug sensitivity test that would be much more rapid than the *in vitro* clonogenic bioassay of human tumor in use at that time.¹⁹ In 1986 they extended their technique to the study of human solid tumors.²⁰ They treated three small cell carcinomas of the lung (CPH SCCL series) with melphalan. Two of the tumors were sensitive to melphalan *in vivo* and showed dose-related S phase accumulation by flow cytometry. There were no cell cycle changes seen in the resistant tumor.

3. SOLID TUMORS

Other researchers have also applied these techniques to solid tumors in the hopes of designing more effective chemotherapy. In 1969, Schabel proposed that as solid tumors increase in size, the growth fraction of the cells that are actively dividing decreases, and that as growth fraction decreases, sensitivity to antimetabolites decreases.²¹ He proposed sequential chemotherapy using first a cell cycle nonspecific agent, such as an alkylator, followed by a cell cycle specific agent, such as an antimetabolite, to optimize cell kill. The use of sophisticated flow cytometric techniques since that time has enabled researchers to pinpoint the stage of the cell cycle most sensitive to application of specific agents, and the phase in which cells arrest after treatment (i.e. the phase of action of the drug). The clinician can use this information to optimize chemotherapeutic trials and to identify specific patients that may have drug-sensitive tumors.

Kuo and Luh studied three patients with small cell cancer of the lung who were treated with cyclophosphamide, doxorubicin, and vincristine.²² They observed that the G1 population of cells decreased from 53.7% to 12.7% and that the G2 population increased from 27.0% to 68.3%. They correlated these cell cycle changes with cytomorphologic findings; the affected cells showed enlarged nuclei. Bergerat et al. treated a human colon cancer cell line (LoVo) with cis dichlorodiamineplatinum (II) and demonstrated a prolongation of cell traverse through S and G2, then a block in S and G2 at up to 24 hours.²³ With higher

concentrations of cis dichlorodiamineplatinum, they were able to demonstrate an additional block in G1 or at the G1-S boundary.

Some researchers have utilized a technique of culturing cells with bromodeoxyuridine (BrdUrd). BrdUrd is a thymidine analog which cells will incorporate into DNA during the S phase of the cell cycle. One can use this labelled DNA to advantage either by quantitating the amount of quenching of Hoechst 33258 fluorescence²⁴ or by using an FITC-conjugated monoclonal antibody (anti-BrdUrd).²⁵ Demarcq et al. used the dual parameter measurement of DNA content and cellular BrdUrd as described by Dolbeare et al. to monitor cell cycle perturbations of a cell line of lung adenocarcinoma (A549) following treatment with cisplatin.²⁶ They observed that the cisplatin induced an S phase delay which was dose dependent but not exposure time dependent, and that after 24 hours the labelling index increased significantly, linked to the prolonged S phase. They also noted that approximately 12 hours after contact with cisplatin, the cells accumulated at the S/G2 transition. This arrest was dependent on both dose and duration of exposure to cisplatin. They predicted from these data that cells were maximally sensitive in G1 and minimally sensitive in G2. They also showed a correlation between the S/G2 accumulation and cytotoxicity in a colony forming assay for chemosensitivity.

Fujikane et al. also utilized BrdUrd-linked fluorescence to study another lung adenocarcinoma cell line, PC-9.²⁷ They exposed the cells to one microgram/ml of CDDP for one hour and 24 hours, and observed a delayed S phase transit and accumulation of cells in G2M. The green fluorescence intensity continued to decrease. With time however early and mid S phase cells were able to recover DNA synthesis.

Although many of these studies have looked at cell lines, researchers have also studied fresh tumors. Of the solid tumors, breast cancers have been more amenable to this type of study due to their relative ease of accessibility by fine needle aspirate. By using sequential aspirations, Briffod et al. studied 27 breast cancer patients treated with three cycles of preoperative adriamycin, vincristine, cyclophosphamide, methotrexate, and 5-fluorouracil.²⁸ They noted three patterns of cell cycle changes. Ten of the 27 patients' tumors showed a single DNA peak without cells in S or G2M prior to therapy and showed no change in this pattern after the first cycle of chemotherapy. Another nine tumors prior to treatment showed a small percentage of cells in S phase and a G2M peak. After the first cycle of chemotherapy this group of tumors showed an increase in the G2M peak. The other eight cases were all aneuploid with a high percentage of cells in S and in G2M prior to chemotherapy, and following treatment showed a lowered G0/G1 peak and an increase in S phase and G2M phase cells with additional values at G2M x 2 and G2M x 4. These three separate groups showed clinical correlation. Of the first ten, only one patient showed clinical regression. Three of the nine patients with an increase in G2M peak showed clinical regression, and all eight of the eight cases with large cell cycle perturbations showed clinical regression with chemotherapy.

Remvikos et al. studied 92 breast cancer patients with similar sequential aspirates before and during treatment with two different therapeutic protocols—5-fluorouracil, cyclophosphamide, and doxorubicin or thiopeta.²⁹ Of their 71 interpretable cases, 66% showed changes in their DNA histograms with treatment, usually accumulation in G2M and some change in the amount of cells in S phase. For the patients in the group who received the regimen with doxorubicin, 33% showed G2M accumulation, whereas only 4.5% of those not receiving doxorubicin showed this change. Of those patients receiving the regimen with thiopeta, S phase was the cell compartment most frequently modified by the chemotherapy. This group of researchers also noted that those patients who showed clinical response were more likely (89%) to have a high pretreatment S phase fraction (>5%) or BrdUrd labelling index (>3.3%).

Spyratos et al. performed flow cytometry on aspirates from 35 primary breast cancers before and during preoperative treatment with doxorubicin, vincristine, cyclophosphamide, methotrexate, and 5-fluorouracil.³⁰ Ten of these tumors were initially diploid and showed no evidence of change in cell cycle parameters during chemotherapy. Only one of these ten showed a clinical response to the chemotherapy. Of the 25 aneuploid tumors, ten showed a change in either DNA content, S phase fraction, or overall pattern. They showed a significant correlation between clinical regression and changes in cell cycle patterns by flow cytometry during chemotherapy. Of interest, the aneuploid tumors were also much more likely to recur, and of those patients who recurred who were available for flow cytometric analysis (N=5), all of their flow cytometric cell cycle patterns were identical to their original pretreatment patterns, even if their original tumors showed change during chemotherapy.

4. GYNECOLOGIC TUMORS

Since the early 1980s, our laboratory has utilized flow cytometry to analyze drug-induced cell cycle perturbations on gynecologic cancer cell lines, nude mouse xenografts, and fresh tumors. An early study used flow cytometry on cells stained with propidium iodide and autoradiography to evaluate cell cycle kinetics and cytomorphologic changes in 12 patients with ovarian cancer and 22 nude mouse xenografts.³¹ This study found a good correlation between needle aspiration samples and biopsy samples for both flow cytometry and autoradiography, verifying the use of serial aspiration as a valid technique for studying the effects of chemotherapy on the cell cycle. Samples were taken by aspiration and biopsy both before and after *in vivo* treatment with agents such as cisplatin, adriamycin, and cyclophosphamide. We were able to discern two types of perturbations by flow cytometry: 1- a decline or disappearance of aneuploid populations of DNA, or 2- progressive changes in relative cell populations in S phase or G2M phase (See Figure 1). When chemotherapy did not affect tumor growth, the flow cytometric pattern generally remained unperturbed. We furthered the analysis by studying nude mouse xenografts treated with intraperitoneal cisplatin and found that this animal model closely mimicked the actual patient situation (Figure 2). As described previously we noted several problems with the single parameter histogram. We were unable to differentiate near diploid tumor cells from nonmalignant host cells. Also we could not separate noncycling G0 phase cells from G1 cells or G2 cells from M cells as they have the same DNA content. Shortly after that study we began to use the dual parameter technique utilizing propidium iodide and fluorescein isothiocyanate simultaneously to label DNA and nuclear protein in order to divide the cell cycle further into six distinct analyzable compartments. In 1987 we took both primary and recurrent ovarian cancer samples from the same patient and prepared nude mouse xenografts.³² The primary tumor had not been exposed to chemotherapy and the recurrent tumor was a sample taken after six courses of *in vivo* cisplatin based chemotherapy. We treated the xenografts with intraperitoneal CDDP and compared pretherapy tumor specimens to multiple tumor samples taken up to 18 days after treatment. Cisplatin caused the primary tumor to show a significant decrease of cells in G1 and an accumulation of cells in S, allowing only a small proportion to continue into G2M. In the recurrent tumor however, cells were able to overcome this block in S phase and a large proportion continued into G2M followed by reentry into G1 (Figure 3). Similarly, measured tumor volume in the xenografts decreased significantly in the primary tumor, but tissue from the recurrence showed at best only a partial reduction in volume.

Our laboratory used the same dual parameter technique to test cell cycle perturbations caused by four different platinum derivatives on two relatively platinum-resistant ovarian

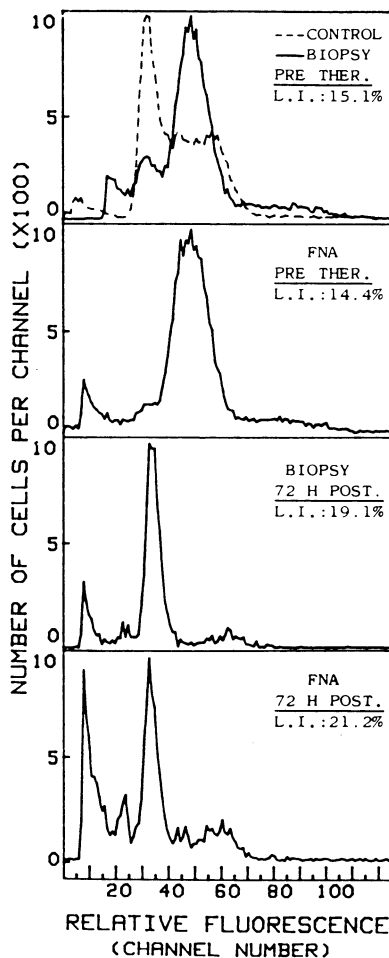


Figure 1. Serial DNA histograms of a patient with ovarian adenocarcinoma treated by CAP chemotherapy. Specimens obtained by both FNA and biopsy.

cancer cell lines, BG-1 and CAOV3.³³ Cisplatin treated cells showed a dose response S phase block at 24 hours which resolved at 48-72 hours at doses lower than the peak plasma concentration. At 48 hours the cells had accumulated in G2. Again recovery from this block varied inversely with dose of cisplatin. The temporal sequence of S then G2 block was lost at doses two and four times peak plasma concentration. These doses produced a concomitant S and G2 block. Carboplatin produced almost identical perturbations in the BG-1 cell line except that the G2 block for the cells dosed with one peak plasma concentration did not recover and instead continued to rise. This change suggests a more potent cell cycle response to carboplatin. Another platinum derivative, 254S, again caused similar cell cycle changes as cisplatin and carboplatin but compared dose for dose, 254S caused more S and G2 blocks than either of the other two agents. The fourth agent, NK 121 showed potency several times that of DDP or carboplatin. Table 1 summarizes the mean effects of each agent. The study demonstrated that various platinum derivatives cause similar cell cycle perturbations but are notably different in potency, or the dose required to produce these effects. These differences were confirmed by measuring cytotoxicity with the ATP-Cell Viability Assay.

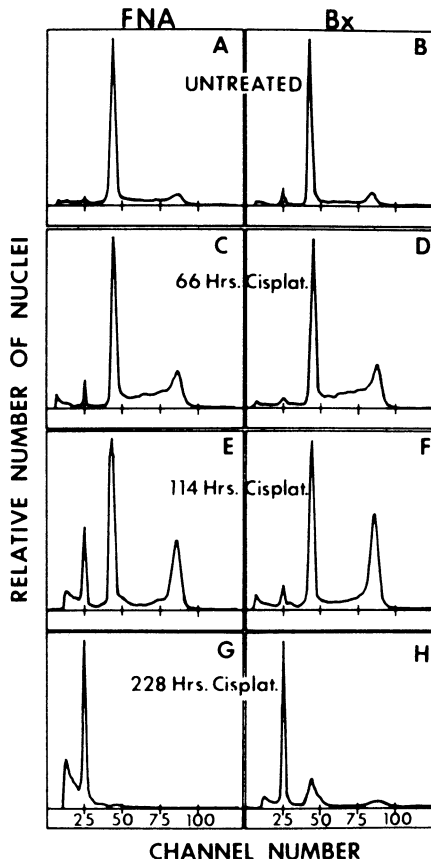


Figure 2. Serial DNA histograms from an ovarian carcinoma nude mouse xenograft treated with intraperitoneal cisplatin.

4.1 Effects of Chemotherapy Modulators

We were also interested in studying the effects of biologic modifiers on the cytotoxicity of cisplatin. Earlier work by other authors had proposed that methylxanthines such as caffeine and pentoxifylline can enhance the cytotoxicity of alkylating agents *in vitro*, presumably by disrupting the repair of DNA damage.^{34,35} We used the dual parameter flow cytometric technique with PI and FITC staining to evaluate the effect of caffeine and pentoxifylline on the cytotoxicity of cisplatin to the cell line BG-1 (a CDDP resistant cell line).³⁶ Cisplatin alone caused an increase in cells in S phase at 24 hours that recovered after 48 hours, and a moderate G2 arrest at 72 hours that recovered by 240 hours.. With the addition of either caffeine or pentoxifylline however we saw a large sustained G1 population decrease and a similar sustained S phase increase. The G2 population showed a similar arrest to that of the cisplatin only treated group, except that it did not recover. It continued to increase over the time course of the experiment. We also performed viable cell counts on the treated cells and confirmed that cells treated with the modulators in addition to cisplatin sustained a growth arrest over the 240 hours studied, comparable to the arrest seen in cells treated with cisplatin alone at two to four times the concentration.

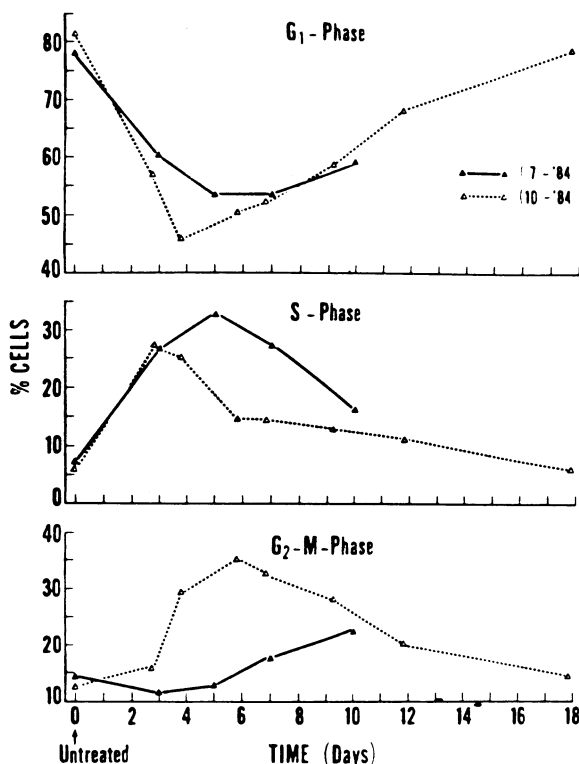


Figure 3. DNA histograms from a primary ovarian tumor xenograft (7-84) and a recurrent tumor xenograft (10-84) after treatment with intraperitoneal cisplatinum. FCM after 10mg/kg CIS-Platinum I.P.

In a similar study, we again looked at the effect of pentoxifylline on cisplatin cytotoxicity but using the bromodeoxyuridine technique.³⁷ By incorporating 5-bromodeoxyuridine into the BG-1 ovarian cancer cell line, stripping the nuclei, and subsequently staining with antibromodeoxyuridine fluorescein conjugate (anti-BrdUrd-F) followed by flow cytometry, we were able to identify cells within G₀/G₁, G₂M, as well as S phases that were actively synthesizing DNA (incorporating BrdUrd). We used this technique to evaluate further the modulating effect of pentoxifylline on cell cycle perturbations caused by cisplatin. Single parameter analysis showed that cisplatin caused a decrease in G₀/G₁ cells for 48 hours, which was followed by a slow recovery in those cells treated with cisplatin only but without recovery in those cells exposed to cisplatin and pentoxifylline. Cisplatin-only treated cells showed a brief increase in S phase for the first 24 hours followed by recovery, but the addition of pentoxifylline caused a maintenance of the cisplatin induced S phase arrest for the entire 168 hours of observation. The G₂M phase also increased in response to platinum with maximum effect seen at 72 hours followed by slow recovery. Cells treated with pentoxifylline in addition to cisplatin showed a delayed but slowly rising G₂M accumulation throughout the 168 hours. The DNA-BrdUrd dual parameter flow cytometric data from these experiments confirmed the results seen in the G₀/G₁ and G₂/M phases. However when analyzing the S phase cells we observed an initial increase in cells synthesizing DNA at 24 hours with a return to control levels at 48 hours. In the cells treated with cisplatin and pentoxifylline this percentage of DNA synthesizing cells at 24 hours was lower than the percentage seen for cisplatin alone, indicating that pentoxifylline inhibited DNA

Table 1. Percentages of BG1 cells in the S phase and G2 phase after treatment with these four platinum derivatives. BG1 control cells had 11+2 percent in the S phase and 12+3 percent in the G2 phase. X=the peak plasma concentration of the drug

	S phase			G2 phase		
	0.2X	0.5X	1X	0.2X	0.5X	1X
DDP	13±3	14±3	16±4	15±4	15±4	19±4
CARBO	13±3	13±2	18±3	14±3	14±3	19±3
254Sc	14±3	17±3	23±3	15±3	19±3	23±5
NK121	17±4	21±4	28±5	21±4	25±4	30±5

synthesis in more of these cells. In addition the accumulation of a cohort of unlabelled nuclei in the S phase, signifying S phase cells that are not actively synthesizing DNA, confirmed this variation between groups. The pentoxifylline modulated group had 35% of its S phase cells unlabelled by BrdUrd whereas the cisplatin only group had 10% and the control group <6%. The results of both of these studies clearly demonstrate the possibility of enhancement of cytotoxicity by methylxanthines.

We have extended studies of cell cycle perturbations to other gynecologic cancer cell types and other chemotherapeutic agents. In 1991 we were interested in Adolezesin, an analog of CC-1065, from a group of very potent alkylating agents. We studied its effect on the cell cycles of five gynecologic cancer cell lines, AN3, AE7, BG1, HEC1A, and SKUT1B.³⁸ This study did not reveal consistent perturbations between cell lines. Some lines exhibited biphasic G2 blocks while others showed reverse dose-dependent G2 blocks or sequential S-G2 blocks. The variation in perturbations seen varied depending on which cell line was examined, its sensitivity to the drug, concentrations of drug used, and sampling time. ATP chemosensitivity assays served as the comparison for cytotoxicity. This study showed that the perturbations produced by Adolezesin could not reliably predict cytotoxicity.

We experienced similar variability when we studied the effects of doxorubicin and one of its derivatives, pirarubicin, at multiple doses on three different gynecologic cancer cell lines, SKUT1B, HEC1A, and BG-1.³⁹ At doses of 0.1, 0.2 and 0.5 times the peak plasma concentration (0.5 micrograms/ml), doxorubicin did not demonstrate significant cell cycle effects on SKUT1B cells however at corresponding doses, the ATP-cell viability assay demonstrated significant cell kill. At higher doses, doxorubicin caused G2 arrest, G1 reduction, and a biphasic S phase (initial reduction, recovery at 48 hours, then arrest after 72 hours). In contrast, doxorubicin affected the HEC1A cell line at all doses, causing a marked G2 arrest and a heterogeneous S phase response. Interestingly, the degree of G2 block showed a *reverse* dose response relationship, possibly because more cells could be delayed in S phase at the higher doses. Pirarubicin in this cell line caused a potent G2 block such that at 0.1 times its peak plasma concentration, 85% of cells were arrested in the G2 phase. At increased concentrations, a larger S phase arrest appeared with a decrease in G2 block. Unlike doxorubicin this reverse dose response relationship continued for the full 168 hours.

The BG-1 cell line after treatment by doxorubicin showed sustained reduction of the S phase population and a dose response pattern of G2 block and G1 depletion. Pirarubicin was approximately four to five times as potent as doxorubicin in causing a G2 block, correlating with the ATP-cell viability data of increased cytotoxicity. Because this study showed such varied cell cycle perturbations in different cell lines, it suggested complexity of cell behaviors and supported the concept of tumor heterogeneity in cell kinetic response. In addition, the cell kinetic responses did not always correspond to the cytotoxicity data, alerting us to some of the limitations of the technique. In particular we became more aware

of the fact that as dead cells undergo karyolysis, only intact surviving cells are being analyzed by flow cytometry, perhaps analyzing only resistant tumor subpopulations.

More recently, we evaluated nine different chemotherapeutic agents on the ovarian cancer cell line BG-1 and saw three patterns of cell cycle changes emerge.⁴⁰ Cisplatin, 4-hydroperoxycyclophosphamide (the active metabolite of cyclophosphamide), and mitomycin C produced a sequential S phase then G2/M phase block. Etoposide, vincristine, and doxorubicin showed a G2/M block only; and 5-fluorouracil, methotrexate, and cytosine arabinoside showed an S phase block only. When compared to previous testing of the *in vitro* chemosensitivity of BG-1 to the various agents by the ATP-cell viability assay, there did not appear to be any correlating pattern of cell cycle perturbation with cytotoxicity. However, analysis *within* the three subgroups of agents showed a positive correlation between the magnitude of cell cycle perturbations and chemosensitivity.

In a similar manner to the evaluation of pentoxifylline's effect on cisplatin cell cycle perturbations, we have evaluated other modulators of chemotherapeutic response. Progestational compounds such as provera are antimitotic and antiproliferative, increasing the number of cells in the resting phase.⁴¹ To study whether provera would diminish the activity of chemotherapeutic agents, we exposed three uterine cancer cell lines (AE7, ECC1, and HEC1A) to continuous provera and chemotherapy with 4hydroperoxycyclophosphamide, adriamycin, and cisplatin (CAP) and then performed dual parameter flow cytometry with PI and FITC.⁴² The addition of provera compromised the cell cycle effects of the chemotherapy by causing a significant reduction of CAP-induced G2 block and increased the amounts of CAP-induced G1 and S reductions. Both cell lines AE7 and ECC1, which are positive for progesterone receptors, showed this dampening of cell cycle perturbations with provera, whereas the kinetics of the progesterone receptor-negative cell line HEC1A treated with chemotherapy did not change with the addition of provera. This study revealed that provera effects correlated with progesterone receptor status, and confirmed that the reduction of the growth fraction of the tumor (increase in noncycling cells) by provera could impair the ability of cytotoxic agents to effect their damage.

4.2 Effects of Radiation

We have also extended this model for testing flow cytometric changes to cells treated with radiation. We studied six uterine cancer cell lines which we treated with radiation from a cobalt⁶⁰ source and then subjected to flow cytometry with PI and FITC.⁴³ We also performed ATP bioluminescence cell viability assays to obtain radiation survival curves and a radiosensitivity index. The cell lines AN3, HEC1A, and HEC1B exhibited a dose dependent severe G2 block caused by radiation, maintained for 168 hours at the higher doses. The S phase population initially decreased at 24 hours then recovered at 48-72 hours and arrested at 168 hours. The G1 population decreased in a dose response relationship. The other three cell lines, SKUT1B, AE7, and ECC1, exhibited a biphasic G1 response, with accumulation at 24 hours then reduction after 48-72 hours. The S phase population also showed a biphasic response with initial reduction then accumulation. The G2 phase was minimally perturbed except at the highest dose of radiation in the SKUT1B cells. At that dose there was a G2 block and a G1 reduction, possibly because the more sensitive cells had died and a resistant subgroup responded differently to the radiation. These cells corresponded to a 3% surviving fraction on ATP sensitivity assay, suggesting some heterogeneity of the tumor cell population. Although the ATP assay in this study appeared to be appropriate for the evaluation of radiosensitivity, the variability of the changes in cell kinetics did not allow the use of flow cytometric evaluation alone to predict radiosensitivity.

We looked at the effects of radiation again on the ovarian cancer cell line BG-1.⁴⁴ In this study we only evaluated BG-1 and treated these cells with radiation alone and caffeine

immediately postirradiation. In these cells we observed a G2 phase accumulation at 24-72 hours. By utilizing the dual parameter technique with both nuclear protein and DNA staining, we were able to subdivide G2 into G2A (low nuclear protein levels) and G2B (high nuclear protein levels). The cells' G2A peak occurred at 24 hours and G2B peak at 48-72 hours. By adding caffeine, we were able to prevent the G2 arrest, allowing cells to traverse rapidly through G2A and G2B back to G1(Figure 4). This change was associated with higher cell kill compared to that of cells treated by radiation alone.

Taxol, as one of the newer chemotherapeutic agents, has rapidly become a first line agent in many gynecologic malignancies, particularly ovarian cancer. As previous studies had shown that taxol could cause G2/M prolongation related to its ability to inhibit the mitotic spindle⁴⁵, we endeavored to show if this cell cycle perturbation could account for the ability of taxol to function as a radiation sensitizer. We treated the ovarian cancer cell line BG-1 with very low doses of taxol (.001 times the peak plasma concentration) followed in 48 hours by a radiation dose of 2 Gray, and then analyzed the cell cycle kinetics of treated cells and

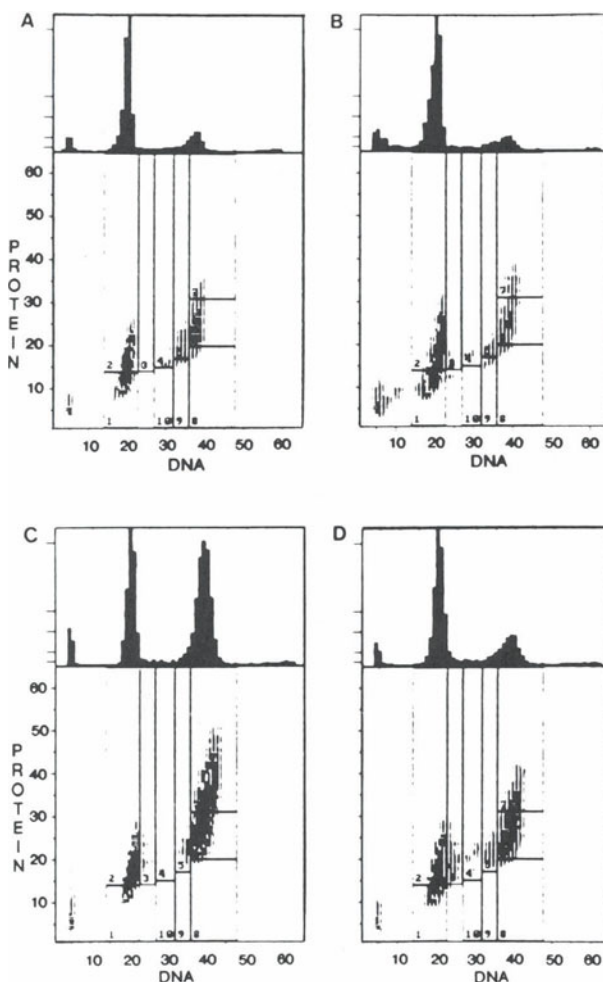


Figure 4. DNA-protein histograms after 48 hours of A-an untreated control, B-caffeine (1 mM) treated alone, C-irradiation alone (5 Gy), and D-irradiation followed by caffeine. Figure 4C shows the typical G2 accumulation, which is suppressed by the caffeine in figure 4D.

controls of radiation alone, taxol alone, and no treatment (Figure 5).⁴⁶ For both the untreated and taxol-only treated samples, most cells were in G0/G1 with a small number in G2M. The radiation only treated cells showed a minor temporary block in G2M. However the combination of taxol and radiation therapy produced cells with a larger and more prolonged G2M block. The cells were followed up to 216 hours after taxol treatment to confirm the persistence of perturbations. Although the G2M accumulation in the taxol and radiation treated group did recover somewhat after 120 hours, it did not fall back to pretreatment values. The use of the ATP-cell viability assay allowed us to calculate a mean inactivation dose (MID) in order to represent radiation sensitivity. Cells treated by radiation alone showed an MID of 6.24 Gray and the cells treated with radiation and taxol showed a significant decrease to an MID of 4.63 Gray. This experiment showed that although the very low dose of taxol used did not cause cell cycle perturbations by itself, that same dose clearly provided radiosensitization, contradicting the earlier theory that taxol induced cell cycle perturbations were necessary for radiation sensitization.

In summary, we have been able to use the techniques of fluorochrome staining for the evaluation of chemotherapy-induced cell cycle perturbations by flow cytometry in many

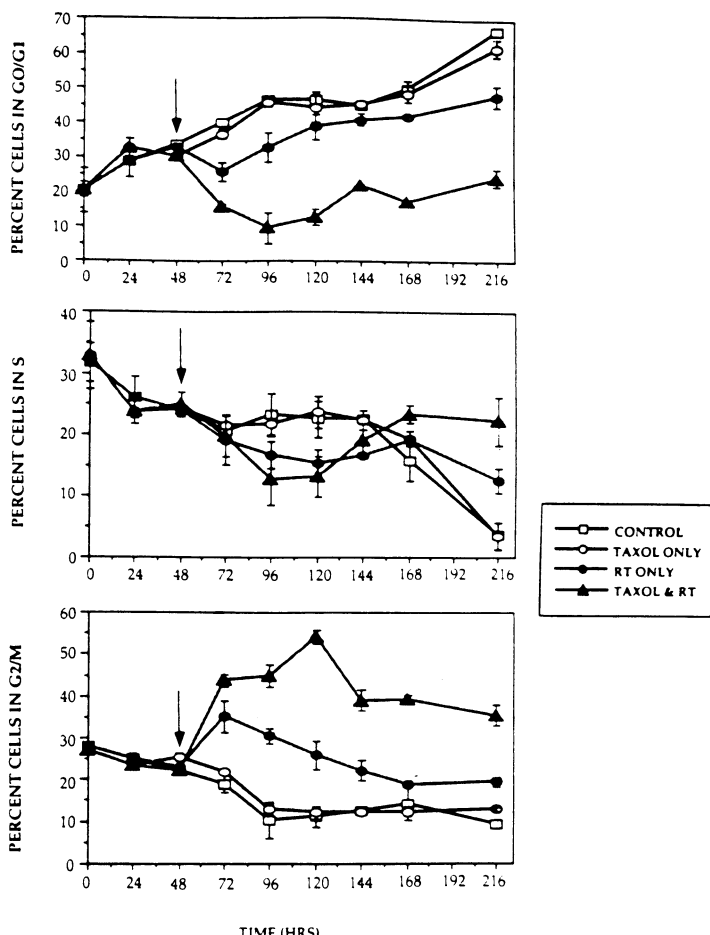


Figure 5. Cell cycle responses of BG-1 cells to taxol, radiation alone, taxol and radiation, and a control (no treatment). The cells treated with taxol and radiation show a larger and longer decrease in the percentage of cells in G0/G1, and a more prolonged block (increase) in G2/M.

ways: a) as a method of testing chemosensitivity by looking for the presence or absence of cell cycle perturbations after treatment, b) for further elucidation of the mechanisms of action of various chemotherapeutic agents, c) as a method to test different derivatives of an agent for relative potencies, d) to study pharmacologic, hormonal, and irradiation modulators of chemotherapeutic response, and e) to collect data in the hopes of correlating cell cycle perturbations with clinical outcomes.

5. CLINICAL RELEVANCE

There are several potential applications of this technique to the clinical arena. Many investigators have already correlated the pretreatment cell cycle kinetics with prognosis for various cancers. Aneuploidy correlates with poorer survival in ovarian cancer,^{47,48,49,50,51,52} cervical cancer,⁵³ endometrial cancer,⁵⁴ bladder cancer,⁵⁵ prostate cancer,^{56,57} and possibly colon cancer.⁵⁸ Among diploid tumors, investigators are looking at increased S phase fraction, the percentage of cells in S phase, as another possible indicator of poor prognosis.⁵² Clinicians can use this information as additional factors to help guide the aggressiveness of therapy.

Another clinically relevant use of the technique, as we and others have demonstrated in the previous examples, is the ability to select in advance chemotherapeutic agents that demonstrate an effect on an individual tumor.⁴⁰ Multiple studies have shown, primarily in cell lines with known response characteristics, that the presence of cell kinetic perturbations from the pretreatment to the posttreatment specimens generally indicates clinical responsiveness. For example, disappearance of an aneuploid cell population from a given tumor indicates strong cytotoxic effects of treatment.³¹ Tumors that are resistant to particular agents show no perturbation or minimal perturbation with recovery. Our studies with multiple chemotherapeutic agents demonstrated that it is important to follow the cell kinetic changes for a prolonged period after treatment, as the peak effect may not be seen for up to 168 hours.⁴⁰ Of course, this technique will not always be appropriate for this type of evaluation. As seen in our studies on adolezesin and the effect of doxorubicin and pirarubicin on gynecologic cancer cell lines, not all agents reliably produce cell cycle effects that correlate with cytotoxicity. In our laboratory, we currently use the technique concomitantly with the ATP bioluminescence cell viability assay for a more exhaustive evaluation of the effect of a particular agent on an individual tumor specimen.

A natural extension of this idea of testing tumors for chemosensitivity would be to use the technique to follow individual patients' progress during therapy. Flow cytometry is ideally suited as a reproducible method of serial analysis due to its speed. This type of use would be limited to tumors that are accessible to serial sampling, such as breast cancer, cervical cancer, and perhaps skin cancer. Perhaps the loss of cell cycle perturbations by an agent that once produced them could signal early the development of resistance in a particular tumor. Both the preselection of specific chemotherapeutic agents and the serial monitoring during therapy could limit the exposure of patients to ineffective, potentially quite toxic drugs. This principle is the impetus behind chemosensitivity testing in general.

Another area of clinical usefulness is the ability to evaluate new chemotherapeutic agents on cell lines or xenografts prior to their use in patients. These flow cytometric techniques can help to elucidate the cellular mechanism of action, the effectiveness, the potency, and also potential modulators of new agents.

Of course, it is important to mention several caveats about the translation of these laboratory studies to the clinical arena: a) different drugs produce different patterns of cell cycle perturbations, b) the degree of perturbation is dose dependent and optimally observed at doses that do not result in total cell kill, and c) cell cycle perturbations vary between

different tumors (inter-tumor heterogeneity) even if they appear morphologically similar. In addition, variations of cell cycle kinetics within the same tumor do exist. We have observed in our laboratory that cell cycle kinetics from a primary site do not always look similar to those kinetics from cells in a metastatic deposit of the same tumor (unpublished data). This heterogeneity may result in differing sensitivities of various areas of the same cancer process to specific chemotherapeutic agents. One must consider many factors such as growth fraction, stage of the cell cycle when an agent is administered, dose, perfusion, and length of exposure as possible modifiers of the *in vitro* to *in vivo* correlation. Nevertheless, these techniques provide an exciting and productive avenue for continued progress in the investigation of chemotherapy and its effects.

REFERENCES

1. van Dilla MA, Trujillo TT, Mullaney PF. Cell microfluoremetry: Its method for rapid fluorescence measurement. *Science* 163, 1213-1218 (1969)
2. Fulwyler MJ. Electronic separation of biological cells by volume. *Science* 150, 910-913 (1965)
3. Kamentsky LA and Melamed MR. Spectrophotometric cell sorter. *Science* 156, 1364-1367 (1967).
4. Crissman HA and Steinkamp JA. Multivariate Cell Analysis: Techniques for correlated measurements of DNA and other cellular constituents, in *Techniques in Cell Cycle Analysis* (JW Gray and Z Darzynkiewicz, Eds.) Humana Press, Clifton, NJ, pp.163-206 (1987).
5. LePecq JB and Paoletti C. A new fluorometric method for RNA and DNA determination. *Anal Biochem* 17, 100 (1966).
6. Krishnan A. Rapid flow cytometric analysis of mammalian cell cycle by propidium iodide staining. *J Cell Biol* 66, 188 (1937).
7. Traganos F, Darzynkiewicz Z, Sharpless R. Simultaneous staining of ribonucleic and deoxyribonucleic acid in unfixed cells using acridine orange in a flow cytometric system *J Histochem Cytochem* 25, 46 (1977).
8. Roti Roti JL, Higashikubo R, Blair OC, Uygur N. Cell-cycle position and nuclear protein content. *Cytometry* 3, 91-96 (1982).
9. Pollack, A., Moulis, H., Block, N., and Irvin, G. Quantitation of cell kinetic responses using simultaneous flow cytometric measurements of DNA and nuclear protein, *Cytometry* 5, 473-481 (1984).
10. Gerner EW and Humphrey RM. The cell-cycle phase synthesis of non-histone proteins in mammalian cells. *Biochem Biophys Acta* 331, 117-123 (1973).
11. Averette HE, Weinstein GD, Frost P. Autoradiographic analysis of cell proliferation kinetics in human genital tissues. I. Normal cervix and vagina, *Am J Obst Gynecol* 108, 8-17 (1970).
12. Averette HE, Weinstein GD, Ford JH, Hoskins WJ, Ramos R. Cell kinetics and programmed chemotherapy for gynecologic cancer, I. Squamous cell carcinoma, *Am J Obst Gynecol* 12, 912-923 (1976).
13. Yataganas X and Clarkson BD. Flow microfluorometric analysis of cell killing with cytotoxic drugs. *J Histochem Cytochem* 22, 651-659 (1974).
14. Sorenson, C. and Eastman, A. Mechanism of *cis*-diaminedichloroplatinum-induced cytotoxicity: Role of G2 arrest and DNA double-strand breaks, *Cancer Res.* 48, 4484-4488 (1988).
15. Sorenson, C., Barry, M., and Eastman, A. Analysis of events associated with cell cycle arrest at G2 phase and cell death induced by cisplatin, *J Natl Cancer Inst* 82, 749-755 (1990).
16. Ormerod, M., Orr, R., and Peacock, J. The role of apoptosis in cell killing by cisplatin: A flow cytometric study, *Br J Cancer* 69, 93-100 (1994).
17. Barlogie, B., Drewinko, B., Schumann, J., and Greireich, E. Pulse cytophotometric analysis of cell cycle perturbation with bleomycin *in vitro*, *Cancer Res* 36, 1182-1187 (1976).
18. Engelholm, S.A., Spang-Thomsen, M., and Vindelov, L.L. A short-term *in vitro* test for tumour sensitivity to adriamycin based on flow cytometric DNA analysis, *Br J Cancer* 47, 497-502 (1983).
19. Hamburger, A.W., and Salmon, S.G. Primary bioassay of human tumor stem cells, *Science* 197, 461 (1977).
20. Engelholm, S., Spang-Thomsen, M., Vindelov, L., and Brunner, N. Chemosensitivity of human small cell carcinoma of the lung detected by flow cytometric DNA analysis of drug-induced cell cycle perturbations *in vitro*, *Cytometry* 7, 243-250 (1986).
21. Schabel, F.M. Use of tumor growth kinetics in planning "curative" chemotherapy in advanced solid tumors, *Cancer Res* 29, 2384-2389 (1969).

22. Kuo, S., and Luh, K. Monitoring tumor cell kinetics in patients receiving chemotherapy for small cell lung cancer, *Acta Cytol* 37, 353-357 (1993).
23. Bergerat, J.P., and Barbologie, B. *In vitro* cytokinetic response of colon cancer cells to cis-dichlorodiammineplatinum, *Cancer Res* 39, 4356-4363 (1979).
24. Latt, S.A. Microfluorometric detection of deoxyribonucleic acid replication in human metaphase chromosomes, *Proc Natl Acad Sci USA* 70, 3395-3399 (1973).
25. Dolbeare, F., Gratzner, H.G., Pallavicini, M.G., and Gray, J.W. Flow cytometric measurement of total DNA content and incorporated bromodeoxyuridine, *Proc Natl Acad Sci USA* 80, 5573-5577 (1983).
26. Demarcq, C., Bastian, G., and Remvikos, Y. BrdUrd/DNA flow cytometry analysis demonstrates *cis*-diamminedichloroplatinum-induced multiple cell-cycle modifications on human lung carcinoma cells, *Cytometry* 13, 416-422 (1992).
27. Fujikane, T. Flow cytometric analysis of the kinetic effects of cis-diamminedichloroplatinum on lung cancer cells, *Cytometry* 10, 788-795 (1989).
28. Briffod, M., Spyrats, F., Hacene, K., Tubiana-Hulin, M., Pallud, C., Gilles, F., and Rouesse, J. Evaluation of breast carcinoma chemosensitivity by flow cytometric DNA analysis and computer assisted image analysis, *Cytometry* 13, 250-258 (1992).
29. Remvikos, Y., Jouve, M., Beuzeboc, P., Viehl, P., Magdelenat, H., and Pouillart, P. Cell cycle modifications of breast cancers during neoadjuvant chemotherapy: A flow cytometry study on fine needle aspirates, *Eur J Cancer* 29, 1843-1848 (1993).
30. Spyrats, F., Briffod, M., Tubiana-Hulin, M., Andrieu, C., Mayras, C., Pallud, C., Lasry, S., and Rouesse, J. Sequential cytopunctures during preoperative chemotherapy for primary breast carcinoma, *Cancer* 69, 470-475 (1992).
31. Sevin, B.-U., Pollack, A., Averette, H., Ramos, R., Greening, S., and Evans, D. *In vivo* chemosensitivity testing in patients with gynecologic malignancies and nude mouse xenografts by monitoring cell kinetic parameters and DNA distribution patterns: A preliminary report, *Gynecol Oncol* 24, 27-40 (1986).
32. Sevin, B.-U., Pollack, A., Averette, H., Ramos, R., and Donato, D. *In vivo* cell kinetic effects of *cis*-platinum on human ovarian cancer xenografts measured by dual parameter flow cytometry, *Cytometry* 8, 153-162 (1987).
33. Nguyen, H., Sevin, B.-U., Averette, H., Perras, J., Ramos, R., Donato, D., Ochiai, K., and Penalver, M. Cell cycle perturbations of platinum derivatives on two ovarian cancer cell lines, *Cancer Invest* 11, 264-275 (1993).
34. Byfield, L.E., Murnine, J., Ward, J.F., Calabro-Jones, P., Lynch, M., and Kulhnia, F. Mice, men, mustards, and methylated xanthines: The role of caffeine and related drugs in the sensitization of human tumours to alkylating agents, *Br J Cancer* 43, 669-683 (1981).
35. Lau, C.C., and Pardee, A. Mechanisms by which caffeine potentiates lethality of nitrogen mustard, *Proc Natl Acad Sci* 79, 2942-2946 (1982).
36. Schiano, M., Sevin B.-U., Perras, J., Ramos, R., Wolloch, E., and Averette, H. *In vitro* enhancement of *cis*-platinum antitumor activity by caffeine and pentoxifylline in a human ovarian cell line, *Gynecol Oncol* 43, 37-45 (1991).
37. Perras, J.P., Ramos, R., and Sevin, B.-U. Demonstration of an S phase population of cells without DNA synthesis generated by cisplatin and pentoxifylline, *Cytometry* 14, 441-448 (1993).
38. Nguyen, H.N., Sevin, B.-U., Averette, H.E., and Perras, J.P. *In vitro* evaluation of a novel chemotherapeutic agent, Adozelesin, in gynecologic cancer cell lines. *Cancer Chemother Pharmacol* 30(1), 37-42 (1992).
39. Nguyen, H.N., Sevin, B.-U., Averette, H.E., Perras, J.P. Untch, M., Ramos, R., Donato, D., and Penalver, M. Comparative evaluation of pirarubicin and adriamycin in gynecologic cancer cell lines, *Gynecol Oncol* 45(2), 164-173 (1992).
40. Petru, E., Sevin, B.-U., Haas, J., Ramos, R., and Perras, J. A correlation of cell cycle perturbations with chemosensitivity in human ovarian cancer cells exposed to cytotoxic drugs *in vitro*, *Gynecol Oncol* 58, 48-57 (1995).
41. Gibbons, W.E., Battin, D.A., and diZerega, G.S. Mechanisms of action of reproductive hormones, in *Infertility, Contraception and Reproductive Endocrinology* (D.R. Mishell, Jr. and Val Davajan, Eds.) Medical Economics Book, New Jersey, pp.31-44 (1986).
42. Nguyen, H.N., Sevin, B.-U., Averette, H.E., Perras, J., Ramos, R., Penalver, M., and Donato, D. The effects of provera on chemotherapy of uterine cancer cell lines, *Gynecol Oncol* 42, 165-177 (1991).
43. Nguyen, H.N., Sevin, B.-U., Averette, H.E., Gottlieb, C.F., Perras, J., Ramos, R., Donato, D., and Penalver, M. The use of ATP bioluminescence assay and flow cytometry in predicting radiosensitivity of uterine cancer cell lines: Correlation of radiotoxicity and cell cycle kinetics, *Gynecol Oncol* 46, 88-96 (1992).

44. Wolloch, E., Sevin, B.-U., Perras, J., Gottlieb, C., Pollack, A., Ramos, R., Schiano, M., and Averette, H. Cell kinetic perturbations after irradiation and caffeine in the BG-1 ovarian cancer cell line, *Gynecol Oncol* 43, 29-36 (1991).
45. Schiff, P.B., Fant, J., and Horowitz, S.B. Promotion of microtubule assembly *in vitro* by taxol, *Nature* 22, 665-667 (1986).
46. Steren, A., Sevin, B.-U., Perras, J., Ramos, R., Angioli, R., Nguyen, H., Kochli, O., and Averette, H. Taxol as a radiation sensitizer: A flow cytometric study, *Gynecol Oncol* 50, 89-93 (1993).
47. Friedlander, M.L., Hedley, D.W., Taylor, J.W., Russel, P., Coates, A.S., Tattersal, M.H.N., Influence of cellular DNA index on survival in advanced ovarian cancer, *Cancer Res* 44, 397-400 (1984).
48. Erba, E., Vaghi, M., Pepe, S., Amato, G., Bistoelfi, M., Ubezio, P., Mangioni, C., Landoni, F., and Morasca, L. DNA index of ovarian carcinomas in 56 patients: *In vivo* and *in vitro* studies, *Br J Cancer* 52, 564-573 (1985).
49. Iverson, O.E., Skaarland, E. Ploidy assessment of benign and malignant ovarian tumors by flow cytometry, a clinicopathologic study, *Cancer* 60, 82-87 (1987).
50. Rodenburg, C.J., Cornelisse, C.H., Heintz, P.A.M., Hermans, J., Fleuren, G.T. Tumor ploidy as a major prognostic factor in advanced ovarian cancer, *Cancer* 59, 317-323 (1987).
51. Kallionemi, O.P., Punnonen, R., Mattila, J., Lehtinen, M., and Koivulla, T. Prognostic significance of DNA index, multiploidy, and S-phase fraction in ovarian cancer, *Cancer* 61, 334-339 (1988).
52. Zanetta, G., Keeney, G., Cha, S., Wieand, H.S., Katzmann, J., Padratz, K.C., and Farr, G. The prognostic significance on long-term survival of flow cytometric DNA measurement in advanced ovarian cancer (abstr), *Proceedings of ASCO* 14, 274 (1995).
53. Jacobsen, A. Prognostic impact of ploidy level in carcinoma of the cervix, *Am J Clin Oncol* 7, 475-480 (1984).
54. Moberger, B., Auer, G., Forslund, G., and Moberger, G. The prognostic significance of DNA measurements in endometrial carcinoma, *Cytometry* 5, 430-436 (1984).
55. Tribukait, B., Gustafson, H., and Esposti, P.L. The significance of ploidy and proliferation in the clinical and biologic evaluation of bladder tumors: A study of 100 untreated cases, *Br J Urol* 54, 130-135 (1982).
56. Tribukait, B., Ronstrom, L., and Esposti, P. Quantitative and qualitative aspects of flow DNA measurements related to the cytologic grade in prostatic carcinoma, *Anal Quant Cytol* 5, 107-111 (1983).
57. Frankfurt, O.S., Arbuck, S.G., Chin, J.L., Greco, W.R., Pavelic, Z.P., Slocum, H.K., Mittelman, A., Piver, S.R., Pontes, E.J., and Rustum, Y.M. Prognostic applications of DNA flow Cytometry for hman solid tumors, in *Clinical Cytometry: Annals of the New York Academy of Sciences*, vol. 468 (M. Andreeff, Ed.), New York, NY, pp. 276-290 (1986).
58. Meyer, J.S., and Prioleau, P.G. S phase fractions of colorectal carcinomas related to pathological and clinical features, *Cancer* 48, 1221-1228 (1981).

THE EFFECTS OF TUMOR HETEROGENEITY ON THE FLOW CYTOMETRIC ANALYSIS OF CLINICAL SPECIMENS

Wade E. Bolton and Melissa O'Brien

Coulter Corporation
11800 S.W. 147th Avenue
Miami, Florida 33196-2500

INTRODUCTION

A combination of accelerated mutation rates and the presence of numerous different cell types in solid tumors creates a degree of stemline and cellular heterogeneity that constitutes a considerable challenge to the flow cytometric analysis of prognostic parameters. While multi-site sampling can circumvent the effect of stemline heterogeneity (2), the solution to the problem of cellular heterogeneity is less straightforward, and has, until relatively recently, been hampered by technological limitations.

Cellular heterogeneity is problematic for a number of reasons, the most obvious of which is numerical dilution. The presence of up to dozens of different cell types, primarily of stromal and reactive origin, in addition to frequently large numbers of apoptotic and necrotic cells, can significantly reduce analytical sensitivity to tumor cells (20,22,23,25). Apart from dilution effects, analysis may be further complicated by heterogeneity of autofluorescence (24), non-specific binding (6,17,19,21), and common antigen expression in different cell types (12), as well as by altered DNA content in (1,7,8,9,10,14,18,20), and artifactual effects on S-phase (14,20) by dead cells.

Light scatter heterogeneity and a dearth of both tumor-specific antigens and viability probes resistant to fixative and permeabilizing agents (for DNA staining) necessitate the use of a multiparametric approach to targeting live breast tumor cells in heterogeneous clinical specimens. We have developed such a panel, consisting of the DNA dye DAPI and antibodies to cytokeratin (CK), epithelial mucin antigen (MC5), tubulin, and proliferating cell nuclear antigen (PCNA). The panel was optimized and tested using a breast tumor model, consisting of an equal mixture of live and dead breast tumor cells of the MDA-MB-175-VII cell line, live lymphoblastic cells of the CEM cell line, and live peripheral blood mononuclear cells (PBMCs). Upon exclusion of non-epithelial, non-tumor, and dead cells by CK, MC5, and tubulin, respectively, PCNA and DAPI staining permitted proliferation and DNA content

analysis of only the targeted live tumor cells. Application of the panel to the breast tumor model is described herein.

MATERIALS AND METHODS

Materials

Anti-tubulin monoclonal antibody was purchased from Zymed Laboratories, Inc. (San Francisco, CA). Goat anti-mouse-PEC45 (GAM-PECY5), PCNA-FITC, MC5-RD1, CK-ECD, and matched isotype controls were from Coulter Corporation (Miami, FL). DAPI, phosphate-buffered saline (PBS), lysophosphatidyl choline, Nonidet P-40 (NP40), and trypan blue were purchased from Sigma Chemical Co. (St. Louis, MO). Fetal bovine serum (FBS) was from HyClone (Logan, UT); absolute methanol, from JT Baker, Inc. (Phillipsburg, NJ); ficoll-hypaque, from Pharmacia LKB Biotechnology (Piscataway, NJ); Paraformaldehyde, from Fluka Chemie A.G. (Buchs, Switzerland); and RPMI and Dulbecco's modified Eagle medium (DMEM), from Biowhittaker (Walkersville, MD).

Sample Preparation

PBMCs were separated by ficoll-hypaque density centrifugation as follows: Up to 8 mL of PBS-diluted (1:1) whole blood was overlaid on 4 ml ficoll-hypaque in 15 mL centrifugation tubes. After centrifugation at 400g for 30 min., the mononuclear layer was removed and placed in a clean tube, which was filled with PBS containing 2.5% FBS (PBSF) and centrifuged at 300g for 10 min. at 4°C. The supernatant was decanted, and the wash step repeated. Finally, the pellet was resuspended in PBSF to a concentration of 1×10^7 /mL.

Cultured cells were maintained in log phase growth in either high glucose DMEM containing 10% FBS (MDAs) or in RPMI with 10% FBS (CEMs), at 37°C and 5% CO₂ in a humidified atmosphere. Cell death was induced in MDA cells by holding them, tightly capped, for one week at 37°C.

Live PBMCs, live MDAs, dead MDAs, and live CEMs were aliquoted, at 1×10^6 cells/test, both individually and in a proportionately equal mixture for cell staining. The staining procedure consisted of four main steps: viability staining; fixation and permeabilization; PCNA, CK, and MC5 staining; and DNA staining. Antibodies were diluted to working concentrations with PBSF (doses were previously established by titration).

Viability staining was performed as follows: Samples were incubated for 15 min. at room temperature in 200µL each of tubulin ascites (1:5 dilution; protein concentration unavailable) or PBSF (for controls), followed by centrifugation at 500g for 5 min. at RT and decanting. The samples were then washed with 2 mL PBSF and centrifuged and decanted as above. The samples were then incubated as above in 200µL GAM-PECY5 (200µg/mL) or PBSF, followed by washing and centrifugation as above. Lastly, the samples were incubated as above in 200 :L MslgG₁ (1 mg/mL; to block any free GAM sites) or PBSF, followed by two washes as above.

To fix and permeabilize the cells for intracellular staining, the samples were incubated first for 2 min. at room temperature in 1 mL of 20µg/mL lysophosphatidyl choline in 1% paraformaldehyde, followed by centrifugation and decanting; secondly, for 10 min. on ice, in 1 mL of absolute methanol, followed by centrifugation and decanting; and finally, for 5 min. on ice, in 1 mL of 0.1% NP40 in PBSF, followed by centrifugation and decanting.

The samples were then labelled sequentially with PCNA-FITC (50µg/mL), CK-ECD (25µg/mL), and MC5-RD1 (7.5µg/mL), or dose-matched isotype controls. All incubations

were for 15 min. at room temperature, followed by a wash, centrifugation, and decanting as above.

Finally, the samples were resuspended in 1 mL of 1.5 μ g/mL DAPI in PBSF or PBSF alone (for controls), vortexed, and incubated for at least 20 min. prior to flow cytometry.

Flow Cytometry

The samples were analyzed on an Elite flow cytometer (Coulter Corporation, Miami, FL), configured with a 488 nm air-cooled laser, operated at 15 mW, for FITC, RD1, ECD, and PECY5 excitation, and a water-cooled argon laser operated at 351 nm and 40 mW for DAPI excitation. Gated amplification was used to collect DAPI in the FITC channel, with the 351 nm line displaced 40 μ sec below the 488 nm line. Hardware settings were optimized for the live MDA samples.

FITC and DAPI emission were collected with a 550 nm dichroic longpass (DL) and a 525 nm bandpass (BP) filter; RD1 emission, with a 600 nm DL and a 575 nm BP filter; ECD, with a 650 nm DL and a 612 nm BP filter; and PECY5, with a 650 nm DL and a 675 nm BP filter.

Ten thousand events for unmixed cell samples and 40,000 for cell mixtures were acquired in listmode format. Analysis was performed with the Elite software (Coulter Corporation, Miami, FL) and MultiCycle software (Phoenix Flow Systems, San Diego, CA).

RESULTS

A series of electronic gates was cumulatively applied to the cell mixture's DAPI, tubulin, CK, and MC5 distributions to exclude, respectively, doublets and dead, non-epithelial, and non-breast tumor cells (Figure 1). PCNA positivity, ploidy, and % S-phase fraction (%SPF) of the tetraploid breast tumor component were determined for each level of gating (Figure 2). Exclusion of doublets yielded an increase in PCNA positivity from 3.0 to

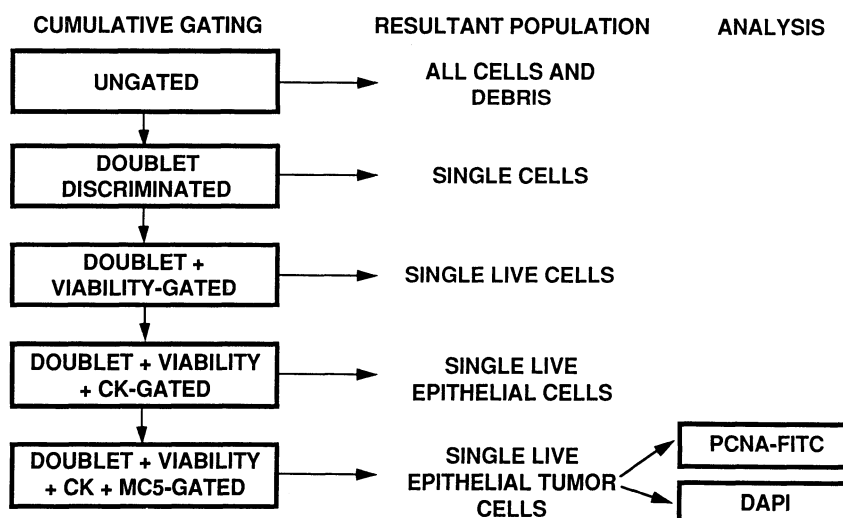


Figure 1. Cumulative gating schematic, illustrating the sequence of gating and resultant populations. After doublets and dead, non-epithelial, and non-tumor cells were gated out, the PCNA expression and DNA content of the targeted live breast tumor cells were analyzed.

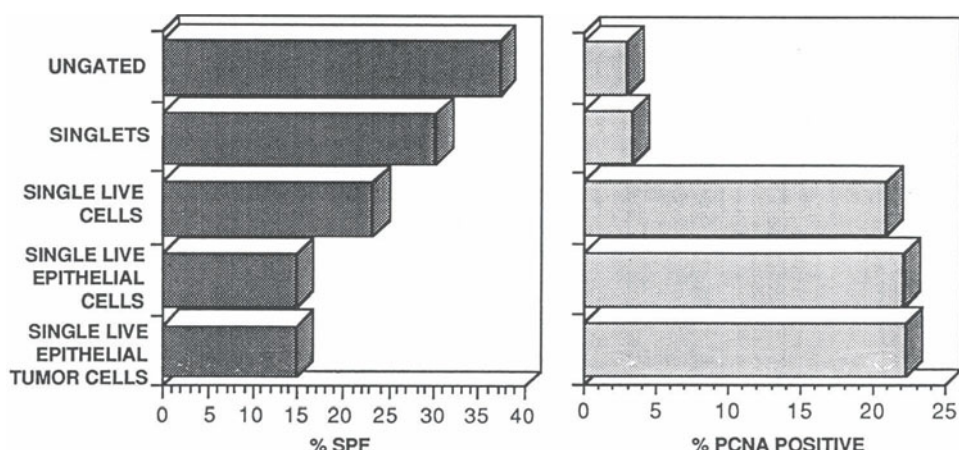


Figure 2. Effects of cumulative gating on %SPF and %PCNA. The %SPF of the tetraploid (live breast tumor cells) cycle and the PCNA positivity of the entire population were calculated for each successive level of gating.

3.4% and a decrease in the tetraploid %SPF from 37.2 to 30.2%. Exclusion of doublets and dead cells increased PCNA positivity from 3.4 to 21%, decreased the tetraploid %SPF from 30.2 to 23.1%, and eliminated a seemingly hypodiploid component from the multiploid cell cycle. Exclusion of doublets, dead cells, and non-epithelial cells increased PCNA positivity from 21.0 to 22.2%, decreased the tetraploid %SPF from 23.1 to 14.9%, and further eliminated the diploid component of the cell cycle. Further gating on MC5 to remove non-breast tumor cells resulted in no significant changes, because MDA cells are positive for both CK and MC5. MC5 is included in the panel, however, for clinical purposes: a small percentage of breast tumors are CK+/MC5- (16); MC5 may have some utility in serum screening; recent reports have suggested that cytokeratin expression may decrease with increasing metastatic potential (15); and CK+/MC5- cells in MC5+ tumors offer a suitable normal control for DNA index calculation (18).

In summary, cumulative gating of the cell mixture to target live breast tumor cells resulted in over a seven-fold increase in PCNA positivity (Figure 3), a 60% decrease in %SPF (Figure 4), and elimination of extraneous hypodiploid and diploid components from the cell cycle. The values obtained by cumulatively gating to target live breast tumor cells in the mixture are consistent with those obtained for unmixed breast tumor cells.

DISCUSSION

One of the major projects in our laboratory is concerned with the accurate assessment of cell proliferation in solid tumors, utilizing flow cytometry and an array of monoclonal antibodies directed against proliferation-associated antigens (PAA), such as PCNA, Ki67, p120, p145 and p105. In our initial experiments several years ago, we refined procedures to permeabilize cells for the detection of nuclear antigens (3), developed methods to preserve PAA expression (13) and, using the aforementioned techniques, quantitated PAA expression during G₀ reentry (5) and in hematogenous malignancies (11). The reagent configuration for the above investigations combined PAA-specific monoclonal antibodies with propidium iodide (PI), and this dual-parameter approach allowed us to quantitate PAA in relation to the stages of the cell cycle (4).

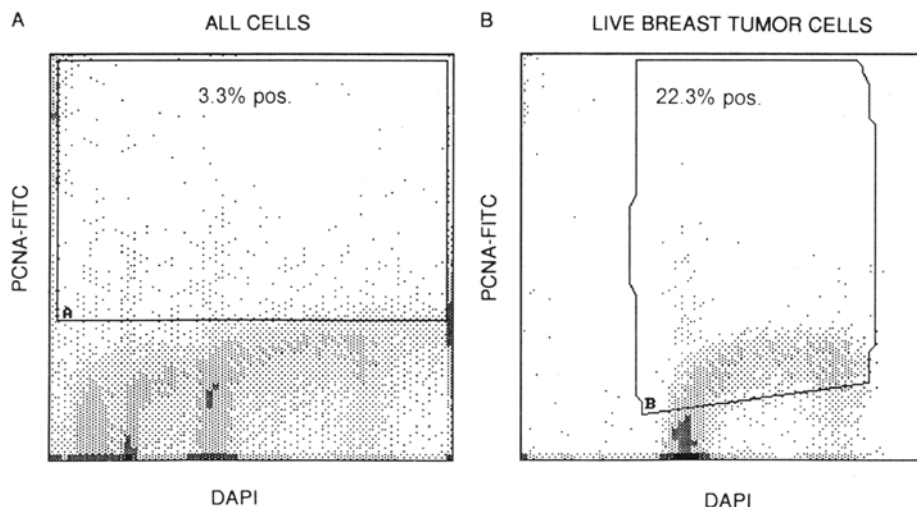


Figure 3. Effect of cumulative gating on PCNA expression. A. PCNA expression in ungated sample. B. PCNA expression of targeted live breast tumor cells, after exclusion of doublets and dead, non-epithelial, and non-tumor cells. Analysis regions were set on isotype controls to include approximately 2% of background.

Having refined the techniques within our laboratory to the point that we felt that we could assess cell proliferation with relative accuracy, our attention was next directed to applying these techniques to solid tumors. It immediately became obvious that the reproducibility and crisp histograms produced by the dual-parameter (PAA + PI) reagent in suspension cultures or hematological tumors was a thing of the past. We began to generate data on human solid tumors that conflicted with the known clinical presentation, obfuscating current biological paradigms. In some instances, rapidly growing tumors yielded percent S phases of <1%, or insignificant PCNA positivity. In other cases, the percent S phase was significantly elevated, while the percent of cells expressing PCNA was extremely low. At this point, it was necessary to reevaluate, in a step-by-step manner, each of the processes and procedures utilized in this type of experiment that could account for these apparent discrepancies, including: 1) length of time post-tumor excision, 2) transport medium, 3) transport mode, 4) tumor dissociation methodologies, 5) cell permeabilization procedures, 6) fluoro-

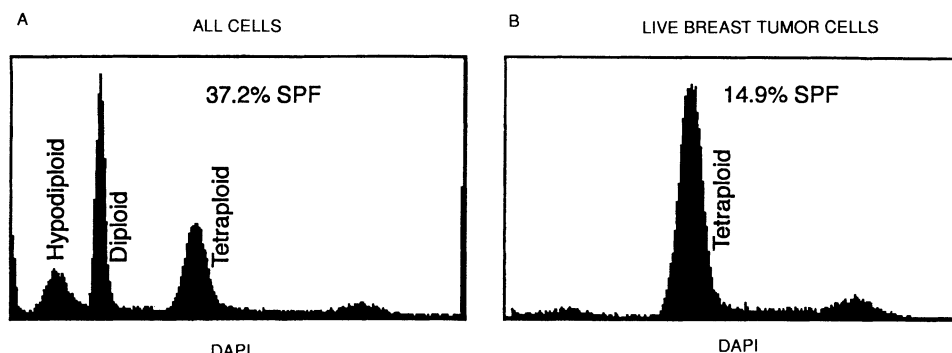


Figure 4. Effect of cumulative gating on cell cycle analysis. A. %SPF of the tetraploid cycle (live breast tumor cells) in the ungated sample. B. %SPF of the targeted live breast tumor cells, after exclusion of doublets and dead, non-epithelial, and non-tumor cells.

phore-to-protein ratios (F:P) of directly labeled antibodies, 7) staining procedure, 8) gating strategies, and 9) tumor heterogeneity. After several months of intense evaluation, tumor heterogeneity appeared to account for most, but not all, of the problems associated with the reproducible and accurate assessment of proliferation status.

The data presented in Figures 2, 3 and 4 illustrate the significant disparity between 'gated' versus 'ungated' samples. In particular, Figure 2 demonstrates significant changes in S phase and PCNA positivity as the tumor cells within the sample were electronically isolated, using monoclonal antibodies prior to analysis. Using these gating techniques, it was possible, in many instances, to resolve apparently contradictory data by targeting the live tumor cells and excluding stromal, apoptotic and dead cells and debris. It is the authors' contention that this type of multiparameter approach, utilizing cumulative gating to refine the accurate assessment of tumor cells, is essential, and will help us better understand both the biology and clinical presentation of tumors in general.

REFERENCES

1. Afanasyev VN, Korol BA, Matylevich NP, Pechatnikov VA, Umansky SR: The use of flow cytometry for the investigation of cell death. *Cytometry* 14:603-609, 1993.
2. Barranco SC, Perry RR, Durm ME, Werner AL, Gregorcyk SG, Bolton WE, Kolm P, Townsend Jr. CM: Intratumor variability in prognostic indicators may be the cause of conflicting estimates of patient survival and response to therapy. *Cancer Res* 54:5351-5356, 1994.
3. Bolton WE, Mikulka WR, Healy CG, Schmittling RJ, Kenyon NS: Expression of Proliferation Associated Antigens in the Cell Cycle of Synchronized Mammalian Cells. *Cytometry* 13:117-126, 1992.
4. Bolton WE, Zeng XR, Lee MYWT, Mikulka W: Expression of PCNA and DNA Polymerase Delta in the Cell Cycle of Synchronized Mammalian Cells. *Journal of Cancer Molecular Biology*, 1, 193-197, 1994.
5. Bolton WE, Freeman JW, Mikulka WR, Healy CG, Kenyon NS: Expression of Proliferation-Associated Antigens (PCNA, p120, p145) during the reentry of G₀ cells into the Cell Cycle. *Cytometry* 17:66-74, 1994.
6. Clevenger CV, Shankey TV: Cytochemistry II: Immunofluorescence measurement of intracellular antigens. In: *Clinical Flow Cytometry: Principles and Applications*, Bauer KD, Duque RE, Shankey TV (eds). Williams & Wilkins, Baltimore, 1993, pp. 157-175.
7. Columbano A: Cell death: Current difficulties in discriminating apoptosis from necrosis in the context of pathological processes *in vivo*. *J Cellular Biochem* 58:181-190, 1995.
8. Darzynkiewicz Z, Bruno S, Del Bino G, Gorczyca W, Hotz MA, Lassota P, Traganos F: Features of apoptotic cells measured by flow cytometry. *Cytometry* 13:795-808, 1992.
9. Gorczyca W, Gong J, Darzynkiewicz Z: Detection of DNA strand breaks in individual apoptotic cells by the *in situ* terminal deoxynucleotidyl transferase and nick translation assays. *Cancer Res* 53:1945-1951, 1993.
10. Gorczyca W, Tuziak T, Kram A, Melamed MR, Darzynkiewicz Z: Detection of apoptosis-associated DNA strand breaks in fine-needle aspiration biopsies by *in situ* end labeling of fragmented DNA. *Cytometry* 15:169-175, 1994.
11. Healy CG, Kenyon NS, Bolton WE: Expression of Proliferation Associated Antigens PCNA, p145 and Ki67 during cell cycle progression in activated peripheral blood lymphocytes: Potential utility in monitoring hematologic malignancies. *Journal Cancer Molecular Biology*, Vol. 1, No. 1, 59-60, 1994.
12. Lockshin RA, Zakeri ZF: Physiology and protein synthesis in programmed cell death: Early synthesis and DNA degradation. *Ann NY Acad Sci* 663:234-249, 1992.
13. Mikulka WR, Bolton WE: Methodologies for the preservation of Proliferation Associated Antigens PCNA, p120, and p105 in tumor cell lines for use in flow cytometry. *Cytometry* 17:246-257, 1994.
14. O'Brien MC, Gupta RK, Lee SY, Bolton WE: Use of a multiparametric panel to target subpopulations in a heterogeneous solid tumor model for improved analytical accuracy. *Cytometry* 21:76-83, 1995.
15. Paine ML, Gibbins JR, Chew KE, Demetrious A, Kefford RF: Loss of keratin expression in anaplastic carcinoma cells due to posttranscriptional down-regulation acting in trans. *Cancer Res* 52:6603-6611, 1992.
16. Peterson JA, Zava DT, Duwe AK, Blank EW, Battifora H, Ceriani RL: Biochemical and histological characterization of antigens preferentially expressed on the surface and cytoplasm of breast carcinoma

- cells identified by monoclonal antibodies against the human milk fat globule. *Hybridoma* 9:221–235, 1990.
17. Riedy MC, Muirhead KA, Jensen CP, Stewart CC: Use of a photolabeling technique to identify nonviable cells in fixed homologous or heterologous populations. *Cytometry* 12:133–139, 1991.
 18. Shankey TV, Rabinovitch PS, Bagwell B, Bauer KD, Duque RE, Hedley DW, Mayall BH, Wheless L: Guidelines for implementation of DNA cytometry. *Cytometry* 14:472–477, 1993.
 19. Terstappen LWMM, Shah VO, Conrad MP, Recktenwald D, Loken MR: Discriminating between damaged and intact cells in fixed flow cytometric samples. *Cytometry* 9:477–484, 1988.
 20. Visscher DW, Zarbo RJ, Jacobsen G, Kambouris A, Talpos G, Sakr W, Crissman JD: Multiparametric deoxyribonucleic acid and cell cycle analysis of breast carcinomas by flow cytometry: Clinicopathologic correlations. *Lab Invest* 62:370–378, 1990.
 21. Wing MG, Montgomery AMP, Songsivilai S, Watson JV: An improved method for the detection of cell surface antigens in samples of low viability using flow cytometry. *J Immunol Meth* 126:21–27, 1990.
 22. Wingren S, Stål O, Carstensen J, Sun XF, Nordenskjöld B: S-phase determination of immunoselected cytokeratin-containing breast cancer cells improves the prediction of recurrence. *Breast Cancer Res and Treatment* 29:179–187, 1993.
 23. Wingren S, Stål O, Nordenskjöld B: Flow cytometric analysis of S-phase fraction in breast carcinomas using gating on cells containing cytokeratin. *Br J Cancer* 69:546–549, 1994.
 24. Zama L, Bareggi R, Santavenere E, Vitale M: Subtraction of autofluorescent dead cells from the lymphocyte flow cytometric binding assay. *Cytometry* 14:951–954 (1993).
 25. Zarbo RJ, Visscher DW, Crissman JD: Two-color multiparametric method for flow cytometric DNA analysis of carcinomas using staining for cytokeratin and leukocyte-common antigen. *Anal Quant Cytol Histol* 11:391–402, 1989.

VIDEOMICROFLUOROMETRY OF PROGESTERONE RECEPTORS AND THEIR GENES IN BREAST CANCER CELLS

Sylvie Cassanelli, Agnès Mialhe, Josette Louis, and Daniel Seigneurin

Equipe de Cytologie Quantitative - Institut Albert Bonniot
Faculté de Médecine - 38700 - La Tronche - France

ABSTRACT

Expression of progesterone receptors (PR) at the cell level is heterogeneous. Quantification by image analysis of several fluorescent immunostainings (PR, Ki-67 antigen, DNA) on breast cancer cell lines shows that this heterogeneity is partially linked to cell proliferation kinetic. Simultaneous detection of chromosome 11 (on which PR gene is located) by *in situ* hybridization and PR immunostaining do not demonstrate any relationship between the number of chromosome 11 and PR cell positivity, probably because numbers of chromosome 11 and of PR gene copies are not correlated, as shown by a double fluorescent *in situ* hybridization on metaphases.

1. INTRODUCTION

Quantification of progesterone receptors (PR) is thought to be a good prognostic parameter in breast cancer (McGuire, 1991) and is therefore generally used. Immunocytochemical studies showed that PR positive tumors stained heterogeneously (Clark, 1983; Seigneurin, 1989). The proportion of stained cells and the intensity of staining vary from tumor to tumor and also within the same tumor. By studying the MCF-7 breast tumor cell line and subclones derived from this cell line by limit dilution, we demonstrated that this heterogeneity can be explained in part by cell kinetic or by genomic alterations (Cassanelli, 1991, 1992, 1995). Most of these studies were done with fluorescent probes, whose quantification needs videomicrofluorometry (Shotton, 1991).

The purpose of this review is to summarize these studies and to define more precisely the genomic alterations which can be responsible for PR heterogeneity, focusing on the number of chromosome 11, on which the human PR gene is located and the number of copies of PR gene.

2. MATERIAL - METHODS

2.1. Biological Material

2.1.1. MCF-7 and MCF-7 Subclones Culture. MCF-7 subclones were obtained as described by Cassanelli (1995); briefly, the concentration of the MCF-7 cell suspension was determined and adjusted to 10 cells per ml. 0.1 ml aliquot of the diluted cells was plated onto two 96 well plates at a concentration of one cell per well. After 15 days, thirty colonies were numbered and some of them transferred to 24 well plates. These cells were grown to confluence and then transferred into a larger flask. The cells of the MCF 7 hormone responsive human breast cancer line and the MCF-7 subclones were grown as a monolayer in plastic flasks (25 cm^2) at 37° C . The culture medium contained 90 % Dulbecco's minimal essential medium (Gibco), supplemented with 10 % fetal calf serum (Gibco) to which was added 1 % L glutamine (Boehringer), 1 % insulin 1 U/ml (Actrapid HM : Novo Industrie Pharmaceutique) and 0.1 % antibiotics (penicillin, streptomycin).

2.1.2. Stainings.

- PR, Ki-67 or BrdU and DNA Triple Immunofluorescent Staining.
 - *PR staining.* After fixation, cells were incubated for 15 min. with goat serum. After the blocking step, cells were incubated with a rat monoclonal anti-PR antibody (PgR-ICA Abbott Laboratories) for 30 min. In a second step, cells were incubated with a second tetramethyl rhodamine isothiocyanate (TRITC) conjugated goat antirat IgG F(ab')₂ fragment (Immunotech) diluted at a 1:50 ratio in PBS for 30 min.
 - *Ki-67 antigen staining.* The murine monoclonal antibody against Ki-67 antigen can be used to assess the growth fraction. It binds to a nuclear antigen expressed in all stages of the cell cycle except G0 . IgG F(ab')₂ fragment (Immunotech) was diluted at a 1:50 ratio in PBS and incubated for 30 min. followed by a second fluorescein isothiocyanate (FITC) conjugated goat antimouse antibody (Immunotech) diluted at a 1:50 ratio in PBS for 30 min.
 - *BrdU staining.* A mouse monoclonal anti BrdU antibody (Becton Dickinson) was incubated for 60 min., followed by a second FITC conjugated antibody as described above.
 - *DNA staining.* Cells were incubated in bisbenzimidazol, a stoichiometric DNA fluorochrome (Hoechst-Behring 33342; 10^{-6}M) for 40 min in the dark. After working in PBS, slides were embedded in an "antifading" medium (Shotton, 1991) and covered with a glass coverslip.
 - *Negative controls.* For each cell batch, controls were obtained by omitting primary antibodies in order to determine the fluorescence background.
- *In situ hybridization*
 - *Probes.* Specific repeated DNA sequences of the centromeric regions of human chromosome 11 and of the RP gene were cloned respectively in the pRB₂ and the pSG₅ plasmids. They were labelled by nick translation with digoxigenin 11 d-UTP. Hybrids were detected with a sheep antidigoxigenin antibody linked to FITC or TRITC.
 - *PR immunocytochemistry and chromosome 11 fluorescent in situ hybridization (FISH).* The final concentration of the probe was 2.5 ng/ml. After treatment with proteinase K, hybridization medium was added to the slides; DNA probe and nuclear target DNA were denatured at 90° C for 8 min.; hybridization was carried out overnight at 37° C . PR was revealed prior to FISH using the alkaline

phosphatase-antialkaline phosphatase (APAAP) method (Mialhe, 1995) and NBT-X-Phosphate substrate. FISH was carried out after the immunocytochemistry detection.

- *Chromosome 11 and RP gene FISH.* The final concentrations of the probes were 10 ng/µl for both pSG₅ and pRB₂. 20 µl of hybridization medium with probes were added to the slides. Hybridization was carried out overnight at 37°C in a moist chamber saturated with 50% formamide. Slides were embedded in Vectashield medium and DAPI.

2.1.3. Cytometry and Image Analysis

• Cytometry

A triple quantification of PR, Ki-67 antigen and DNA staining in a representative number of cell nuclei was performed with a SAMBA 2005 Image Analysis System coupled to a silicon-intensified target camera (LH 4036 Lhesa Electronique), a microcomputer and a epiillumination microscope (Zeiss Axioplan). Measurements were made with a plan-apochromat 40 x objective, the Optovar magnification was 2 x, the final magnification was 800 x. The following filters were used : a bandpass filter BP 546/121nm, a chromatic beam splitter FT 580 and a longwave pass filter LP 590 nm for red TRITC fluorescence ; a bandpass filter BP 485/20 nm, a chromatic beam filter splitter FT 510, and a longwave pass filter LP 515/575 for green FITC fluorescence ; a band pass filter BP 365/12 nm, a chromatic beam filter splitter FT 395 and a longwave pass filter LP 397 nm for blue bisbenzimidazol fluorescence. The excitation source was a 50 W. Hg lamp. Images were digitized in a 512 x 512 array and fluorescence intensity levels were coded on 8 bits (256 values, 0 for black and 255 for white).

Analysis began with the segmentation of the nuclei. This was performed in fluorescent light by a grey level threshold on DNA stain. The DNA staining was used to segment the nucleus and allow PR and antigen Ki-67 quantification in each nucleus and to determine DNA content. Then, PR, Ki-67 antigen and DNA cell quantities were calculated by integration of the grey level for each pixel (integrated fluorescences PR-IF, Ki-67-IF and DNA-IF). Fluorescence staining of negative controls was adjusted and set to obtain a zero or one IF value, corresponding to the TRITC and FITC backgrounds. For comparative and reproducible studies, all quantifications were performed on slides simultaneously immunostained with identical sensitivity settings.

• FISH image analysis

Visualisation of fluorescent hybridization signals was carried out with an epiillumination microscope HBO 100 W Axiophot (Zeiss) coupled to a cooled CCD camera (Hamamatsu Photonics). For each metaphase, 3 images, corresponding to DAPI, FITC and TRITC, were placed in the memory and treated, in order to decrease background noise and to increase the resolution of the signals.

3. RESULTS

3.1. PR Expression According to Cell Kinetics

The microscopic observation of triple PR, Ki 67 and DNA staining shows that strongly Ki-67 labeled cells have a high PR level and Ki-67 negative cells demonstrated a low PR level. Figure 1 presents the variations of PR expression in relation to cell kinetics: non cycling cells (cells in G0) express significantly less PR than cycling cells.

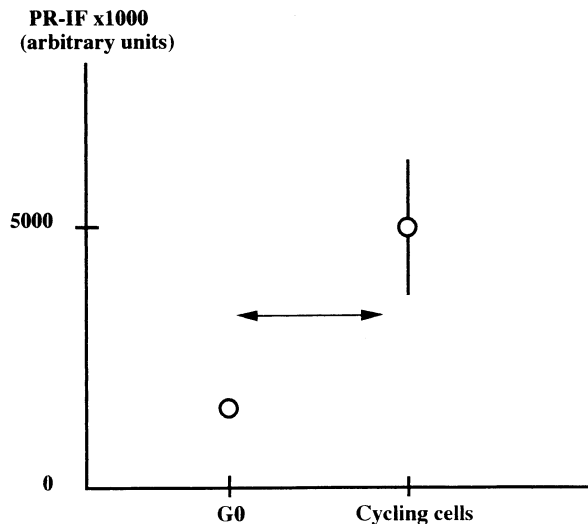


Figure 1. Variations of the progesterone expression according to resting or cycling characteristics of the cells. Difference in the PR fluorescent intensities is statistically significant at the 0.05 level (Mann and Whitney test).

During the cell cycle, PR expression changes (Figure 2) : level is high in G1 phase ; in late G1 and early S the PR amount decreases; it is again high in middle and late S and in G2 phase.

3.2. PR Expression According to Genomic Alteration

3.2.1. MCF-7 Subclones. Thirty MCF-7 subclones were present on microscopic slides after 15 days of culture. Immunofluorescent staining of PR allows the characterization of two kinds of clones : PR positive and PR negative ones; 20 were PR negative and 10 were PR positive with an heterogeneous PR expression. PR positive and PR negative clones differed by their proliferative features, demonstrated by the number of cells after 15 days of culture and the percentage of Ki-67 antigen positive cells, both parameters being lower in PR negative than in PR positive clones. PR negative clones grew slowly and died, whereas PR positive continued to proliferate.

3.2.2. Immunocytochemistry of PR and Chromosome II FISH. The number of chromosome 11 varies considerably in the cell line studied, whether cells contain PR or not. A majority of PR negative cells contain four, five or six copies of the centromere of chromosome 11. The same observations were obtained in PR positive cells. The evaluation of chromosome 11 number in about 300 cells showed that PR positive and PR negative nuclei had similar percentages of cells with 4, 5 or 6 chromosomes. Indeed, statistical analysis (χ^2 test) has shown that there is no significant correlation between PR expression and the number of copies of chromosome 11 (χ^2 - 9.33 ; $p < 0.1$) - (Table 1).

3.2.3. Chromosome 11 Centromere and PR Gene FISH. Analysis of metaphases of MCF-7 cells showed that the number of chromosome 11 varies from cell to cell and that each chromosome 11 does not always carry two PR gene hybridization spots. Some chromosome 11 have no PR gene, others only one. In MCF-7 cell line no relation between the number of chromosome 11 and the number of copies of PR gene was demonstrated. This may be due

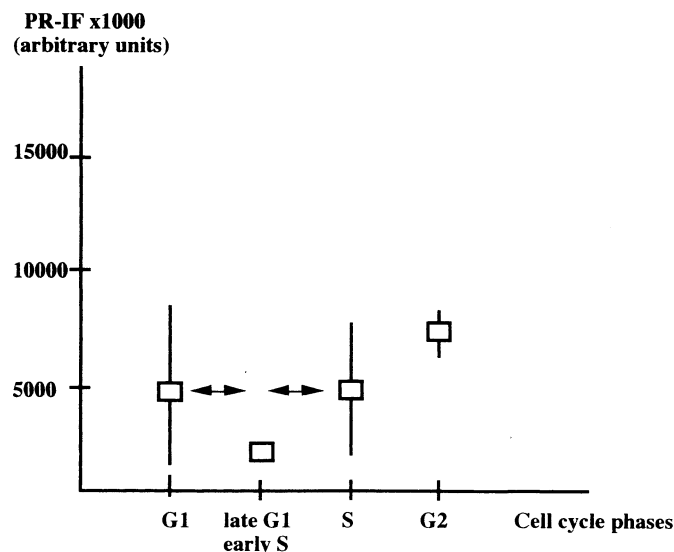


Figure 2. Variations of the progesterone expression during the cell cycle according to cell cycle phases. Differences in the PR fluorescent intensities between late G1-early S and S are statistically significant at the 0.05 level (Mann and Whitney test).

to translocations or deletions; indeed in some of the cells in metaphase one can see PR genes on chromosomes other than the 11. The double FISH of chromosome 11 centromere and PR gene on MCF-7 subclone number 4 gave very different results. This clone expresses PR with a high level and is very homogeneous according to the number of chromosome 11 and of copies of PR gene : 94% of the cells have 4 chromosomes and 8 copies of PR gene. We did not demonstrate PR gene deletion.

Table 1. Heterogeneity of number of chromosome 11 and progesterone receptor (PR) expression

Number of chromosome 11 in T47-D cell line	PR negative		PR positive	
	n	% of cells	n	% of cells
4	42	(33,5)	69	(38,5)
5	23	(18)	48	(26,5)
6	46	(36,5)	52	(29)
7	10	(8)	10	(5,5)
8	5	(4)	1	(0,5)
total number of analyzed cells	126		180	

$\chi^2 = 9,33$
 $p < 0,1$

4. DISCUSSION

4.1. About Methods Used

Cell heterogeneity is a morphologic observation ; to study it, we used methods of *in situ* evaluation of proteins and nucleic acids such as immunocytochemistry and *in situ* hybridization. These methods, however, have their own drawbacks, mainly due to a sometimes poor reproducibility and the lack of usable references. A high level of standardisation is necessary.

Fluorescent labelling has many advantages : very small amount of label can be detected if an intensified video-camera is used ; the intensity of emitted light is proportionnal to label concentration; specimens can be multiply-labelled without interfering with images of each stain (Lockett, 1991).

Quantification of fluorescent labels by videomicrofluorometry gives unsatisfactory results if artefacts due to the instrument are not eliminated or reduced. Corrections according to Vigo (1991) using background and reference of homogeneity images permitted the reduction of videomicrofluorometry errors.

4.2. About PR Expression and Cell Kinetics

In MCF-7 and MCF-7 subclones, non cycling cells express less PR than cycling cells. This result is in agreement with data from Jakesz (1984) who studied Estrogen Receptors (ER) in MCF-7 cell line. Thus, both types of steroid receptors (PR and ER) seem to follow the same expression rules. However, our results are in contradiction with data obtained on human breast tumors (Kute, 1981). In fact, an inverse relationship between ER and PR expression and cell proliferation (estimated by the percentage of cells in S phase) has been demonstrated ; highly proliferative tumors most often express a low level of PR or none at all. It is not clear if this inverse relationship persists when only PR positive tumors are studied. During the cell cycle, the variations of PR expression are significant of the time of their synthesis and degradation. PR synthesis begins at the end of the S phase and persists during G2 phase. It may stop at that time. The low level of PR at the end of G1 and early S phases can be explained by the PR short half life (28 hours for Nardulli, 1988) compared to the duration of the cell cycle of MCF-7 cell line (37 to 41 hours).

4.3. About PR Expression and the Cell Genome

4.3.1. Clonal Origin of the Cells in MCF-7 Cell Line. Resnicoff (1987) hypothesized that ER expression in MCF-7 cell line depends on the clonal origin of the cells. This is not the opinion of Kodama (1985) who demonstrated that, in this cell line, ER positive colonies derived from ER negative stem cells and that ER expression appeared during cell differentiation. Our results on subclones obtained by limit dilution are in favour of Resnicoff's hypothesis. Indeed some subclones do not express PR, while some do. All culture conditions being the same, the subclones are different only according to the genome of their stem cells.

4.3.2. PR Expression and Chromosome 11. Dutrillaux (1991) showed that breast tumor cells may have lost the long arm of chromosome 11 on which PR gene is located; this may explain the loss of PR expression (Magdalénat, 1994). On the other hand, an increase in chromosome 11 number should be associated with a high PR expression. This was the hypothesis of Savouret for the T47-D cell line. However, our results do not confirm it: we

found that the number of chromosome 11 varies from 4 to 8 and that PR expression does not seem to be correlated with chromosome 11 number. Of course, presence of chromosome 11 centromere does not necessarily imply the presence of PR gene since chromosome deletions or translocations may occur.

4.3.3. Chromosome 11 and PR Gene. In the MCF-7 cell line we did not find any relationship between numbers of chromosome 11 and PR gene copies: the spots corresponding to chromosome 11 centromere are not always associated with two PR gene spots. However, this is the case in MCF-7 subclone number 4, where 94% of the cells have 4 chromosomes 11 and 8 copies of PR gene.

These results are a sign of the great complexity of the PR expression.

FISH on interphase cells, associated with immunofluorescence of PR expression, may give useful insight into the relation at the cell level between the number of copies of PR gene and the amount of expressed PR.

REFERENCES

- Cassanelli S., Guillaud P., Louis J. and Seigneurin D., 1991, Image cytometry of progesterone receptor expression during the cell cycle in the MCF-7 cell line, *J. Histochem. Cytochem.* 39: 1713-1718.
- Cassanelli S., Louis J. and Seigneurin D., 1995, Progesterone receptor heterogeneity in MCF-7 cell subclones is related to clonal origin and kinetics, *Tumor Biology* 16: 222- 229.
- Cassanelli S., and Seigneurin D., 1992, Video microfluorometry of hormonal receptors in breast cancer cells; *J. Cell. Pharmacol.* 3: 146-150.
- Clark G.M., McGuire W.L., Hubay C.A., Pearson O.H. and Marshall J.S., 1983, Progesterone receptors as a prognostic factor in stage II breast cancer, *Engl. J. Med.* 309: 1343-1347.
- Dutrillaux B., Gerbault-Seureau M., Remvikos Y., Zafrahi B and Prieur M., 1991, Breast cancer evolution : I. Data from cytogenetics and DNA content; *Breast Cancer Res. Treat.* 19: 245-255.
- Jakesz R., Smith C.A., Aitken S., Huff K., Schuette W., Shackney S. and Lippman M., 1984, Influence of cell proliferation and cell cycle phase on expression of estrogen receptor in MCF-7 breast cancer cells, *Cancer Res.* 44: 619-625.
- Kodama F., Greene G.L. and Salmon S.E., 1985, Relation of estrogen receptor expression to clonal growth and antiestrogen effects on human breast cancer; *Cancer Res.* 45: 2720- 2724.
- Kute T.E., Muss H.B. and Anderson D., 1981, Relationship of steroid receptor, cell kinetics, and clinical status in patients with breast cancer; *Cancer Res.* 41: 3524-3529.
- Lockett S., O'Rand M., Rinehart C.A., Kaufman D.G., Herman B. and Jacobson K., 1991, Automated fluorescence image cytometry: DNA quantification and detection of chlamydia infections; *Anal. Quant. Cytol. Histol.* 13:27-44.
- Magdelénat H., Gerbault-Seureau M. and Dutrillaux B., 1994, Relationship between loss of estrogen and progesterone receptor expression and of 6q and 11q chromosome arms in breast cancer, *Int. J. Cancer* 57: 63-66.
- McGuire W.L., 1991, Breast cancer prognostic factors: evaluation guidelines, *J. Natl. Cancer Inst.* 83: 154-155.
- Mialhe A., Cassanelli S., Louis J. and Seigneurin D., 1996, Methods for simultaneous interphase *in situ* hybridization and nuclear antigen immunocytochemistry in T47-D cells, *J. Histochem. Cytochem.* 44: 193-197.
- Nardulli A.M. and Katzenellenbogen B.S., 1988, Progesterone receptor regulation in T47D human breast cancer cells : analysis by density labeling of progesterone receptor synthesis and degradation and their modulation by progestin, *Endocrinology* 122: 1532-1536.
- Resnicoff M., Medrano E.E., Podhajcer O.L., Bravo A.I., Bover L. and Mordoh J., 1987, Subpopulation of MCF-7 cells separated by percoll gradient centrifugation: a model to analyze the heterogeneity of human breast cancer, *Proc. Natl. Acad. Sci. USA* 84: 7295-7299.
- Savouret J.F., Rauch M., Redeuilh G., Sar S., Chauchereau A., Woodruff K., Parker M.G. and Milgrom E., 1994, Interplay between estrogens, progestins, retinoic acid and AP- 1 on a single regulatory site in the progesterone receptor gene, *J. Biol. Chem.* 269: 28955-28962.

- Seigneurin D., Cohen O. and Louis J., 1989, Immunocytochemistry and image cytometry of progesterone receptors in breast carcinoma imprints; expression of tissular and cellular heterogeneity; relationship to biochemical and histological parameters and DNA analysis, *Anal. Cell. Pathol.* 1:97-104.
- Shotton D.M., Video and optodigital imaging microscopy, 1991, in: "Topics in molecular and structural biology, vol.15. New techniques of optical microscopy and microspectroscopy", RJ Cherry, ed, Macmillan Press, London, England pp 1-47.
- Vigo J., Salmon J.M., Lahmy S. and Viallet P., 1991, Fluorescent image cytometry: from qualitative to quantitative measurements, *Anal. Cell. Pathol.*.. 3: 145-165.

IMMUNOPHOTODETECTION OF CANCER BY ANTIBODY-INDOCYANIN CONJUGATES

Experimental and Preliminary Clinical Results

S. Folli,¹ P. Westermann,¹ D. Braichotte,² A. Pèlegelin,⁵ J. Mizeret,²
 G. Wagnières,² H. van den Bergh,² J-F. Savary,³ P. Monnier,³
 J-P. Cerottini,⁴ J-C. Givel,⁴ and J-P. Mach¹

¹ Institute of Biochemistry
 University of Lausanne
 1066 Epalinges, Switzerland

² Institute of Environmental Engineering
 Ecole Polytechnique Fédérale 1015 Lausanne

³ Department of Otolaryngology, CHUV 1010 Lausanne

⁴ Department of Surgery, CHUV 1011 Lausanne

⁵ Centre Val d'Aurelle
 Service de Médecine Nucléaire
 34094 Montpellier, France

ABSTRACT

We have recently shown that immunophotodetection of human colon carcinomas in nude mice and in patients is possible by using anti-carcinoembryonic antigen (CEA) monoclonal antibodies (MAb) coupled to fluorescein. Here we show, by using a new fluorescent dye, indocyanin, coupled to either anti-CEA or anti-squamous cell carcinoma MAbs, that the efficiency of tumor immunophotodetection in nude mice bearing either human colon carcinoma or squamous cell carcinoma xenografts, can be markedly improved. This improvement is due to the higher absorption and emission wavelengths of indocyanin (652 - 667 nm) as compared to fluorescein (488-515 nm), which give a deeper tissue penetration and lower tissue autofluorescence. Preliminary clinical studies in patients with SCC, however, showed that the tumor to normal tissue ratios obtained after injection of ¹²⁵I-MAb E48-indocyanin conjugates were not sufficient to allow satisfactory immunophotodiagnosis. In contrast, when we used our chimeric anti-CEA antibody coupled to indocyanin in patients with colon carcinomas, we obtained very elegant and specific tumor immunophotodetection. The overall results demonstrate the feasibility of a new form of *in vivo* tumor diagnosis called immunophotodetection, which may open

the way to the development of a more specific approach to phototherapy of early carcinomas.

INTRODUCTION

One way to improve the prognosis of cancer patients is to detect small tumors earlier. In this regard the use of dyes was shown to be helpful for the photodiagnosis of early bronchial carcinoma^{1,2,3,4,5}. Such diagnostic procedures, although limited to tumors accessible to the exciting light and to the detection of the emitted fluorescence, can theoretically be applied to a large number of cancers including carcinomas from the respiratory, gastrointestinal, and urogenital systems, as well as to ocular and skin cancers³. However an important limiting factor of this technology is that the presently used fluorescent dyes have a relatively low tumor localization specificity. To overcome this problem, it was proposed to couple dyes to antibodies directed against tumor-associated antigens. The obvious advantage of using a MAb as a vector for tumor localization of a dye is the property of MAb to bind specifically to a marker which is more abundant in tumor than in normal tissue. Furthermore, this technique allows selection of the dye on the basis of its photochemical properties, independently of its weak tumor-localizing properties, since the tumor selectivity is provided by the MAb specificity.

Dyes have already been coupled to MAbs for photodiagnostic purposes, but they were essentially tested *in vitro*^{6,7,8,9,10,11}, or in one instance by local application in the stomach¹². To our knowledge, no *in vivo* tumor immunophotodiagnosis studies after systemic injection of antibody-dye conjugate have been reported and the few immunophototherapy experiments performed did not yield highly significant results⁶.

We have first shown that MAbs directed against the CEA, conjugated with up to 10 molecules of fluorescein per MAb molecule, were able to localize specifically into human colon carcinomas in a nude mouse xenograft model¹³. Furthermore, in a pilot clinical study¹⁴, we have demonstrated that the small amount of fluorescein (15 to 80 ng/g), specifically localized in the tumor by the antibody, was sufficient to allow clearly detectable laser-induced fluorescent signal in the tumor. However due to the fact that the fluorescein absorption and emission wavelengths are too low (respectively 488 and 515 nm) their tissue penetration is not optimal, thus only the fluorescein molecules which are localized at the surface of the lesion can be excited by the laser light. In addition, an important non-specific yellowish autofluorescence is induced by the excitation at the 488 nm wavelength of endogenous chromophores which are present in several normal tissues such as the rectal mucosa¹⁴. Despite sophisticated computerized technology, this autofluorescence can sometimes interfere with optimal detection of the specific green fluorescence due to fluorescein. To overcome these limitations we have chosen a new dye, indocyanin, which had never been used previously for *in vivo* photodetection. This dye has been selected on the basis of its higher absorption and emission wavelengths of 652 nm and 667 nm, respectively, its very high extinction coefficient (> than 200.000) and its favourable quantum yield of fluorescence.

The purpose of the present study was to determine whether the encouraging results of immunophotodetection obtained after injection of anti-CEA or anti-SCC indocyanin conjugates in nude mice grafted with either human colon carcinoma or human SCC A431¹⁵ could be reproduced at the clinical level. In addition we tried to make a correlation between direct fluorescent measurements¹⁶ and the radioactivity counting obtained in nude mice bearing the A431 SCC xenografts, which received intravenous injection of conjugates consisting of indocyanin coupled to ¹²⁵I trace labeled MAb E48. This correlation should help

to determine the meaningfulness of the direct fluorescence measurements¹⁶ which have been used at clinical level in the context of photodiagnosis and therapy.

MATERIALS AND METHODS

Monoclonal Antibodies

The anti-CEA MAb 35 was purified from mouse ascites using ammonium sulfate (45% saturation at 4°C) precipitation followed by DE52 cellulose (Whatman, Balston, UK) ion exchange chromatography using 0.03 M or 0.05 M phosphate buffer, pH 8. The mouse-human chimeric anti-CEA MAb (CGP44290) of human IgG4 K isotype (X4) used was derived from one of our murine anti-CEA Mabs B7-25. Both mouse and chimeric anti-CEA Mabs have been used clinically for tumor diagnosis by immunoscintigraphy^{18,19}.

Monoclonal E48 (IgG1), kindly provided by Centocor Inc. (Leiden, The Netherlands), was derived from mice immunized with cells from a metastasis of a moderately differentiated SCC of the larynx²⁰. The antigen recognized by MAb E48 was reported to be expressed by 98 % of primary head and neck tumors (N = 110) and the majority of cells within these tumors. The LOVO-D1 MAb²¹ was derived from mice immunized with cells from the human colon carcinoma cell line LOVO. This MAb recognized a pancarcinoma antigen also similar to that identified by Mab 17-1A which is also known to be expressed in SCC²².

In several experiments we used as control an irrelevant mouse IgG1 (PxIgG1), purified from ascites produced by the secreting mouse myeloma P3X63²³.

Radiolabeling of Monoclonal Antibodies

Batches of 4 mg MAb were trace labeled with 100 µCi ¹²⁵I by the chloramine T method. Free ¹²⁵I was separated from labeled MAb on a Sephadex G25 column (Pharmacia, Uppsala, Sweden) equilibrated in 0.15 M sodium bicarbonate buffer, pH 9.5, yielding a specific activity of 0.01 to 0.02 µCi/µg (1 Ci = 37 GBq).

Preparation of Indocyanin-Monoclonal Antibody Conjugates

Various amounts of indopentamethinecyanin N-hydroxysuccinimidyl ester produced under the name of CY5.18 by Biological Detection System Inc. (Pittsburgh, PA, USA) and thereafter called indocyanin, were dissolved in pure dimethylformamide and progressively added to the ¹²⁵I-labeled MAb, in sodium bicarbonate buffer, at a constant concentration of 2 mg/ml. The final dimethylformamide concentration did not exceed 10% (V/V) of the reaction volume. After gentle shaking overnight at 4°C, the conjugates were filtered through a Sephadex G200 gel column (Pharmacia) to remove free indocyanin and any (<1%) aggregated material generated by the labelling process (Fig.1).

Indocyanin/MAb ratios were determined using absorbance at 652 nm for the indocyanin concentration and radioactive measurement for MAb quantitation. For injection to patients the same procedure was used except that the last filtration was performed in pyrogen free physiological saline buffer from our hospital and the conjugate was sterilized by filtration through 0.22-µm Millipore filter as described¹⁴. Immunoreactivity of each anti-CEA indocyanin conjugate preparation was determined before injection and on a sample from the patient's serum (collected 2 hr after injection) by direct binding assay¹³ to an excess of purified CEA coupled to CNBr-activated Sepharose (Pharmacia). For indocyanin MAb

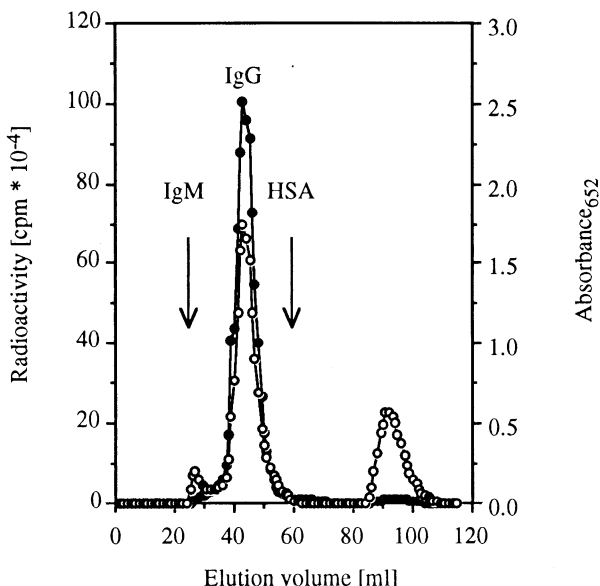


Figure 1. Elution profile on Sephadex G200 column of ^{125}I -MAb E48 after a coupling reaction with indocyanin N-hydroxysuccinimidyl ester, demonstrating the separation of the MAb E48 indocyanin conjugate from the unreacted free indocyanin. ^{125}I -radioactivity (●—●) and absorbance (○—○) at 652 nm are expressed in arbitrary units ; the arrows indicate the three peaks of the human serum : IgM, IgG and human serum albumin (HSA).

E48 conjugates the immunoreactivity was determined by direct binding assay to cells from SCC line A431 as described¹⁵.

In Vitro Stability of the Conjugates

To test the stability of the conjugates, conjugate samples were incubated for 24 hr at 37°C with normal human serum containing 0.02 % sodium azide. After separation by gel filtration on a Sephadex G200 column (Pharmacia), the eluent was analyzed for optical absorption at 280 nm and 652 nm and ^{125}I radioactivity as described^{14,15}.

Samples of the conjugates were also tested on 7.5% SDS-PAGE under reducing and non reducing conditions as an additional experiment to study the stability of the coupling. After the migration of the conjugate, the gel was analyzed by autoradiography and by laser induced fluorescence at 667 nm after excitation at 640 nm. A Kodak Wratten filter 70 was used to eliminate the 640 nm excitation light as described¹⁵.

Tumor Localization Studies of Indocyanin–MAb Conjugates in Nude Mice Xenografts

Human colon carcinoma T380 serially transplanted subcutaneously into "Swiss" nude mice²⁴ (Iffa Credo, L'Arbresle, France) was used as target for the anti-CEA MAb 35 -indocyanin conjugates, as previously described²⁵ for radiolabeled MAb. This tumor is well vascularized²⁶ and shows few necrotic areas before it reaches a size of more than 1 gram²⁴. The human SCC A431²⁷ serially transplanted into nude mice was used as target for the MAb E48-indocyanin conjugate. Mice had their thyroids blocked by adding Lugol's (0.05%) (vol/vol) iodine solution in the drinking water.

Twenty µg of iodinated MAb conjugates were injected intravenously into mice bearing T380 or A431 tumors weighing 0.2 to 0.6 g. The amounts of injected indocyanin varied with the indocyanin to MAb ratio, ranging from 0.1 to 0.3 µg. To determine the biodistribution of the indocyanin E48 conjugates, groups of 3 or 4 mice were sacrificed at different time intervals (6, 12, 24, 48 and 96 hr). The tumor and all normal organs including a 0.5 ml sample of blood were weighed and their ^{125}I radioactivity was measured in a scintillation counter^{28,29}. The results were expressed as percentages of the injected dose of radioactivity (% ID) per gram of tissue. The tumor to normal tissue ratios were calculated by dividing the % ID per g in the tumor by that measured in each individual organ.

Immunophotodetection of Colon Carcinoma or SCC in Nude Mice Xenografts

For photodetection of the human tumor xenografts in nude mice, the animals were sacrificed 24 hr after the injection of 100 µg of ^{125}I -MAb 35 -(indocyanin)₂ conjugate corresponding to 1 µg of indocyanin. The mice were placed under a homogenous laser beam illuminating a 13 cm diameter circle with an intensity of 13 mW cm^{-2} at 640 nm excitation light. A Kodak Wratten filter 70 was used to eliminate the 640 nm excitation light as described¹⁵.

Fluorescence Measurements in Nude Mice Xenografts

Twenty four hours after intravenous injection of 100 µg of ^{125}I -(indocyanin)₂ MAb E48 conjugate, the mice were sacrificed and the excised tumor, skin and muscle were analyzed by light induced fluorescence (LIF) using a previously described experimental set-up for endoscopic measurements¹⁶. Fluorescence excitation was performed at 633 nm and the induced fluorescence was detected at 667 nm. The fluorescence spectra thus obtained were displayed by an optical multichannel analyser (OMA) and were processed by a computer. The weak background signal due to the tissue autofluorescence was determined by measuring the fluorescence of A431 tumor bearing mice which had not been injected and was subtracted. The fluorescence intensity was expressed in relative arbitrary units and calibrated using a fluorescence standard. We also tried to perform sequential tumor fluorescence measurements *in vivo* at different time intervals during the 24 hrs before the sacrifice of mice. These measurements were performed through the skin of the mice which covered the human tumor xenografts and the normal organs. The fluorescence signals in different organs, however, cannot be directly compared because of their different optical properties (absorption and scattering).

The % ID of radioactivity per g tissues obtained after the sacrifice of mice at the corresponding time intervals were compared with the direct measurements of the fluorescence intensity obtained *in vivo* at 667 nm.

Patients and Antibody Perfusion

A series of five patients with known primary SSC carcinoma and one patient with known primary carcinoma of the colon were investigated. Each patient gave informed consent before inclusion in the study. Table 4 shows the clinical features of each patient and the amounts of each type of antibody-indocyanin conjugates injected. Patients had their thyroid blocked by Lugol's 5% (vol/vol) iodine solution, and they received an antihistaminic drug and prednisolone 30 min before the slow i.v. injection of the antibody conjugate, as described^{14,30}. Patients 1, 2, 3, 5 and 6 received in the same perfusion 1 mg of the same MAb

not conjugated with indocyanin and labeled with 0.2 mCi of ^{131}I . Patient 5 received ^{131}I E48 MAb used as comparison with ^{125}I -LOVO D1-MAb (indocyanin)₂ conjugate.

Immunophotodetection of Tumors and Radioactivity Counting in Patients

Surgery was performed on the six patients 24 or 48 hrs after injection. The resected tumor and normal tissues were analyzed *ex vivo* for fluorescence as described for nude mice bearing human SCC or T380 colon carcinoma. Radioactivity measurements were performed on samples from different parts of the surgically resected tumor and from the dissected adjacent normal tissues. Each tumor and normal tissue sample was weighed, the specific radioactivity of ^{125}I and of ^{131}I was determined in a dual channel scintillation counter³¹. Results were expressed as % ID of radioactivity per g of tissue¹⁴ and the tumor to normal tissue ratios were calculated by dividing % ID per g of tumor by that of the different adjacent normal tissues.

RESULTS

In Vitro Characterization of Indocyanin-Monoclonal Antibody Conjugates

Indocyanin was solubilized in pure dimethylformamide and incubated at room temperature with MAb E48 previously labeled with trace amounts of ^{125}I . After the coupling reaction, the conjugate preparation contained no detectable MAb aggregates as determined by Sephadex-G200 gel filtration. The eluted conjugate gave a single peak of radioactivity at a retention volume identical to that of the IgG peak of the human serum, which was in complete correlation with the absorbance peak of indocyanin at 652 nm (Fig. 1). The same procedure was used for the anti-CEA MAbs (35 and X4) and the LOVO-D1 MAb.

To test the stability of the indocyanin conjugates, a sample of the ^{125}I -indocyanin mouse anti-SCC MAb E48 was incubated in normal human serum at 37°C during 24 hrs.

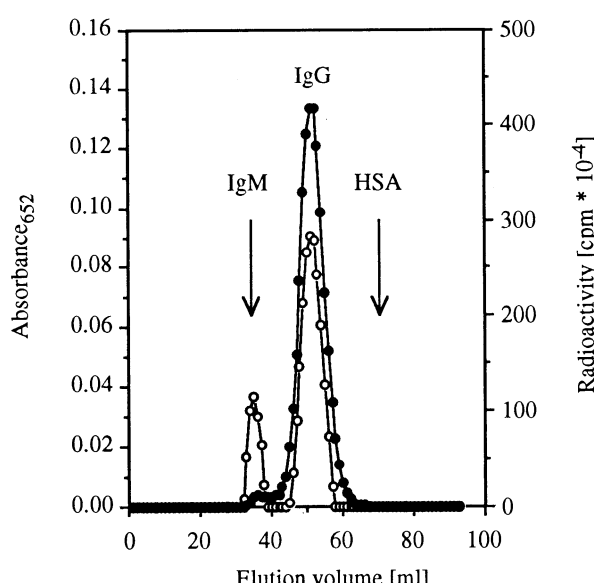


Figure 2. Elution profile on Sephadex G200 column of the ^{125}I -(indocyanin)₂ MAb E48 conjugate after a 24 hrs incubation in human mouse serum at 37°C, demonstrating the *in vitro* stability of the E48 anti-SCC MAb-indocyanin conjugate. ^{125}I -radioactivity (•••) and absorbance (○○○) at 652 nm are expressed in arbitrary units. The arrows indicate the three peaks of the human serum: IgM, IgG and human serum albumin (HSA).

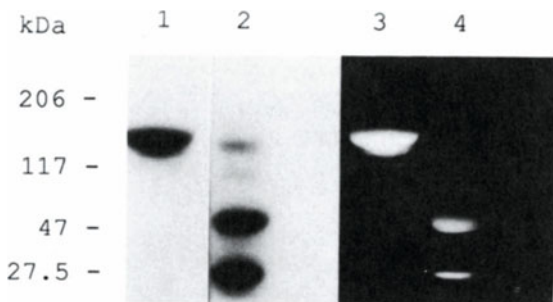


Figure 3. SDS-PAGE analysis of ^{125}I -(indocyanin)₂ MAb E48 conjugate. Lane 1 and 2: detection by autoradiography of indocyanin- ^{125}I -MAb E48 conjugate under non-reducing and reducing conditions; lanes 3 and 4: detection by laser induced fluorescence of the same conjugate under non-reducing and reducing conditions.

Subsequent filtration of the conjugate on Sephadex-G200 showed a major peak of absorption at 652 nm correlating with the radioactivity and with the elution of the IgG peak from human serum (Fig. 2). An additional peak of fluorescence eluted at the exclusion of the column suggests the formation of a small percentage of aggregate during the 24 hr incubation at 37°C.

An additional analysis of the conjugate on 7.5% SDS-PAGE was performed to test the stability of the indocyanin conjugates and to rule out non-covalent binding of the dye to the MAbs. Fig. 3 shows that under non-reducing conditions, a single band of about 150 kDa were detected after autoradiography (lane 1) and laser induced fluorescence after excitation at 640 nm (lane 3). Under reducing conditions, as expected, the molecule dissociated into H and L chain monomers, with molecular weights of about 50 and 25 KDa respectively, and the two bands detected by autoradiography (lane 2) were in complete correlation with those obtained by laser induced fluorescence (lane 4), demonstrating that the dye was covalently linked to both heavy and light chains of the MAb.

Table 1 shows that the percentages of binding of the indocyanin MAb 35 conjugates to CEA-Sepharose were high, ranging from 78.7 to 92.3 % for indocyanin MAb molar ratios ranging from 1 to 10. With 10 indocyanin per MAb, the binding to CEA showed only a moderate decrease to 78.7 % and the non-specific binding on an irrelevant protein coupled to Sepharose slightly increased to 1.4 %. Percentages of binding of the ^{125}I -E48 MAb (indocyanin)₂ conjugate to A431 SCC line were almost as high as those obtained¹⁵ with the unconjugated E48 MAb.

***In Vivo* Tumor Localization and Biodistribution of ^{125}I -Indocyanin Conjugates**

The influence of increasing indocyanin/MAb molar ratios on the *in vivo* properties of the conjugate was tested in nude mice bearing CEA-producing human colon carcinoma xenografts. The results in Table 2 shows that with a indocyanin/MAb ratio of 2 (or less), the

Table 1. *In vitro* binding activity of Indocyanin-MAb 35 conjugates

Indocyanin/MAb molar ratio	% binding to CEA	% nonspecific binding
0	91.0	1.0
1	92.3	0.6
2	90.3	1.0
5	85.8	1.2
10	78.7	1.4

Table 2. Influence of indocyanin to MAb 35 molar ratio on *in vivo* biological half-life and tumor localization of the conjugates

Indocyanin/MAb molar ratio	% ID/g tumor	% ID recovered*
0	37.1	77.2
1	37.6	75.6
2	36.7	73.8
3	28.5	51.5
5	15.9	35.4

*Whole mouse radioactivity including tumor

Results were obtained with mice dissected 24 hrs after the I.V. injection of 20 µg of conjugate

% ID of the conjugate localized per gram of tumor was optimal, i.e. not significantly different from unconjugated MAb. For greater molar ratios, the tumor localization as well as the whole body biological half-life markedly decreased. For all these experiments, the conjugates were trace labeled with a constant amount of ^{125}I and the results were obtained by direct radioactivity measurements of the dissected tumor and normal tissues. Similar results were obtained with ^{125}I -MAb E48 indocyanin conjugates in nude mice bearing human SCC A431 xenografts¹⁵.

The ^{125}I -(indocyanin)₂ MAb E48 conjugate was selected for a more extensive kinetic study of tumor localization and biodistribution. Groups of four and three mice bearing the SCC A431 xenografts were given injections i.v. of 20 µg of the ^{125}I -(indocyanin)₂ MAb E48 conjugate. At different time intervals after injection (6, 12, 24, 48 and 96 hrs) the % ID per gram of tumor, liver, kidneys, lung, spleen, muscle, skin, carcass and blood were determined by radioactivity measurement as described¹⁵. In addition, laser-induced tumor fluorescence analysis was performed *in vivo* at different time intervals directly through the skin to determine if there was a good correlation between this direct fluorescence analysis and the radioactivity measurements. Table 3 shows that the increasing fluorescence intensities directly detected from the tumor without removing skin at 6, 12 and 24 hrs post injection, corresponded to the increasing tumor concentrations of the ^{125}I -(indocyanin)₂ MAb E48 conjugate and that they already reached a plateau at 12 hrs post-injection.

At 24 hrs post injection of either ^{125}I -(indocyanin)₂ MAb E48 or irrelevant ^{125}I -(indocyanin)₂ PX conjugate, the mice were sacrificed and the % ID per gram tissue of both conjugates were compared with the direct measurement of the fluorescence intensity of each dissected organ, namely tumor, skin and muscle. Figure 4 shows that the recorded fluores-

Table 3. *In vivo* kinetics of the biodistribution of ^{125}I -(indocyanin)₂ MAb E48 conjugate in tumor, muscle and/or skin 24 hrs after the injection

Dissection	Observed fluorescence intensity ¹ (A.U.)		% ID/g tissue of the conjugate ²		
	Tumor (and skin)	Muscle (and skin)	Tumor	Muscle	Skin
6	50.00±8.40	18.67±1.87	11.99±1.32	0.62±0.14	2.62±0.24
12	74.70±7.16	24.40±3.33	14.81±1.02	0.73±0.09	3.48±0.33
24	74.70±7.67	25.33±1.60	15.54±2.35	0.79±0.13	3.93±0.07

¹Direct fluorescence measurements performed through the mouse skin were measured at 667 nm after excitation at 633 nm. Background fluorescence, determined by analyzing organs from A431 tumor bearing mice, which did not receive any conjugate, was subtracted.

²The concentration of radioactivity expressed in % ID/g tissue was determined by radioactivity measurement in a dual channel scintillation counter.

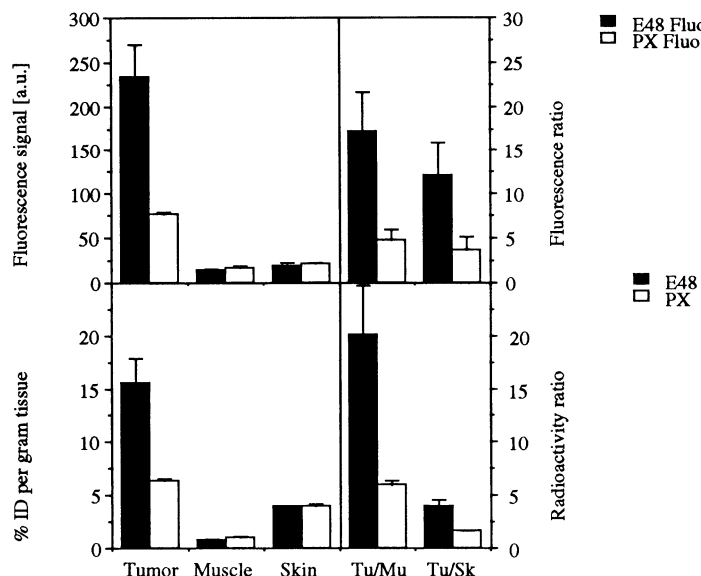


Figure 4. Comparison of the direct fluorescence measurements (upper panel) and the radioactivity counting (lower panel) of the *in vivo* tumor localization and distribution in muscle and skin of the ^{125}I -(indocyanin)₂ MAb E48 conjugate 24 hrs after intravenous injection in nude mice bearing a subcutaneous xenograft of the human SCC A431. The fluorescence was measured on dissected tumor, muscle and skin as described in Methods. The % ID per gram tissue was determined by measurement of radioactivity. ^{125}I radioactivity and fluorescence at 667 nm after excitation at 633 nm are expressed in arbitrary units.

cence signals were much higher in the tumor than in the normal organs studied, for the MAb E48 indocyanin conjugates, as also demonstrated with the radioactivity. However, there was also an increased fluorescent signal in the tumor for non-specific IgG-Px indocyanin conjugate, also confirmed by radioactivity counting. These results suggest that part of the conjugate localization of the antibody conjugate in the tumor is due to its better vascularization. The specificity of the tumor localization of the antibody is still clearly demonstrated by the tumor to muscle ratios which reach 17 and 20 in the fluorescence and radioactivity measurements respectively, as compared with values of only 4.6 and 6.2 for similar ratios observed with non-specific conjugate.

Figure 5 illustrates the photodetection of a 250 mg human colon carcinoma in its original position on the left flank of a mouse without removing skin. The mouse was killed 24 hrs after intravenous injection of 100 μg of ^{125}I -(indocyanin)₂ MAb 35 conjugate, corresponding to only 1 μg of indocyanin coupled to MAb. An intense red fluorescence from the indocyanin-MAb conjugate specifically localized in the tumor could be observed after laser irradiation at 640 nm, using Kodak Wratten filter 70 for cutting the excitation light.

Immunophotodetection of SCC and Colon Carcinomas in Patients

None of the six patients injected with the immunoconjugates (Table 4) showed any adverse effect during or after the injection. Photodetection was performed *ex vivo* on surgically resected tissues.

Immediately after surgery, the resected tumors and adjacent normal tissues were homogenously irradiated with a laser light at 640 nm. For the first 5 patients with SCC, there



Figure 5. Photograph showing the detection of fluorescence emitted by a human colon carcinoma xenograft T380 in a nude mouse which received an intravenous injection of 100 µg of ^{125}I -anti-CEA (indocyanin)₂ MAb 35 conjugate representing only 1 µg of indocyanin 24 hrs earlier. A homogenous laser irradiation was performed at 640 nm within a 13 cm diameter. The photograph was taken through a Wratten filter 70 in order to cut the irradiation light.

was no need of further dissection of the resected tumor, whereas for the patient with colon carcinoma, the resected colon segment was opened by longitudinal incision before laser irradiation. In patients with SCC, who were injected either with the indocyanin E 48 MAb conjugate (patients 1 to 4) or with the indocyanin LOVO-D1 MAb conjugate (patient 5), visual examination, through the cut-off filter that eliminates the reflected excitation light, showed a red fluorescence of the entire resected pieces which didn't allow one to differentiate the tumor from normal adjacent mucosa. In contrast, the colon carcinoma from the 6th patient, who had received an i.v. injection of the chimeric anti-CEA indocyanin MAb conjugate (X4), showed, by visual examination through the filter, a strong red fluorescence limited to the tumor with almost no detectable fluorescence on the normal bowel mucosa. Fig. 6 shows a color photograph of the tumor and adjacent normal tissue from this last patient, on the left during illumination by normal light (Fig. 6 A), and on the right during laser irradiation (Fig. 6 B).

Table 4. Clinical features and description of antibody-indocyanin conjugates for 6 patients studied

Patient			Primary tumor	Tumor's stage	Type of MAb	Indocyanin to MAb molar ratio	Amounts injected (mg)	Injected indocyanin (µg)
N°	Age	Sex						
1	34	M	Mouth	T2NB	E48	1.6	6.0	48
2	47	M	Tongue	T2NO	E48	1.8	6.0	56
3	60	M	Larynx	T3NO	E48	1.6	6.5	52
4	70	M	Larynx	T2N2C	E48	3.5	8.2	144
5	52	M	Larynx	T2NB	LOVO.D1	3.3	8.2	158
6	59	F	Recto-sigmoid	B	X4	2.3	7.7	89

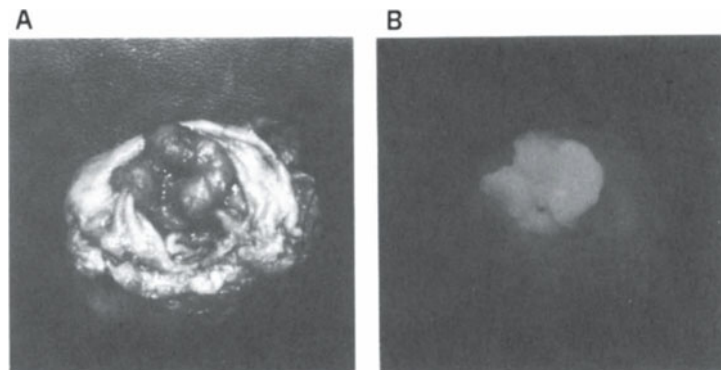


Figure 6. Laser-induced fluorescence in the resected sigmoid large-bowel carcinoma from patient 6 who received an i.v. injection of 7.7 mg of the chimeric anti-CEA indocyanin MAb conjugate containing about 90 µg of indocyanin 48 hrs before surgery. (A) Tumor and adjacent normal bowel mucosa illuminated with normal light, (B) the same tumor and normal tissue after homogenous laser excitation at 640 nm, photographed through a filter cutting only the exciting light. The red fluorescence is homogenously distributed in the tumor tissue and almost undetectable in adjacent normal bowel mucosa. Size of the tumor was about 3.0 cm in the largest diameter.

¹²⁵I-Labeled Mab Conjugate and ¹³¹I-Labeled Unsubstituted MAb Concentrations in Resected Tumor and Normal Tissues from Patients

To confirm the photodetection results and give a more precise quantitative evaluation of the tumor localization of the trace radiolabeled MAbs conjugates, the percentages of injected dose of ¹²⁵I-labeled MAbs indocyanin conjugates and those of ¹³¹I-unconjugated MAbs, simultaneously injected in all 6 patients were determined on several tumor biopsy specimens and adjacent normal tissues by differential radioactivity counting.

Figure 7 presents the results of the calculated percentage of injected dose in the different tumor fragments and normal tissues, as well as the ratios of radioactivity concentration between tumor and normal mucosa for the different indocyanin conjugates used. The results showed that both E48 or LOVO-D1 MAb indocyanin conjugates gave low tumor to normal mucosa ratios (0.7 to 2.2) in agreement with the negative immunophotodetection obtained in SSC. In contrast the chimeric anti-CEA MAb-indocyanin conjugate injected in the patient with sigmoid carcinoma gave a tumor to normal mucosa ratio of 3.8 in agreement with the well detectable red fluorescence selectively localized in the tumor.

DISCUSSION

The concept of using photoactive dyes coupled to antibodies for photodiagnosis or therapy of cancer has been proposed by several groups. Most of the reported dye-antibody conjugates, however, remained at the stage of *in vitro* testing^{7,8,9,10,11} or in the few instances in which they were injected into tumor bearing animals for the purpose of phototherapy, the results were very poor and there was no *in vivo* biodistribution or tumor localization results⁶. One reason for the absence of biokinetic results from *in vivo* studies of dye-antibody conjugates is that the most commonly used photoactive dyes, such as hemato- or benzo-porphyrins and chlorins have hydrophobic properties which may have been responsible for their weak intrinsic tumor localizing properties. However, when these hydrophobic molecules

were coupled to antibodies, either directly or even through dextran polymer, polypeptide or polyvinyl alcohol intermediates^{6,7,8,10,11}, the solubility and consequently the circulating half-life of the antibodies may have been drastically reduced, precluding satisfactory tumor localization.

Conceptually, the advantage of the use of antibody as vector for tumor localization is that one can select entirely new photoactive dyes primarily on the basis of their photochemical properties independently of their alleged weak tumor localizing properties. In addition, our experience showed that more satisfactory *in vivo* results are obtained when hydrophilic dyes are coupled to antibodies^{13,14,15}.

It may appear surprising that fluorescent probes coupled to antibodies which have been among the most commonly used immunological reagents *in vitro* for identification of antigen on tissue sections and on cell surface, particularly for flow cytofluorimetry and cell sorting, have never been used for tumor diagnosis *in vivo*. Although fluoresceinated anti-CEA antibodies have been sprayed directly on resected stomach tissue to detect carcinoma cells¹², no study of *in vivo* tumor localization of i.v. injected fluoresceinated MAb was done.

We have first shown in nude mice, that murine anti-CEA MAb substituted with as many as 10 fluorescein isothiocyanate molecules could localize efficiently in human colon carcinoma xenografts and that their *in vivo* half-life was only reduced by 50 % as compared with the same unconjugated ¹²⁵I-labeled anti-CEA MAb¹³. This experience was confirmed in a small series of colorectal carcinoma patients, in which an intravenously injected

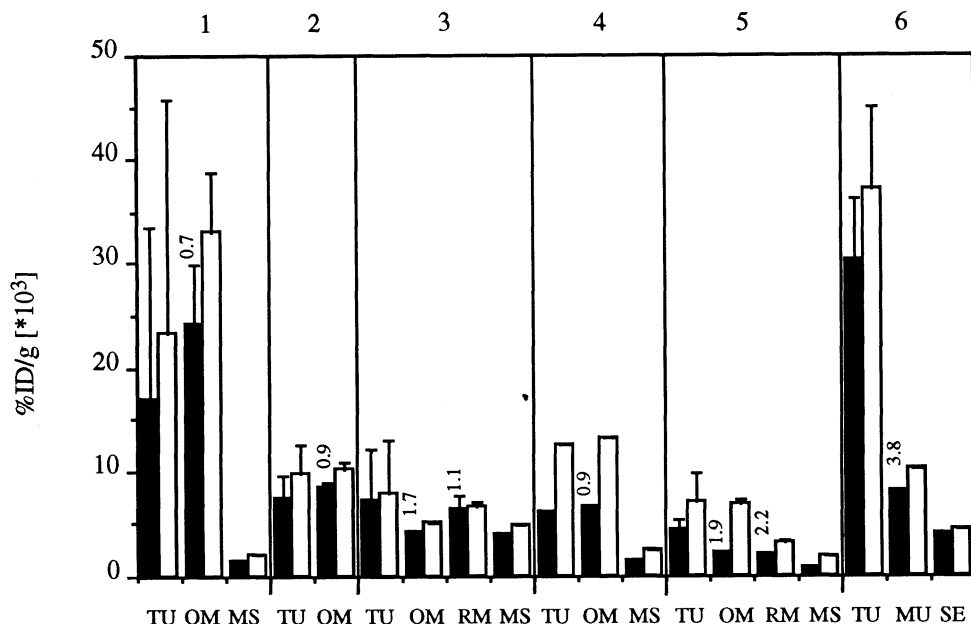


Figure 7. Percentage of injected dose per g (10^3) of tumor and adjacent normal tissues measured and calculated for the different indocyanin-conjugated (dark bars) and unconjugated (open bars) MAbs 48 hrs after injection in all 6 patients presented. All patients received a simultaneous i.v. injection of ^{125}I MAb-indocyanin conjugate and an ^{131}I -unsubstituted E48. For patients 1-4, the antibody-indocyanin conjugate was MAb E48, for patient 5, it was LOVO-D1 and for patient 6, the chimeric anti-CEA X4 was used conjugated to indocyanin or unsubstituted. The numbers over the black columns represent the tumor to normal tissue ratios of the immunoconjugate for the adjacent normal mucosa. TU, tumor; MS, muscle; OM, oral mucosa; RM, respiratory mucosa; MU, mucosa; SE, serosa.

mouse-human chimeric anti-CEA MAb, also substituted with 10 to 14 fluorescein isothiocyanate molecules, was shown to localize in tumors with a high degree of specificity¹⁴.

Although the fluorescein-MAb conjugates appeared to have many advantages for *in vivo* tumor detection, in terms of circulating half-life and the high absorption coefficient and fluorescent quantum yield of fluorescein, the excitation and emission wavelengths of fluorescein at 488 nm and 515 nm respectively, were found to be too low for efficient tissue penetration and the laser excitation at this wavelength gave a too high tissue autofluorescence, which could interfere with optimal immunophotodiagnosis^{13,14}.

In order to optimize immunophotodetection, we introduced into this field a new dye, indocyanin, which has higher excitation and emission wavelengths of 652 nm and 667 nm, respectively. This dye was coupled to either anti-CEA MAb 35 or anti-SCC MAb E48¹⁵ and the excellent immunoreactivity and stability of the conjugates were demonstrated *in vitro*. After *in vitro* characterization, the newly prepared indocyanin-MAbs conjugates were tested *in vivo* in nude mice bearing either the CEA-producing human colon carcinoma T380 or the human SCC A431 xenografts. The comparison of the *in vitro* immunoreactivity data and the *in vivo* tumor localization results (Tables 1 and 2) clearly illustrates that in this field, it is not possible to predict *in vivo* results from those obtained *in vitro*. For instance, the indocyanin-anti-CEA MAb conjugate with a molar ratio of 5, which showed 85.8 % binding to immobilized CEA, gave less than half % ID per g in the tumor, as compared to the unsubstituted MAb, whereas the conjugate with an indocyanin-MAb molar ratio of 2, with a very similar binding to CEA gave almost as good tumor localization as the unsubstitute MAb. This demonstrates the importance of *in vivo* evaluation of new conjugates, which should take place at a relatively early stage in the development of such compounds. Indeed, it does not appear rational to construct highly sophisticated conjugates for any form of *in vivo* detection or therapy without verifying that their biodistribution is compatible with satisfactory tumor localization.

Comparison of direct light induced fluorescence (LIF) measurements with precise counting of the radioactivity linked to the immunoconjugates in the different tissues from injected mice gave interesting information. At the clinical level for the precise planning of phototherapy, an efficient, minimally invasive and non-destructive method is needed for pharmacokinetic measurements. LIF appears to meet these requirements and could also be used in animal pharmacokinetic studies to reduce the number of animals sacrificed to obtain a kinetic measurement. Two types of fluorescence measurements have been performed in this study: a) *ex vivo* contact measurements on the various dissected organs, b) *in vivo* "through the skin" measurements of the site of interest. Fluorescence measurements performed *ex vivo* directly on the organs of interest show a good correlation with radioactivity measurements (Fig. 4). This is true for the tumor and the muscle. In the case of the skin, the obtained LIF signals are about twice as small as they should be according to radioactivity measurements, leading to two times higher tumor/skin fluorescence ratio. This is probably due to the small thickness of the skin as compared to the more bulky tumor and muscle. This implies that when a small volume of tumor or normal tissue is excited with penetrating red light, one should expect a smaller amount of fluorescence than that obtained with a larger volume of tissue. Thus, we should take this into account when comparing tumor and normal tissue by LIF in patients. The results obtained with the "through skin" LIF measurements performed *in vivo* (Table 3) show that it is possible to obtain some useful qualitative information in this way. For instance, the maximum of concentration of MAb E48 conjugate in the tumor was determined. However, such information can be obtained only if the LIF signal of the organ under measurement is several times higher than that of the overlaying skin. From these two animal experiments one can conclude that fluorescence pharmacokinetics are efficient for superficial directly accessible tumors¹⁷, which can be directly probed,

but of lower interest for subcutaneously implanted tumor, due to the screening effect of the skin.

The major finding of the experimental tumor immunophotodetection data presented here is that the conjugate with an indocyanin MAb molar ratio of only 2 was more efficient in tumor detection than a fluorescein MAb conjugate with a molar ratio of 6¹⁵. This improvement is most likely due to the higher excitation and emission wavelengths of indocyanin, allowing a better penetration of the excitation light and the emission signal through the tissue. This is clearly illustrated by the fact that the indocyanin-MAb conjugate was detectable in the tumor through the mouse skin (Fig. 5), while without removal of the skin the fluorescein-MAb signal was not detectable^{13,15}. The second important information gained from the *in vivo* use of this new dye coupled to MAbs is that the laser excitation at 640 nm gave almost no non-specific tissue autofluorescence, while it induced a specific fluorescence emission at 667 nm by the indocyanin conjugate localized in the tumor by the MAb¹⁵.

The preliminary clinical results presented here show that when using the chimeric mouse human anti-CEA MAb coupled to two molecules of indocyanin, the advantage of this new conjugate demonstrated in nude mice could be reproduced in a first colon carcinoma patient by the elegant *ex vivo* immunophotodetection of the tumor. For the SCC patients, however, despite the excellent results obtained in nude mice grafted with the human SCC A431¹⁵, the E48 MAb-indocyanin conjugate did not give sufficient tumor to normal tissue ratios in the clinical condition to allow any satisfactory immunophotodetection.

As shown in Figure 7, the SCC tumor to normal adjacent mucosa ratios and the % ID/g tumor obtained in patients injected with either the indocyanin E48 MAb conjugate or LOVO-D1 conjugate were very low. In contrast, in the first patient tested with colon carcinoma, the tumor to normal mucosa ratio and the % ID/g of tumor were higher and definitively sufficient to visualize a well contrasted tumor image of red fluorescence, 48 hrs after intravenous injection of 7.7 mg of the mouse chimeric MAb conjugated to only 0.09 mg indocyanin (Fig. 6 B). The red signal was homogenously distributed through the tumor and a very precise delineation between the tumor and the normal adjacent tissue was observed. The more homogenous distribution of the indocyanin emission light in this tumor, as compared to the heterogenous signal observed in a tumor from a patient injected with the same chimeric MAb coupled to fluorescein¹⁴, is likely to be due to the higher excitation and emission wavelengths of indocyanin which allowed a better penetration of the laser light and the emission signal through the tissue. Thus, an increased number of dye molecules localized more deeply into the tumor could be excited and could transmit their signal, resulting in an overall amplification of the fluorescence intensity detectable in the tumors. In addition, with the use of this new immunoconjugate, almost no non-specific tissue autofluorescence was observed in normal mucosa adjacent to the tumor during the laser light excitation.

Our extensive experimental data on immunophotodetection^{13,14,15}, as well as these first very encouraging clinical results with anti-CEA MAb-indocyanin conjugates, which extend our previous clinical results of anti-CEA-fluorescein conjugates¹⁴, open the way to a new form of clinical immunophotodiagnosis and possibly to the development of a more specific approach to the phototherapy of early carcinomas.

ACKNOWLEDGMENTS

This work has been supported by the CHUV-UNIL-EPFL Fund, the Swiss National Priority Program in Optics and the Swiss National Foundation for Scientific Research, Grant 3229857.90. The authors are grateful to Françoise Flejszman for editorial assistance.

REFERENCES

1. J.H. Kinsey and D.A. Cortese, Endoscopic system for simultaneous visual examination and electronic detection of fluorescence, *Rev Sci Instrum.* 51:1403 (1980).
2. A.E. Profio, O.J. Balchum, and F. Carstens, Digital background subtraction for fluorescence imaging, *Med Phys.* 13:717 (1986).
3. A.E. Profio, Fluorescence diagnosis and dosimetry using porphyrins, in: "Photodynamic therapy of neoplastic disease", D. Kessel, ed., CRC Press Inc., Boca Raton, Florida p. 77 (1990).
4. H. Kato, T. Imaizumi, K. Aizawa, H. Iwabuchi, H. Yamamoto, N. Ikeda, T. Tsuchida, Y. Tamachi, T. Ito, and Y. Hayata, Photodynamic diagnosis in respiratory tract malignancy using an excimer dye laser system, *J Photochem Photobiol B.* 6:189 (1990).
5. G. Wagnières, D. Braichotte, A. Châtelain, Ch. Depersinge, Ph. Monnier, M. Savary, Ch. Fontollet, J.-M. Calmes, J.-C. Givel, G. Chapuis, S. Folli, A. Pèlegrin, F. Buchegger, J.-P. Mach, and H. van den Bergh, Photodetection of early cancer in the upper aerodigestive tract and the bronchi using Photofrin II and colorectal adenocarcinoma with fluoresceinated monoclonal antibodies, *Proc Soc Photo Opt Inst.* 1525:219 (1991).
6. D. Mew, C.K. Wat, G.H.N. Towers, and J.G. Levy, Photoimmunotherapy : treatment of animal tumors with tumor-specific monoclonal antibody-hematoporphyrin conjugates, *J Immunol.* 130:1473 (1983).
7. D. Mew, V. Lum, C.K. Wat, G.H.N. Towers, C.H.C. Sun, R.J. Walter, W. Wright, M.W. Berns, and J.G. Levy, Ability of specific monoclonal antibodies and conventional antisera conjugated to hematoporphyrin to label and kill selected cell lines subsequent to light activation, *Cancer Res.* 45:4380 (1985).
8. A.R. Oseroff, D. Ohuoha, T. Hasan, J.C. Bommer, and M.L. Yarmush, Antibody-targeted photolysis : selective photodestruction of human T-cell leukemia cells using monoclonal antibody-chlorin E6 conjugates, *Proc Natl Acad Sci USA* 83:8744 (1986).
9. A.R. Oseroff, G. Ara, D. Ohuoha, J. Aprille, J.C. Bommer, M.L. Yarmush, J. Foley, and L. Cincotta, Strategies for selective cancer photochemotherapy: antibody-targeted and selective carcinoma cell photolysis, *Photochem Photobiol.* 46:83 (1987).
10. T. Hasan, C.W. Lin, and A. Lin, Laser-induced selective cytotoxicity using monoclonal antibody-chromophore conjugates, *Progress in Clin Biol Res.* 288:471 (1989).
11. F.N. Jiang, D.J. Liu, H. Neyendorff, M. Chester, S.Y. Jiang, and J.G. Levy, Photodynamic killing of human squamous cell carcinoma cells using a monoclonal antibody-photosensitizer conjugate, *J Natl Cancer Inst.* 83:1218 (1991).
12. M. Tatsuta, H. Lishi, M. Ichii, M. Baba, R. Yamamoto, S. Okuda, and K. Kikuchi, Diagnosis of gastric cancers with fluorescein-labeled monoclonal antibodies to carcinoembryonic antigen, *Lasers Surg Med.* 9:422 (1989).
13. A. Pèlegrin, S. Folli, F. Buchegger, J.-P. Mach, G. Wagnières, and H. van den Bergh, Antibody-fluorescein conjugates for photoimmunodiagnosis of human colon carcinoma in nude mice, *Cancer* 67:2529 (1991).
14. S. Folli, G. Wagnières, A. Pèlegrin, J.-M. Calmes, D. Braichotte, F. Buchegger, Y. Chalandon, N. Hardman, Ch. Heusser, J.-C. Givel, G. Chapuis, A. Chatelain, H. van den Bergh, and J.-P. Mach, Immunophotodiagnosis of colon carcinomas in patients injected with fluoresceinated chimeric antibodies against carcinoembryonic antigen, *Proc Natl Acad Sci USA* 89:7973 (1992).
15. S. Folli, P. Westermann, D. Braichotte, A. Pèlegrin, G. Wagnières, H. van den Bergh, and J.-P. Mach, Antibody-indocyanin conjugates for immunophotodetection of human squamous cell carcinoma in nude mice, *Cancer Res.* 54:2643 (1994).
16. D. Braichotte, R. Bays, G. Wagnières, A. Châtelain, C.K. Burckhardt, and H. van den Bergh, Photofrin II pharmacokinetics and optical dosing in tissue:apparatus and clinical measurements for the pharynx, esophagus and tracheobronchial tree, in: "Photodynamic therapy: Basic principle and clinical applications", B.W. Henderson and T.J. Dougherty, eds., Dekker, New York p. 425 (1991).
17. D. Braichotte, G. Wagnières, R. Bays, Ph. Monnier, and H. van den Bergh, Clinical pharmacokinetic studies of photofrin by fluorescence spectroscopy in the oral cavity, the esophagus, and the bronchi, *Cancer* 75:2768 (1995).
18. B. Delaloye, A. Bischof Delaloye, F. Buchegger, V. von Fließner, J.-P. Grob, J.C. Volant, J. Pettavel, and J.-P. Mach, Detection of colorectal carcinoma by emission-computerized tomography after injection of ^{123}I -labeled Fab or $\text{F}(\text{ab}')_2$ fragments from monoclonal anti-carcinoembryonic antigen antibodies, *J Clin Invest.* 77:301 (1986).
19. A. Bischof Delaloye, B. Delaloye, F. Buchegger, A. Pèlegrin, C. Heusser, N. Hardman, and J.-P. Mach, Prospective immunoscintigraphy (IS) with chimeric ^{123}I -anti-CEA MAb in patients with raising serum-CEA, *J Nucl Med.* 32:941-Abstract (1991).

20. J.J. Quak, F.J. Balm, J.G. Brakkee, R.J. Schepers, C.J. Meijer, and G.B. Snow, Production of monoclonal antibodies to squamous cell carcinoma antigens, *Arch. Otolaryngol. Head. Neck. Surg.* 116:181 (1990).
21. Ch. Girardet, A. Vacca, A. Schmidt-Kessen, M. Schreyer, S. Carrel, and J.-P. Mach, Immunochemical characterization of two antigens recognized by new monoclonal antibodies against human colon carcinoma, *J. Immunol.* 136:1497 (1986).
22. M. Herlyn, Z. Steplewski, D. Herlyn, and H. Koprowski, Colorectal carcinoma-specific antigen: detection by means of monoclonal antibodies, *Proc Natl Acad Sci USA* 76:1438 (1979).
23. G. Kohler, S.C. Howe, and C. Milstein, Fusion between immunoglobulin-secreting and non-secreting myeloma cell lines, *Eur J Immunol.* 6:292 (1976).
24. K.W. Martin, and S.E. Halpern, Carcinoembryonic antigen production, secretion and kinetics in BALB/c mice and a nude mouse-human tumor model, *Cancer Res.* 44:5475 (1984).
25. J.-P. Mach, S. Carrel, C. Merenda, B. Sordat, and J.C. Cerottini, *In vivo* localization of radiolabelled antibodies to carcinoembryonic antigen in human colon carcinoma grafted into nude mice, *Nature* 248:704 (1974).
26. S. Folli, A. Pèlegrin, Y. Chalandon, X. Yo, F. Buchegger, F. Lejeune, and J.-P. Mach, Tumor necrosis factor can enhance radio-antibody uptake in human colon carcinoma xenografts by increasing vascular permeability, *Int J Cancer* 53:829 (1993).
27. G. van Dongen, H. Leverstein, J.C. Roos, J.J. Quak, M. van den Brekel, A. van Lingen, H. Martens, J. Castelijns, G. Visser, C. Meijer, G. Teule, and G. Snow, Radioimmunoscintigraphy of head and neck cancer using ^{99m}Tc-labeled monoclonal antibody E48 F(ab')₂, *Cancer Res.* 52:2569 (1992).
28. C.M. Haskell, F. Buchegger, M. Schreyer, S. Carrel, and J.-P. Mach, Monoclonal antibodies to carcinoembryonic antigen: ionic strength as a factor in the selection of antibodies for immunoangiography, *Cancer Res.* 43:3857 (1983).
29. F. Buchegger, A. Vacca, S. Carrel, M. Schreyer, and J.-P. Mach, Radioimmunotherapy of human colon carcinoma by ¹³¹I-labelled monoclonal anti-CEA antibodies in a nude mouse model, *Int J Cancer* 41:127 (1988).
30. A. Bischof Delaloye, B. Delaloye, F. Buchegger, W. Gilgien, A. Studer, S. Curchod, J.C. Givel, F. Mosimann, J. Pettavel, and J.-P. Mach, Clinical value of immunoangiography in colorectal carcinoma patients: a prospective study, *J Nucl Med.* 30:1646 (1989).
31. F. Buchegger, C. Pfister, K. Fournier, F. Prevel, M. Schreyer, S. Carrel, and J.-P. Mach, Ablation of human colon carcinoma in nude mice by ¹³¹I-labelled monoclonal anti-carcinoembryonic antigen antibody F(ab')₂ fragments, *J Clin Invest.* 83:1449 (1989).

THREE-DIMENSIONAL OPTICAL FUNCTIONAL IMAGING OF TISSUE WITH TWO-PHOTON EXCITATION LASER SCANNING MICROSCOPY

Barry R. Masters

Department of Anatomy and Cell Biology
Uniformed Services University of the Health Sciences
4301 Jones Bridge Road
Bethesda, Maryland 20814

1. INTRODUCTION

This chapter demonstrates the use of two-photon excitation microscopy to monitor cellular metabolism in ocular tissue. Light can be used as a noninvasive probe to monitor cellular function in cells, tissues and organs. Cellular metabolism can be noninvasively optically monitored by the technique of redox fluorometry.¹ This optical technique has been applied to the eye²⁻⁴ and quantitative analysis of the various pyridine nucleotides have been measured in individual cellular layers of the normoxic and anoxic eyes. The noninvasive optical probes are the intrinsic fluorescent pyridine nucleotides, and the flavoproteins. The pyridine nucleotides, nicotinamide adenine dinucleotide, NAD(P)H are excited in the region 365 nm and fluoresce in the region 400-500 nm. The flavoproteins are excited in the region 450 nm and fluoresce in the region 500-600 nm. Typically the fluorescence is imaged and changes in fluorescence intensity follow changes in cell oxidative metabolism. Optical sections of micron thickness can be combined to visualize the full three-dimensional image of thick tissues.

Three-dimensional metabolic imaging based on redox fluorometry has two limitations. First, there is photobleaching of the fluorescent molecules during the measurement period. Second, the short wavelengths preclude deep penetration of highly scattering tissues such as human skin. Our previous work on the cornea in which we have used redox fluorometry is due to the low light scatter of the normal cornea.⁵⁻⁹ However, further developments and applications of optical metabolic redox imaging of the ocular lens, and normal and pathological skin require longer wavelengths of light to penetrate deep into these highly scattering tissues.

Cells contain two intrinsic fluorescent probes which can be used for functional metabolic monitoring together with two-photon excitation microscopy. The fluorescent

intensity from intrinsic oxidized flavoproteins present in mitochondria of cells is a noninvasive measure of cellular respiratory function. The fluorescence from the reduced pyridine nucleotides NAD(P)H is another intrinsic probe to study cellular metabolism. The fluorescence intensity from these intrinsic probes provides a noninvasive optical method to monitor cellular respiration. The fluorescence from NAD(P)H has been used to study cellular metabolism in many tissues and organs due to the strong fluorescence intensity. The NAD(P)H fluorescence intensity occurs in two compartments, the mitochondrial and the cytosolic; this complicates the interpretation of the fluorescence studies. However, in some tissues, i.e. rat cardiac myocytes, the NAD(P)H fluorescence is predominantly from the mitochondrial space.

The main advantage of measuring the fluorescence intensity from the oxidized flavoproteins is that the fluorescence is localized in the mitochondrial space. The light absorption of oxidized flavoproteins has a broad maximum at 460 nm and extends from 430 to 500 nm. The fluorescence intensity from oxidized flavoproteins in the cornea epithelium occurs in the region from 520 nm to 590 nm with a broad maximum at 540 nm. This chapter will illustrate the use of two-photon excitation microscopy to image NAD(P)H fluorescence in ocular tissue.

The cornea is a semitransparent, avascular tissue in the anterior portion of the eye. The rabbit cornea is about 400 microns thick and is composed of several layers: the 40 micron thick epithelial layer which is directly adjacent to the tear film, the stromal portion (354 microns) or middle region of the cornea, and the endothelial cell layer (6 microns) on the posterior side of the cornea. The epithelial cell layer is itself composed of 5-6 layers of epithelial cells.

This study demonstrates that the cellular respiratory function of corneal epithelial and endothelial cells can be noninvasively optically monitored with two-photon excitation scanning microscopy.

2. METHODS

M. Göppert-Mayer¹⁰ developed the theoretical foundation for two photon excitation processes in 1931. Two-photon excitation arises from the simultaneous absorption of two photons; their combined energies result in the electronic transition to the excited state of the chromophore.

The use of a laser scanning microscope for fluorescence imaging based on two-photon excitation microscopy was first developed by Denk et al., 1990.¹¹ The principle of two-photon excitation spectroscopy is the simultaneous absorption of two photons; two photons of wavelength in the near infrared induce an electronic transition that normally requires an ultraviolet photon. The absorption process is nonlinear. The experimental verification of the two-photon absorption process is that the number of electronic transitions from the ground state to the excited states is proportional to the square of the instantaneous intensity.

The technique of 2-photon excitation laser scanning microscopy has been used to overcome the two problems cited previously; photobleaching and tissue penetration. The practical instrument consists of a laser scanning microscope that is used for scanning the laser beam and for detection of the specimen fluorescence. The typical light source is a self-mode-locked Ti: sapphire laser, which is pumped by a CW argon-ion laser. This provides light in the range 700 nm to about 1050 nm. An alternative system is a hybrid mode-locked dye laser. A Satori ultrafast dye laser is used to form 150 fsec pulses of 705 nm light at a repetition rate of 76 MHz. A series of 150-fsec pulses of 705 nm light from the Nd:YAG pumped Satori dye laser are directed into the optical path of a scanning confocal microscope

with the aperture opened up. To keep the biological samples in a viable state a pulse duty cycle of 10^{-5} keeps the average power near 10 mW which is in the range of power normally used in a laser scanning confocal microscope.

The diffraction-limited focusing of the laser beam and the temporal concentration of the 100-fsec pulses generated by the mode-locked laser result in two-photon excitation processes only in the region of focus. Outside of the focal region there is insufficient photon density, and therefore no absorption process occur. Therefore, outside of the focal region there is no signal; this is the origin of the optical sectioning. The optical sectioning is derived from the physics of the optical system and an aperture in front of the light detector is not required to obtain the optical sectioning capability of the microscope.

Prior to the development of two-photon excitation microscopy, in order to excite chromophores which absorb in the ultraviolet region, it was necessary to use ultraviolet excitation light. When ultraviolet fluorescence microscopy is used to image living cells and tissues it was observed that cell viability was compromised and that there was photobleaching of the chromophore.

The advantages of two-photon excitation microscopy are: (1) the near infrared light is less damaging to living cells and tissues, (2) there is deeper tissue penetration, and (3) photobleaching is limited to the region of focus. The 700 nm light results in deeper tissue penetration since both tissue absorption and scatter are reduced.

3. RESULTS

Two-photon excitation laser scanning microscopy was used to monitor the metabolic state of both an *ex vivo* rabbit eye and an *ex vivo* human ocular lens. These studies are based on the two-dimensional monitoring of NAD(P)H fluorescence intensity. The figures below show the applications of the methodology. The temporal changes in NAD(P)H were monitored over a two-fold change in fluorescence intensity following chemical induced cellular hypoxia.

In order to demonstrate the capability of two-photon excitation microscopy to monitor NAD(P)H fluorescence intensity in thick tissues we used an *ex vivo* rabbit eye as a biological specimen.¹² The cornea is 400 microns thick in the central region and is an almost transparent object. Two photon-excitation microscopy could obtain one micron optical sections across the full thickness of the tissue. Figures 1 and 2 illustrate the optical sections obtained in two different optical sections in the basal epithelium of the cornea. The cell nuclei appear black due to the absence of NAD(P)H fluorescence. The bright NAD(P)H fluorescence occurs in the cytoplasmic space outside of the nucleus. Both of these images are located about 50 microns below the surface of the cornea.

To demonstrate the ability of two-photon excitation microscopy to image NAD(P)H fluorescence across thick tissue we imaged the corneal endothelial cells in an intact eye. The endothelial cell layer is located 400 microns below the surface of the cornea. These cells are only four microns thick and therefore the NAD(P)H fluorescence intensity is very weak. Figure 3. illustrated the ability of two-photon excitation microscopy to image this thin cell layer across 400 microns of cornea. The dark bean shaped cell nuclei are shown in Figure 3. In order to verify that the bean shaped structures are cell nuclei they were stained for DNA with Hoechst 33342. Figure 4. shows the fluorescent image of the Hoechst stained cornea. The corneal endothelial cells appear dark except for the bright fluorescence from the bean shaped structures. Since the Hoechst dye is specific for DNA this test confirms that the bean shaped structures in Figure 3. are cell nuclei.

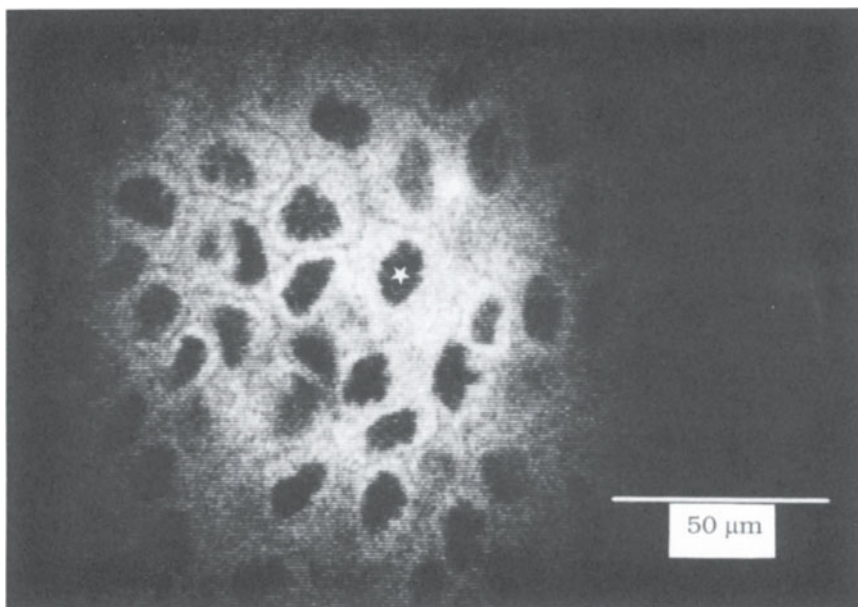


Figure 1. NAD(P)H fluorescence image showing basal epithelial cells in an *ex vivo* rabbit cornea. This image is located 50 μm below the surface of the cornea. A white star indicates the nucleus of the basal epithelial cell.

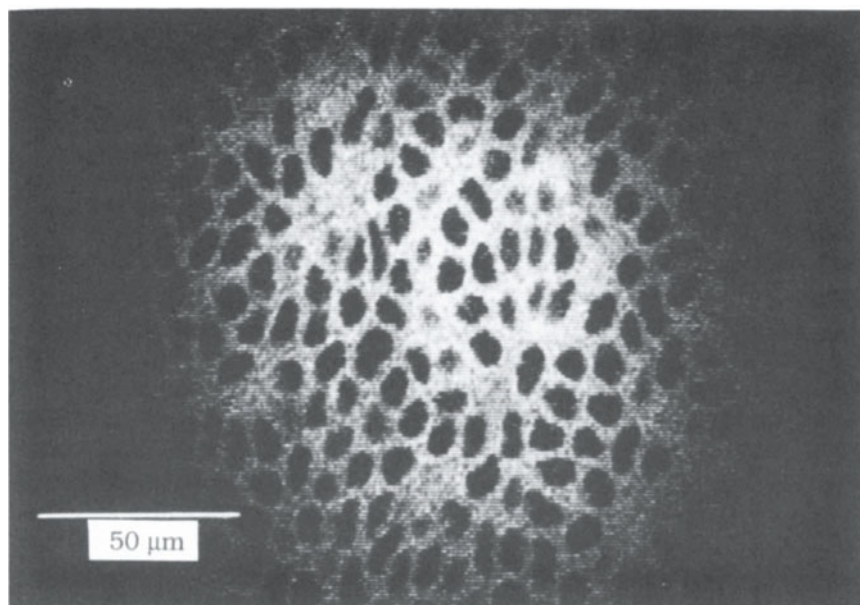


Figure 2. NAD(P)H fluorescence image showing basal epithelial cells in an *ex vivo* rabbit cornea. This image is located 55 μm below the surface of the cornea. The dark oval shapes are nuclei of basal epithelial cells.

4. DISCUSSION

These studies demonstrate the feasibility of two-photon excitation microscopy to provide three-dimensional functional imaging of ocular tissue. The images are acquired through a tissue thickness of 400 nm. The studies in this chapter illustrate the use of two-photon excitation microscopy for functional metabolic imaging based on the fluorescence of NAD(P)H.¹³ It was demonstrated that one micron optical sections could be obtained across 400 microns of ocular tissue.

Prior to the use of two-photon excitation microscopy we used a laser scanning confocal microscope to image the NAD(P)H in the basal epithelial cells of the cornea. The light source was an argon ion laser with a line in the ultraviolet. In order to obtain a three-dimensional visualization of the full thickness of the cornea we obtained one micron optical sections across the cornea. In this case there was photobleaching both in the focal plane of the microscope objective and in the double cone of light from the objective.

The use of two-photon excitation microscopy (with 700 nm excitation light) as described in this chapter shows three advantages over the use of an ultraviolet laser coupled to a confocal microscope to obtain optical sections of tissue with intrinsic functional metabolic probes such as NAD(P)H. The advantages include: photobleaching is restricted to the focal point of the microscope objective which results in diminished photobleaching when the thick tissue is optically sectioned, the near infrared light caused less phototoxicity than the ultraviolet light, and the near infrared light results in deeper tissue penetration. The last point is critical when thick, highly scattering tissues such as skin are imaged.

Further developments in progress involve the application of the methods to *in vivo* imaging of thicker and more highly scattering tissues such as normal and pathological skin. The use of flavoprotein fluorescence as a second intrinsic probe of cellular metabolism is

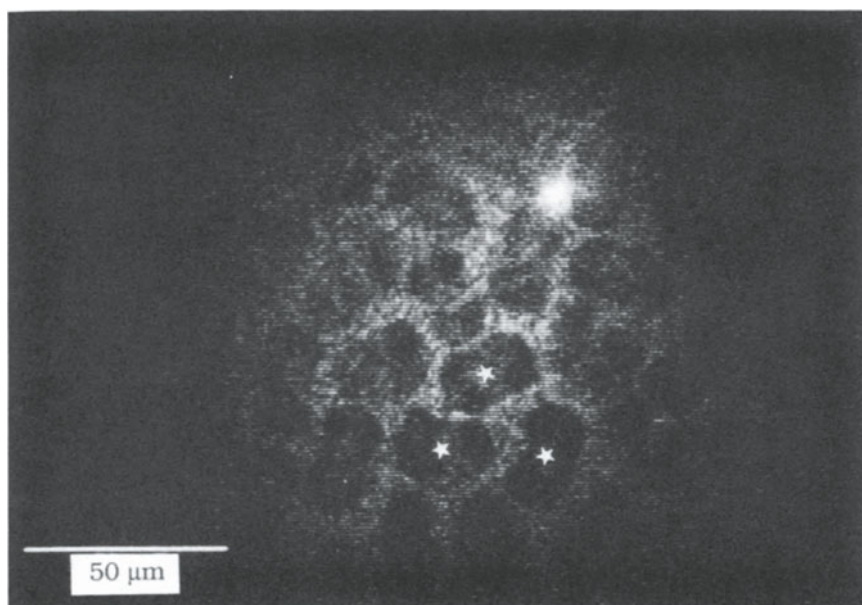


Figure 3. NAD(P)H fluorescence image showing corneal endothelial cells in an *ex vivo* rabbit eye. This image is located 400 μm below the surface of the cornea. White stars indicate the bean shaped nuclei of endothelial cells.

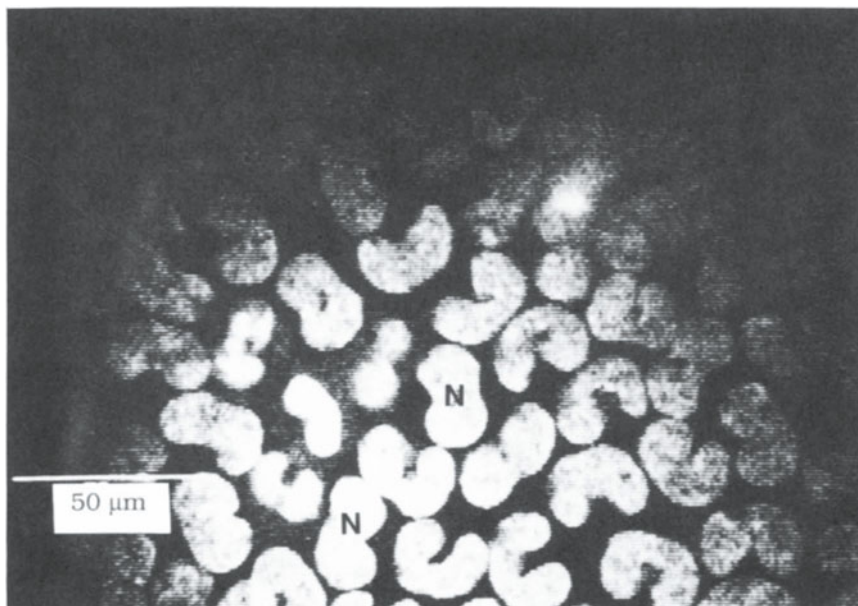


Figure 4. Fluorescence image showing corneal endothelial cell nuclei in an *ex vivo* rabbit eye. This image is located 400 μm below the surface of the cornea. The nuclei of the endothelial cells were stained with the DNA stain Hoechst-33342. The bean shaped nuclei are labeled with the letter N.

currently under investigation. Our goal is the further development of non-invasive optical methods for the diagnosis of pathology in human cells and tissues.

5. ACKNOWLEDGMENTS

This work was supported by a grant from the National Institutes of Health, National Eye Institute, EY-06958.

6. REFERENCES

1. B. Chance, and B. Thorell, Localization and kinetics of reduced pyridine nucleotide in living cells by microfluorometry. *J. Biol. Chem.* 234, 3044-3050 (1959).
2. B. R. Masters, S. Falk, B. Chance, *In vivo* flavoprotein redox measurements of rabbit corneal normoxic-anoxic transitions. *Curr. Eye Res.* 1, no. 10, 623-627 (1982).
3. B. R. Masters, M. V. Riley, J. Fischbarg, B. Chance, Pyridine nucleotides of rabbit cornea with histotoxic anoxia: chemical analysis, non-invasive fluorometry and physiological correlates. *Exp. Eye Res.* 36, 1-9 (1983).
4. B. R. Masters, A. K. Ghosh, J. Wilson, F. M. Matschinsky, Pyridine nucleotides and phosphorylation potential of rabbit corneal epithelium and endothelium. *Invest. Ophthalmol. Vis. Sci.* 30, no. 5, 861-868 (1989).
5. B. R. Masters, Effects of contact lenses on the oxygen concentration and epithelial mitochondrial redox state of rabbit cornea measured noninvasively with an optically sectioning redox fluorometer microscope, in "The Cornea: Transactions of the World Congress on the Cornea III," H.D. Cavanagh, ed., Raven Press, New York, pp. 2810-3860 (1988).

6. B. R. Masters, *In vivo* corneal redox fluorometry. "Noninvasive Diagnostic Techniques in Ophthalmology" B. R. Masters, ed., Springer-Verlag, New York, pp. 223-247 (1990).
7. B. R. Masters, A. Kriete, and J. Kukulies, Ultraviolet confocal fluorescence microscopy of the *in vitro* corneal: redox metabolic imaging. *App. Opt.* 32, 592-596 (1993).
8. B. R. Masters, Functional imaging of cells and tissues: NADP(H) and flavoprotein redox imaging. in: "Medical Optical Tomography: Functional Imaging and Monitoring," G. Müller et al. eds, SPIE Press, Bellingham, pp. 555-575 (1993).
9. B. R. Masters, , B. Chance, Redox confocal imaging: intrinsic fluorescence probes of cellular metabolism. in: "Fluorescent and Luminescent Probes for Biological Activity," W. T. Mason, ed., Academic Press, pp. 44- 57, (1993).
10. M. Göppert-Mayer, Über Elementarakte mit zwei Quantsprüngen. *Ann. Phys.* 9, 273-294 (1931).
11. W. Denk, J.H. Strickler, and W.W. Webb, Two-photon laser scanning fluorescence microscopy. *Science*, 248, 73-76 (1990).
12. D. W. Piston, B. R. Masters, W. W. Webb, Three-dimensionally resolved NAD(P)H cellular metabolic redox imaging of the *in situ* cornea with two-photon excitation laser scanning microscopy. *J. Micros.* 178, Pt. 1, 20-27 (1995).
13. W. Denk, , D. W. Piston, and W. W. Webb, Two-photon molecular excitation in laser-scanning microscopy. in: "Handbook of Biological Confocal Microscopy," J. B. Pawley, ed., Plenum Press, New York, pp. 445-458 (1995).

ESTROGEN RECEPTOR IMAGING USING INTRINSICALLY FLUORESCENT LIGANDS

Richard J. Miksicek¹ and John A. Katzenellenbogen²

¹ Department of Physiology
Michigan State University
East Lansing, Michigan 48824

² Department of Chemistry
University of Illinois
Urbana, Illinois 61801

INTRODUCTION

This article will summarize recent advances in the development of fluorescent probes that bind as ligands to the estrogen receptor (ER). While fluorescent steroid derivatives have been investigated for decades as potential probes for cytofluorometric analysis of steroid receptors, only recently has it been possible to convincingly demonstrate their utility for receptor visualization within cells by *in situ* fluorescence microscopy. We have recently shown that inherently fluorescent ligands such as the naturally occurring plant estrogen coumestrol¹ and synthetic tetrahydorchrysene (THC) estrogens² are able to visualize ER within cells in a cell culture model for ER expression. Reversibly binding fluorescent ligands have several distinct advantages compared to using chemically conjugated antibodies for the analysis of receptor expression and distribution. Notable among these are an improvement in localization of the target protein due to the small size of these probes and the fact that upon binding, they become effectively immobilized at the ligand binding site of their receptor. In contrast, analysis by immunohistochemical methods involves the deposition of a potentially diffusible chromophore in proximity to the target protein, directed by an antigen-antibody interaction on the protein surface. An increase in resolution is afforded by immunofluorescence analysis; however, this technique is still indirect since the imaging fluorochrome is coupled to either a primary or a secondary antibody rather than to the target protein under investigation.

Due to their neutral character and small size, several of the fluorescent estrogenic ligands differ also from conjugated antibodies by being freely diffusible into cells. This property permits them to be used for cytological staining without prior fixation or permeabilization of tissue specimens and enables them to be used for receptor visualization in viable cells^{1,2}. This feature, combined with the immobilization of probe that occurs upon receptor binding, creates a unique opportunity to apply anisotropy techniques such as the

measurement of fluorescence polarization towards an analysis of receptor mobility within cells. The change in solvation associated with receptor binding results in a significant increase in the intensity of fluorescence emission, accompanied by a substantial Stokes shift in the emission spectra²⁻⁴. Intrinsically fluorescent ligands of ER therefore provide excellent opportunities for the development of new applications such as the use of fluorescence video cinematography to study the dynamics of real-time motion of ER within the cell nucleus, quantitative flow cytometry to analyze the heterogeneity of ER expression within populations of ER-positive cells, and the analysis of ER expression as a function of the cell cycle. This report will focus on ER imaging techniques using epifluorescence microscopy and will discuss current limitations of this methodology. A long term goal of this work continues to be the development of new reagents, protocols, and instrumentation that may one day make fluorescence microscopy using intrinsically fluorescent ligands a reliable method for quantitatively assessing the level and heterogeneity of ER expression in tumor samples.

INTRINSICALLY FLUORESCENT LIGANDS WITH HIGH AFFINITY FOR THE ESTROGEN RECEPTOR

Several classes of compounds have been investigated over the preceding two decades for their potential to serve as fluorescent probes for the estrogen receptor. The majority of these fall into one of two categories: 1) nonfluorescent ligands (usually steroidal estrogens) that have been chemically conjugated to a well characterized fluorochrome such as fluorescein^{3,5-9} and 2) intrinsically fluorescent ligands.^{3,10-13} Fluorescent conjugates have proven largely unsatisfactory for use with ER since conjugation of the steroid nucleus with a bulky fluorochrome tends to dramatically reduce affinity of these ligands for receptor and since their fluorescence properties are largely unaffected by receptor binding. Consequently, they typically show high levels of background fluorescence due to nonspecific binding of the fluorochrome to other cellular components and due to leaching of the fluorochrome from the steroid conjugate. The fact that most of the commonly used fluorochromes such as fluorescein carry ionic charges at neutral pH also represents an undesirable feature since this reduces the membrane permeability of the corresponding steroid conjugate.

Many of the shortcomings of fluorescent steroid conjugates are circumvented by the use of intrinsically fluorescent ligands. It has proven difficult, however, to identify compounds that display strong fluorescence and still retain good binding affinity for ER. With the exception of 12-oxo-9(11)-dehydroestradiol¹⁰, most intrinsically fluorescent ligands of ER are nonsteroidal compounds. The best studied fluorescent probes from the standpoint of receptor imaging are coumestrol,^{1,3,14} a naturally occurring phytoestrogen found in many legumes¹⁵ and derivatives of 5,6,11,12-tetrahydrochrysene (THC), synthetic estrogens that were rationally designed to optimize their fluorescence properties.^{16,17} The remarkable fluorescence of these compounds compared with nonfluorescent steroidal estrogens such as 17 β -estradiol can be ascribed to charge delocalization afforded by the presence of electron donor/acceptor pairs on a highly conjugated ring system (see Figure 1).

The spectral properties of these fluorochromes have been thoroughly investigated^{16,17,18} and are briefly summarized in Table 1. Each of these probes are excited optimally by near *uv* light (340-380 nm), but emit all or a portion of their fluorescence energy as visible light. In each case, the emission spectra are shifted towards longer wavelengths when these probes become protein bound.^{1,18} These probes are also highly solvatochromic and tend to fluoresce with significantly less intensity in aqueous buffers compared with neat organic solvents. It should also be noted, particularly for coumestrol, that extensive overlap exists between its excitation spectrum and the emission spectrum of protein tryptophanyl residues,

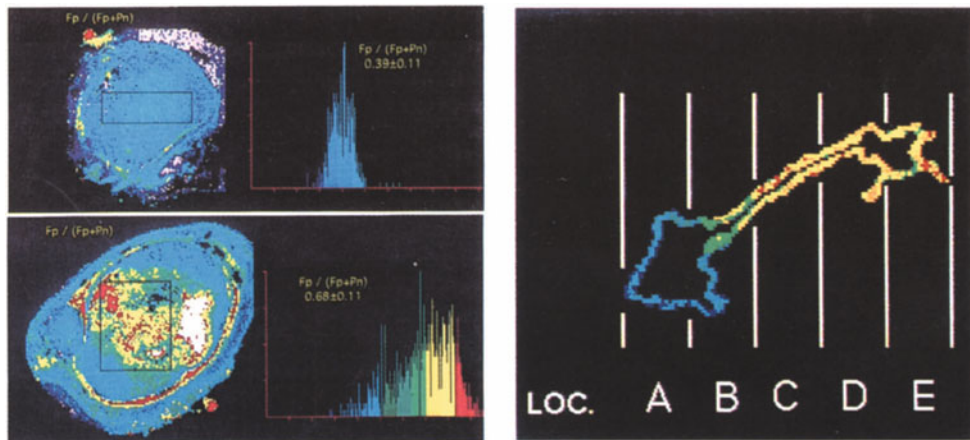


Figure 6. (Chance, p. 29) **(A)** Illustrating a trans-forma-tion from a highly hypoxic state, near state 5 of Fig. 1 for a rat 9L tumor grown on the flank of a rat and studied by freeze trapping and redox scanning. **(B)** The effect of breathing 95% oxygen, 5% carbon dioxide (carbogen) to increase the oxygen delivery to a 9L tumor and increase the oxidation of flavoprotein in diminishing the reduction of NADH, as best depicted by the ratio of the flavoprotein to the pyridine-nucleotide signal.

Figure 1A. (Gross *et al.*, p. 251) A map of the intramembrane electric field along the surface of a single NIE-115 neuroblastoma cell. Each cell was divided into five equally sized zones, each of which covers a distinct location as shown.

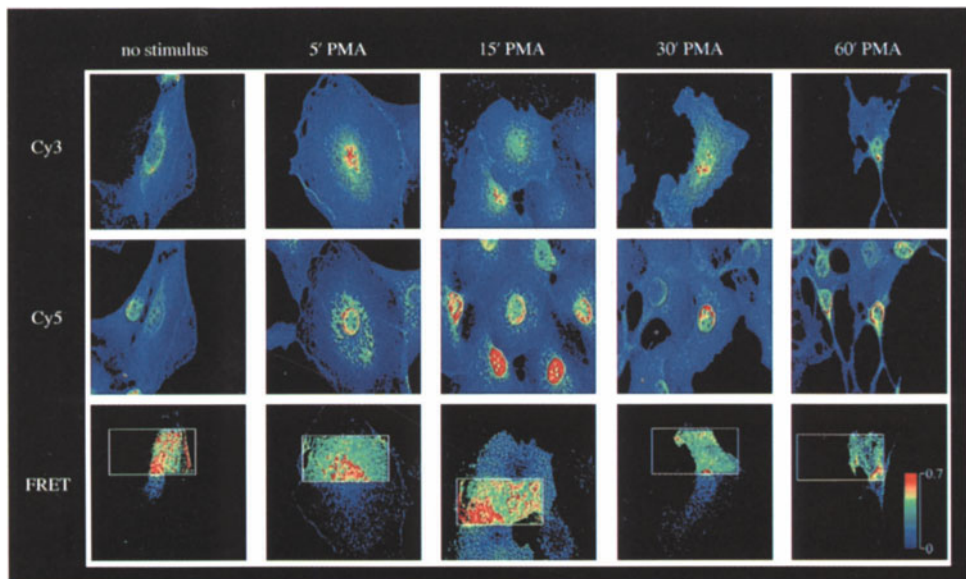


Figure 2. (Bastiaens and Joven, p. 56) Confocal images demonstrating localization and proteolytic processing of PKC β I in Balb/c 3T3 cells.

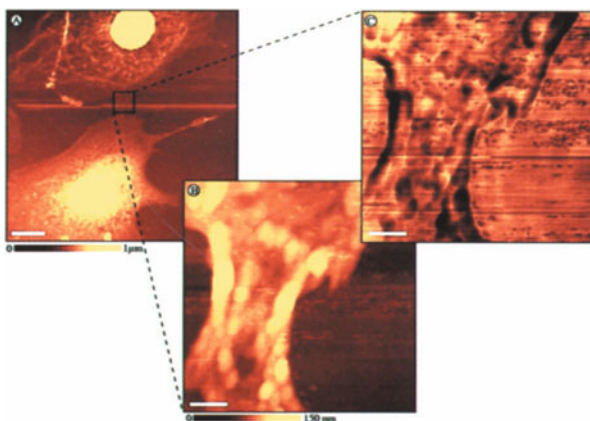


Figure 3. (Kirsch *et al.*, p. 320) Images of dried BALB/c-3T3 cells.

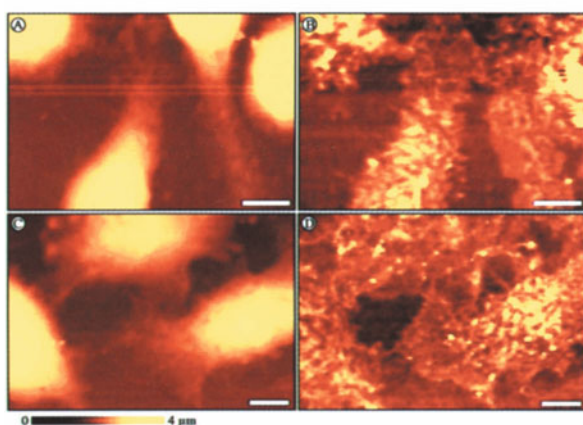


Figure 4. (Kirsch *et al.*, p. 320) Images of Cy5 labeled RBL-2H3 cells.

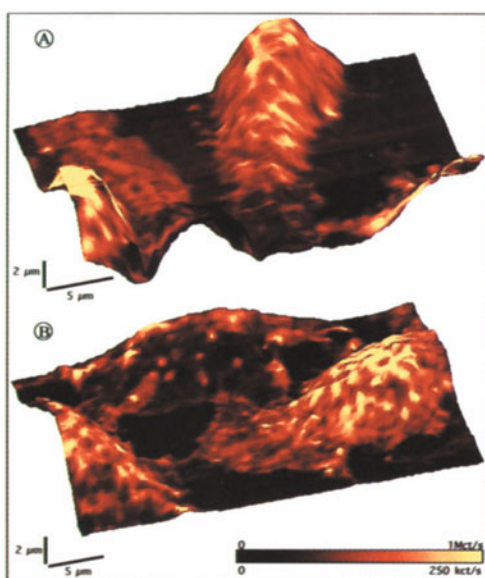


Figure 5. (Kirsch *et al.*, p. 321) Combined topography/fluorescence images of Cy5 labeled RBL-2H3 cells.

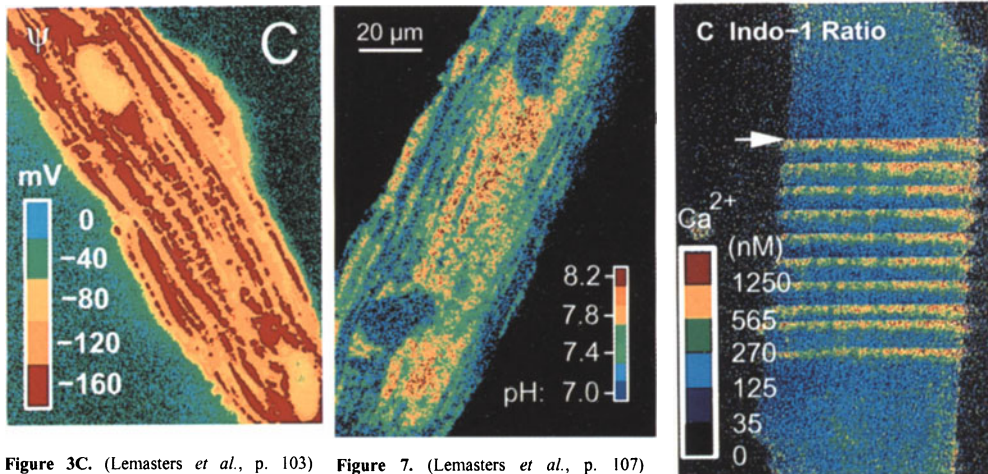


Figure 3C. (Lemasters *et al.*, p. 103) Electrical potential in a cardiac myocyte. A processed image that is pseudocolored to show the intracellular distribution electrical potential. After Chacon *et al.* (1994).

Figure 7. (Lemasters *et al.*, p. 107) Intracellular pH in a SNARF-1-loaded cardiac myocyte. Fluorescence was imaged simultaneously at 584 nm and >620 nm using 568 nm laser excitation, ratioed and pseudocolored to represent the distribution of pH. After Chacon *et al.* (1994).

Figure 9C. (Lemasters *et al.*, p. 109) Indo-1 ratio-imaging of a cardiac myocyte during electrical stimulation. The ratio image is scaled to represent free Ca^{2+} concentrations occurred in both cytosolic and mitochondrial compartments, the latter identified by rhodamine 123 labeling. After Ohata *et al.* (1994).



Figure 2. (Viklicky *et al.*, p. 335) Distribution of vimentin and GFAP in astrocytoma. Tissue section was stained with anti-vimentin antibody (red), anti-body to GFAP (green) and DNA-binding dye (blue).

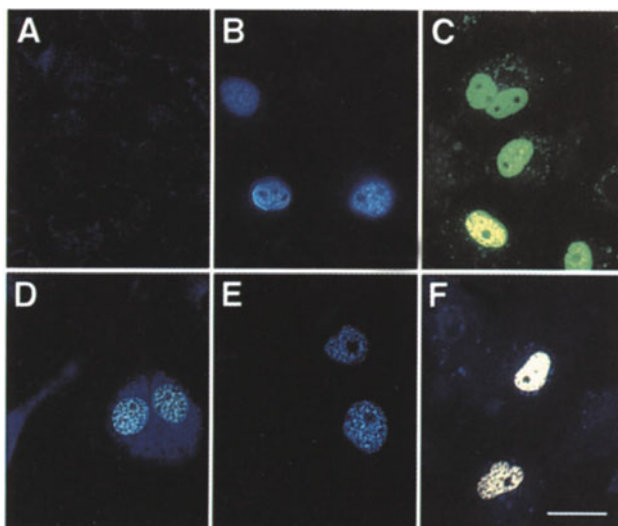


Figure 2. (Miksicek and Katzenellenbogen, p. 217) Fluorescence visualization of ER in Cos7 cells transfected with pCMV-ER (B-F) compared with control cells transfected with expression vector alone (A). Cells were stained without prior fixation by incubation together with 10^{-7} coumetrol (A & B), 10^{-5} M THC-nitrile (C), 10^{-5} M THC-amide (D), 10^{-5} M THC-ester (E), or 10^{-5} M THC-ketone (F), as described in Miksicek *et al.*, 1995².

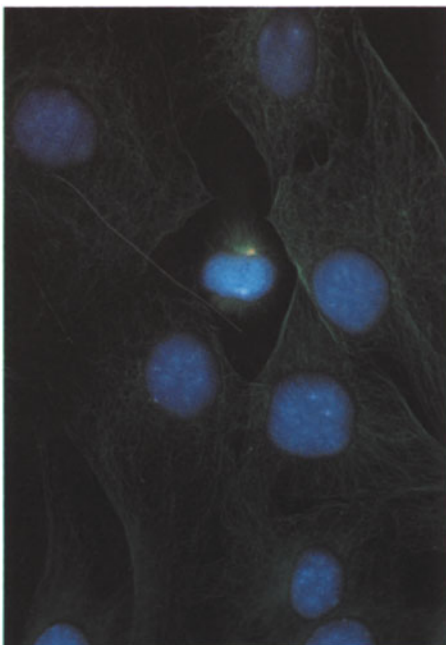


Figure 3. (Dráber *et al.*, p. 263) Distribution of γ -tubulin in interphase and mitotic 3T3 cells. Cells were stained with anti-tubulin antibody (green), antibody TU-30 to γ -tubulin (red) and DNA-binding dye (blue).

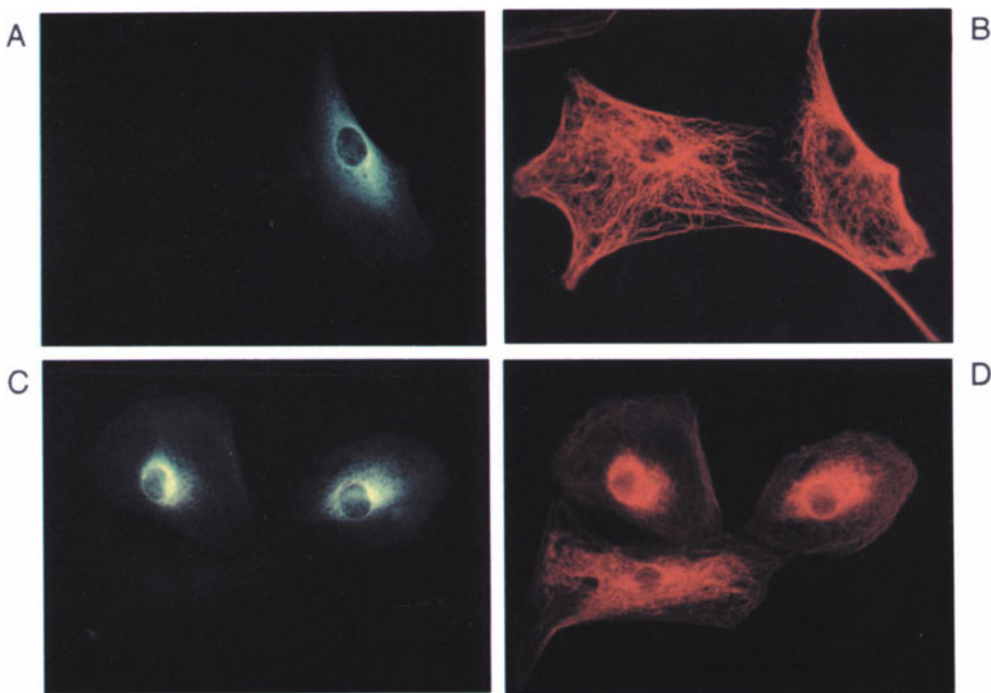


Figure 3. (Dráberová and Dráber, p. 270) Effect of MA-01 antibody injection on the distribution of microtubules and intermediate filaments of vimentin-type. 3T3 cells were injected with MA-01 antibody at a concentration of 5 mg/ml, fixed after 3 hours and processed for immunostaining. Distribution of MA-01 antibody (A,C), microtubules (B) and vimentin filaments (D) is shown by double-label immunofluorescence. Antibodies TU-04 and VI-01 were directly conjugated with rhodamine. Each pair (A-B and C-D) represents the same cells. Bar=10 μ m.

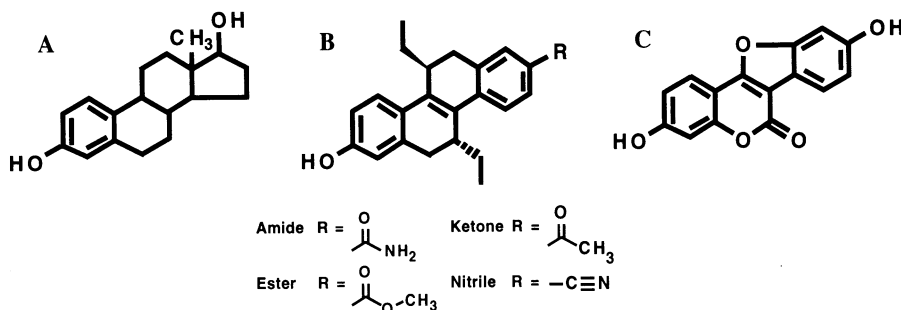


Figure 1. Structural comparison of 17 β -estradiol (A) with the fluorescent tetrahydrochrysene estrogens (B) and coumestrol (C).

enabling fluorescence energy transfer techniques to be applied to an analysis of the coumestrol / ER complex.³ Finally, as evidenced by relative binding activities (RBAs) marginally less than 17 β -estradiol itself, each of these fluorescent ligands retains excellent affinity for ER and is capable of fully saturating this receptor at concentrations as low as 10 nM. High binding affinity is a crucial factor with respect to the specificity of receptor imaging since it enables these probes to be used at concentrations that serve to minimize nonspecific interactions with other cellular components.

CONDITIONS FOR ESTROGEN RECEPTOR IMAGING WITH FLUORESCENT LIGANDS

A number of previous attempts have been made to employ reversibly binding fluorescent ligands to image ER within cells and tissues. By and large, these studies were performed using fixed or frozen specimens from estrogen-responsive tissues such as the breast and uterus, or using tumors or tumor cell lines derived from these tissues. While several of these investigators claimed success in being able to visualize ER within tissues and cells²⁰⁻²³, these studies can be criticized on several grounds,^{24,25} including the use of excessively high concentrations of probe, choice of fixation conditions that tend to inactivate ligand binding by ER, and difficulties in demonstrating that the observed staining was sensitive to competition by nonfluorescent estrogens. In addition, the fact that the cellular

Table 1. Biochemical and spectral properties of intrinsically fluorescent estrogens

Compound	RBA ¹	$\lambda_{\max, ab}^2$ (nm, EtOH)	$\lambda_{\max, em}^2$ (nm, EtOH)	Φ_F^2 (EtOH)	ε^2 (M ⁻¹ cm ⁻¹ , EtOH)
coumestrol	13.3	345	399	0.67	21,100
THC-amide	14.5	350	472	0.58	18,608
THC-ester	19.5	364	482	0.69	42,200
THC-nitrile	13.6	366	456	0.69	28,300
THC-ketone	33.3	380	525	0.43	22,801

¹Relative Binding activities (RBA) are defined as their ability to compete for binding to ER (either human or lamb receptor) using estradiol (=100%) as a tracer (values from references 1,19).

²Absorbance maxima ($\lambda_{\max, ab}$), fluorescence emission maxima ($\lambda_{\max, em}$), fluorescence quantum yields (Φ_F), and Molar absorptivities (ε) were measured in absolute ethanol (as reported in references 4,18).

fluorescence observed in most of these studies was largely cytoplasmic, conflicts with our current understanding that ER is a predominantly nuclear protein.²⁶

While coumestrol was included in several of these earlier studies, they relied most heavily on the use of micromolar concentrations of the lower affinity fluorescent steroid conjugates. In retrospect, it appears that the tissue staining observed at this time corresponded primarily to an interaction of high concentrations of these probes with a class of abundant, lower affinity estrogen binding sites (so called type II sites) that are distinct from ER and are present in a wide variety of cells.²⁷ For this reason, documenting the specificity of ER staining by fluorescent ligands requires that this staining reaction occurs at concentrations of probe close to the equilibrium binding constant (K_d) for ER (i.e., type I binding sites), as well as a clear demonstration that this staining is sensitive to competition by nonfluorescent estrogens.

A key to successfully demonstrating the utility of ligands such as coumestrol and the fluorescent THCs for visualizing ER within cells has been our adoption of a transiently transfected cell culture system in which ER expression can be manipulated as an independent variable.^{1,2} To achieve high levels of ER expression, we have chosen to transfect cells with an expression plasmid, pCMV·ER, in which the wild type human ER cDNA has been placed under transcriptional control of the human cytomegalovirus transcriptional promoter. A direct assessment of the specificity of cell staining using coumestrol or the estrogenic THCs can be made by comparing the fluorescence staining pattern of pCMV·ER-transfected cells with mock-transfected cells that have not received the ER cDNA. An example of such an experiment is shown in Figure 2 and reveals intense nuclear fluorescence that is limited to cultures that express ER, but is entirely lacking in control cultures. In contrast, all of the cells regardless of their exposure to the pCMV·ER expression plasmid display a low level of background fluorescence that appears to correspond largely to vesicular organelles such as the perinuclear golgi complex. It is expected that only a fraction of the cells in pCMV·ER-transfected cultures (typically 1-10%) display nuclear fluorescence, since the transient transfection technique is inherently inefficient and is unable to achieve uniform expression throughout the culture. Based on an independent determination of ER levels using a radiometric ligand-binding assay corrected for the percentage of cells that are positive for fluorescence staining, we have estimated that the threshold for nuclear staining by these probes using a conventional epifluorescence microscope equipped with standard optics is approximately $0.2-2 \times 10^6$ receptor sites per cell.²

DISCUSSION

Intrinsically fluorescent ligands such as coumestrol and the estrogenic THCs possess excellent potential to be used as target-specific probes for imaging ER in cells and tissues. The principal features that distinguish these compounds from conjugated fluorescent probes that have been examined in earlier studies is their high affinity for the ligand-binding site of ER, combined with their neutral charge and high intrinsic fluorescence. We have previously demonstrated^{1,2} that fluorescent imaging of ER using any one of the fluorescent estrogens shown in Table 1 is specific for this receptor, since this fluorescence requires expression of ER and is restricted to the nuclear compartment where this karyophilic protein is known to accumulate. Furthermore, this pattern of nuclear fluorescence is sensitive to competition by an equimolar concentration of a nonfluorescent estrogen such as 17 β -estradiol or diethylstilbestrol and nuclear staining has been shown to be coincident with the distribution of ER expression as independently assessed by indirect immunofluorescence analysis. By all of these criteria, nuclear staining using these fluorescent estrogens accurately reflects the distribution of ER within cells.

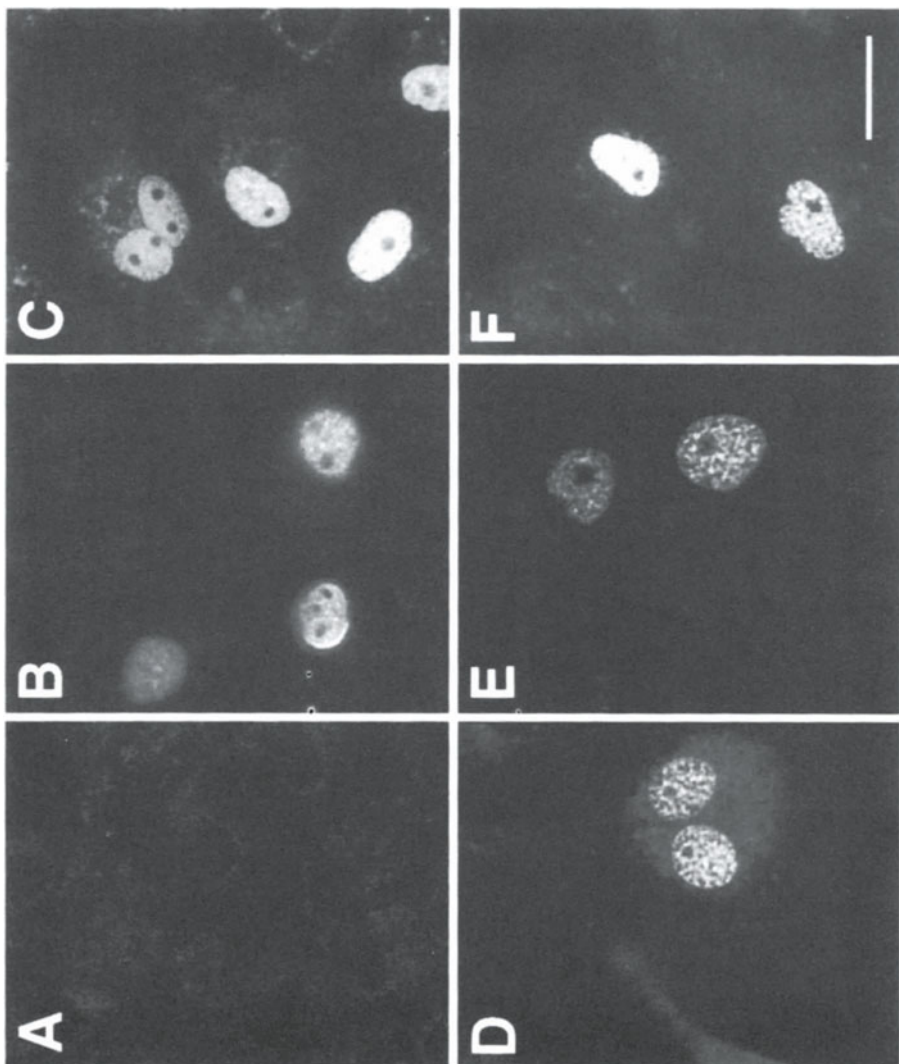


Figure 2. Fluorescence visualization of ER in Cos7 cells transfected with pCMV-ER (B-F) compared with control cells transfected with expression vector alone (A). Cells were stained without prior fixation by incubation together with 10^{-7} M coumestrol (A & B), 10^{-8} M THC-nitrile (C), 10^{-8} M THC-amide (D), 10^{-8} M THC-ester (E), or 10^{-8} M THC-ketone (F), as described in Miksicek *et al.*, 1995. A color representation of this figure can be found facing p. 214.

The protocol for cell staining with these ligands is remarkably simple and exceedingly flexible. It can be used for *in situ* analysis of ER expression in unfixed cells under physiological conditions, as well as in aldehyde-fixed preparations suitable for immunofluorescence analysis. The sensitivity of detecting fluorescence from receptor-bound ligand continues to be the major limitation of this technique.² So far, it has not been possible to visualize ER in the nuclei of estrogen-responsive cell lines such as MCF7 cells that express physiological levels of ER. However, our demonstration of the feasibility of this method is an important breakthrough that represents a realistic starting point for the further technical development of this method.

CONCLUDING REMARKS

It is hoped that improvements in the sensitivity of ER detection using intrinsically fluorescent estrogens can be made by further refinements in the probes themselves, by changes in the conditions for cell staining, and by optimization of the instrumentation and optics used for fluorescence visualization. The many advantages of this novel imaging technique are already reaping benefits for basic research on the structure and function of steroid receptors. This methodology should also one day be of benefit for the assessment of steroid receptor expression and its role in the management of mammary and reproductive tumors.

REFERENCES

1. R.J. Miksicek, *In situ* localization of the estrogen receptor in living cells with the fluorescent phytoestrogen coumestrol, *J Histochem Cytochem* 41:801 (1993).
2. R.J. Miksicek, K.E. Carlson, K.-J. Hwang, and J.A. Katzenellenbogen, Studies using fluorescent tetrahydrochrysene estrogens for *in situ* visualization of the estrogen receptor in living cells, *Mol Endocrinol* 9:592 (1995).
3. Y.J. Lee, A.C. Notides, Y.-G. Tsay, and A. Kende, Coumestrol, NBD-nor- hexestrol, and dansyl-norhexestrol, fluorescent probes of estrogen-binding proteins, *Biochemistry* 16:2896 (1977).
4. K.J. Hwang, K.E. Carlson, G.M. Anstead, and J.A. Katzenellenbogen, Donor-acceptor tetrahydrochrysenes, inherently fluorescent, high-affinity ligands for the estrogen receptor: binding and fluorescence characteristics and fluorometric assay of receptor, *Biochemistry* 31:11536 (1992).
5. B.R. Rao, C.G. Fry, S. Hunt, R. Kuhnel, and W.B. Dandliker, A fluorescent probe for rapid detection of estrogen receptors, *Cancer* 46:2902 (1980).
6. S.H. Lee, Hydrophilic macromolecules of steroid derivatives for the detection of cancer cell receptors, *Cancer* 46:2825 (1980).
7. B.G. Joyce, R.I. Nicholson, M.S. Morton, and K. Griffiths, Studies with steroid-fluorescein conjugates on oestrogen target tissues, *Eur. J. Cancer Clin. Oncol.* 18:1147 (1982).
8. T.L. Fevig, J.E. Lloyd, J.A. Zablocki, and J.A. Katzenellenbogen, Preparation, receptor binding, and fluorescence properties of hexestrol-fluorophore conjugates: evaluation of site of attachment, fluorophore structure, and fluorophore-ligand spacing, *J. Med. Chem.* 30:156 (1987).
9. K.E. Carlson, M. Coppey, H. Magdelenat, and J.A. Katzenellenbogen, Receptor binding of NBD-labeled fluorescent estrogens and progestins in whole cells and cell-free preparations, *J. Steroid Biochem.* 32:345 (1989).
10. J.A. Katzenellenbogen, K.E. Carlson, R.D. Bindal, R.L. Neeley, P.M. Martin, and H.P. Magdelenat, Fluorescence-based assay of estrogen receptor using 12-Oxo-9(11)-dehydroestradiol-17 β , *Anal. Biochem.* 159:336 (1986).
11. K. Nelson, E.J. Pavlik, J.R. van Nagell, Jr, M.B. Hanson, E.S. Donaldson, and R.C. Flanigan, Estrogenicity of coumestrol in the mouse: fluorescence detection of interaction with estrogen receptors, *Biochemistry* 23:2565 (1984).

12. G.M. Anstead and J.A. Katzenellenbogen, Optimizing of 2,3-diarylindenes as fluorescent estrogens: Variation of the acceptor group, ortho substitution of the 2-ring, and C-1 methylation, *J. Med. Chem.* 31:1754 (1988).
13. K.-J. Hwang, J.P. O'Neil, and J.A. Katzenellenbogen, 5,6,11,12-Tetrahydro-chrysenes: synthesis of rigid stilbene systems designed to be fluorescent ligands for the estrogen receptor, *J. Org. Chem.* 57:1262 (1992).
14. P.M. Martin, H.P. Magdelenat, B. Benyahia, O. Rigaud, and J.A. Katzenellenbogen, New approach for visualizing estrogen receptors in target cells using inherently fluorescent ligands and image intensification, *Cancer Res.* 43:4956 (1983).
15. E.M. Bickoff, A.N. Booth, R.L. Lymanm A.L. Livingston, C.R. Thompson, and F. De Eds, Coumestrol, a new estrogen isolated from forage crops, *Science* 126:969 (1957).
16. G.M. Anstead, K.-J. Hwang, and J.A. Katzenellenbogen, Characterization of the spectroscopic properties of a tetrahydrochrysene system containing a rigidified hydroxynitrostilbene chromophore: an inherently fluorescent ligand designed for the estrogen receptor, *Photochem. Photobiol.* 57:616 (1993).
17. G.M. Anstead, K.E. Carlson, P.R. Kym, K.-J. Hwang, and J.A. Katzenellenbogen, The effect of acceptor group variation on the solvatochromism of donor-acceptor fluorophores, *Photochem. Photobiol.* 58:785 (1993).
18. O.S. Wolfbeis and K. Schaffner, Solvent and acidity dependence of the absorption and fluorescence of coumestrol, *Photochem. Photobiol.* 32:143 (1980).
19. R.J. Miksicek, Interaction of naturally occurring nonsteroidal estrogens with expressed recombinant human estrogen receptor, *J. Steroid Biochem. Molec. Biol.* 49:153 (1994).
20. L.P. Pertschuk, E.H. Tobin, P. Tanapat, E. Gaetjens, A.C. Carter, N.D. Bloom, R.J. Macchia, and K.B. Eisenberg, Histochemical analysis of steroid hormone receptors in breast and prostatic carcinoma, *J. Histochem. Cytochem.* 28:799 (1980).
21. G.H. Barrows, S.B. Stroupe, and J.D. Rhiem, Nuclear uptake of a 17 β -estradiol-fluorescein derivative as a marker of estrogen dependence, *Am. J. Clin. Pathol.* 73:330 (1980).
22. I. Nenci, W.B. Dandliker, C.Y. Meyers, E. Marchetti, A. Marzola, and G. Fabris, Estrogen receptor cytochemistry by fluorescent estrogen, *J. Histochem. Cytochem.* 28:1081 (1980).
23. S.H. Lee, The histochemistry of estrogen receptors, *Histochem.* 71:491 (1981).
24. G.C. Chamness and W.L. McGuire, Questions about histochemical methods for steroid receptors, *Arch. Pathol. Lab. Med.* 106:53 (1982).
25. E.M.J.J. Berns, E. Mulder, F.F.G. Rommerts, R.A. Blankenstein, E. de Graf, and H.J. van der Molen, Fluorescent ligands, used in histochemistry, do not discriminate between estrogen-receptor-positive and receptor-negative human tumor cell lines, *Breast Cancer Res. Treat.* 4:195 (1984).
26. W.J. King and G.L. Greene, Monoclonal antibodies localize oestrogen receptor to the nuclei of target cells, *Nature (London)* 307:745 (1984).
27. J.H. Clark, J.W. Hardin, and S. Upchurch, Heterogeneity of estrogen receptor binding sites in the cytosol of the rat uterus, *J. Biol. Chem.* 253:7630 (1978).

VIDEOMICROFLUOROMETRY AND INTRACELLULAR IONIC CONCENTRATION IN SINGLE LIVING CELLS

From Toy to Tool

P. Viallet, J. M. Salmon, M. Yassine, and J. Vigo

Group of Quantitative Microfluorometry
University of Perpignan
52 Av. de Villeneuve F66860 Perpignan

ABSTRACT

The measurement of the intracellular concentrations of ions is one of the challenges of modern cell biology. For that purpose, different kinds of fluorescent probes are now available. For some of them, the complexation induces a shift in the position of the excitation and/or the emission fluorescence spectrum. In that case the popular two-wavelength ratio method allows the determination of the intracellular pH although some problems have been reported in the obtaining of intracellular calibration curves.

We have previously demonstrated that the fluorescence emission or excitation spectrum of most of these probes was pH sensitive in the range of biological pH. Moreover it has also been proven that they are able to bind with intracellular proteins. So we have proposed another data processing method that allows us to extract quantitative information on each of these interactions from the cell fluorescence spectrum. That method was used to monitor pH_i variations with the fluorescent probe C-SNARF-1.

The scope of this contribution is to present a protocol of data processing allowing to use video-imaging techniques for monitoring the changes in intracellular ionic concentrations. For sake of clarity, only applications to the determination of the kinetics of pH_i equilibration following some external stimuli will be considered.

INTRODUCTION

The measurement of the intracellular concentrations of ions is one of the challenges of modern cell biology. The recognition of the interdependency of these concentrations¹, the potential role of some ions in the triggering of some biological processes^{2,3} and in the intracellular transfer of information⁴ point out the need for accurate data obtained in real

time on living material. From this point of view fluorescence techniques look promising, for they are both non invasive, specific, and generally sensitive enough to require only low concentrations of the probes. Although the concentrations of anions such as chloride and bicarbonate are of primary importance in the intracellular ionic balance, chemical constraints have mainly limited the use of fluorescence to the intracellular detection of cations such as proton, magnesium, calcium and more recently sodium.

Different kinds of fluorescent probes are now available. Some of them have been designed so that the complexation of the cation results only in a variation in the intensity of their excitation and/or emission spectrum^{5,6}. In that case the intracellular ionic concentration could be obtained from measurements at only one wavelength if one can assume that the intra and/or extracellular distribution of the probe remains unchanged during the whole experiment.

Data are more reliable when obtained with probes for which the complexation induces a shift in the position of the excitation and/or the emission fluorescence spectrum. A large enough spectral shift allows an easy determination of the ratio of the respective molar fraction of the free and bound fluorescent probe with the popular two-wavelength ratio method⁷. Such a method has been widely used for the determination of the intracellular pH although some problems have been reported in the obtaining of intracellular calibration curves⁸.

Indo-1 and Fura-2 have been designed to monitor the intracellular concentration of calcium. Unfortunately it has also been demonstrated that the fluorescence emission or excitation spectrum of these probes was pH sensitive in the range of biological pH. Moreover it has also been proven that they are able to bind with intracellular proteins^{9,10}. All these cation-unspecific interactions preclude the use of the two-wavelength ratioing method. Fortunately these interactions generally result in specific shifts of the fluorescence spectrum. So another data processing method has been proposed that allows to extract quantitative information on each of these interactions from the cell fluorescence spectrum. That method was used to monitor pHi variations with the fluorescent probe C-SNARF-1. It gives access to the respective molar fraction of the free and of the protonated forms of the probe. Its main advantages compared to the two-wavelength method are that it allows to detect any unexpected chemical interaction of the probe with other intracellular chemicals as well as potential physical modifications of the probe microenvironment. For these reasons it has been shown more reliable to correlate pHi measurements with data obtained in cuvettes. That would allow avoiding the cytotoxic consequences of any excessive ion-loading inside the cell^{11,15}.

The scope of this contribution is to present a protocol of data processing allowing one to use video-imaging techniques for monitoring the changes in intracellular ionic concentrations. For sake of clarity, only applications to the determination of the kinetics of pHi equilibration following some external stimuli will be considered.

MATERIALS AND METHODS

Reagents

The carboxy-SNARF™-1 (C-1270), 5i(and 6i)-carboxy-10-dimethylamino-3-hydroxy-spiro[7H-benzo[c]xanthene-7,1i(3iH)-isobenzofurans]-3i-one and the acetoxy-methyl-ester derivative, carboxy-SNARF-1/AM, (C-1271), were from Molecular Probes Inc. (Eugene, OR, USA). Water solutions were made from decarbonated and deionized water. The fluorescence spectra of C-SNARF1 were found identical to those published by Molecular Probes Inc. for the recommended excitation wavelengths.

Cell Culture

Experiments were performed on an established human leukemic cell line (CCRF-CEM) kindly provided by Dr. W. T. Beck (St. Jude Children Hospital, Memphis, TN, USA). The cells were grown at 37°C with 5% CO₂ in RPMI 1640 medium (Flow) supplemented with 2 mM glutamine, 10% fetal calf serum (Gibco) and antibiotics. The cells were seeded every 2 or 3 days at 2,105 cells per ml, to maintain continually exponential growth. In all experiments the cell viability was measured by trypan blue exclusion and was always higher than 95%. The doubling time was evaluated at 24 hours.

Loading Procedures

An aliquot of 500 µl of CCRF-CEM cells suspension at 37°C (106 cells per ml) was incubated with 10µM C-SNARF1/AM (0.5% DMSO) in RPMI for 30 min.. After that time-lag the level of C-SNARF1 intracellular fluorescence reached a plateau. Cells were then rinsed three times with cold PBS and resuspended in PBS for observation. Fluorescence spectra were recorded after plating cells in Sykes-Moore chambers. Temperature in Sykes-Moore chambers was controlled during measurements (37°C).

For experiments in the presence of nigericin, after 10 min. treatment with the pH probe, the incubation medium was complemented, for 20 min., with nigericin (8 µM or 20 µM) and KCl to reach an extracellular concentration of 140 mM KCl. The cells were then washed as stated above while nigericin and KCl were maintained at the same concentrations during the entire experiments.

Equipment

Microspectrofluorometer. The microspectrofluorometer was composed of an inverted microscope (Leitz) connected to an Optical Multichannel Analyzer (OMA, Princeton Applied Research Corp.) equipped with a Silicon Intensified Target (SIT) as detector. The excitation wavelength was selected at 500 nm. from the emission of a Xenon lamp with a monochromator. The fluorescence spectra were recorded between 550 and 750 nm. (200 channels, 0.72 nm per channel) and resulted from the accumulation of 500 frame scans (recording duration 15 sec.). The fluorescence intensity was evaluated in counts, each count corresponding to about 25 photons in the spectral range recorded. Data were transferred to a PDP 11/73 (Plessey) microcomputer for storage and calculations. This equipment was used to record the fluorescence emission from single living cells as well as from solutions.

Digitized Video Fluorescence Microscope. The digitized video fluorescence imaging microscopy system has been previously described¹⁶. The system consists of an inverted fluorescence microscope (Olympus, IMT2) equipped with an epi-illuminator (block B), a 40x objective (Leitz) (final magnification 60x) and a silicon intensified target camera from Lhesa (LH 4036) was coupled with a TITN SAMBA 2002 image processor. The light source for fluorescence excitation was a Xenon lamp (150W). Illumination of the microscopic field was electronically controlled by a shutter. A special data acquisition program that includes subtraction of the background, correction of the nonlinearity of the digitizer and pixel to pixel heterogeneity of the camera gain allowed quantitative measurements of dye fluorescence intensities.

Data Processing

Fluorescence Spectrum Analysis. The complex fluorescence spectrum was analyzed with a method previously described in detail¹⁷. Briefly, using a microcomputer this method of spectral analysis has allowed us to identify all the components of the intracellular fluorescence spectrum and to quantify their participation. Graphic (weighted residues curve) and numeric (Chi-square : χ^2) estimators were calculated to estimate the fit of the resolution of the fluorescence spectrum into its different components. To analyze the complex fluorescence, two characteristic fluorescence spectra were recorded for C-SNARF1: i) at pH 5.5 for the acid form, ii) at pH 9.5 for the basic form.

Numerical Image Analysis. The method was derived from the above mentioned method of resolution of complex cell fluorescence spectra. It has been described in full detail in a recent paper¹⁸ so that only the salient features will be given below. When the complex fluorescence issuing from a pixel results from the fluorescence of N chemicals, its intensity at each wavelength can be described as a linear combination of the intensities of each component at the same wavelength.

Use of a set of N convenient filters, each of them being defined by a transfer function $\Phi_j(\lambda)$ allows us to generate the set of N equations needed to resolve that system. The whole system can be expressed in matricial writing as :

$$(M) [A] = [B]$$

Each element of the matrix (M) is the convolution product of the characteristic fluorescence spectrum of a component i of the mixture by a filter function $\Phi_j(\lambda)$.

[A] is the unknown column vector; its components are the participation coefficients of the components to the whole cellular fluorescence spectrum.

[B] is an experimental vector; its components are the convolution product of the experimental cellular spectrum by each filter function $\Phi_j(\lambda)$.

An efficient use of this process requires that some conditions are fulfilled :

1. first, the images which will be used in the calculations have to be registered under conditions which have been previously described in detail¹⁸ in order to minimize the errors and bias due to the experimental conditions and to the equipment ;
2. second, the functions Φ_j, λ must be chosen to minimize both the error in the matrix coefficients m_{ij} and the amplification error resulting from the calculations. That means that both the wavelength and the bandwidth of each optical filter must be selected to minimize the final error;
3. finally, preliminary experiments must have been performed to evaluate the minimal number of pixels from which significant data can be obtained.

After resolution of the matrix equation it is first necessary to verify that the error amplification induced by the mathematical treatment is minimal. That is done by calculation of the "conditioning" of the matrix.

Then the validation of the model is performed by adding another filter to the N strictly required to solve the system. The comparison between the experimental intensity obtained with that filter and the theoretical value resulting from the calculation allows one to detect the presence of any unexpected fluorescent compound.

RESULTS AND DISCUSSION

Intracellular Validation of the Method Used to Determine the Respective Molar Fraction of the Protonated/Deprotonated Probe

The respective characteristic fluorescence spectra of the protonated and deprotonated probe were first used to resolve fluorescence spectra recorded in solution at different intermediate pH measured by a conventional electrode. The molar fractions of the protonated probe (AH) and/or the deprotonated probe (A-) calculated from such experiments were used to build up a calibration curve at different ionic strengths. Because it was claimed that the difficulties met in the obtaining of an intracellular calibration curve may result from interactions between C-SNARF-1 and some proteins, such interactions were searched for in solution using BSA as a model. No interaction between BSA and purified C-SNARF-1 was evidenced using the method of molecular filtration. Moreover the effects of pH variations on the fluorescence spectrum of a C-SNARF-1 solution containing 0.2% of BSA were studied. The presence of an isobestic point clearly demonstrated that no new fluorescent compound resulting from an interaction of BSA with either AH or A- or both of them can be detected. Finally, calibration curves were drawn in the presence of BSA (0.2%) and were found identical to those recorded without BSA.

Experiments were then performed on single living cells incubated with C-SNARF-AM in their usual culture medium. Because a pH probe is supposed to be located in a water-phase environment, the fluorescence emission spectra of C-SNARF1/AM treated cells were resolved using a combination of the respective characteristic fluorescence spectra obtained from water solutions of protonated and deprotonated C-SNARF1. The fit between the experimental fluorescence spectrum and the calculated spectrum was checked using both the statistical distribution around zero of the weighted residues and the chi-square value close to 1. Such results indicate that only these two species are necessary to account for the intracellular fluorescence. That excludes the presence of other fluorescent species, which could have resulted from interactions between the probe and intracellular macromolecules or components.

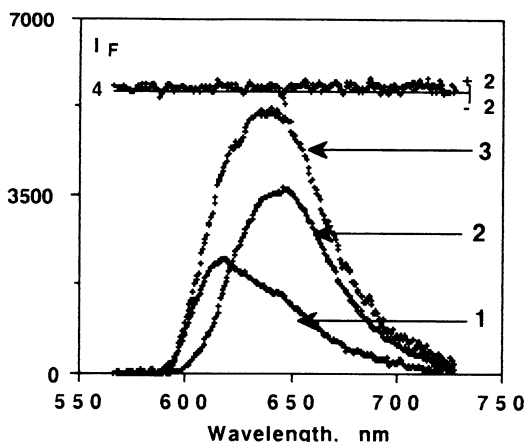


Figure 1. Resolution of a single cell fluorescence spectrum (CCRF-CEM): 1 Participation of protonated C-SNARF-1; 2 Participation of deprotonated C-SNARF-1; 3 experimental complex fluorescence spectrum; 4 weighted residues.

Such an excellent fit between the experimental and calculated curve also suggests that both protonated and deprotonated C-SNARF1 should have a chemical environment identical to that they experience in water solutions. So the intracellular pH was evaluated using the physical parameters determined in solution : pKa=7.5, fluorescence quantum yield ratio (K_{A^+}/K_{AH}) = 1.61. The obtained pH value was 7.52, a value that was not surprising for tumor cells. It might be of importance that taking into account the intrinsic cell fluorescence is not necessary to get a good fit between experimental and calculated spectra.

That set of experiments suggested that the proposed method of resolution of fluorescence spectra may be convenient for intracellular pH measurements. The question now is to prove that the measured values are the actual ones. That will be done by using a ionophore and recording the pH_i variations during the pH_e/pH_i equilibration.

Microspectrofluorometric analysis allows the recording of a complete fluorescence spectrum in less than 15 seconds. That allows to follow the kinetics of equilibration in about 12 individual cells at a time. In these experiments C-SNARF1 - loaded cells were maintained for 20 minutes in the culture medium with 20 mM nigericin and 140 mM KCl (see Material and methods), before the extracellular pH was set at a given value. The cell fluorescence spectrum was then recorded at different times until its stabilization. The successive pH_i values were calculated from these recorded fluorescence spectra.

As a general rule, a continuous increase of the intracellular pH of a single cell follows the setting of pH_e . A plateau is reached only after about 25 minutes after extracellular pH setting. The final pH_i value is the same for all the cells, and equal to that of pH_e , but the time required to reach that value may differ from cell to cell.

That finding suggests that the differences between the calibration curves presented by different scientists may be due to the time lag necessary to obtain a true pH_e/pH_i equilibration. That may also explain the observed cell to cell difference especially for pH_e far from physiological pH.

Application of Numerical Image Analysis to the Study of Kinetics of pH_i Equilibration After a Modification of the pH_e

Applying videomicrofluorometry to the study of the kinetics of pH_i variations on living cells requires some conflicting prerequisites. First the signal/noise ratio must be good enough to allow the use of our method of data treatment. Second, the time necessary to get that signal/noise value must be small compared to the speed of the expected pH_i variations. Third, both the probe concentration and the excitation flux must be kept minimal to avoid any biological damage. These conditions limit the minimal cytosolic volume from which significant data can be acquired.

As stated above numerical image analysis allows simultaneously recording the kinetics of pH_i variations on a larger number of cells. That method was used to monitor the pH_i variations with time, after addition of NH₄Cl to the buffered (pH_e 7.2) culture medium of CCRF- CEM cells. As has been previously published¹⁹ addition of ammonium chloride first produces a rapid rise in pH_i due to the entry of NH₃, which rapidly combines with intracellular protons. That increase is then followed by a slow and “exponential” decrease of the pH_i which was reported to result both from a specific activation of the (Na⁺/H⁺) antiport and/or a slow entry of NH₄⁺. But a cell to cell analysis seems to indicate that the cell responses are more complicated (Figure 2).

First, the upper value of the pH_i seems to be independent of the initial pH_i value. That looks consistent with the fact that the rise in pH_i results from the NH₃ concentration gradient. But the subsequent pH_i decrease seems to depend on other parameters than the initial pH_i value. If the initial pH_i reflects the way that each cell accommodates its physiological status

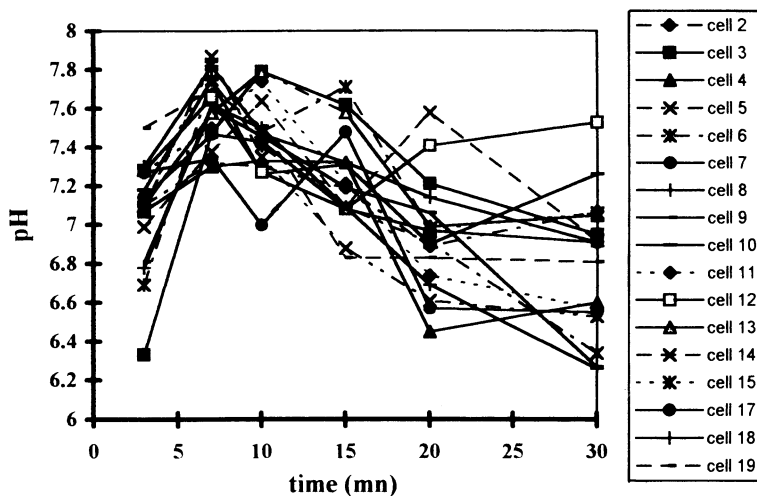


Figure 2. Concomitant variations with time of the pH_i of some CCRF-CEM cells after addition of NH_4Cl to the culture medium.

to the fixed extracellular pH, it could be expected that activation of the (Na^+/H^+) antiport allows each cell to reach its initial pH_i . To obtain a confirmation of that finding, the curves corresponding to cells with initial pH_i value close to 7.1, i.e. around the pH_e value, were selected and presented in the Figures 3A and 3B.

These figures clearly show that there is no correlation between the initial and the final pH_i values. That difference may come from the fact that addition of ammonium chloride to the culture medium induces not only a change in the extracellular ammonium ion concentration, but also an increase of the extracellular chloride ion concentration. Such an increase may activate the $\text{HCO}_3^-/\text{Cl}^-$ exchangers resulting for each cell in a new acidobasic equilibrium.

These preliminary experiments demonstrate that Videomicrofluorometry might be useful to study the relative importance of pH-regulating cation and anion antiport mecha-

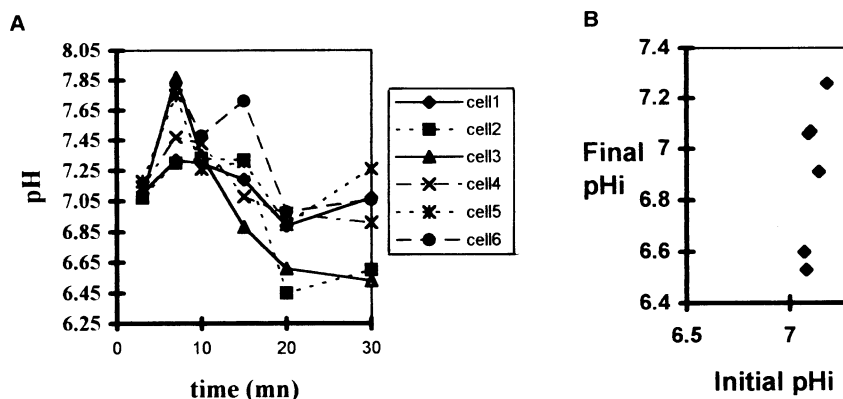


Figure 3. Variations with time of the pH_i of some CCRF-CEM after addition of NH_4Cl to the culture medium. **3A:** Cells with initial pH_i values close to 7.1; **3B** Final pH_i values compared to initial pH_i .

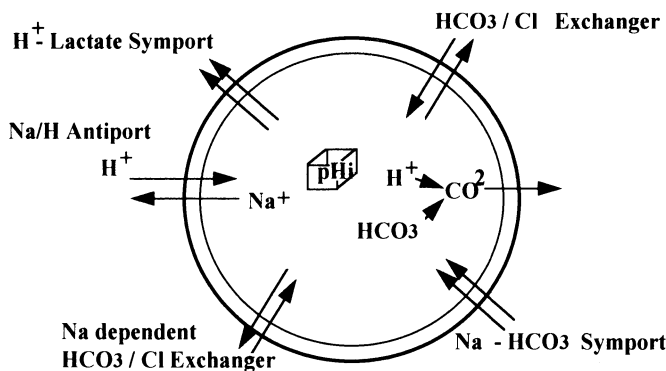


Figure 4. Different pathways involved in pH_i regulation.

nisms. It could also be expected that they could be used to monitor the activation of the (Na^+/H^+) antiport by growth factors.

4. CONCLUSIONS

1. C-SNARF-1 used with convenient methods of data processing allows avoiding the preparation of intracellular calibration curves; it is a convenient probe both for basal pH_i determinations and to monitor pH_i variations following an external stimulus of the different pathways involved in the pH_i homeostasis.
2. Due to the interdependency of these pathways, the interpretation of these pH_i variations requires specific informations on the status of at least some of these pathways. For instance the influence of a cation on a cationic antiport, through an increase of its extracellular concentration, cannot be assessed without taking into account the potential role of the accompanying anion.
3. Conversely these pH_i variations can be used to study selectively the changes of activity of antiports, ports and exchangers in response to extracellular stimuli.
4. Future breakthroughs are expected from simultaneous determination of intracellular concentrations of different ions in the same cell.

REFERENCES

1. "Bicarbonate, Chloride, and Proton Transport Systems" Annals of the New York Acad. Sci. Vol 574 J.H. Durham and M.A. Hardy Eds. New York, 1989.
2. "Membrane Transport driven by ion gradients" Annals of the New York Acad. Sci. Vol 456 G. Semenza and R. Kinne Eds. New York, 1985.
3. R. J. Aets, A. J. Durston, and W. H. Moolenaar, "Cytoplasmic pH and the regulation of the dictyostelium cell cycle" Cell, 43, 653-657 (1985).
4. C. N. Abboud, S. P. Scully, A. H. Lichtman, J. K. Brennan, and G. B. Segel, "The requirement for ionized calcium and magnesium in lymphocyte proliferation" J. Cell. Physiol. 122, 64-72 (1985).
5. R. Y. Tsien "New calcium indicators and buffers with high selectivity against magnesium and protons: Design, synthesis, and properties of prototype structures" Biochemistry, 19, 2396-2404 (1980).
6. T. J. Rink, R. Y. Tsien, T. Pozzan, "Cytoplasmic pH and free Mg^{2+} in lymphocytes" J. Cell Biol. 95, 189-196 (1982).

7. G. Grynkiewicz, M. Poenie, and R. Y. Tsien, "A new generation of Ca^{2+} indicators with greatly improved fluorescence properties" *J. Biol. Chem.* 260 (6), 3440-3450 (1985).
8. P. S. Blank, H. S. Silverman, O. Y. Chung, B. A. Hogue, M. D. Stern, R. G. Hansford, E. G. Lakatta, and M. C. Capogrossi, "Cytosolic pH measurements in single cardiac myocytes using carboxy-seminaphthorhodafluor-1" *Am. J. Physiol.* 263 (Heart Circ. Physiol. 32) H276-H284 (1992).
9. F. Bancel, J.M. Salmon, J. Vigo, and P. Viallet, "Microspectrofluorometry as a tool for investigation of non-calcium interactions of Indo-1" *Cell Calcium* 13, 59-68 (1992).
10. F. Bancel, J.M. Salmon, J. Vigo, T. Vo-Dinh, and P. Viallet, "Investigation of noncalcium interactions of Fura-2 by classical and synchronous fluorescence spectroscopy" *Anal Biochem.* 204, 231-238 (1992).
11. D. Molenaar, T. Abbe, and W.N. Konings, "Continuous measurement of the cytoplasmic pH in Lactococcus lactis with a fluorescent pH indicator" *Biochim. Biophys. Acta* 1115, 75-83 (1991).
12. B. J. Fuller, J.D. Gower and C.J. Green, "Free radical damage and organ preservation: fact or fiction" *Cryobiol.* 25, 377-393 (1988).
13. J. L. Farber "The role of calcium in cell death" *The Life Sci.* 29, 1289-1295 (1981).
14. E. C. LeGrande "Free radicals in tissue culture: Part V calcium, magnesium, cytotoxicity and cellular death" *Art to Science in tissue culture*, HyClone Laboratories, Inc., 10 (2) XX (1991).
15. D. A. Eisner, N. A. Kenning, S. C. O'Neil, G. Pocock, C. D. Richards, and M. Valdeolmillos, "A novel method for absolute calibration of intracellular pH indicators" *Pflügers Arch.* 413, 553-558 (1989).
16. J. Vigo, J.M. Salmon, S. Lahmy and P. Viallet, "Fluorescence image cytometry: from qualitative to quantitative measurements" *Anal. Cell Path.* 3, 145-165 (1991).
17. J. M. Salmon, J. Vigo, and P. Viallet, "Resolution of complex fluorescence spectra recorded on single unpigmented living cells using a computerized method" *Cytometry* 9, 25-32 (1988).
18. J. Vigo, M. Yassine, P. Viallet, and J. M. Salmon, "Multiwavelength fluorescence imaging: the pre-requisites for the intracellular applications" *Journal of Trace and Microprobe techniques* 13, (3) (1995) in press.
19. I. G. Madshus, "Regulation of intracellular pH in eukaryotic cells" *Biochem. J.* 250, 1-8, (1988).

MULTIWAVELENGTH MICROFLUOROMETRY TO INVESTIGATE CYTOTOXIC PROCESSES ON SENSITIVE AND RESISTANT HUMAN LYMPHOBLASTOID CCRF-CEM LINES

Jean-Marie Salmon, Emmanuelle Rocchi, Jean Vigo, and Pierre Viallet

Laboratoire de Chimie Physique

Microfluorimétrie Quantitative et Pharmacocinétique cellulaire

Université de Perpignan

66860 Perpignan, France

INTRODUCTION

Chemotherapy continues to be, along with radiotherapy and surgery, an extremely efficient approach in cancer therapy. Much progress has been made in the last 25 years that allows us to consider several types of cancer as "curable" by chemotherapy. These cures can be obtained for cancers as different as: Hodgkin's disease, large cell lymphoma, acute lymphocytic leukemia, testicular cancer and early stage breast cancer¹. Furthermore with the development of combination chemotherapy, other malignancies such as ovarian, small cell lung cancer, and advanced breast cancer, though not yet curable, demonstrate interesting clinical responses in many patients.

The failure of these treatments as well as those used when a relapse occurs can usually be associated with the development of a drug resistance, intrinsic or acquired, that induces a limited response to chemotherapy.^{2,3}

This resistance results from the genetic instability of malignant cell populations which leads to the spontaneous generation of variant forms presenting different phenotypic and genotypic properties including the intrinsic resistant cell populations and the resistance acquired by cell populations under a selection pressure, for example the Multidrug Resistance phenotype.^{4,5}

In consequence, for precise investigations of cytotoxic processes on cell populations it is of interest to be capable not only to obtain individual information on cells of the population, but also to evaluate the maximum of parameters that could be related to the cytotoxic process. Usually the evaluation of the cytotoxicity of drugs is performed using the growth inhibition of cell cultures. This does not give direct information on intracellular

events. However it can be expected that cytotoxicity may induce changes in: i) cell or nucleus sizes, ii) DNA or mitochondria labelling, iii) intracellular ionic concentrations, depending on the cytotoxic process involved.

Some of this intracellular information can be obtained by the multiparametric non destructive approach we used to monitor the MDR phenotype on cell populations.⁶ That approach by multiwavelength microfluorometry on single living cells associated with numerical image analysis uses the simultaneous intracellular labelling with: i) the nuclear probe Hoechst 33342 (Ho 342), ii) the mitochondrial probe Rhodamine 123 (R123), iii) the membrane probe Nile Red (NR), which allows us to delineate each cell studied through the plasma membrane labelling.

Based on accumulation differences existing for Ho342 and R123 between sensitive and MDR resistant cell this protocol has allowed us:

- to discriminate between sensitive and resistant cell lines, not only for cells presenting rather high resistance degrees (>10 for CCRF-CEM-VLB) but also for cells presenting low resistance degrees (1.4 to 2 for L1210),⁷
- to study the effect of different drugs (verapamil, vinblastine, colchicine) on the R123 efflux by the Pgp.⁸

Thus multiwavelength microfluorometry has been used, in a first step, to test the potentialities of such an approach for a multiparametric study of the effects of cytotoxic drugs. This test has been performed on an established human lymphoblastoid line (CCRF-CEM) and related resistant cell lines. The cytotoxic drugs Adriamycin (ADR) and Vinblastine (VLB) have been used, ADR being a typical intercalating drug while VLB is able to bind tubulin. Rhodamine 110 has also been used as a compound that did not present cytotoxic effects at doses as high as 50 µg/l.⁹

MATERIALS AND METHODS

Cell Culture

Experiments were performed on an established human lymphoblastoid line (CCRF-CEM) and the resistant derivative lines obtained after selection with: i) VLB (CEM-VLB100), ii) Teniposide (CEM-VM1). CCRF-CEM, CEM-VLB100 and CEM-VM1 cells were a gift from Dr. W.T. Beck (St. Jude Childrens Research Hospital, Memphis, TN, USA). CEM-VLB100 cells displayed the "classic" MDR phenotype¹⁰, with overexpression of Pgp while CEM-VM1 express an atypical MDR phenotype¹¹. They were grown at 37°C in RPMI 1640 supplemented with 10% heat-inactivated fetal calf serum and antibiotics as previously described¹². CEM-VLB100 cells (CEM-VLB) were seeded in VLB-free medium 8 days before experiments. To maintain continuous exponential growth, cells were seeded at 2 x 10⁵ cells/ml every 3 days. In all experiments, the viability of the cells was checked by trypan blue exclusion, and was always > 95%.

Conditions of Labeling

Stock solutions of Ho342 (1 mM) from Aldrich, R123 (0.1 mM), R110, ADR and VPL (1 mM) from Sigma were prepared in PBS. Nile red (1 mM) from Sigma was made up in DMSO. Ten µl of Ho342 were added to 1 ml (1 x 10⁶ cells) of cell suspension and the suspension incubated for 2 h at 37° C. After the first hour of incubation, 100 µl of R123 solution were added to the cell suspension. The cells were then incubated for 1 h simultaneously with the two probes centrifuged and rinsed with cold PBS. The cells were then stained

with NR (5 μ M, final concentration) for 5 min at 37°C, rinsed with cold PBS and resuspended in HANKS for observation. Numerical image analyses were performed after plating cells in Sykes-Moore chambers. In experiments where the effects of VLB, ADR and R110 were studied, the cells were grown for 72 hours in the presence these drugs, before being labeled as previously described.

Numerical Image Analysis

The fluorescence digital imaging microscopy system has been previously described in detail.^{13,14} Briefly, an inverted fluorescence microscope (Olympus, IMT2) equipped with an epi-illuminator, a 40x Leitz objective (final magnification 60x), and a Silicon Intensified Target (SIT) camera (Lhesa), was coupled to an image processor (TITN SAMBA 2002). The light for fluorescence excitation was generated from a high-pressure mercury lamp (100W). The Hg line 365 nm or 435 nm was selected by dichroic mirrors for the respective excitation of Ho342 and of R123 and NR. A computer-controlled filter holder allowed to switch automatically the filters necessary for recording the specific fluorescence of the dyes: no filter for Ho342; interference filter $\lambda_{\text{max}} = 525$ nm, half bandwidth = 10 nm for R123; interference filter $\lambda_{\text{max}} = 610$ nm, half bandwidth = 20 nm for NR. A specific data acquisition program that included the background subtraction, the correction of non-linearity of the digitizer and the pixel-to-pixel heterogeneity of the camera gain, permitted quantitative measurements of dye fluorescence intensities. The excitation intensity was adjusted with neutral density filters to keep each fluorescent probe image on scale. A protocol was developed to record the NR-stained plasma membrane fluorescence using image segmentation by thresholding, followed via a cell contour smoothing via opening and closing sequences. NR fluorescent image of the cells was required for 2 reasons: i) it allowed the determination of cell size by plasma membrane staining as well as the determination of parameters related to shape and size of the cells¹³. Such parameters were necessary to exclude the data related to subcellular debris or cell clumps and gave an estimation of cell integrity; ii) R123 fluorescence was heterogeneous because R123 was distributed in clusters, so that a segmentation process was not possible from R123 fluorescence images. The mask for each cell was generated from NR fluorescence images to delineate the cell contour. This contour was then superimposed to the R123 fluorescent image and the fluorescence of R123 was quantified after subtraction of the background corresponding to the fluorescence of the medium¹⁵. The corresponding nucleus was isolated by thresholding and contour smoothing by closing and opening sequences. Thus, besides the parameters related to shape and size of cells and nuclei, we recorded the total fluorescence intensity as well as the mean fluorescence intensity and related standard deviation that can be used to monitor the fluorescence distribution of each probe

Cytotoxicity

The growth-inhibitory effect of drugs was evaluated by plating cells in dishes (35 mm diameter) at a final concentration of 10^6 cells/ml. After 72 h the cells were Coulter-counted and the data were expressed as percentages of surviving cells compared with untreated cells. The IC₅₀ was defined as the concentration of drug that inhibits cell growth by 50%. Using the trypan blue exclusion test the percentage of dead cells was found to be below 3%.

RESULTS

In all experiments the ADR and VLB treated cells were grown for 72 h with IC₅₀ doses.

CEM-WT Cells

We can observe in Figure 1A that VLB treatment induces, compared to control, a slight shift of the cell distribution toward higher values of Ho342 fluorescence intensities while a larger shift is observed for the R123 fluorescence intensity. On the contrary ADR treatment induces simultaneously : i) a large shift of the cell distribution toward higher values of Ho342 and R123 fluorescence intensities, ii) a large increase of the area of the cells' distributions that suggests an important heterogeneity of the cell population.

Concomitantly we can observe, Figure 1B, that ADR induces an important increase of the nuclei and cellular sizes (shift of the cell population toward higher values) and again an increase of the dispersion of the cell distribution. On the contrary, treatment by VLB results only in an increase of the cell size without any significant modification of the nuclear size.

The distribution of these cell populations as a function of the R123 intracellular mean fluorescence intensity versus the corresponding Standard Deviation (SD) of R123 intracellular fluorescence distribution is shown in Figure 1C. It indicates that when the R123 fluorescence increases from control to VLB and ADR treated cells we observe a simultaneous increase of the heterogeneity of the R123 fluorescence distribution that suggests that R123 remains localized in mitochondria. This observation can be taken as a proof that they remain highly energized.

At least a close relation between the cell size and the R123 intracellular fluorescence was observed. That increase of R123 fluorescence intensity should be the result of an increase of the amount of intracellular R123 resulting either from the augmentation of the mass of mitochondrial material or from an augmentation of the mitochondrial energetic level. A similar relation was also observed between the Ho342 fluorescence intensity and the nuclear size, indicating an increase of the nuclei DNA content. As can be seen in Figure 1A, the Ho342 fluorescence intensity is greatly increased for ADR treated cells, out of the range of the values observed for control cells. On the contrary, if we also observe a general increase of the Ho342 fluorescence intensity for VLB treated cells, the distribution of that cell population remains in the range of the values observed for control cells. We only observe a diminution of the number of cells presenting low Ho342 intranuclear accumulation. These results suggest an increase of the number of cells in G2 + M phases for VLB treated cells while for ADR treated cells we observe, at least for part of the cell population, a DNA synthesis that continues far away from the nuclear DNA content of the G2 phase.

CEM-VLB Cells

In Figure 2A the distribution of the ADR and VLB treated cell population remains in the same range of Ho342 fluorescence intensities as for controls. On the contrary, we observe an increase of the R123 fluorescence intensity with a simultaneous increase of the area in which are spread the distribution of the cell populations. That indicates an increase in the cell population heterogeneity. Furthermore the distributions of the cell populations as a function of cell and nuclear sizes suggests an increase of the cell size for ADR and VLB cells while the nuclear sizes remain in the range of that of control cells. However, the curves of Figure 2B indicate a diminution of the number of cells presenting a low Ho342 intranuclear accumulation (IF= 32000), corresponding to an increase in the number of cells in G2+M phases with a higher intranuclear accumulation of Ho342.

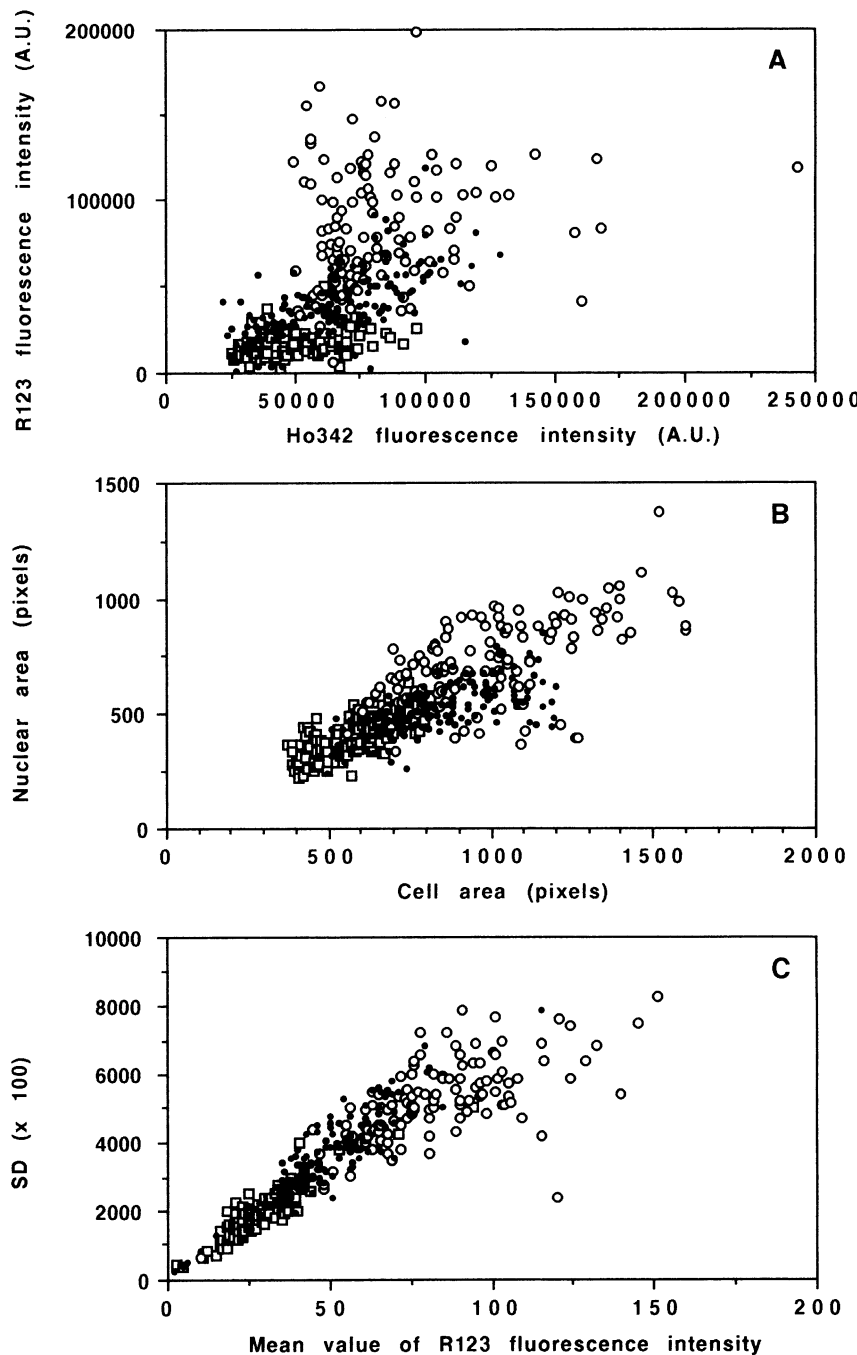


Figure 1. Distribution of CEM-WT cell populations (□) control or grown for 72 h in the presence of (○) ADR 60 ng/ml or (●) VLB 5 ng/ml corresponding to their respective IC₅₀ dose, as a function of: A) R123 versus Ho342 fluorescence intensities; B) cell versus nuclear area; C) standard error of R123 cellular fluorescence distribution versus the corresponding mean value.

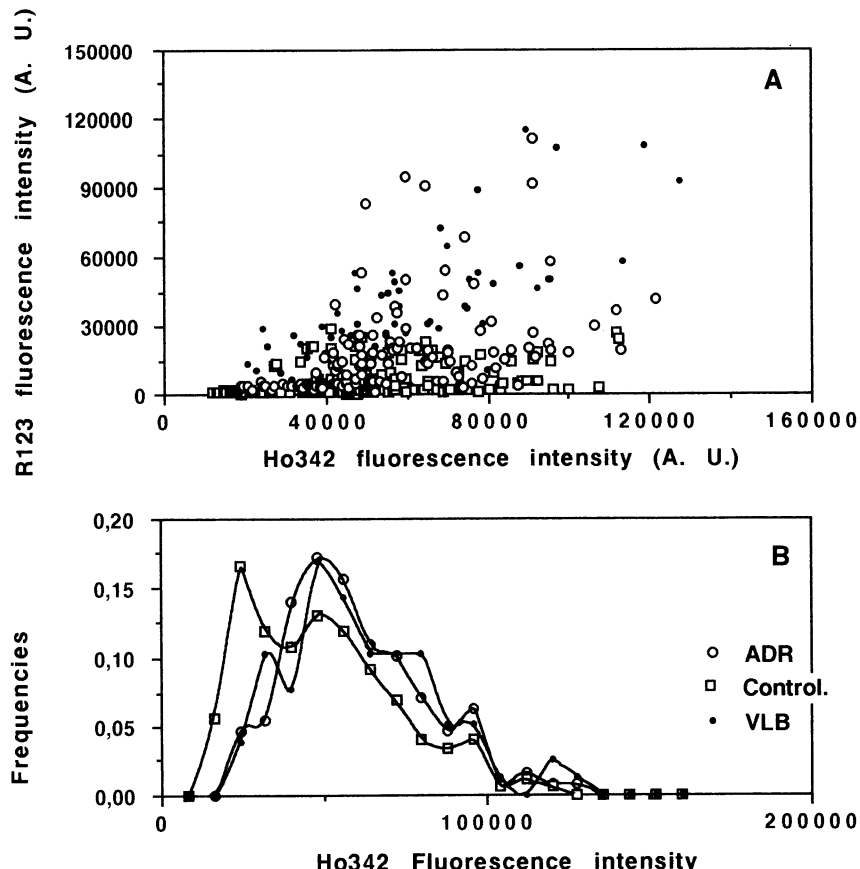


Figure 2. CEM-VLB cell populations (□) control or grown for 72 h in the presence of (○) ADR 500 ng/ml or (●) VLB 1000 ng/ml corresponding to their respective IC₅₀ dose: A) distribution as a function of R123 versus Ho342 fluorescence intensities; B) frequency distribution of Ho342 nuclear fluorescence.

CEM-VMI Cells

The distributions of Figure 3 shows that for ADR treated cells we observe for some cells a slight increase of the nuclear labelling (Ho342) compared to control cells. On the contrary, an important decrease is observed for the cellular staining by R123. That decrease should indicate a reduction of the energetic level of the mitochondria. This figure shows also that some ADR treated cells exhibit an increase of the nuclear and cellular areas.

For the VLB treated cells we only observe a significant increase of the intracellular fluorescence of R123, Figure 3, while the cell areas remain in the range of the values obtained for control cells. Thus the increase of the mitochondrial labeling could be related more to a higher mitochondrial energetic state than to an augmentation of the amount of mitochondrial material. As for CEM-VLB cells, the distribution of the Ho342 fluorescence intensities as well as that of the nuclei's areas remain in the same range of values as that for control cells. We only observe a relative increase of the number of cells presenting higher levels of Ho342 accumulation. That should again indicate an increase of the number of cells in G2+M phases.

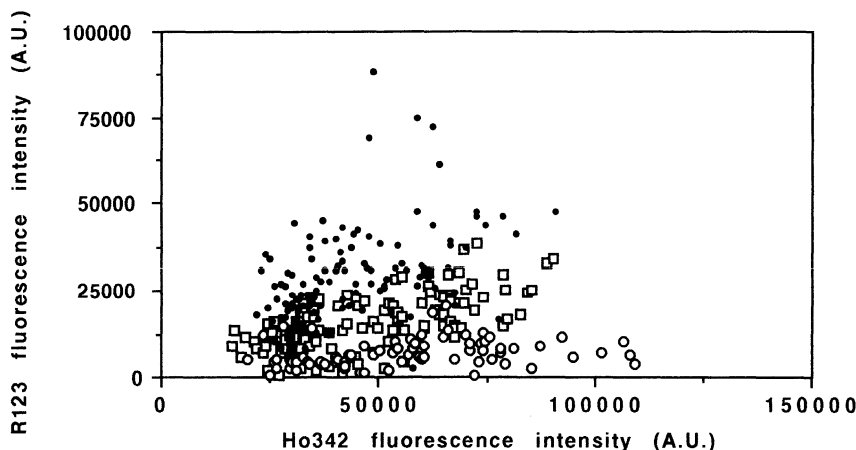


Figure 3. Distribution of CEM-VM1 cell populations (□) control or grown for 72 h in the presence of (○) ADR 100 ng/ml or (●) VLB 42 ng/ml corresponding to their respective IC₅₀ dose, as a function of: A) R123 versus Ho342 fluorescence intensities.

Effect of R110 Treatment on CEM-WT Cells

Figure 4 shows the differences, between R110 treated and control cells, in the distribution of these cell populations. While differences can be observed in the Ho342 nuclear labelling, an important decrease is seen for the mitochondrial staining of R110 treated cells by R123. This decrease should be correlated to a reduction of the energetic level of mitochondria, representing a strong alteration of the cellular metabolism, though R110 has no effect on the cell growth even at the high dose used, 50 µg/ml.

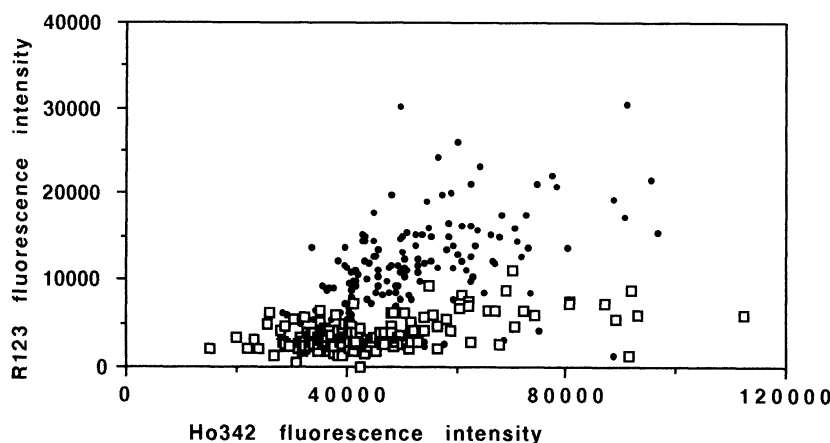


Figure 4. Distribution of CEM-WT cell populations (□) control or (●) grown for 72 h in the presence of R110 50 µg/ml as a function of R123 versus Ho342 fluorescence intensities.

CONCLUSION

The results obtained show the very different responses of the cells' strains to the treatment by ADR and VLB at IC₅₀ doses.

Vinblastin appears to affect the cell cycle by increasing the percentage of the cell population in G₂+M phases. This effect can be related to the blocking of the cell cycle resulting from the binding of VLB to tubulin that blocks the cells in G₂+M phases, as already reported by Beck et al.¹⁰ Furthermore we have been able to observe the notable increase of the mitochondrial energetic level following VLB treatment.

These observations are also valid for CEM-WT cells as well as for the related resistant ones CEM-VLB and CEM-VM1.

On the contrary Adriamycin induces, for CEM-WT, a strong increase of the nuclear and cellular sizes as well as of the labelling of the nuclei and mitochondria. That indicates a nuclear DNA content higher than the one of G₂ and M phase, and probably an increase of the amount of mitochondrial material. That observation, which agrees with the increase of the nuclear DNA content observed for 3T3 ADR treated cells,¹⁶ seems to rule out, as possible mode of action of the ADR, the inhibition of DNA replication.

This effect is less obvious for CEM-VLB and CEM-VM1 cells for which it seems that we only observe an increase in the number of cells presenting a nuclear DNA content corresponding to G₂+M phases. However these cell types differ strongly in the mitochondria labelling level that can be taken as an indicator of mitochondrial activity. While for CEM-VLB we observe an increase of the mitochondria energetic level, CEM-VM1 exhibits a drastic decrease of the mitochondria energetic state.

These differences in the effects of ADR on these three cell lines suggest that this drug should have different modes of action depending on the cell type and on the doses used for the treatment. These observations can be related to the multimodal mode of action of ADR¹⁷ that could be differently expressed depending on doses and cell properties.

At least the effect of R110 on the CEM-WT cells, strong decrease on mitochondria's activity, also shows that apparently non toxic chemicals can deeply modify the cellular metabolism.

These preliminary results are a good example of the possibilities of the association of microfluorometry and numerical image analysis for the studies of the modification of intracellular mechanisms in single living cells. Thus, this approach can be an interesting tool to investigate the effects and the mode of action of cytotoxic drugs or other active substances.

However and more precisely, the modification of the cells' sizes points out the necessity to complete the set of evaluated parameters by the evaluation of intracellular ionic concentrations: pH, Na⁺, Mg⁺⁺..., that could influence the cell volume depending on osmotic pressure related to ionic transports.

REFERENCES

1. B. A. Chabner, R. L. Fine, C. L. Allegre, Cancer chemotherapy: progress and expectations, *Cancer* 54: 2599 - 2608 (1984).
2. W. R. Waud and D.P. Griswold, Therapeutic Resistance in Leukemia, in "Drug Resistance in Oncology", B. A. Teicher, ed., Dekker, N-Y, 227 - 250 (1993).
3. B. A. Teicher, *In vivo* resistance to antitumor alkylating agents, in "Drug Resistance in Oncology", B. A. Teicher, ed., N-Y, 263 - 290 (1993).
4. J. D. Hayes and C.R. Wolf, Molecular mechanisms of drug resistance, *Biochem. J.* 272:281 - 230 (1985).
5. J. H. Goldie, A. J. Coldman, Genetic instability in the development of drug resistance, *Semin. Oncol.* 12: 222 - 230 (1985).

6. Y. Canitrot, D. Lautier, S. Lahmy, J. Vigo, P. Viallet and J. M. Salmon, Nile red labeling of single living cells for contour delineation to quantity and evaluate the distribution of rhodamine 123 with fluorescence image cytometry, *Histochem. Cytochem.* 41: 1785 - 1793 (1993).
7. Y. Canitrot, Chimiothérapie et résistance: la rhodamine 123 comme marqueur de la résistance pléiotropique. Apport de l'analyse d'images de fluorescence numérisées à la discrimination de cellules sensibles et résistantes, Thèse, Université de Perpignan: 201 p.(1994).
8. D. Lautier, Y. Canitrot and J. M. Salmon, Effects of vinblastine, colchicine and verapamil on rhodamine 123 accumulation in human p-glycoprotein- positive leukemia cells, *Anticancer Research* 14: 2589- 2596 (1994).
9. T.J. Lampidis, C. Castello, A. Del Giglio, B. Pressman, P. Viallet, H. W. Ptirvorow, G. K. Valet, Tapiede H. and N. Savaraj, Relevance of the chemical charge of Rhodamine dyes multiple drug resistance, *Biochem. Pharmacol.* 38: 4267- 4271 (1989).
10. W. T. Beck, M. C. Curtin, A. T. Look and R. A. Ashum, Reversal of vinca alkaloid resistance but not multiple drug resistance in human leukemic cells by verapamil, *Cancer Research* 46: 778 - 784 (1986).
11. M. K. Danks, J. C. Yalowich and W. T. Beck, Atypical multiple drug resistance in a human leukemia cell line selected for resistance to tenoposide (VM -26), *Cancer Research* 47: 1297 - 1301 (1987).
12. W.T. Beck, T.J Mueller and L.R. Tanzer, Altered surface membrane glycoproteine in Vinca alkaloid-resistant human leukemic lymphoblasts, *Cancer Research* 39: 2070-2076 (1979).
13. J. M. Salmon, Y .Canitrot, D . Lautier, S .Lahmy, J .Vigo and P. Viallet, Multiwavelenght videomicrofluorimetry and multiparametric analysis: application to the detection of multidrug resistance in single living cells, *J. Cell Pharmacol.* 3: 86-94 (1992).
14. J. Vigo, J. M. Salmon, S. Lahmy and P. viallet, Fluorescence image cytometry: from qualitative measurement, *Anal. Cell Pathol.* 3: 145-165 (1991).
15. Y. Canitrot, D. Lautier, J. Vigo, P. Viallet and J. M Salmon, Nile red labeling of single living cells for contour delineation to quantify and evaluate the distribution of rhodamine 123 with fluorescence image cytometry, *J. Histochem. Cytochem.* 41: 1785-1793 (1993).
16. S. Lahmy, J. M. Salmon, J. Vigo and P. Viallet, pH and DNA content modifications after ADR treatment in 3T3 fibroblasts. A microfluorometric approach, *Anticancer Research* 9: 929-936 (1989).
17. M. Israel, R. Seshadri, Y. Yoseki, M. Potmesil, S. Kirschenbaum, R. Silber, A. Bodley, L.F. Liu and T.P. Brent, New anthracyclines analogues against DNA topoisomerase II, in *Anticancer drugs*, Eds. H. Tapiero, J. Robert, T.J. Lampidis, Colloque INSERM/John Libbey Eurotext, 191: 39-47 (1989).

LASER-INDUCED AUTO FLUORESCENCE OF NORMAL AND TUMOR BLADDER CELLS AND TISSUES

In Vitro and in Vivo Studies

Maurice Anidjar,¹ Olivier Cussenot,¹ Jocelyne Blais,² Olivier Bourdon,² Sigrid Avrillier,³ Dominique Ettori,³ Jean-Marie Villette,⁴ Pierre Teillac,¹ and Alain Le Duc¹

¹Département de Recherche en Urologie
Hôpital Saint-Louis, Paris

²L.P.B.C. CNRS URA 2056
Université P. et M. Curie, Paris

³Laboratoire de Physique des Lasers
Université Paris XIII, Villetaneuse

⁴Laboratoire de Biologie Hormonale
Hôpital Saint-Louis, Paris

INTRODUCTION

Urothelial carcinoma *in situ* (CIS) is clearly related to tumor recurrence and subsequent cancer progression¹. CIS detection remains a challenge for urologists since this lesion, which is only a few cell layers in thickness, may be asymptomatic and/or not visible under conventional white light cystoscopy.

These last few years, laser induced fluorescence spectroscopy has appeared as a sensitive, selective and non-invasive technique which can be used as a tool to discriminate tumors from normal surrounding tissues². Since the penetration depth of light in biological tissues is less than a few millimeters, superficial regions such as urothelial mucosa would be ideally studied using fluorescence. However, most of the fluorescence studies in urology, have been carried out using the laser induced emission of fluorescent tumor markers such as Hematoporphyrin derivative (HpD)³, the commercially available drug (Photofrin) or more recently, chlorin derivatives, a second generation sensitizer.

One of the major drawbacks of these exogenous dyes are their cutaneous side effects⁴. The use of endogenous protoporphyrin IX induced by 5-aminolevulinic acid (ALA), a precursor in the heme biosynthetic pathway, has been recently shown to give promising results. The fluorescent detection of neoplastic urothelial lesions using intravesical instilla-

tion of ALA has been performed by Kriegmair et al.⁵. However, ALA instillation time was quite long with a median time of 204 min. which represents a major burden for the patient.

An alternative method could be to take advantage of tissue endogenous fluorophores. Laser-induced autofluorescence spectroscopy (LIAFS) avoids any intravenous or topical drug administration and has demonstrated its ability for demarcating lung, colonic and cerebral tumors from normal surrounding tissues.² Tissue autofluorescence results from the overlapping of the emission of various endogenous chromophores (tryptophan, collagen, NADH, flavins etc.). The observed emission thus depends on the excitation wavelength, the relative absorption of the various chromophores and their molecular environment. In addition, *in vivo* fluorescence is affected by various parameters such as scattered light, tissue thickness, hemoglobin absorption².

In an attempt to demonstrate whether changes in urothelial tissue autofluorescence upon urothelial tumor development are sufficient to be used for diagnostic purposes we present here a comparative study of the *in vitro* and *in vivo* autofluorescence of normal and tumor bladder cells and tissues. First, the autofluorescence of single living cells has been studied using argon laser microspectrofluorimetry. The *in vivo* autofluorescence of normal and tumor bladder areas was studied *in vivo* using an optical fiber fluorimeter.

MATERIALS AND METHODS

Cell Cultures

Five different urothelial cell types including normal urothelial cells (NU) and tumor cells of different stage and grade (epidermoid carcinoma G1, Ta G2, T24 and J82) were studied. All cells were cultured in RPMI 1640 supplemented with foetal calf serum, glutamine and antibiotics, in a humidified atmosphere of 5 % CO₂ in air.

Microspectrofluorimetric Experiments

The microspectrofluorimeter used for these experiments has been previously described.⁶ In our working conditions, excitation was performed with the 488 nm line of an ionized Argon laser, the light intensity was 0.1 μW at the cellular level and the emission was provided by a subcellular volume of about 5 μm³. The fluorescence spectra were recorded with an accumulation time of 1 sec.

In Vivo Fluorimetry

The *in vivo* fluorimetric experiments were performed with an experimental set up specially built in our laboratory . A multifiber catheter composed, in the same bundle, of 6 excitation fibers and 13 detection fibers (Polymicro 200/220/240 μm, optical aperture 0.22) was connected to a 1-mm core monofiber which was introduced through a regular cytoscope under saline irrigation and maintained in close contact with each bladder area studied. The acquisition was performed by a spectrometer coupled with an optical multichannel analyzer system, adjusted to collect the whole spectrum for a single few ns excitation pulse. Normal, suspicious red-looking and tumor bladder areas have been studied with this device on 25 patients, using three different laser wavelengths for excitation: a coumarin dye laser (480 nm, 4 μJ per pulse) pumped by a nitrogen laser, a nitrogen laser (337 nm, 14 μJ per pulse) and an XeCl excimer laser (308nm, 40 μJ per pulse). Spectroscopic results were correlated to histological findings.

RESULTS AND DISCUSSION

In Vitro Fluorimetric Studies

Argon laser induced autofluorescence (488 nm) of a subcellular volume of normal and several tumor urothelial cell lines (Figure 1) appeared as a broad structureless band with a maximum in the 550-560 nm range whatever the cell type, corresponding most likely to oxidized flavoproteins.⁷

The fluorescence maximum intensity was found to be strongly responsive to the normal or tumor character of cell lines (Figure 2). The analysis of maximum intensity values clearly shows that autofluorescence was much more intense - by a factor of 10 ($p < 0.0001$) - in the case of normal urothelial cells than for any of the tumor cells we studied, specially for the two most undifferentiated cell types, T24 and J82. Nevertheless, no statistically significative correlation could be drawn between the grade of the tumor cell types and the autofluorescence intensity.

These data suggest that flavin concentration may be drastically reduced in tumor urothelial cells, particularly in the poorly differentiated types. This observation is consistent with Pollack's early work⁸ who showed, after extensive extraction from human tumor samples, that riboflavin concentration was lower in tumor tissues, suggesting a "deficient" aerobic oxidation system. According to Chance⁹, the fluorescence yield depends on the

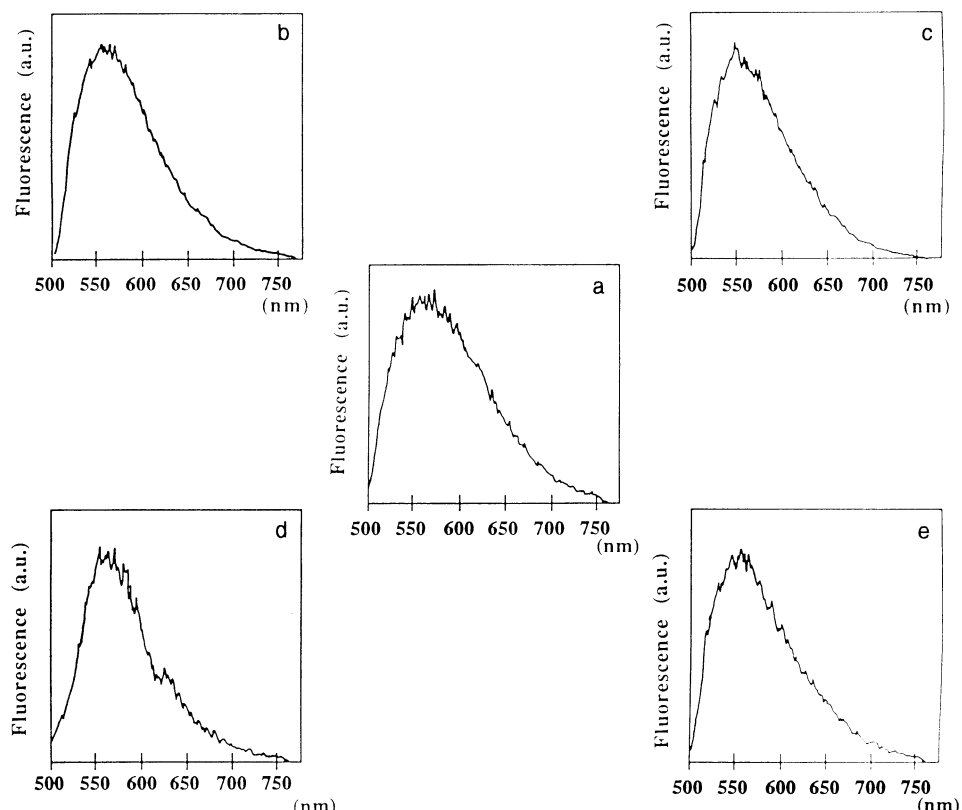


Figure 1. Typical auto-fluorescence emission from a single living urothelial cell. All spectra were normalized to the maximum intensity. a) normal urothelial cell, b) epidermoid carcinoma G1 cell, c) TaG2 cell, d) T24 cell e) J82 cell.

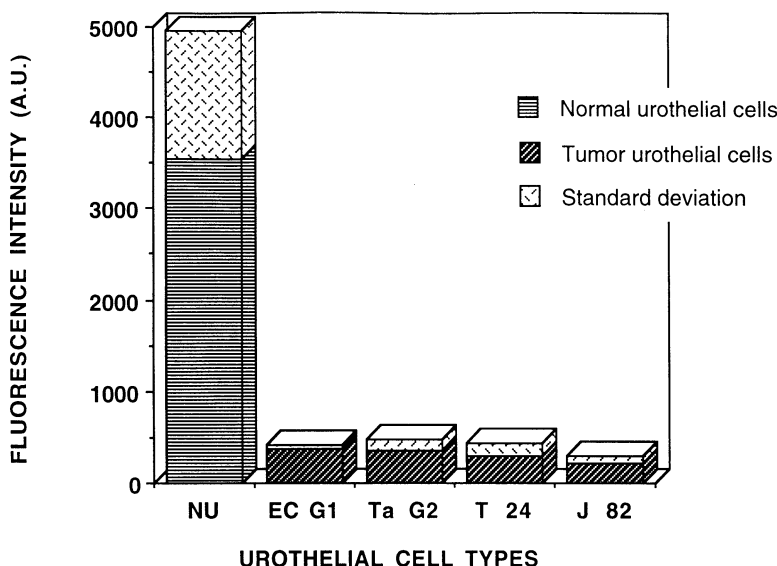


Figure 2. Maximum autofluorescence intensities of normal and tumor urothelial cells.

oxidation-reduction state of flavins, the fluorescence being partially quenched in anaerobic conditions. In the present work, it may thus be assumed that the decrease of the fluorescence intensity we observed for all tumor cells demonstrates a lower concentration of oxidized flavoproteins.

***In Vivo* Liafs Experiments**

Figure 3 shows typical fluorescence emission spectra upon 480 nm excitation of normal bladder mucosa, non specific inflammatory bladder mucosa, a visible bladder tumor regardless of stage and grade and a CIS. In each case, a very similar fluorescence spectrum was observed, with one band centered around 580 nm. In comparison with normal mucosa, the fluorescence intensity was reduced for inflammatory areas, but much less than for any visible bladder tumor including CIS.

In vivo and *in vitro* results are very consistent. In both cases, the emission observed may be ascribed to endogenous flavins. The strong decrease of the fluorescence intensity of tumor cells and tissues seems then to indicate a lower oxidized flavin concentration. Such a decrease could allow for a clear demarcation between normal or inflammatory mucosa and any tumor type including CIS ($p < 0.05$). However, it must be pointed out that for all bladder areas studied, the fluorescence signal was quite weak.

This prompted us to investigate the autofluorescence characteristics using different excitation wavelengths. Upon excitation at 337 nm, the fluorescence emission of normal bladder mucosa, non specific inflammatory bladder mucosa and bladder tumors including CIS showed a fluorescence emission with a maximum around 450 nm, which can be ascribed to NADH emission.¹⁰ In comparison with normal mucosa, the fluorescence intensity was reduced for inflammatory areas, but much less than for any visible bladder tumor including CIS (Figure 4) This observation indicates a reduced NADH expression in bladder tumors and is thus consistent with results obtained at 480 nm, indicating different redox conditions in bladder tumors.⁸

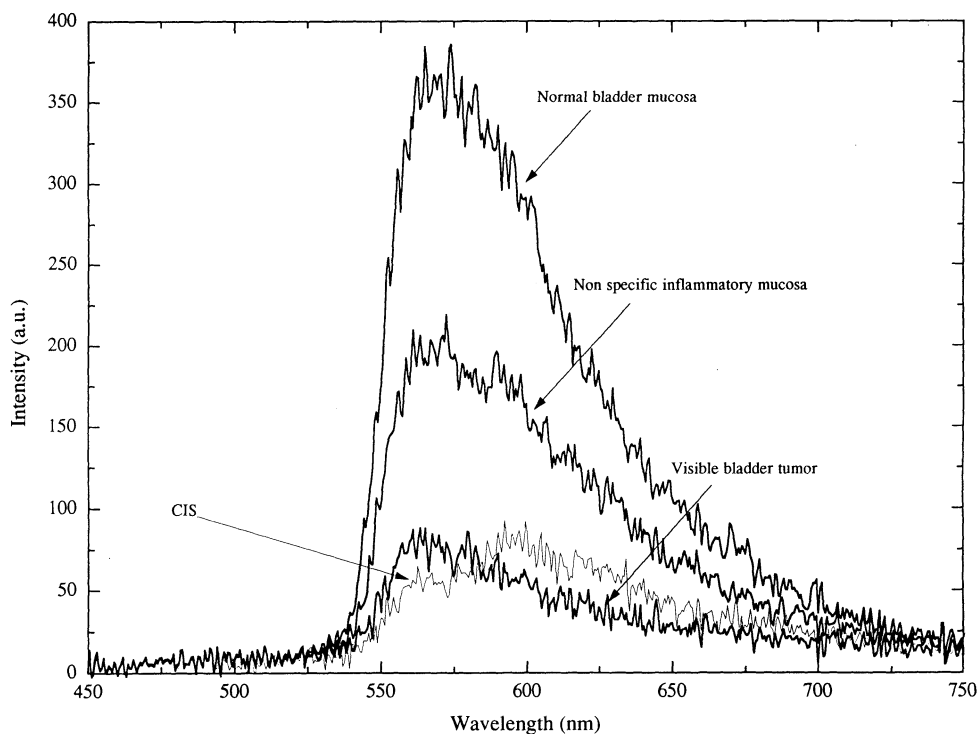


Figure 3. 480 nm induced fluorescence of normal bladder mucosa, non-specific inflammatory mucosa, visible bladder tumors and CIS

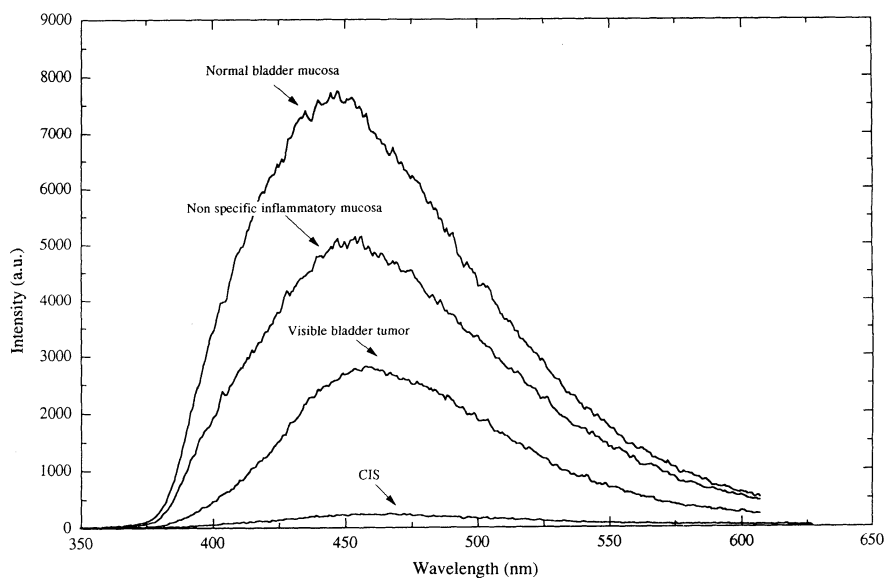


Figure 4. 337 nm induced fluorescence of normal bladder mucosa, non specific inflammatory mucosa, visible bladder tumors and CIS

Finally, excitation was performed using an excimer laser emitting at 308 nm, corresponding to the absorption spectral region of chromophores such as Tryptophan (Trp) or collagen.^{11,12} The emission of normal bladder mucosa appeared as a composite emission with two poorly resolved maxima around 380 nm and 450 nm (Figure 5) corresponding respectively to collagen fluorescence arising from the lamina propria and NADH emission from urothelial cells. Visible bladder tumors spectra, regardless of stage and grade, were strongly modified, with a maximum at 360 nm assigned to Trp and a second band at 450 nm of weak intensity attributed to NADH. Despite an overall reduction in intensity, CIS spectral shape was very similar to that of any visible bladder tumor (Figure 5).

Thus upon 308 nm excitation, two main features appear in tumor spectra: i) a screening of collagen fluorescence by a thickened urothelium preventing excimer laser light from reaching the lamina propria. ii) a reduced expression of NADH confirming the presence of different redox conditions. Therefore, when using 308 nm for excitation, the presence of two distinct fluorescence bands allowed the use of absolute intensity ratioing $R = I_{360} / I_{440}$ nm, in order to get rid of variations of experimental parameters such as excitation energy and geometrical position of the area studied. This ratio could allow for an accurate diagnosis since the difference was statistically highly significant between normal or inflammatory bladder mucosa and any bladder tumor including CIS ($p < 0.0001$) (Table 1).

In conclusion, in the present study we demonstrate that LIAFS has a real potential in demarcating normal from tumor bladder tissues including CIS. The use of 308 nm excitation provides, information related to endogenous fluorophores (i.e. Trp, collagen, NADH) and allows a more accurate diagnosis using fluorescence intensity ratios at 360 and 440 nm.

We are currently developing a prototype of autofluorescence ratio imaging using an ultraviolet continuous source for excitation and a detection system composed of two narrow band-pass filters (360-380 nm and 440-460 nm) and a charge-coupled device (CCD) camera.

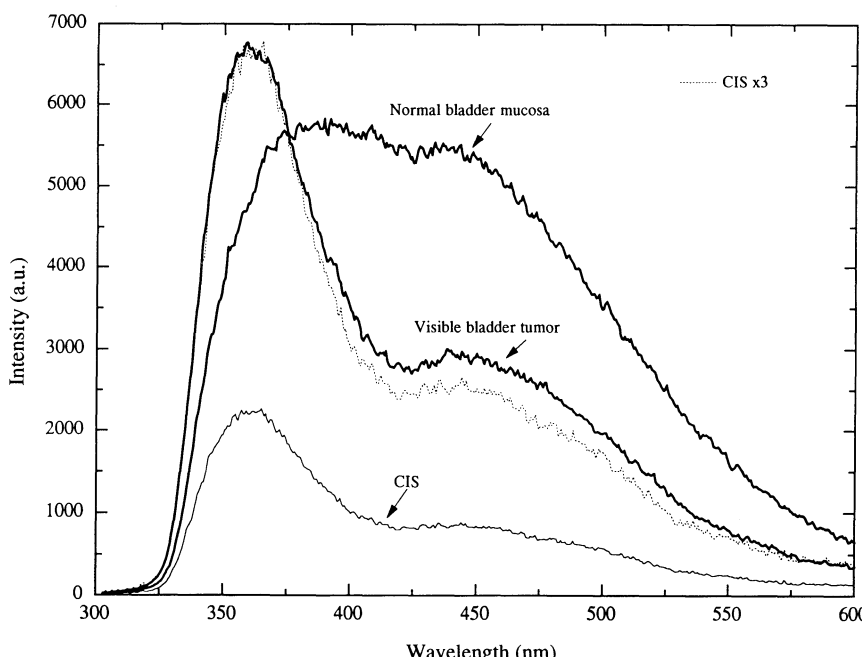


Figure 5. 308 nm induced fluorescence of normal bladder mucosa, visible bladder tumors and CIS

Table 1. Mean fluorescence intensities at 360 and 440nm and ratio values together with standard deviations. CIS are included into bladder tumor group.

	I 360 (a. u.)	I 440 (a. u.)	R
Normal bladder mucosa (n=25)	6570 ± 3747	7450 ± 3819	0.87 ± 0.19
Non specific inflammatory mucosa (n=13)	5893 ± 4270	4853 ± 3847	1.28 ± 0.40
Bladder tumors(n=26)	6097 ± 3742	1979 ± 1084	3.04 ± 0.64
	NS a NS b	* a * b	** a ** b

* p < 0.05

** p< 0.0001

NS not significantly different

a compared to normal bladder mucosa

b compared to non specific inflammatory mucosa

We believe that this instrumentation could become in the near future a useful adjunct for precise mapping of urothelial CIS of the bladder.

REFERENCES

1. M.L.A. Hudson , H.W.Herr: Carcinoma *in situ* of the bladder.*J. Urol.*, 153:564 (1995).
2. T.G. Papazoglu : Malignancies and atherosclerotic plaque diagnosis - is laser induced fluorescence spectroscopy the ultimate solution. *J. Photochem. Photobiol. B-Biol.* 28:3 (1995).
3. R.C. Benson, G.M.Jr. Farrow, J.H.Kinsey: Detection and localization of *in situ* carcinoma of the bladder with hematoporphyrin derivative. *Mayo Clin. Pro.* 548 (1982).
4. T.J. Dougherty, M.Cooper, T.S. Mang : Cutaneous phototoxic occurrences in patients receiving photofrin. *Laser Surg. Med.* 10: 485 (1990).
5. M. Kriegmair, R.Baumgartner, R.Knuechel, P.Steinbach , A.Ehsan , W. Lumper, F.Hofstädter, A.Hofstetter: Fluorescence photodetection of neoplastic urothelial lesions following intravesical instillation of 5-aminolevulinic acid. *Urology.* 44:836 (1994).
6. J. Blais, C. Amirand, J.P. Ballini, P. Debey, MT. Foultier, T.Patrice : Photofrin-induced fluorescence in progressive and regressive murine colonic cancer cells : correlation with cell photosensitivity. *J. Photochem. Photobiol. B-Biol.* 27:225 (1995).
7. R.C. Benson, R.A.Meyer, M.E..Zaruba, G.M. McKann: Cellular autofluorescence. Is it due to flavins ? *J. Histochem. Cytochem.* 27:44 (1979).
8. M.A. Pollack, A.Taylor, J.Taylor, RJ.Williams: B vitamins in cancerous tissues. I. Riboflavin. *Cancer Res.* 2:739 (1942).
9. B.Chance, B.Schoener , Fluorometric studies of flavin component of the respiratory chain. in: Flavins and Flavoproteins p 510, Slater, ed, Elsevier Publishing Company, New York (1966).
10. B.Chance, P.Cohen, F.Jöbsis, B.Schoener.: Intracellular oxidation-reduction states *in vivo*, *Science*: 137:499 (1962).
11. J.R. Lakowicz : Protein fluorescence. in: Principles of fluorescence spectroscopy, p.341, New York Plenum Press (1983).
12. K.T.Schomacker, J.K.Frisoli, C.C.Compton, T.J.Flotte, J.M.Richter, N.S.Nishioka , T.F.Deutsch: Ultra-violet laser-induced fluorescence of colonic tissue : Basic biology and diagnostic potential. *Lasers Surg. Med.*12:63 (1992).

FLUORESCENT IMAGING OF MEMBRANE POTENTIAL COMPONENTS

Eitan Gross,^{1,2} Richard S. Bedlack, Jr.,² and Leslie M. Loew²

¹ Department of Physiology and Biophysics
Case Western Reserve University
10900 Euclid Ave., Cleveland, Ohio, 44106-4970

² Department of Physiology
University of Connecticut Health Center
Farmington, Connecticut, 06030-3505

INTRODUCTION

The behavior of a given channel can be different in different regions of a cell. Belardetti et al.¹ pointed out that Na channels in invertebrate axons and growth cones inactivate much faster than Na channels in somata. Upon severing the neurite of a crustacean peptidergic neuron, Meyers² displayed current-voltage curves for both Na and Ca currents that appear to be shifted to less depolarized voltage in the isolated lamellipodium relative to the soma. Llinás and his coworkers have shown that calcium influx occurs almost exclusively in the dendrites of Purkinje cells³⁻⁶ even though the Ca channels responsible for this current can also be found in somata⁷; this group found subtle differences in the electrophysiological properties of the Ca channels in these two regions of Purkinje cells⁷. Taken as a whole, these observations are important because they suggest that different regions of a neuron could respond differently to the same stimulus *without differences in channel distribution* between the regions.

The mechanism underlying such regional variations in channel function remains unclear. Although voltage-gated channels are usually described in terms of voltage dependence, it is important to emphasize that the regulatory elements within them (e.g. gating charges) are, fundamentally, responding to the potential gradient at their specific location in the plasmalemma - the intramembrane electric field. Therefore, structurally similar ion channels might behave differently along the surface of a neuron if the endogenous intramembrane electric field they are experiencing is non-uniform.

As a first step toward testing this hypothesis, we have developed a method for mapping the intramembrane electric field along the surface of a cell by dual wavelength ratiometric imaging of a membrane-soluble potential-sensitive fluorescent dye, di-8-ANEPPS^{8,9}. In most of the systems that have been investigated, the dye response can be understood in terms of an electrochromic mechanism^{10,11} in which its absorbance and

fluorescence spectra are shifted in the presence of an electric field. Since ratiometric measurements eliminate artifacts due to uneven dye concentration¹², the probe can be used to measure regional variations in intramembrane electric field.

EXPERIMENTAL PROCEDURES

Liposomes

Liposomes were prepared as described previously⁹. Briefly, egg phosphatidylcholine was mixed with di-8-ANEPPS (in ethanol). Cholesterol, 6-ketocholestanol, or phloretin, in an organic solvent were added to this solution. The solvent was evaporated and 2 ml aqueous solution was added to the dried lipid film. A clear liposome suspension was formed by sonicating for 5 min with a probe sonicator. Unless otherwise stated, the final lipid and dye concentrations in the experiment were 2.5 mg/ml and 9.0 μ M, respectively.

Fluorescence Ratios (R)

Fluorescence ratios of the liposomal dye were measured on a dual wavelength fluorescence spectrophotometer. Emission at 620 nm was excited from two excitation monochromators set at 440 nm and 530 nm. Excitation was rapidly alternated between the two excitation wavelengths via a 400-Hz chopper.

Measuring Intramembrane Electric Fields

Differentiating N1E-115 cells on glass coverslips were stained with di-8-ANEPPS, mounted in a thermostated chamber and visualized using a Nikon Diaphot microscope with a 63x 1.4 N.A. objective as described previously¹³. Dual wavelength image pairs (excitation at 440 nm and 530 nm; emission > 570 nm) of single cells were acquired with a CCD camera before and after an exchange of the salt solution. Fluorescence ratios (R) were calibrated against valinomycin-mediated K⁺ diffusion potentials⁸. Membrane potential was converted to intramembrane electric field by dividing by 8 Å, taken as the extended length of the di-8-ANEPPS molecule. To facilitate comparisons, intramembrane electric field variations were mapped relative to the soma, which was set to zero.

RESULTS

Dual wavelength ratiometric imaging of di-8-ANEPPS in the membrane of differentiating N1E-115 mouse neuroblastoma cells provided us with a striking result: the intramembrane electric field along the surface of these cells was not uniform (Fig. 1A). When the cells were divided into five equally sized zones of membrane; analysis of variance testing confirmed that there was a difference ($p < 0.001$) in intramembrane electric field between the regions (Fig. 1B). Two distinct populations within the regions have been defined: a population corresponding to the somata (regions "A" and "B") and a population corresponding to the neurites ("C", "D" and "E"). Defining the "positive" field direction to be from the cytosolic to the external face of the membrane, the mean intramembrane local electric field associated with the neurites was 9.5 ± 2.0 (S.E.) mV/Å more positive than the mean intramembrane electric field associated with the somata.

Intramembrane electric fields have three components (Fig. 2): transmembrane potentials (arising from differences in ion concentrations between the extracellular and intracel-

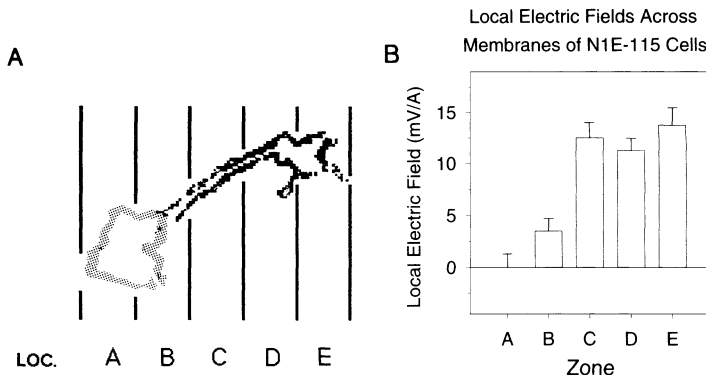


Figure 1. (A) A map of the intramembrane electric field along the surface of a single N1E-115 neuroblastoma cell. Each cell was divided into five equally sized zones, each of which covers a distinct location as shown. (B) The average intramembrane electric field in a zone as a mean of 20 different N1E-115 cells. Intramembrane electric field variations were referenced to the average in zone "A", taken as 0. Note that the zones appear to fall into two distinct populations, one from the soma and a separate one from the neurite. A color representation of this figure can be found following p. 214.

lular fluids)⁽¹⁴⁾, surface potentials (arising from differences in charge density along the surface of the outer and inner faces of the membrane)⁽¹⁵⁾ and dipole potentials (arising from the aligned molecular dipoles of lipid ester groups or the water molecules adjacent to them)⁽¹⁶⁻¹⁹⁾. Only transmembrane potentials are amenable to measurement using the standard electrophysiological methods. Dual wavelength excitation of di-8-ANEPPS can be analyzed ratiometrically⁸ to measure a local sum of the intramembrane electric fields associated with transmembrane potentials, surface potentials and dipole potentials⁹. The approximate location of the sensor portion of the dye is indicated in Figure 2 and defines the transverse position within the membrane at which di-8-ANEPPS measures an electric field.

We initially considered that the intramembrane electric field variation might be due to transmembrane potential differences between the neurites and the somata (cf Fig 2a.). It has been observed, for example, that ion channels are not uniformly distributed over the neuronal plasmalemma; indeed, in N1E-115 cells, L-type calcium channels are much more prevalent in neurites than in somata²⁰. An uneven distribution of channels could lead to

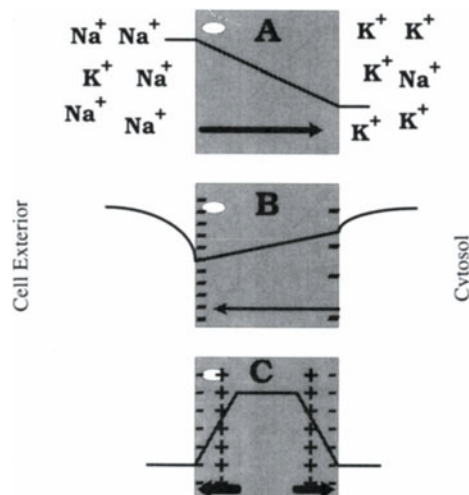


Figure 2. The components of intramembrane electric fields. The intramembrane electric field is depicted as an arrow pointing in the field direction and with a thickness representing the field intensity. (a) The transmembrane potential. (b) The surface potential. (c) The dipole potential. The putative location of one di-8-ANEPPS molecule in the membrane, with respect to the electric potential profile, is also shown.

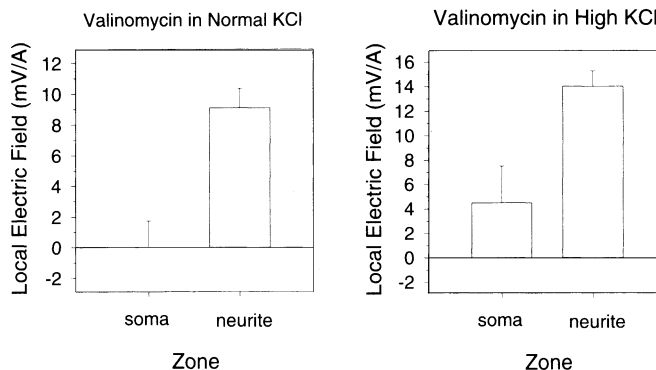


Figure 3. (left) Intramembrane local electric field profile averaged across 10 different NIE-115 cells in a balanced salt solution supplemented with 0.3 μ M valinomycin. Cells were divided into two zones: neurite and soma. (right) The intramembrane electric field profile of the same cells after a solution exchange in which the [KCl] is increased from 5.5 to 35.5 mM and [NaCl] is reduced from 130 to 100 mM, in the presence of valinomycin.

uneven ion conductances, non-uniform transmembrane potentials and thus, a non-uniform intramembrane electric field. We tested this hypothesis by adding valinomycin, a potassium ionophore, to our cells (Fig. 3). This should set the transmembrane potential equal to the potassium equilibrium potential over all regions of the cell membrane, thereby overwhelming any intrinsic heterogeneities in ion channel distribution. The overall intramembrane electric field was offset by varying concentrations of KCl in the presence of valinomycin. However, the regional variation in intramembrane electric field remained, despite such normalization of the transmembrane potential. Thus, the measured non-uniformity could not have been caused by unequal ion conductances between neurites and somata.

Next, we attempted to determine whether the intramembrane electric field variation could be explained by surface potential differences between neurites and somata. Unequal surface charge densities between the neurite and the soma can, in principle, lead to unequal surface potentials (Fig. 2b.) and a non-uniform intramembrane electric field. However, an extremely large difference in surface charge would be required to fully explain the measured intramembrane electric field variation. Assuming a 40 Å membrane thickness, the gradient in surface potential would have to be 80-90 mV; using the Guoy-Chapman theory²¹; this means that the neurite would need a mole fraction of negative lipids near 100% on its outer surface, with the soma and the entire inner surface being neutral. Nevertheless, we directly tested the surface potential hypothesis by increasing the concentration of calcium in the extracellular fluid (Fig. 4). This manipulation should screen surface charge along the outer surface of the neuron, thereby decreasing the intramembrane electric field. Figure 4 shows that the intramembrane electric field all over the cell did slightly decrease with calcium elevation. However, if a greater density of negative charge on the outer surface of neurites compared to somata was the origin of the non-uniform intramembrane electric field, high extracellular calcium should have normalized it. Since the intramembrane electric field remained significantly different in the neurite compared with the soma after elevation of calcium, the non-uniformity could not have been caused by unequal surface charge distribution between these regions.

A final possibility was that the source of the non-uniform intramembrane electric fields was a difference in dipole potential (Fig 2c.) between the neurites and the somata. Dipole potential is highly dependent on the cholesterol to phospholipid ratio in the mem-

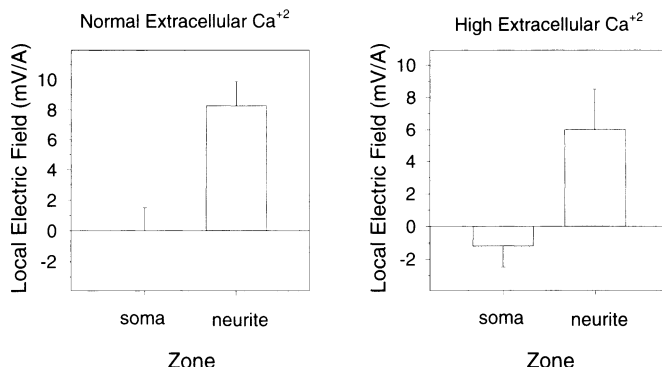


Figure 4. (left) Intramembrane local electric field profile averaged across 10 cells in a balanced salt solution. (right) Same cells after a solution exchange with [CaCl₂] increased from 1.8 to 11.8 mM and [NaCl] decreased from 130 to 120 mM.

brane²². Differences in cholesterol to phospholipid ratio between the membranes of neurites and the membranes of somata have been recently described²³. We studied the effect of cholesterol on the dye's fluorescence ratio in a bilayer model system where cholesterol to phospholipid ratio can be easily manipulated.

In Figure 5, we show the effect of increasing the mole fraction of cholesterol in phosphatidyl choline liposomes on fluorescence ratio (R) of the dye incorporated into the liposomal bilayer. As can be seen, 50% cholesterol causes a 1.5-fold increase in R. 6-Ketocholestano (6-KC) and phloretin are known to increase and decrease, respectively, the internal dipole potential when incorporated into bilayers^{19,24}. We thus measured the effects of these compounds, incorporated into liposomal bilayer, on R. Increasing the mole fraction of 6-KC from 0 to 30% caused a 2.5-fold increase in R, while a 3-fold decrease was obtained by 15% phloretin (Fig. 5). The effects of cholesterol, 6-KC and phloretin on R suggest that R is sensitive to changes in the intrinsic bilayer dipole potential.

A total potential model was developed in which the dipole potential is explicitly derived from an array of dipoles¹⁷. This model was recently extended by Franklin and Cafiso¹⁹ to explain the effects of 6-KC and phloretin on the rate of hydrophobic ion currents through PC vesicle membranes. We used dipole potential values from this work to plot R as a function of dipole potential in Fig. 6. Dipole potential for pure PC is taken as the reference point at which R is set to unity by appropriate normalization (or, equivalently, by balancing the dual wavelength optics). The line is the linear least-squares fit to the data. Although over such large changes a linear fit is not strictly theoretically valid, it permits a useful approximate comparison to the sensitivity of R to transmembrane potential. R changes by 0.8 units

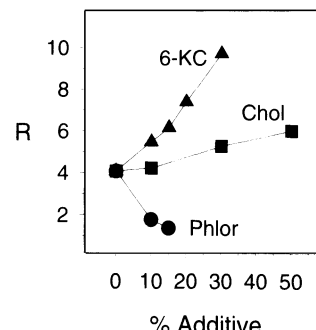


Figure 5. The ratio of the fluorescence intensity excited at 440 nm to that excited at 530 nm, R, as a function of the mole fractions of the indicated membrane additives. The emission wavelength was 620 nm.

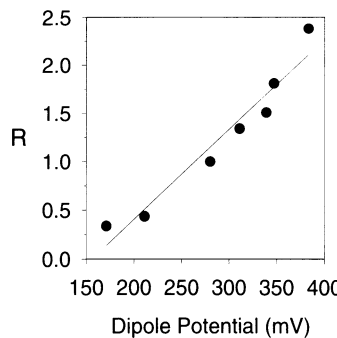


Figure 6. The dependence of R on the dipole potential.

for a change of 100 mV in dipole potential, as compared to a change of 0.1 for a 100 mV change in transmembrane potential. This difference is so large because the electric field (i.e. voltage gradient) at the location of the dye in the membrane is much greater for the dipole potential than for a transmembrane potential of the same size. Taking the data a step further, they imply that for dipole potential, the voltage gradient spans a distance $\leq 1/8$ that of the transmembrane potential.

DISCUSSION

Links between cholesterol to phospholipid ratio, intramembrane electric field, and electrophysiology, may prompt a reexamination of how cholesterol influences the biology of cells. An especially pertinent example involves differentiation of the N1E-115 neuroblastoma cells used in this study. N1E-115 cells increase their cholesterol to phospholipid ratio concomitant with developing neurites, and preventing this increase (with inhibitors of cholesterol synthesis) can block the formation of neurites²⁵. A possible explanation may involve cholesterol's effect on dipole potential and intramembrane electric field. Depolarizing the transmembrane potential across N1E-115 plasmalemmæ by increasing extracellular potassium promotes neurite outgrowth and initiation, presumably by activating voltage gated calcium channels²⁶. It is important to appreciate that the channel moieties which sense these depolarizations are really responding to local intramembrane electric field. An increased cholesterol content would affect the intramembrane electric field within the outer leaflet of the bilayer in the same direction as the described depolarizations, sensitizing, or perhaps even initiating, the cascade that culminates in enhanced neurite growth.

Examination of the image in Figure 1 shows that the intramembrane electric field may be heterogeneous on a still more microscopic level than the statistically significant differences between somata and neurites that we have been able to show in this study. Some regions of the growth cone are particularly irregular, with excursions toward both polarized (green) and depolarized (red) potentials within membrane patches of just a few hundred nanometers. We have not established any statistical significance for this more focal variability, but it could correspond to localized electric fields set up by charged residues within clusters of membrane proteins. Indeed, this could, in principle, be a source for variations in intramembrane electric field on a molecular scale both laterally along the surface and within the thickness of a cell membrane.

In summary, we have shown that the intramembrane electric field in neurons, which regulates several components of signal transduction, is intrinsically different in neurites and

somata. The most likely explanation for this phenomenon is a difference in dipole potential, perhaps stemming from a difference in cholesterol-to-phospholipid ratio, between neurites and somata. Thus, the distribution of lipids within the plasmalemma may influence the process of differentiation and the ability of the cell to sustain spatially distinct structures and functions.

REFERENCES

1. Belardetti, F., Schacher, S. & Siegelbaum, S. A. (1986). Action potentials, macroscopic and single channel currents recorded from growth cones of *Aplysia* neurones in culture. *J. Physiol.*, 374, 289-313.
2. Meyers, D. E. (1993). Distribution of ionic currents in the soma and growing region of an identified peptidergic neuron in defined culture. *J. Neurophysiol.*, 69, 406-415.
3. Llinás, R. & Sugimori, M. (1980). Electrophysiological properties of *in vitro* Purkinje cell somata in mammalian cerebellar slices. *J. Physiol.*, 305, 171-195.
4. Llinás, R. & Sugimori, M. (1980). Electrophysiological properties of *in vitro* Purkinje cell dendrites in mammalian cerebellar slices. *J. Physiol.*, 305, 197-213.
5. Tank, D. W., Sugimori, M., Connor, J. A. & Llinás, R. R. (1988). Spatially resolved calcium dynamics of mammalian Purkinje cells in cerebellar slice. *Science*, 242, 773-777.
6. Sugimori, M. & Llinás, R. R. (1990). Real-time imaging of calcium influx in mammalian cerebellar Purkinje cells *in vitro*. *Proc. Natl. Acad. Sci. U. S. A.*, 87, 5084-5088.
7. Usowicz, M. M., Sugimori, M., Cherksey, B. & Llinás, R. (1992). P-type calcium channels in the somata and dendrites of adult cerebellar Purkinje cells. *Neuron*, 9, 1185-1199.
8. Montana, V., Farkas, D. L. & Loew, L. M. (1989). Dual wavelength ratiometric fluorescence measurements of membrane potential. *Biochemistry*, 28, 4536-4539.
9. Gross, E., Bedlack, R. S. & Loew, L. M. (1994). Dual-wavelength ratiometric measurement of the membrane dipole potential. *Biophys. J.*, 67, 208-216.
10. Loew, L. M., Bonneville, G. W. & Surow, J. (1978). Charge shift optical probes of membrane potential. Theory. *Biochemistry*, 17, 4065-4071.
11. Loew, L. M., Scully, S., Simpson, L. & Waggoner, A. S. (1979). Evidence for a charge-shift electrochromic mechanism in a probe of membrane potential. *Nature*, 281, 497-499.
12. Tsien, R. Y. & Poenie, M. (1986). Fluorescence Ratio Imaging: A new window into intracellular ionic signaling. *TIBS*, 11, 450-455.
13. Bedlack, R. S., Wei, M.-d., Fox, S. H., Gross, E. & Loew, L. M. (1994). Distinct electric potentials in soma and neurite membranes. *Neuron*, 13, 1187-1193.
14. Hille, B. (1992). *Ionic Channels of Excitable Membranes*, (Sinauer Associates Inc., Sunderland, MD, USA), 2nd Ed.
15. McLaughlin, S. (1989). The electrostatic properties of membranes. *Ann. Rev. Biophys. Biophys. Chem.*, 18, 113-136.
16. Hladky, S. B. & Haydon, D. A. (1973). Membrane conductance and surface potential. *Biochim. Biophys. Acta*, 318, 464-468.
17. Flewelling, R. F. & Hubbell, W. L. (1986). The membrane dipole potential in a total membrane potential model. Applications to hydrophobic ion interactions with membranes. *Biophys. J.*, 49, 541-552.
18. Honig, B. H., Hubbell, W. L. & Flewelling, R. F. (1986). Electrostatic interactions in membranes and proteins. *Ann. Rev. Biophys. Biophys. Chem.*, 15, 163-193.
19. Franklin, J. C. & Cafiso, D. S. (1993). Internal electrostatic potentials in bilayers: measuring and controlling dipole potentials in lipid vesicles. *Biophys. J.*, 65, 289-299.
20. Silver, R. A., Lamb, A. G. & Bolsover, S. R. (1990). Calcium hotspots caused by L-channel clustering promote morphological changes in neuronal growth cones. *Nature*, 343, 751-754.
21. McLaughlin, S. (1977). Electrostatic potentials at membrane-solution interfaces. In Bronner, F. & Kleinzeller, J. (eds.), *Current Topics Membranes and Transport*, Academic Press, New York, NY, USA Vol. 9, pp. 71-144.
22. Szabo, G. (1974). Dual mechanism for the action of cholesterol on membrane permeability. *Nature*, 252, 47-49.
23. Igarashi, M., Waki, H., Hirota, M., Hirabayashi, Y., Obata, K. & Ando, S. (1990). Differences in lipid composition between isolated growth cones from the forebrain and those from the brainstem in the fetal rat. *Dev. Brain Res.*, 51(1), 1-10.

24. Bechinger, B. & Seelig, J. (1991). Interaction of electric dipoles with phospholipid head groups. A ^2H and ^{31}P NMR study of phloretin and phloretin analogues in phosphatidylcholine membranes. *Biochemistry*, 30, 3923-3929.
25. de Laat, S. W., Bluemink, J. G., Boonstra, J., Mummery, C. L., van der Saag, P. T. & van Zoelen, E. J. J. (1984). Membrane fluidity in growth and differentiation; the neuroblastoma cell model. In Shinitzky, M. (ed.), *Physiology of Membrane Fluidity*, CRC Press, Boca Raton, FL, USA Vol. 2, pp. 21-51.
26. Anglister, L., Farber, I. C., Shahar, A. & Grinvald, A. (1982). Localization of voltage-sensitive calcium channels along developing neurites: their possible role in regulating neurite elongation. *Dev. Biol.*, 94, 351-365.

PROBING OF MICROTUBULE STRUCTURES WITH MONOCLONAL ANTIBODIES AND IMMUNOFLUORESCENCE MICROSCOPY

Pavel Dráber, Eduarda Dráberová, and Vladimír Viklický

Institute of Molecular Genetics
Academy of Sciences of the Czech Republic
142 20 Prague 4, Czech Republic

1. INTRODUCTION

Microtubules are filamentous polymers that combine stability of structure with an ability to organize rapidly in response to internal and external signals. Microtubules are assembled from $\alpha\beta$ -tubulin heterodimers and a collection of microtubule-associated proteins. γ -Tubulin is a relatively new member of the tubulin family that is restricted to the microtubule organizing centers. It was hypothesized that γ -tubulin plays a crucial role in nucleation and anchorage of microtubules¹. In vertebrates α - and β -tubulin subunits exhibit high heterogeneity, and more than 20 tubulin charge variants (isotubulins) can be distinguished by horizontal high-resolution isoelectric focusing². Some of the isoforms result from the expression of multiple tubulin genes. Gene products differ primarily in the C-terminal variable domain consisting of 15 amino acids. On the basis of these variable domains and cell type distribution several evolutionary conserved isotypic classes were identified³. The tubulin heterogeneity is further increased by post-translational modifications. The following variations have been described for brain tubulin: reversible removal of C-terminal tyrosine, acetylation, polyglutamylation, phosphorylation and removal of penultimate glutamyl at the C-terminal end leading to $\Delta 2$ -tubulin. Except for acetylation, all of these modifications occur in the C-terminal, hypervariable regions of both subunits⁴. Although the structure of microtubules is known from electron microscopy combined with image reconstruction, X-ray scattering and video microscopy, information on tubulin structure is indirect and derived mostly from biochemical experiments. A high resolution crystal structure for $\alpha\beta$ -tubulin heterodimer is still missing and our knowledge of actual exposition of tubulin surfaces in microtubules in living cells is limited. Immunofluorescence microscopy with specific antibodies directed to small chemically defined zones of the tubulin molecule is indispensable when investigating tubulin isotype expression, post-translational modifications, low-resolution structure and function. Here we report on the application of immunofluorescence microscopy in the probing of microtubules with domain-specific

antibodies, in the study of expression of neuron-specific class-III β -tubulin and in the localization of γ -tubulin in taxol-treated cells.

2. MATERIAL AND METHODS

2.1. Antibodies

Preparation and characterization of mouse monoclonal antibodies against tubulin subunits were described previously^{5,6}. Monoclonal antibody YL 1/2 against tyrosinated form of α -tubulin⁷ was kindly provided by Dr. J. Kilmartin (Cambridge, UK), monoclonal antibody 6-11B-1 against acetylated α -tubulin⁸ was a kind gift from Dr. G. Piperno (New York, NY, USA) and monoclonal antibody GT335 against glutamylated forms of α - and β -tubulin subunits⁹ was kindly donated by Dr. A. Wolff (Paris, France). Reactivity of antibodies with tubulin structural domains⁵ is summarized in Table 1. For double-label experiments the TU-04 antibody against α -tubulin was directly conjugated with lissamine rhodamine B sulphonylchloride. Fluorescein isothiocyanate (FITC)-conjugated anti-mouse Ig antibody was from Sevac (Prague, Czech Republic), FITC-conjugated antibody against mouse IgG was from Sigma Chemie (Deisenhofen, Germany), indocarbocyanine (Cy3)-conjugated antibody against mouse IgM was from Jackson Immunoresearch Laboratories, Inc. (West Grove, PA, USA).

Table 1. Binding of monoclonal antibodies to interphase microtubules of 3T3 cells

Antibody	Domain specificity*	Microtubules**		
		Fixed	Unfixed	In living cells
TU-01	α_N	+	-	-
TU-02	α_N	+	-	-
TU-03	α_N	+	-	-
TU-05	α_N	+	-	-
TU-09	α_N	+	-	-
6-11B-1	α_N	+	-	ND
TU-04	α_C	+	-	-
YL 1/2	α_C	+	+	+
TU-07	α	+	+	+
TU-10	$\alpha\beta$	+	+	+
GT335	$\alpha_C\beta_C$	+	+	ND
TU-06	β_N	+	-	-
TU-13	β_N	+	-	-
TU-11	β_C	+	+	+
TU-12	β_C	+	+	+
TU-14	β_C	+	+	+
TU-20***	β_C	+	+	ND

* α_N , N-terminal domain of α -tubulin, α_C , C-terminal domain of α -tubulin, β_N , N-terminal domain of β -tubulin, β_C , C-terminal domain of β -tubulin.

**Microtubules: Fixed, cells extracted with 0.2% Triton X-100 and fixed in 3% formaldehyde; Unfixed, cells extracted with 0.2% Triton X-100 in a stabilizing buffer containing 10 μ M taxol; In living cells, cells injected with antibodies.

***TU-20 antibody was tested on mouse neuroblastoma Neuro2a cells. +, decoration of microtubules; -, no decoration of microtubules; ND, not done

2.2. Preparation of Anti-Peptide Monoclonal Antibodies

A 16-amino-acid peptide EYHAATRPDYISWGTQ corresponding to the human γ -tubulin sequence 434-449¹⁰ was synthesized. A cystein had been added to the amino terminus of the peptide in order to allow oriented coupling to the maleimide activated keyhole limpet hemocyanin (KLH) or bovine serum albumin (BSA) using Imject Activated Immunogen Conjugation Kit (Pierce, Rockford, IL, USA). Mice were immunized with peptide coupled to KLH. Sera were monitored for antibody activity by enzyme-linked immunosorbent assay (ELISA) on peptide coupled to BSA. Construction of hybridomas and production of monoclonal antibodies followed standard procedures. Antibody TU-30 was selected for further studies. A similar strategy was used for preparation of monoclonal antibody against neuron-specific class-III β -tubulin. The 8-amino-acid peptide ESESQGPK, corresponding to the human class-III β -tubulin sequence 441-448³, with cystein added to the amino terminus of the peptide was used as an antigen.

2.3. Cells

Mouse embryonic fibroblasts 3T3, mouse neuroblastoma Neuro 2a and human cervical adenocarcinoma HeLa S3 were grown on coverslips in RPMI-1640 medium supplemented with L-glutamine, sodium pyruvate, antibiotics and 10% heat-inactivated fetal calf serum. Neuro-2a cells were also cultured in serum-free medium for 3 days to allow formation of projections. To some of the cultures, taxol at 10 μ M was added for 1, 6, 18 and 24 hours.

2.4. Microinjection and Immunofluorescence

3T3 cells were microinjected with purified antibodies at a concentration of 1-2 mg/ml in microinjection buffer using a Leitz Diavert microscope and a Leitz micromanipulator⁵. Approximately one tenth of a cell volume was usually injected. After injection the cells were incubated at 37°C for 1 hr before fixation. Extraction and fixation steps were carried out in microtubule stabilizing buffer (MSB) consisting of 0.1 M KMes, 2 mM EGTA, 2 mM MgCl₂ and a 4% polyethylene glycol 6000, pH 6.9. Cells were usually extracted for 1 min with 0.2% Triton X-100 at 37°C and fixed for 20 min in 3% formaldehyde at the same temperature. Alternatively, the cells were fixed for 10 min in methanol at -20°C followed by 6 min in acetone at -20°C. To prepare unfixed detergent-extracted cytoskeletons, the cells were rinsed at 37°C with MSB, extracted for 1 min at 37°C with 0.2% Triton X-100 in MSB containing microtubule-stabilizing drug taxol at 10 μ M concentration and rinsed in MSB at the same temperature. Indirect immunofluorescence and double-label indirect/direct immunofluorescence with two monoclonal antibodies was performed as described¹¹. Immunoglobulin class-specific secondary anti-mouse antibodies were used for double-label immunofluorescence employing two monoclonal antibodies of different classes. The slides were incubated 10 min with HOECHST 33258 dye at a concentration of 1 μ g/ml in PBS to detect DNA, mounted in MOWIOL 4-88 and examined with a Leitz Orthoplan microscope equipped with 50/1.00 fluorescence water-immersion objective, epi-illumination using the filter combination cubes N2, I2 and D, and an Orthomat 35 mm camera. Photographs were taken on Kodak Tri-Xpan 400 film and printed on high contrast paper. Neither the control antibody HTF-14 against human transferrin nor the conjugates alone gave any specific staining. Tracing of prints prepared from overexposed negatives helped to place the arrows into identical positions in each pair of prints.

3. RESULTS AND DISCUSSION

To gain insight into the accessibility of tubulin epitopes on microtubules *in vivo*, the distribution of antigenic determinants recognized by corresponding monoclonal antibodies was investigated on microtubules in unfixed detergent-extracted 3T3 cells. For this study we have selected antibodies that react with non-identical antigenic determinants on tubulin structural domains^{5,6} and antibodies against post-translationally modified tubulins, namely YL 1/2 to tyrosinated α -tubulin⁷, 6-11B-1 to acetylated α -tubulin⁸ and GT335 against glutamylated α - and β -tubulins⁹. While all antibodies reacted with fixed microtubules, the antibodies with epitopes located in N-terminal structural domains did not decorate microtubules in unfixed cells. In contrast, only antibodies with epitopes located on C-terminal domains and antibodies TU-07 and TU-10 labelled microtubules on unfixed detergent-extracted cells (Table 1). Double-label experiments revealed that lack of labelling of microtubules was not due to disruption of microtubules with antibodies. As the neuron-specific antibody TU-20 did not react with 3T3 microtubules, immunofluorescence was performed on neuroblastoma Neuro2a cells. To confirm this finding in living cells, the antibodies were injected into interphase 3T3 cells at a concentration of 1-2 mg/ml and the cells were incubated 1 hour at 37°C before fixation. Injection of antibodies YL 1/2, TU-07, TU-10, TU-11, TU-12 and TU-14 resulted in a bright staining of microtubules. On the other hand, only a diffuse staining of cytoplasm was observed after injection of other antibodies (Table 1.) After injection of control antibodies microtubules were not decorated and the appearance of cytoplasmic microtubules was unchanged.

Data summarized in Table 1 indicate that tubulin epitopes on N-terminal structural domains are either unexposed on the microtubule surface of interphase microtubules or are effectively masked by other proteins. The determinants are therefore cryptic in native microtubules and become exposed only after structural distortion produced by fixation. The unreactivity of TU-04 with native microtubules can be explained in a similar way, i.e. the epitope is either located in the more internal part of C-terminal domain or is masked. The sedimentation experiments with antibodies TU-01, TU-02, TU-03, TU-13 and microtubules prepared of purified tubulin indicate, however, that corresponding epitopes are probably occluded by the interaction between tubulin molecules in microtubule wall. The results support a model for orientation of the tubulin dimer in the microtubule wall in which the C-terminal part of both subunits is exposed on the surface of microtubules, whereas considerable regions of the N-terminal domains are either not exposed on the surface of cytoplasmic microtubules or are masked by interacting proteins. Immunofluorescence experiments also demonstrated that stainability of microtubules in detergent-extracted cells with antibodies reflected their reactivity in living cells. A similar finding was recently reported for sea urchin eggs¹².

The sequence variation at the C-terminal zones of β -tubulin isotypes enabled preparation of monoclonal antibodies¹³ that were employed to investigate the differential expression of tubulin isotypes in cultured cell lines and tissues. Previously we have shown that TU-14 antibody reacted in brain with all β -tubulin isotypes, except neuron-specific class-III β -tubulin isotype². To have a complementary antibody, reacting only with class-III β -tubulin, anti-peptide monoclonal antibody TU-20 was prepared. Combination of high-resolution isoelectric focusing with antibodies TU-14, TU-20 and GT335 enabled us to make correlation between individual isotubulins, their isotype origin and post-translational polyglutamylation. Immunofluorescence microscopy on tissue cryosections as well as on formaldehyde-fixed paraffin-embedded material confirmed that TU-20 antibody reacted only with cells of the central or peripheral nervous systems. It is therefore a useful marker for cells of neuronal origin. Example of triple-label staining with antibodies TU-14 and

TU-20 in mixed culture of mouse embryonic 3T3 cells and mouse neuroblastoma Neuro2a is shown in Figure 1. Whereas the TU-14 antibody stained both cell types (Figure 1A), the TU-20 antibody reacted only with neuroblastoma (Figure 1B).

In order to have a specific and standard reagent for detection of γ -tubulin in various cell models, we have prepared monoclonal antibodies against phylogenetically conserved C-terminal peptide of γ -tubulin. As affinity-purified polyclonal antibodies are usually available only in limited amounts, monoclonal antibodies with proper binding characteristic could be useful for isolation of γ -tubulin and its associated proteins. Such antibodies could also help answer the question whether γ -tubulin is the substrate for post-translational modifications and if so, whether γ -tubulin charge variants change during development as was shown for β -tubulins. From the panel of prepared antibodies we have selected the antibody TU-30 for further studies. Specificity of the antibody was confirmed by immunoblotting, ELISA and competition experiments. During the cell cycle TU-30 decorated all typical γ -tubulin-containing structures. Figure 2 shows triple-label staining with anti- α -tubulin antibody, TU-30 antibody and fluorescent DNA-binding dye in 3T3 cells. The TU-30 antibody stained centrosomes and duplicated centrosomes in interphase (Figure 2A-C), spindle poles and two half-spindles within metaphase (Figure 2D-F) and microtubule bundles forming midbodies within telophase (Figure 2G-I). Distribution of γ -tubulin in interphase and mitotic cells is shown also in Fig. 3. The antibody did not decorate interphase microtubules or short aster microtubules at the spindle poles. The antibody reacted with centrosomes in all tested cell lines from evolutionary distant species including avian cells and cultured plant cells from *Nicotiana tabacum*. Testing of the accessibility of antigenic determinant recognized by TU-30 in animal cells prepared under various fixation conditions and in unfixed cells revealed that cold methanol/acetone provided the best visualization of γ -tubulin. When cells were extracted with Triton X-100 and fixed by formaldehyde or glutaraldehyde the antibody did not decorate centrosomes in indirect immunofluorescence with FITC-conjugated anti-mouse antibody. The same negative results were obtained in unfixed, detergent-extracted cells.

Taxol, a microtubule stabilizing drug, causes in interphase cells a rearrangement of microtubules into bundles, and in mitotic cells it induces a spindle disruption and assembly

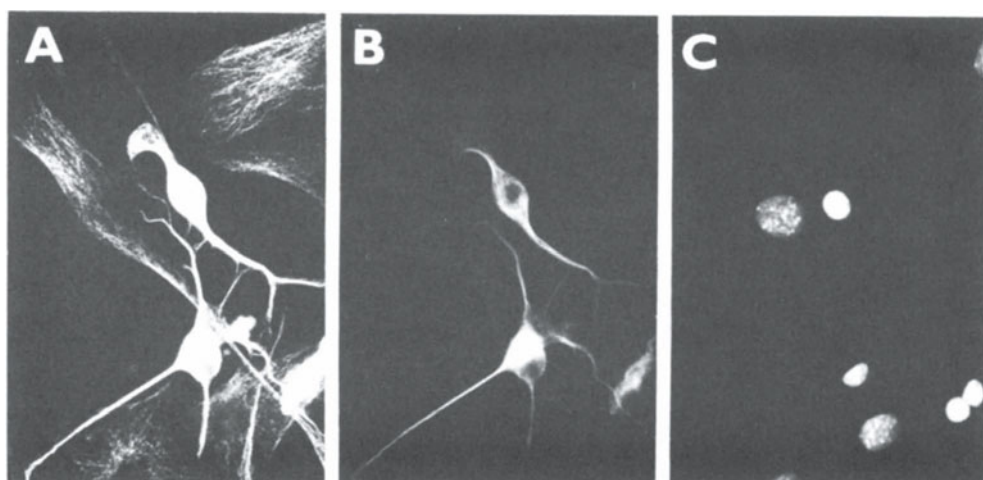


Figure 1. Immunofluorescence triple-label staining of a mixture of Neuro 2a and 3T3 cells with β -tubulin isotype-specific antibodies. Cells were stained with antibody TU-14 specific for β -tubulin isotypes I, II and IV (A), antibody TU-20 specific for β -tubulin isotype III (B) and DNA-binding dye (C). Bar, 10 μ m.

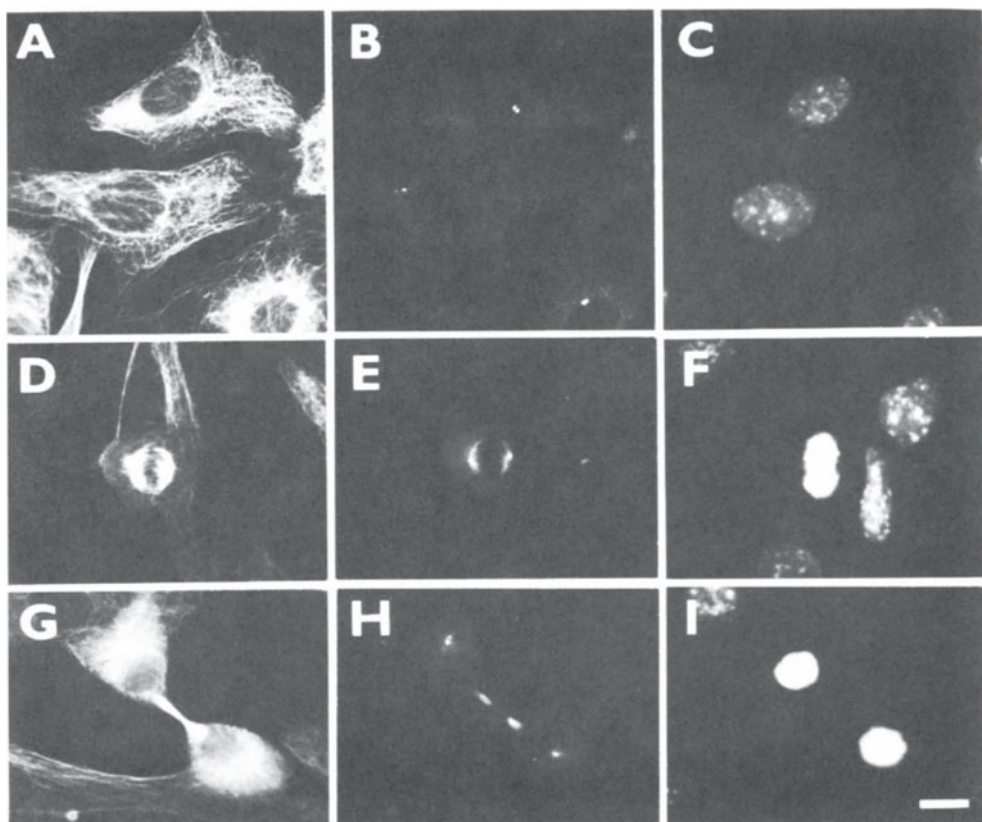


Figure 2. Immunofluorescence triple-label staining of 3T3 cells in various stages of the cell cycle with antibody TU-30 against γ -tubulin. Cells were stained with anti- α -tubulin antibody TU-04 (A, D, G), antibody TU-30 (B, E, H) and DNA-binding dye (C, F, I). The cells in (A-C) are in interphase, the cell in (D-F) is in metaphase and the cell in (G-I) is in telophase. Bar, 10 μ m.

of new microtubule asters¹⁴. 3T3 cells treated with 10 μ M taxol for 18 hours were characterized by multiple nuclei and by typical microtubule arrangements. Triple-label staining with anti- α -tubulin antibody, TU-30 and DNA-binding dye showed that in cells that had entered the mitosis, γ -tubulin was sometimes located in the area where induced aster-like aggregates of short microtubules were found (Arrows in Figure 4A-B). Some 4-20 microtubule asters were found in a single cell. TU-30, however, stained only 1-4 spots in such cells. The localization of γ -tubulin in the microtubule asters was thus limited to only a few asters in one mitotic cell. In the remaining asters no γ -tubulin was detected using immunofluorescence microscopy. The γ -tubulin was also found outside the center of microtubule asters in cells treated with taxol for a shorter (1 and 6 hours) or longer (24 hours) period.

Differential localization of microtubule-asters and γ -tubulin in taxol-treated mitotic cells was not just limited to 3T3 cells. A similar distribution of γ -tubulin was also observed in taxol-treated mitotic HeLa and PtK₂ cells. Figure 4 D-F demonstrates the results of triple-label staining of HeLa cells with anti- α -tubulin antibody, TU-30 and DNA-binding dye. In all taxol-treated mitotic cells the number of microtubule asters exceeded that of γ -tubulin positive spots. These data indicate that in taxol-treated

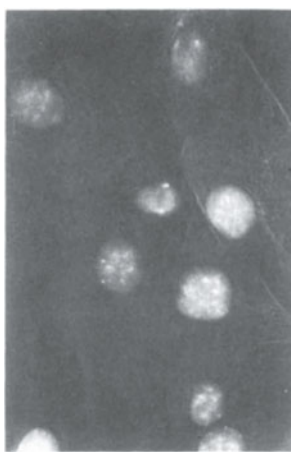


Figure 3. Distribution of g-tubulin in interphase and mitotic 3T3 cells. Cells were stained with anti-tubulin antibody, antibody TU-30 to g-tubulin and DNA-binding dye. A color representation of this figure can be found following p. 214.

mitotic cells microtubule asters are nucleated independently of γ -tubulin or that γ -tubulin is present in amounts undetectable by immunofluorescence microscopy. Other nucleator(s) are probably necessary for generation of taxol-induced asters in cultured somatic cell lines.

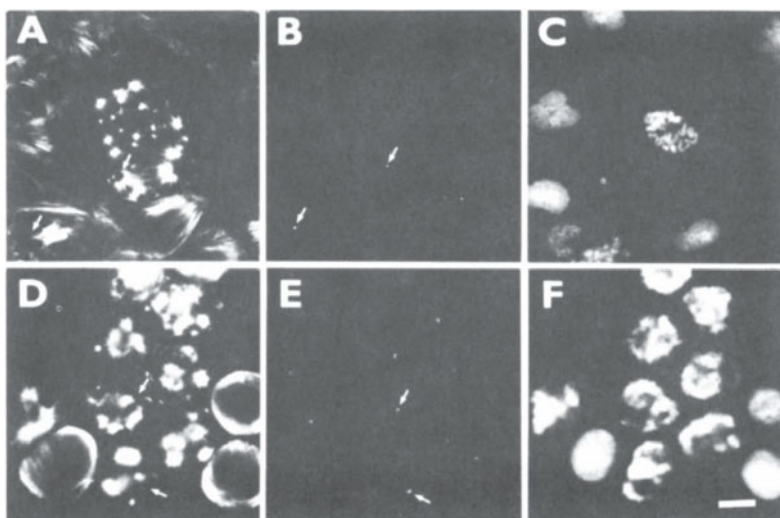


Figure 4. The distribution of γ -tubulin in taxol-treated mitotic 3T3 (A-C) and HeLa (D-F) cells. Cells were incubated for 18 hours with 10 μ M taxol, fixed and triple-label stained with anti- α -tubulin antibody TU-04 (A, D), anti- γ -tubulin antibody TU-30 (B, E) and DNA-binding dye (C, F). Arrows in each pair of prints are placed in identical positions. Bar, 10 μ m.

ACKNOWLEDGMENTS

This work was supported in part by grant 301/94/1674 from the Czech Grant Agency and partly by ERB 3510 PL92 7710 grant from the Commission of the European Communities. The taxol was a generous gift of the Drug Synthesis and Chemistry Branch, Division of Cancer Treatment, National Cancer Institute (Bethesda, MD).

4. REFERENCES

1. H.C. Joshi, M.J. Palacios, L. McNamara, and D.W. Cleveland, γ -Tubulin is a centrosomal protein required for cell cycle-dependent microtubule nucleation, *Nature* 356:80 (1992).
2. I. Linhartová, P. Dráber, E. Dráberová, and V. Viklicky, Immunological discrimination of β -tubulin isoforms in developing mouse brain. Posttranslational modification of non-class III β -tubulins, *Biochem. J.* 288:919 (1992).
3. K.F. Sullivan, and D.W. Cleveland, Identification of conserved and isotype-defining variable region sequences for four vertebrate β tubulin polypeptide classes, *Proc. Natl. Acad. Sci. U.S.A.* 83:4327 (1986).
4. E. Mandelkow, and E.-M. Mandelkow, Microtubules and microtubule-associated proteins, *Curr. Opin. Cell Biol.* 7:72 (1995).
5. P. Dráber, E. Dráberová, I. Linhartová, and V. Viklicky, Differences in the exposure of C- and N-terminal tubulin domains in cytoplasmic microtubules detected with domain-specific monoclonal antibodies, *J. Cell Sci.* 92:519 (1989).
6. P. Dráber, E. Dráberová, I. Linhartová, and V. Viklicky, Tubulin orientation in microtubules probed with domain-specific antibodies, *Acta histochemica, Suppl.* 41: 9 (1992).
7. J.V. Kilmartin, B. Wright, and C. Milstein, Rat monoclonal antitubulin antibodies derived by using a new nonsecreting rat cell line, *J. Cell Biol.* 93:576 (1982).
8. G. Piperno, and M.T. Fuller, Monoclonal antibodies specific for an acetylated form of α -tubulin recognize the antigen in cilia and flagella from a variety of organisms, *J. Cell Biol.* 101:2085 (1985).
9. A. Wolff, B. de Néchaud, D. Chillet, H. Mazarguil, E. Desbruyères, B. Eddé, F. Gros, and P. Denoulet, Distribution of glutamylated α and β -tubulin in mouse tissues using a specific monoclonal antibody, GT335, *Eur. J. Cell Biol.* 59:425 (1992).
10. Y. Zheng, M.K. Jung, and B.R. Oakley, Gamma-tubulin is present in *Drosophila melanogaster* and *Homo sapiens* and is associated with centrosome, *Cell* 65:817 (1991).
11. E. Dráberová, and P. Dráber, A microtubule-interacting protein involved in coalignment of vimentin intermediate filaments with microtubules, *J. Cell Sci.* 106:1263 (1993).
12. M.T. Oka, T. Arai, and Y. Hamaguchi, Different reactivity with monoclonal anti-tubulin antibodies between native and fixed mitotic microtubules in sea urchin eggs, *Cell Motil. Cytoskel.* 29:241 (1994).
13. R.F. Ludueña, Are tubulin isotypes functionally significant, *Mol. Biol. Cell* 4:445 (1993).
14. M. De Brabander, G. Geuens, R. Nuydens, R. Willebrords, F. Aerts, and J. De Mey, Microtubule dynamics during the cell cycle: the effects of taxol and nocodazole on the microtubule system of PtK2 cells at different stages of the mitotic cycle, *Int. Rev. Cytol.* 101:215 (1986).

IMMUNOFLUORESCENCE DETECTION OF CYTOSKELETAL STRUCTURES

Eduarda Dráberová and Pavel Dráber

Institute of Molecular Genetics
Academy of Sciences of the Czech Republic
142 20 Prague 4, Czech Republic

1. INTRODUCTION

Eukaryotic cells possess a complex network of protein filaments that extends throughout the cytoplasm. This network, called cytoskeleton, is a highly dynamic structure involved in such diverse essential cellular functions as segregation of chromosomes at mitosis, signal transduction and cell motility. The diverse activities of the cytoskeleton depend on three types of filaments - tubulin microtubules, actin microfilaments and intermediate filaments. According to their sequence homologies and tissue distribution intermediate filament proteins can be divided into five types. In mesenchymal cells the building component of intermediate filaments is vimentin. One of the major tools for studying of cytoskeletal proteins in cells is immunofluorescence microscopy with monoclonal or affinity purified polyclonal antibodies¹. Invention of secondary antibodies coupled with new fluorophores enabled to perform multiple immunodetection of individual cytoskeletal proteins and their relative locations². Potential of these approaches is further enhanced by the technique of microinjection of purified antibodies to study *in vitro* the function of individual cytoskeletal components and their structural domains. Microinjection experiments also brought out new data on dynamics of cytoskeletal systems and on interaction of cytoskeletal filaments with each other. The key steps in preparation of samples for immunofluorescence detection of cytoskeletal components are to make cells permeable for antibody molecules and to achieve optimal structural preservation of supramolecular polymers³. An optimization of fixation conditions is also necessary with respect to the used antibodies, as corresponding antigenic determinants can be strongly affected by the applied fixation, especially in the case of monoclonal antibodies.

Here we summarize our results of probing cytoskeletal structures in adherent cells using multiple immunofluorescence microscopy and microinjection of monoclonal antibodies.

2. MATERIAL AND METHODS

2.1. Antibodies

Mouse monoclonal antibodies TU-04 against α -tubulin⁴, VI-01 against vimentin⁵ and MA-01 against 210 kDa microtubule-interacting protein⁶ were used as diluted ascitic fluids or were purified according to standard procedures. For microinjection experiments the MA-01 antibody was dialysed against microinjection buffer⁷. Affinity purified rabbit antibody against tubulin was described previously⁸. The antibodies TU-04 and VI-01 were labelled with lissamine rhodamine B sulphonyl chloride according to Brandtzaeg⁹. Anti-mouse and anti-rabbit antibodies conjugated with fluorescein isothiocyanate (FITC) were from Sevac (Prague, Czech Republic), 7-amino-4-methylcoumarin-3-acetic acid (AMCA)-conjugated anti-rabbit antibody was from Jackson Immunoresearch Laboratories, Inc. (West Grove, PA).

2.2. Extraction of Cytoskeletons

Extraction and fixation steps on 3T3 cells grown on coverslips were carried out in a microtubule stabilizing buffer (MSB) consisting of 0.1 M KMes, 2 mM EGTA, 2 mM MgCl₂, 4% polyethylene glycol 6000, pH 6.9. Fixed cytoskeletons were prepared as described¹⁰. A brief description of the fixation protocols, with abbreviations in parentheses, follows. Cells grown on coverslips were fixed for 10 min in methanol at -20°C followed by 6 min in acetone at -20°C (M/A). Alternatively cells were extracted for 1 min with 0.2% Triton X-100 at 37°C and fixed for 20 min in 3% formaldehyde at the same temperature (Tx/F). Cells were also fixed for 30 min in 3% formaldehyde before extraction for 4 min with 0.5% Triton X-100 at 37°C (F/Tx); or cells were fixed at 37°C for 3 min in 0.25% glutaraldehyde/0.5% Triton X-100 mixture, followed by 20 min incubation at the same temperature in 1% glutaraldehyde and then three times (5 min each) in 0.5 mg/ml NaBH₄ (G/Tx). To prepare unfixed detergent-extracted cytoskeletons, cells were rinsed at 37°C with MSB, extracted for 1 min at 37°C with 0.2% Triton X-100 in MSB containing microtubule-stabilizing drug taxol at concentration 10 μ M and rinsed in MSB at the same temperature (Unfixed). For triple-label experiments samples were prepared according to the Tx/F protocol.

2.3. Microinjection

Microinjection of antibodies into the cells was carried out according to Graessman and Graessman¹¹. Approximately one tenth of a cell volume was injected with purified antibodies at a concentration ranging from 0.5 - 10 mg/ml. Injected cells were incubated at 37°C for various time periods prior to extraction and fixation. Cytoskeleton preparations were used for double-label immunofluorescence to visualize whether or not the injected antibody induced a re-organization of cytoskeletal networks.

2.4. Immunofluorescence

Immunofluorescence staining was performed as described¹⁰. For double-label indirect/direct fluorescence fixed cytoskeletons were incubated first with MA-01 antibody and after washing with FITC-conjugated anti-mouse antibody. Coverslips were washed again and the remaining binding sites on the FITC-conjugated antibody were blocked by incubation with normal mouse serum. Samples were thereafter incubated with rhodamine-conjugated anti-tubulin or anti-vimentin antibodies. For triple-label immunofluorescence fixed

cytoskeletons were first incubated with a mixture of rabbit anti-tubulin and mouse anti-vimentin VI-01 antibodies, and after washing with a mixture of AMCA-conjugated anti-rabbit antibody and FITC-conjugated anti-mouse antibody. Coverslips were washed again and incubated with rhodamine-conjugated phalloidin. The slides were mounted in MOWIOL 4-88 (Calbiochem AG, Lucerne, Switzerland) and examined with a Leitz Orthoplan microscope equipped with 50/1.00 Fluorescence water-immersion objective, epi-illumination using the filter combination cubes N2, I2 and A, and an Orthomat 35 mm camera. Photographs were taken on Kodak Tri-Xpan 400 film and printed on hard paper. Neither the control antibody against human transferrin nor the conjugates alone gave any specific staining.

3. RESULTS AND DISCUSSION

Selection of proper extraction and fixation conditions is necessary for preparation of cytoskeletal samples for immunofluorescence microscopy. This is especially important when monoclonal antibodies and multiple labelling techniques are intended. In general, the aim is to achieve optimal structural preservation and intense antibody labelling. But reactivity of many antibodies is dependent on the used fixation. As microtubules belong to the most fragile cytoskeletal structures, we have used MSB for preparation of samples. Table 1. demonstrates the effect of fixation conditions on the degree of preservation of corresponding antigenic determinants. For example, polyclonal anti-tubulin antibody decorated microtubules under all tested fixation protocols, whereas monoclonal antibody MA-01 strongly stained microtubules after extraction of cells by non-ionic detergent and subsequent fixation with formaldehyde, but no interphase microtubules were detected in samples fixed by cold methanol and acetone. Successful double or triple immunofluorescence labelling thus requires that the selected fixation protocol is suitable for each of the used antibodies. Individual primary antibodies must provide intense staining with a clean background when used alone.

The primary antibodies used for multiple labelling are often prepared in different species and secondary species-specific antibodies conjugated with fluorophores are then used. Alternatively primary antibodies can be detected by conjugated protein A and protein G. To enhance the staining, secondary antibodies are sometimes biotinylated and the bound biotin is detected, for example, with fluorophore-conjugated streptavidin. It is essential to check that the secondary antibodies are negative when used alone, and that there is no cross-reactivity of the secondary antibodies with antibodies used in the experiment. Selection of fluorophores depends on the available filter sets in particular fluorescence microscope. Control experiments may be needed to verify the absence of bleed-through of one colour

Table 1. Effect of fixation procedure on reactivity of antibodies and phalloidin with cytoskeletal structures

Antibody	Structure	Fixation protocol*				
		M/A	Tx/F	F/Tx	G/Tx	Unfixed
Polyclonal	microtubules	+	++	++	++	++
TU-04	microtubules	+	++	++	++	-
MA-01	microtubules	-	++	+	+	-
VI-01	vimentin filaments	+	++	+	-	++
Phalloidin	actin filaments	-	++	++	++	++

*. Description of fixation protocols is in Material and methods.

M, methanol; A, acetone; Tx, Triton X-100; F, formaldehyde; G, glutaraldehyde.

++, strong; +, moderately strong; -, negative.

into the wrong channel. To reduce bleaching, especially of FITC, anti-bleach agents are often added into the mounting medium. However, in multiple-label experiments it is necessary to test beforehand that the anti-bleaching compound does not diminish fluorescence of the other fluorophores. A combination of red, green and blue fluorescence with proper filter sets is most often used for triple labelling of cytoskeletal structures. Example of triple-labelling of microtubules, vimentin filaments and microfilaments in 3T3 cells, using AMCA, FITC and rhodamine as fluorophores, is shown in Figure 1. Even quadruple fluorescence labelling of microtubules, vimentin filaments, mitochondria and endoplasmatic reticulum was reported. Fluorescence detection of endoplasmic reticulum and mitochondria with cyanine dye was followed by extraction of the dye and triple-label immunofluorescence¹². Immunofluorescence staining of a single cell with four different antibody probes was also developed. It consisted of triple-label immunofluorescence followed by removal of all bound antibodies with low pH buffer, which allowed further staining with a fourth primary antibody. The whole procedure however required 14 steps¹³.

When primary mouse monoclonal antibodies are used in multiple immunofluorescence, it is possible to detect them with commercially available class or subclass-specific anti-mouse antibodies. If two monoclonal antibodies of the same class are intended for double-label immunofluorescence, it is possible to directly conjugate one antibody with fluorophore. Unlabelled antibody is then detected by indirect immunofluorescence and the directly conjugated monoclonal antibody is applied after blocking the remaining binding sites on secondary anti-mouse antibody. An example of indirect/direct immunofluorescence is shown in Figure 2. Microtubule-interacting protein, detected by indirect immunofluorescence with mouse monoclonal antibody MA-01 and FITC-conjugated anti-mouse antibody (Figure 2A), co-localized with microtubules detected with rhodamine-conjugated anti-tubulin antibody TU-04 (Figure 2B). As shown in Figure 2C and 2D, mouse serum effectively blocked the remaining binding sites on secondary FITC-conjugated anti-mouse antibody since mitotic spindles with midbodies were not visualized with rhodamine-conjugate anti-vimentin antibody (Figure 2D) used in double-label staining.

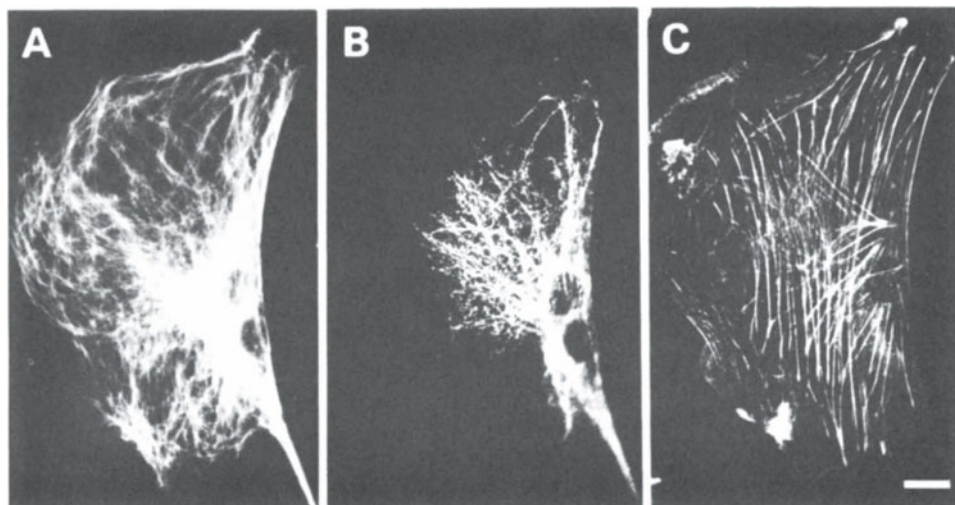


Figure 1. Triple-label immunofluorescence staining of 3T3 cytoskeleton with rabbit anti-tubulin antibody (A), mouse anti-vimentin antibody (B) and rhodamine-conjugated phalloidin (C). Secondary anti-rabbit antibody was conjugated with AMCA (A), secondary anti-mouse antibody was conjugated with FITC (B). Bar, 10 µm.

Combination of microinjection of MA-01 antibody into living cells and double-label immunofluorescence made it possible to localize the MA-01 antigen in living cells and estimate its effect on the integrity of cytoskeletal structures. After microinjection, extraction and fixation the antibody was found distributed diffusely in cytoplasm and no cytoskeletal structures were stained. However, with prolonged incubation the MA-01 immunofluorescence was accumulated around the nucleus, and after 3 hours the pattern was characterized by a perinuclear cap and faint diffuse staining. Double immunofluorescence with anti-tubulin antibody showed that the microtubule network remained unchanged (Figure 3A and 3B). Double immunofluorescence with anti-vimentin antibody revealed that injection of antibody induced gradual change of the network of the intermediate filaments and after 3 hours vimentin filaments were completely disrupted (Figure 3C and 3D). Microinjection of control monoclonal antibody against human transferrin at concentrations between 1-10 mg/ml and subsequent incubation for 1-6 hours did not give rise to collapsed vimentin filaments, eliminating the possibility that the collapse was a response to microinjection. When injected cells were stained with rhodamine-conjugated phalloidin, stress fibres of microfilaments resembled those observed in cells injected with control antibody.

The collapse of filaments started 30 min after an injection of the antibody at concentration of immunoglobulin 2 mg/ml and higher. Time-course experiments demonstrated that the collapse was reversible and was most marked 3 hours after injection. With time the degree of filament collapse in individual cells decreased and extended vimentin filaments reappeared after 20 hours. The combined data indicate that the MA-01 antigen is a new microtubule-interacting protein that mediates, directly or indirectly, an interaction between microtubules and vimentin-type intermediate filaments¹⁴. These immunofluores-

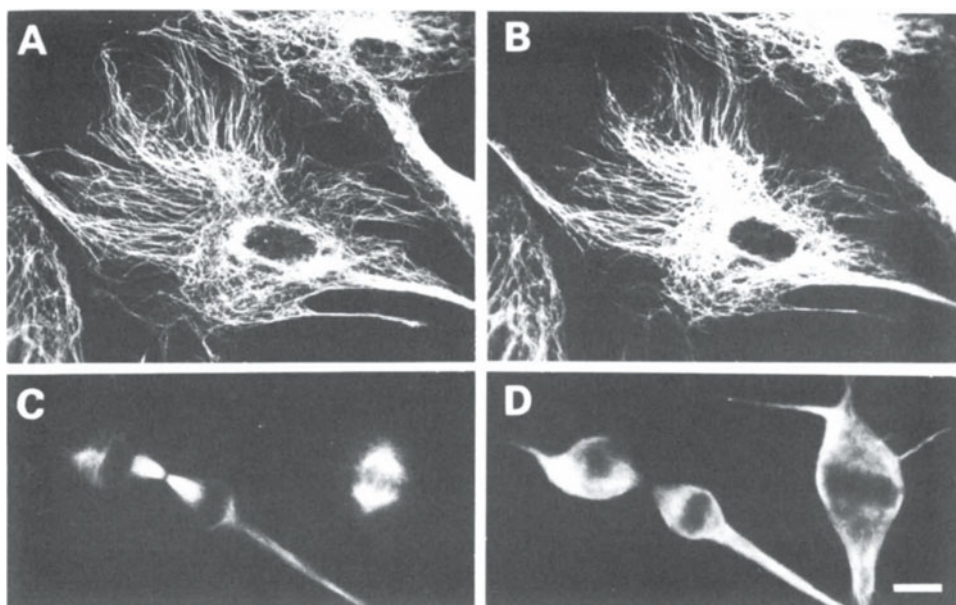


Figure 2. Double-label indirect/direct immunofluorescence staining of 3T3 cytoskeleton with MA-01 antibody (A, C), anti-tubulin TU-04 (B) and anti-vimentin VI-01 (D) antibodies. Antibodies TU-04 and VI-01 were directly conjugated with rhodamine. Each pair (A-B and C-D) represents the same cells. Bar, 10 µm. (Dráberová et al., 1993, with permission of J. Cell Sci.)

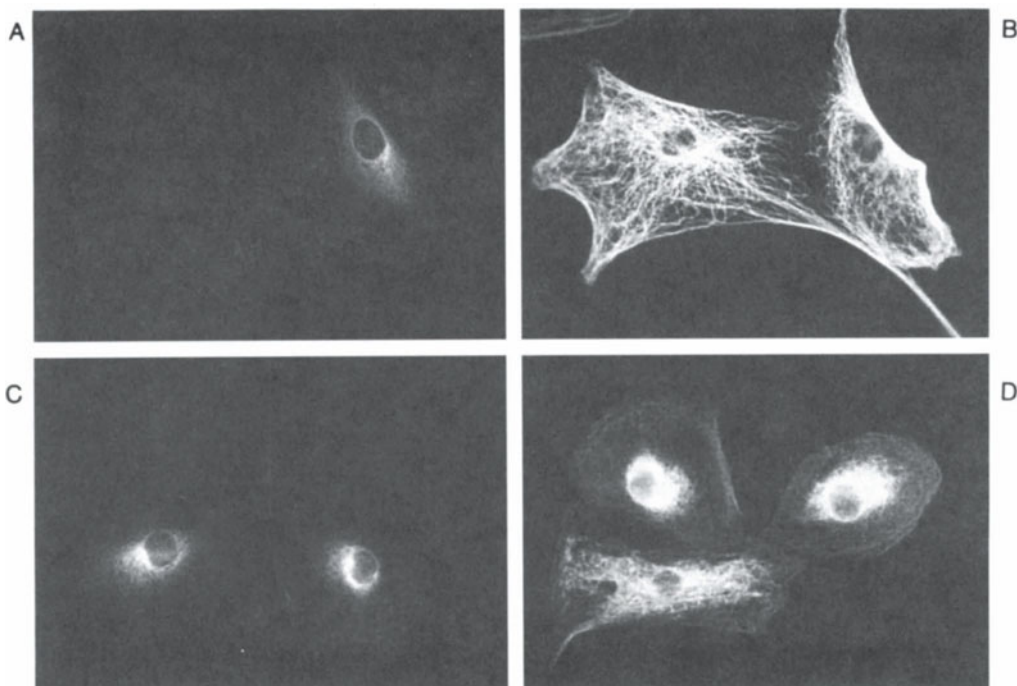


Figure 3. Effect of MA-01 antibody injection on the distribution of microtubules and intermediate filaments of vimentin-type. 3T3 cells were injected with MA-01 antibody at a concentration of 5 mg/ml, fixed after 3 hours and processed for immunostaining. Distribution of MA-01 antibody (A,C), microtubules (B) and vimentin filaments (D) is shown by double-label immunofluorescence. Antibodies TU-04 and VI-01 were directly conjugated with rhodamine. Each pair (A-B and C-D) represents the same cells. Bar, 10 µm. A color representation of this figure can be found following p. 214.

cence studies also document that intermediate filaments can be withdrawn from the cytoskeleton with no effect on distribution of microtubules and cell morphology.

ACKNOWLEDGMENTS

This work was supported in part by grant 552407 from the Czech Academy Grant Agency. Taxol was a generous gift of the Drug Synthesis and Chemistry Branch, Division of Cancer Treatment, National Cancer Institute (Bethesda, MD). Rhodamine-labelled phalloidin was a generous gift of Dr. T. Wieland.

4. REFERENCES

1. M. Osborn and K. Weber, Immunofluorescence and immunocytochemical procedures with affinity purified antibodies: Tubulin containing structures, in: "Methods in Cell Biology," L. Wilson, ed., Vol. 24, pp 97, Academic Press, New York (1982).
2. J.V. Small, S. Zobele, G. Rinnerthaler, and H. Faulstich, Coumarin-phalloidin: A new actin probe permitting triple immunofluorescence microscopy of the cytoskeleton, *J. Cell Sci.* 89:21 (1988).

3. M. Herzog, A. Draeger, E. Ehler, and J.V. Small, Immunofluorescence microscopy of the cytoskeleton: Double and triple immunofluorescence. in: "Cell Biology. A Laboratory Manual", J.E. Celis, ed., Vol.2, pp 355, Academic Press, San Diego (1994).
4. P. Dráber, E. Dráberová, D. Zicconi, C. Sellito, V. Viklicky, and P. Cappuccinelli, Heterogeneity of microtubules recognized by monoclonal antibodies to alpha-tubulin, *Eur. J. Cell Biol.* 41:82 (1986).
5. E. Dráberová, P. Dráber, F. Havlícek, and V. Viklicky, A common antigenic determinant of vimentin and desmin defined by monoclonal antibody, *Fol. Biol. (Praha)* 32:295 (1986).
6. E. Dráberová, P. Dráber, and V. Viklický, Cellular distribution of protein related to neuronal microtubule-associated protein MAP-2 in Leydig cells, *Cell Biol. Int. Rep.* 10:881 (1986).
7. M.W. Klymkowsky, Intermediate filaments in 3T3 cells collapse after intracellular injection of a monoclonal anti-intermediate filament antibody, *Nature* 291:249 (1981).
8. P. Dráber, E. Dráberová, and V. Viklický, Immunostaining of human spermatozoa with tubulin domain-specific monoclonal antibodies, *Histochemistry* 195:519 (1991).
9. P. Brandtzaeg, Conjugates of immunoglobulin G with different fluorochromes. I. Characterization by anionic exchange chromatography, *Scand. J. Immun., Suppl.* 2:273 (1973).
10. P. Dráber, E. Dráberová, I. Linhartová, and V. Viklický, Differences in the exposure of C- and N-terminal tubulin domains in cytoplasmic microtubules detected with domain-specific monoclonal antibodies, *J. Cell Sci.* 92:519 (1989).
11. M. Graessman, and N. Graessman, "Early" simian-virus-40-specific RNA contains information for tumour antigen formation and chromatin replication, *Proc. Natl. Acad. Sci. U.S.A.* 73:366 (1976).
12. B.J. Soltys, and R.S. Gupta, Interrelationships of endoplasmic reticulum, mitochondria, intermediate filaments, and microtubules - a quadruple fluorescence labelling study, *Biochem. Cell Biol.* 70:1174: (1992).
13. T. Maekawa, and R. Kuriyama, Differential pathways of recruitment for centrosomal antigens to the mitotic poles during bipolar spindle formation, *J. Cell Sci.* 100:533 (1991).
14. E. Dráberová, and P. Dráber, A microtubule-interacting protein involved in coalignment of vimentin intermediate filaments with microtubules, *J. Cell Sci.* 106:1263 (1993).

CELL EXPRESSION SYSTEM IN V79 CELLS TRANSFECTED WITH CYTOCHROME P450 AND ITS PERFORMANCE IN METABOLISM STUDIES

Johannes Doehmer, Wolfgang A. Schmalix, and Helmut Greim

Institut für Toxikologie und Umwelthygiene
der Technischen Universität München
Lazarettstrasse 62
D-80636 München, Germany

INTRODUCTION

Cytochromes P450 play key roles in pharmacology and toxicology, because they are the key enzymes in the metabolism of exogenous chemicals, e.g. drugs and pollutants, and of endogenous chemicals, e.g. steroids. Cytochromes P450 are hemoproteins with Fe as the central atom. They are membrane bound enzymes either anchored in the endoplasmatic reticulum adjacent to electron delivering cytochrome P450 reductase or in the mitochondrial membrane adjacent to ferredoxin reductase. They catalyze thousands of oxidative and reductive reactions by using oxygen. These reactions may be grouped according to similarities (Guengerich, 1993).

Today, more than 300 different cytochrome P450 isoforms across all species are known, either as cloned cDNA and/or purified enzyme. Substrate specificities of cytochromes P450 vary. A few isoforms are highly specialized; most isoforms overlap in their substrate specificity. Both the large number and overlapping specificities are the reasons for the plasticity of this enzyme system, which is sufficiently wide to handle all sorts of chemicals. Cytochrome P450 genes are evolutionary related and are believed to originate from an ancestral cytochrome P450 gene. Based on their sequence homology, cytochromes P450 have been grouped in families and subfamilies (Nelson et al., 1996). Cytochromes P450 of family 1 through 4 are of toxicological and pharmacological interest, since those cytochromes P450 preferentially handle drugs, pollutants or other exogenous chemicals, e.g. food additives. Other cytochromes P450, e.g. those of families 11 or 17, play key roles in the synthesis of hormones.

Most cytochrome P450 genes are under control of various receptor binding sequences adjacent to the expression signals. Therefore, expression of cytochrome P450 genes may

depend on developmental stage, sex, tissue or presence of inducing chemicals (Sogawa and Fujii-Kuriyama, 1993; Bresnick, 1993).

THE GENE TECHNOLOGICAL APPROACH FOR THE STUDY OF CYTOCHROMES P450

With the advent and development of gene technology, tools and procedures became available which allow unlimited access to genes and gene products. This has turned out to be particularly useful for the complex cytochrome P450 enzyme system. Cloning cytochrome P450 genes started in the 1980s (Fujii-Kuriyama et al., 1981) and since then has been a very efficient way to elucidate relationships among cytochromes P450 or to identify the genetic elements responsible for the inducibility of cytochromes P450 genes.

Cloning cytochrome P450 genes as cDNAs for heterologous expression in bacteria, yeast, insect and mammalian cells yielded new possibilities to gain access to virtually unlimited amounts of any cytochromes P450 (Doehmer and Greim, 1993). This was especially important for those cytochrome P450 isoforms which are difficult to prepare from native tissues, because of low abundance or because of limited availability of human tissue, for ethical and practical reasons.

THE PRINCIPLE OF HETEROLOGOUS EXPRESSION OF CYTOCHROMES P450

The principle of heterologous expression is the transfer of a gene from its native tissue into a cultivated cell (Figure 1). The cultivated cell serving as recipient in gene transfer is mainly chosen for its genetic and phenotypical features to support cytochrome P450 related metabolism studies. For mass production of purified cytochromes P450, bacterial, yeast and insect cells are the preferred hosts of the cytochrome P450 cDNA. For cytochrome P450-related metabolism studies, mammalian cells may be preferred when biological endpoints and metabolism should be combined. For whatever host cell is chosen for heterologous

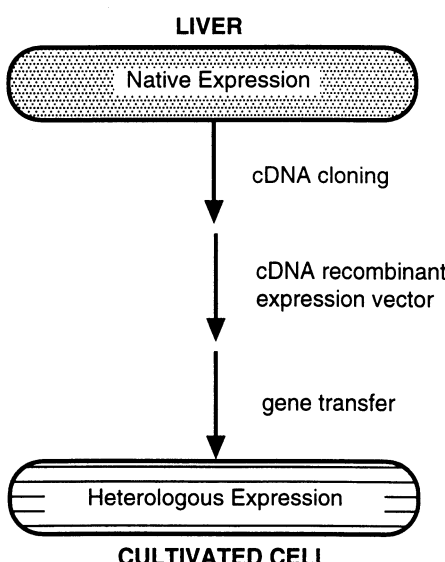


Figure 1. The principle of heterologous expression means the dislocation of a single gene from its native genetic and cellular environment into a new genetic and cellular environment. The new cellular environment may be bacterial, yeast, insect or mammalian.

expression a few criteria should be observed, if the genetically engineered expression system is experimentally better suited than native tissue. Authenticity of the cDNA product is shown by Sequence analysis, Western analysis and substrate specificity. The host cell should have genetic and phenotypic features which allow for special studies, where those features are an essential prerequisite. If these criteria are fulfilled, then full experimental advantage may be taken from a reduction of a very complex *in vivo* to a very defined *in vitro* cytochrome P450 situation.

HETEROLOGOUS EXPRESSION OF CYTOCHROMES P450 IN V79 CELLS

Based on these general criteria for selecting the most appropriate host cell, V79 cells of Chinese hamster lung fibroblast origin have been genetically engineered for stable expression of human and rat cytochromes P450 (Doehmer, 1993). V79 cells are attached growing cells which have very unusual and useful genetic and phenotypic features which made them the preferred study object for now more than 30 years in toxicology for studies on cytotoxicity, mutagenicity, chromosomal aberration, sister chromatid exchange or micronuclei formation. What is so unusual about these cells is their extreme fast growth with a generation time of less than 12 hours and at the same time maintaining an intact karyotype with no variation in their chromosome number. They also show a cloning efficiency of more than 90%. V79 cells have the HGPRT gene locus on a single X-chromosome. However, for all these years, it was well known and well documented that V79 cells do not metabolically activate chemicals. Metabolic deficiency in these cells was overcome by using liver homogenate for metabolism, very much the same as Salmonella bacterial strains were used in the Ames mutagenicity testing.

Both metabolic deficiency and special cell characteristics were the reasons for picking V79 cells to serve as host cell for cDNA mediated expression of cytochromes P450. In the course of these developments it was repeatedly observed, that V79 cells do not express cytochromes P450 neither as mRNA nor as protein nor as enzyme activity. What was a disadvantage in the parental V79 cell turned into an advantage in the genetically engineered V79 cells. Because of zero cytochrome P450 background V79 cells are defined for the cDNA encoded cytochrome P450. Indeed, further studies have shown that the genetically engineered V79 cells function as expected from purified cytochrome P450 isoform. The experimental strategy was aimed at construction of a cytochrome P450 source for constant supply. For this purpose, the cDNA was placed under control of the SV40 early promotor, which ensures stable and high level expression (Fig. 2).

In addition, genetically engineered V79 cells were selected for stable integration of the expression vector into the V79 cell chromosomal DNA. Successfully transfected V79 cells show expression of their cDNA encoded cytochrome P450 in Western analysis (Fig. 3) and by *in situ* immunofluorescence staining (Fig. 4). A list of the available genetically engineered V79 cell lines is given in Table 1.

APPLICATION OF V79 CELLS GENETICALLY ENGINEERED FOR CYTOCHROMES P450

V79 cells genetically engineered for cytochromes P450 have been applied in several metabolism studies related to pharmacological and toxicological problems. A few examples will be presented.

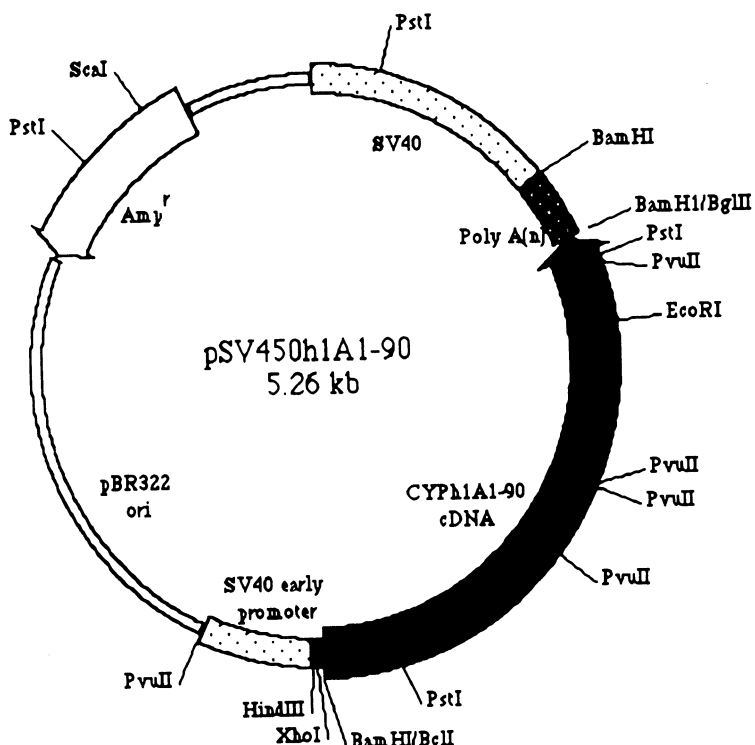


Figure 2. Recombinant expression vector for human cytochrome P450 1A1 cDNA for stable expression by the SV40 Early promoter in V79 Chinese hamster cells upon stable integration of this vector into V79 genomic DNA.

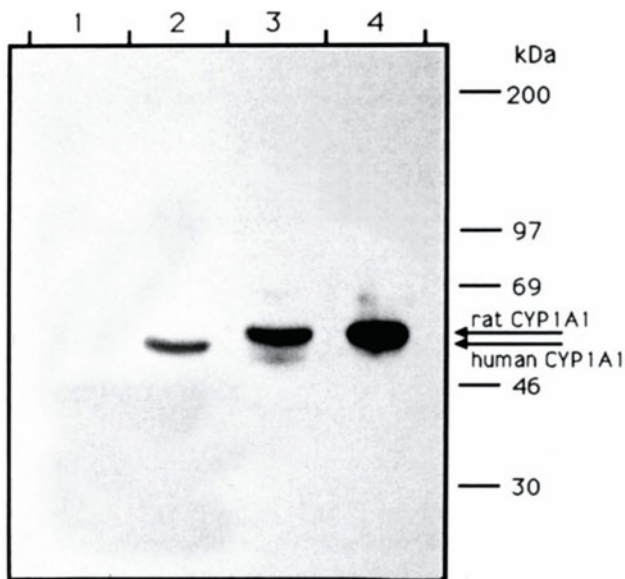


Figure 3. Western analysis of cDNA directed expression of cytochrome P450 1A1 in V79 Chinese hamster cells. Lane 1: V79 parental cell; Lane 2: V79 expressing human cytochrome P450 1A1; Lane 3: V79 expressing rat cytochrome P450 1A1; Lane 4: rat liver homogenate. Each lane was loaded with 50 μ g of total protein.

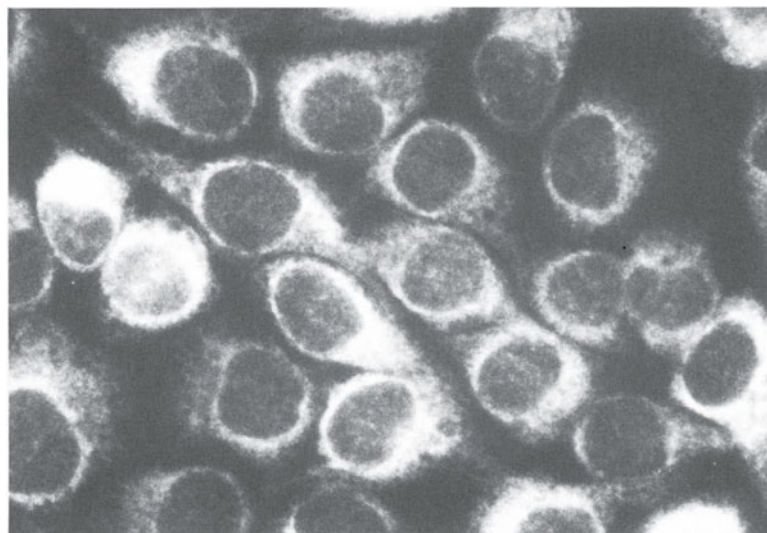


Figure 4. *In situ* immunofluorescence staining of V79 cells expressing the human cytochrome P450 1A1 using a specific antibody and FITC-conjugated anti-rabbit IgG. Cytochrome P450 1A1 is detected in the nuclear membrane and in the cytoplasm associated with the endoplasmic reticulum.

Metabolic activation by cytochromes P450 may turn noncarcinogenic chemicals into carcinogenic metabolites. A classical example is the conversion of benzo[a]pyrene into its ultimate carcinogenic form of 7,8-diol-9,10-epoxid (Fig. 5). The principle of this reaction was extensively studied some time ago (Sims et al., 1974). However, those and following studies were mostly performed with rats, rat tissues or preparations of rat cytochrome P450. Due to species-dependent differences in cytochromes P450 the results from those studies may not necessarily be valid for humans. But studies on human homologues of cytochromes P450 are extremely limited. Heterologous expression of homologous rat and human cytochromes P450 is the most appropriate experimental way to bypass these limitations. Thus, V79 cells were constructed for

Table 1. Listing of cytochrome P450 expressing V79 cell lines

Cytochrome P450 expressed	Typical and specific activity (pmol product formed/min/mg total protein)	
Rat:		
1A1	52	ethoxyresorufin- <i>O</i> -deethylation
1A2	7	ethoxyresorufin- <i>O</i> -deethylation
2B1	30	pentoxyresorufin- <i>O</i> -deethylation
2E1		to be characterized for activity
Human:		
1A1	48	ethoxyresorufin- <i>O</i> -deethylation
1A2	5	ethoxyresorufin- <i>O</i> -deethylation
2A6	80	ethoxycoumarin-7-hydroxylation
2E1	70	chlorzoxazone-6-hydroxylation
3A4	80	testosteron-6 β -hydroxylation

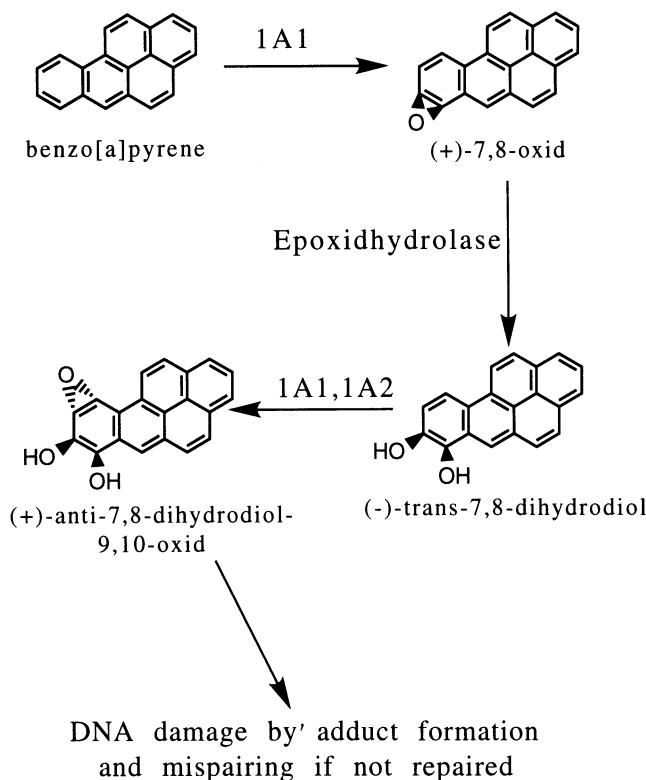


Figure 5. Pathway of benzo[a]pyrene leading to its ultimate genotoxic and carcinogenic metabolite.

expression of rat and human cytochrome P450 1A1, which is considered to be the most potent and important cytochrome P450 in the metabolic activation of benzo[a]pyrene. Both V79 derived cell lines are directly comparable, since they have almost identical cytochrome 1A1 activities (Table 1). Yet, when tested for metabolite profile and cytotoxicity, it was observed that the human cytochrome P450 1A1 preferentially oxidized benzo[a]pyrene in the 7,8-position, the so-called pre-bay region, leading to the ultimate carcinogenic metabolite 7,8-diol-9,10-epoxide, whereby the rat cytochrome P450 1A1 yielded more oxidation in the 4,5-position, to so-called K-region, which is readily detoxified (Fig. 6). This explains the higher cytotoxicity of benzo[a]pyrene in the human cytochrome P450 1A1 expressing V79 cells as compared to the rat cytochrome P450 1A1 expressing V79 cells (Fig. 7). This is not the only reason why it makes a difference if a rat or a human smokes. In addition to differences in metabolite profiles, the human cytochrome P450 1A1 is preferentially expressed in lung, and the rat cytochrome P450 1A1 is predominantly expressed in liver.

For many drugs metabolic activation by cytochromes P450 influences their pharmacological potency quantitatively and qualitatively, either by degradation, conversion, activation of drugs, or by inhibition of cytochromes P450. The identification of the metabolically competent cytochrome P450 isoform and metabolite profile are essential information for studies of drug efficacy. Failure of prodrug activation because of low cytochrome P450 levels in target tissue is a major reason for drug resistance. This information may be obtained from cytochrome P450 expressing V79 cells. Expressing human cytochromes P450 is of particular

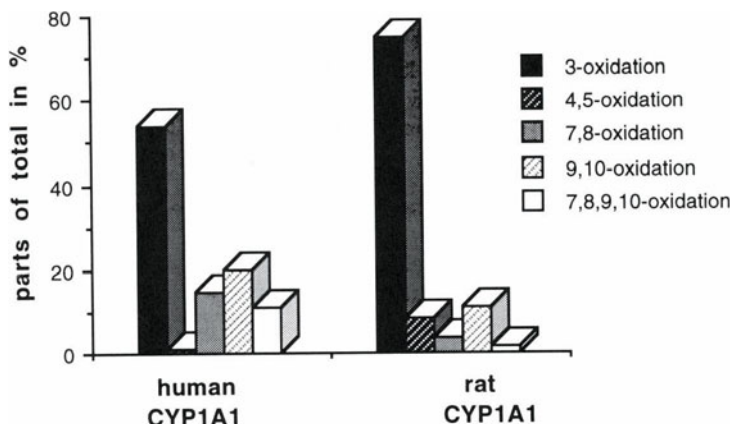


Figure 6. Species dependent metabolite profile of benzo[a]pyrene by cytochrome P450 1A1 from human and rat.

advantage by yielding data, which are of immediate relevance for humans, already at the preclinical stage of drug development.

The cytostatic potency of cyclophosphamide and ifosfamide is dependent on rat cytochrome P450 2B1 or human cytochromes P450 2B6 and 3A4 mediated 4-hydroxylation to yield the cytostatic acting metabolites (Fig. 8). V79 parental cells and cells expressing these cytochromes P450 or the rat homologue 2B1 were exposed to various concentrations of cyclophosphamide (Fig. 9). No cytotoxic effect was observed in the V79 parental cells or V79 cells expressing cytochromes P450 other than 2B1 even at very high concentrations. A cyclophosphamide dose dependent cytotoxicity was only observed in the 2B1 expressing cell line (Doehmer et al., 1990).

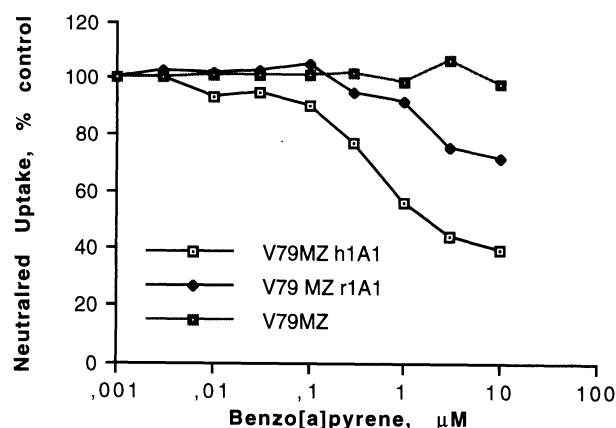


Figure 7. Cytotoxicity of benzo[a]pyrene in V79 cells expressing human and rat cytochromes P450 1A1 or 1A2; V79MZ means parental cell.

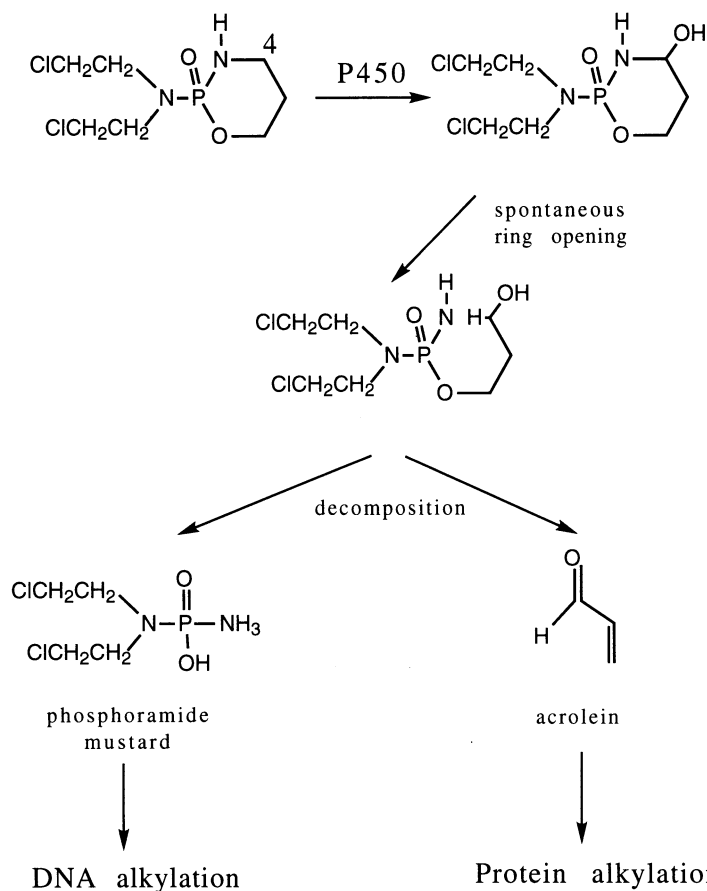


Figure 8. Metabolic activation of cytostatic drugs by cytochrome P450, e.g. cyclophosphamide.

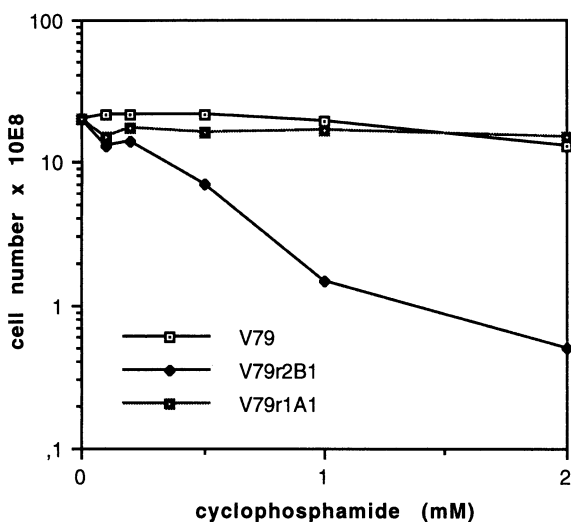


Figure 9. Cytochrome P450 2B1 mediated effect on V79r2B1 cells, but not in V79r1A1 or V79 parental cells.

EXPERIMENTAL CONDITIONS FOR THE IDENTIFICATION OF METABOLITES IN V79 CELLS

Experimental procedures have been established to use V79 cells as microsomal preparation, cell homogenate or live cells in metabolism studies for the identification and quantitation of metabolites by HPLC or GC / MS and are described in detail (Waxman et al. 1989, Platt et al. 1989, Fuhr et al. 1992, Denner et al. 1995). These procedures have in common that only at given and fixed time points accumulated metabolites will be measured. Using live V79 cells combined with an appropriate detection device may allow single cell metabolism studies following metabolite formation in real time. This approach may be considered an immense progress in obtaining information on metabolite formation and metabolite mediated cellular damage. Detection devices or procedures have been suggested and may be discussed for application on genetically engineered cytochrome P450 expressing V79 cells.

Another interesting approach would make use of chromophore carrying substrates combined with video imaging systems. This would allow metabolism studies on a single cell and possibly follow the fate of metabolites. This would establish a new technology in toxicology and pharmacology with new insights into metabolic activation of chemicals and drugs and their cellular consequences. For toxic chemicals it would be interesting to follow metabolites, e.g. for DNA binding or organelle sorting in a cell. This would improve our knowledge of the mechanisms when, how, and where these chemicals work in a cell. Risk assessment and drug safety would profit from these new methodologies.

ACKNOWLEDGMENT

The construction of V79 cell lines was supported by ZEBET, Zentralstelle zur Erfassung und Bewertung von Ersatzmethoden zum Tierversuch. Studies on metabolic activation of cyclophosphamide and polycyclic aromatic hydrocarbons was supported by the Deutsche Forschungsgemeinschaft.

REFERENCES

- Bresnick, E., Induction of cytochromes P450 1 and P450 2 by xenobiotics, in "Cytochrome P450," J.B. Schenkman and H. Greim, eds., Springer Verlag, New York, Berlin, Heidelberg (1993).
- Denner, K., Vogel, R., Schmalix, W., Doehmer, J., and Bernhardt, R., 1995, Cloning and stable expression of the human mitochondrial cytochrome P450 11B1 cDNA in V79 Chinese hamster cells and their application for testing of potential inhibitors, *Pharmacogenetics* 5:89.
- Doehmer, J., Seidel, A., Oesch, F., and Glatt, H.R., 1990, Genetically engineered V79 Chinese hamster cells metabolically activate the cytostatic drugs cyclophosphamide and ifosfamide, *Env. Health Persp.* 88:63.
- Doehmer, J.: V79 Chinese hamster cells genetically engineered for cytochrome P450 and their use in mutagenicity and metabolism studies. *Toxicology*, 82: 105-118 (1993).
- Doehmer, J., and Greim, H., Cytochromes P450 in genetically engineered cell cultures: The genotechnological approach, in "Cytochrome P450," J.B. Schenkman and H. Greim, eds., Springer Verlag, New York, Berlin, Heidelberg (1993).
- Fuhr U., Doehmer J., Battula N., Wölfel C., Kudla C., Keita Y., and Staib A.H., 1992, Biotransformation of caffeine and theophylline in mammalian cell lines genetically engineered for expression of single cytochrome P450 isoforms, *Biochem. Pharmacol.* 43:225.
- Fujii-Kuriyama, Y., Taniguchi, T., Mizukami, Y., Saki, M., Tashiro, Y., Muramatsu, M., 1981, Construction and identification of a hybrid plasmid containing a DNA sequence complementary to phenobarbital-inducible cytochrome P-450 messenger RNA from rat liver, *J. Biochem.* 89:1869.

- Guengerich, F.P., Metabolic reactions: Types of reactions of cytochrome P450 enzymes, in "Cytochrome P450", J.B.Schenkman and H. Greim, eds. Springer-Verlag, New York, Berlin, Heidelberg (1993).
- Nelson, D.R., Kamataki, R., Waxman, D.J., Guengerich, F.P., Estabrook, R.W., Feyereisen, R., Gonzalez, F.J., Coon, M.J., Gunsalus, I.C., Gotoh, O., Okuda, K., and Nebert, D.W., 1996, CYP450 superfamiliy: Update on new sequences, gene mapping, accession numbers, and nomenclature, Pharmacogenetics, in press.
- Platt K.L., Molitor E., Doehmer J., Dogra S., and Oesch F., 1989, Genetically engineered V79 Chinese hamster cells express monooxygenase activity of purified cytochrome P450IIB1, *J Biochem. Toxicol.* 4:1.
- Sims, P., Grover, P.L., Swaisland, A., Pal, K., and Hewer, A., 1974, Metabolic activation of benzo[a]pyrene proceeds by a diol-epoxide, *Nature* 252:326.
- Sogawa, K., and Fujii-Kuriyama, Y., Regulation of cytochrome P450 expression, in "Cytochrome P450," J.B. Schenkman and H. Greim, eds., Springer Verlag, New York, Berlin, Heidelberg (1993).
- Waxman D.J., Lapenson D.P., Morrissey J.J., Park S.S., Gelboin H.V., Doehmer J., and Oesch F., 1989, Androgen hydroxylation catalyzed by a cell line (SD1) that stably expresses rat hepatic P-450 PB-4 (IIB1), *Biochem. J.* 260:81.

DIRECT TRANSFER OF CONTROL AND MULTIDRUG RESISTANCE

Hans V. Westerhoff,^{1,2} Johann M. Rohwer,² Marc Heijn,^{1,3} Sipko Mülder,
Rick I. Ghauharali, Peter Wielinga,³ Boris N. Kholodenko,¹
Ellen C. Spoelstra, and Jan Lankelma³

¹ Department of MicroPhysiology, Faculty of Biology
Free University
De Boelelaan 1087, NL-1081 HV Amsterdam, The Netherlands

² E.C. Slater Institute
University of Amsterdam

³ Department of Medical Oncology
Academisch Ziekenhuis Vrije Universiteit

SUMMARY

Ultimately the distribution of control among the various factors in the cell depends on the kinetic properties of all the components in the cell. These properties may again differ between the isolated state and the intact system. Consequently it is important to be able to study the kinetic properties both in well-defined states and in the intact cell.

We review our studies on the function of P-glycoprotein as measured in intact cells by monitoring daunorubicin fluorescence in a flow-through system. To interpret the experimental findings, a mathematical model was set up. Multidrug resistance is not only controlled by the drug efflux pump. Part of the control resides in the passive permeability of the plasma membrane for the drug.

The control distribution between pump and the passive permeability should depend on how the pumping rate of P-glycoprotein depends on the intracellular daunorubicin concentration. Interestingly, the latter dependence was more than linear. This co-operativity in terms of daunorubicin concentration was confirmed when studying active drug pumping into plasma membrane vesicles loaded with DNA, by following fluorescence quenching of the transported daunorubicin.

The intricate organisation of cellular processes brings with it special kinetic and control properties. Here we discuss this for the case of ‘vacuum cleaning’ multidrug pumps and for the bacterial phosphotransferase system (PTS), which combines transport with regulation. The distinction between ‘vacuum cleaning’ and ‘non vacuum cleaning’ multidrug pumps may be less strict than anticipated and we define a “Vacuum Cleaner Index” which may serve to quantify the extent to which a drug pump behaves as a “vacuum cleaner”. Using

the PTS as a model system for channelling and signal transduction, we show experimentally that the sum of the flux control coefficients of the PTS enzymes may come close to 2.

FLUORESCENCE ASSESSMENT OF MULTIDRUG RESISTANCE AND DRUG-EFFLUX PUMP KINETICS IN INTACT CELLS

Tumor cell populations treated with any of a variety of anti-tumor drugs may develop resistance simultaneously to this drug and to many other such drugs. Part of this classical multidrug resistance (MDR) is associated with the enhanced expression of an MDR gene [review: Gottesmann and Pastan, 1994]. In the mouse the *mdrla* and *mdrlb* genes encode so-called P-glycoproteins. The *mdrla* gene product appears to be involved in the transport of substances across the blood-brain barrier [Schinkel *et al.*, 1994]. The homologous *mdr2* gene encodes a glycoprotein associated with the transport of phospholipid into bile [Smit *et al.*, 1993]. Overexpression of the former gene (and homologues from other organisms) in tissue culture cells leads to multidrug resistance and to active extrusion of the drugs from the cells. For overexpression of the latter gene, such an effect has not yet been demonstrated. Similar proteins such as the Multidrug Resistance associated Protein (MRP), also give rise to multidrug resistance by active extrusion of drugs across the plasma membrane [Müller *et al.*, 1994; Zaman *et al.*, 1994]. Also the so-called multispecific organic anion transporter has been implicated in multidrug resistance [Oude Elferink and Jansen, 1994].

Fluorescence methods have been important in the elucidation of the biochemical activity of P-glycoprotein and MRP [Spoelstra *et al.*, 1992]. Because the fluorescence of some of the anti-tumor drugs changes as they enter or leave the cell, measurement of their fluorescence constitutes a non-invasive method for measuring drug transport. Here we shall discuss four aspects: (i) efflux measurements from cells, (ii) evidence for the presence of an active drug efflux pump in the plasma membrane by steady state experiments, (iii) drug transport into plasma membrane vesicles, and (iv) detection of drug in the plasma membrane.

Daunorubicin is one of the anti-tumor drugs that is pumped by P-glycoprotein. When daunorubicin binds to DNA its fluorescence decreases. Because the corresponding affinity is high, most of the intracellular daunorubicin is bound to the DNA in most kinetic experiments. The association and dissociation of this drug to the DNA is rapid, such that at time scales of minutes if not seconds, the binding can be assumed to be at equilibrium. When daunorubicin is added to cells its fluorescence decreases and the rate at which this happens reports the rate of net influx. After a while the fluorescence decrease halts and a steady state obtains. When the cells are washed and placed in medium without daunorubicin, the total fluorescence increases. The rate of this increase of daunorubicin fluorescence is smaller in cells lacking P-glycoprotein, or in the presence of the inhibitor verapamil.

The rate of pumping of daunorubicin should be a function of the intracellular free concentration of the drug. To determine the kinetics of this dependence it is necessary to determine the intracellular free concentration of the drug. Because the binding constant of daunorubicin is in the same range as the daunorubicin concentrations used in these experiments and because there may be various binding sites with various affinities, the binding of daunorubicin cannot be assumed to be a *linear* function of the intracellular free concentration of daunorubicin. Because the assumption that these binding sites are in rapid equilibrium at the time scale of efflux (half time of several minutes) seemed safe, Ghauharali *et al.* [1996] solved this problem by making a calibration curve of daunorubicin fluorescence in non-pumping cells versus the concentration of extracellular daunorubicin. Assuming that in the calibration experiment at steady state the extracellular concentration equalled the intracellular concentration, the daunorubicin fluorescence in the efflux experiments was recalculated

to a scale of the intracellular free daunorubicin concentration, and then the rate of daunorubicin efflux was plotted versus this concentration [Ghauharali *et al.*, 1996]. The result was the demonstration that the P-glycoprotein mediated efflux of daunorubicin was saturable with a K_M of approximately 2 μM . Because it also deals with the fact that intracellular daunorubicin fluoresces to some extent, the calculation procedure is complicated, but the experiment is simple, such that the method may well become of interest for clinical applications. Recently, we have devised a variant of this method, in which the cells are kept out of the light path, such that fluorescence only reflects extracellular daunorubicin.

An earlier variant of this method was the flow-through system developed by Lankelma and colleagues [1982]. Drug containing medium is flowed over the cells attached in a monolayer to a glass plate, and the drug fluorescence in the effluent is monitored as a function of time. At steady state there is no net flux of drug into the cells and the drug concentration in the effluent equals that in the influent. When any drug pump is inactivated, drug flows transiently into the cells until a new steady state at higher intracellular drug concentration is attained. At that point the drug concentration in the effluent will have returned to its original value. Transiently, however, the drug concentration in the effluent will have been lowered. The extent of this lowering is proportional to the net influx rate of drug into the cells.

In one assay of daunorubicin pumping by MDR cells, the MDR reverser verapamil is injected so as to give a constant concentration that is sufficient to inhibit P-glycoprotein pumping of daunorubicin completely [Spoelstra *et al.*, 1992]. Almost as soon as the verapamil reaches the effluent, the daunorubicin fluorescence in the effluent decreases, indicative of net daunorubicin influx into the cells. The minimum of the daunorubicin concentration in the effluent can be taken as indicative of the maximum net influx rate. Subsequently the net influx rate begins to decrease because the intracellular drug concentration increases. After 30-60 minutes, the intracellular daunorubicin concentration appears to reach a steady state, and the daunorubicin concentration in the effluent has returned to its initial value.

Importantly, this situation has been achieved by adding an inhibitor of the pump, which results in influx of the drug. Similarly, depletion of ATP leads to such a net influx. When verapamil was removed from the influx medium in this type of experiment, the daunorubicin concentration in the effluent increased, indicating efflux of daunorubicin against its own concentration gradient, hence proving that there must be an active extrusion mechanism [Lankelma *et al.*, 1990].

There has been a surge in possibilities described for the molecular characterisation of important cellular factors. These possibilities have been of crucial importance in the identification of the drug efflux pumps involved in MDR and in the identification of their normal function. However, these successes should not detract from the fact that the drug efflux pump functions in a context that is not solely set by itself, but rather by itself in conjunction with various other molecular properties. Accordingly, even though the primary cause of MDR may be the overexpression of MDR genes, its appearance may be influenced by other cellular properties. To help evaluate experiments with the drug-efflux pumps in their cellular context and to help elucidate implications of properties of the drug-efflux pump for therapy, we have constructed an arithmetic model for the drug-efflux pump in a cell with a drug target and a passive plasma-membrane permeability of the pump. The fundamental rate equations are kept simple. For the pumping rate, v_p , we here write [Demant *et al.*, 1990; Spoelstra *et al.*, 1994]:

$$v_p = \frac{\left(\frac{x}{K_x}\right)^n \cdot V_{\max}}{1 + \left(\frac{x}{K_x}\right)^n + \left(\frac{d}{K_d}\right)^n} \quad (1)$$

Here x represents the intracellular free concentration of daunorubicin, K_X the Michaelis constant of the pump with respect to the intracellular drug, V_{max} the maximum pumping rate, d the extracellular free drug concentration and K_D the corresponding Michaelis constant. The pump is assumed to be effectively irreversible owing to the large input of ATP hydrolytic free energy. n is the index of co-operativity, equal to 1 in the simplest case.

The leakage of drug into the cells, $-v_L$, is written as:

$$v_L = L \cdot (x - d) \quad (2)$$

Here L is the passive permeation coefficient [volume/time/unit cell] of the plasma membrane for the drug. At steady state the intracellular drug concentration predicted by these equations is found by setting the sum of equations 1 and 2 to zero and solving for x . For the case that $n=2$ (see below), and for low intracellular concentrations of drug ($x \ll K_X$ and $d \ll K_D$), one finds:

$$x = \frac{L \cdot (K_X)^2}{2 \cdot V_{max}} \cdot \left(-1 + \sqrt{1 + 4 \cdot \frac{V_{max} \cdot d}{L \cdot (K_X)^2}} \right) \quad (3)$$

The number of drug pump molecules per cell occurs as a proportionality factor in V_{max} . Consequently, this equation shows that the intracellular concentration of the drug is not only a function of the concentration of the drug efflux pump, but also of its kinetic properties, and of properties unrelated to the drug efflux pump such as the extracellular concentration of the drug (d , in a non-linear fashion) and the passive permeability of the membrane for the drug (L). Indeed, genetic modifications of cells that affect plasma membrane properties may well modulate multidrug resistance that is caused by a drug-efflux pump.

The above-described model for the functioning of P-glycoprotein was validated in studies in intact cells by Spoelstra *et al.* [1994]. Most notably, both saturability and positive co-operativity ($n \approx 2$) could be detected in these intact systems.

FLUORESCENCE STUDIES OF DRUG UPTAKE INTO VESICLES

The analysis of the kinetics of the P-glycoprotein in intact cells required an arithmetic model, to correct for the passive drug leakage that occurs in parallel. Therefore it was important to confirm the observed kinetic characteristics in a more direct system. Drug uptake assays into plasma membrane vesicles did not seem promising because of the small internal volume and the possibility of rapid drug efflux upon filtration or centrifugation of the vesicles. Here the property that daunorubicin fluorescence is quenched when this drug binds to DNA, has proven quite useful. DNA enclosed in the vesicles trapped transported daunorubicin and quenched its fluorescence, such that fluorescence quenching became a transport assay. In this manner Guiral *et al.* [1994] have shown that P-glycoprotein pumps daunorubicin with a K_M of approximately 2 μM and a positive co-operativity of 2.

METABOLIC CONTROL ANALYSIS

For fluxes through metabolic pathways, Metabolic Control Analysis (MCA) has shown that there need not be a single rate-limiting step [Heinrich and Rapoport, 1973; Kacser

and Burns, 1973; Groen *et al.*, 1982; Westerhoff and Van Dam, 1987; Fell, 1992; Kacser, 1995; Westerhoff and Kell, 1996]. This is true *a fortiori* for a steady-state concentration set by a number of metabolic reactions [Westerhoff and Van Dam, 1987]. For the concentration of a substance, the extent of control by an enzyme is defined by the log-log derivative of the steady state concentration with respect to the activity of that enzyme [Burns *et al.*, 1985; in fact we use concentration of the enzyme here denoted by e_j ; for a further discussion of the difference and of the distinction between Response and Control Coefficients, see Schuster and Heinrich, 1992; Hofmeyr *et al.*, 1993; Kholodenko *et al.*, 1995]. For the concentration, x , of a drug inside a cell and enzyme concentration e_j , this reads:

$$C_{e_j}^x = \left(\frac{d \ln x}{d \ln e_j} \right)_{\text{at steady state}} \quad (4)$$

By way of illustration, the lower line in Fig. 1 shows how the kinetic model described above and in Spoelstra *et al.* [1994] predicts this control coefficient to vary with the activity of the drug efflux pump. The control exerted by the pump on the intracellular drug concentration is negative; as the pump is activated, the intracellular drug concentration decreases (upper curve). At low pump activities, the control exerted by the pump on the intracellular drug concentration is close to zero, whereas for higher concentrations of the drug efflux pump this control is stronger, approaching -0.5 at very high pump activities. Because of the summation theorem for concentration control coefficients [Kacser and Burns, 1973; Westerhoff and Van Dam, 1987], the control by the drug permeability of the plasma membrane on the intracellular drug concentrations must be the opposite of this control by the pump. At even higher activities of the drug efflux pump, either control should return to zero as the thermodynamic limit for the drug gradient across the plasma membrane is reached, but this phenomenon is not contained in the above equations, since the pump was assumed to be effectively irreversible.

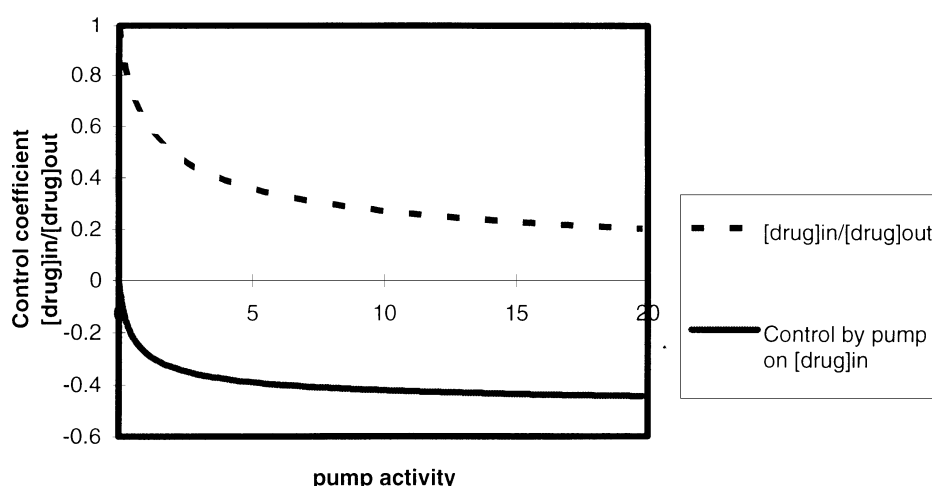


Figure 1. Control of intracellular drug concentration (upper curve) by drug pump activity (lower curve), as calculated for the arithmetic model in the text.

NON-IDEALITY IS REALITY? THE VACUUM CLEANING DRUG EFFLUX PUMP

The above account of multidrug resistance and its control was based on what two of us have defined as the concept of ideal metabolism [Khodolenko and Westerhoff; 1995b]: a cell consisting of well-defined homogeneous aqueous compartments, in which direct interactions between enzymes are absent. In such ideal metabolism the enzymes bind their substrates at a well defined thermodynamic activity from the aqueous medium. In the case of the drug efflux pump in the above model of multidrug resistance, this meant that the drug efflux pump bound substrate from the cytoplasm.

This picture of the pumping of the generally rather hydrophobic drugs by P-glycoprotein is somewhat paradoxical, because the binding site of the P-glycoprotein for the drug resides where that protein is: in the membrane. Moreover, the concentration of the drug in the membrane tends to exceed that in the cytoplasm because the drug is hydrophobic. Accordingly, the drug will be pumped from the membrane, where the most likely interpretation of ‘membrane’ is the interface between membrane and cytoplasm. How then should one interpret the concept of ideal metabolism for this case?

The essence of ideal metabolism for the case of drug efflux pumping is that the drug at the binding site of the pump is in more rapid exchange with the aqueous cytoplasm than with the membrane or that the latter equilibrates rapidly with the cytoplasm anyway. ‘Rapid’ here should be taken relative to the time scale of the depletion of the drug reservoir in closest contact with the drug binding site. By consequence, non-ideal efflux pumping should arise if the drug binding site of the pump equilibrated more readily with the membrane phase than with the aqueous cytoplasm and if the membrane phase and the cytoplasm did not equilibrate at the time scale of drug pumping. We stress the importance of the latter condition. Many authors have pointed at the likeliness that the drug binding site is in rapid drug exchange contact with the membrane. However likely this may be, it is not at all a sufficient condition for the occurrence of non-ideal kinetic behaviour. Importantly, the additional condition is much less likely, i.e., absence of rapid equilibration of drug between cytoplasm and membrane phase.

In the scientific area of multidrug resistance, the relevant non-ideal behaviour has been called the ‘vacuum cleaning’ effect [Gottesman, 1993]. ‘Vacuum cleaning’ drug efflux pumps have been proposed rapidly to expell drug from the plasma membrane, preventing any drug from entering the cytoplasm. Of course, in the absolute sense the latter prevention is thermodynamically impossible at steady state. Some drug will always make it to the cytoplasm, and unless there is a steady active sink for drug in the cell, at steady state the cytoplasmic drug concentration should equilibrate with that in the membrane. Effectively then, the ‘vacuum cleaner’ model should be regarded as a three compartment system; outside, cytoplasm and membrane phase. The transfer of drug between pump and membrane should be quicker than the transfer between pump and cytosol, and the transfer of drug between membrane (-phase) and cytoplasm should be slow at the time scale of drug pump operation. Vacuum cleaning is enhanced when the membrane is asymmetrical such that the drug more readily moves between membrane and extracellular medium than between membrane and cytoplasm.

An arithmetic model for this type of ‘vacuum cleaner’ for a symmetrical membrane showed that, in the absence of pumping, the drug concentration in the membrane should increase quickly upon administration of the drug to the cells [Mülder *et al.*, 1993]. This quick phase should be followed by a slower but equally extensive increase, witnessing equilibration of the drug with the cytoplasm. A ‘vacuum cleaner’ should reduce the extent of the first phase, whereas a protein pumping from the cytoplasm should only reduce the extent of the

second phase. Using the membrane soluble fluorescent compound 1-(4-trimethylammoniumphenyl)-6-phenyl-1,3,5-hexatriene (TMA-DPH) and its fluorescence energy transfer to daunorubicin in the plasma membrane, Mülder *et al.* [1993] observed ‘vacuum-cleaner’ behaviour in one cell-line, whereas in a different cell line there was no or less ‘vacuum cleaning’.

The above contention that the occurrence of ‘vacuum cleaning’ depends on the relative kinetics of the exchanges of drug between the pump and the membrane phase and cytosol, suggests that the distinction between vacuum cleaner and classical drug pump should not be taken too far. Depending on the substrate or on the host cell a pump protein may exhibit more or less ‘vacuum cleaning’. Indeed, it may be useful to implement a ‘vacuum cleaning index’, perhaps defined by [Lankelma *et al.*, in preparation]:

$$VCI = (1 + a) \cdot \frac{\frac{v_i^{\text{inhibited}} - v_i}{v_i}}{\frac{x_{ss}^{\text{inhibited}} - x_{ss}}{x_{ss}}} \quad (5)$$

Here v_i refers to the initial rate of drug uptake into the cells (zero *trans*), x_{ss} refers to the steady-state intracellular drug concentration, a is an asymmetry factor equal to the relative drug permeability of the inner membrane surface relative to the outer membrane surface (e.g., 1 for a symmetrical membrane) [Mülder *et al.*, 1993]. The superscript ‘*inhibited*’ refers to complete inhibition of the pump such as achieved by the addition of excess Verapamil, which effectively inhibits drug pumping by the drug efflux pump. The equation has been derived for a model where a nonsaturable drug efflux pump either pumps from the membrane or from the cytoplasm. If the pump only communicates with the cytoplasm the *VCI* becomes 0 because such a pump does not affect the initial influx rate. A nonsaturable pure ‘vacuum cleaner’ (i.e., a protein pumping from the membrane more quickly than the drug equilibrates between cytoplasm and membrane) will exhibit a *VCI* of 1. This may be understood intuitively for the example of a symmetrical membrane with a partition coefficient of 1, where the pump is equally active as the leak, such that the steady state membrane activity of the drug will be half that in the external medium. This leads to 1 for the denominator of Eq. 5. The pre-steady state (membrane being already at steady state, but not so the cytoplasm) membrane concentration in the absence of pumping is half the outside concentration; in the presence of the aforementioned pumping activity this becomes one third. Consequently, the initial influx becomes one third rather than half of the unidirectional influx, making the numerator in Eq. 5 equal to $\frac{1}{2}$ and the *VCI* equal to 1. Importantly, if the pump pumps from the membrane, but the drug equilibration between membrane and cytosol is faster than drug pumping, then the *VCI* approaches zero; the drug loses its vacuum cleaner character.

METABOLIC CONTROL ANALYSIS AND NON-IDEALITY

The traditional Metabolic Control Analysis (MCA) treated metabolism as if it were ideal in the above described sense. Non-ideal metabolism, such as direct transfer of metabolites between enzymes, leads to control properties different from those prescribed by the summation property of MCA that total control on flux must equal 1 [Kell and Westerhoff, 1985]. Kholodenko and colleagues [Van Dam *et al.*, 1993; Kholodenko and Westerhoff, 1993, 1995b] have developed MCA for non-ideal metabolism, by defining control coefficients in terms of control by steps in reaction schemes rather than per enzyme. In this sense,

Table 1. Experimental summed control coefficients for all PTS enzymes plus the boundary substrates on the flux of phosphorylation of α -MG, as a function of the concentration of the extract.
E. coli extracts were incubated at various dilutions. PTS mediated phospho transfer from PEP to α -MG was measured *in vitro*

Protein (g/l)	Sum of flux control coefficients
0.5	2.1
1.0	1.9
2.0	1.4

the control of drug uptake into MDR cells should be dissected into control by all steps, including those of the transfer of the drug between the cytosol, the membrane interface and the drug binding site on the pump.

DIRECT METABOLITE TRANSFER AND ENHANCED CONTROL IN SIGNAL TRANSDUCTION

In vivo non-ideal metabolism may well be the rule rather than the exception. Hence, there is a great interest in the special control properties arising in the complex organisation of cell metabolism [Welch and Keleti, 1987]. The phosphotransferase system (PTS) is an interesting system in this respect. It is involved in the import of glucose into *E. coli*, but also in the catabolite repression linked signal transduction. A phosphoryl group is transferred from phosphoenolpyruvate (PEP) through a chain of proteins to glucose. One of the intermediary proteins, i.e., factor IIA^{Glc}, is a key intermediate in regulating some entry systems for other sugars than glucose, as well as the production of cAMP [Postma *et al.*, 1993]. The PTS appears regulated by the cellular free-energy state [Rohwer *et al.*, 1996]. In addition to this actual role, the system may also serve as a model for the extreme case of direct transfer of metabolites between enzymes (metabolite channelling), as the phosphoryl group is never free in solution on its way from PEP to glucose.

We have been able to show that the PTS may exhibit special control properties. First, at low enzyme concentrations, the sum of the control coefficients of the enzymes with respect to the flux of the phosphoryl group through the pathway should equal 2 rather than the 1 prescribed for fluxes through ideal metabolic pathways [but see Van Dam *et al.*, 1993]. Second, at higher enzyme concentrations, where the enzyme-enzyme complexes may persist, this sum should drop to, or even below 1 [Kholodenko and Westerhoff, 1995a]. Table 1 shows the results of an experiment where the sum of all the control coefficients was determined for methyl- α -glucoside (α -MG; an analogue of glucose) phosphorylation in an extract from *E. coli*. The sum of the enzymes' control (response) coefficients was shown greatly to exceed 1 and to decrease at higher protein concentrations.

CONCLUSIONS

With this contribution we hope to have shown that the control of important processes in the live cell, such as the transport of cytotoxic drugs and signal transduction is a complex resultant of various molecular processes and not always in line with sheer intuition. Biomathematical modelling and quantitative experimentation (e.g., by fluorescence methods [Kohen *et al.*, 1983]) appear to be essential for a scientific understanding of these processes in their functional habitat.

ACKNOWLEDGMENTS

HVW thanks Prof. dr. E. Kohen, for many stimulating discussions on the essence of the living cell. This work has been supported by the Netherlands' Organisation for Scientific Research (NWO), the Netherlands' Cancer Foundation (KWF), and the Netherlands' Association of Biotechnology Research Schools (ABON).

REFERENCES

- Burns J.A., Cornish-Bowden A., Groen A.K., Heinrich R., Kacser H., Porteous J.W., Rapoport S.M., Rapoport T.A., Stucki J.W., Tager J.M., Wanders R.J.A. and Westerhoff H.V. (1985). Control analysis of metabolic systems. *Trends Biochem. Sci.* 10, 16.
- Demanet E.J.F., Sehested M. and Buhl Jensen P. (1990) A model for computer simulation of P-glycoprotein and transmembrane delta pH-mediated anthracycline transport in multidrug-resistant tumor cells. *Biochim. Biophys. Acta* 1055, 117 - 125.
- Fell D.A. (1992) Metabolic Control Analysis: a survey of its theoretical and experimental development. *Biochem. J.* 286, 313-330.
- Ghauharali RI, Westerhoff HV, Dekker H, Lankelma J (1996) Saturable P-glycoprotein kinetics assayed by fluorescence studies of drug efflux from suspended human KB8-5 cells. *Biochim. Biophys. Acta*, in press.
- Gottesman M.M. (1993) How cancer cells evade chemotherapy. *Cancer Res.* 53, 747 - 754.
- Gottesman M.M. and Pastan I. (1994) Biochemistry of multidrug resistance mediated by the multidrug transporter. *Annu. Rev. Biochem.* 62, 385 - 427.
- Groen A.K., Wanders R.J.A., Westerhoff H.V., Van der Meer R. and Tager J.M. (1982). Quantification of the contribution of various steps to the control of mitochondrial respiration. *J. Biol. Chem.* 257, 2754-2757.
- Guiral M, Viratelle O, Westerhoff, HV and Lankelma, J (1994). Cooperative P-glycoprotein mediated daunorubicin transport into DNA-loaded plasma membrane vesicles. *FEBS Lett.* 346, 141-145.
- Heinrich R. and Rapoport T.A. (1973). Linear theory of enzymatic chains: its application for the analysis of the crossover theorem and of the glycolysis of human erythrocytes. *Acta Biol. Med. Germ.* 31, 479-494.
- Hofmeyr, J-H S., Cornish-Bowden, A. and Rohwer, J M (1993). Taking enzyme kinetics out of control: putting control into regulation. *Eur J. Biochem.* 212, 833-837.
- Kacser H. (1995). Recent developments beyond metabolic control analysis. *Biochem. Soc. Trans.* 23, 387-391.
- Kacser H. and Burns J.A. (1973). The control of flux. *Symp. Soc. Exp. Biol.* 27, 65-104.
- Kell D.B. and Westerhoff H.V. (1985). Catalytic facilitation and membrane bioenergetics. In *Organized Multienzyme Systems. Catalytic Properties* (Welch G.R., ed.) pp. 63-138, Academic Press, New York, NY, USA.
- Kholodenko B.N. and Westerhoff H.V. (1993). Metabolic channelling and control of flux. *FEBS Lett.* 320, 71-74.
- Kholodenko B.N. and Westerhoff H.V. (1995a). Control theory of group-transfer pathways. *Biochim. Biophys. Acta* 1229, 256-274.
- Kholodenko B.N. and Westerhoff H.V. (1995b). The macroworld versus the microworld of biochemical regulation and control. *Trends Biochem. Sci.* 20, 52-54.
- Kholodenko B.N., Molenaar, D., Schuster S., Heinrich, R. and Westerhoff H.V. (1995) Defining control coefficients in non-ideal metabolic pathways. *Biophys. Chem.* 56, 215-226.
- Kohen E., Kohen C., Hirschberg J.G., Wouters A.W., Thorell B. and Westerhoff H.V. (1983) Metabolic Control and Compartmentation in Single Cells and Multicellular Assemblies. *Cell. Biochem. Function* 1; 3 - 16.
- Lankelma J., Laurensse E. and Pinedo H.M. (1982) A flow-through tissue culture system with fast dynamic response. *Anal. Biochem.* 127, 340 - 345.
- Lankelma J., Spoelstra E.C., Dekker H. and Broxterman H.J. (1990) Evidence for daunomycin efflux from multidrug-resistant 2780^{AD} human ovarian carcinoma cells against a concentration gradient. *Biochim. Biophys. Acta* 1055, 217 - 222.
- Mülder H.S., Van Grondelle R., Westerhoff H.V. and Lankelma J. (1993) A plasma membrane "vacuum cleaner" for daunorubicin in multidrug resistant SW-1573 human non-small cell lung carcinoma cells. *Eur. J. Biochem.* 218, 871 - 882.

- Oude Elferink R.P.J. and Jansen P.L.M. (1994) The role of the canicular multispecific organic anion transporter in the disposal of endo- and xenobiotics. *Pharmacol. Therap.* 64, 77 - 97.
- Postma P.W., Lengeler J.W. and Jacobson G.R. (1993) Phosphoenolpyruvate: carbohydrate phosphotransferase systems of bacteria. *Microbiol. Rev.* 57, 543 - 594.
- Rohwer J.M., Jensen P.R., Shinohara Y., Postma P.W. and Westerhoff H.V. (1996) Changes in the cellular energy state affect the activity of the bacterial phosphotransferase system. *Eur. J. Biochem.* 235, 225 - 230.
- Schinkel A.H., Smit J.J.H., Van Tellingen O., Wagenaar E., Van Deemter L., Mol C.A.A.M., Van der Valk M.A., Robanus-Maandag E.C., Te Riele H.P.J., Berns A.J.M., and Borst P. (1994) Disruption of the mouse *mdr1a* P-glycoprotein gene leads to a deficiency in the blood-brain barrier and to increased sensitivity to drugs. *Cell* 77, 491 - 502.
- Schuster S. and Heinrich R. (1992). The definitions of metabolic control analysis revisited. *BioSystems* 27, 1-15.
- Smit J.J.M., Schinkel A.H., Oude Elferink R.P.J., Groen A.K., Wagenaar E., Van Deemter L., Mol C.A.A.M., Ottenhof R., Van der Lugt N.M.T., Van Roon M.A., Van der Valk M.A., Offerhaus G.J.A., Berns A.J.M. and Borst P. (1993) Homozygous disruption of the murine *mdr2* P-glycoprotein gene leads to a complete absence of phospholipid from bile and to liver disease. *Cell* 75, 451 - 462.
- Spoelstra E.C., Westerhoff H.V., Dekker H. and Lankelma J. (1992) Kinetics of daunorubicin transport by P-glycoprotein of intact cancer cells. *Eur. J. Biochem.* 207, 567 - 579.
- Spoelstra E.C., Westerhoff H.V., Pinedo H.M., Dekker H. and Lankelma J (1994) The multidrug reverser verapamil interferes with cellular P-glycoprotein mediated pumping of daunorubicin as a non-competing substrate. *Eur. J. Biochem.* 221, 363 - 373.
- Van Dam K., Jansen N., Postma P., Richard P., Ruijter G., Rutgers M., Smits, H.P., Teusink B., Van der Vlag J., Walsh M. and Westerhoff H.V. (1993). Control and regulation of metabolic fluxes in microbes by substrates and enzymes. *Anthonie van Leeuwenhoek* 63, 315-321.
- Welch, G R and Keleti, T (1987) Is cell metabolism controlled by a 'molecular democracy' or by a 'supramolecular socialism? *Trends Biochem. Sci.* 12, 216 - 217.
- Westerhoff H.V. and Kell D.B. (1996) What BioTechnologists knew all along.....?? *J. theor. Biol., in the press.*
- Westerhoff H.V. and Van Dam K. (1987) Thermodynamics and Control of Biological Free Energy Transduction Elsevier, Amsterdam, the Netherlands.
- Zaman G.J.R., Flens M.J., Van Leusden M.R., De Haas M., Mülder H.S., Lankelma J., Pinedo H.M., Scheper R.J., Baas F., Broxterman H.J. and Borst P. (1994) The human multidrug resistance-associated protein MRP is a plasma membrane drug-efflux pump. *Proc. Natl. Acad. Sci. USA* 91, 8822 - 8826.

INSTRUMENTATION DESIGN FOR STUDY OF METABOLIC CONTROL IN LIVING CELLS

Joseph G. Hirschberg and Elli Kohen

Department of Physics and Department of Biology
University of Miami
Coral Gables, Florida

INTRODUCTION

For the study of living cells in culture using the fluorescence microscope it is important to make provision for the widest possible instrumental armamentarium, including real-time parameter interactive experimental control (RIPEC). In an ideal apparatus (Kohen *et al* 1991) one might include, for example, (Figure 1) provision for excitation and emission fluorescence spectra, video-optical phase visualization with a long working-distance phase condenser (Hirschberg 1990), scanning near-field microscopy (SNOM), total internal reflection microscopy (TIRM), confocal fluorescence optics, and modulated laser excitation for fluorescent lifetime measurements. The living cells must be contained in a special chamber with regulated temperature and humidity and with sufficient working distance to facilitate micromanipulation and micro-injection. The resulting data are to be displayed in real time, used for computer controlled interactive experimentation, and stored, all by a dedicated computer.

Since many of these subjects have been described elsewhere, (Hirschberg *et al* 1993, Ince 1995, Jovin 1995 and Lansing-Taylor 1995) we will concentrate here on only one aspect, the desirability and provision for excitation fluorescence spectra.

BACKGROUND

The fluorescent excitation spectrum is the dependence of the intensity of fluorescent light on the wavelength of the exciting radiation. Emission fluorescence spectra have been often used but excitation spectra have been comparatively neglected. Excitation spectra have, however, a number of advantages for the study of living cells:

- a. Combined with emission fluorescence spectra, they give an additional parameter which, as has been pointed out (Weber 1961) may help to identify the sources of fluorescence arising from several different fluorophores.

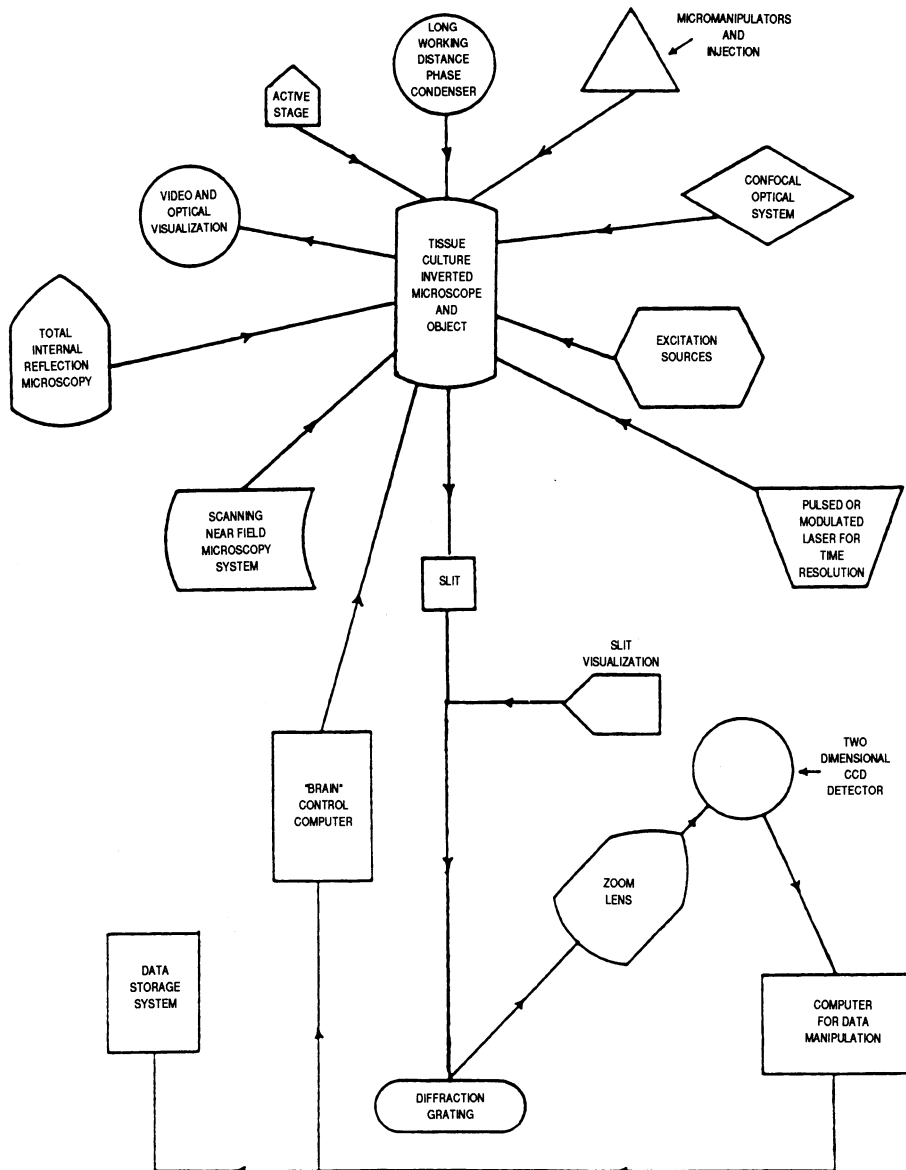


Figure 1. This is a diagrammatic representation of a model multi-option microspectrofluorometer with real-time interactive parameter experimental control (RIPEC) for the study of metabolic processes in living cells. The apparatus is built around a Leitz Diavert tissue-culture microscope (A). Shown clockwise from the top are provision for: B) visible illumination with a custom-built long range phase condenser, C) micromanipulators for dissection of and injection into living cells, D) confocal optical system for z-axis localization of fluorescence, E) excitation sources, including the apparatus for excitation spectrum measurements and (F) pulsed or modulated illumination for fluorescence lifetimes, G) adjustable aperture, together with its visualization lamp (H) for observing the size of the field presented to the emission spectrometer and the topographic measurement of fluorescence, I) interchangeable diffraction gratings and mirror for the selection of spectroscopic dispersion and for topography, J) zoom lens for varying the size of the topographic image and fine adjustment of spectroscopic dispersion, and (K) the CCD detector. L is a dedicated computer affording real-time visualization, data storage capability and "brain control" for interactive control of experiments, N represents a system for scanning near-field and (M) internal reflection microscopy, O and P are eyepiece and video or film cameras for fluorescence visualization and Q is the microscope stage, equipped with temperature and other controls for living cell retention, with micromanipulator access and (R) piezoelectric positioners for interactive study.

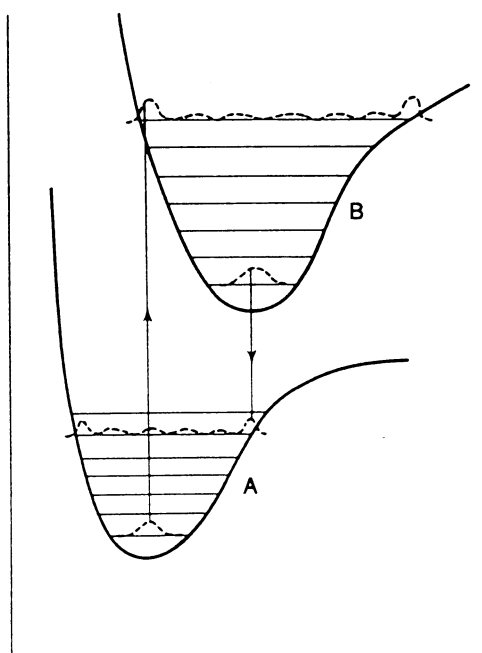
- b. Because the shapes of excitation spectra often reflect the vibrational levels of higher excited electronic states than those of emission spectra, (Figure 2) they can be more indicative of the environment in which the fluorophore is immersed.
- c. The limiting factor in the amount of exciting radiation that is used for living cell fluorescence is often the cell itself. If too much energy falls on the cell it can be damaged or its fluorescence altered. When excitation spectroscopy is used, the spectroscopic selection of the light is carried out in the optical train *before* it strikes the cell instead of after, as is the case with emission fluorescence spectroscopy. Since the spectrum selector element, be it a spectrometer, an interferometer or an interference filter decreases the intensity of the light, from the point of view of light burden on the living cell it may be better to place the selector element before rather than after the cell. The fluorescence from the cell is then brought to the detector by the very efficient light train of the high numerical aperture microscope. In this way damage to the cell can be minimized, even where the fluorescent efficiency is small.

METHOD

There are two distinct ways to perform measurements of the excitation fluorescence spectrum:

- a. Perhaps the most straightforward of these is the sequential method, which is to change the wavelength of the exciting radiation and record the resulting fluorescence, both as a function of time. This has the disadvantage, however, that different parts of the spectrum are recorded at different times. If the cell processes vary in time so that the intensity of the fluorescence changes, the results will not be correct.

Figure 2. This shows the energy levels for the lowest two states of a fluorescing molecule. The excitation spectrum represents transitions ordinarily originating from the lowest vibrational level of the ground electronic state of the molecule and ending on the various vibrational levels of a higher electronic state; thus its shape reflects the population of the vibrational levels of the upper (excited) electronic state. The emission spectrum, on the other hand, originates from the lowest vibrational level of the upper state and ends on the levels of the lowest (ground) electronic state, reflecting the populations of the vibrational levels of the ground electronic state. The excited state will be, on the average, more distant from the nuclei than is the ground state, and therefore the excitation spectrum will tend to be more affected by the environmental conditions surrounding the molecule than is the emission spectrum.



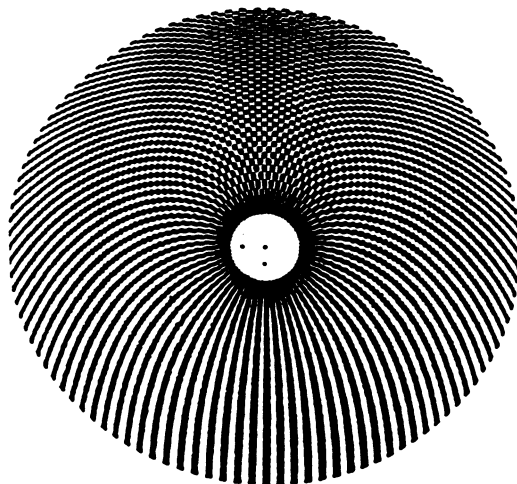


Figure 3. This shows a sample chopping disk, in which the number of transparent and opaque areas in each zone depends on the distance from the pattern center. Two such disks are placed concentric and close to one another in the focal plane of a grating or prism spectrometer fed with a continuum of radiation in the excitation region for the molecule to be measured. When one disk is rotated and the other held fixed, the spectrum will be modulated with a frequency depending on the wavelength of the light.

- b. It is also possible to gather the whole excitation fluorescence spectrum at the same time, using simultaneous spectral encoding (SSE). This has the double advantage that changes in the fluorescence during the time of observation will not result in a false picture of the spectrum, and that the whole spectrum is observed at once, leading to more efficient use of the light.

We have suggested two SSE methods of measuring the emission spectrum:

1. the first employs a continuous light source followed by a prism or grating monochromator with its exit slit replaced by a pair of identical disks, one rotating and the other fixed. (Figure 3). The spectrum is modulated by the two disks in such a way that each band of wavelengths is chopped at a different audio frequency. The resulting fluorescence emission contains the excitation spectral information since the intensity recorded for each frequency corresponds to that from each wavelength band.
 2. In the second method two interferometers are used, a Fabry-Perot and a Michelson. The interferometers have two important advantages over the grating or prism monochromator.
- a. The interferometer patterns have circular symmetry, which matches the aperture of a microscope, and approximately that of a cell.

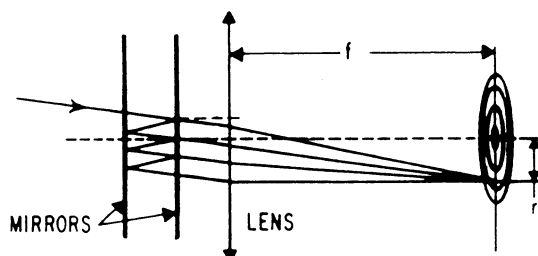


Figure 4. This shows a Fabry-Perot interferometer. It consists of two flat parallel partially-reflecting mirrors, separated by an optical distance nh , where n is the index of refraction of the inter-mirror medium and h is the distance between the mirrors.

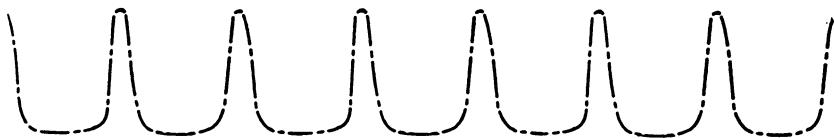


Figure 5. This shows the focussed central pass bands of a Fabry-Perot interferometer as a function of wavelength when the interferometer is illuminated by a continuous-wavelength source. The wavelength space between the bands is the free spectral range. The height of the curve is arbitrary.

- b. The use of an interferometer yields a luminosity advantage of a factor approaching ten compared to a grating or prism monochromator (Jacquinot 1954).

The interferometers are to be used as follows: Light from a continuous source falls on a Fabry-Perot interferometer (Figure 4) adjusted, for example, so that its free spectral range, $\Delta\lambda$ is about 10 nm. The expression for the free spectral range of a Fabry Perot is:

$$\Delta\lambda = \lambda^2/nh$$

where n is the inter-mirror refractive index and h is the geometrical distance between the mirrors. This will result in a “comb spectrum” with peaks 10 nm apart. For example, between 350 and 450 nm, there will be 10 peaks. (Figure 5) This light will then fall on a collimated Michelson interferometer arranged so that one of its mirrors can be accurately translated perpendicularly to its surface with constant speed in a sawtooth motion. The result will be that each band of wavelengths will be modulated at a different frequency. A blanking pulse will stop recording during the sawtooth return periods. The collimated Michelson fringe maxima occur according to:

$$n\lambda = 2x$$

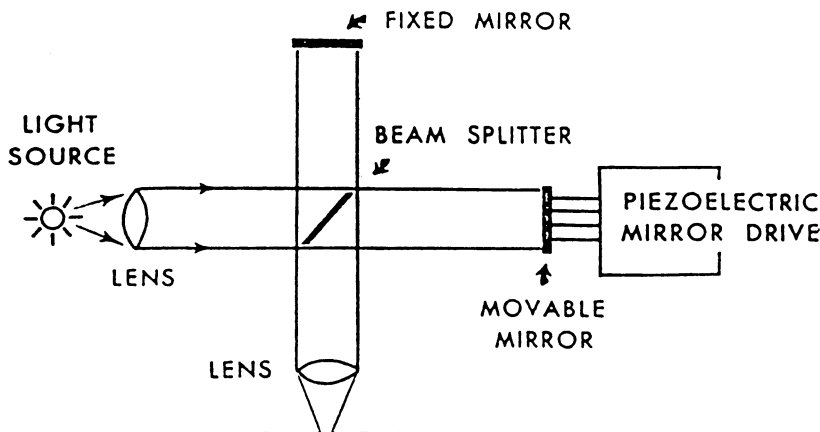


Figure 6. This shows a Michelson interferometer. The light from the Fabry-Perot falls on a 50-50% beam-splitter and is sent in two perpendicular directions. Two flat mirrors, one movable and one fixed, reflect the light which is recombined by the beam-splitter and the fringes focussed by a lens. To change the optical path difference of the two light paths, one of the mirrors is moved by a piezo-electric mounting perpendicular to the axis in a smooth sawtooth as a function of time, like the horizontal motion of the electron beam in an oscilloscope. (As in an oscilloscope the rapid sawtooth return is periodically blanked out by momentarily shutting off the signal from the detector.) The light emerging from the Michelson is focussed by a lens and passed through an aperture in the center of the resulting circular fringe pattern. Each Fabry-Perot peak is then modulated by the Michelson with a frequency inversely proportional to its wavelength.

Differentiating:

$$\frac{dm}{dt} / \lambda = 2 dx/dt$$

From this we obtain:

$$f = 2v/\lambda$$

where f is the frequency of the light variations and v the speed of the moving mirror. Each wavelength will then be modulated at a different frequency in the same way as for the grating system described above, but with significantly greater efficiency. Again, light from the interferometer falls on the cell, and the resulting fluorescence is collected, measured and analyzed.

CONCLUSION

We have described a future multi-option fluorescent microscope for the study of metabolic control in living cells, and have treated in detail one of the options, an interferometric method for the measurement of the fluorescence excitation spectrum. We have also expressed some advantages of the fluorescence excitation spectrum.

ACKNOWLEDGMENTS

This work was supported in part by National Science Foundation SGER award BIR-9521478 and by the University of Miami General Support Award: "Microspectrofluorometry of Detoxification Mechanisms in Transplanted Cells".

REFERENCES

- Hirschberg, J.G., Fried, W.I. and Hazleton, L. Jr. (1971) "Multiplex Fabry-Perot interferometer", *Appl. Optics* 10 1979-1980.
- Hirschberg, J.G. (1990) "A long range microscope phase condensing system" *Appl. Optics* 29 1409-1410.
- Hirschberg, J.G., Kohen, E. and Kohen, C. "Microspectrofluorometry" in *Advances in Optical and Electron Microscopy*, Vol. 14, pp. 121-211, Academic Press, London.
- Ince, C. (1995) "Creating physiological conditions for single cell investigations on the stage of a microscope", Proceedings of NATO Advanced Research Workshop: *Analytical Use of Fluorescent Probes in Oncology*, Hollywood, FL, USA.
- Jacquinot, P. (1954) "The luminosity of spectrometers with prisms, gratings or Fabry-Perot étalons." *J. Opt. Soc. Am.* 44, 761-765.
- Jovin, T.M. (1995) "Integration of scanning probe microscopy with optical techniques", Proceedings of NATO Advanced Research Workshop: *Analytical Use of Fluorescent Probes in Oncology*, Hollywood, FL, USA.
- Kohen, E., Kohen C., Hirschberg, J.G., Santus, R., Morliere, P., Kasten F.H. and Ghadially, F.N. (1991) "Optical methods in cell biology" in *Encyclopedia of Human Biology*, Vol. 5, pp. 561-585.
- Lansing-Taylor D. (1995) "N-dimensional imaging of cells", Proceedings of NATO Advanced Research Workshop: *Analytical Use of Fluorescent Probes in Oncology*, Hollywood, FL, USA.
- Weber, G. (1961) "Enumeration of components in complex systems by fluorescence spectroscopy", *Nature* 190, 27-29

USE OF FLUORESCENT DERIVATIVES FOR LABELING CELLS; DIAGNOSING, PREVENTING, AND CORRECTING GENETIC DISEASES; PHOTOSYNTHESIZING AND KILLING OF TUMORS, PARASITES, AND VIRUSES

Shimon Gatt, Tama Dinur, Sara Cerbu-Carabat, Vered Agmon, and
Arie Dagan

Department of Biochemistry
Hebrew University — Hadassah School of Medicine
Jerusalem 91120, Israel

1. INTRODUCTION

Our laboratory has been involved in enzymatic and cell-biological studies using fluorescent derivatives since the late 1970's. Although a few of the fluorescent compounds were purchased, most were novel derivatives synthesized by us. They were used for the following purposes:

1.1. Use as Substrates for Following Enzymatic Activity *in Vitro* and *in Situ*

Because of our involvement in studies of the metabolism of the sphingolipids, we synthesized numerous fluorescent derivatives of the various glycosphingolipids and the corresponding phospholipid sphingomyelin. They were used as substrates for determining the activities of the respective enzymes which hydrolyze this group of complex lipids, i.e., glycosidases and sphingomyelinases. For this purpose purified enzymes or, alternatively, cell extracts were used. In parallel, an alternative approach was developed, i.e., hydrolysis of the fluorescent substrates in intact cells. For this purpose the fluorescent glyco- and phosphosphingolipids were administered into intact cells in culture and their intracellular metabolism, as well as secretion of the metabolic products from the cells into the culture medium was extensively studied. These studies were done using normal cells and those derived from patients with sphingolipid storage disorders, such as Gaucher, Krabbe, Fabry,

Schindler, Tay-Sachs, GM1-gangliosidosis and Niemann-Pick diseases. In a more recent molecular-biological approach, the fluorescent sphingolipids were employed for selecting cells derived from a lipid storage disease that had been enzymatically corrected and normalized by transfection with a vector containing the gene encoding the normal enzyme. And, in another study, for characterizing intracellular activities of cells of a lipid storage disorder that had been transfected with genes encoding various mutations of a sphingolipid hydrolase.

1.2. Analytical Use for Labeling of Specific Cell Types

For this purpose fluorescent compounds were administered into cells and used for labeling specific cell populations. Thus, differences in fluorescence-emission were obtained between normal and leukemic cells as well as the latter and their differentiated counterparts. Differences in fluorescence emission were also obtained between normal cells and those derived from patients with lipid storage diseases. And, in a separate study, fluorescent compounds were used for labeling parasites infecting host cells, as well as their specific, intracellular components (e.g., malaria parasites in intact erythrocytes).

1.3. Photosensitization and Selective Killing of Cells

For this purpose we employed two groups of fluorescent compounds. The first had the polycyclic hydrocarbon pyrene and required illumination with a long wavelength ultraviolet light source (UVA). It was used mostly for selective killing of leukemic cells and those derived from patients with lipid storage disorders. The second was composed of derivatives of pheophorbide prepared from chlorophyll of the algae *Spirulina* or of bacteriochlorophyll prepared from *Rhodobacter*. These compounds were employed for cleanup of blood infected with parasites or viruses and for killing of cancer cells as well as eradicating solid tumors in animals.

2. EXPERIMENTAL PROCEDURES

2.1. Synthesis of Fluorescent Compounds

1. Though we have tested numerous fluorescent probes, we ended up using two main probes: pyrene, a non-polar polycyclic hydrocarbon, and lissamine-rhodamine (LR) or sulforhodamine (Texas Red, SR or TR), polar probes which contain a negatively-charged sulfonate and two positively-charged amines, a tertiary and a quaternary. Most pyrene-containing derivatives contained the probe, linked to a 12-carbon fatty acid, i.e., pyrene dodecanoic acid (P12). The latter was purchased from Molecular Probes (Eugene, OR) and linked, following activation of its carboxyl group, via an amide group to lysosphingolipids (i.e., sphingolipids from which the original fatty acyl residue was removed by hydrolysis). In a later development, the pyrene was linked to aminoundecanoic acid via a sulfonylamido linkage. The latter (i.e., pyrene sulfonylamido undecanoic acid (PSA-11) was then attached via an amide linkage to the respective lysosphingolipids.
2. The LR or SR were purchased as their sulfonylchlorides and the latter were linked to amino fatty acids. As with pyrene, fatty acids of various chain length were tested and the most suitable for our studies was again found to be $\text{LRSO}_2\text{NH}(\text{CH}_2)_{11}\text{COOH}$, i.e., lissamine (or sulfo) rhodamine dodecanoic acid (LR12 and SR12), which was linked to the various lysosphingolipids.

3. Numerous fluorescent derivatives of pyrene and lissamine rhodamine other than sphingolipids were also synthesized and used for cell biological studies. Their syntheses and applications will not be discussed in this article.
4. For preparing pheophorbide, the dried algae *Spirulina* was extracted with organic solvents and its chlorophyll treated with trifluoroacetic acid, converting it to pheophorbide (Ph-0).¹ A similar procedure was used for extracting bacteriochlorophyll from *Rhodobacter* and converting it to bacteriopheophorbide (B-Ph-0). The pheophorbide and bacteriopheophorbide were then derivatized via their respective carboxyl groups, producing a variety of compounds which were fluorescent and acted as very efficient photosensitizers. To exemplify some of these compounds: Pheophorbide fatty acids [pheophorbide acetate (Ph₂COOH), butyrate (Ph₄COOH), hexanoate (Ph₆COOH), octanoate (Ph₈COOH), decanoate (Ph₁₀COOH), dodecanoate (Ph₁₂COOH)]; pheophorbide amines (Ph₂NH₂, Ph₄NH₂, Ph₆NH₂, Ph₈NH₂) and alcohols (Ph₂OH, Ph₄OH, Ph₆OH, Ph₈OH); pheophorbide ethane (Ph₂CH₃); pheophorbide ethyl sulphydryl (Ph₂SH); pheophorbide ethyl sulfonate (Ph₂SO₃⁻); pheophorbide ethyl trimethyl amine (Ph₂-N⁺(CH₃)₃); pheophorbide hexylphosphate (Ph₆-PO₃H₂); and others.

2.2. *In Vitro Assay of Enzymatic Activity of Sphingolipid Hydrolases*

When using pyrene, LR or other fluorescent sphingolipids as substrates for the respective sphingolipid hydrolases the product, as well as the substrate were fluorescent. Therefore, it was necessary to separate the product from the substrate. For this purpose we worked out three analytical procedures.

2.2.1. Thin Layer Chromatography (TLC). The entire reaction mixture is applied to a thin layer chromatography plate or aluminium-based sheet of silica gel or alumina. The latter is dried with a fan and developed with a suitable solvent mixture which results in a different migration of the substrate and product and permits collection of the latter. Illumination of the TLC plate with a long-wavelength ultraviolet light source (UVA) permits identification of the fluorescent product, and through its fluorescence emission strength, a qualitative evaluation of the degree of hydrolysis of the substrate. For quantitation the fluorescent spot of the product is scraped from the plate into a tube (or, when using a sheet, the spot is cut out with scissors and introduced into the tube). The fluorescent product is then extracted with a suitable solvent mixture (usually by heating for about 10 minutes at 50–60°C) and its fluorescence emission quantified in a spectrofluorometer using the peak absorption and emission spectra for the respective probe used.

2.2.2. Mini-Column Chromatography. The reaction mixture is applied to a mini-column of silica or alumina in a Pasteur pipette; the product is selectively eluted using a suitable solvent mixture and its fluorescence quantified in a spectrofluorometer. Alternatively, a commercial mini-column pre-filled with silica or alumina is used.

2.2.3. Solvent Partition. For many of the assays, advantage was taken of differences in the respective polarities of the substrate and product to selectively transfer the latter into one portion of a bilayered solvent mixture while the as yet undegraded substrate remained in the second portion. To exemplify, when pyrene sphingomyelin was hydrolyzed by sphingomyelinase to ceramide, the product (i.e., pyrene ceramide) which is very non-polar, partitioned into the heptane phase of a bilayered solvent mixture composed of equal volumes

of heptane, isopropylalcohol and water ("Dole's mixture"). In contrast, the substrate, which contains the polar phosphocholine residue, partitioned to the aqueous-alcoholic phase. Another example is the hydrolysis of ceramide to sphingosine and pyrene fatty acid using the same solvent mixture. In this case the fluorescent fatty acid, in the presence of NaOH partitioned to the aqueous-alcoholic phase while the remaining undegraded substrate (i.e., pyrene ceramide) partitioned to the upper heptane phase.

2.3. Administration of Fluorescent Lipids into Cultured Cells

Most of our interest was in studying the degradation of sphingolipids by lysosomal hydrolases. Therefore, for studying intracellular hydrolysis of the fluorescent sphingolipids our aim was to direct them to the lysosomal compartment of the intact cells. When using pyrene sphingolipids, this was achieved as follows: the respective sphingolipid was mixed with a 4 or 9 mole excess of lecithin (phosphatidylcholine), the organic solvent was evaporated, water and buffer were added and the suspension was subjected to ultrasonic irradiation, resulting in the formation of small unilamellar liposomes (SUV). Apolipoprotein E (a generous gift of Biotechnology Inc., Nes Ziona, Israel) was added and the liposomes containing the fluorescent sphingolipid were thereby administered into the cells by receptor mediated endocytosis via the LDL-receptor and trafficked to the cells' lysosomes, where the substrate was degraded.

When the highly polar lissamine or sulforhodamine sphingolipids were added to the culture medium as solutions in ethanol or dimethyl sulfoxide, they translocated across the plasma membrane of the cell and reached the lysosomes without the need for apolipoprotein E or any other carrier, though frequently they were incorporated into phosphatidylcholine liposomes.

2.4. Analysis of the Fluorescence of Intact Cells

Following administration of a fluorescent sphingolipid, the cells were subjected to a "pulse and chase", i.e., they were incubated in the presence of the fluorescent compound for a period of 2 to 96 hours ("pulse"). The medium was then removed and replaced with fresh medium devoid of the fluorescent substrate and the incubation was continued for 1 day up to 1 week. Analysis was as follows:

- a. The cells were washed and, when adhering to the matrix (e.g., using skin fibroblasts) trypsinized briefly, the trypsin was neutralized with fetal calf serum, the cell suspension washed and its fluorescence emission recorded in a spectrophotometer.
- b. For analyzing the metabolic products the cells were extracted with mixtures of chloroform and methanol and the fluorescence of the cells' extract recorded. The solvent was then evaporated under a stream of nitrogen, argon or air and the residue spotted on a thin layer chromatography plate or sheet. Development of the latter provided a fluorescent image of the metabolic products. Scraping the respective spots, extracting with solvent and recording their fluorescence provided a quantitation of the respective metabolic products.
- c. An alternative procedure was sorting of the cell suspension in the Fluorescence Activated Cell Sorter (FACS Becton-Dickinson). This provided the distribution of the fluorescence in each individual cell.
- d. Still another procedure involved growing the cells on microscopic glass cover slides and analyzing the cell fluorescence by fluorescence microscopy and, even more efficiently, by confocal computerized fluorescence microscopy (imaging;

microspectrofluorometry). The latter provided a quantitative value of fluorescence per cell, as well as an image of the intracellular distribution of the fluorescence in the subcellular components.

2.5. Photosensitization

The photosensitizing molecule was administered into the cells and the latter were subjected to illumination with a suitable light source. Cell damage was measured as follows:

1. Cells adhering to the matrix were preincubated with radioactive chromate. Following illumination, damaged cells leaked radioactivity into the medium.
2. Adhering fibroblasts were suspended by trypsin, illuminated and left to readhere to the matrix. Only undamaged cells readhered.
3. Cell death could also be followed using vital stains, loss of reproduction capacity, etc.
4. Animals with solid tumors were infused with the respective photosensitizer and the tumor was illuminated with laser terminals. Tumor size and weight was then determined at various times following the illumination.

3. SUMMARY OF EXPERIMENTAL APPROACHES AND RESULTS

3.1. Selective Labeling and Cell-Killing by Pyrene Dodecanoic Acid²⁻¹⁶

These studies were done in close collaboration with Dr. E. Fibach of the Hematology Department of the Hadassah University Hospital in Jerusalem.

When added to the culture medium, pyrene dodecanoic acid (P12) was taken up by cells and metabolized. Extraction of the cells, followed by thin layer chromatography, indicated absence of free P12 and its presence in the cells neutral- and phospholipid phases. We assumed that when translocated across the plasma membrane P12 is activated to form pyrene dodecanoic coenzyme-A ester which transfers the P12 to the glycerol moiety of the lipids. The degree of incorporation and the ratio of fluorescence in the neutral and phospholipids varied considerably with the cell type. To exemplify: When compared to that of the red or various white cell lines, leukemic cell lines exhibited a considerably higher fluorescence emission, e.g., when measured in the fluorescence activated cell sorter. But, even in this case variability was observed. Thus, HL-60 cells (established from a patient with acute promyelocytic leukemia) had a considerably higher fluorescence per cell than murine erythroleukemia (MEL) cells. When undifferentiated leukemic cells (e.g., erythroleukemic MEL-60) cells were differentiated, their fluorescence per cell was considerably modified. But the fluorescence per cell depended on the type of differentiation. Thus, differentiation of MEL cells with hexamethylene bis acetamide (HMBA) resulted in formation of hemoglobin-containing normoblasts which exhibited a considerably lesser fluorescence. When HL-60 cells were differentiated, the fluorescence per cell in the differentiated cells depended markedly on the inducer molecule. Thus, when HL-60 cells were incubated with dimethylsulfoxide they were converted to granulocytes and, when incubated with TPA, they were differentiated to macrophages which exhibited a considerably higher fluorescence.

Pyrene is also an effective photosensitizer. Thus, when illuminated with a long wavelength ultraviolet light source at 366 nm (UVA) for periods of 0.5–5 min., cells which have been pretreated with P12 were killed.¹¹⁻¹⁶ Similar irradiation had no effect on cells that had not been exposed to P12. The time necessary to induce the toxic process was related to

the quantity of P12 incorporated. Thus, MEL cells were more prone to phototoxicity than the differentiated, hemoglobin-containing normoblasts.

3.2. Use of Fluorescent Sphingolipids for Studying Lipid Storage Disorders

In our studies of the genetic disorders, named the lipid storage diseases (lipidoses), we aimed at using fluorescent sphingolipids for the following three approaches: a. Diagnosis, b. Prevention of birth of infants afflicted with lipidoses. c. Gene therapy. The respective approaches are herewith described.

A. Diagnosis

A1. In vitro. ¹⁷⁻²⁸ We have synthesized fluorescent derivatives of the various sphingolipids to which we have linked the following probes: anthracene, pyrene, NBD, fluorescein; rhodamine, lissamine rhodamine, sulforhodamine and Bodipy. They were used for determining the activities of the respective hydrolases, such as ceramidase, β -glucosidase, α - and β -galactosidases; α - and β -N-acetylhexosaminidases, arylsulfatases and sphingomyelinases. Since in all cases both the substrate and product were fluorescent, techniques have been worked out for separating the product from the as yet undegraded substrate by solvent partition, thin layer or mini-column chromatography (see Experimental Procedures). Quantification of the fluorescence emission of the product was by spectrofluorometry using the specific peak excitation and peak emission wavelengths for the respective probes.

A2. In situ. ²⁹⁻³³ The principle of this mode of diagnosis is as follows: A fluorescent substrate is administered into intact cultured cells, trafficked to the lysosomes where it is degraded by the respective hydrolases and the product secreted into the medium. This procedure follows two stages: a "pulse", during which the substrate is present in the medium and taken up by the cells. This is followed by a "chase" in which the original medium is removed, fresh medium devoid of fluorescent substrate added and incubation continued. Thus, during the pulse period the fluorescence peaks and during the chase it decreases considerably. When using cells derived from patients with lipid storage diseases which lack a specific hydrolase, the substrate is not degraded and the fluorescence remains high even following a prolonged "chase" period. Thus, a higher fluorescence relative to that of intact normal cells indicates an enzymatic defect related to a specific genetic disorder (lipidosis). Analysis was done by recording the fluorescence of a suspension of intact cells or, alternatively, of an extract in organic solvent in the spectrofluorometer. Subsequently, thin layer chromatography of the extracted lipids, followed by quantification of the fluorescence of the product, indicated the degree of degradation of the substrate. Two alternative modes of analysis of the fluorescence of the intact cells were done using the fluorescence activated cell sorter or by computerized, confocal fluorescence microscopy (imaging; microspectrofluorometry).

When sphingolipids to which the hydrophobic probe pyrene was linked were used, they were incorporated into unilamellar liposome of lecithin and the latter coated with apolipoprotein E. This resulted in their uptake by receptor mediated endocytosis via the LDL-receptor and trafficking to the lysosomes. Lissamine- or sulfo-rhodamine sphingolipids translocated across the cell membrane in the absence of apolipoprotein E and because of their net positive charge they trafficked to and accumulated in the lysosomes. Using the latter probes the following sequence of events occurs: The sphingolipid in the lysosome is degraded to LR- or SR-ceramide. The latter translocates across the lysosomal membrane to

the Golgi, where it is converted to LR- or SR-sphingomyelin. The latter is trafficked (by vesicular flow) to the plasma membrane (PM) and, probably due to its high polarity, is not maintained in the PM but is secreted into the medium. In lipidotic cells where, because of an enzymatic deficiency LR ceramide is not formed from LR-glycolipids, LR-sphingomyelin is not present in the culture medium. Thus, quantifying the LR-sphingomyelin in the medium permits an *in situ* diagnosis without having to disrupt the cells.

B. Potential Prevention of Birth of Lipidotic Infants³⁴

This study was done in collaboration with Dr. N. Laufer of the Hadassah Hospital. The principle was to analyze an embryo as healthy or sick at the pre-implantation stage of *in vitro* fertilization (IVF) using one cell that would be removed from the embryo for *in situ* fluorescence-based diagnosis. Since use of human embryos for research is forbidden, we used murine embryos as a model. The latter were pulsed with fluorescent glucosylceramide (glucocerebroside) for 2 hours and then chased overnight in fresh medium. In parallel, embryos were incubated in medium containing bromoconduritol B-epoxide (Br-CBE), an inhibitor of β -glucosidase. The embryos were then analyzed by computerized fluorescence microscopy—those incubated in the presence of Br-CBE were found to have a much higher fluorescence than those incubated in its absence. This experiment, used as a model for Gaucher disease, indicated the feasibility of this approach.

C. Models for Gene Therapy of Niemann–Pick Disease (NPD)^{35–37}

This study was done in collaboration with Dr. E.A. Schuchman, R.J. Desnick and their coworkers at the Mount Sinai Medical Center in New York City. Fibroblasts from a patient with Niemann–Pick type B (the milder form) were transduced with retroviral vectors expressing the normal, lysosomal (acid) sphingomyelinase (ASM). For isolating those cells which had incorporated the gene and consequently expressed ASM activity (“normalized”), the entire cell population was labelled with a fluorescent sphingomyelin (lissamine rhodamine dodecanoyl sphingosylphosphocholine, LR-SPM). The metabolically-corrected cells which degraded the LR-SPM, and consequently had a reduced fluorescence, were sorted and collected under sterile conditions in the FACS and subsequently regrown. Quantitative PCR analysis demonstrated that the enzymatically-corrected cells were indeed enriched in vector sequences. And, the corrected cells could be regrown and continued to express high levels of ASM activity after numerous passages, consistent with the fact that they were stably transduced by the normal ASM. The above provided a procedure in which gene-corrected cells of a genetic disease could be isolated by a fluorescence-based procedure stemming from modified metabolic activity, obviating the need for inclusion of cotransfected marker genes (e.g., the neomycin resistance gene). Subsequently, we grew together the above gene-corrected cell and the original NPD cells. Fluorescence-based techniques (i.e., FACS sorting and computerized fluorescence microscopy) indicated a correction of the NPD cells, most probably by transfer of acid sphingomyelinase from the gene-corrected to the NPD cells. Thus, this was a model of gene therapy at a level of tissue culture, indicating that “bystander correction” may occur following autologous transplantation of retrovirally-transduced cells into NPD patients.

3.3. Photosensitization by Pheophorbide and Bacteriopheophorbide Derivatives^{38–40}

Pheophorbide, bacteriopheophorbide and their respective derivatives were synthesized in our laboratory in Jerusalem and were used for two main approaches:

1. Photosensitization and killing of cancer cells in culture and eradication of solid tumors in animals. These studies were done in collaboration with Drs. J. Donald Chapman and his colleagues at the Fox Chase Cancer Center in Philadelphia, PA, USA as well as Drs. R. Santus and J.C. Maziere of the Museum of Natural History in Paris, France.
2. Photosensitization and killing of parasites and viruses in blood. These studies were done in collaboration with Drs. J. Schrevel, Ph. Grellier, R. Santus and J.C. Maziere of the Museum of Natural History in Paris, France.

3.3.A. Photosensitization and Killing of Cultured Cancer Cells and Solid Tumors in Animals

The various pheophorbide derivatives, in which the functional group was linked at the C7 carboxylic group, were added to the culture medium of several cell lines: murine mammary (EMG) MT-29 (colon), Ovar10 and A2780 (ovary) tumor lines; U937 monocyte-like cells and HLG-cells. Irradiation was by a laser source at 663 nm. Addition of lipoprotein (e.g., HDL, LDL or VLDL) resulted in a marked increase of the fluorescence emission of many of the pheophorbide derivatives, and administration of lipoproteins into the culture medium assisted in the removal of the pheophorbide derivatives from the cells. The most efficient photosensitizers were pheophorbide butanol (Ph4OH) and pheophorbide ethane (Ph_2CH_3). The relative effectiveness of pheophorbide butanol (Ph4OH) and bacteriochlorophyll butanol (B-Phe 4OH) towards cancer cells in culture exceeded that of Photofrin 1,500- and 2,400-fold, respectively.

In a parallel study done by J.D. Chapman and his collaborators, pheophorbide derivatives were injected into mice into which EMT-6 tumor cells were injected subcutaneously into the backs of C.B.17/ICR scid (severely compromised immune deficiency) mice or rats in which Dunning prostate carcinomas (R3327-AT) were grown subcutaneously on the flanks. Laser light was generated and delivered by 7 or 9-fiber illuminators, spread around the solid tumor. For pheophorbide and bacteriopheophorbide derivatives light at 637 and 753 nm respectively was used. Complete tumor eradication was obtained, probably because of perfusion shutdown and secondary ischemic cell death. In intact animals, Ph4OH and B-Ph4OH were at least 100-fold more potent than Photofrin in photo-eradicating the solid tumors.

3.3.B. Cleanup of Blood from Parasites and Viruses

Cultures of the malaria parasites (e.g., *Plasmodium falciparum*) or babesiosis (e.g., *Babesia divergens*) in red blood cells or whole blood were incubated with pheophorbide derivatives and irradiated with a light source at 660 nm, resulting in total eradication of the respective parasites. As with tumor cells, pheophorbide butanol was the most efficient photosensitizer. Under the conditions used, red blood cells devoid of parasites were not lysed or damaged. Preliminary experiments using AIDS virus in blood also indicated that Ph4-OH can be used for its total eradication.

REFERENCES

1. M.R. Wasiliewski and W.A. Svec, Synthesis of covalently linked dimeric derivatives of chlorophyll, pyrochlorophyll-a, chlorophyll-b and Bacteriochlorophyll-a. *J. Org. Chem.* 45:1968–1971 (1980).

2. O. Morand, E. Fibach, A. Dagan, and S. Gatt, Transport of fluorescent derivatives of fatty acids into cultured human leukemic myeloid cells and their subsequent metabolic utilization. *Biochem. Biophys. Acta* 711:539–550 (1982).
3. O. Morand, E. Fibach, and S. Gatt, Effect of albumin, low temperature and metabolic inhibitors on transport of fatty acids into cultured human leukemic myeloid cells. *Biochim. Biophys. Acta* 693:143–150 (1982).
4. O. Morand, E. Fibach, N. Livni, and S. Gatt, Induction of lipid storage in cultured leukemic myeloid cells by pyrene-dodecanoic acid. *Biochim. Biophys. Acta* 793:95–104 (1984).
5. E. Fibach, N. Nahas, H. Giloh, and S. Gatt, Uptake of fluorescent fatty acids by erythroleukemia cells: Effect of differentiation. *Exp. Cell Res.* 166:220–228 (1986).
6. E. Fibach, E. Morand, and S. Gatt, Phosphosensitization to UV-irradiation and selective killing of cells following uptake of pyrene fatty acid. *Cell Sci.* 85:149–159 (1986).
7. N. Nahas, E. Fibach, H. Giloh, and S. Gatt, Use of Fluorescence Activated Cell Sorter for studying uptake of fluorescent fatty acids into cultured cells. *Biochim. Biophys. Acta* 917:66–71 (1987).
8. S. Gatt, N. Nahas, and E. Fibach, Continuous spectrofluorometric measurements of uptake by cultured cells of 12-(1-pyrene)-dodecanoic acid from its complex with albumin. *Biochem. J.* 253:977–980 (1988).
9. S. Gatt and E. Fibach, Spectrofluorometric measurements of the dispersion state of pyrene dodecanoic acid and its uptake by cultured cells and liposomes. *Biochim. Biophys. Acta* 943:447–453 (1988).
10. E. Fibach, H. Giloh, E.A. Rachmilewitz, and S. Gatt, Flow cytometric analysis of the uptake of the fluorescent fatty acid pyrene-dodecanoic acid by human peripheral blood cells. *Cytometry* 9:525–528 (1989).
11. E. Fibach and S. Gatt, Clonal analysis of the response of human promyelocytic leukemia (HL-60) cells to photosensitization induced by a pyrene containing fatty acid. *Leuk. Res.* 11:1019–1126 (1987).
12. E. Fibach, E.A. Rachmilewitz, and S. Gatt, Analysis of cellular heterogeneity in the response of human leukemic cells to photosensitization induced by pyrene-containing fatty acid. *Leuk. Res.* 13:1099–1104 (1989).
13. Fibach, E., S. Gatt, and E.A. Rachmilewitz, Selective photosensitization of human leukemic cells by a pyrene-containing fatty acid. *Exp. Hematol.* 18:89–93 (1990).
14. S. Abou-Rabia, E. Fibach, M. Kotler, and S. Gatt, Inactivation of Vesicular Stomatitis virus by photosensitization following incubation with a pyrene fatty acid. *FEBS Letters* 270:9–10 (1990).
15. E. Fibach, S. Abou-Rabia, and S. Gatt, Pyrene butanol — an efficient, selective and non-metabolized photosensitizing agent for human myeloid leukemia cell. *Leuk. Res.* 16:1453–1462 (1992).
16. E. Fibach, E.A. Rachmilewitz, and S. Gatt, Photosensitization of human bladder carcinoma cells by pyrene dodecanoic acid: Quantitative analysis of the cytotoxicity. *Res. in Exp. Med.* 192:185–196 (1992).
17. T. Dinur, G.A. Grabowski, J.R. Desnick, and S. Gatt, Synthesis of a fluorescent derivative of glucosyl ceramide for the sensitive determination of glucocerebrosidase activity. *Anal. Biochem.* 136:223–234 (1984).
18. M. Zeigler, J. Zlatogora, R. Regev, A. Dagan, S. Gatt, and G. Bach, Prenatal diagnosis of Krabbe disease using a fluorescent derivative of galactosylceramide. *Clin. Chim. Acta* 142:313–328 (1984).
19. R. Salvayre and S. Gatt, Use of mixed dispersions of fluorescent galactosylceramide and sodium dodecylsulfate for assaying galactoceramide β -galactosidase and diagnosing Krabbe disease. *Enzyme* 33:175–180 (1985).
20. D.E. Negre, R. Salvayre, A. Dagan, and S. Gatt, New fluorometric assays of lysosomal acid lipase and its application to the diagnosis of Wolman and cholesteryl ester storage disease. *Clin. Chim. Acta* 149:81–88 (1985).
21. G. Bach, A. Dagan, B. Herz, and S. Gatt, Diagnosis of arylsulfatase-A deficiency in intact cultured cells using a fluorescent derivative of cerebroside sulfate. *Clin. Genet.* 31:211–217 (1987).
22. R. Klar, T. Levade, and S. Gatt, Synthesis of pyrene sulfonylamidosphingomyelin and its use as substrate for determining sphingomyelinase activity and diagnosing Niemann-Pick disease. *Clin. Chim. Acta* 176:259–268 (1988).
23. S. Marchesini, P. Viani, B. Cestaro, and S. Gatt, Synthesis of pyrene derivatives of cerebroside sulfate and their use for determining arylsulfatase A activity. *Biochim. Biophys. Acta* 1002:14–19 (1989).
24. P. Viani, S. Marchesini, B. Cestaro, and S. Gatt, Correlation of the dispersion state of pyrene cerebroside sulfate and its uptake and degradation by cultured cells. *Biochim. Biophys. Acta* 1002:20–27 (1989).
25. A. Negre, A. Dagan, and S. Gatt, Pyrene-methyl lauryl ester, a new fluorescent substrate for lipases: Use for diagnosis of acid lipase deficiency in Wolman's and cholesteryl ester storage diseases. *Enzyme* 42:110–117 (1989).
26. A. Negre, R. Salvayre, A. Dagan, and S. Gatt, Pyrene methyl laurate, a new fluorescent substrate for continuous kinetic determination of lipase activity. *Biochim. Biophys. Acta* 1006:84–88 (1989).

27. S. Marchesini, A. Preti, M.F. Aleo, A. Casella, A. Dagan, and S. Gatt, Synthesis, spectral properties and enzymatic hydrolysis of fluorescent derivatives of cerebroside sulfate containing long-wavelength emission probes. *Chem. Phys. Lipids* 53:165–175 (1990).
28. V. Agmon, S. Cherbu, A. Dagan, M. Grace, G.A. Grabowski, and S. Gatt, Synthesis of novel fluorescent glycosphingolipids for estimating β -glucosidase activity *in vitro* in the absence of detergents and subtyping Gaucher disease variants following administration into intact cells. *Biochim. Biophys. Acta* 1170:72–79 (1993).
29. T. Levade, S. Gatt, and R. Salvayre, Uptake and degradation of several pyrene-sphingomyelins by human skin fibroblasts from controls and Niemann-Pick disease: Effect of the structure of the fluorescent fatty acyl residue. *Biochem. J.* 275:211–218 (1991).
30. T. Levade, S. Gatt, A. Maret, and R. Salvayre, Different pathways of uptake and degradation of sphingomyelin by lymphoblastoid cells and the potential participation of the neutral sphingomyelinase. *J. Biol. Chem.* 266:13519–13529 (1991).
31. V. Agmon, T. Dinur, S. Cherbu, A. Dagan, and S. Gatt, Administration of pyrene lipids by receptor-mediated endocytosis and their degradation in skin fibroblasts. *Exp. Cell Res.* 196:151–157 (1991).
32. V. Agmon, E. Monti, A. Dagan, A. Preti, S. Marchesini, and S. Gatt, Diagnosis of lipid storage diseases using the culture medium of skin fibroblasts. *Clin. Chim. Acta* 218:139–147 (1993).
33. T. Levade, F. Vidal, S. Vermeersch, N. Andrieu, S. Gatt, and R. Salvayre, Degradation of fluorescent and radiolabelled sphingomyelins in intact cells by a non-lysosomal pathway. *Biochim. Biophys. Acta*, in press.
34. M. Epstein, Y. Avital, V. Agmon, T. Dinur, E. Fibach, S. Gatt, and N. Laufer, Use of fluorescent lipids for diagnosing a murine embryo model of Gaucher disease. *Human Reproduction* 8(2):302–309 (1993).
35. M. Suchi, T. Dinur, R.J. Desnick, S. Gatt, L. Pereira, E. Gilboa, and H. Schuchman, Retroviral-mediated transfer of the human acid sphingomyelinase cDNA: Correction of the metabolic defect in cultured Niemann-Pick disease cells. *Proc. Natl. Acad. Sci.* 89:3227–3231 (1992).
36. T. Dinur, E.H. Schuchman, E. Fibach, A. Dagan, M. Suchi, R.J. Desnick, and S. Gatt, Toward gene therapy for Niemann-Pick disease (NPD): Separation of retrovirally corrected and non-corrected NPD fibroblasts using a novel fluorescent sphingomyelin. *Human Gene Therapy* 3:633–699 (1992).
37. P. Levy-Yeati, V. Agmon, C. Fillat, T. Dinur, A. Dagan, R.J. Desnick, S. Gatt, and E.H. Schuman, Fluorescence-based selection of retrovirally-transduced cells in the absence of a marker gene: direct selection of transduced Type B Niemann-Pick disease cells and evidence for bystander correction. *Human Gene Therapy* 6:975–983 (1995).
38. J.D. Chapman, C.C. Stobbe, E.L. Engelhardt, M.C. Fenning, D.Q. Brown, A. Dagan, and S. Gatt, Exploitation of interstitial brachytherapy techniques for the photodynamic therapy of solid tumors. Proceedings of the SPIE Conference, Los Angeles, Vol. 2133, 128–139 (1994).
39. A. Dagan, S. Gatt, S. Cerbu-Karabat, J.C. Maziere, C. Maziere, R. Santus, E.L. Engelhardt, K.A. Yeh, C.C. Stobbe, M.C. Fenning, and J.D. Chapman, Uptake by cells and photosensitizer effectiveness of novel pheophorbide derivatives *in vitro*. *Int. J. Cancer*, 63: 831-839 (1995).
40. P. Grellier, V. Agmon, P. Palud, J.C. Maziere, D. Rogomier, A. Dagan, R. Santus, S. Gatt, and J. Schrevet, Photosynthesized inactivation of *Plasmodium falcifarum* and *Babesia divergens* infected erythrocytes in whole blood by pheophorbide derivatives. In preparation.

CA²⁺ SIGNALING AND CYTOSKELETON REORGANIZATION IN ENDOTHELIAL CELLS STIMULATED BY BRADYKININ

Lilly Y. W. Bourguignon, Leya Mathew, Lucia Sobrin, and Gerard J. Bourguignon

Department of Cell Biology and Anatomy
School of Medicine
University of Miami
Miami, Florida 33101

ABSTRACT

In this study we have examined the activation events which occur following the binding of bradykinin (BK) to its receptor on cultured bovine endothelial cells. Using Fura-2 and a fluorescence spectrophotometer, we have found that intracellular Ca²⁺ mobilization occurs within seconds after the addition of BK to the cells and reaches a maximal level within 20 seconds. Subsequently, the [Ca²⁺]_i decreases to a constant level after about 3 min following the addition of BK to the cells. After Ca²⁺ mobilization the cytoskeletal protein, ankyrin, is readily reorganized and accumulated in the perinuclear region. This event is followed by the onset of DNA synthesis. Cytoskeletal protein inhibitors, such as cytochalasin D (known to impair microfilament function) and W-7 (a calmodulin antagonist) have no effect on BK-induced Ca²⁺ mobilization, but block BK-induced cytoskeleton reorganization and the onset of BK-induced DNA synthesis. These findings suggest that the ankyrin-associated microfilament system and a calmodulin-dependent event are required for BK-stimulated endothelial cell proliferation.

INTRODUCTION

Ca²⁺ is known to play an important role in a number of biological responses including cytoskeleton reorganization and cell proliferation¹⁻⁶. In endothelial cells, intracellular Ca²⁺ mobilization by physiologically relevant stimuli (e.g. bradykinin) is closely associated with the hydrolysis of inositol-4,5-bisphosphate (PIP₂) to diacylglycerol and inositol triphosphate (IP₃)⁷. IP₃ is known to cause the release of internal Ca²⁺ as shown in permeabilized endothelial cells⁸.

Cytoskeletal proteins are well known to be important participants in certain cellular regulation mechanisms^{2,3,6,9}. Because the cytoskeletal network can potentially form a physical link between the plasma membrane, organelle membranes and nuclear membranes, it has been suggested that they may be directly involved in signal transduction^{2,3,6,9}. Ankyrin, a cytoskeletal protein which links certain membrane proteins [such as erythrocyte band 3⁹ and lymphocyte GP85(CD44)¹⁰⁻¹⁷] to spectrin/fodrin-associated microfilaments, has recently been found to bind to IP₃ receptors in brain¹⁸ and lymphoma cells^{19,20}. In addition, the binding of ankyrin to the IP₃ receptor inhibits IP₃ binding and IP₃-mediated internal Ca²⁺ release^{19,20}. In platelets, both IP₃ binding and IP₃-induced Ca²⁺ release are also inhibited by cytochalasin D (an inhibitor for microfilament function) and colchicine (an agent known to disassemble microtubules)²¹. These findings further support the hypothesis that the cytoskeleton is directly involved in regulating important cellular activities. The fact that ankyrin not only binds to the surface molecules, but also binds to intracellular proteins (such as the IP₃ receptor), suggests that ankyrin may be involved in multiple functions during cellular regulation.

In this study we have examined the effects of bradykinin (BK) on Ca²⁺ mobilization, cytoskeleton rearrangement and DNA synthesis in bovine endothelial cells stimulated by bradykinin.

MATERIALS AND METHODS

Cell Culture

The endothelial cells used in this study were a chemically transformed bovine aorta cell line (Gm7372a)^{8,16}. The cells were cultured in eagle minimal essential medium (EMEM) with Earle's Salts, two-fold-concentrated essential and nonessential amino acids, two-fold-concentrated vitamins, plus 10% fetal bovine serum at 37° in a 5% CO₂ atmosphere. Confluent cultures were passaged by using trypsin-EDTA to detach the cells and then plated at a 1:8 dilution onto uncoated, plastic tissue culture dishes as described previously^{8,16}. The endothelial cells grew with a population doubling time of about 30 H and formed a flat cobblestone-like monolayer. Subconfluent endothelial cells were used for all experiments.

Measurement of Intracellular Ca²⁺ Mobilization by a Fluorescence Spectrophotometer

Bovine endothelial cells were first incubated with 5µM fura-2/AM (Calbiochem, LaJolla, CA, USA) at 37°C for 20 min in a buffer solution containing 140 mM NaCl, 5mM KCl, 1mM MgCl₂, 1mM CaCl₂, 10mM glucose and 10mM Na HEPES (pH 7.4). Cells were then washed three times with the same buffer, resuspended in 0.1M phosphate saline buffer (pH 7.0) and finally incubated simultaneously with an equal volume of 0.1M phosphate saline buffer (pH 7.0) containing 100nM bradykinin (BK) (Sigma Chemical Co., St. Louis, MO, USA) into a 20 microliter cuvette alternately illuminated by 340 nm and 380 nm every 4 milliseconds using a fluorescence spectrophotometer system designed by Scientific Instruments (Heidelberg Germany). In some cases, cells loaded with fura-2/AM were pretreated with various drugs [e.g. cytochalasin D (10 µM) and W-7 (10µM)] in the same buffer at 37°C for 30 min. Subsequently, the fura-2 loaded endothelial cells (with or without drug treatment) were incubated with HEPES buffer in the absence or presence of bradykinin (BK) (either 10nM or 100nM) at room temperature. The concentration of intracellular Ca²⁺ was determined using the following equation: $[Ca^{2+}]_i = K_d * ((R - R_{min}) / (R_{max} - R)) * F/B$ where

[Ca²⁺]_i is intracellular Ca²⁺ concentration, K_d is the dissociation constant of Fura-2 for Ca²⁺, R is the ratio of the fura-2 fluorescence excited at 340nm divided by the fluorescence excited at 380 nm, R_{min} and R_{max} minimal and maximal fluorescence ratios respectively obtained in ionomycin in the presence of 7 mM EGTA or 2.0 mM Ca²⁺. F and B are the fluorescence voltage signals at 380 nm in 1.0 μM ionomycin in the presence of 7 mM EGTA and 2 mM Ca²⁺, respectively, as described previously²².

Immunofluorescence Staining

Bovine endothelial cells were washed with EMEM medium and resuspended in the same medium. Then, bradykinin (BK) (10nM or 100nM) was added directly to the cells at room temperature. Subsequently, cells were fixed in 2% paraformaldehyde containing 0.1M phosphate buffer (pH 7.2) and rendered permeable by 90% ethanol. These cells (with or without BK treatment) were then stained with fluorescein (FITC)-conjugated monoclonal mouse anti-ankyrin antibody (ANK 016) (22). To detect any non-specific antibody binding, cells were incubated with normal mouse serum followed by rhodamine-conjugated secondary antibodies (FITC-goat anti-mouse IgG). No staining was observed in such control samples. The fluorescence labeled samples were then examined using an Ar/Kr laser confocal scanning microscope (MultiProbe 2001 Inverted CLSM system, Molecular Dynamics, Sunnyvale, CA, USA).

DNA Synthesis Measurement

DNA synthesis was determined by incubating the endothelial cells in complete growth medium containing 0.2% fetal bovine serum for 48h at 37° in a 5% CO₂ atmosphere followed by bradykinin (5-100nM) treatment for 18h. Cells were then pulse-labeled with [³H]thymidine (0.1 Ci/ml) for 4h. The incorporation of nucleoside into DNA was terminated by adding ice-cold 10% trichloroacetic acid (TCA) to the medium. The TCA-precipitated materials were collected on Milipore filters which were then dried and counted in a Beckman liquid scintillation counter.

RESULTS

(A) Bradykinin (BK)-Induced Ca^{2±} Mobilization

Intracellular Ca²⁺ mobilization is known to be involved in various agonist-induced biological responses¹⁻⁶. In this study we have used a fluorescence indicator, fura-2, to measure the intracellular free Ca²⁺ concentration [Ca²⁺]_i following BK binding to cultured bovine endothelial cells. Endothelial cells were first loaded with fura-2 and then stimulated with bradykinin (BK) while they were monitored by the Ca²⁺ fluorescence measuring system. The ratio of the fura-2 fluorescence signal (at 340 and 380 nm excitation) was measured to determine the [Ca²⁺]_i in a large number of monolayer-grown cells (at least 1 x 10⁵ cells/sample) during BK treatment. Our results indicate that the level of [Ca²⁺]_i begins to increase within seconds after the addition of BK to the cells and reaches a maximal level within ≈20 seconds (Fig. 1). The [Ca²⁺]_i then decreases to a constant lower level after about 3 min following the addition of BK to the cells (Fig. 1). These data suggest that intracellular Ca²⁺ mobilization is one of the early signalling events which occur following BK binding to bovine endothelial cells.

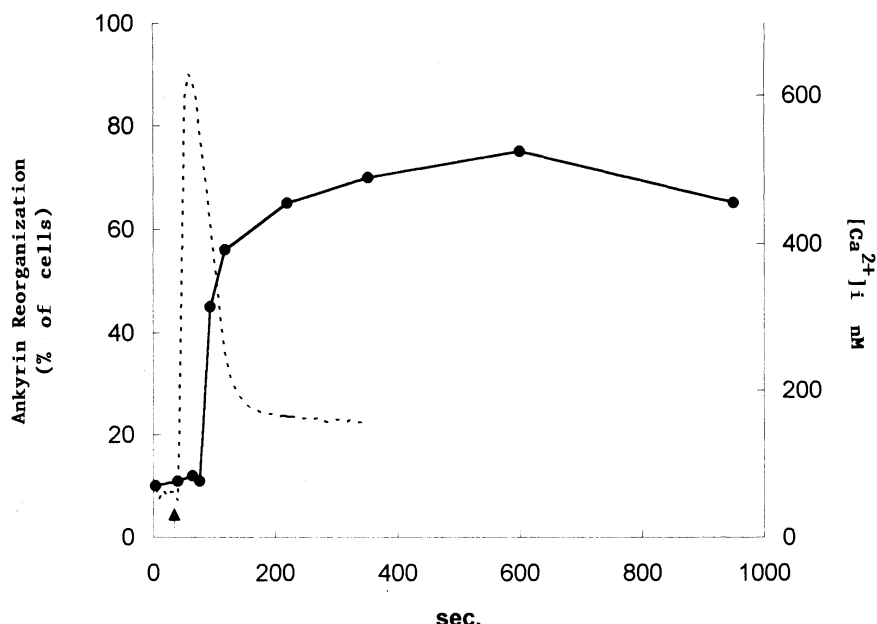


Figure 1. Ca^{2+} mobilization and ankyrin rearrangement in endothelial cells during BK stimulation. Ca^{2+} mobilization was measured by a fluorescence spectrophotometer using 1×10^6 cells loaded with fura-2. Localization of ankyrin was detected by staining cells with mouse anti-ankyrin and FITC-conjugated goat anti-mouse IgG as described in the Materials and Methods. (Arrow represents BK treatment; Dotted line represents BK-induced Ca^{2+} transient using fura-2-loaded cells; Solid line represents BK-induced ankyrin rearrangement).

(B) BK-Induced Reorganization of the Cytoskeletal Proteins Such as Ankyrin

Immunofluorescence staining data indicate that cytoskeletal proteins such as ankyrin were randomly distributed throughout the cytoplasm in unstimulated (resting) endothelial cells (Fig. 2A). After BK treatment, ankyrin is rapidly reorganized and accumulated in the perinuclear region (Fig. 2B). Further analyses indicate that the ankyrin reorganization is induced by BK in a concentration-dependent manner (Table 1). The BK concentrations which stimulate ankyrin reorganization also cause the subsequent onset of DNA synthesis (Table 1). These findings suggest that the reorganization of the cytoskeletal protein, ankyrin, is a physiologically-relevant event that is directly correlated with BK-stimulated endothelial proliferation.

Kinetic analysis indicates that elevation of the intracellular free Ca^{2+} concentration ($[\text{Ca}^{2+}]_i$) occurs before the onset of ankyrin reorganization (Fig. 1). The ankyrin reorganization to the perinuclear region is observed after 45 sec BK treatment (Fig. 1), and reaches a maximal level within 10 min after BK addition to the cells (Fig. 1).

In addition, we have found that certain cytoskeleton inhibitors, such as cytochalasin D (a microfilament disrupting agent known to prevent actin polymerization) and W-7 (a calmodulin antagonist) have no effect on BK-induced Ca^{2+} mobilization (data not shown). However, cytochalasin D and W-7 have a marked inhibitory effect on BK-induced ankyrin reorganization (Table 2) and subsequent DNA synthesis (Table 2). These findings suggest that an ankyrin-associated microfilament system and a calmodulin-dependent event are involved in BK-induced endothelial cell proliferation.

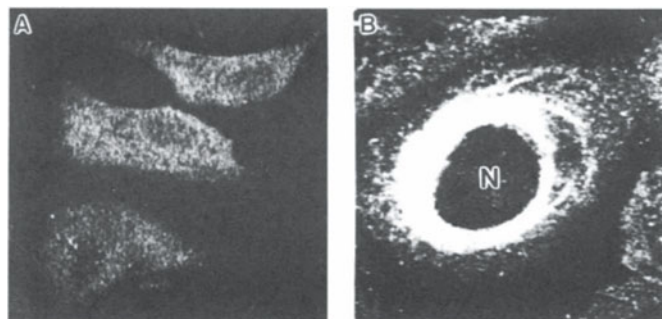


Figure 2. Immunofluorescence staining of ankyrin in endothelial cells. A: Intracellular ankyrin staining of resting (unstimulated) endothelial cells using monoclonal mouse anti-ankyrin antibody followed by fluorescein (FITC)-conjugated goat anti-mouse IgG. B: Intracellular ankyrin staining of endothelial cells stimulated by BK using monoclonal mouse anti-ankyrin antibody followed by fluorescein (FITC)-conjugated goat anti-mouse IgG.

DISCUSSION

Ankyrin is well known to bind to a number of plasma membrane-associated proteins including band 3, two other members of the anion exchanger gene family^{23,24}, Na⁺/K⁺-AT-Pase²⁵⁻²⁷, amiloride-sensitive Na⁺ channel²⁸, the voltage-dependent Na⁺ channel^{29,30} and GP85(CD44)¹⁰⁻¹⁷. The fact that ankyrin also binds to lymphocyte intracellular Ca²⁺ channels, such as the IP₃ receptors^{20,21} and ryanodine receptors³¹, suggests that ankyrin may be involved in multiple functions during cellular regulation. Using immunofluorescence staining techniques, we have found that ankyrin (Fig. 2A) is randomly distributed in the cytoplasm in unstimulated endothelial cells. However, immediately after the onset of BK-induced Ca²⁺ mobilization, intracellular ankyrin becomes relocated to the perinuclear region of the cell (Fig. 2B). The close association between ankyrin and perinuclear structures following BK stimulation may be required for the onset of DNA synthesis (see Table 1).

The fact that ankyrin reorganization occurs immediately after the increase in intracellular Ca²⁺ suggests that Ca²⁺ may be needed for the rearrangement process. This result is similar to that found in other biological systems^{2-6,32}. For example, in smooth muscle cells Ca²⁺ transients always precede contraction and decrease to near baseline levels before contraction begins. (32). In lymphocytes, the elevation of [Ca²⁺]_i always occurs before the cytoskeleton-mediated receptor patching/capping formation²⁻⁶.

Table 1. Effects of bradykinin (BK) on ankyrin rearrangement and DNA Synthesis

Treatments	Ankyrin reorganization (% of total cells)	DNA synthesis (CPM x 10 ⁻³)
Control (No treatment)	<5	110
BK (10nM)	40	925
BK (100nM)	64	1,600

Endothelial cell ankyrin reorganization (after 10min BK treatment) and DNA synthesis (after 18h BK treatment) were analyzed according to the procedures described in the Materials and Methods. The values expressed in this table represent an average of 3-5 experiments with a SD<5%.

Table 2. Effects of various drugs on ankyrin rearrangement and DNA synthesis

Treatments	Ankyrin reorganization ^{a,b} (% of total cells)	DNA synthesis (CPM x 10 ⁻³)
Control (No treatment)	<5	100
BK alone	65	1650
Cytochalasin D + BK	4	90
W-7 + BK	5	98

a: The concentrations of various drugs used in these experiments were: cytochalasin D (10 mM) and W-7 (10mM). The effects of various drugs on endothelial cell ankyrin rearrangement and DNA synthesis (with or without 10min BK treatment) were analyzed according to the procedures described in the Materials and Methods.b: The values expressed in this table represent an average of 3-5 experiments with a SD<5%.

We now propose that the reorganization of ankyrin to the perinuclear region is regulated by a Ca²⁺/calmodulin-dependent microfilament system which may be one of the required steps for the onset of endothelial cell proliferation.

ACKNOWLEDGMENTS

The authors gratefully acknowledge Dr. W.G. Kerrick's assistance in Ca²⁺ measurement using a fluorescence spectrophotometer. This work was supported by National Institutes of Health Grants CA 66163 and GM36353, a Department of Defense grant, and American Heart Association grants. L.M. is a predoctoral fellow of the American Heart Association.

REFERENCES

1. R. P. Rubin, G.B. Weiss, and J. W. Putney. Calcium In Biological Systems, Plenum, New York, NY, USA(1985).
2. L.Y.W. Bourguignon and G.J. Bourguignon. Capping and the cytoskeleton, in: "Int. Rev. Cytol.", G.H. Bourne and J. E. Danielli, ed., Academic Press, New York, NY, USA 87:195 (1984).
3. L.Y.W. Bourguignon. Receptor-ligand mediated transmembrane interactions. in:"Energetics of Secretory Responses", J.W.N. Akkerman, ed., CRC Press, Boca Raton, FL, USA 1:83 (1988).
4. L.Y.W. Bourguignon, W. Jy, M.H. Majercik, and G.J. Bourguignon. Lymphocyte activation and capping of hormone receptors. *J. Cell Biochem.* 37:131 (1988).
5. W. Jy, N. Fregien, G.J. Bourguignon, and L.Y.W. Bourguignon. Role of Ca²⁺ in the regulation of hormone receptor exposure during lymphocyte activation. *Biochem. Biophys. Acta* 983:153 (1989).
6. L.Y.W. Bourguignon. Membrane skeleton linker proteins in immune cells. in: "Encyclopedia of immunology", I.M. Roitt and P. J. Delves, Academic Press, New York, NY, USA (1992).
7. T. L. Lambert, R. S. Kent, and A.R. Whorton. Bradykinin stimulation of inositol polyphosphate production in porcine aortic endothelial cells. *J. Biol. Chem.* 261:15288 (1986).
8. L.Y.W. Bourguignon, N. Iida, L. Sobrin, and G.J. Bourguignon, Identification of an IP₃ receptor in endothelial cells. *J. Cell Physiol.* 159L:29 (1994).
9. V. Bennett, Spectrin-based membrane skeleton: a multipotent adaptor between plasma membrane and cytoplasm. *Physiol. Rev.* 70:1029 (1990).
10. L. Y. W. Bourguignon, G. Walker, S. Suchard, and K. Balazovich, A lymphoma plasma membrane-associated protein with ankyrin-like properties. *J. Cell Biol.* 102:2115 (1986).
11. E. L. Kalomiris and L.Y.W. Bourguignon, Mouse T-lymphoma cells contain a transmembrane glycoprotein (GP85) which binds ankyrin. *J. Cell Biol.* 106,319 (1988).
12. E. L. Kalomiris and L. Y. W. Bourguignon, Lymphoma protein kinase C is associated with the transmembrane glycoprotein, GP85, and may function in GP85-ankyrin binding. *J. Biol. Chem.* 264:8113 (1989).

13. V. B. Lokeshwar and L. Y. W. Bourguignon, Post-translational protein modification and expression of ankyrin-binding site(s) in GP85 and its biosynthetic precursors during T-lymphoma membrane biosynthesis. *J. Biol. Chem.* 266:17983 (1991).
14. L. Y. W. Bourguignon, E. L. Kalomiris, and V. B. Lokeshwar, Acylation of the lymphoma transmembrane glycoprotein, GP85, may be required for GP85-ankyrin interaction. *J. Biol. Chem.* 266:11761(1991).
15. V. B. Lokeshwar, and L. Y. W. Bourguignon, The lymphoma transmembrane glycoprotein GP85 (CD44) is a novel G-protein which regulates GP85(CD44)-ankyrin interaction. *J. Biol. Chem.* 267:22073 (1992).
16. L.Y.W. Bourguignon, V.B. Lokeshwar, J. He, X. Chen, and G.J. Bourguignon, A CD44-like endothelial cell transmembrane glycoprotein (GP116) interacts with extracellular matrix and ankyrin. *Mol. and Cell Biol.* 12:4464 (1992).
17. V. B. Lokeshwar, N. Fregien, and L.Y.W. Bourguignon, Ankyrin binding domain of CD44(GP85) is required for the expression of hyaluronic acid-mediated adhesion function. *J. Cell Biol.* 126:1099 (1994).
18. S. K. Joseph and S. Samanta, S. Detergent solubility of inositol triphosphate receptor in rat brain membranes. *J. Biol. Chem.* 268:6477 (1993).
19. L. Y. W. Bourguignon, H. Jin, N. Iida, N. Brandt and S. H. Zhang, The involvement of ankyrin in the regulation of IP₃ receptor-mediated internal Ca²⁺ release from Ca²⁺ storage vesicles in mouse T-lymphoma cells. *J. Biol. Chem.* 268:7290 (1993).
20. L. Y. W. Bourguignon and H. Jin, Identification of the ankyrin-binding domain of the mouse T-lymphoma cell IP₃ receptor and its role in the regulation of IP₃-mediated internal Ca²⁺ release. *J. Biol. Chem.* 270:7257 (1995).
21. L. Y. W. Bourguignon, N. Iida, and H. Jin, The involvement of the cytoskeleton in regulating IP₃ receptor-mediated internal Ca²⁺ release in human blood platelets. *Cell Biol. Int.* 17:751 (1993).
22. L.Y.W. Bourguignon, V. B. Lokeshwar, X. Chen and W. G. L. Kerrick W.G.L. Hyaluronic acid (HA)-induced lymphocyte signal transduction and HA receptor (GP85/CD44)-cytoskeleton interaction. *J. Immunol.* 151:6634 (1993).
23. V. Bennet, Ankyrins. *J. Biol. Chem.* 267:8703 (1992).
24. J. Davis, S.E. Lux, and V. Bennet, Mapping the ankyrin binding site of human erythrocyte anion exchanger. *J. Biol. Chem.* 264:9665(1989).
25. W. J. Nelson, and P. J. Veshnock, Ankyrin binding to Na⁺/K⁺-ATPase and implications for the organizations of membrane domains in polarized cells. *Nature (Lond)*. 328:533(1987).
26. J. S. Morrow, C. D. Cianci, A. S. Ardito, and M. Kashgarian, Ankyrin links fodrin to the alpha subunit of Na⁺/K⁺-ATPase in Madin-Darby canine kidney cells and in intact renal tubule cells. *J. Cell Biol.* 108,455 (1989).
27. M. M. Shull, D. G. Pugh, and J. B. Lingrel, Characterization of the human Na⁺/K⁺-ATPase α 2 gene and identification of the intragenic restriction fragment length polymorphism. *J. Biol. Chem.* 264:17532 (1989).
28. P. R. Smith, G. Saccomani, E. H. Joe, K. J. Angelides, and D. J. Benos, Amiloride sensitive sodium channel is linked to the cytoskeleton in renal epithelial cells. *Proc. Natl. Acad. Sci. (USA)* 88:6971 (1991).
29. E. Kordeli, and V. Bennet, Distinct ankyrin isoforms at neuron cell bodies and nodes of Ranvier resolved using erythrocyte ankyrin-deficient mice. *J. Cell Biol.* 114:1243 (1991).
30. E. Kordeli, S. Lambert, V. Bennet, and Ankyrin G, A new ankyrin gene with neural-specific isoforms localized at the axonal initial segment and node of Ranvier. *J. Biol. Chem.* 270:2352 (1995).
31. L.Y.W. Bourguignon, A. Chu, J. Jin and N. R. Brandt. Ryanodine receptor-ankyrin interaction regulates internal Ca²⁺ release in mouse T-lymphoma cells. *J. Biol. Chem.* 270:17917 (1995).
32. F. S. Fay, H. H. Shlebin, W. C. Granger,Jr., S. R. Taylor "Aequorin luminescence during activity of single isolated smooth muscle cells" *Nature (London)* 280;506 (1979).

INTEGRATION OF OPTICAL TECHNIQUES IN SCANNING PROBE MICROSCOPES

The Scanning Near-Field Optical Microscope (SNOM)

Achim Kirsch, Christoph Meyer, and Thomas M. Jovin

Department of Molecular Biology
Max Planck Institute for Biophysical Chemistry
P.O. Box 2841, D-37018 Göttingen, Germany

1. INTRODUCTION

During the last 15 years scanning probe microscopes (SPM), in particular the scanning force microscope (SFM) and scanning tunneling microscope (STM), have developed into highly sophisticated instruments for the investigation of surfaces and surface structures under a broad range of environmental conditions. Applications range from imaging single atoms in ultrahigh vacuum¹, to the visualization of strands of DNA on freshly cleaved mica surfaces², and the investigation of the activation of platelets under physiological conditions^{3,4}.

Despite their outstanding high lateral and vertical resolution, SFM and STM are literally “blind” to the electromagnetic spectrum and thus cannot exploit contrast mechanisms associated with light. This circumstance provided the impetus in the mid 1980s for the development of a different class of scanning probe instruments: the scanning near-field optical microscope (SNOM)⁵⁻⁷. In their present implementation, these microscopes combine a force or tunneling current sensor and a detection scheme for optical signals in a multifunctional probe^{8,9}. In addition to the simultaneous acquisition of topographic and optical images of a surface, SNOM offers an improved lateral optical resolution due to the extremely small distance between the optical probe and the structure(s) being examined. Conventional optical microscopes employ lenses that operate in the far-field regime, in which propagating waves constitute the appropriate solutions to Maxwell’s equations; their resolution is diffraction limited. In the SNOM the distance between probe and sample is smaller than the wavelength and the resolution is on the order of the probe (usually a micropipette or an optical fiber) aperture¹⁰⁻¹².

We have constructed an SNOM head as an add-on to a commercial SFM (NanoScope III, Digital Instruments) using an uncoated fiber tip as a combined illumination and detection element¹³⁻¹⁵. The distance between the tip and the sample is maintained constant via the measurement of shear-force interactions^{16, 17}. In this communication we describe the

configuration of the system, including the shear-force detection unit. Reflection images of 3T3 mouse fibroblasts and fluorescence images of RBL-2H3 (rat basophilic leukemia) cells labeled with the sulfoindocyanine dye Cy5 demonstrate the performance of the SNOM.

2. SNOM SYSTEM

The heart of our SNOM system (Fig. 1) is a tip produced from an optical fiber (Siecor) by heating and pulling with a CO₂ laser-based commercial pipette puller (Sutter Instruments). The tip illuminates the sample with the emission of a 633 nm HeNe laser (Research Electro-Optics) coupled into the input end of the fiber. The same tip collects light reflected and emitted from the sample surface. The fluorescence is focused onto a single photon-counting avalanche photo diode (EG&G, Princeton, NJ, USA) and the bright-field reflection is detected by a standard photodiode (Centronics).

The scanning of the sample by the fiber tip is under control of the commercial scanning probe system (NanoScope III). The shear force detection is depicted in Fig. 2A. The fiber tip is vibrated parallel to the surface of the sample at its resonance frequency (12 - 40 kHz). The amplitude of this vibration is determined from the motion of the diffraction pattern of a laser diode oriented parallel to the sample surface and focused on the tip. The vibration of the fiber tip is damped in the proximity of the sample surface due to mechanisms which are as yet poorly understood¹⁶. A typical calibration of vibration amplitude [measured with a lock-in amplifier (Stanford Research Systems)] vs. sample-probe distance is shown in Fig. 2B. During the scanning process, the z-position of the sample is varied by a feedback mechanism so as to maintain the vibration amplitude constant at ~60% of that obtained with the retracted tip. The distance between the sample and the probe is thereby kept approximately constant.

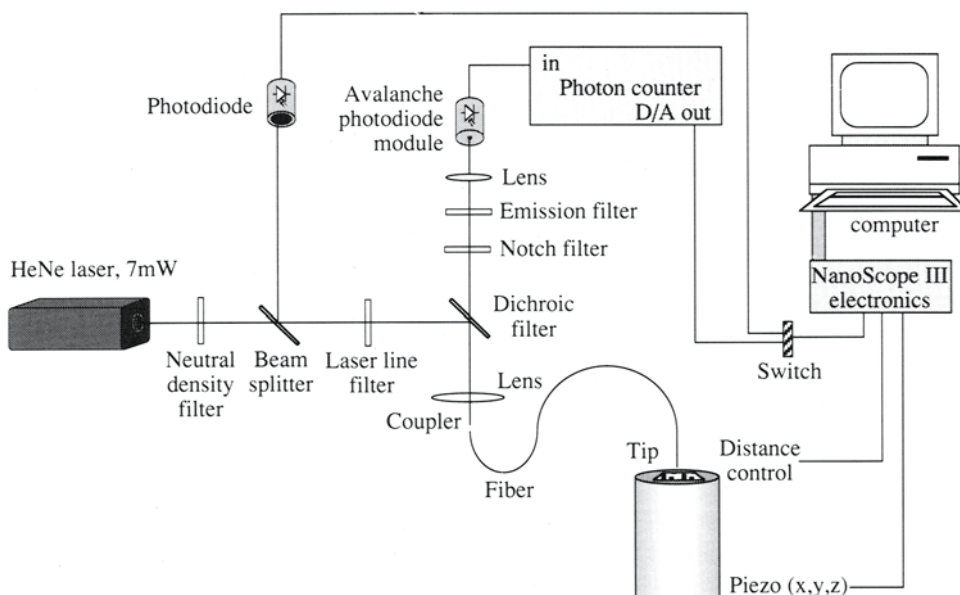


Figure 1. Schematic set up of the SNOM system.

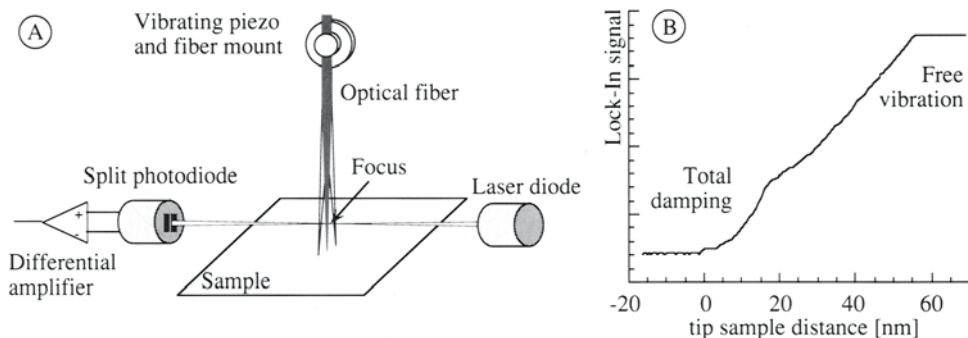


Figure 2. Shear force detection. (A) Schematic view of the optical configuration. (B) Vibration amplitude of the fiber tip (lock-in signal) vs. distance from the sample. The origin for the distance axis is defined as the point at which the vibration vanishes.

3. CELL AND PROBE PREPARATIONS

Mouse fibroblasts (BALB/c-3T3) were grown at 37 °C on glass coverslips under standard conditions in Dulbecco's modified Eagle's medium (DMEM) with 10% fetal calf serum (FCS). They were washed with phosphate-buffered saline (PBS: 137 mM NaCl, 2.7 mM KCl, 7.9 mM Na₂HPO₄, 1.5 mM KH₂PO₄, pH 7.2), dehydrated in methanol and stored at -20 °C. The cells were air dried prior to imaging with the SNOM. Living RBL-2H3 (rat basophilic leukemia) cells ¹⁸ were washed free of medium and serum with RAB buffer (135 mM NaCl, 10 mM KCl, 1 mM CaCl₂, 0.4 mM MgCl₂, 5.6 mM glucose, 10 mM Hepes-Na, pH 7.2) and then fluorescence labeled according to the following procedures.

- *Procedure 1:* Excess buffer was aspirated, 20 µl of Cy5 N-hydroxysuccinimide ester (Biological Detection Systems; stock solution 50 µg/µl in DMSO diluted to 0.1 µg/µl in RAB buffer containing 50 mM borate pH 8.5) were added per coverslip and reacted with the cells for 2 min. The cells were then washed copiously with buffer.
- *Procedure 2:* 20 µl of 20 nM Cy5-labeled IgE ¹⁸ per coverslip were reacted for 30 min at room temperature with the cells, after which they were washed three times with buffer.

After labeling, all 2H3 cell preparations were fixed with 3% paraformaldehyde in buffer for 15 min at room temperature, washed in Tris-saline buffer, rinsed once, quickly in water, and then dehydrated in an ethanol series (5 min each in 70%, 80%, 90% and 100% v/v ethanol). Cells were air dried prior to imaging with the SNOM.

4. RESULTS

4.1 3T3 Fibroblasts

Shear-force and bright field reflection images of 3T3 fibroblasts were taken simultaneously. The topography of two adjacent cells is shown in Fig. 3A. The area enclosed by the black box was also imaged at higher magnification (Fig 3B, topography; Fig 3C, reflection intensity). The height of the cell in the zoomed area varied between 15 and 75 nm, and the modulation of the optical signal was approximately 6%. The smallest structures

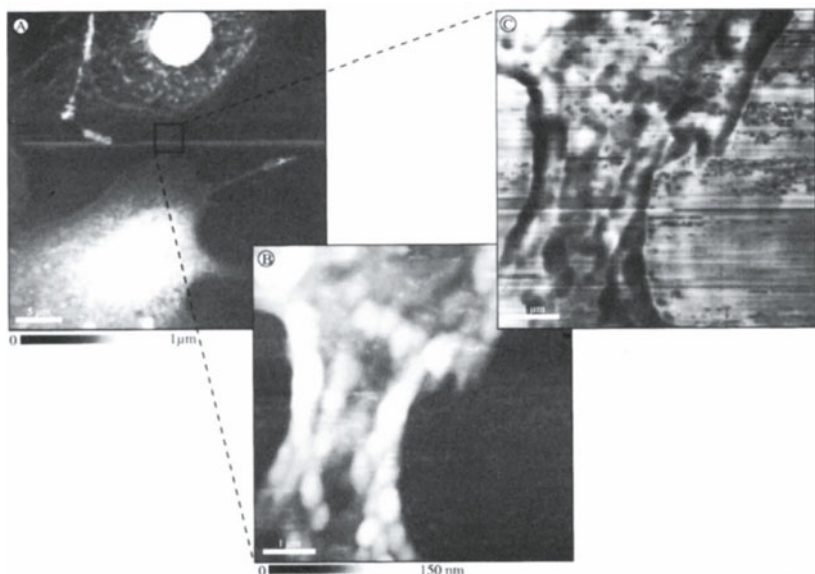


Figure 3. Images of dried BALB/c-3T3 cells. (A) topography overview. (B) and (C) topography and bright field reflection of the area depicted in (A). In (C) a dark color signifies lower reflection intensity. A color representation of this figure can be found facing p. 215.

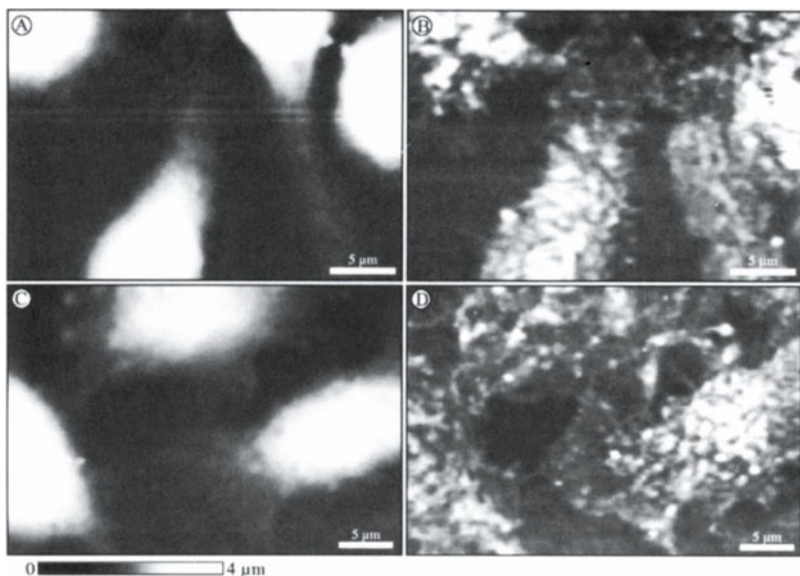


Figure 4. Images of Cy5 labeled RBL-2H3 cells. Topographic (A and C) and fluorescence (B and D) images. (A, B) cells directly labeled with Cy5; (C, D) cells labeled with Cy5-IgE. In (B) the color scale is 1 Mcp/s (cp/s = counts per s) with a background of 200 kcp/s. 4.5 μW of excitation light was coupled into the fiber. In (D) the color scale is 250 kcp/s with a background of 50 kcp/s; 2.5 μW of light was coupled into the fiber. A color representation of this figure can be found facing p. 215.

revealed in the optical signal were 100 nm in width, corresponding to $\sim 1/6$ of the wavelength of the laser.

4.2 RBL-2H3 Rat Basophilic Leukemia Cells

Shear-force topographic and fluorescence images of the RBL cells are shown in Fig 4. Panels A and B are for cells labeled directly with the fluorescence dye Cy5, panels C and D for cells labeled with the IgE ligand specific for the Fc_e receptors mediating the immediate allergic response of mast cells. There are approximately 10^5 such receptors located on the surface of the RBL cells.

The differences due to the labeling techniques are clearly evident. Whereas the cells labeled with the reagent directed against all moieties bearing a free amino group (glycolipids, glycoproteins) showed a fairly homogeneous distribution (Fig. 4 B), the IgE-receptors were distributed in more discrete arrangements (Fig. 4D). This circumstance can be better appreciated in a three-dimensional representation in which the topographic relief was augmented with the color-coded intensity of the fluorescence signal (Fig. 5). This innovative form of display was achieved with the image processing software SxMIMAGE (Centre Suisse d'Electronique et de Microtechnique).

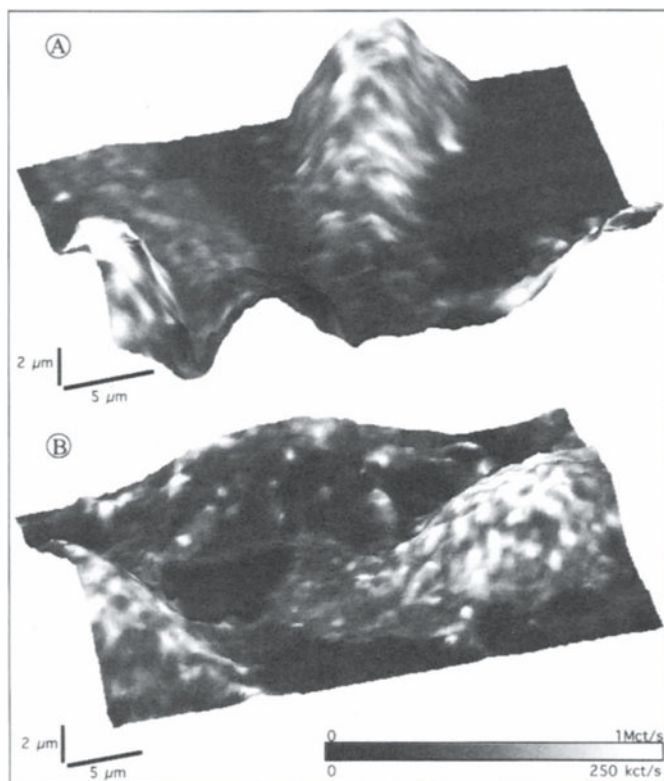


Figure 5. Combined topography/fluorescence images of Cy5 labeled RBL-2H3 cells (same data as Fig. 4 represented with the SxMIMAGE software). 3D surface (topography) plots with color encoding of the fluorescence intensity. (A) Combined data from panels A and B of Fig. 4. (B) Combined data from panels C and D of Fig. 4. A color representation of this figure can be found facing p. 215.

The images of Figs. 4 and 5 demonstrate vividly the capability of SNOM for simultaneously recording topographic and optical (fluorescence) data with very satisfactory contrast and spatial resolution. For example, substrate between the cells is revealed clearly. One should note that in contrast to other techniques such as confocal laser scanning microscopy, the topographic information is deduced from physico-mechanical interactions of the fiber tip with the sample and not derived from optical signals.

5. SUMMARY AND CONCLUDING REMARKS

We have presented the construction and operational features of a scanning near-field optical microscope (SNOM) working in an epi-illumination mode. The optical head was designed as an add-on to a commercial Nanoscope III scanning force microscope. The system permits simultaneous measurements of sample topography via shear-force detection and optical signals on a nanometer scale. The performance characteristics have been demonstrated with images of bright field reflection of 3T3 cells and fluorescence measurements of Cy5 labeled RBL-2H3 cells. These and other experiments carried out in the combined mode of operation are very encouraging. We anticipate a widespread application of the SNOM technique with configurations similar to ours as well as in very different implementations.

6. ACKNOWLEDGMENTS

We thank C. Schnetter for the 3T3 cell preparations and Dr. D. Arndt-Jovin for the preparation of the RBL-2H3 cell samples. A. K. is a graduate student of the University of Konstanz, Germany and C. M. a Diplomand of the University of Göttingen, Germany.

7. REFERENCES

1. Eigler, D. M., P. S. Weiss, E. K. Schweizer, and N. D. Lang. 1991. Imaging Xe with a low-temperature scanning tunneling microscope. *Phys. Rev. Lett.* 66:1189-1192.
2. Schaper, A., J. P. P. Starink, and T. M. Jovin. 1994. The scanning force microscopy of DNA in air and in n-propanol using new spreading agents. *FEBS Lett.* 355:91-95.
3. Fritz, M., M. Radmacher, and H. E. Gaub. 1994. Granula motion and membrane spreading during activation of human platelets imaged by atomic-force microscopy. *Biophys. J.* 66:1328-1334.
4. Radmacher, M., R. W. Tillmann, M. Fritz, and H. E. Gaub. 1992. From molecules to cells-imaging soft samples with the atomic force microscope. *Science* 257:1900-1905.
5. Betzig, E., A. Lewis, A. Harootunian, M. Isaacson, and E. Kratschmer. 1986. Near-field scanning optical microscopy (nsom) - development and biophysical applications. *Biophys J.* 49:269-279.
6. Pohl, D. W., W. Denk, and M. Lanz. 1984. Optical stethoscopy: image recording with resolution $\lambda/20$. *Appl. Phys. Lett.* 44:651.
7. Pohl, D. W. 1991. Scanning near-field optical microscopy (SNOM). *Adv. Optical Electron Microsc.* 12:243-312.
8. Garcia-Parajo, M., J. Rosiu, and C. Yong. 1994. On the way to a multi-task near field optical microscope-simultaneous STM/SNOM and PSTM imaging. *Microsc. Microanal. Microstruct.* 5:399-407.
9. Moers, M. H. P., R. G. Tack, N. F. van Hulst, and B. Bölger. 1994. Photon scanning tunneling microscope in combination with a force microscope. *J. Appl. Phys.* 75:1254-1257.
10. Courjon, D., and C. Bainier. 1994. Near-field microscopy and near-field optics. *Rep. Prog. Phys.* 57:989-1028.
11. Vigoureux, J. M., and D. Courjon. 1992. Detection of nonradiative fields in light of the Heisenberg uncertainty principle and the Rayleigh criterion. *Appl. Opt.* 31:3170-3177.
12. Novotny, L., D. W. Pohl, and P. Regli. 1994. Light-propagation through nanometer-sized structures - the 2-dimensional-aperture scanning near-field optical microscope. *J. Opt. Soc. Am. A.* 11:1768-1779.

13. Spajer, M., D. Courjon, K. Sarayeddine, A. Jalocha, and J. M. Vigoureux. 1991. Reflection near-field optical microscopy. *J. de Phys. III.* 1:1-12.
14. Bielefeldt, H., I. Hörsch, G. Krausch, M. Lux-steiner, J. Mlynek, and O. Marti. 1994. Reflection-scanning near-field optical microscopy and spectroscopy of opaque samples. *Appl. Phys. A.* 59:103-108.
15. Jalocha, A., and N. F. van Hulst. 1995. Dielectric and fluorescent samples imaged by scanning near-field optical microscopy in reflection. *Opt. Com.* 119:17-22.
16. Betzig, E., P. L. Finn, and J. S. Weiner. 1992. Combined shear force and near-field scanning optical microscopy. *Appl. Phys. Lett.* 60:2484-2486.
17. Toledo-Crow, R., P. C. Yang, Y. Chen, and M. Vaez-Iravani. 1992. Near-field differential scanning optical microscope with atomic force regulation. *Appl. Phys. Lett.* 60:2957-2959.
18. Jürgens, L., D. J. Arndt-Jovin, I. Pecht, and T. M. Jovin. 1996. Proximity relationships between the type I receptor for Fc_ϵ ($\text{Fc}_\epsilon\text{RI}$) and the mast cell function-associated antigen (MAFA) studied by donor photobleaching fluorescence resonance energy transfer microscopy. *Eur. J. Immunol.* in press.

PERFUSION, TEMPERATURE, AND PO₂ CONTROL IN A LEIDEN CULTURE BATH FOR SINGLE CELL MEASUREMENTS AND MANIPULATIONS

C. Ince,¹ A. de Vos,² G. Verschragen,² M. Sinaasappel,³ and B. Van Duijn³

¹ Department of Physiology

² Department of Anesthesiology

³ Academic Medical Center

University of Amsterdam

² the Department of Physiology

Leiden University, The Netherlands

INTRODUCTION

Cell physiological investigations in single living cells have provided much insight into the underlying mechanisms of the functional activities of cells and their components in health and disease. Investigating living cells provides the investigator the opportunity of following sequences of physiological events in time. This is in contrast to a histological approach where a physiological process is frozen in time. Techniques which can be applied to the study of single living cells during their functional activity include microscopical observations (e.g. video-timelapse or confocal observations), use of vital fluorescent or phosphorescent indicator dyes (for e.g. intracellular ion concentration measurements, cellular or mitochondrial membrane potential measurements, intracellular pO₂ measurements) ion channel measurements using patch clamp techniques or mechanical measurements such (e.g force-length measurements). Besides such cellular measurements, manipulations of cells (i.e intracellular injections of DNA or manipulations of cell functions with e.g. caged compounds) are also important activities which need to be performed under microscopic control. A major condition for making such measurements is that cells have to be maintained under physiological conditions in which optical conditions are achieved suitable for all types of microscopical investigations. We have over the years developed a number of tools for achievement of such conditions.

The conditions which first have to be created on the stage of a microscope include temperature and gas pressure control while free access for microelectrode for making single cell measurements is maintained. Besides these requirements humidity, osmolality and sterility need to be adequately maintained. We developed the Leiden Culture Bath which is

a chamber meeting these conditions and in which a standard 35 mm tissue culture dish can be placed for use on an inverted microscope (Ince et al., 1983). With this chamber the same conditions as exist in a commercial CO₂ incubator can be achieved on the stage of a microscope. In a subsequent study we developed a teflon culture dish which can be fitted into the Leiden Culture Bath and in which standard glass coverslips with adherent cells can be fitted (Ince et al., 1985). This dish enables 100x oil immersion optics to be used and thereby most other types of microscopic modalities for single living cell investigations where good optics are required while maintaining free access to cells for measurements and manipulations. Several studies including video time lapse, micro-manipulations, intracellular calcium measurements and patch clamp measurements have made use of these properties of the tissue culture dish (e.g. van Duijn and Inouye, 1991, Wiltink et al., 1995, Ince et al., 1988). A subsequent teflon dish was developed by Atsma et al. 1994 which divides the dish into two compartments. This construction enables simultaneous measurements in a single cell culture by switching from one compartment to the other. Furthermore a closed perfusion micro chamber was developed for single cell fluorescence studies when optimal control of the cell environment is desired (Ince et al. 1990).

In this study we present a simple device called the convector heater which can be placed on to the Leiden Culture Bath. With this attachment the incoming perfusate is heated by the culture bath from room temperature to 37°C and directs the perfusate into dish. An aspirator positioned in the culture dish ensures by suction that a constant level of perfusate is maintained in the dish. This study further shows the ability of the Leiden Culture Bath to achieve low pO₂ conditions. This property of the culture system is demonstrated by Pd-porphine quenching of phosphorescence measurements of oxygen pressures in the cell medium (Sinaasappel and Ince, 1996).

MATERIALS AND METHODS

The Leiden Culture Bath is illustrated in Fig. 1A. Described elsewhere in detail (Ince, 1983), the culture bath essentially consists of a number of toroidal rings screwed together to comprise one large heating ring in which standard 35 mm disposable plastic tissue culture dishes with adherent cells in cell medium can be placed. The heating ring consists of a heating coil which is fed current under control by a temperature controller unit (TC-202 Temperature Controller, Medical System Corp. Greenvale, NY) attached to a thermistor immersed in the culture medium. Inside the heating ring are ducts which can heat gas mixtures entering through the inlet of these ducts and direct them onto the surface of the cell medium. A second ring with a metal top is placed around the metal heating ring for attachment of small magnets holding sensors such as, (as shown in Fig. 1A), a temperature sensor for heating control and inlets and outlets for medium when cells perfusion is desired. For no perfusion conditions the cell medium is covered by a thin layer of mineral oil (Ince et al. 1983).

Temperature is controlled by direct contact of the heating ring with the side of the dish and by air heated in the heating ducts of the ring and directed over the surface of the mineral oil layered over the cell medium. This heated air stream heats the center of the dish and ensures uniform temperature control over the whole dish. By choice of suitable gas mixtures, it also controls the gas pressures in the cell medium such as pCO₂ (for pH control in bicarbonate-buffered medium) and pO₂, such as shown in this paper. For perfusion, the gas pressure is controlled in the perfusate reservoir outside the system.

In this study we present a small ring-shaped device which we have termed the convector heater which can be placed on the metal heating ring holding the dish with cells. The heat being generated by the ring is sufficient to heat perfusate flowing through the tubing in the convector heater. Under conditions of perfusion, perfusate at room temperature flows

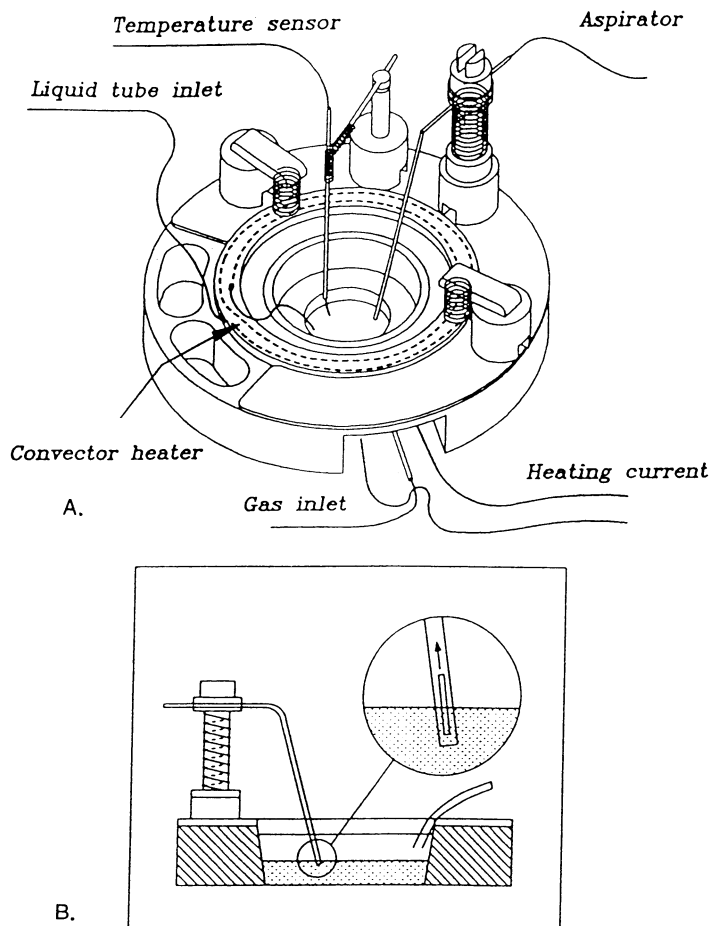


Figure 1. (A) Perfusion of the Leiden Culture Bath by use of a convector heater. The culture bath is essentially a heating ring as described in the Methods section. The convector heater is a holder for tubing placed on the culture bath through which the perfusate is allowed to flow. The convector heater brings the tubing with perfusate into contact with the heating ring and thus allows it to heat the perfusate flowing through the tubing. (B) The level of the perfusate in the dish is controlled by an aspirator placed in the dish. A close up of the tip of the aspirator is shown. The aspirator is a hollow stainless steel tube under suction with a slit in its tip.

into the tubing of the heater convector and during two cycles around the heating ring it is heated from room temperature to the temperature set by the temperature controller by the heat generated from the heating ring below. The temperature of the heating ring is regulated by current supplied by the temperature controller and the temperature sensed by a thermistor placed in the dish. The perfusate flows out of the outlet of the convector heater into the dish with cells. The level of the perfusate entering the dish is controlled by an aspirator which suctions off excess perfusate. As shown in Fig 1B the aspirator consists of a hollow stainless steel tubing with a small slit at the bottom. The tubing, which is under suction, can be positioned at a desired height by adjustment of a screw. By adjustment of the slit to a desired height, any fluid level exceeding this level is suctioned off. The aspirator is attached to a support magnet which can be positioned around the culture dish at a desired position.

We present two types of experiments. The first is shown in Fig.2 and is an example of how temperature control of the perfusate can be achieved using the convector heater. At time = 0 the set-point of the temperature controller is set at 36° C and perfusate at room temperature allowed to flow into the tubing and into the dish at two different flows. The change in perfusate temperature is measured in the dish by the thermistor of the temperature controller.

To monitor the time course of oxygen concentration in the cell medium, Pd-porphine quenching of phosphorescence as developed by Wilson and co-workers (1991) was applied. To this end Pd-porphine bound to bovine serum albumin was added to the medium. A phosphorimeter (Sinaasappel and Ince, 1996) was attached to a Y-shaped light guide with the leg of the guide fastened to the bottom of the dish. One arm of the guide was attached to a Xe-flash lamp and the other to a gated photomultiplier device for detection of the quenching of phosphorescence of the Pd-porphine compound following excitation by a Xe-flash lamp. Oxygen pressures were calculated according to the Stern Volmer relation with parameters obtained from calibration experiments (Sinaasappel and Ince, 1995).

RESULTS AND DISCUSSION

The temperature change of the perfusate as measured by the temperature sensor of the temperature regulator is shown following change of the temperature set point from room temperature to 36°C for two flow rates commonly used during such experiments (0.66 ml/min and 1.33 ml/min). As can be seen the set temperature is achieved satisfactorily taking about 15 minutes to reach the steady state temperature set in the controller. At high flow rates, however, the perfusate will not remain long enough in the tubing of the convector heater to be heated to the set temperature and a discrepancy will be found between the set point and the temperature of the perfusate. If such high flow levels are desired calibration experiments need to be made to compensate for this discrepancy.

Achievement of low pO₂ conditions is desired for cell physiological experiments aimed at understanding the pathophysiology of ischemia-reperfusion. The closed perfusion chamber has been used for this purpose for intracellular pO₂ measurements in single macrophages (Sanders et al. 1995) as well as in the study of intracellular calcium measure-

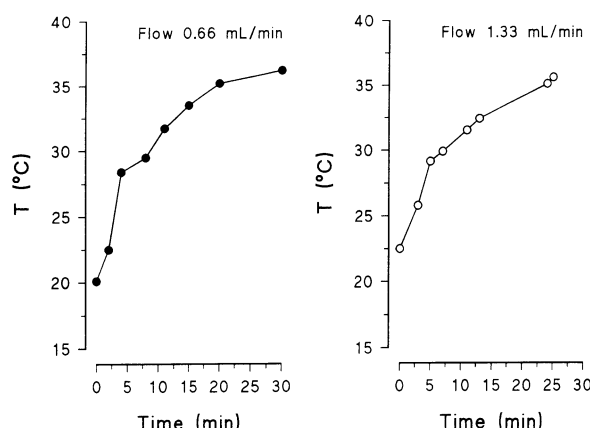


Figure 2. The temperature change of the medium in the perfused dish is shown when the set point of the temperature controller is changed from room temperature to 36 degrees C. The temperature changes in two levels of flow are shown , 0.66 ml/min and 1.33 ml/min are shown.

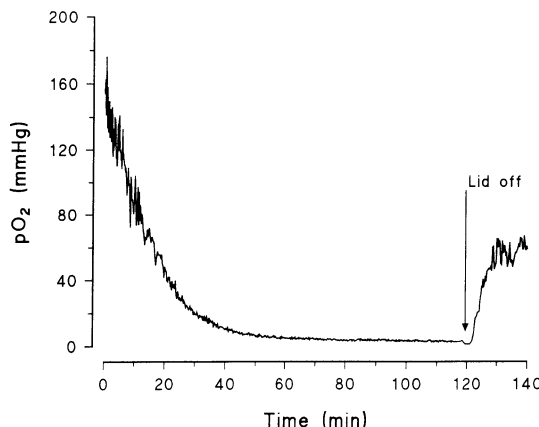


Figure 3. The time course of pO_2 in the cell medium of a tissue culture dish in a Leiden Culture Bath during argon perfusion is shown. The cell medium is covered by a thin layer of mineral oil. The dish is covered by a lid with a section removed to enable electrode access. Argon gas is directed over the gas permeable oil layer. As can be seen from the trace of pO_2 in the cell medium, oxygen levels go down to almost zero. Lifting the lid off at the arrow results in a rise in pO_2 as the argon gas mixes with the ambient air.

ments in cardiomyocytes during hypoxia (Rose et al. 1993). To show that low pO_2 can be achieved in the Leiden Culture Bath while maintaining open access for electrodes to make single cell measurements, a lucid lid with 60 degree slice taken out (for access to cells by electrodes) was placed on the heating ring. Argon gas was then passed through the heating ducts and directed over the surface of the mineral oil layer covering the cell medium containing Pd porphine compound. Argon gas was used because it is a relatively heavy gas and settles on the cell medium instead of mixing with the surrounding air. The O_2 pressure was measured from lifetime measurements of the quenching of phosphorescence of the Pd porphine compound. The trace in Fig. 3 shows the time course of pO_2 of the medium when argon is directed over the cell medium. As can be seen very low oxygen levels can be achieved. At the end of the experiment the lid covering the culture dish is lifted and a rise in pO_2 is seen. This illustrates the need for the lid if truly low O_2 levels are required. It is concluded that the Leiden Culture Bath is suitable for studies where low pO_2 conditions are desired.

ACKNOWLEDGMENTS

M. Sinaasappel is supported by the Netherlands Science Foundation (grant nr. 900-519-110).

All the devices described in this paper are available from Medical Systems Corp., 1 Plaza Road, Greenvale, NY, USA.

REFERENCES

- Atsma DE, Bastiaanse EML, Ince C, van der Laarse A (1994) A novel two-compartment culture dish allows microscopic evaluation of two different treatments in one cell culture simultaneously. *Pflüg Arch Eur J Physiol* 428:296-299.

- Van Duijn B, Inouye K (1991) Regulation of movement speed by intracellular pH during Dictyostelium discoideum chemotaxis. *Proc Natl Acad Sci (USA)* 88:4951-4955.
- Ince C, Beekman RE, Verschragen G (1990) A micro-perfusion chamber for single-cell fluorescence measurements. *J Immunol Meth* 128:227-234.
- Ince C, Coremans A, Ypey DL, Leijh PCJ, Verveen AA, van Furth R (1988) Phagocytosis by human macrophages is accompanied by changes in ionic channel currents. *J Cell Biol* 106:1873-1878.
- Ince C, van Dissel JT and Diesselhoff-den Dulk MMC (1985) A Teflon culture dish for high magnification observations and measurements from single cells. *Pflügers Arch Eur J Physiol* 203:240-244.
- Ince C, Ypey DL, Diesselhof-den Dulk MMC, Visser JAM, de Vos A, van Furth R (1983) Micro-CO₂-incubator for use on a microscope. *J Immunol Meth* 60:269-275.
- Rose UM, Bindels RJM, Vis A, Jansen JWCM, van Os CH (1993) The effect of L-type Ca²⁺ channel blockers on anoxia-induced increases in intracellular Ca²⁺ concentration in rabbit proximal tubule cells in primary culture. *Pflüg Arch Eur J Physiol* 423:378-386.
- Sanders R (1995) Imaging of oxygen-concentrations in single cells. In: *Fluorescence lifetime as a contrast mechanism in confocal imaging*. Ph.D.Thesis University of Utrecht, the Netherlands ISBN no. 90-393-0648-6, pp. 45- 53.
- Sinaasappel M, Ince C, van der Sluijs JP, Bruining HA. (1995) A new phosphorimeter for the measurement of oxygen pressures using pd-Porphine phosphorescence. *Adv Exp Medicine* 361:105-110.
- Wilson DF, Pastuszko A, DiGiacomo JE, Pawlowski M, Schneiderman R, Dellvoria-Papadopoulos M. (1991) Effect of hyperventilation on oxygenation of the brain cortex of newborn piglets. *J Appl Physiol* 70(6): 2691-2696.
- Wiltink A, Nijweide PJ, Scheenen WJJM, Ypey DL, van Duijn B. (1995) Cell membrane stretch in osteoclasts triggers a self-reinforcing Ca²⁺ entry pathway. *Pflüg Arch Eur J Physiol* 429:663-671.

IMMUNOFLUORESCENCE STUDY OF INTERMEDIATE FILAMENT PROTEIN EXPRESSION UNDER NORMAL AND PATHOLOGICAL CONDITIONS

Vladimír Viklický, Zdeněk Lukáš,* and Pavel Dráber

Institute of Molecular Genetics
Academy of Sciences of the Czech Republic
142 20 Prague 4, Czech Republic
*2nd Department of Pathology
Medical Faculty of Masaryk's University
662 63 Brno, Czech Republic

1. INTRODUCTION

Intermediate filaments are polymers of fibrous proteins found in the cytoplasm of most multicellular animals and represent, in addition to microtubules and actin filaments, the third major component of the cytoskeleton. The presence of intermediate filaments in plants remains to be confirmed by primary sequence analysis data. All major intermediate filaments have similar ultrastructure, show diameters between 7-18 nm and can be reconstituted from isolated proteins¹. All known intermediate filament proteins have a similar protein domain structure consisting of a central α -helical rod domain flanked by non-helical head and tail domains. On the basis of sequence similarities in the rod domain, five classes of intermediate filaments are recognized². Their expression is tissue-specific and developmentally regulated. Two basic concepts have been proposed with regard to the function of intermediate filaments: filaments as mechanical support for positioning of nucleus and other cellular components³ and filaments as regulators⁴. Recent data indicate that intermediate filaments play an important role in the maintenance of axonal caliber and in strengthening of the epidermis. First results are beginning to appear demonstrating that changes in the expression of intermediate proteins can also affect the transformed phenotype of cells⁵.

Intermediate filament proteins have been used by clinical pathologists as suitable markers of tumor cell origin⁶. In certain cases in which only very few tumor cells are present (metastases), or in which diagnosis cannot readily be made by normal histological procedures, antibodies against these proteins appear to be very useful as an aid in tumor classification⁶. Different intermediate filament proteins are associated with histologically distinct cell types, and the majority of the cell types in an adult human contain a single

intermediate filament type. In some cases two and more intermediate filament proteins occur in tumor cells. Their detection then significantly helps in diagnosis. For example cells of the round-cell carcinoma of lung also express beside keratins, neurofilament triplet proteins. A positive immunostaining for both intermediate filament protein types in single cell is then sufficient for proper diagnosis. Knowledge of the timing of intermediate filament protein expression in ontogenesis is an essential feature of human neuropathology. During embryonic development there is a highly stereotyped progression in the pattern of intermediate filaments. In various animal models a common expression pattern exists in non-epithelial cells. The initial transient appearance of vimentin is followed by the appearance of differentiation-specific intermediate filaments and later on by the disappearance of vimentin⁷. Analogical studies in the human nervous system are scarce. Here we report on differential expression of intermediate filament proteins in human developing dorsal root ganglia, spinal cord and neuroblastic and glial neoplasms as detected by immunofluorescence microscopy with monoclonal antibodies.

2. MATERIAL AND METHODS

2.1. Tissues

Twenty human embryos and foetuses of gestation ages from 6 weeks to term were examined. Specimens of neuroblastic and glial neoplasms were obtained from surgically removed tumors and from biopsies. Samples were covered with Tissue-Tek II OCT (Miles Laboratories, Vienna, Austria), snap frozen in a mixture of propane-butane precooled in liquid nitrogen, and stored at -70°C.

2.2. Antibodies

Mouse monoclonal antibodies VI-01 against vimentin⁸, GF-01 against glial acidic protein⁹ and NF-01 against phosphorylated high molecular weight neurofilament protein (NF-H)¹⁰ were used as diluted ascitic fluids. For double-label experiments VI-01 antibody was directly labelled with lissamine rhodamine B sulphonyl chloride as described. Mouse monoclonal antibody against the phosphorylated variant of NF-H was purchased from Amersham (Aylesbury, UK). Mouse monoclonal antibody reacting with NF-H independently of the state of its phosphorylation was bought from Boehringer Manheim (Vienna, Austria). Anti-mouse antibody conjugated with fluorescein isothiocyanate (FITC) was from Sevac (Prague, Czech Republic).

2.3 Immunofluorescence Microscopy

Frozen sections were cut at -20°C at a thickness of 5 µm and air-dried at room temperature on glass slides precoated with 0.1% poly-L-lysine. The sections were fixed with methanol for 10 min at -20°C and transferred to acetone for 6 min at the same temperature. Alternatively, samples were fixed in 3% paraformaldehyde for 30 min with subsequent treatment with 0.1% Triton X-100 in PBS. In some cases, sections from archival formaldehyde-fixed paraffin-embedded samples were used. For double-label immunofluorescence the slides were subsequently incubated with NF-01 or GF-01 FITC-labelled anti-mouse antibody, normal mouse serum and VI-01 antibody labelled with rhodamine. Mouse serum effectively blocked the remaining binding sites on FITC-conjugated anti-mouse antibody. Incubations were at room temperature for 30 min in a humidified chamber. The slides were thoroughly washed with PBS after each incubation step and just before mounting in 90%

glycerol in PBS, pH 9.0. The preparations were examined with a Leitz Orthoplan fluorescence microscope equipped with epi-illumination using the filter combination cubes N2 and I2. Photographs were taken on Kodak Tri-Xpan film. In control tests the primary antibodies were omitted.

3. RESULTS AND DISCUSSION

3.1. Immunolocation of Vimentin and GFAP in Neural Tube and Spinal Cord of Human Embryos and Foetuses

In 6-8 week-old human embryos vimentin was found present in radial fibres or processes. These fibres were located very close to the nuclei, predominantly in the vicinity of the central canal. In addition, mesenchymal derivatives reacted positively. No trace of positive staining with GF-01 antibody was found up to that stage of development. In 10-week embryos vimentin was also present in the first differentiation stages of the glia. GFAP positive cells were noted in the radial processes of the marginal layer, later extending into the mantle zone. GFAP was co-expressed in some cells reacting positively for vimentin, but the number of GFAP-positive cells was smaller than that of vimentin-positive cells. In 23-week-old foetuses, the fibres of glial cells gave a positive reaction with both antibodies. The majority of ependymal cells gave a positive reaction with anti-vimentin antibody, while only a minority of them reacted positively with antibody against GFAP. The pattern of distribution of the two intermediate filament proteins in 30-and 40-week foetuses was very similar to that of the 23-week stage with the exception of ependymal cells. These cells retained reactivity for vimentin, whereas the reactivity for GFAP disappeared. Results of expression of vimentin and GFAP in the developing spinal cord are summarized in Table 1.

3.2. Immunolocation of Vimentin and Phosphorylated NF-H in Dorsal Root Ganglia and Spinal Cord of Human Embryos and Foetuses

The phosphorylated variant of NF-H protein was present in both ventral and dorsal roots, as well as in bundles of nerve fibres containing the differentiating perikarya of ganglion cells in the ganglia of 6- and 8-week-old embryos. The fibrillar structures contained vimentin. The reactivity of NF-01 antibody was similar and strong during the whole period

Table 1. Expression of vimentin and GFAP in glial cells of neural tube and spinal cord in developing human embryos

Week	Marginal layer (white matter)		Mantle layer (grey matter)		Ependymal layer	
	Vim.	GFAP	Vim.	GFAP	Vim.	GFAP
6	++	-	++	-	++	-
8	++	-	++	-	++	-
10	++	+	++	-	++	-
23	++	++	++	++	++	+
30	++	++	+	++	++	+
40	++	++	+	++	++	-

++, indicates strong reactivity; +, indicates medium reactivity; -, indicates no reactivity.

Vimentin (Vim.) was detected by antibody VI-01, GFAP was detected by antibody GF-01.

under investigation (till 30 weeks). Vimentin was detected, apart from its presence in mesenchymal derivatives, only in some ganglion cells and nerve processes. In 30-week-old foetuses no co-expression of phosphorylated NF-H and vimentin was observed.

Contrary to the finding in dorsal root ganglia we have not found any reactivity with either antibody in the ganglion cell perikarya in developing spinal cord. Vimentin positivity was present only in some nerve processes in the 6-and 8-week-old embryos, phosphorylated NF-H was present in longitudinal bundles of nerve processes in the marginal layer, in the loose network of fibres in the mantle zone and later on in some radial fibres in the ventral part of the mantle layer. Co-expression of the two proteins was observed in just a few of the radial fibres in this area. In the spinal cord of 23- and 30-week-old foetuses, phosphorylated NF-H was located in the axons of both spinal cord and nerve roots. The same staining pattern was provided with commercial antibody against phosphorylated NF-H. A typical example

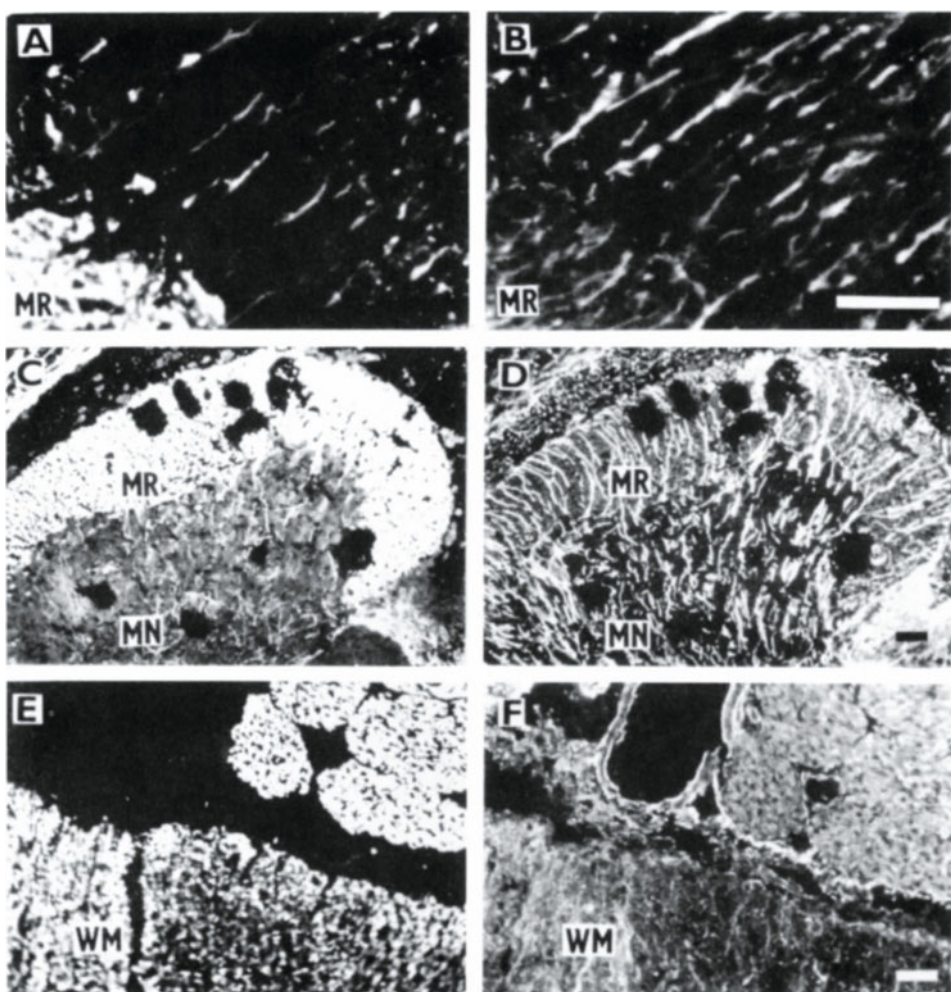


Figure 1. Double-label immunofluorescence analysis of frozen sections of neural tube and spinal cord in 6-week (A, B) and 8-week-old (C, D) embryos, and in a 23-week-old foetus (E, F) using antibodies against phosphorylated NF-H (A, C, E) and vimentin (B, D, F). MN, mantle zone; MR, marginal layer; WM, white matter of the spinal cord. Bar, 50 µm. (Lukáš et al., 1993, with permission of Histochemistry).

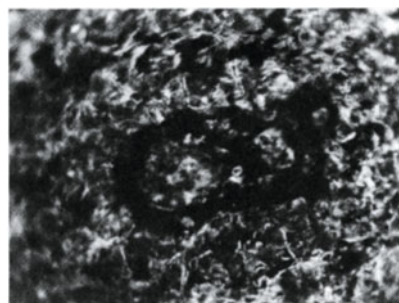


Figure 2. Distribution of vimentin and GFAP in astrocytoma. Tissue section was stained with anti-vimentin antibody, antibody to GFAP and DNA-binding dye. A color representation of this figure can be found facing p. 214.

of double-label experiments is shown in Figure 1. Results of immunolocalization of vimentin and phosphorylated NF-H in developing dorsal root ganglia and spinal cord are summarized in Table 2.

3.3. Co-Expression of Intermediate Filament Proteins in Neuroblastic and Glial Neoplasms

The findings of intermediate filament proteins in neoplasms derived from neuroglial differentiation confirmed the opinion that GFAP is a reliable marker for this tumor type. It was found in all cases studied. Important from our point of view is the fact that small groups of proliferating cells positive for vimentin were found without having been stained by antibodies against GFAP, namely in some glioblastomas and anaplastic astrocytomas. The co-expression of vimentin with GFAP in astrocytomas and glioblastomas was found in well differentiated as well as in undifferentiated tumors or anaplastic astrocytomas, so that its presence does not indicate a lower degree of differentiation*. Expression patterns of the two intermediate filament proteins in individual glial cells can be characterized as follows: some processes express only GFAP or only vimentin, while a certain proportion of them express both proteins. In neuroblastomas staining for phosphorylated NF-H was present in perikarya

Table 2. Immunolocation of phosphorylated NF-H and vimentin in developing dorsal root ganglia and spinal cord

Wks	Ganglion cell perikarya				Nerve processes			
	NF-H		Vimentin		NF-H		Vimentin	
	DRG	SC	DRG	SC	DRG	SC	DRG	SC
8	++	-	++	-	++	++	++	+
14	++	-	+	-	++	++	+	-
30	++	-	-	-	++	++	-	-

++, indicates strong reactivity; +, indicates medium reactivity; -, indicates no reactivity; DRG, dorsal root ganglia; SC, spinal cord. Phosphorylated high molecular weight neurofilament protein (NF-H) was detected by antibody NF-01; vimentin was detected by antibody VI-01.

* An example of co-expression of vimentin and GFP in astrocytoma is shown in Figure 2

Table 3. Coexpression of NF-H and vimentin in neuroblastomas and ganglioneuromas

Cell localization	NF-H(PID)	NF-H(PD)	Vimentin
Perikarya	+	+/-	+/-
Processes		+	+/-

++, indicates strong reactivity; +, indicates medium reactivity; +/-, up to 5% positive cells; -, indicates no reactivity; PID, phosphorylation independent epitopes; PD, phosphorylation dependent epitopes.

and processes of the neuroblasts. Phosphorylation-dependent epitopes were found in the rim of the cytoplasm of a small proportion of neuroblasts (up to 5% of the cells). Phosphorylated epitopes of NF-H were also present in all processes of the ganglion cells in ganglioneuroblastomas and ganglioneuromas, whereas the perikarya of these cells usually were stained weakly. This finding is in agreement with the fact that neurofilament subunits are synthesized in neuronal perikarya and undergo slow axonal transport¹¹. During this process additional phosphorylations occur¹². Vimentin positivity was recorded in variably developed blood vessels and in areas with astroglial differentiation. A proportion of neuroblasts and differentiating ganglion cells (up to 5%) show the co-expression of this filament protein with NF-H protein. Results of immunolocalization of NF-H and vimentin on the single cell level are summarized in Table 3.

In conclusion, indispensable tools for immunofluorescence detection of intermediate filament proteins are highly specific monoclonal antibodies that make it possible to distinguish closely related building proteins. Changes in the expression of vimentin, GFAP and NF-H observed during human embryogenesis are in agreement with data obtained on animal models. In the tested differentiated as well as undifferentiated tumors no substantial differences were observed in the expression of GFAP and NF-H. However, double-label immunofluorescence with monoclonal antibodies revealed that rapidly proliferating cells in some parts of undifferentiated glioblastomas expressed only vimentin. A similar staining pattern characterized by expression solely of vimentin was observed in glial cell in early stages of embryogenesis.

ACKNOWLEDGMENTS

This work was supported in part by grant 301/93/0323 from the Czech Grant Agency and in part by grant 752101 from the Czech Academy Grant Agency.

4. REFERENCES

- M. Osborn, N. Geisler, G. Shaw, G. Sharp and K. Weber, Intermediate filaments, *Cold Spring Harbour Symp.* 46:413 (1982).
- M.W. Klymkowsky, Intermediate filaments: new proteins, some answers, more questions. *Curr. Opin. Cell Biol.* 7:46 (1995).
- P.A. Janmey, U. Euteneur, P. Traub, and M. Schliwa, Viscoelastic properties of vimentin compared with other filamentous biopolymer networks, *J. Cell Biol.* 113: 155 (1991).
- P. Traub, and R.L. Shoeman, Intermediate filament proteins: cytoskeletal elements with a gene-regulatory function? *Int. Rev. Cytol.* 154: 1 (1994).
- W.H.I. McLean, and E.B. Lane, Intermediate filaments in disease, *Curr. Opin. Cell Biol.* 7: 118 (1995).
- M. Osborn, and K. Weber, Intermediate filaments: cell-type-specific markers in differentiation and pathology, *Cell* 31: 303 (1982).

7. R.A. Nixon, and T.B. Shea, Dynamics of neuronal intermediate filaments: a developmental perspective, *Cell Motil. Cytoskel.* 22: 81 (1992).
8. E. Dráberová, P. Dráber, F. Havlíček and V. Viklický, A common antigenic determinant of vimentin and desmin defined by monoclonal antibody, *Fol. Biol. (Praha)* 32:295 (1986).
9. Z. Lukáš, P. Dráber, J. Buček, E. Dráberová, V. Viklický, and Z. Stašková, Expression of vimentin and glial fibrillary acidic protein in human developing spinal cord, *Histochem. J.* 21:693 (1989).
10. Z. Lukáš, P. Dráber, J. Buček, E. Dráberová, V. Viklický, and S. Doležel, Expression of phosphorylated high molecular weight neurofilament protein (NF-H) and vimentin in human developing dorsal root ganglia and spinal cord, *Histochemistry* 100:495 (1993).
11. B.M. Riederer, Some aspects of the neuronal cytoskeleton in development, *Eur. J. Morphol.* 28: 347 (1990).
12. P.J. Hollenbeck, The transport and assembly of the axonal cytoskeleton, *J. Cell Biol.* 108: 223 (1989).

THE USE OF FLUORESCENT PROBES IN CHARACTERIZING DRUG RESISTANCE IN CULTURED CELLS

Anna-Marija Helt,¹ Gary D. Kruh,² and Kenneth D. Tew¹

¹ Department of Pharmacology

² Department of Medical Oncology

Fox Chase Cancer Center

Philadelphia, Pennsylvania 19111

1. INTRODUCTION

Confocal microscopy in conjunction with fluorescent probes have greatly facilitated the study of antimicrotubule drugs such as vinblastine, taxol and estramustine, and have been particularly useful in the characterization of drug resistant phenotypes associated with these and other drugs. By elucidating drug resistance mechanisms, ways of circumventing them can then be sought. This article will focus on structural, morphological and drug efflux studies aimed ultimately at uncovering how cancer cells develop resistance to the drug, estramustine.

Studies were undertaken using the imaging capabilities of a beam-scanning confocal microscope for several reasons. With conventional fluorescence optics, light from the entire thickness of the specimen reaches the image plane and obscures fine detail. With confocal optics, only one point in the specimen is being illuminated at any given moment¹. Fluorescence originating from this point will hit the pinhole detector and contribute to image formation. Light originating from outside of this point will be physically blocked¹. This results in a higher signal-to-noise ratio and, consequently, in better lateral resolution and shallower depth-of-field. Use of a high numerical aperture objective results in resolution of a fraction of a micron along the optical axis, thus allowing for a three-dimensional composite to be built up from a series of closely-spaced images scanned sequentially along the Z-axis¹. These capabilities were applied to studies on intracellular distribution and trafficking, in space and time, of discreet spots of fluorescently-tagged drug. Another application performed was three-dimensional measurements of cells. A third application was in the comparison of cytoskeletal elements in wild type and drug-resistant cells avoiding artifacts stemming from out-of-focus light or from electron microscopy specimen-fixation procedures.

Estramustine (EM) is an antimicrotubule agent with efficacy in combination treatment of hormone-refractory prostate cancer^{2,3}. It consists of estradiol linked to nor-nitrogen

mustard through a carbamate-ester bond^{2,4} (see left panel, Figure 1). The estradiol moiety was supposed to localize the drug in tissue having estrogen receptors (malignant breast tissue, for example)⁴. Here the alkylating agent, nor-nitrogen mustard, was to be cleaved off, thereby inducing damage to proteins and nucleic acids⁴. Clinical and *in vitro* studies using EM showed no effects stemming from alkylating agent activity. In fact, the carbamate bond between the steroid and nitrogen mustard molecules proved to be stable, indicating that the EM molecule acts intact to produce cytotoxic effects⁴. The molecule has been shown to bind noncovalently to tubulin and a number of microtubule-associated proteins (MAPS)⁵. Exposure to EM results in depolymerization of microtubules starting at the distal ends⁶. Spindle fibres involved in chromosome segregation appear to be especially sensitive to the drug; cells treated with low doses of EM are effectively blocked at the G2/M phase of the cell cycle^{2,6}.

Two sets of EM-resistant cell lines were clonally-selected by exposing a human prostate carcinoma cell line, DU145, to incrementally increasing drug doses. The first set of clones, "E4" and "E9", showed an approximate 5-fold resistance to EM while the more recently cloned lines, "EM12" and "EM15", displayed an 8- to 9-fold level of resistance⁷, also unpublished data. Work with E4 and E9 cells has shown that resistance to EM is not mediated by the multi-drug resistance (MDR) phenotype. Evidence for this lies in the absence of upregulated p-glycoprotein mRNA and glutathione-S-transferase activity, and in the lack of cross-resistance to other chemotherapeutic drugs such as doxorubicin, taxol and vinblastine⁷.

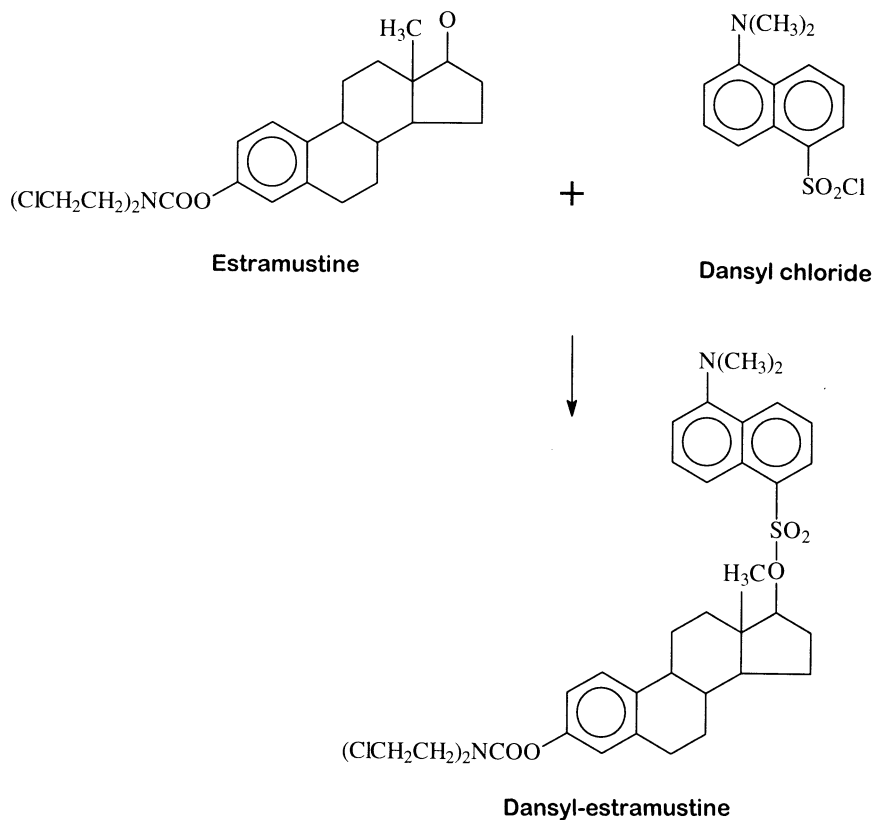


Figure 1. Dansylation of the estramustine molecule.

2. DANSYLATED ESTRAMUSTINE EFFLUX STUDIES

EM is non-fluorescent. In order to follow its uptake, intracellular distribution and efflux on an individual cell basis, a fluorescent EM-conjugate was needed. Dansyl chloride (dnsCl), 5-dimethylaminonaphthalene-1-sulfonyl chloride, is a fluorochrome commonly used for labeling non-fluorescent compounds. The dansylation reaction was used to attach the fluorochrome to the 17- β hydroxyl group on the EM molecule⁸ (Figure 1). This hydroxyl group is readily substitutable. The clinical formulation has a 17 β phosphate which makes the molecule more hydrophilic, thereby facilitating clinical administration of the drug³. The 17- β position has also been used in photoaffinity labeling for protein binding studies⁵. Though the dansylated drug was more hydrophobic than estramustine alone, colony-forming assays demonstrated that the cytotoxicity of the two compounds was similar⁸.

The fluorescence excitation and emission spectra for dansylated EM (dnsEM) was determined using a fluorimeter. Red shifted from the maximum excitation peak was a smaller peak. Though it was not the most efficient wavelength for dnsEM excitation, this secondary peak was sufficient to produce fluorescence detectable above the background, and coincided with the available laser line of the imaging system. Fluorescence emission reached far enough into the green to pass through a 515 LP collection filter and reach the detector.

EM-resistant cells (E4) and wild type DU145 cells were grown on coverslips and used to do short-term time course experiments on the intracellular distribution of dnsEM. The purpose of this was to compare how drug-sensitive and resistant cells dealt with the drug immediately after uptake. In each experiment, a coverslip was placed cell-side-down on a slide. (To prevent the coverslip from pressing down on the cells, spacers had been fastened to the slide.) DnsEM in media was injected under the coverslip. After one minute, fresh media was perfused under the coverslip to wash out extracellular drug. Image collection was initiated immediately following the rinse. A small enough image frame size was used so that a full series of optical sections could be scanned through the cells every 15 seconds. Using this setup, cells were followed for a maximum of ten minutes. To aid in drug localization within the cells, phase images were collected and superimposed with corresponding fluorescence images. (Figure 2) A difference in drug localization and efflux rates was apparent between the parental DU145 and drug resistant cells. Bright, punctate fluorescence was concentrated around the nucleus in wild type cells. Over the course of the experiment, this distribution did not change much, nor did the amount of fluorescence decrease dramatically. Fluorescent spots were spread throughout the cytoplasm of resistant cells. Individual spots could be seen migrating towards the periphery of E4 cells where they were presumably extruded. A more dramatic drop in fluorescence occurred in E4 cells than in wild type DU145 cells by the end of the timecourse. The cell lines also differed in the distribution of dnsCl, but no significant difference could be seen in terms of fluorescence decrease (Figure 3).

These time course studies indicate that some sort of drug efflux mechanism may play a role in resistance to EM. It is not certain whether the extrusion of dnsEM is due to a specific interaction with EM or to a more general interaction with hydrophobic compounds. (DnsCl is less hydrophobic than dnsEM and was not extruded from E4 cells as rapidly.) EM uptake into cells is not energy-dependent⁵ and it is presently not clear if efflux is.

3. CELL VOLUME STUDIES

Another difference between the wild type prostatic cells and their EM-resistant counterparts was size. The E4, E9, EM12 and EM15 cells were smaller than the parental DU145 cells. Measurements of cell dimensions were desired to see if this change was a

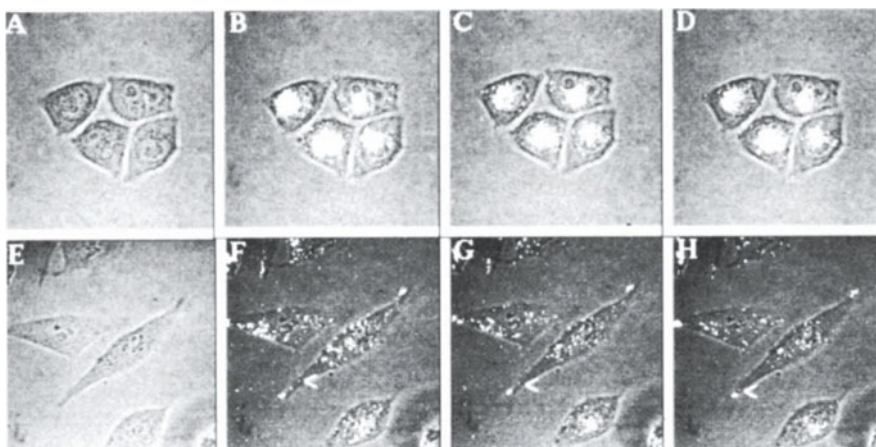


Figure 2. Dansylated Estramustine Time Course in DU145 Cells. The distribution of dnsEM (bright white areas) in wild type (B-D) and EM-resistant (F-H) cells differed dramatically. Also, resistant cells effluxed the drug more rapidly than did wild type cells. (A) and (E) are phase images collected before the addition of dnsEM. (B) and (F) show drug distribution 15 seconds after the time course was started. (C) and (G) are after 75 seconds; and, (D) and (H) are after 135 seconds. The white arrows indicate a discreet spot of drug moving out towards the cell periphery, presumably to be effluxed.

consistent feature of the EM-resistant phenotype. An optical method for size measurement was preferred because it allowed for the exclusion of dead, mitotic or giant, multinucleate cells. Area measurements were not satisfactory since morphological changes along the optical axis may not be taken into account; therefore, a cell volume-measuring assay was performed.

A number of techniques have been used by investigators to determine cell volume and cell volume changes. Some methods were based on the inverse relationship of intracellular fluorescent dye concentration (as judged by fluorescence intensity) and cell size^{9,10}.

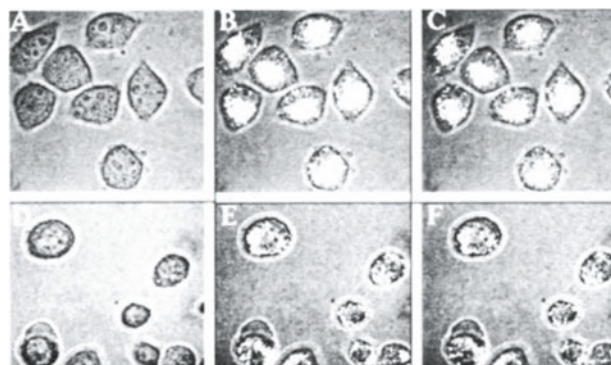


Figure 3. Dansyl Chloride Time Course in DU145 Cells. Dansyl chloride (bright white areas) distribution differed in wild type (B) and (C) and EM-resistant (E) and (F) DU145 cells; though the rate of efflux did not seem to differ. Additionally, dnsCl efflux was not as rapid as dnsEM efflux. (A) and (D) are phase images collected before the start of the time course. (B) and (E) show dnsCl distribution 45 seconds into the time course. (C) and (F) are after 135 seconds.

Optical sectioning with DIC optics has been used to get cell area and perimeter measurements for use in volume calculations¹¹. For EM studies, confocal imaging and three-dimensional volume-rendering software were used for volume comparison between wild type and resistant cells. To accomplish this, the live-cell marker, calcein (Molecular Probes, Eugene, OR, USA), was employed. The method used was modified from one tested by Farinas¹⁰.

Calcein-acetoxymethyl ester (calcein-AM) is a cell permeant fluorescein derivative that is non-fluorescent until the "AM" moiety (which enables cellular uptake of the dye) is cleaved off by intracellular esterases¹². Calcein fills the entire cell with a bright green fluorescence upon excitation with blue light¹². Calcein-loaded cells on coverslips were placed cell-side-down on slides. Stacks of sections were scanned along the optical ("Z") axis of randomly chosen fields of cells. Though the Z-resolution of the system was determined to be 0.70 mm, Z-sections were scanned at 1.0-micron intervals to save time and disk space. The stacks of sections were exported to a Silicon Graphics workstation (SGI, Mtn. View, CA, USA) where image dimensions were entered into the image header file for translation to real world units. Images were displayed using Voxel View Ultra Volume Rendering software (Vital Images, Fairfield, Iowa, USA). For each cell, the number of voxels above a specified grey level was detected using the "Voxelseed" function¹³ provided in the volume

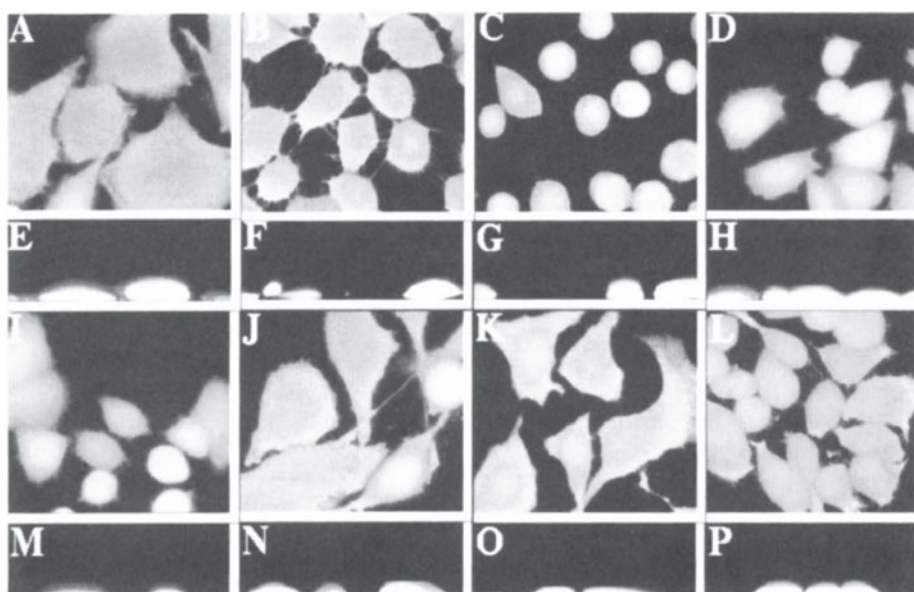


Figure 4. Cell Volume Measurements. Cells grown on coverslips were loaded with 3 μ M calcein-AM (Molecular Probes) for 40 minutes. Coverslips were placed cell-side-down on spacers fastened to a slide. Randomly chosen cells were imaged using the 488nm line and standard FITC-collection filters on a Bio-Rad MRC-600 LSCM. Using a 60X, 1.4 N.A. Nikon PlanApo objective lens, sections were scanned at 1.0- μ M intervals along the optical axis. Images were exported to a Silicon Graphics workstation where image frame size, in pixels and microns, and the number and spacing of Z-sections were entered into the image header files. The number of voxels above a specified gray level in each cell was counted using Voxel View software (Vital Images). Voxel number was translated to cubic microns based on dimensions in the image header file. X/Y image planes are displayed in (A)-(D) and (I)-(L). Y/Z image planes are displayed in (E)-(H) and (M)-(P). E4 (B) and (F), E9 (C) and (G), EM12 (D) and (H) and EM15 (I) and (M) were smaller than the wild type DU145 cells (A) and (E). EM-resistant ovarian carcinoma cells (L) and (P) were also smaller than the wild type cells (K) and (O) from which they were derived. Vinblastine-resistant DU145 cells (J) and (N) showed no size decrease compared to wild type cells.

Table 1. Summary of DU145 cell volumes

Cell Line	% of wild type cell size* ± SEM
DU145/E4	66 ± 6
DU145/E9	74 ± 4
DU145/EM12	62 ± 12
DU145/EM15	54 ± 4
DU145/VLB	110 ^{xx}
OVEM15	83 ± 1

* average size of wild type DU145 cells was about 9,000 μm^3

**one experiment

rendering software. The threshold value, which was held constant for all experiments, was chosen such that extracellular spaces were not included in the detection.

On average, cells of the four EM-resistant prostatic lines were 30% to 50% smaller than the parental cells (Figure 4). Nuclear volume decreased by the same factor (Figure 5). (Nuclear volumes were determined the same way as cell volumes, but with propidium iodide replacing calcein as the space filler.) A drop in modal chromosome number, as determined by karyotyping procedures, paralleled this size decrease. For a summary of volume measurements, see Table 1.

To see if a change in size occurred in cells derived from non-prostatic tissue, volume measurements were carried out on EM-resistant ovarian carcinoma cells clonally-selected in the same fashion as the prostatic lines. A noticeable decrease in size occurred after the cells had become resistant to low doses of the drug. Currently, ovarian cells growing in 15 micromolar EM show a 20% decrease in size compared to the parental line (Figure 4). It is plausible that this cell shrinkage is due, at least in part, to EM-induced cytoskeletal alterations in the prostatic and ovarian cell lines.

4. CYTOSKELETAL STUDIES

Previous studies using differential interference contrast (DIC) and conventional fluorescence microscopy revealed several cytoskeletal alterations, including unusual microfilament organization and smaller mitotic spindles in E4 and E9 cells⁶. Confocal optics were used to look for these cytoskeletal changes in the more recent clones.

Microfilament organization in DU145, EM12 and EM15 cells was examined using a rhodamine-phalloidin conjugate (Molecular Probes, Eugene, OR, USA). Like E4 and E9, EM12 and EM15 had altered microfilament arrangements (Figure 6). In contrast to the smooth array of microfilaments found just below the plasma membrane of wild type cells,

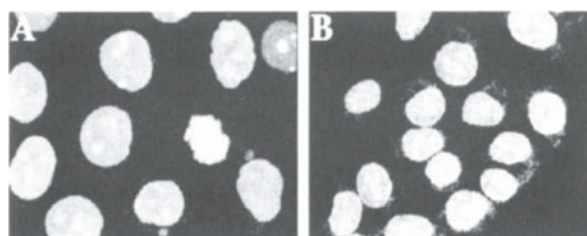


Figure 5. PI-Stained Nuclei. Nuclei were measured the same way cells were, but with propidium iodide (Sigma) used as the space filler. Nuclei of EM-resistant cells were about 50% smaller than nuclei of wild type cells. E4 cells (B) and wild type DU145 cells (A) are shown here.

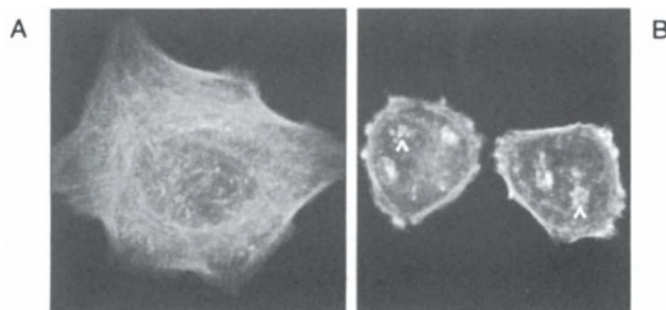


Figure 6. Microfilament Organization. Wild type (A) and EM-resistant (B) DU145 cells were labeled with rhodamine-phalloidin. A smooth network of microfilaments can be seen in wild type cells, while clumps and punctate areas of actin are visible in resistant cells (arrows).

actin was distributed in clumps and punctate areas at the periphery and throughout the cytoplasm of resistant cells. Interestingly, the EM-resistant clones exhibited increased sensitivity to the microfilament poison, cytochalasin B⁷. If this increased sensitivity is related to the change in microfilament organization, then this alteration does not seem to be an evolutionarily-favorable one, indicating that it may be just an indirect effect of resistance to EM.

To compare mitotic spindle structures, EM12, EM15 and wild type DU145 cells were immunofluorescently-labeled for β -tubulin and stained with propidium iodide. Metaphase and anaphase cells were imaged confocally. Spindle-pole and pole-pole distances were measured on the digitized images using the "LENGTH" macro provided with the confocal operating software (SOM 4.1, Bio-Rad, Hercules, CA). In addition, interphase cells from these slides were imaged to demonstrate the greater density of microtubules in the resistant clones (Figure 7).

Mitotic spindles in the EM-resistant cells were about 25% smaller than those in the parental DU145 cells. To see if spindle size would be altered in resistant cells of non-prostatic origin, EM-resistant ovarian carcinoma cells were labeled, scanned and measured in the same manner. A 25% drop in mitotic spindle size was apparent in these cells as well. (Figure 8) Given that microtubule poisons such as taxol and vinblastine produce cytotoxic effects through drug-induced spindle anomalies^{14,15} and that EM elicits microtubule effects on mitotic cells similar to those caused by these drugs⁵, it is possible that the smaller spindles of EM-resistant cells are an adaptation that aids in surviving insult by the drug. It has been

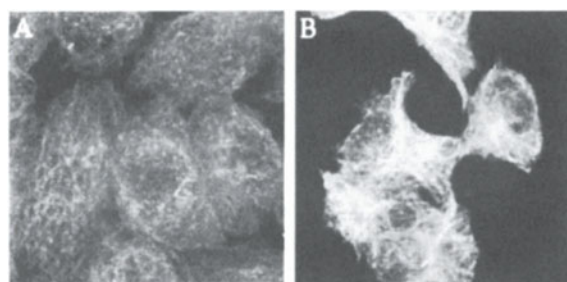


Figure 7. Microtubule Organization. DU145 cells were labeled immunofluorescently for β -tubulin. EM-resistant cells (B) consistently showed a greater density of microtubules than did wild type cells (A).

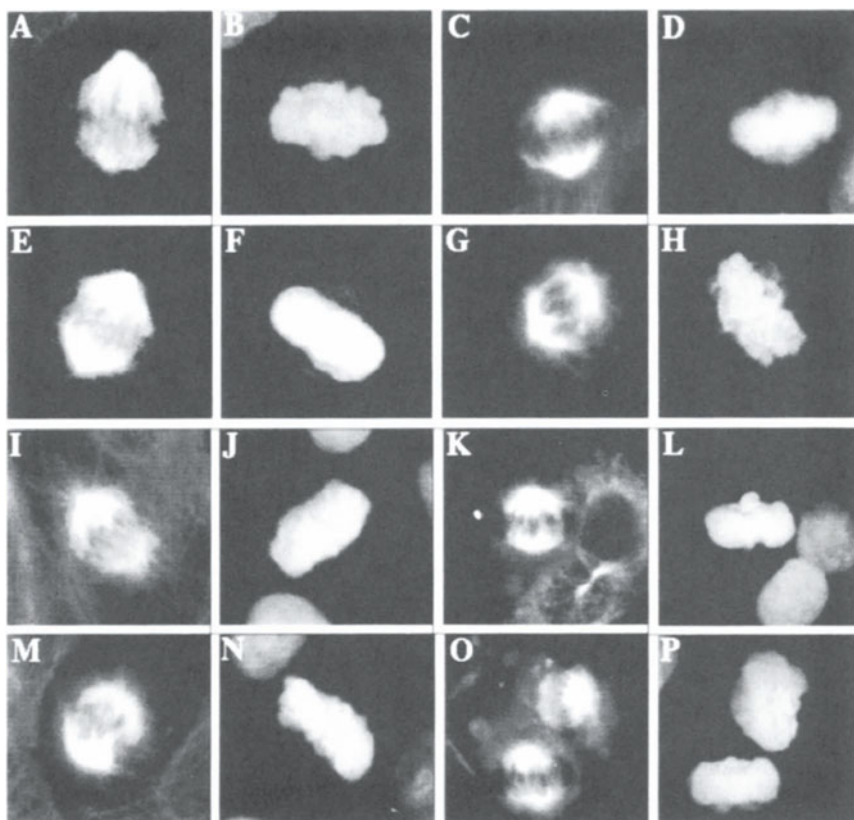


Figure 8. Mitotic Spindle Size. Mitotic spindles of EM-resistant prostatic (C) and (G) and ovarian carcinoma (K) and (O) cells were 25% smaller than that of the parental DU145 (A) and (E) and FCOV5 (I) and (M) cells. Spindles were visualized immunofluorescently with anti-B-tubulin antibodies. Propidium iodide was used to stain the chromosomes. Chromosomes images (B,D,F,H,J,L,N and P) are directly to the right of the corresponding tubulin images.

hypothesized that reduced chromosome number and reduced spindle size are related⁵; however, the cause/effect relationship between the two has yet to be confirmed.

CONCLUSIONS

Fluorescent probes have provided clues as to how resistant cells are able to survive and grow despite drug treatment. Studies utilizing radio-labeled drugs are standard in following drug uptake and efflux in cell populations. However, fluorescence allows the visualization of individual cell responses to insult with drug both initially (as in death or in drug efflux mechanisms), and after long term exposure (as in morphological and structural changes).

Based on the studies described, it seems that EM-resistant cells are able to efflux some of the drug within the first few minutes following exposure. This could be one of the early defenses the resistant cell has to protect itself from toxicity. It is not clear how EM binding to microtubule proteins specifically causes microtubule disassembly. However, the

dense microtubule arrays found in the EM-resistant cells may be another defense, especially if small cell size and drug efflux mechanisms limit the overall amount of drug that can interact with tubulin and/or MAPS. Though it is unclear, whether smaller mitotic spindle size in EM-resistant prostatic cells is due, to or causes, the loss of chromosomes, this change could affect the cells' ability to pass through M-phase while wild type cells are blocked at G2/M. Additionally, preliminary data suggest that resistant cells may express different tubulin isotypes compared to wild type and this may be another possible adaptation employed by the cells¹⁶.

Resistance to toxins that target cytoskeletal proteins may well be manifested in structural and regulatory changes in such proteins. This makes fluorescent probes, particularly in combination with confocal microscopy, valuable in the investigation of cytoskeletal drug resistant phenotypes.

REFERENCES

1. T. Wilson, D. J. R. Sheppard. "Theory and Practice of Scanning Optical Microscopy", Academic Press, Inc., NY (1984).
2. B. Hartley-Asp. Estramustine induced mitotic arrest in two human prostatic carcinoma cell lines. *Prostate*. 5: 93-100 (1984).
3. L. A. Speicher, L. R. Barone, K. D. Tew. Combined antimicrotubule activity of estramustine and taxol in human prostatic carcinoma cell lines. *Cancer Res.* 52: 4433- 4440 (1992).
4. K. D. Tew, B. Hartley-Asp. Cytotoxic properties of estramustine unrelated to alkylating and steroid constituents. *Urology*. 23: 28-33 (1984).
5. L. A. Speicher, L. R. Barone, J. D., Robbins, K. B. Seamon, K. D.Tew. Interaction of estramustine with cytoskeletal proteins and alteration in their regulation in drug resistant prostate carcinoma cells. *Mol. Pharm.* 46: 866-872 (1994).
6. V. R. Sheridan, L. A. Speicher, K. D. Tew. The effects of estramustine on metaphase and anaphase in DU145 prostatic carcinoma cells. *Eur. J. Cell Biol.* 54: 268- 276 (1991).
7. L. A. Speicher, V. R. Sheridan, A. K. Godwin, K. D. Tew. Resistance to the antimitotic drug estramustine is distinct from classic multi-drug resistance phenotype. *Br. J. Cancer* 64: 2767-2773 (1991).
8. M. E. Stearns, D. P. Jenkins, K. D. Tew. Dansylated estramustine, a fluorescent probe for studies of estramustine uptake and identification of intracellular targets. *Proc. Natl. Acad. Sci. USA* 82: 8483-8487 (1985).
9. S. Muallem, B. Zhang, P. A. Loessberg, R. A. Star. Simultaneous recording of cell volume changes and intracellular pH or Ca^{2+} concentration in osteosarcoma cells UMR-106-01. *J. Biol. Chem.* 267: 17658-17664 (1992).
10. J. Farinas, V. Simanek, A. S. Verkman. Cell volume measured by total internal reflection microfluorimetry: application to water and solute transport in cells transfected with water channel homologs. *Biophys J.* 68: 1613-1620 (1995).
11. K. Strange, K. R. Spring. Water permeability of rabbit cortical collecting ducts. *J. Membr. Biol.* 96: 27-43 (1987).
12. Haugland, R. P. Handbook of Fluorescent Probes and Research Chemicals (1992-1994). Molecular Probes, Eugene, OR, (1992).
13. P. Holden, W. Bounouar, J. Argiro. "Voxel View Ultra 2.1 User's Guide", Vital Images, Fairfield (1993).
14. M. A. Jordan, D. Thrower, L. Wilson. Mechanism of inhibition of cell proliferation by vinca alkaloids. *Cancer Res.* 51: 2212-2222 (1991).
15. B. H. Long, C. R. Fairchild. Paclitaxel inhibits progression of mitotic cells in G1 phase by interference with spindle formation without affecting other microtubule functions during anaphase and telophase. *Cancer Res.* 54: 4344-4361 (1994).
16. S. Rangonatham, D.W. Dexter, C. Benetatos, A.E. Chapman, K.D. Tew, G.R. Hudes. Increase of bIII and b IV tubulin isotypes in human carcinoma cells as a result of estramustine resistance. *Cancer Res.* 56: 2584-2589 (1996).

A HIGH RESOLUTION MULTIMODE DIGITAL IMAGING SYSTEM FOR FLUORESCENCE STUDIES OF MITOSIS

E. D. Salmon and J. C. Waters

Department of Biology
University of North Carolina
Chapel Hill, North Carolina 27599-3280

I. INTRODUCTION

Multimode digital fluorescence microscopy, in combination with other optical modes of image formation¹, is a powerful method for investigating many questions about the mechanisms of mitotic spindle assembly, chromosome movement and cell cycle control of chromosome segregation and cytokinesis. The dynamics of specific molecules in the spindle can be recorded using fluorescent analog cytochemistry where the molecules of interest are labeled with a fluorophore and introduced into the cell^{2,8}. For example, spindle organization in living cells and *in vitro* systems can be quantitatively determined by adding X-rhodamine labeled tubulin subunits to the cellular tubulin pool to selectively label microtubule polymers. The assembly dynamics of spindle components can be measured in real time using photoactivatable fluorophores^{2,3,6}. More recently, spindle proteins conjugated to green fluorescent protein (GFP) are being developed and expressed *in vivo*^{9,10}. In *in vitro* systems, chromosomes can be selectively labeled with fluorescent DNA-binding dyes like DAPI^{2,4,5,7,8}. Other fluorescent probes can be used to track the dynamics of membranes and other organelles or molecular complexes within the spindle¹¹. Fluorescence techniques are often used in combination with interference contrast. In transparent specimens, the movements of chromosomes and centrosomes can be recorded from transmitted light with phase contrast or differential interference contrast (DIC) optics¹². Polarization methods reveal spindle fiber microtubule dynamics and provide a quantitative measure of microtubule assembly and orientation¹³.

A multimode digital fluorescence microscope system capable of providing 3-D structural detail from stacks of optical sections through specimens stained with specific molecular probes has important advantages. The mitotic apparatus is often 5 μm or more in depth so that a single 200 to 1000 nm thick optical section reveals only a small fraction of spindle or chromosome organization. As computer power and large amounts of digital image storage capacity becomes economically affordable, the development of 4-D (3-D time lapse)

image acquisition and analysis will have a major impact on our understanding of mitotic mechanisms^{14,15}.

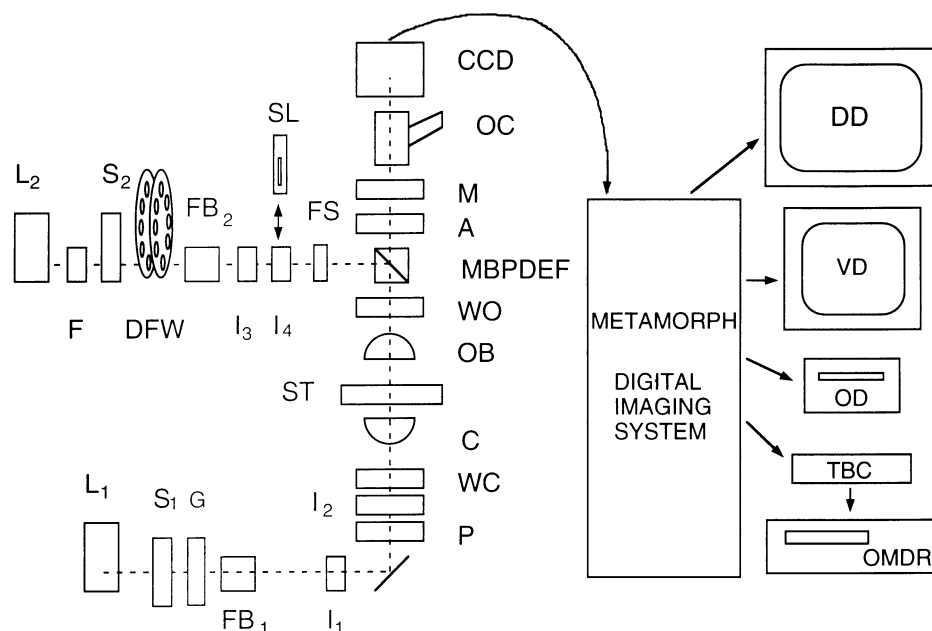
In this paper, we describe the high resolution multimode digital microscope system we have constructed for our mitosis studies and present a few examples of the application of this instrumentation. Many of our studies involve investigations of spindle assembly dynamics and chromosome movements in live cells or unfixed reconstituted preparations *in vitro* in which photodamage and phototoxicity are a major concern. As a consequence, a major factor in the instrument design was optical efficiency: achieving the highest image quality with the smallest number of excitation or illumination photons. This was important for both fluorescence and interference contrast modes.

II. INSTRUMENT DESIGN

The multimode digital imaging system we have constructed for our mitosis studies is diagrammed in Figure 1 (see Fig. 1 for manufacturer information and part numbers)*. We used a Nikon FXA microscope stand, in part because its efficient optical path provides diffraction limited resolution in transmitted and fluorescence modes for images projected onto a cooled CCD camera (Figure 2C). We chose to use a cooled CCD camera over other detectors, and wide field imaging rather than confocal laser scanning, because of their higher quantum efficiency. The camera is mounted directly above the objective at the major intermediate image plane and par-focal with the oculars in the binocular tube. A moveable prism in the FXA stand allows all the light to be projected to either the oculars or to the camera. An Optivar within the body tube provides selectable intermediate magnifications to the camera of 1X, 1.25X, 1.5X or 2X.

Cooled CCD cameras have a number of advantages for digital imaging over unintensified and intensified video detectors, including dynamic range, linearity, low noise and small

* Component parts are: L1, 100 W quartz halogen lamp; S1, Uniblitz shutter (#225L2A1Z523398, Vincent Associates, Rochester, NY); G, ground glass diffuser; FB1, manual filter changers including KG4 heat cut and green interference filters; I1, field iris diaphragm; I2, condenser iris diaphragm; P, AP, high transmission Nikon polaroid polarizer and removable analyzer; WC, WO, DIC Wollaston prisms for condenser and objective; C, Nikon NA = 1.4 CON A, Achr-Apl condenser; ST, rotatable stage with focus position controlled by z-axis stepper motor (Mac2000, Ludl Electronic Products, LTD., Hawthorne, NY); OB, 20x/NA= .75 or 60x/NA=1.4 Nikon objectives; MBPDEF, epi-filter block with multiple bandpass dichromatic mirror and emission filter (#83101 and #83100, Chroma Technology Corp., Brattleboro, VT); L2, 100 W HBO Hg lamp; F, KG4 heat cut filter; S2, DFW, shutter and dual 8 position filter wheel (Metaltek, Raleigh, NC), one wheel containing neutral density filters (#FNG011, Melles Griot, Irvine, CA), and the other a series of narrow bandpass excitation filters (#83360, #83490, #83570, Chroma Technology Corp.); FB2 manual filter changer; I3, epi-condenser iris diaphragm; I4, epi-field diaphragm slider; SL, slit (25 µm width, #04PAS004, Melles Griot, Irvine, CA) cemented to Nikon pinhole slider (#84060) for photoactivation; FS, filter slider; M, optivar magnification changer, 1X-2X (Nikon, Garden City, NJ, USA); OC, oculars; CCD, cooled CCD camera (#C4880, Hamamatsu Photonics, Bridgewater, NJ, USA); DD, 1024 x 768 pixel, 20 inch digital graphics display monitor (#2082, Viewsonic); VD, RGB video display monitor (#PVM1271Q, Sony); MetaMorph digital imaging system (Universal Imaging Corp., West Chester, PA) using a EISA bus, 64 MByte RAM memory, Imaging Technology AFG digital and video image processing card, Hamamatsu C4880 CCD controller card, Matrox MGA Ultima graphics display card, graphics display to S-VHS converter card (Hyperconverter, PC Video Conversion Corp., San Jose, CA), 1.4 MByte floppy drive, 580 MByte hard drive, ethernet card, parallel port cards for controlling shutter S1 and driving laser printer; 8 serial port card for controlling MetalTek filter wheel, Ludl z-axis stepper, CCD camera, and OMDR; OD, Pinnacle Micro 650 MByte optical drive (Pinnacle Micro Inc., Irvine, CA, USA); TBC, Personal Time-Base Corrector III, Digital Processing Systems, Fluorence KY; OMDR, Panasonic 2028 Optical Memory Disk Recorder. Modified from Salmon et al., 1994.



NIKON FXA LIGHT MICROSCOPE

Figure 1. Multimode digital microscope system for mitosis studies *in vivo* and *in vitro*.

geometrical distortion. The Hamamatsu C4880 was chosen because it has a high quantum efficiency, specified by Hamamatsu to be 55% at 730 nm. It also has two readout modes: a fast scan mode (up to 7 frames/sec) which is useful for focusing, and a slow scan mode (12 bit/pixel, 500,000 bytes/sec readout rate), which gives the most useful dynamic range (about 4000 grey levels above a noise floor of about 50 ± 10).

Our digitally enhanced (DE-) DIC images are recorded typically with 600 msec on-chip integration. This on-chip integration represents a 20 fold gain in sensitivity in comparison to image acquisition at video rates (about 30 msec exposure per frame). As a result, the high intensity illuminators and optical scramblers needed for high resolution video-enhanced DIC microscopy¹⁶⁻¹⁸ are not necessary. The full and even illumination of the objective aperture needed for high optical resolution¹⁹ can be achieved using the standard Nikon 100 W Quartz-halogen illuminator, heat reflecting filter, green filter, and a ground glass diffuser within the trans-illumination pathway in the base of the Nikon FXA stand (Figure 1). The standard test specimen for high resolution in the light microscope is the frustule pore lattice of the diatom *Amphipleura*. These pores in the silica shell are aligned with about 0.19 μm separation along rows and 0.24 μm separation between rows. As seen in Figure 2C, the rows of pores are clearly resolved by our DE-DIC system and the individual pores are almost resolvable with green light illumination. A major advantage of this illumination system for living cells is the low illumination intensity and the computer control of shutters, which illuminates the specimen only during the camera exposure. As a result, cells are viable for long periods of time-lapse recording.

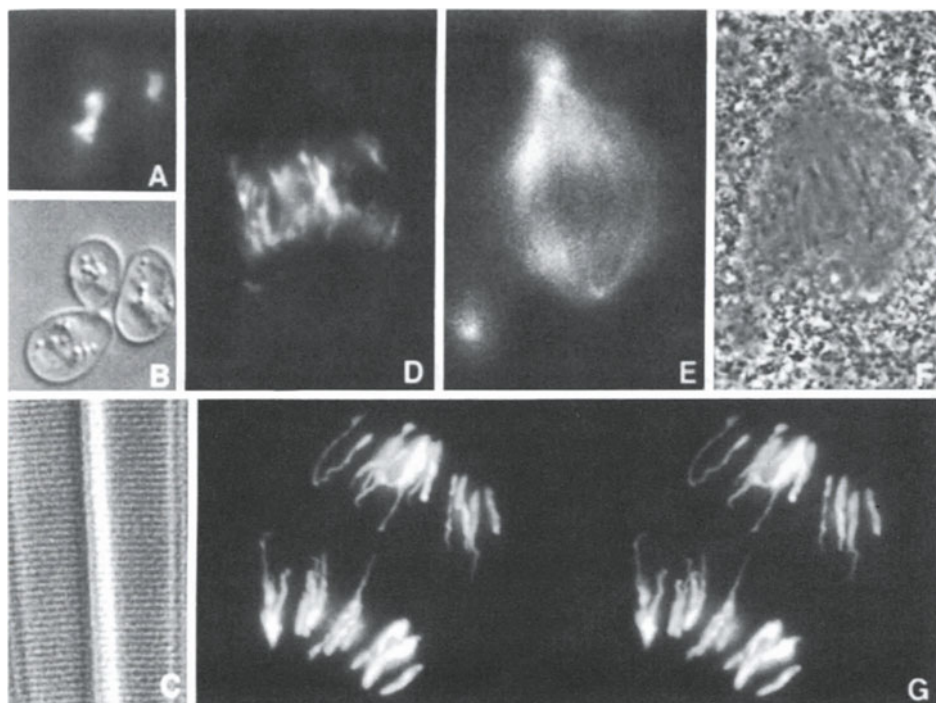


Figure 2. Views of a living, dividing yeast *Saccharomyces cerevisiae* by (A) fluorescence in the fluorescein channel of GFP protein bound to nuclear histones and (B) DIC*. (C) Image in DIC of the 0.24 μm spacing between rows of frustular pores of the diatom *Amphipleura* illuminated with green light*. Images of a spindle undergoing *in vitro* anaphase in *Xenopus* cytoplasmic egg extracts: (D) DAPI stained chromosomes, (E) X-rhodamine-tubulin labeled spindle and aster microtubules and (F) phase contrast (Nikon 20X/NA=0.75 Fluar Phase 3 objective). See^{7,8} for details. Stereo pair images (F) of DAPI stained chromosomes generated from a stack of 0.5 μm optical sections through a *Xenopus* spindle fixed in the extracts in mid-anaphase*. (*, Nikon 60X/NA=1.4 Plan Apo DIC objective and NA=1.4 condenser illumination for DIC). With permission from Salmon *et al.*⁷

An important criterion in our mitosis studies is that all the epi- and trans-illumination images be aligned and in focus at the same position on the CCD detector. This was accomplished using a single Chroma filter cube containing a multiple bandpass dichromatic mirror and emission filters designed for the DAPI (blue), fluorescein (green) and X-rhodamine (red) emission wavelengths (Figure 1). A MetalTek dual filter wheel is used to control excitation intensity and wavelength by selecting one of 8 neutral density filters in one wheel and one of 8 narrow bandpass filters in the other wheel. Further manual control of illumination intensity and field of illumination is provided by other filters and iris diaphragms in the epi- and trans-illumination paths (Figure 1). Focus position along the z-axis is controlled by a Ludl stepper motor attached to the Nikon FXA fine focus.

The MetaMorph digital imaging system is programmed to control image acquisition from the CCD camera. We have found that the central area (300x300 pixels) of the 1000x1000 pixel detector provides sufficient resolution and field of view for most of our mitosis studies, while reducing the time required to process the digital images and the amount of digital storage required (180 kBytes/image). Another important feature of the C4880 camera which can be controlled with Metamorph is the binning of adjacent pixels during the camera readout. For many fluorescence studies, resolution is not as critical as the sensitivity

of the camera. Binning 2x2, 4x4 or 8x8 provides increased sensitivity and reduces the number of pixels in the image by 4, 16 or 64 respectively.

In addition, the MetaMorph digital imaging system has programs and drivers to control for either time-lapse or z-axis stepping, shutters in the light paths, filter wheel positions, and image storage into stacks identified by their mode of acquisition [eg. DAPI, X-rhodamine (Xrhod), phase, DIC, etc.]. Image stacks are initially stored within the 64 MBytes of RAM memory then archived on the hard drive or the Pinnacle optical disk drive. MetaMorph also provides comprehensive functions for quantitative analysis of intensity and motion, multi-color overlays of different image stacks (e.g. DAPI and rhodamine channels), and movie presentation either on the high resolution graphics screen, or by conversion of the digital images to video through a VGA to S-VHS video converter. Large stacks of images can also be converted to video for storage on an optical memory video disk (Figure 1).

Journals are an important feature of Metamorph for customized control of the parameters, sequence and timing of image acquisition and storage. Journals are a sequence of instructions to the Metamorph imaging software generated by recording a sequence of selections from the program menus. For example, to take phase contrast, DAPI and rhodamine images of the same spindle in time lapse, journals are recorded which control image acquisition for each optical mode. These journals are then called by a time-lapse journal which controls the timing and sequence of image acquisition. For phase, the transmitting shutter is opened, the camera instructed to open its shutter for say 600 msec, close the camera shutter and then transfer the 16 bit image into the bottom of a stack of phase images. For each image, the time of acquisition is appended. Similarly, journals are written to control image acquisition for DAPI and rhodamine epi-fluorescence which specify the exposure time of the camera, the neutral density filter, the excitation filter, and the opening and closing of the epi-fluorescent light shutter. The timelapse journal can call the phase, DAPI and rhodamine journals in sequence at specified time intervals.

III. EXAMPLE APPLICATIONS

Using this system we were able to obtain high resolution real-time images of yeast nuclear motion in the cell division cycle^{7,20}. In one series of experiments⁷, GFP-histones were expressed to visualize the nucleus (Figure 2A) and cellular structural detail recorded by DIC (Figure 2B). The GFP fluorescence was photoactivated using a several sec pulse of 360 nm light; then images were recorded using the fluorescein channel and excitation filter. In other studies²⁰, we discovered that the cooled CCD camera produces unexpectedly high contrast and high resolution DE-DIC images, such that the positions of the spindle pole bodies and the anaphase elongation of the mitotic spindle within the 2 μ m diameter preanaphase nucleus can be clearly seen (Figure 3).

The multimode microscope system has also been particularly useful for recording anaphase spindle dynamics and chromosome segregation for the first time *in vitro*^{7,8}, by reconstituting mitosis in a test tube from sperm nuclei and cytoplasmic extracts prepared from *Xenopus* eggs^{4,5} (Figure 2D, 2E, 2F). Here phase and/or DAPI fluorescence image stacks record chromosome movements while X-rhodamine labeled tubulin fluorescence shows spindle microtubule assembly dynamics. The spindles in cytoplasmic extracts are pipetted from a test-tube and held in a chamber between a slide and a coverslip separated by 12 μ m latex beads and sealed with halocarbon oil and valap (1:1:1 mixture of vaseline, lanoline and paraffin). For time-lapse, sequential 600 msec exposures of rhodamine and DAPI and/or phase images are recorded to their respective image stacks at either 30 or 60 sec intervals. The *Xenopus* egg cytoplasm is very optically dense making the rhodamine and DAPI fluorescent images the most useful for recording spindle and chromosome dynamics.

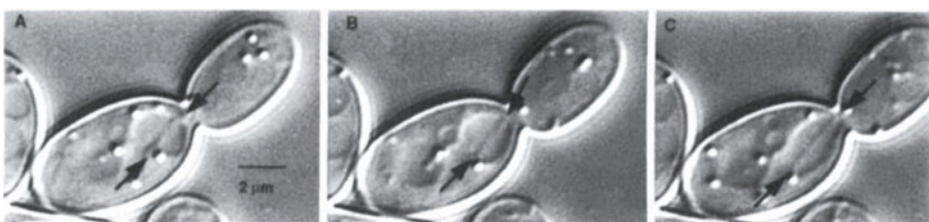


Figure 3. DE-DIC images of a dividing yeast *Saccharomyces cerevisiae* (A) preanaphase, (B) the beginning of anaphase spindle and nuclear elongation and (C) the end of the initial fast phase of spindle elongation. The spindle extends through the center of the nucleus and is formed from an overlapping bundle of microtubules extending from opposite spindle pole bodies (arrows). Modified from Yeh *et al.*¹⁴

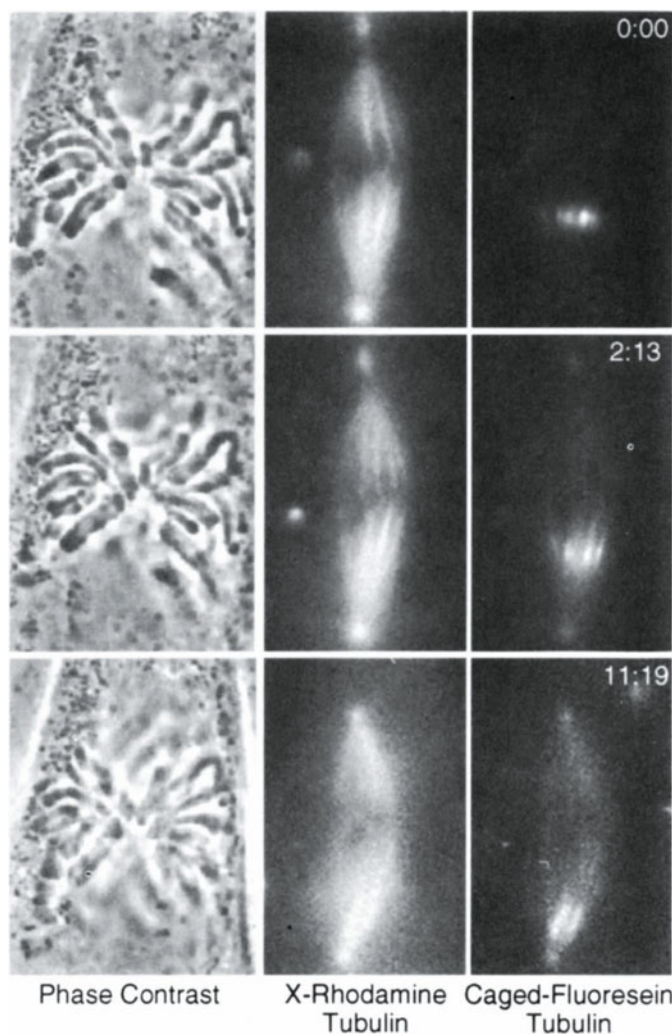


Figure 4. Multi-mode imaging and local fluorescence photoactivation to see the dynamics of kinetochore fiber microtubules in metaphase newt lung epithelial cells. Cells were injected in early mitosis with X-rhodamine labeled tubulin and C2CF caged fluorescein labeled tubulin. At each time point a phase image showed chromosome position; an X-rhodamine image showed spindle microtubule assembly and the C2CF fluorescein image recorded the poleward flux and turnover of photoactivated fluorescent tubulin within the kinetochore fiber microtubules. Time is given in min after photoactivation. See²¹ for details Scale = 10 μm.

3-D images derived from a single time-point stack of optical sections have also proved very useful for determining the behavior of all of the chromosomes and their kinetochore regions within the spindle^{7,8} (Figure 3G).

Another application of our multimode system has been in the analysis of the dynamics of kinetochore microtubules within mitotic tissue cells using fluorescence photoactivation methods^{3,21}. Figure 4 shows a metaphase newt lung epithelial cell which has been microinjected with X-rhodamine labeled tubulin to label all the spindle microtubules and C2CF caged-fluorescein labeled tubulin for photoactivation of tubulins within the spindle fiber microtubules as developed by Mitchison²². For photoactivation, the field diaphragm in the epi-illuminator is replaced with a 25 μm slit cemented to a Nikon pinhole slider (Figure 1). With the Nikon 60X/ NA = 1.4 Plan Apochromat objective, a 2 mm thick optical glass flat is also inserted into the light path, using the filter slider which is just after the slit, to bring the image of the slit with 360 nm excitation light onto the same focal plane as illumination between 450-600nm without the slit and optical flat. The spindle is marked with 360nm illumination for 2 sec using the Chroma DAPI exciter filter within the excitation filter wheel and no neutral density filters. Image stacks for rhodamine, fluorescein and phase are acquired at 30 sec intervals. The exposures are 600 msec using 1 OD neutral filters in front of the 100 watt Hg lamp and using a 2x binning of pixels in the Hamamatsu cooled CCD detector. The 2X pixel binning reduces the 300 x 300 central image capture area to 150 x 150 pixels and increases image sensitivity by 4 fold. This has proven to be important in allowing lower excitation light intensity, which reduces photobleaching, and has not significantly reduced useful resolution in these low light level images. The images in Figure 4 show that photoactivated marks on the kinetochore fibers flux poleward, demonstrating that at metaphase the kinetochore microtubules, which connect the chromosomes to the poles, have a net addition of tubulin subunits at their kinetochore ends and a net disassembly of subunits at their polar ends. In anaphase, this poleward flux of kinetochore microtubules persists as chromosomes move poleward^{3,6}. Photoactivation has also been used to show that poleward flux of spindle microtubules occurs in other cell types^{2,6}. This has important implications for how kinetochore microtubule dynamics are coupled to force generation for chromosome movement and proper alignment of the chromosomes for accurate segregation during mitosis^{3,6,18,21}.

IV. REFERENCES

1. D. Farkas, G. Baxter, R. DeBiasio, A. Gough, M. Nederlof, D. Pane, J. Pane, D. Patek, K. Ryan, and D. Taylor. Multimode light microscopy and the dynamics of molecules, cells and tissues. *Ann. Rev. Phys.* 55: 785 (1993).
2. K.E. Sawin and T.J. Mitchison. Poleward microtubule flux in mitotic spindles assembled *in vitro*. *J. Cell Biol.* 112: 941 (1991).
3. T.J. Mitchison and E.D. Salmon. Poleward kinetochore fiber movement occurs during both metaphase and anaphase-A in newt lung cell mitosis. *J. Cell Biol.* 119: 569 (1992).
4. C.E. Shamu and A.W. Murray. Sister chromatid separation in frog egg extracts requires DNA topoisomerase II activity during anaphase. *J. Cell Biol.* 117: 921 (1992).
5. S.L. Holloway, M. Glotzer, R.W. King, A.W. Murray. Anaphase is initiated by proteolysis rather than by the inactivation of maturation-promoting factor. *Cell* 73: 1393 (1993).
6. Y. Zhai, P. Kronebusch, and G. Borisy. Kinetochore microtubule dynamics and the metaphase-anaphase transition. *J. Cell Biol.* 131:721 (1995).
7. E.D. Salmon, T. Inoue, A. Desai, and A.W. Murray. High resolution multimode digital imaging system for mitosis studies *in vivo* and *in vitro*. *Biol Bull.* 187: 231 (1994).
8. A. Murray, A. Desai, and E. Salmon. Real time observation of anaphase *in vitro*. *Molec. Biol. Cell* 5: 255a (1995).
9. T. Stearns. Green fluorescent protein: The green revolution. *Current Biol.* 5: 262 (1995).

10. K. Olson, J. McIntosh, and J. Olmsted. Analysis of MAP4 function in living cells using green fluorescent protein (GFP) chimeras. *J. Cell Biol.* 130: 639 (1995).
11. C.M. Waterman-Storer, J.W. Sanger, and J.M. Sanger. Dynamics of organelles in the mitotic spindles of living cells: membrane and microtubule interactions. *Cell Motil. Cytoskel.* 26: 19 (1993).
12. R.V. Skibbens, V.P. Skeen, and E.D. Salmon. Directional instability of kinetochore motility during chromosome congression and segregation in mitotic newt lung cells: a push-pull mechanism. *J. of Cell Biol.* 122: 859 (1993).
13. L. Cassimeris, S. Inoue, and E.D. Salmon. Microtubule dynamics in the chromosomal spindle fiber: analysis by fluorescence and high-resolution polarization microscopy. *Cell Motil.* 10: 185 (1988).
14. S. Inoué and T.D. Inoué. 3-D and 4-D imaging of living cells with DIC and polarization microscopy. *Mole Biol. of Cell* 5:247a (1995).
15. C.F. Thomas, P.J. DeVries, V.E. Centonze, J.D. Hardin and J.G. White. 4-Dimensional digital imaging and display system for dynamic processes. *Mole Biol. of Cell* 5:247a (1995).
16. T. Salmon, R.A. Walker, and N.K. Pryer. Video-enhanced differential interference contrast light microscopy. *BioTechniques* 7: 624 (1989).
17. R.A. Walker, N.R. Glikman, and E.D. Salmon. Using video-enhanced differential interference contrast microscopy to analyze the assembly dynamics of individual microtubules in real time, *In "Optical Microscopy for Biology."* B. Herman and K. Jacobson, eds., Wiley-Liss, Inc. New York, NY, USA (1990).
18. E.D. Salmon. VE-DIC light microscopy and the discovery of kinesin. *Trends in Cell Biol.* 5: 154 (1995).
19. S. Inoué. "Video Microscopy": Plenum Publishing, New York (1986).
20. E. Yeh, R. Skibbens, J. Cheng, E. Salmon, and K. Bloom. Spindle dynamics and cell cycle regulation of dynein in the budding yeast, *Saccharomyces cerevisiae*. *J. Cell Biol.* 130: 687 (1995).
21. J.C. Waters, T. Mitchison, and C.L. Rieder, and E. Salmon. The kinetochore microtubule minus-end disassembly associated with poleward flux produces a force that can do work. *Molec. Biol. Cell.* in press (1996).
22. T.J. Mitchison. Polewards microtubule flux in the mitotic spindle: evidence from photoactivation of fluorescence. *J. Cell Biol.* 109: 637 (1989).

USE OF PHOTODIODE ARRAY FLUORESCENCE SPECTROSCOPY IN BIOCHEMISTRY, PHARMACOLOGY, AND ONCOLOGY

Roy Pottier¹ and James C. Kennedy²

¹ Department of Chemistry and Chemical Engineering
The Royal Military College of Canada
Kingston, Ontario, Canada K7K 5L0

² Department of Oncology
Queen's University, Kingston
Ontario, Canada K7L 3N6

INTRODUCTION

All materials are partially transparent in some part of the electromagnetic spectrum, and it is thus logical that the transmission of light has found wide use as a probing tool to characterize and study a large variety of samples. Dual beam spectrophotometric systems, in which the intensity of light transmitted through a sample is directly compared with the same light transmitted through a reference material, have found wide use in many areas such as analytical chemistry, geology, physics and medicine. The fact that all atomic and molecular systems absorb light at some wavelengths (ultraviolet, visible or infrared) has made absorbance spectroscopy a general and widely applicable tool.

The main disadvantage of absorbance spectroscopy for use in biological systems is related to the inhomogeneity of the sample. The simple linear Beer-Lambert absorbance law shows significant deviation when applied to turbid, highly scattering media. Thus the use of absorbance spectroscopy for the study of biological samples often requires prior sample preparation in order to render the samples homogeneous. Further, the requirement that at least some of the probing light traverses the sample is a severe limitation, since it precludes such a technique from being applied for many *in vivo* investigations.

Many molecules of biological interest are capable of re-emitting part of their absorbed energy in the form of fluorescence. Further, the fluorescence originating from the excited states of a large variety of biomolecules is found in the visible part of the electromagnetic spectrum, a region that is partially transparent for many types of tissues. Thus fluorescence spectroscopy has, in general, been more useful than absorbance spectroscopy as a technique to study turbid biological systems.

While it is true that not all molecules in biological tissue exhibit a high fluorescence quantum yield, the fact that emitted photons can be easily measured (down to the single photon level) makes this approach attractive. This manuscript briefly describes the instrumentation used and provides examples of applications of photodiode array fluorescence spectroscopy in biochemistry, pharmacology and oncology.

DIODE ARRAY FLUORESCENCE SPECTROSCOPY

Instrumentation

There are three main components of a system used to measure fluorescence spectra. These are: light sources, dispersive elements and photon detection devices.

Light Sources. The first component of any fluorescence spectroscopy system consists of a light source that is capable of exciting molecules to their excited states, from which they will lose some of their energy in the form of emission (fluorescence, in this case). A variety of light sources can be used for such a purpose, including incandescent lamps, arc lamps and lasers. Incandescent lamps have the advantage of being cheap, long lasting, easy to manipulate and air cooled. Their disadvantages are that they are not very intense in their light output, are not easily focused, and are not easily pulsed for short time temporal measurements. Arc lamps have much more intense output powers, but are less stable, and often require water cooling. Their power supply requirements are often cumbersome and costly. Optical feedback systems can be incorporated on arc lamps in order to stabilize their output over time. Their higher output power means that they can be used with light guides or large (1-2 mm diameter) optical fibers. Such lamps are often used for the investigation of biological systems where the probing fibers can be installed in large natural body cavities, for example, mouth, anus, or vagina.

Laser sources are capable of generating highly monochromatic light with extremely high intensities. Lasers can be either of the continuous wave (CW) type, whereby the laser emits a relatively steady output intensity, or pulsed, where the light output is emitted at discrete times. These pulses of laser light can reach extremely high peak powers (Gigawatts), but are often of very short duration (as short as femtoseconds). Pulsed laser excitation is very useful for the study of ultrashort phenomena, and is required for characterizing the emission lifetimes of molecules being investigated. The main disadvantages of laser light sources are their high cost and limited availability of wavelengths. The cheaper laser diodes show great promise in this respect.

Dispersive Elements. In order to render fluorescence spectroscopy most useful, it is necessary to separate into their constituent wavelengths both the excitation energy from the source, and the emitted fluorescence from the sample. If a laser is used as an excitation source, one needs only to separate the emitted fluorescence, since laser light is already highly monochromatic.

Two types of dispersive elements are readily available. The simplest of these is the filter. Filters can be used to isolate parts of the excitation light (for example, to match the excitation light with the absorption characteristics of the molecule being investigated, or to selectively excite a part of the emitted fluorescence). Filters are available in two types: absorbing or reflecting. Absorbing filters are usually cheaper, and are composed of glass or plastic in which is embedded absorbing material that will stop all the light except a small bandpass that is of interest. Reflecting filters have a reflective coating that selectively reflects

certain regions of wavelengths. These are usually more expensive, but can withstand higher light energies without breaking.

By far the most widely used dispersing elements in fluorescence spectroscopy are monochromators. These contain a dispersive element, either a prism or a diffraction grating, that separates the various wavelengths of light in space. Two such monochromators are found in conventional (non-laser) fluorescence spectrophotofluorimeters, one to separate the excitation light into its constituents, another to separate the emitted fluorescence into its various wavelengths. The sample to be studied is placed between these two dispersive elements. A scanning of the emission monochromator produces a fluorescence spectrum, while a scanning of the excitation monochromator enables one to obtain a fluorescence excitation spectrum, this latter being related to the absorbance properties of the chromophore. Simultaneous scanning of both monochromators leads to synchron spectra. These are useful in the verification of the purity of compounds under study.

Light Detection Devices. Once the excitation light has excited the sample to be investigated, and the emitted fluorescence has passed through the second monochromator (called the emission monochromator), the fluorescence emission must be quantitatively measured. Until relatively recently, photomultipliers were the most widely used measurement devices in fluorescence spectroscopy. They are still the most sensitive devices available to measure photons, and as such, are expected to be found in use in the future, especially for the measurement of low level fluorescence. Photomultipliers are normally placed at the exit slit of the emission monochromator, and the dispersive element is rotated in order to scan the emission spectrum.

Alternately, in the past two decades, photodiode arrays have been used to rapidly measure the full emission spectrum simultaneously. Photodiode arrays are a series of very sensitive photodiodes that are placed at the exit port of a polychromator. The array views the entire dispersed spectrum simultaneously, thus permitting a rapid collection of spectral data without the need for a mechanical rotation of the dispersive element. The main advantage of such an approach is that the entire spectrum can be collected during a very short time, even on a nanosecond time scale.

A typical photodiode array spectrophotofluorimeter system that is adapted for *in vivo* use is illustrated in Fig. 1. In such a system, the excitation light is delivered to the biological subject under investigation by the use of a bifurcated optical fiber bundle. The emitted fluorescence is similarly delivered to the emission polychromator by the other branch of the bifurcated optical fiber bundle. Alternately, it is possible to image the sample with a two dimensional array, in order to obtain a "picture" of the substance under investigation. The use of such devices, called charged coupled devices (CCD's) are discussed in more details in other chapters of these proceedings.

APPLICATIONS OF PHOTODIODE ARRAY FLUORESCENCE SPECTROSCOPY TO BIOLOGICAL SYSTEMS

Biochemical Applications

Nature of the Chromophores Responsible for Naturally Occurring Fluorescence in Rodent Skin. In order to unambiguously detect and measure the emission properties of a particular chromophore *in vivo*, it is necessary to clearly separate the emission properties of the molecule under study from the emission properties of the host sample. Many such *in vivo* studies are carried out in rodents. One example is the use of mice as a model, in order to

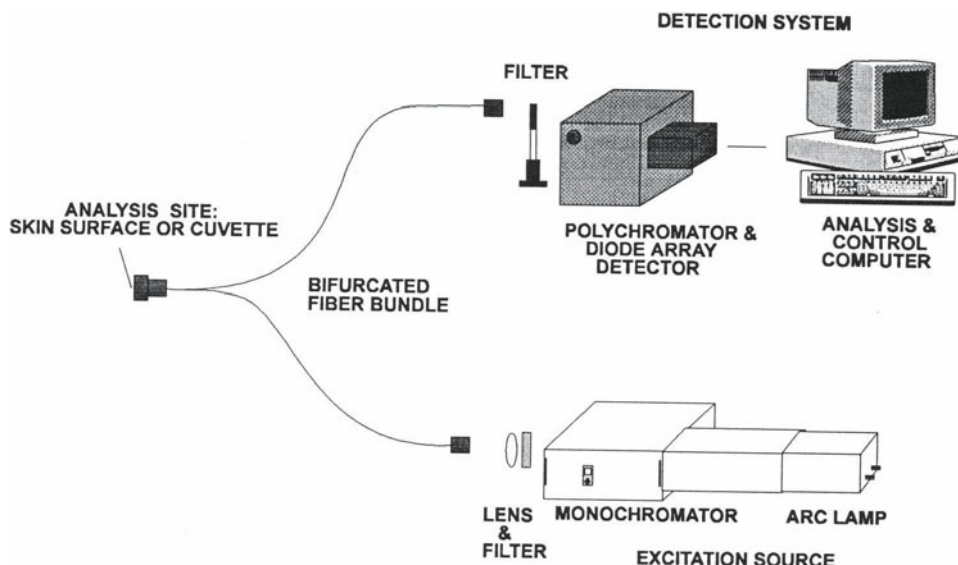


Figure 1. Typical photodiode array spectrophotofluorimeter system suitable for *in vivo* measurements.

characterize the amount of photochemotherapeutic agent localized in the skin or in internal organs. Surface detected *in vivo* fluorescence spectroscopy can be used for such a purpose, using systems such as that shown in Fig. 1.

During the surface detected fluorescence measurements of porphyrins, it was observed that the background fluorescence contained an interfering chromophore in the wavelength range of emission of the porphyrins. When a sample mouse was sacrificed and fluorescence spectra were obtained from the stomach area, it was revealed that the interfering fluorescence was due to partially degraded chlorophyll products derived from rodent food¹. In order to eliminate the presence of such interfering substances, it is necessary to keep rodents on a special chlorophyll-free diet for at least two weeks prior to carrying out fluorescence measurements².

Rate of Formation and Clearance of 5-Aminolevulinic Acid Induced Protoporphyrin IX. Another biochemical application of photodiode array fluorescence spectroscopy can be seen in the monitoring of the biochemical conversion of 5-aminolevulinic acid (ALA) into protoporphyrin IX *in vivo*. This reaction is part of the metabolic energy production scheme in all cells, and is also part of the mechanism responsible for the production of heme. The administration of ALA into a rodent quickly leads to the observation of the protoporphyrin IX (PP) fluorescence, characterized by its emission peaks at 635 and 700 nm. The rate of conversion of ALA into PP can thus be monitored via the intensity of PP fluorescence as a function of time (post-ALA administration). For intraperitoneal injection of ALA in mice, the maximum PP fluorescence is observed 2-4 hours post injection (dose dependent), with complete PP clearance in less than 24 hrs.

Applications in Pharmacology

Pharmacokinetic Behaviour of Drugs as a Function of Hydrophobicity. The rate at which a drug is cleared from a body is an important parameter to be measured in pharmacology. Surface detected fluorescence spectroscopy is ideally suited for such a purpose,

provided, of course, that the drug to be monitored has a appreciable fluorescence quantum yield.

In an attempt to correlate the structural properties of a series of porphyrin derivatives with their clearance times, the pharmacokinetic behaviour of 17 porphyrin derivatives was studied by surface detected fluorescence spectroscopy³, in order to provide a correlation between the hydrophilic nature of the various porphyrin derivatives to the time required for drug clearance. A notable exception to the general trend of slow clearance for hydrophobic drugs was the natural porphyrin, protoporphyrin IX. This exception can be explained by the action of iron and the enzyme ferrochelatase, resulting in the rapid conversion of PP into heme, a non-fluorescent metalloporphyrin.

Multiphasic Drug Pharmacokinetics. The rapid scanning ability of photodiode arrays permit one to quickly obtain full *in vivo* emission of fluorescent drugs on a quasi-continuous basis. Detailed *in vivo* pharmacokinetic studies are made possible. When such measurements are carried out on an individual rodent, large fluctuations, superimposed on the classic biphasic drug clearance curves, are often observed. For example, the *in vivo* fluorescence pharmacokinetic behaviour of zinc phthalocyanine as characterized by fluorescence at its peak emission wavelength, shows an oscillatory pattern in its clearance curve. The oscillations are believed to be related to interfering fluorescence arising from chromophores in rodent food⁴.

Applications in Oncology

Tissue pH. Tumour tissue is often found to have a pH significantly lower than that of adjacent normal tissue⁵. While microelectrodes are available for the measurement of tissue pH, such electrodes are very fragile and disrupt the pH equilibrium of the system due to their invasive nature. *In vivo* pH can be measured non-invasively by the use of pH dependent fluorescence probes. Fluorescent dyes, such as bis-carboxyethylcarboxy fluorescein, have different fluorescence characteristics at different pH values, and can be exploited for such *in vivo* measurements. This technique can be rendered more sensitive by the use of two excitation wavelengths. One excitation wavelength corresponds to an isoemissive point, the other wavelength corresponds to a pH sensitive region. The ratio of the emission observed from the excitation at these two wavelengths leads to an enhanced pH sensitive probing system⁶.

Optical Biopsy. The most important use of *in vivo* fluorescence spectroscopy in oncology is undoubtedly related to the concept of the “optical biopsy” to characterize the shape and depth of a particular lesion. Rather than removing a tissue sample for subsequent analysis, the optical biopsy would probe the tissue *in vivo* via the use of harmless, non-invasive photons. Slight changes in the chemical profile of endogenous fluorescent chromophores, such as NADH and protoporphyrin IX, can be rapidly detected by surface-detected *in vivo* fluorescence spectroscopy. Further, the presence of anti-tumour agents, such as adriamycin, can also be monitored by such a technique. The appreciable fluorescence quantum yield of most photochemotherapeutic agents, which localize selectively in various diseased tissues, (e.g. porphyrins, chlorins, phthalocyanines, merocyanine 540, etc.) has led to an increase in attempts to develop a quantitative optical biopsy system.

The rationale for the use of visible electromagnetic radiation in tumour diagnostics is straightforward. Visible photons are harmless and non-invasive. Further, the use of different excitation wavelengths can, in theory, be used to probe different tissue depths due to their different tissue penetration characteristics. Unfortunately, several problems have to

be solved before such an optical biopsy system can be rendered quantitative. First, the penetration depth of visible light in tissue is severely limited, typically a few millimeters. Second, the optical properties of tissue are quite complex and vary significantly amongst different tissue types and from patient to patient. Light scattering is also a complex phenomenon that has to be accommodated in the interpretation of tissue/chromophore fluorescence data. Thus while it is relatively straightforward to obtain *in vivo* fluorescence spectral data from both normal and malignant tissue, the quantitative aspect of such data is far from simple. At present, surface-detected *in vivo* fluorescence spectroscopy can easily delineate the region of tumour tissue at the surface, but the depth profiling of the tumour is still in the experimental stage. The increased use of tissue optics modelling will hopefully help in the refinement and usefulness of the important concept of the optical biopsy for use in oncology.

ACKNOWLEDGMENTS

This work was financially supported in part by a Department of National Defence (Canada) ARP Grant and by DUSA Pharmaceuticals.

REFERENCES

1. G. Weagle, P.E. Paterson, J. Kennedy and R. Pottier, The nature of the chromophore responsible for naturally occurring fluorescence in mouse skin, *J. Photochem. Photobiol.B:Biol.* 2:313 (1988).
2. H. Holmes, J.C. Kennedy, R. Pottier, F. Rossi and G. Weagle, A recipe for the preparation of a rodent food that eliminates chlorophyll-based tissue fluorescence, *J. Photochem. Photobiol.B:Biol.* 29: 199 (1995).
3. J.C. Kennedy, P. Nadeau, Z.J. Petryka, R.H. Pottier and G. Weagle, Clearance times of porphyrin derivatives from mice as measured by *in vivo* fluorescence spectroscopy, *Photochem. Photobiol.* 55:729 (1992).
4. E.F. Gudgin Dickson, H. Holmes, G. Jori, J.C. Kennedy, P. Nadeau, R.H. Pottier, F. Rossi, D.A. Russell and G.E. Weagle, On the source of oscillations observed during *in vivo* zinc phthalocyanine fluorescence pharmacokinetic measurements in mice. *Photochem. Photobiol.* 61: 506 (1995).
5. A.J. Thistlethwaite, D.B. Leeper, D.J. Moyler III and R.E. Nerlinger, pH distribution in human tumors, *Int. J. Radiat. Oncol. Biol. Phys.*, 11:1647 (1985).
6. D.A. Russell, R.H. Pottier and D.P. Valenzeno, *In vivo* spectroscopic properties of the fluorescent pH indicator biscarboxyethyl carboxyfluorescein, *J. Photochem. Photobiol.B:Biol.* 29:17 (1995).

HYDROPHOBIC PHOTOSENSITIZERS DELIVERY TO TUMOR TISSUES BY AN AMPHIPHILIC PEPTIDE

In Vitro and in Vivo Fluorimetric Studies

O. Bourdon,¹ J. Blais,¹ J. Bolard,¹ V. Vonarx,² L. Morlet,² T. Patrice,²
C. Bedel,³ N. Cempel,³ and D. Guillochon³

¹ LPBC- CNRS URA 2056 - Université P. et M. Curie
T 22, case 138 , 4 Place Jussieu
75252 Paris Cedex 05-France

² Département Laser

CHRU Nantes - BP10045- 44035-Nantes- France

³ Laboratoire des Substances Naturelles IUT A
Lille I, BP179-59653 Villeneuve d'Ascq- France

INTRODUCTION

Photodynamic therapy (PDT) of cancers has been developed over the last few years, giving promising results in clinical assays in different medical fields. It is based on the activation of photosensitizers that show some preferential accumulation in tumor tissues¹. The photodynamic processes involve the formation of active oxygen species such as singlet oxygen (${}^1\text{O}_2$), a very cytotoxic form of molecular oxygen which has been shown to cause damage to tumor cellular constituents^{1,2}. HpD, and the commercialy available drug Photofrin® have been commonly used in PDT but these compounds have cutaneous side effects. Efficient second generation sensitizers, such as chlorin and benzoporphyrin derivatives, are now under investigation.

Hydrophobic sensitizers are shown to exhibit good photodynamic ability which could be due to possible interactions with cellular lipid constituents resulting in a better accumulation ability in tumors^{3,4}. However the hydrophobicity remains a limiting factor to their use for clinical assays and various delivery system like cremophores, liposomes, microspheres, nanoparticles or lipoproteins have been proposed^{1,5,6}.

Recently, an amphiphilic peptide isolated from bovine haemoglobin⁷ has been shown to highly improve the solubility of hydrophobic compounds, forming a non-covalent association.

In the present work, we have studied the interaction of the non-covalent association between this peptide and the hydrophobic protoporphyrin IX (PpIX) chosen as a model.

First, the possible penetration of P_pXI-peptide within cells has been studied by microspectrofluorimetry. In a second step, the biodistribution in nude mice grafted with human adenocarcinoma has been investigated using an optical fiber spectrofluorimeter.

EXPERIMENTAL

Peptide Purification and Characterization

The bovine haemoglobin hydrolysate was purified by gel chromatography. One of the fractions was selected with regards to its ability to solubilize PpIX and was purified by reversed phase HPLC (for details see 7). The amphiphilic peptide sequence identified by mass spectrometry (FAB and MS-MS) was as follows:

Ala-Ser-His-Leu-Pro-Ser-Asp-Phe-Thr-Pro-Ala-Val-His-Ala-Ser-Leu which represents the 110-125 fragment of the α chain of bovine haemoglobin.

Preparation of the [P_pIX-Peptide] Complex

PpIX free base was dissolved in acetone-phosphate buffer 50mM (50:50 v/v). The peptide in phosphate buffer (20ml) was added to the porphyrin solution (20ml). Acetone was then removed under vacuo and insoluble residues were eliminated. The porphyrin concentration of [PpIX-peptide] was determined by spectrophotometry on the basis of a calibration curve .

Culture Cells

Human colorectal adenocarcinoma (HT29) cells were allowed to grow to confluence in RPMI 1640 without phenol red and supplemented with 10% fetal calf serum, glutamine (2mM) and antibiotics. Cells were subcultured by dispersal with 0.025% trypsin and replated (10^5 cells/ml).

Microspectrofluorimetry Experiments

The experimental set up developed in our laboratory has been previously described⁸. In the present work, the excitation was performed with the 488nm line of an ionized argon laser. The exciting beam was focused on a cell area of $1\mu\text{m}^2$. The excitation power was $0.1\mu\text{W}$ at the sample level. The analyzed cellular volume was about $10\mu\text{m}^3$.

Adherent cells were incubated in Petri dishes in RPMI medium with L-glutamine and without phenol red in the presence of [PpIX-peptide] at 37°C and kept in the dark.

In Vivo Fluorimetric Experiments

The optical fiber spectrofluorimeter (Figure 1) used for the *in vivo* experiments has recently been described in detail by Morlet⁹. Excitation light (514nm) from an argon laser was delivered by an optical fiber which was in direct contact with the target tissue. The power density at the fiber tip was 0.5mW.cm^{-2} .

Seven to nine week old male Swiss nude mice were grafted with HT29 cells from a human colorectal adenocarcinoma. Before the fluorimetric experiments, mice received an intraperitoneal injection of [PpIX-peptide].

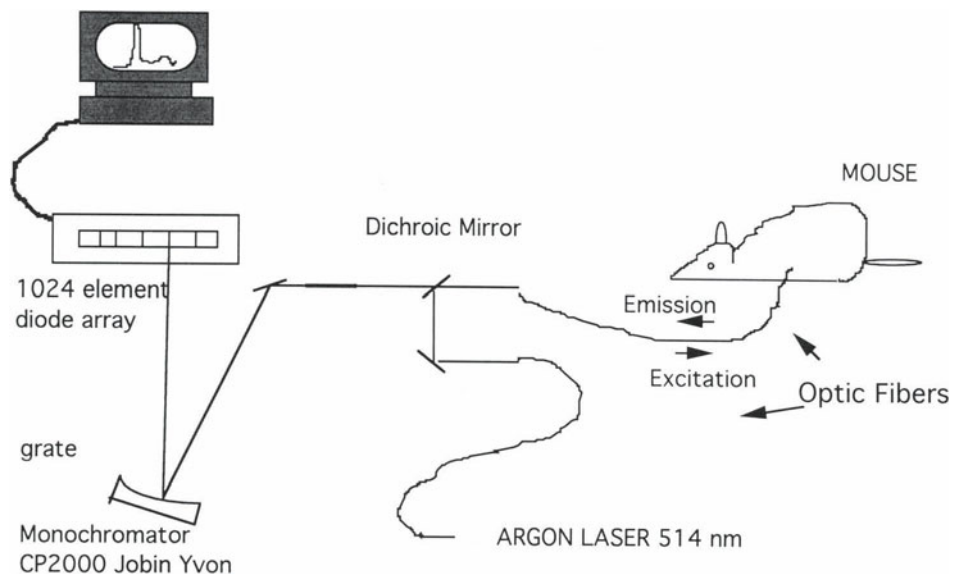


Figure 1. Optical fiber spectrofluorimeter.

RESULTS AND DISCUSSION

Spectroscopic Characteristics of Aqueous Solution of the [PpIX-Peptide] Non-Covalent Association

The absorption spectrum of an aqueous solution of [PpIX-peptide] is characteristic of this association with maxima located at similar wavelengths to those for a solution of PpIX (acetone/water 50/50 v:v) but with different relative absorption band intensities. In particular, the Soret band appears as a shoulder, whereas the two transitions 480 and 360 nm are well resolved (Figure 2A).

As seen in Figure 2B, the symmetrical molecule PpIX exhibited an anomalous optical activity when in association with the peptide. An induced circular dichroism was observed with positive and negative CD signals at 360nm and 480nm respectively. The whole CD spectrum appeared as well correlated with the absorption spectrum of the solution.

The large hypochromicity of the Soret band is suggestive of self-porphyrin association¹⁰. As already reported in the literature^{11,12}, the induced CD we observed could indicate a strong interaction between porphyrin aggregates and a helically arranged peptide group.

The fluorescence emission spectrum (Figures 3A and 3B) with two bands maxima at 620 and 654nm was found very different from that of PpIX in solution which has a characteristic intense band at 636nm. Moreover, the fluorescence intensity was very low, about two orders of magnitude lower than for an acetone-water solution of PpIX. Due to our experimental conditions, it was not possible to determine a fluorescence quantum yield accurately. This strong fluorescence quenching would be consistent with the formation of porphyrin aggregates.

Cellular Fluorescence from HT29 Incubated with [PpIX-Peptide]

The fluorescence emission from a microvolume of a cytoplasmic area of HT29 cells incubated with an aqueous solution of [PpIX-peptide] is displayed in Figure 4. An intense

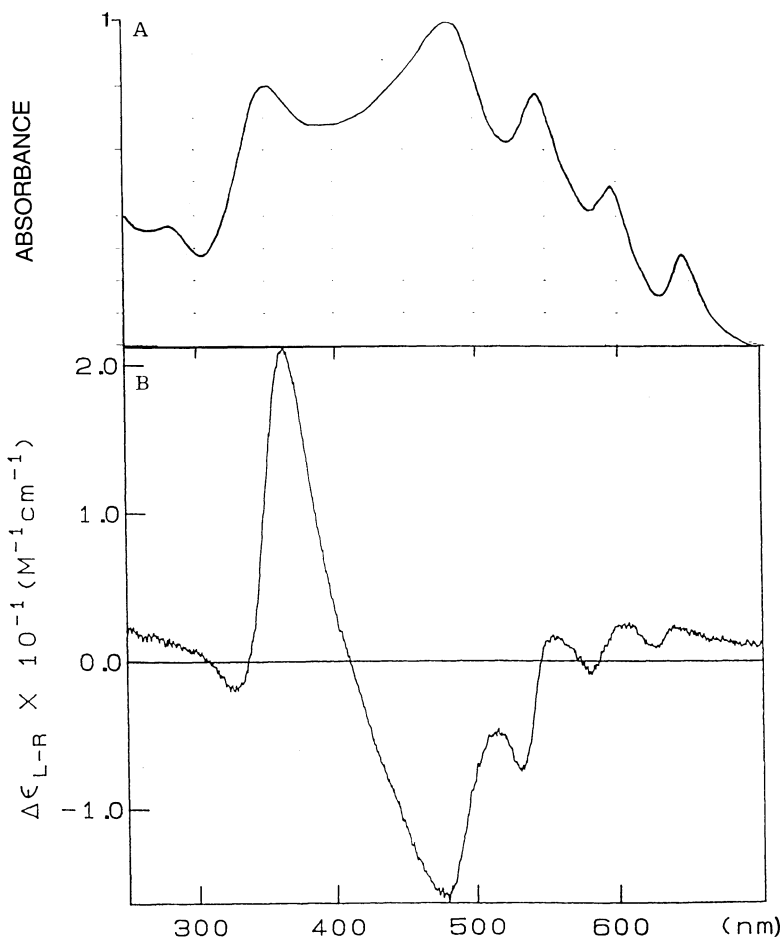


Figure 2. A) Absorption spectrum of aqueous solution of [PpIX-peptide] ($\epsilon_{539} = 14500 \text{ M}^{-1} \text{ cm}^{-1}$) B) Induced circular dichroism of [PpIX-peptide] in aqueous solution.

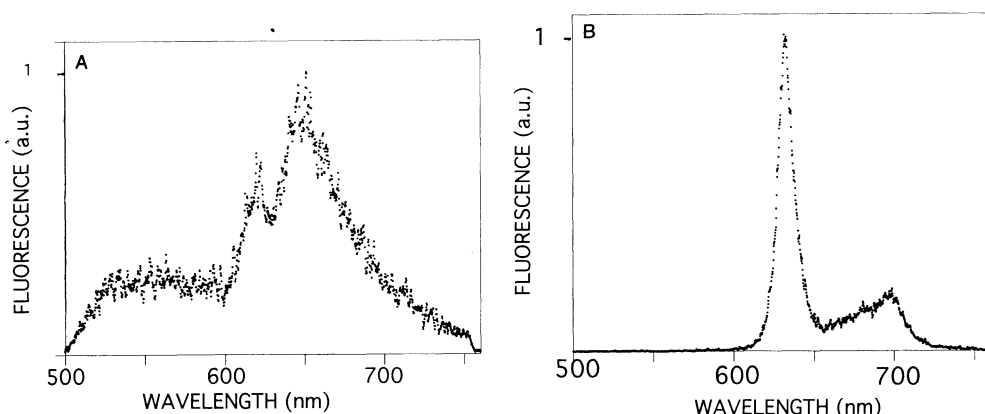


Figure 3. A- Typical fluorescence spectrum of [PpIX-peptide], [PpIX] = 5 $\mu\text{g}/\text{ml}$, in aqueous solution $I_{\text{max}} = 157 \text{ a.u.}$ B- Typical fluorescence spectrum of PpIX in solution (acetone water 50:50 v/v) $I_{\text{max}} = 17000 \text{ a.u.}$. Spectra are normalized in both cases; solution absorbances measured at 488nm were identical.

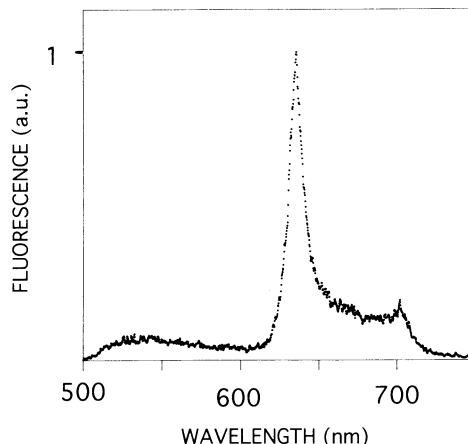


Figure 4. Typical fluorescence spectrum from a cytoplasmic area of HT 29 cells incubated with aqueous solution of [PpIX-peptide] (47 µg PpIX / mg of peptide and [PpIX]=5µg/ml, incubation time 2h ; Imax = 3313 a.u. arbitrary units). The fluorescence spectra were recorded with an accumulation time of 0.2 to 2s.

emission characterized by two bands, one well resolved maximum at 636nm and a lower one at 700nm was observed. The large weak band in the 570nm region was caused by the cellular autofluorescence and was observed for non-treated cells. Emission from the extracellular medium was always found negligible.

5-aminolevulinic acid (ALA) is known to stimulate endogenous PpIX formation, an intermediate precursor in the heme biosynthesis pathway in most nucleated cells. In order to identify without any ambiguity the cellular emission we observed in the presence of [PpIX-peptide], HT 29 were incubated with ALA (100µg/ml ,1h). The cellular fluorescence observed was found identical to the cellular fluorescence of HT29 incubated with [PpIX-peptide]. The occurrence of the dissociation of the [PpIX-peptide] association with the PpIX release within cells may be assumed.

It may be noted that prolonged laser exposure of a cellular area induced a photodegradation of PpIX as shown by the decrease of fluorescence intensity (70% for a 40 s. exposure time) and by the modification of the emission shape in the 650-670nm region^{13,14}. In our experimental conditions (exposure times from 0. 2 to 2sec), such a process could be neglected.

The PpIX cellular uptake was determined from the fluorescence intensity measured at 636nm (Figures 5A and 5B).

The PpIX penetration was quite fast for incubation periods lower than 30 minutes and then was slowing down. Similar kinetics were found for a PpIX concentration of 2 and 5µg/ml showing that these concentrations do not correspond to saturation conditions. However, when the same PpIX concentration was used, the increase of the relative peptide concentration seemed to favor the PpIX penetration (Figure 5B a upper curve).

PpIX cellular amount was found to be lowered by a factor of 2 when incubations were performed at 4°C, indicating that PpIX taken up would partially occur by endocytosis (about 50%).

***In Vivo* Fluorescence Spectra of [PpIX-Peptide]**

Administration of [PpIX-peptide] solution to mice resulted in the appearance of tissue fluorescence characterized by an intense band at 632 nm and another peak at 700nm typical of PpIX emission (Figure 6).

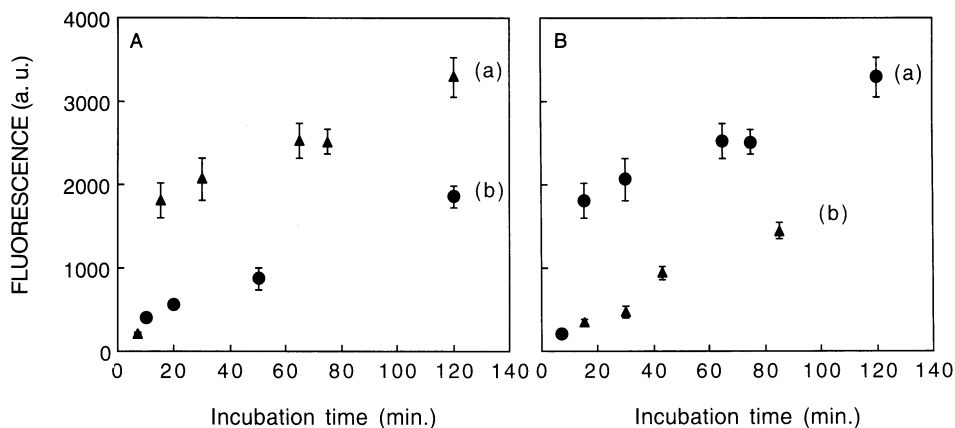


Figure 5. PpIX uptake by HT 29 cells as determined from 636 nm fluorescence intensity (a.u. arbitrary units) Each experimental point was obtained from the averaged intensity determined for 50 distinct cells. Standard error is reported for each value. A) $[PpIX] = a$ 5 $\mu\text{g}/\text{ml}$ or b) 2 $\mu\text{g}/\text{ml}$ [PpIX-peptide]composition is 47 μg PpIX / mg of peptide. B) $[PpIX] = 5 \mu\text{g}/\text{ml}$ [PpIX-peptide]composition are : a) 47 or b) 90 μg PpIX / mg of peptide.

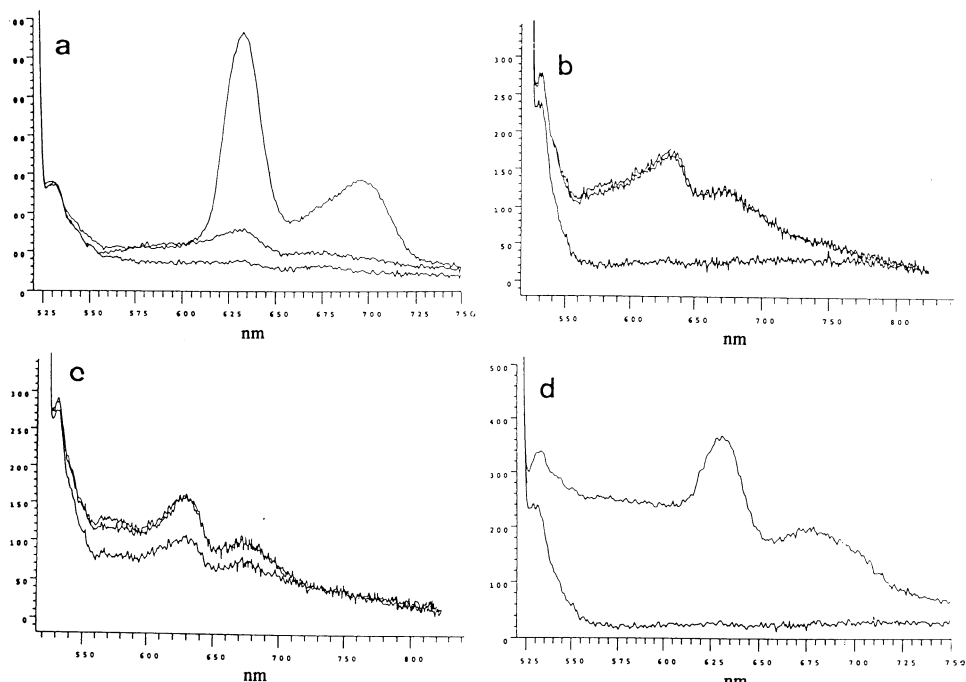


Figure 6. Fluorescence emission from mice tissues; excitation at 514 nm after injection of aqueous solution of [PpIX-peptide] obtained with an optical fiber spectrofluorimeter. PpIX dose was 6mg/kg, total injected volume was 0.7 ml, mice were sacrificed 3h30 after injection. a) eyes 1h, 2h, 3h30 after injection, b) liver 3h30, c) tumor 1h, 2h 3h30, d) gall bladder 3h30. Spectrum recording time was 20ms and was accumulated over 3sec. Excitation was performed at 514nm to minimize scattered light from tissues.

Table 1. Fluorescence intensity (632nm) of organs of nude mouse after injection of aqueous solution of [PpIX - peptide] (PpIX dose 6mg/kg)
The maximum intensity was found in the eyes and was measured
1, 2 and 3h30 after injection. For other organs, the fluorescence
was measured at sacrifice time

Organs	1 h	2 h	3h30
Eyes	+	++	++++
Gall Bladder			+++
Tumor	++	++	++
Liver			++
Lung			+
Kidney			+
Brain			±
Spleen			±
Heart			-
Bladder			-
Skin	?	?	?

The fluorescence intensity was dependent on the tissue and results are summarized in Table I. A broad band was also observed in the 670nm region with an intensity depending of the PpIX emission intensity suggesting a possible contribution of a porphyrin metabolite. The non resolved band observed in the 550nm region could be provided by some compounds similar to bilirubin.

CONCLUSION

Dissociation of the [PpIX-peptide] has been shown to occur at the cellular level with the release of the drug PpIX within the cells. The use of this peptide thus appears as a convenient way to make hydrophobic drugs soluble.

The association of microspectrofluorimetry and *in vivo* optical fiber spectrofluorimetry allows us to acquire useful pharmacokinetics data for any fluorescent drugs (with or without carrier).

REFERENCES

1. J. Moan and C. Berg, Photochemotherapy of cancer: experimental research, *Photochem Photobiol.* 55:931 (1992).
2. B. Henderson and T. Dougherty, How does photodynamic therapy work?, *Photochem Photobiol.* 55:145 (1992).
3. M. R. Hamblin and E. Luke Newman, On the mechanism of tumor-localising effect in photobiology, *J Photochem. Photobiol. B-Biol.* 23:3 (1994).
4. S. Sommer, Porphyrin derivatives having physical and chemical characteristics similar to those of the active components of hematoporphyrin derivatives and with very strong photosensitizing effects, *J Photochem Photobiol. B-Biol.* 1:241 (1987).
5. M. R. Hamblin and E. L. Newman, Photosensitizer targeting in photodynamic therapy .I. Conjugates of haematoporphyrin with albumin and transferrin, *J Photochem Photobiol B-Biol.* 26:45 (1994).
6. A. Richter, E. Waterfield, A. Jain, A. Canaan, B. Allison and J. Levy, Liposomal delivery of a photosensitizer benzoporphyrin derivative monoacid ring A (BPD), to tumor tissue in a mouse tumor model, *Photochem. Photobiol.* 57:1000 (1993).

7. N. Cempel, J.-M. Aubry, J.-M. Piot and D. Guillochon, Isolation from bovine haemoglobin of a peptide that might be used as a potential hydrophobic photosensitizer carrier, *Biotechnol. Appl. Biochem.* 21:287 (1995).
8. J. Blais, C. Amirand, J. P. Ballini and P. Debey, Photofrin induced fluorescence in progressive and regressive murine colonic cancer cells: correlation with cell photosensitivity, *J. Photochem. Photobiol. B-Biol.* 27:225 (1995).
9. L. Morlet, V. Vonarx, P. Lenz, M.-T. Foultier, L. Xavier de Brito, C. Stewart and T. Patrice, Correlation between meta(tetrahydroxyphenyl)chlorine (m-THPC) biodistribution and photodynamic effects in mice, *J. Photochem. Photobiol. B-Biol.* 28:25 (1995).
10. E.J.Gibbs, I.Tinoco, M.F.Maestre, P.A.Ellinas, and R.F.Pasternack, Self-assembly of porphyrins on nucleic acids, *Biochem.Biophys.Res.Comm.* 157:350 (1988).
11. S. Ikeda, N. Takashi and G. Ebert, Induced CD and interaction of some porphyrin derivates with alpha-helical polypeptides in aqueous solutions, *Biopolymers.* 31:1257 (1991).
12. R. F. Pasternack, A. Giannetto, P. Pagano and E. J. Gibbs, Self-assembly of porphyrins on nucleic acids and polypeptides, *Journal of the American Chemical Society.* 113:(1991).
13. J. Moan, C. Rimington and Z. Malik, Photoinduced degradation and modification of Photofrin II in cells *in vitro*, *Photochem. Photobiol.* 47:363 (1988).
14. J. Rotomskiene, B. Kapocjute, R. Rotomskis, G. Jonusauskas, T. Szito and A. Nizhnik, Light induced transformation of hematoporphyrin diacetate and hematoporphyrin, *J. Photochem. Photobiol. B-Biol.* 2:373 (1988).

MEROCYANINE 540—A FLUORESCENT DYE AND A BIOLOGICAL PROBE

Cyril Párkányi,¹ Alain Adenier,² and Jean-Jacques Aaron²

¹ Department of Chemistry
Florida Atlantic University
777 Glades Road, P.O. Box 3091
Boca Raton, Florida 33431-0991

² Institut de Topologie et de Dynamique des Systèmes (Associé au C.N.R.S., URA 34)
Université Denis Diderot - Paris 7
1, Rue Guy de la Brosse
F-75005 Paris, France

ABSTRACT

Merocyanine 540 (MC-540) is an anionic, lipophilic fluorescent dye which is used as a photosensitizer in phototreatment of human cancer cells (leukemia) and as a biological probe in membrane studies (transmembrane potentials). Within the framework of our systematic studies of biologically important heterocycles, we have investigated solvent effects upon the photophysical properties of MC-540. The electronic absorption and fluorescence emission spectra of MC-540 were determined at 298 K in a number of solvents of different polarity and solvent effects were evaluated using the solvatochromic shift method (McRae, Suppan, Bakhshiev, Kawski-Chamma-Viallet correlations). Also, the ground and first excited singlet state dipole moments of MC-540 were measured and compared with the corresponding calculated values and a tensiometric study of MC-540 has been carried out. The results indicate that the polarity of MC-540 is lower in the first excited singlet state than in the ground state. In aqueous solutions, MC-540 forms stacked aggregates (dimers, trimers) at low concentrations and micelles at higher concentrations.

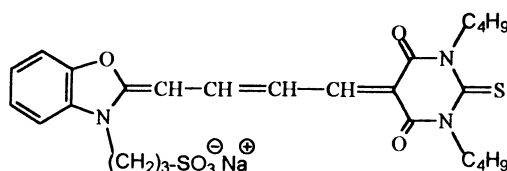
INTRODUCTION

For a number of years, we have been interested in physical and chemical properties of various biologically important systems in general and of aromatic heterocycles and organic dyes in particular. These properties include, but are not limited to, solubilities in different solvents, electronic absorption, fluorescence, and phosphorescence spectra and the

respective concentration and solvent effects, excited-state lifetimes, ground- and excited-state dipole moments and ionization constants, linear free energy relationships, micellization processes, etc. In addition to the experimental data, the corresponding quantities can be obtained by theoretical calculations or the experimental results can be correlated with calculated quantum-chemical quantities.

In this contribution, we wish to report our new results obtained with merocyanine 540.

Merocyanine 540 (MC-540) is an anionic, lipophilic fluorescent dye with many uses. It is a sodium salt of sulfonic acid, with a chain of four conjugated methine groups, a substituted benzoxazole ring at one end, and substituted thiobarbituric acid at the other end.



MEROCYANINE-540

MC-540 was originally developed as a photosensitizer for photographic emulsions.¹ However, its main importance today is in biology and medicine. It is widely used as a biological probe in membrane studies (fluorescent probe for studies of membrane systems, optical probe for transmembrane potentials), for characterization of the multidrug resistance phenotype, for photoinduced cytotoxicity as a highly effective drug against human malignant cells (photodynamic purging of neoplastic cells in bone marrow explants - leukemia, treatment of lymphomas and metastatic neuroblastomas) and other diseases (malaria, *Herpes simplex*, HIV), and for preclinical assessment and sterilization of blood and blood products.²⁻²⁵ Also, MC-540 is a selective stain for leukemic and immature hemopoietic cells.²⁶⁻²⁸

One of the very interesting physical characteristics of MC-540 is its electrochromism (changes in electronic absorption and emission spectra in the presence of an external electric field).^{6, 29-32} These optical changes show a linear dependence on applied voltage. Because MC-540 is amphiphilic, many of its physical and chemical properties depend on the polarity of the solvent.^{2, 6, 31, 32} Thus, its fluorescence response to membrane potential changes (variations in surface potential) and polarity changes in the microenvironment can be monitored as λ_{max} shifts^{3, 33} (cf. also^{34, 35}).

An intriguing feature is that membrane-associated MC-540 becomes more monomeric with decreasing dielectric constant of the solvent or microenvironment. This change from a dimer to a monomer manifests itself as a solvatochromic shift, with λ_{max} at 532 nm in water and at 570 nm in benzene.³ The monomer-dimer mixtures of MC-540 are governed by numerous other factors.³ Micellization takes place at higher concentrations.

Only a limited number of papers devoted to these effects from the photophysical point of view has been published. Several solvent-polarity related spectroscopic studies have appeared in the literature.^{3, 6, 32} The plots of the maximum absorption wavenumber against the macroscopic dielectric constant of the medium reveal a partially linear hypsochromic shift of the spectral data with increasing solvent polarity. However, the scope of these studies is limited as the number of solvents was small or only alcoholic mixtures were used.

Also, only one value of the experimental dipole moment of MC-540 was reported so far; the dipole moment was obtained in water (in a membrane with $\epsilon = 2$).^{2, 29} In another

publication, ground- and excited-state dipole moments of MC-540 were estimated from solvent-induced spectroscopic shifts, in a series of aliphatic nitrile solvents.³²

In this contribution, we wish to present a new value of the ground-state dipole moment of MC-540 in a mixed organic solvent (dioxane-dimethylformamide, 15 : 1, v/v), a calculated value of the ground-state dipole moment, and the first excited singlet-state dipole moment obtained by the solvatochromic method. Also, as a part of our studies of the photophysical properties of MC-540, we report a comparison of the concentration effects upon its electronic absorption and fluorescence spectra in ethanol and in water, determination of the oscillator strength, and micellization of MC-540 at higher concentrations supported by the results of tensiometric study.

EXPERIMENTAL

Merocyanine 540 (MC-540) was obtained from Sigma Chemical Company, St. Louis, MO, and was purified by recrystallization from ethanol. The ground-state dipole moment of MC-540 was determined in a dioxane-dimethylformamide mixture (15 : 1, v/v) at 298 K using a WTW dipole meter model DM-01 (Wissenschaftlich-Technische Werkstätten, Weilheim, Germany) as described in our previous publications.^{36,37} Spectroscopic grade solvents were used for spectroscopic measurements. Electronic absorption spectra were taken in different solvents at 298 K using a Cary 118 spectrophotometer with a thermostatted cell holder and fluorescence emission and excitation spectra were measured on a Perkin-Elmer LS-50 spectrofluorometer, with 10^{-6} - $10^{-7} M$ solutions as MC-540 aggregates at higher concentrations. Solid-state density of MC-540 needed for the determination of the first excited singlet-state dipole moment (Onsager cavity radius) was determined pycnometrically with a suspension of MC-540 in kerosene.

Several values of the first excited singlet-state dipole moment of MC-540 were obtained using the solvatochromic method and four formulas developed for this purpose (McRae, Suppan, Bakhshiev, Kawski-Chamma-Viallet) as previously described.³⁶⁻⁴³

A combination of the PPP method (Pariser-Parr-Pople, π -LCI-SCF-MO) and the empirical σ -bond moment contributions was used to obtain the total calculated ground-state dipole moment of MC-540, $\mu_{g(\text{calc})}$. The π -contribution was obtained by the usual version of the PPP method, with the Mataga-Nishimoto formula employed for the bicentric electronic repulsion integrals as described in our previous publications.^{37,44} A model of MC-540 with a simplified $(\text{CH}_2)_3\text{SO}_3^-\text{Na}^+$ group was used. The calculations were carried out on a Hewlett-Packard HP 150 II Touchscreen computer.⁴⁵

RESULTS AND DISCUSSION

Ground-State Dipole Moment

Our value of the experimental ground-state dipole moment of MC-540, $\mu_{g(\text{exp})}$, is 5.25 ± 0.43 D, close to our theoretical value, $\mu_{g(\text{calc})} = 4.70$ D. This experimental value compares relatively well with a reported value of 8.6 ± 2.3 D obtained in water-membrane interface,^{2,29} and an approximate value of 9.6 D roughly estimated for MC-540 in n-alkane-nitrile solvents.³² An experimental value of 9.70 D was found for another structurally similar merocyanine.^{25,46} Our calculated angle for the orientation of the dipole moment indicates that it is directed approximately along the long axis of MC-540.

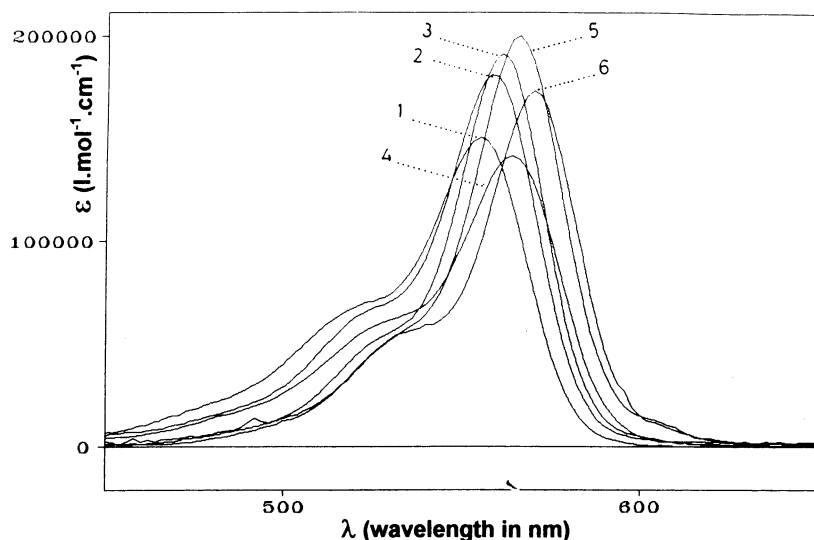


Figure 1. Effect of the solvent on the electronic absorption spectra of $5 \times 10^{-7} M$ MC-540 at 298 K. 1 Methanol; 2 acetonitrile; 3 methyl acetate; 4 dimethyl sulfoxide; 5 dioxane; 6 chloroform.

Table 1. Effect of the solvent on the electronic absorption and fluorescence emission spectral data of merocyanine 540 at 298 K^a

Solvent	λ_A^b	λ_F^c	$\epsilon \times 10^{-5}d$	f ^e
Dimethyl sulfoxide	564.5	580.0	1.42	1.02
Acetonitrile	558.5	574.0	1.82	1.16
Nitromethane	561.0	576.0	1.64	1.10
Methanol	555.0	572.0	1.51	1.11
Ethanol	560.0	576.0	1.66	1.11
Acetone	560.0	575.0	1.82	1.14
Chloroform	571.0	584.0	1.74	1.04
Toluene	570.0	584.0	1.83	1.02
Dioxane	566.0	580.0	2.00	1.12
Methyl acetate	561.0	579.0	1.92	1.10
Diethyl ether	565.0	575.0	1.00	0.95
Triethylamine	565.0	579.0	1.61	0.93
Pyridine	570.0	592.0	1.44	1.29
Water ^f	534.0	568.5	0.61	1.03

^a In all solvents, the concentrations of MC-540 were $5 \times 10^{-7} M$ for the absorption and fluorescence measurements, unless otherwise indicated.

^b Electronic absorption band maximum wavelength in nm.

^c Fluorescence absorption band maximum wavelength in nm.

^d Molar absorption coefficient (in $L \text{ mol}^{-1} \text{ cm}^{-1}$).

^e Experimental oscillator strength obtained from the integrated molar absorption coefficient over the total absorption spectrum using the Spectra Calc software (Galactic Industries Corporation).

^f Another maximum was observed at 502 nm ($\epsilon = 0.62 \times 10^5 L \text{ mol}^{-1} \text{ cm}^{-1}$; [MC-540] = 1 μM).

Solvent Effects on the Electronic Absorption and Emission Spectra

We have investigated the effects of fourteen solvents of different polarities on the electronic absorption and fluorescence spectra of MC-540. Typical examples of absorption spectra of MC-540 ($5 \times 10^{-7} M$), recorded in different solvents (Fig. 1), show the existence of a band of maximum absorbance with additional maxima at shorter wavelengths. No significant changes of the shape of the absorption curve take place when changing the solvent.

The electronic absorption spectral properties are presented for all solvents under study (Table 1). It can be seen that the absorption wavelengths of MC-540 are located between 555-571 nm for the entire solvent polarity range (dielectric constants 4.8 to 32.7), and that they do not vary significantly with the solvent, although a moderate blue shift trend is noted with increasing dielectric constant of the solvent. Water is an exception. In water, the MC-540 absorption spectrum contains two bands of similar intensity at about 502 and 534 nm which are considerably blue-shifted relative to the other solvents. This particular behavior can be attributed to the existence of specific solute-solvent interactions in aqueous medium.^{3,47}

The molar absorption coefficients ϵ_{\max} of the maximum intensity band are between 1.00×10^5 and $2.00 \times 10^5 \text{ L mol}^{-1} \text{ cm}^{-1}$ in organic solvents, while in water the ϵ_{\max} value is $0.6 \times 10^5 \text{ L mol}^{-1} \text{ cm}^{-1}$. This indicates an important apparent hypochromic effect. Similar high ϵ_{\max} values in organic solvents were previously observed for other analogous cyanine dyes, and are typical of extensively conjugated amidic tetramethine systems.⁴⁸ However, the experimental oscillator strength values (f) are practically identical for all solvents under study, including water (median $f = 1.08 \pm 0.15$). This quasi-invariability of the f values indicates that only one MC-540 species is present at the very low concentrations used for all solvents. It shows that even in water, only MC-540 monomers participate in $\pi-\pi^*$ electronic transitions, because of these submicromolar concentrations.

For all the solvents under study, the MC-540 fluorescence excitation spectrum is homothetic to its absorption spectrum (Fig. 2). In each solvent, including water, an identical

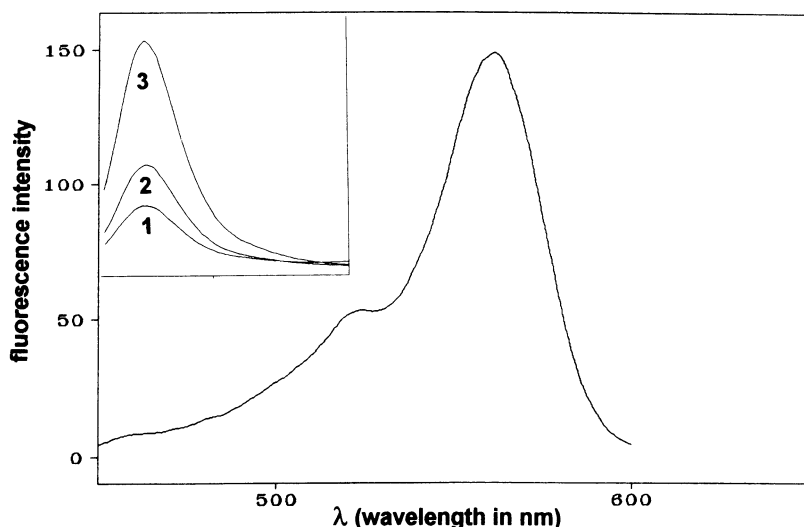


Figure 2. Fluorescence excitation spectrum of a $5 \times 10^{-7} M$ ethanolic solution at 298 K. The upper left-hand box: emission spectra ($\lambda_{\max} = 576 \text{ nm}$) obtained by exciting at 480 nm (1), 520 nm (2), and 550 nm (3).

Table 2. Statistical treatment of the solvatochromic shift correlations of MC-540

Correlation ^a	Slope ^b	Intercept ^b	r ^c	n ^d
McRae (A)	170.1	17566 ^e	0.969	7
Suppan (A)	388.6	17487 ^e	0.937	8
Bakhshiev (AE)	60.4	421 ^f	0.974	7
Kawski-Chamma-Viallet (AE)	421.8	17341 ^g	0.929	8

^a A - absorption data only; AE - absorption and emission data.

^b In cm⁻¹.

^c r = correlation coefficient.

^d n = number of data.

^e The intercept represents the ν_A value at the origin.

^f The intercept represents the ($\nu_A - \nu_F$) value at the origin.

^g The intercept represents the ($\nu_A + \nu_F$)/2 value at the origin.

fluorescence emission spectrum is obtained when exciting over any band of the MC-540 absorption spectrum. This confirms the existence of only one emitting MC-540 species. As in the case of the absorption spectra, a moderate blue shift of the emission maxima of MC-540 is observed with increasing solvent polarity (Table 1). In contrast to the dramatic blue shift of the absorption spectrum noted in an aqueous medium ($\Delta\lambda_A = 26$ nm for ethanol), the MC-540 emission spectrum undergoes a less important hypsochromic effect upon changing from an organic solvent to water ($\Delta\lambda_F = 12.5$ nm for ethanol).

Solvatochromic Correlations and the First Excited Singlet-State Dipole Moment

Spectral blue shifts observed with increasing solvent polarity are usually called a negative solvatochromism.⁴⁹ They occur when the ground state is more polar than the first excited singlet state (i.e., when the ground-state dipole moment is higher than the excited-

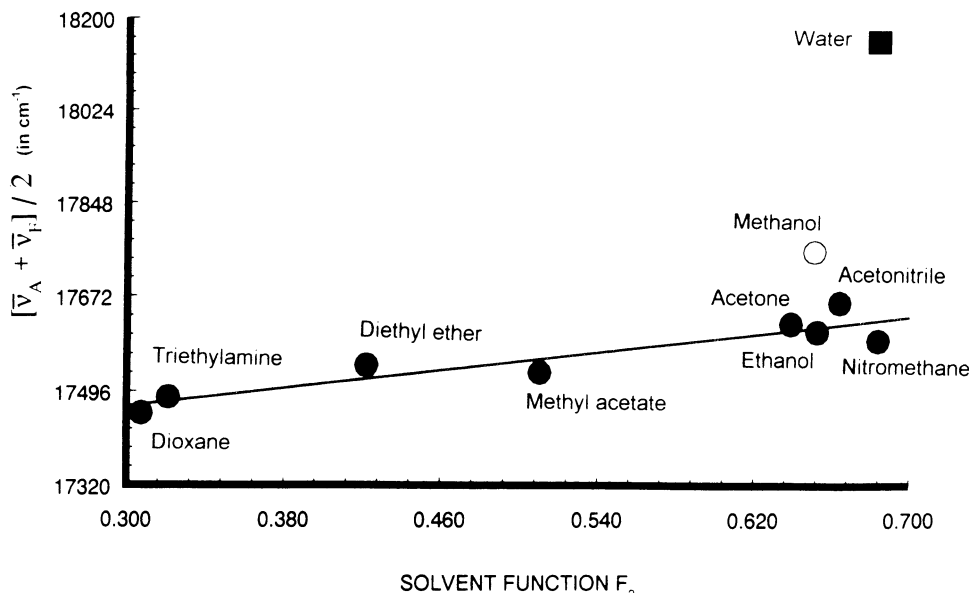


Figure 3. Kawski-Chamma-Viallet correlation between the solvent spectral shifts and the F_2 solvent polarity function^{36, 37, 42-44} for MC-540. Methanol and water are not included in the correlation.

Table 3. Comparison of the experimental ground-state and the first excited singlet-state dipole moments of merocyanine 540^a

$\mu_g(\text{exp})^b$	$\mu_e(\text{exp})^b$			
5.25 (± 0.43) ^c	4.15 ^d	2.72 ^e	4.23 ^f	4.51 ^g

^a All values are in Debye units (D).^b $\mu_g(\text{exp})$ ground-state dipole moment; $\mu_e(\text{exp})$ first excited singlet-state dipole moment.^c Literature values: 8.6 (± 2.3) D (measured in water-membrane interface)^{2, 29} and 9.6D (roughly estimated in n-alkanenitrile solvents)³² for MC-540; 9.70 D for a structurally similar merocyanine.^{25, 46, 48}^d McRae correlation.^e Suppan correlation.^f Bakhshiev correlation; value obtained by taking the negative root of $(\mu_g(\text{exp}) - \mu_e(\text{exp}))^2$.^g Kawski-Chamma-Viallet correlation.

state dipole moment). In order to determine the first excited singlet state dipole moment of MC-540, the Stokes shift ($v_A - v_F$) and $(v_A + v_F)/2$ values were plotted against the solvent functions in the McRae,³⁸ Suppan,^{39, 40} Bakhshiev,⁴¹ and Kawski-Chamma-Viallet^{42, 43} equations. The respective formulas and solvent functions and their use for the evaluation of excited-state dipole moments are described in detail in our publications (e.g.^{36, 37, 44}).

The results of the statistical treatment of the solvatochromic correlations, i.e., the slopes, intercepts, and correlation coefficients are presented in Table 2. For all correlations, the correlation coefficients are at least 0.93 or higher. This indicates a satisfactory linear behavior for a majority of solvents (Fig. 3). Due to the specific MC-540-solvent interactions and/or the approximations included in the solvatochromic method, some solvents had to be excluded from the correlations (excessive deviations). A very significant deviation is observed in the case of water, confirming the existence of strong specific interactions between MC-540 and water molecules.

The ground-state dipole moment and several values of the first excited singlet-state dipole moment, determined from the slopes of the solvatochromic correlations, are presented in Table 3.

Except for the Suppan correlation, a good agreement was obtained among the values of the excited singlet-state dipole moments based on the three remaining correlations. The dipole moment of MC-540 is slightly lower in the first excited singlet state than in the ground state, indicating the weakly negative solvatochromic behavior of this compound. If the 2.72 D value (Suppan correlation) is not considered, the decrease of the dipole moment upon excitation is about 0.8–1.1 D. This difference compares reasonably well with the $|\Delta\mu| = 0.46 (\pm 0.05)$ D value estimated from electrochromic measurements for MC-540 incorporated in phospholipid layers.³¹ The small decrease of the polarity of the first excited singlet state with respect to the ground state may be attributed to slightly more stabilized polar resonance structure of MC-540 in the ground state and/or to contraction of the dipole in the excited state. In the second case, a change from the all *trans*-configuration to a *cis*-configuration of the tetramethine chain would take place upon excitation of MC-540.

Concentration Effects on the Electronic Absorption and Emission Spectra: Ethanolic and Aqueous Media

Among the mechanisms proposed for the phototherapeutic activity of MC-540 in biological systems,^{18, 50} the possible involvement of singlet molecular oxygen has been related to the monomeric MC-540 bound to membranes, even under conditions where dimeric forms are predominant.⁵¹ For mechanistic purposes, it is very important to obtain information on the

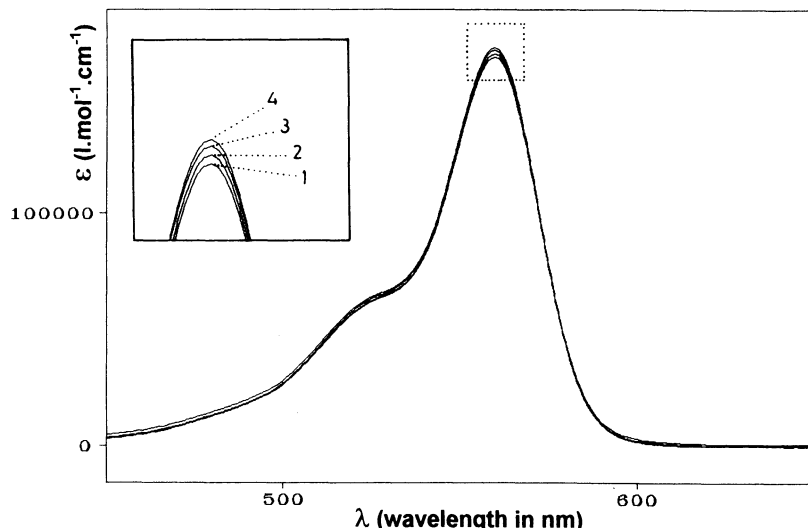


Figure 4. Effect of concentration of MC-540 on the electronic absorption spectra in ethanol at 298 K. Concentrations: $1.5 \times 10^{-7} M$; $2.1 \times 10^{-5} M$; $3.5 \times 10^{-5} M$; $4.1 \times 10^{-4} M$.

concentration-dependent monomer-dimer equilibrium, even in the absence of the biological target of MC-540. However, until now, only a few studies have been devoted to the effect of concentration on both the absorption and emission spectra of MC-540.^{3, 15} Therefore, we have decided to compare the influence of concentration on the electronic absorption and emission spectra of MC-540 in two different media - ethanol and water.

In ethanol, no significant change of the shape of the absorption curve, wavelength, and ϵ_{\max} values was observed upon varying the concentration of MC-540 between $5 \times 10^{-7} M$

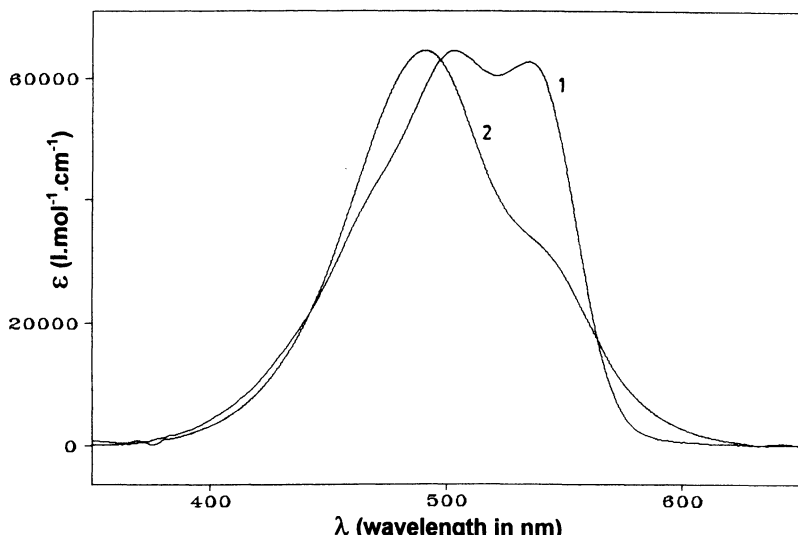


Figure 5. Effect of concentration of MC-540 on the electronic absorption spectra in water at 298 K. Concentrations: $1.1 \times 10^{-6} M$; $2.2 \times 10^{-6} M$.

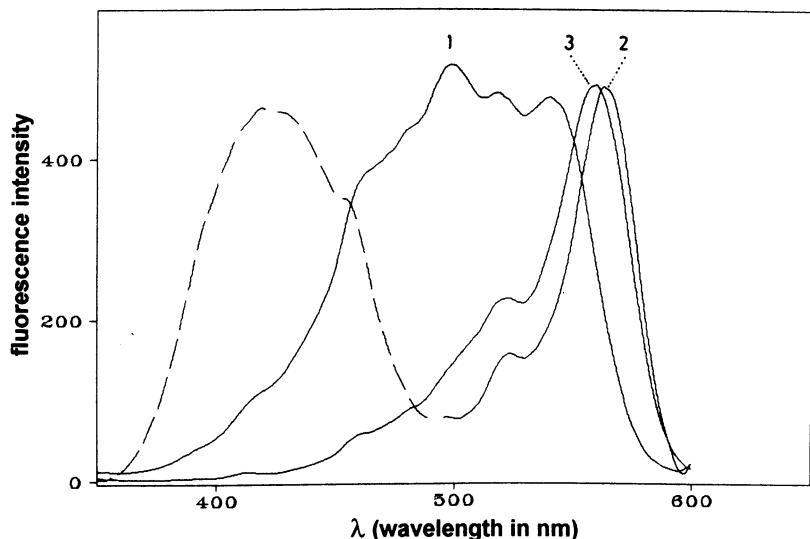


Figure 6. Effect of concentration of MC-540 on the excitation spectra in aqueous media at 298 K. 1 $1 \times 10^{-6} M$ in water; 2 $2.6 \times 10^{-5} M$ in water; 3 $3.5 \times 10^{-7} M$ in anionic micelles ($0.1 M$ aqueous sodium n-dodecyl sulfate, SDS); dotted line: spectral distortion due to an inner filter effect of MC-540.

and $10^{-4} M$ (Fig. 4). In contrast, the position of the fluorescence emission maximum changed continuously from 576 nm to 599 nm upon going from the concentration of $5 \times 10^{-7} M$ to $10^{-4} M$ MC-540. This surprising concentration-dependent spectral shift can be attributed either to the gradual formation of MC-540 aggregates in the excited singlet state, or to the presence of differently solvated MC-540 species in this ethanolic solution.

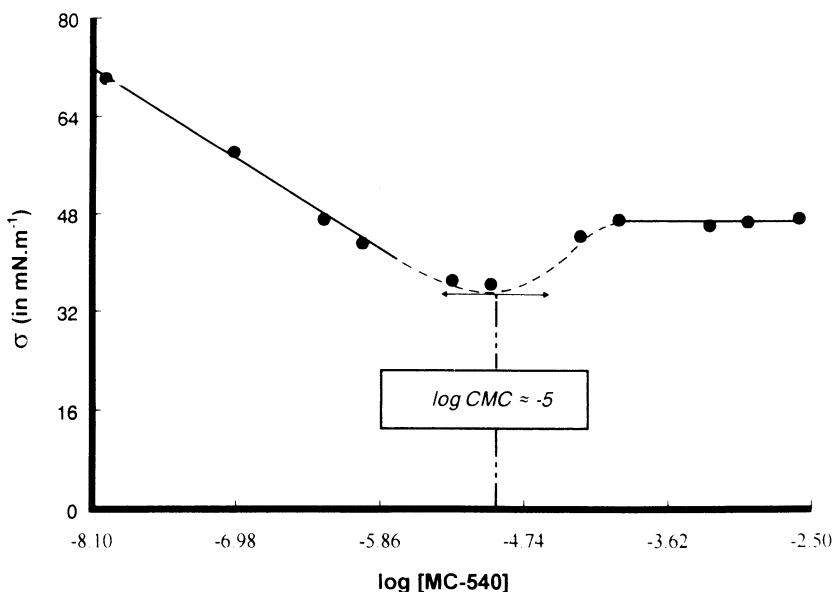


Figure 7. Plot of the surface tension σ against the concentration of MC-540 ($\log [MC-540]$). The critical micelle concentration (CMC) was approximately $10^{-5} M$.

In contrast, in an aqueous solution, an increase of the concentration of MC-540 from $10^{-6}M$ to $10^{-4}M$ leads to a gradual decrease of the intensity of the 534 nm band, while the absorbance of the 502 nm band does not change significantly, although its position is weakly blue-shifted (Fig. 5). This spectral behavior can be explained by self-stacking of the MC-540 monomeric species leading to the formation of dimers, trimers, tetramers, etc. in an aqueous solution.^{52,53} In the case of the fluorescence excitation spectra, a similar increase of the concentration of MC-540 produced a very different change of the spectral curve (Fig. 6). At low concentrations, the excitation spectrum of MC-540 is homothetic to the absorption spectrum, obtained at the same concentration. However, at higher concentrations ($6 \times 10^{-5}M$), the excitation spectrum exhibits two distinct components centered at approximately 580 and 420 nm. The long-wavelength component is very close to the excitation spectrum of a very diluted ($5 \times 10^{-7}M$) MC-540 micellar solution (0.1 M sodium n-dodecyl sulfate, SDS) which suggests the formation of micelles of MC-540 in an aqueous solution at high concentrations.

On the other hand, the short-wavelength component of the excitation spectrum obtained at $6 \times 10^{-5}M$ concentration of MC-540 can be due to self-absorption (inner filter effect) resulting from a very high optical density of such a concentrated solution.

Similarly, an increase of concentration of MC-540 from $1.2 \times 10^{-6}M$ to $6 \times 10^{-4}M$ leads to an important and progressive red shift of the fluorescence emission maximum from 568 nm to 617 nm, resulting from dimerization processes at relatively low MC-540 concentrations and from micellization at higher concentrations.

In order to confirm this micelle formation process of MC-540 in concentrated aqueous solutions, we have carried out a tensiometric study. The curve of the surface tension (σ) plotted against $\log [MC-540]$ is characterized by an initial linear decrease of σ at relatively low MC-540 concentrations, followed by a plateau at higher concentrations (Fig. 7). This curve is typical of the behavior of classical surfactants such as sodium n-dodecyl sulfate (SDS) and n-cetyltrimethylammonium bromide (CTAB) above and below the critical micelle concentration (CMC).⁵⁴ In our case, a CMC value of about $10^{-5}M$ can be estimated from this curve for MC-540. It should be pointed out that the unusual shape of the curve in the transition region, observed around the CMC value, can be explained as due to the fact that micelle formation may take place simultaneously with the occurrence of small aggregates such as the dimers, trimers, tetramers, etc. Comparable aggregation processes (self-stacking dimerization and micellization) have been previously reported with some biomedically important oxazolopyridocarbazoles including those with a long alkyl chain, and with the cytostatically active ellipticine chromophore.^{55, 56}

In addition to a preliminary communication,⁵⁷ more detailed spectroscopic results on MC-540 concerning the various aggregation processes will be reported in a subsequent full-length paper.

REFERENCES

1. F.M. Hamer, "The Cyanine Dyes and Related Compounds," J. Wiley, New York, NY (1964).
2. P. Dragsten and W. Webb, Mechanism of the membrane potential sensitivity of the fluorescent membrane probe merocyanine, *Biochemistry* 17:5228 (1978).
3. P.I. Lelkes and I.R. Miller, Perturbations of membrane structure by optical probes. I. Location and structural sensitivity of merocyanine 540 bound to phospholipid membranes, *J. Membrane Biol.* 52:1 (1980).
4. A.S. Verkman and M.P. Frosch, Temperature-jump studies of merocyanine 540 relaxation kinetics in lipid bilayer membranes, *Biochemistry* 24:7117 (1985).
5. F. Sieber, Antineoplastic and antiviral properties of merocyanine 540, *Proc. SPIE - Int. Soc. Opt. Eng.* 997:128 (1989).

6. L. Šikurová and T. Janíková, Effect of solvents on the absorption spectra of merocyanine 540, *Stud. Biophys.* 118:189 (1987).
7. A.S. Verkman, Mechanism and kinetics of merocyanine 540 binding to phospholipid membranes, *Biochemistry* 26:4040 (1987).
8. P.F. Aramendía, M. Krieg, C. Nitsch, E. Bittersmona, and S.E. Braslavsky, The photophysics of merocyanine 540. Comparative study in ethanol and in liposomes, *Photochem. Photobiol.* 48:187 (1988).
9. L. Šikurová, R. Franková, and D. Chorvát, Dimers of merocyanine 540. III. In dimyristoyl lecithin liposomes, *Stud. Biophys.* 133:67 (1991).
10. L. Šikurová and R. Franková, Temperature induced changes in monomer-dimer distribution of merocyanine 540 in dimyristoyl lecithin liposomes, *Stud. Biophys.* 140:21 (1991).
11. R.J. Singh, J.B. Feix, T.J. Pintar, A.W. Girotti, and B. Kalyanaraman, Photodynamic action of merocyanine 540 in artificial bilayers and natural membranes: action spectra and quantum yields, *Photochem. Photobiol.* 53:493 (1991).
12. A. Kalenak, R.J. McKenzie, and T.E. Conover, Response of the electrochromic dye, merocyanine 540, to membrane potential in rat liver mitochondria, *J. Membrane Biol.* 123:23 (1991).
13. P. Kaschny and F.M. Goñi, The components of merocyanine-540 absorption spectra in aqueous, micellar and bilayer environments, *Eur. J. Biochem.* 207:1085 (1992).
14. M. Krieg, Singlet oxygen production and fluorescence yields of merocyanine 540: a comparative study in solution and model membrane systems, *Biochim. Biophys. Acta* 1105:333 (1992).
15. B. Ehrenberg and E. Pevzner, Spectroscopic properties of the potentiometric probe merocyanine-540 in solutions and in liposomes, *Photochem. Photobiol.* 57:228 (1993).
16. F. Sieber, J.L. Spivak, and A.M. Sutcliffe, Selective killing of leukemic cells by merocyanine 540-mediated photosensitization, *Proc. Natl. Acad. Sci. USA* 81:7584 (1984).
17. F. Sieber, Yearly review: merocyanine 540, *Photochem. Photobiol.* 46:1035 (1984).
18. J. Davila, K.S. Gulliya, and A. Harriman, Inactivation of tumours and viruses via efficient photoisomerization, *J. Chem. Soc., Chem. Commun.* 1215 (1989).
19. F. Sieber, G.J. Krueger, J.M. O'Brien, S.L. Schober, L.L. Sensenbrenner, and S.J. Sharkis, Inactivation of Friend erythroleukemia virus and Friend virus-transformed cells by merocyanine 540-mediated photosensitization, *Blood* 73:345 (1989).
20. J.M. O'Brien, R.R. Montgomery, W.H. Burns, D.K. Gaffney, and F. Sieber, Evaluation of merocyanine 540-sensitized photoirradiation as a means to inactivate enveloped viruses in blood products, *J. Lab. Clin. Med.* 116:439 (1990).
21. J.C. Smith, Potential-sensitive molecular probes in membranes of bioenergetic relevance, *Biochim. Biophys. Acta* 1016:1 (1990); and references therein.
22. J. Davila, A. Harriman, and K.S. Gulliya, Photochemistry of merocyanine 540: the mechanism of chemotherapeutic activity with cyanine dyes, *Photochem. Photobiol.* 53:1 (1991).
23. D.K. Gaffney, J.M. O'Brien, and F. Sieber, Modulation by thiols of the merocyanine 540-sensitized photolysis of leukemia cells, red cells, and Herpes simplex virus type 1, *Photochem. Photobiol.* 53:85 (1991).
24. J.M. O'Brien, R.J. Singh, J. B. Feix, B. Kalyanaraman, and F. Sieber, Action spectra of the antileukemic and antiviral activities of merocyanine 540, *Photochem. Photobiol.* 54:851 (1991).
25. A. Harriman, (Photo)isomerization dynamics of merocyanine dyes in solution, *J. Photochem. Photobiol. A* 65:79 (1993).
26. J.E. Valinsky, T.G. Easton, and E. Reich, Merocyanine 540 as a fluorescent probe of membranes: selective staining of leukemic and immature hemopoietic cells, *Cell* 13:487 (1978).
27. G.M.K. Humphries and J.P. Lovejoy, Cholesterol-free phospholipid domains may be the membrane feature selected by N-ε-dansyl-L-lysine and merocyanine 540, *Biochem. Biophys. Res. Commun.* 111:768 (1983).
28. R.C. Meagher, F. Sieber, and J.L. Spivak, Susceptibility to merocyanine 540-mediated photosensitization: a differentiation marker on murine hematopoietic progenitor cells, *J. Cell. Physiol.* 116:118 (1983).
29. P.R. Dragsten, Mechanism of voltage-induced fluorescence changes of the membrane probe merocyanine 540. A fluorescence polarization study, Ph.D. Thesis, Cornell University, Ithaca, NY (1977).
30. S. Krasne, Interactions of voltage-sensing dyes with membranes. III. Electrical properties induced by merocyanine 540, *Biophys. J.* 44:305 (1983).
31. L. Šikurová and R. Franková, Electrochromism of merocyanine dye in phospholipid layers, *Acta Phys. Univ. Comenianae* 29:169 (1989).
32. D.R. Bessire and E.L. Quitevis, Effect of temperature and viscosity on rotational diffusion of merocyanine 540 in polar solvents, *J. Phys. Chem.* 98:13083 (1994).

33. P.D. Aramendía, R. Duchowicz, L. Scaffardi, and J.O. Tocho, Photophysical characterization of a photochromic system: the case of merocyanine, *J. Phys. Chem.* 94:1389 (1990).
34. L.G.S. Brooker, G.H. Keyes, R.H. Sprague, R.H. VanDyke, E. VanLare, G. Van Zandt, F.L. White, H.W.J. Cressman, and S. R. Dent, Jr., Color and constitution. X. Absorption of the merocyanines, *J. Am. Chem. Soc.* 73:5332 (1951).
35. E.G. McRae, Solvent effects on merocyanine spectra, *Spectrochim. Acta* 12:192 (1958).
36. C. Párkányi, S. R. Oruganti, A.O. Abdelhamid, L. von Szentpály, B. Ngom, and J.J. Aaron, Dipole moments of indoles in their ground and the first excited singlet states, *J. Mol. Struct. (Theochem)* 135:105 (1986).
37. J.J. Aaron, M.D. Gaye, C. Párkányi, N.S. Cho, and L. von Szentpály, Experimental and theoretical dipole moments of purines in their ground and lowest excited singlet states, *J. Mol. Struct.* 156:119 (1987).
38. E.G. McRae, Theory of solvent effects on molecular electronic spectra. Frequency shifts, *J. Phys. Chem.* 61:562 (1957).
39. P. Suppan, Solvent effects on the energy of electronic transitions: experimental observations and applications to structural problems of excited molecules, *J. Chem. Soc. A* 3125 (1968).
40. P. Suppan and C. Tsiamis, Absolute excited state dipole moments from solvatochromic shifts, *Spectrochim. Acta* 36A:971 (1980).
41. N.G. Bakhshiev, Universal intermolecular interactions and their effect on the position of the electronic spectra of molecules in two-component solutions. VII. Theory (general case of an isotropic solution), *Opt. Spektrosk.* 16:821 (1964).
42. A. Kawski, Zur Lösungsmittelabhängigkeit der Wellenzahl von Elektronenbanden lumineszierender Moleküle und über die Bestimmung der elektrischen Dipolmomente im Anregungszustand, *Acta Phys. Polon.* 29:507 (1966).
43. A. Chamma and P. Viallet, Détermination du moment dipolaire d'une molécule dans un état excité singulet: application à l'indole, au benzimidazole et à l'indazole, *C.R. Acad. Sci. Sér. C.* 270:1901 (1970).
44. C. Párkányi, C. Boniface, J.J. Aaron, M.D. Gaye, L. von Szentpály, R. Ghosh, and K.S. RaghuVeer, Electronic absorption and fluorescence spectra and excited singlet-state dipole moments of biologically important pyrimidines, *Struct. Chem.* 3:277 (1992).
45. Details concerning the calculations, the parameterization, and the additional references are available upon request from the authors (C.P.).
46. L. Kushner and P. Smyth, Resonance and polarity in the molecules of three colored compounds, *J. Am. Chem. Soc.* 71:1401 (1949).
47. A. Adenier and J. Aubad, Détermination par spectrophotométrie d'absorption différentielle et relaxation chimique part saut de température des paramètres caractérisant l'autoassociation de colorants en solution aqueuse, *J. Chim. Phys.* 84:921 (1987).
48. L.G.S. Brooker, G.H. Keyes, R.H. Sprague, R.H. VanDyke, E. VanLare, G. Van Zandt, and F.L. White, Studies in the cyanine dye series. XI. The merocyanines, *J. Am. Chem. Soc.* 73:5326 (1951).
49. C. Reichardt, "Solvents and Solvent Effects in Organic Chemistry", pp. 285, 409, VCH Verlagsgesellschaft, Weinheim (1988).
50. B. Kalyanaraman, J.B. Feix, F. Sieber, J.P. Thomas, and A.W. Girotti, Photodynamic action of merocyanine 540 on artificial and natural cell membranes: involvement of singlet molecular oxygen, *Proc. Natl. Acad. Sci. USA* 84:2999 (1987).
51. R.J. Singh, J.B. Feix, T.J. Pintar, A.W. Girotti, and B. Kalyanaraman, Photodynamic action of merocyanine 540 in artificial bilayers and natural membranes: action spectra and quantum yields, *Photochem. Photobiol.* 53:493 (1991).
52. W. West and S. Pearce, The dynamic state of cyanine dyes, *J. Phys. Chem.* 69:1894 (1965).
53. E. Rabinowitch and L.F. Epstein, Polymerization of dyestuffs in solution. Thionine and methylene blue, *J. Am. Chem. Soc.* 63:69 (1941).
54. P.H. Elworthy, A.T. Florence, and C.B. MacFarlane, "Solubilization by Surface Active Agents", Chapman, London (1968).
55. A. Adenier, J. Aubard, and M.A. Schwaller, Thermodynamics and kinetics of aggregation processes in aqueous media of ellipticine derivatives: the alkylloxazolopyridocarbazole series, *J. Phys. Chem.* 96:8785 (1992).
56. A. Adenier, M.A. Cordonnier, M.F. Ruasse, and M.A. Schwaller, Self-association mechanisms in aqueous media: dimerization versus micellization of alkylellipticinium derivatives, *J. Chem. Soc., Perkin Trans. 2* 839 (1993).
57. A. Adenier, J.J. Aaron, C. Párkányi, G. Deng, and M. Sallah, Solvent effects on the electronic absorption and fluorescence emission spectra of merocyanine 540, a biological probe, *Heterocycl. Commun.*, in press.

HIGH PRESSURE INFRARED SPECTROSCOPY IN BIOLOGICAL AND BIOMEDICAL STUDIES

Adnan Taymaz¹, Ghaith Breiki¹, Ipek Kanat¹, Ali Karaman¹, and Patrick T. T. Wong²

¹ Department of Nuclear Physics
Science Faculty, Vezneciler Campus
Istanbul University, 34459 Istanbul, Turkey

² Steacie Institute For Molecular Sciences
National Research Council of Canada
Ottawa, Ontario K1A OR6, Canada

ABSTRACT

Recent advances in infrared spectroscopy have made it possible to study structural and dynamic properties of biomembranes and model systems at molecular level by spectral analysis. Using pressure tuning infrared spectroscopy we studied intermolecular interactions in 1,2 dioleoyl phosphatidylcholine (DOPC), 1,2 dipalmitoyl phosphatidylcholine (DPPC). Infrared spectra from model biomembranes and abnormal tissues were measured and compared to their normal species under 0 to 45 kbar pressure. Discontinuities in the pressure dependencies of various infrared spectral parameters indicate that structural phase transitions occur at 4.2, 5 and 15 kbar. More than two correlation field components of CH₂ scissoring modes are observed in spectra of the high-pressure phases, suggesting that more than two acyl chains are present in the unit cell of these phases.

INTRODUCTION

Interest in the structure of biological systems or their models at molecular level under elevated pressure has grown rapidly during the last decade (Macdonald, 1984; Wong, 1994), while the experimental pressure range of interest has reached up to 45 kbar. The effect of pressure on the lipid volume permits us to study the variation in intermolecular distances, and allows us to understand the intermolecular interactions and mechanism of phase transitions.

Various physical techniques have been applied in recent years in order to study the structural and dynamic changes in molecular level of the model lipid (3). The necessity of

non-perturbing techniques, i.e., those not requiring the use of molecular probes, has been emphasized (4). Infrared spectroscopy has benefited from a number of technical developments, which allow us to overcome the difficulty of very intense water absorption in the infrared region. For the reasons above, computerized and Fourier-transform (5) infrared spectroscopy have been developed to overcome the technical and methodological difficulties (6).

EXPERIMENTAL

Samples of 1,2 dioleoyl phosphatidylcholine (DOPC) and dipalmitoylphosphatidylcholine (DPPC) were obtained from AVANTI Polar-Lipids Inc. (Birmingham, AL). Other materials were of analytical grade. The DOPC:DPPC-d₆₂ mixtures prepared for high pressure infrared experiments were 1:1 and 1:4 molar ratio respectively.

The solid samples were dissolved in chloroform in order to obtain a homogenous mixture of the two specimens, and followed by evaporating the chloroform, first under nitrogen gas, then under high vacuum. The solid mixtures were then dispersed into thirst-buffers made with D₂O 30% w/w. Later, the lipid mixture was heated to 60°C in a closed vial, followed by vortexing and cooling down to 0°C. The heating-vortexing and cooling cycle was repeated at least five times in order to obtain purified and homogeneous graded samples. At room temperature, lipid samples, together with some powdered alpha-quartz and KRS-5, were placed in a 0.34 mm diameter hole on a 0.23 mm thick stainless-steel gasket that was mounted on a diamond anvil cell. The KRS-5 served as a substrate; the alpha-quartz was used in order to determine the internal pressure from the alpha-quartz phonon bands in the infrared spectra (7). Infrared spectra were measured at room temperature with a Bomen Model DA3.02 Fourier-transform infrared spectrometer equipped with a liquid-nitrogen cooled mercury cadmium telluride detector. The infrared beam was condensed by a sodium chloride lens system onto a pinhole on the diamond anvil cell. A total of 120 spectra were

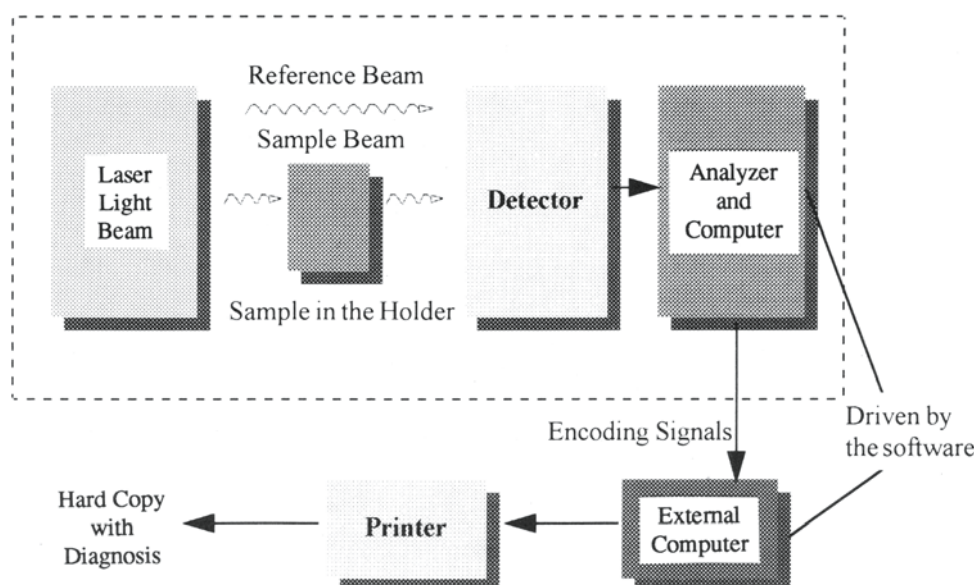


Figure 1.

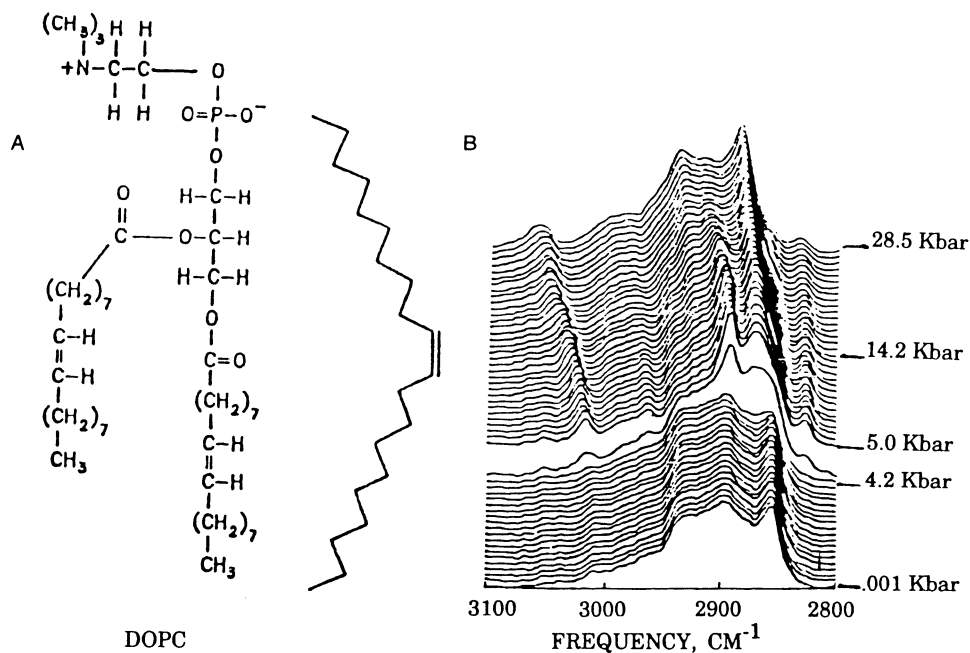


Figure 2.

recorded at different pressures up to 45 kbar. For each spectrum 512 scans were co-added; the spectral resolution was 2 cm⁻¹. Data reduction was performed using software developed by the molecular spectroscopy laboratory at NRC of Canada. The electronic system used in this infrared spectroscopic study is shown in Figure 1.

RESULTS AND DISCUSSIONS

Spectral Regions Useful for Lipids and Membranes Studies

The spectral features of these samples, which originate from molecular vibrations of the various functional groups in the head group, are initiated from: a) carbon-hydrogen (C-H) and b) carbon-oxygen (C-O) bands.

a. The carbon-hydrogen (=C-H, CH₂ and CH₃) stretching vibrations give to the bands a characteristic spectral region of 2800-3100 cm⁻¹. The CH₂ antisymmetric stretching modes at around 2850 cm⁻¹ are generally the strongest bands in the spectra of lipids. Other infrared modes are associated with the different bending vibrations of acyl chains as in methylene and methyl groups. Examples include the CH₂ scissoring between 1462-1474 cm⁻¹, the symmetric CH₃ deformation at 1375 cm⁻¹, the CH₂ wagging band progression of regularly spaced bands between 1190-1345 cm⁻¹, and the CH₂ phospholipids (15) rocking/twisting band progression with a strong head band between 720-730 cm⁻¹.

b. The carbonyl vibration, the C=O stretching bands, which occur in the spectral range 1715-1745 cm⁻¹, are sensitive to both conformational and environmental factors. Thus, it is not surprising that the gel to liquid-crystalline phase transition also produces changes in the C=O stretching band. It was noticed quite early that

the C=O stretching band of phospholipids in aqueous dispersions displays an asymmetry, which changed when the lipid passed from the gel into the liquid-crystalline phase. For illustration purpose we will discuss the results of lamellar membranes consisting of unsaturated DOPC and DPPC respectively.

DOPC is a phospholipid with a rigid cis double bond in the middle of each of the two hydrocarbon chains, shown in Figure 2A. At ambient conditions, DOPC aqueous bilayers are in the liquid crystalline state in which the conformational and orientational structures of the hydrocarbon chains are highly disordered. It has been shown (6) that external pressure can order a disordered liquid crystalline phase and induce a transition from the disordered liquid crystalline phase into an ordered gel phase. This phase transition is indicated by discontinuous changes in the infrared spectra (see Figure 2B).

Dramatic changes in the infrared and Raman spectra of DOPC bilayers and discontinuities in the pressure dependencies of all the infrared spectra were observed at 5 kbar. This indicates that the liquid crystalline phase and gel phase of liquid DOPC undergoes a phase transition into the gel phase at this pressure. For instance, the Raman spectra in the frequency region of the C-H stretching vibrations shown in Figure 3 exhibit distinct changes at 5 kbar. The spectra in this region below and above 5 kbar are the same type as those of the liquid crystalline phase and the gel phase of liquid bilayers respectively (3,6).

The bend configuration of a hydrocarbon chain in the gel phase of DOPC is also evident from the changes at 5 kbar in other regions of the infrared and Raman spectra. For example, a decrease in the frequency of the C=C double stretching mode takes place above 5 kbar in the gel phase (see Figure 3).

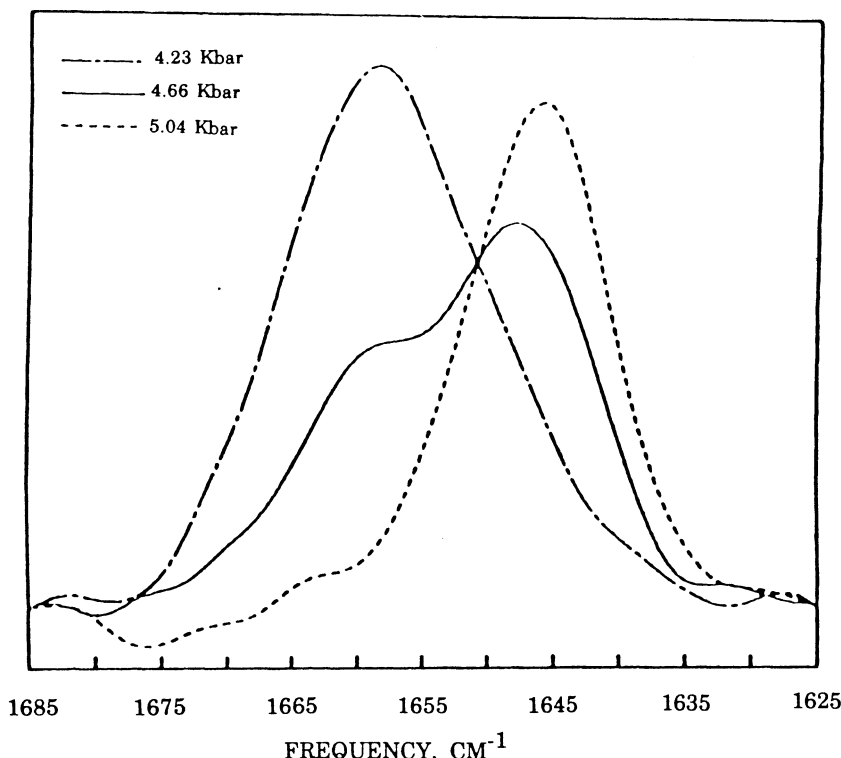


Figure 3.

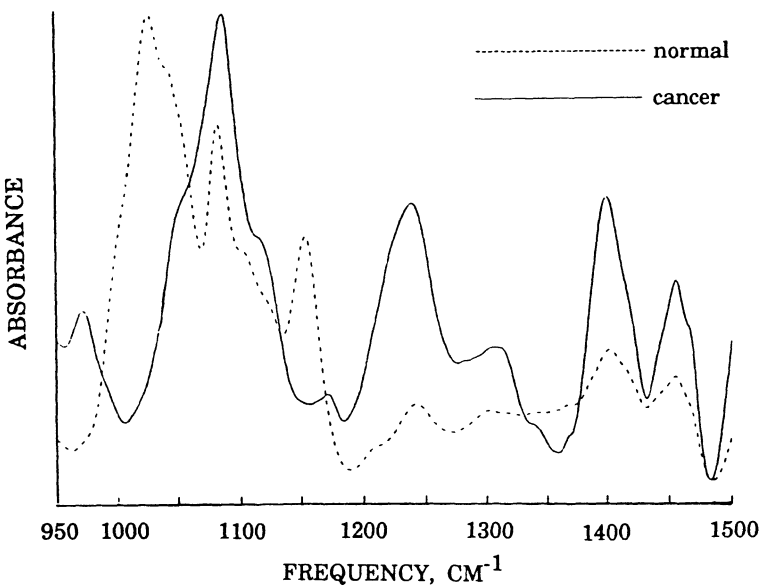


Figure 4.

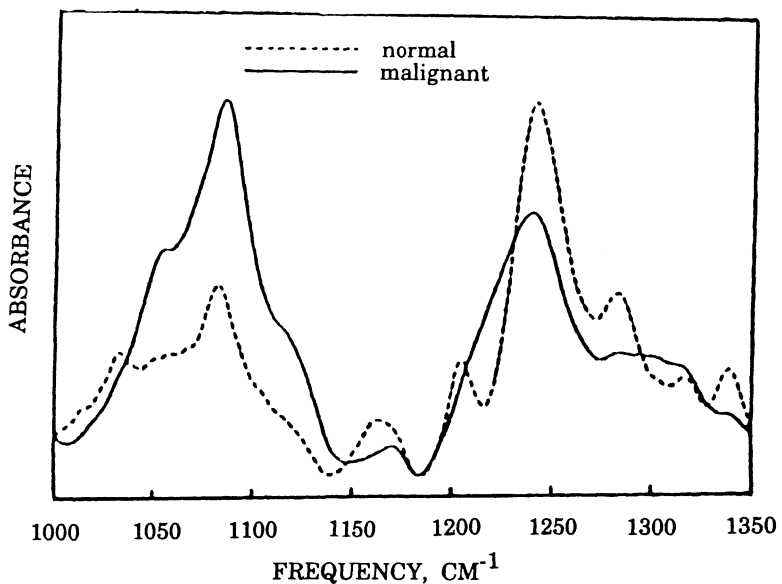


Figure 5.

These results suggest that the conformational structure of the hydrocarbon chains is highly ordered and that the hydro-carbon chain segments on both sides of the cis double bond are highly extended. Consequently, the two zig-zag CH₂ chain segments on both sides of the cis double bond in each oleoyl chain form a bent structure such as that shown in Figure 2.

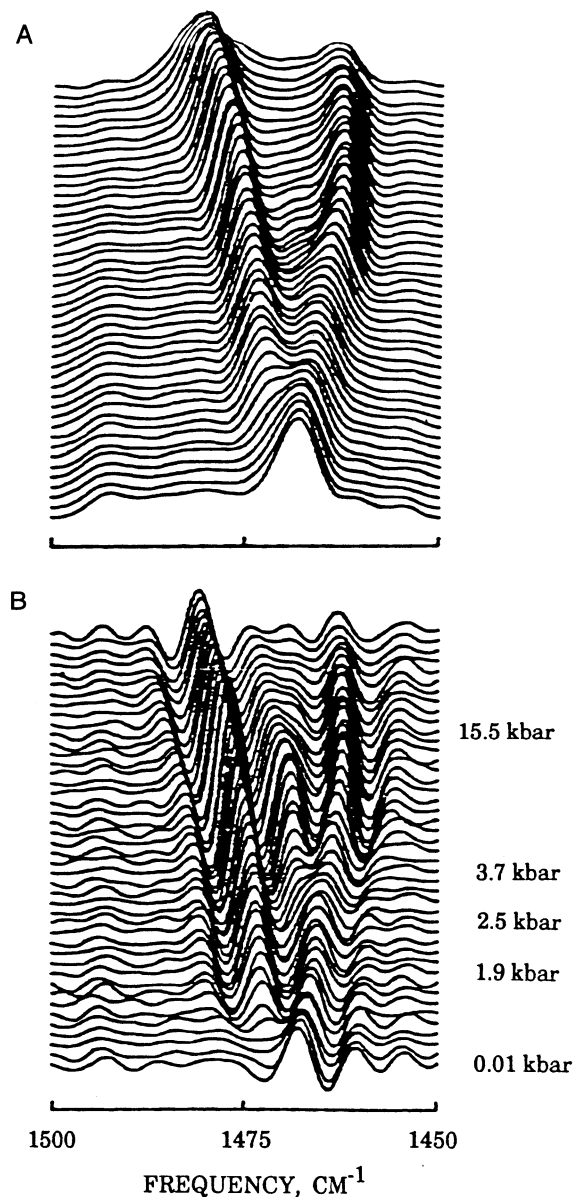


Figure 6.

Biological and Biomedical Studies

Here, some of the biomedical studies will be included. These are carcinogen-induced exfoliated cells (8,9), cultured human cell lines (10,11) and structural modifications at the molecular level in human cancers (12,13).

Figure 4 shows the infrared spectra of exfoliated cells from a pair of normal and malignant cervical tissues in the frequency region 950-1500 cm⁻¹. The spectra are similar to those of other glycogen-rich tissues such as the liver and vaginal tissues.

The infrared spectra of a pair of normal and malignant colon tissues in the frequency region 1000-1350 cm⁻¹ are shown in Figure 5. The spectrum of the normal colon tissue and its changes in the malignant tissue are similar to those of other tissues such as tissues of stomach skin and breast. Extensive control studies are required, because comparison of normal vs. malignant tissue necessitates precise determination of cell populations in each case. Otherwise the observed difference cannot be interpreted.

Model Biomembranes

Results from our studies demonstrated that there are a number of advantages in using the pressure-tuning infrared spectroscopic technique for spectral analysis of biological tissues in distinguishing the normal cell from the malignant one. One example is the phospholipid 1,2 dipalmitoyl phosphatidylcholine (DPPC), which forms multilamellar bilayers when dispersed in excess water and provides a widely used model system for biomembranes. The infrared spectra of aqueous DPPC provide details of the system's interchain structure. Furthermore, when the effect of elevated pressure on the infrared spectra of aqueous DPPC is combined with the existing data regarding the effect of pressure on the Raman spectra of the same system (14), it becomes possible to establish the pressure effect on the dispersion of the normal modes of the acyl chains. The pressure induced field splitting can be visualized by contour spectra as shown in Figure 6. As the hydrostatic pressure

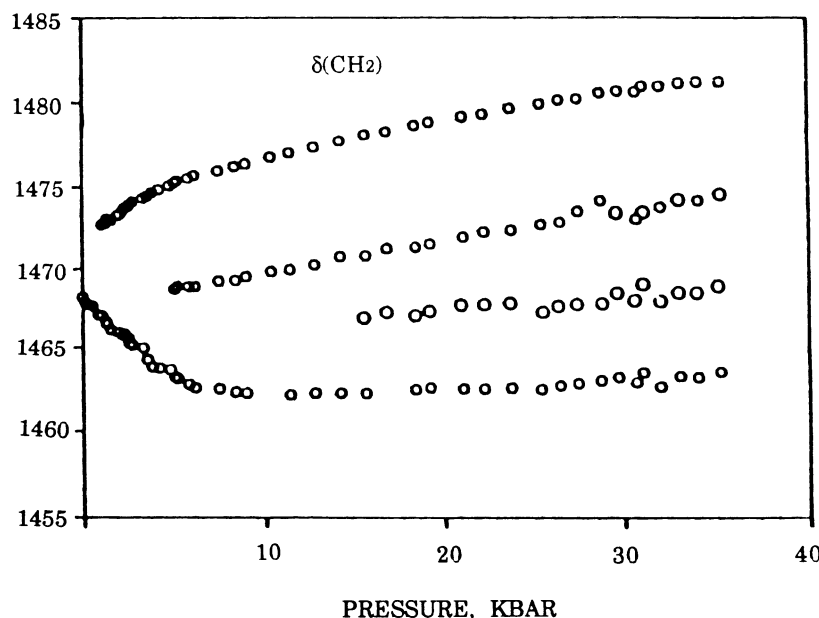


Figure 7.

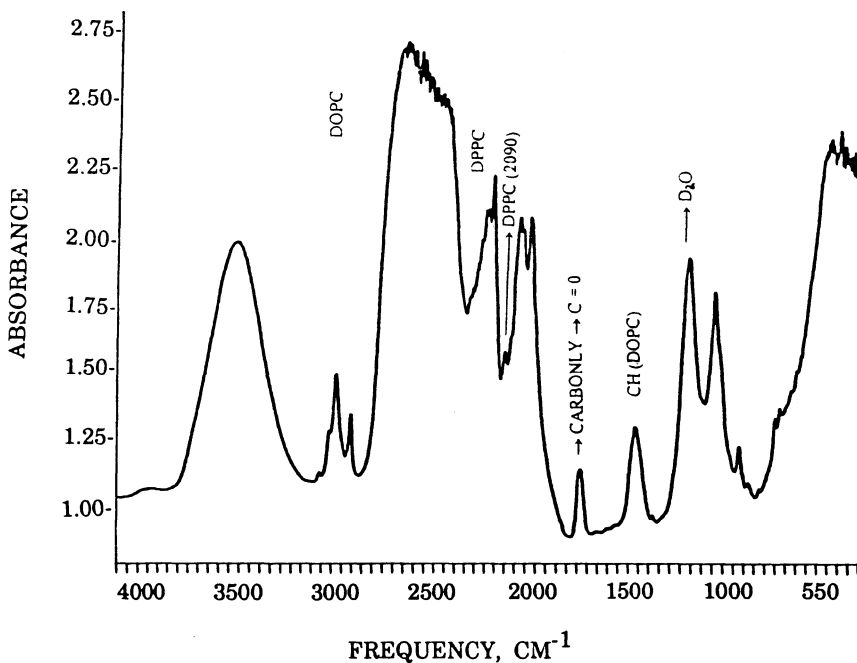


Figure 8.

increases, the correlation field band, $\delta'\text{CH}_2$, first evident as a shoulder on the high frequency side of δCH_2 , gains intensity and becomes even stronger than the δCH_2 band when the pressure reaches 1.8 kbar. At still higher pressure, a new band appears between δCH_2 and $\delta'\text{CH}_2$; this band can be seen more clearly in Figure 6B, which shows the same spectra after resolution enhancement by band narrowing (3). Furthermore, the newly developed band first broadens and then splits into two components at pressures above 15 kbar. The pressure dependencies of the frequencies of the components of the CH_2 scissoring modes are shown in Figure 7. The overall splitting between $\delta'\text{CH}_2$ and δCH_2 increases considerably as pressure increases from 1.9 to 4.8 kbar. Thereafter the frequency of the δCH_2 band remains constant at 1463 cm^{-1} , whereas that of the $\delta'\text{CH}_2$ band increases further from 1475 cm^{-1} at 4.8 kbar to 1481 cm^{-1} at 35.2 kbar.

The representative infrared spectra shown in Figure 8 in the frequency region $4000\text{-}550 \text{ cm}^{-1}$ of DOPC:DPPC are due to different modes of the methylene and methyl groups respectively.

Over most of the pressure range investigated, it can be seen that these frequencies vary linearly within experimental error, and phase transitions can be easily determined from well-defined departures from this linear dependence, manifested either by discontinuities or by changes in slope. Specifically, in the spectrum of DOPC:DPPC, discontinuity in the $\text{t}(\text{CH}_2)$ and $\gamma_s(\text{C-C})$ frequencies occur at 6.2 kbar (see Fig. 9). The infrared band of DOPC alone and DOPC:DPPC observed in the frequency region $1460\text{-}1476 \text{ cm}^{-1}$ is shown in Figure 9. External pressure is known to reduce intermolecular distance and thus increase the intermolecular interactions. The splitting pressure of DOPC:DPPC is 6.7 kbar, which coincides with the ordering pressure of DOPC molecules in the DPPC mixture. It is interesting that the splitting pressure in DOPC is also 6.5 kbar, although the ordering pressure of methylene chains in DOPC is 0.2 kbar lower. Therefore, the driving force for the

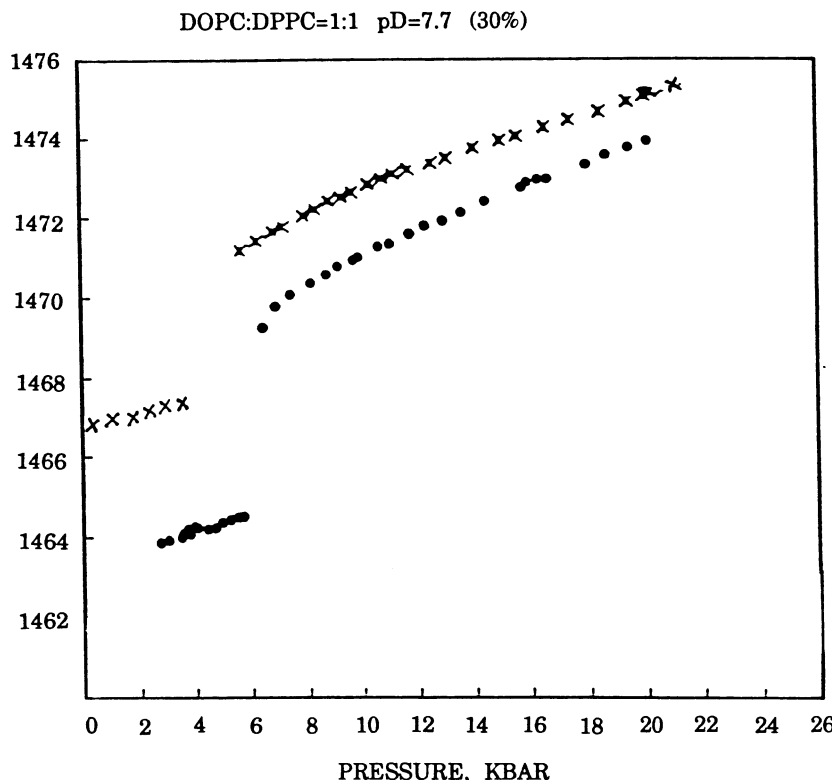


Figure 9.

pressure-induced ordering of the methyl groups differs considerably from that of the ordering of the methylene chains in the DPPC systems.

ACKNOWLEDGMENTS

The authors would like to acknowledge Mr. Baturalp Bal's assistance in the preparation of this manuscript.

REFERENCES

1. Macdonald A.G., *Philos. Trans. R. Soc.*, 47:304 (1984)
2. Wong P.T.T., and Mantsch H.H., *J. Chem. Phys.*, 81:6367 (1984)
3. Cameron D.G., and Mantsch H.H., *Biochem. and Biophys.*, 83 (1978)
4. Wong P.T.T., and Mantsch H.H., *Biophys J.*, 54:781 (1988)
5. Wong P.T.T., High Pressure Vibrational Spectroscopy Studies Of Aqueous Biological Systems: From Model Systems To Intact Tissues, in: "High Pressure Chemistry, Biochemistry and Material Sciences," 511, R. Winter, and J. Sonas, Kluwer Academic Publishers (1993)
6. P.T.T. Wong, US Patent No. 4970396 (1990)
7. P.T.T. Wong, *Cancer Research*, 52:84 (1992)
8. P.J. Siminovitch, et. al., *Biophys. J.*, 51:465 (1987)
9. P.T.T. Wong, M. Cadrin, and S.W. French, *Exp. Mol. Pathology*, 55:289 (1991)

10. Mao H.K., Bell P.M. XU..J., and Wong P.T.T., *Annu. Rep. Geophys. Lab.*, 82:419-421 (1983)
11. P.T.T. Wong, and B. Rigas, *Appl. Spectrosc.*, 49:1715 (1990)
12. P.T.T. Wong, R.K. Wong, T.A. Godwin, and B. Rigas, *Proc. Natl. Acad. Sci. USA*, 88:10988 (1991)
13. P.T.T. Wong, and H.H. Mantsch, *J. Chem. Phys.*, 81:6367 (1984)
14. J.K. Kaupinnen, D.J. Moffat, H.H. Mantsch, and D.G. Cameron, *Appl. Spectrosc.*, 35:271 (1981)
15. D.J. Siminovich et. al., *Biochemistry*, 26:3277 (1987)

FLUORESCENCE SPECTROSCOPY FOR DIAGNOSIS OF CANCEROUS TISSUES

T. Rézio,¹ M. L. Fraser Monteiro,^{1,2} William H. Clode,³ and
J. M. G. Martinho⁴

¹ Centro de Física Molecular
Complexo I, I.S.T.
1000 Lisboa, Portugal

² Departamento de Física
C1, Universidade de Lisboa
1700 Lisboa, Portugal

³ Biotério
Instituto Português de Oncologia
1000 Lisboa, Portugal

⁴ Centro de Química-Física Molecular
I.S.T.
1000 Lisboa, Portugal

ABSTRACT

The autofluorescence of cancerous and normal mouse BALB/c strain tissues was measured *in vitro*, by fluorescence spectroscopy within three hours of surgery ablation. Three emission bands were observed in the 320-600 nm wavelength range.

For UVB excitation at 295 nm, one emission band is centered around 340 nm for cancerous tissue and 330 nm for normal tissue. For UVA excitation at 340 nm, the emission band for the cancerous mouse tissue, is centered about 400 nm and is practically absent for the normal mouse tissue when excited at the same wavelength. For both tissues a band centered at 470 nm is also observed. In our previous study of the fluorescence spectroscopy of cancerous human stomach tissue we found an emission band centered around 380 nm that is practically absent in the normal tissue, when both tissues are excited at 340 nm. We found in this work with mouse tissue a very similar spectral behaviour concerning the differences between cancerous and normal human stomach tissues, with just some shift on the band centers and also some difference in the intensities. In an attempt to understand this behaviour we introduce some discussion about the tryptophan photophysics, and tryptophan metabolism, as the tryptophan amino acid seems to be the responsible for the fluorescence emission bands characteristics of the cancerous tissues.

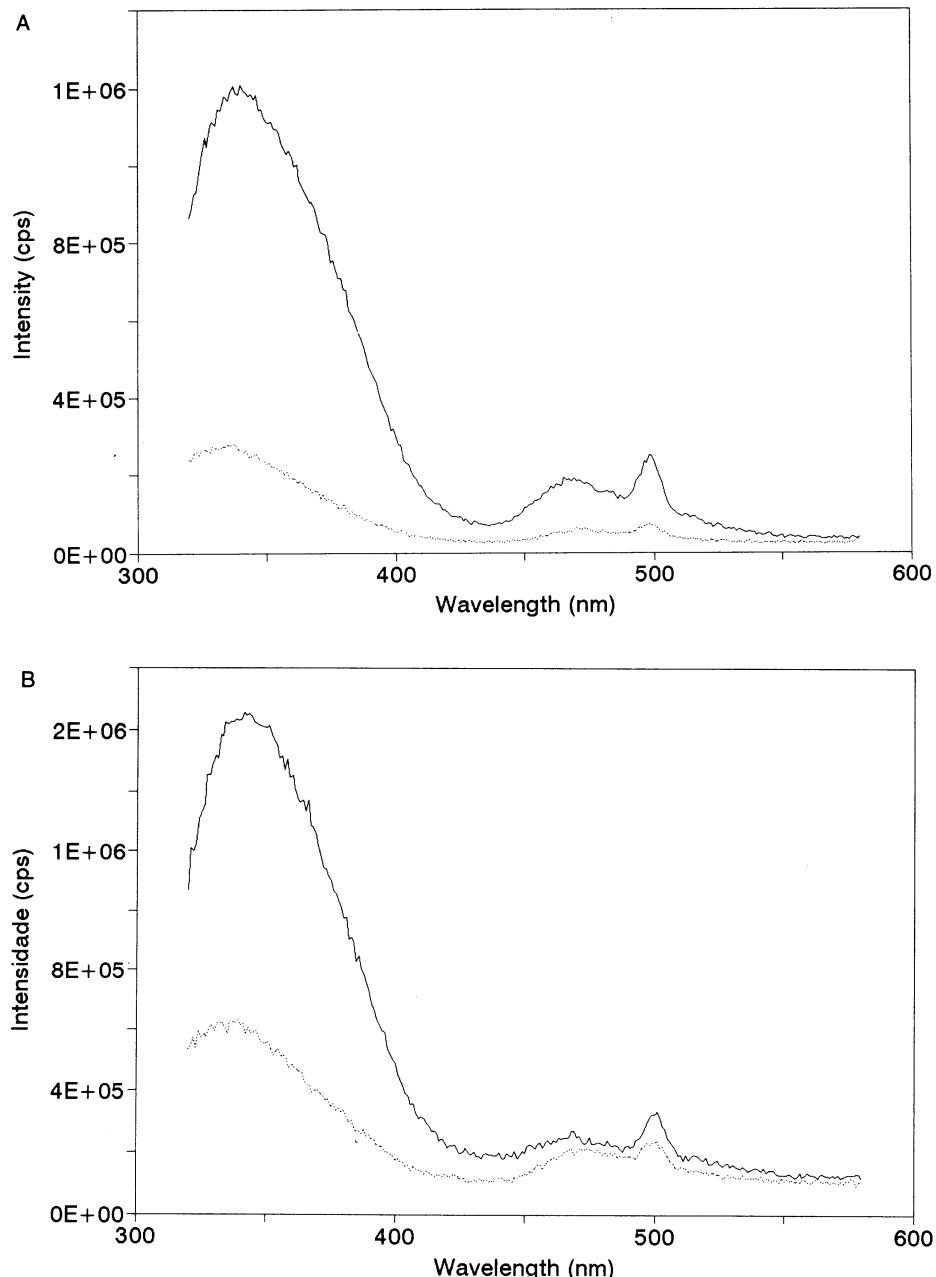


Figure 1. Fluorescence spectra of normal (.....) and tumor (—) mouse tissue from groups A and B excited at 295 nm, A - tumor induced by inoculation of cells, B - tumor induced by ionizing radiation.

INTRODUCTION

Autofluorescence spectroscopy as a method for diagnosis of diseased tissues has increased rapidly during recent years¹⁻⁷.

We have studied the autofluorescence *in vitro* of normal and cancerous human stomach tissues⁸. We found a new fluorescence emission band centered of about 380 nm for the cancerous tissue when excited at 340 nm. This band is practically absent for normal tissue when excited at the same wavelength. As the samples of human stomach tissues were not easy to obtain and analyse immediately after the operation, we decided to study mouse cancerous and normal tissues to compare with our previous results. In this paper we report these studies on two groups of mouse cancerous tissues obtained by two different methods:

Group A - is composed of mouse tissues obtained from mice that have been inoculated with cancerous cells from mammary carcinoma under the skin and which developed a tumor about 10 days later;

Group B - consist of cancerous mouse tissues from mice that develop tumors spontaneously after they have been exposed to ionizing radiation about 11-12 months previously.

MATERIAL AND METHODS

The samples were obtained at the “bioterio” of Instituto Português de Oncologia de Francisco Gentil, transported in an icebox and analysed within 3 hours of surgery. A Fluorolog 2 spectrofluorimeter (SPEX Industries and Company, Edison, NJ, USA) was used with a frontal face geometry to get the fluorescence emission spectra. The samples were chunks of about less than 0.5 cubic centimeter, placed in quartz cuvettes. The exit aperture of the excitation monochromator was about 1 mm diameter. The photon source of the spectrophotometer is a xenon lamp and the instrument corrects the spectrum for constant light intensity. The photomultiplier signal is treated by computer.

All the spectra presented are not corrected for apparatus sensitivity for different wavelengths, as we were interested in doing only comparative measurements between the diseased and normal tissues always at the same conditions.

RESULTS

Three fluorescence emission bands were observed in the 320-600 nm wavelength region. Fig.1(A and B) presents the emission spectra obtained for tissues from group A and B respectively, at the excitation of 295 nm.

The emission bands from the cancerous tissues of groups A and B are centered in both cases at about 340 nm and the emission bands of the normal tissue have the center at about 330 nm, 10 nm shifted to the blue. The emission bands of the cancerous tissue have in general higher intensities than the corresponding bands for the normal tissue.

Fig.2 shows the emission spectra of the cancerous and normal tissues when excited at 340 nm.

The emission band for the cancerous tissue is centered at about 400 nm when the sample is excited at 340 nm, and is practically absent for the normal tissue excited at the same wavelength. For both tissues there is also an emission band centered at about 470 nm, and the intensity of the cancerous tissues is generally higher than for the normal tissue. We have analysed 29 samples of group A and 11 samples of group B. Of the 29 samples of group

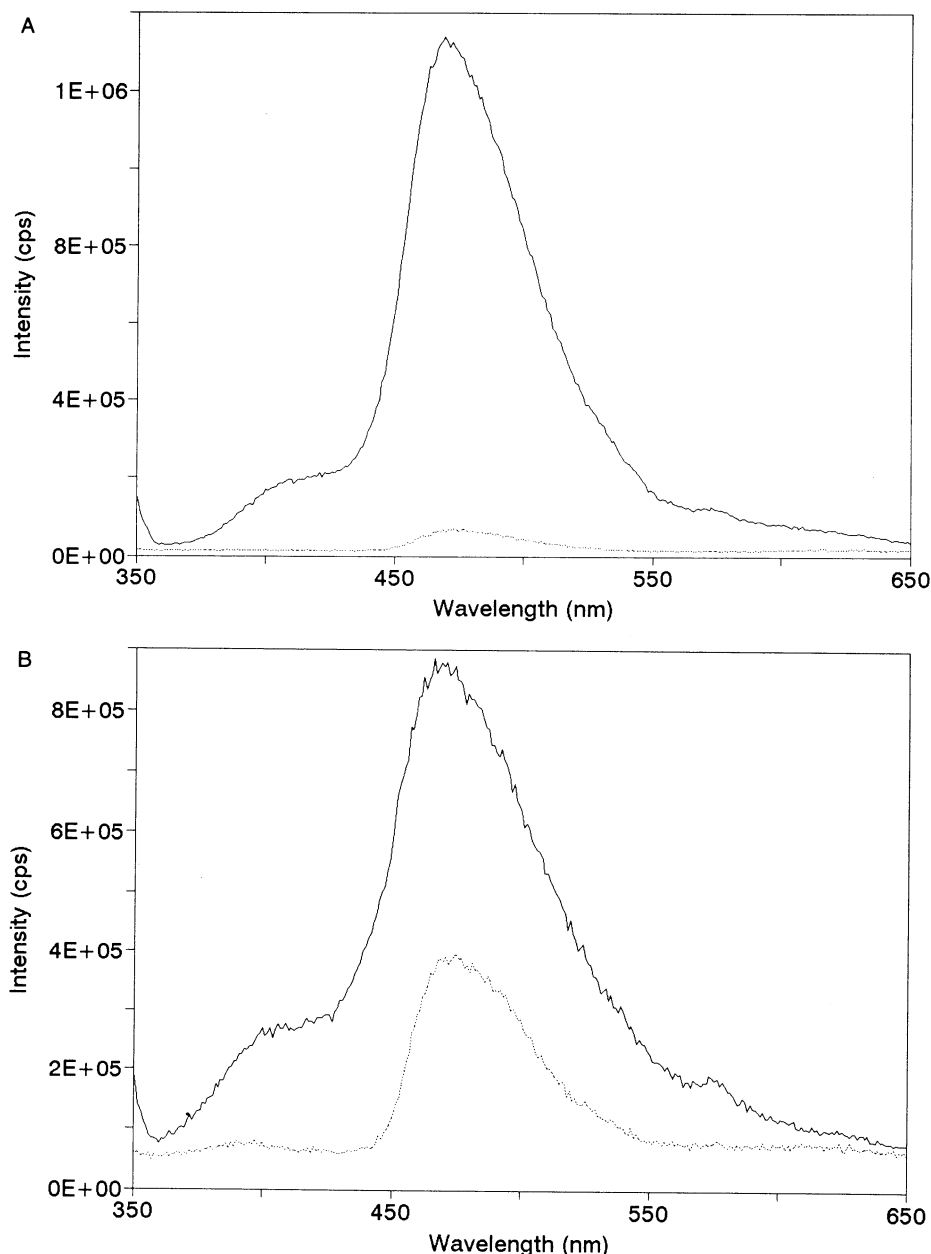


Figure 2. Fluorescence spectra of normal (.....) and tumor (—) mouse tissue from groups A and B excited at 340 nm, A - tumor induced by inoculation of cells, B - tumor induced by ionizing radiation.

A, 20 presented emission spectra exactly like the ones in figure 2A, and the remaining 9 samples presented variations of the standard spectra, possibly due to a contamination of the normal tissues or tissues with metastases. Of the 11 samples of group B, 9 of these presented emission spectra exactly like the ones on figure 2B, and the remaining 2 presented variations of the standard spectra. These numbers represent 69% for group A and 82% for group B of

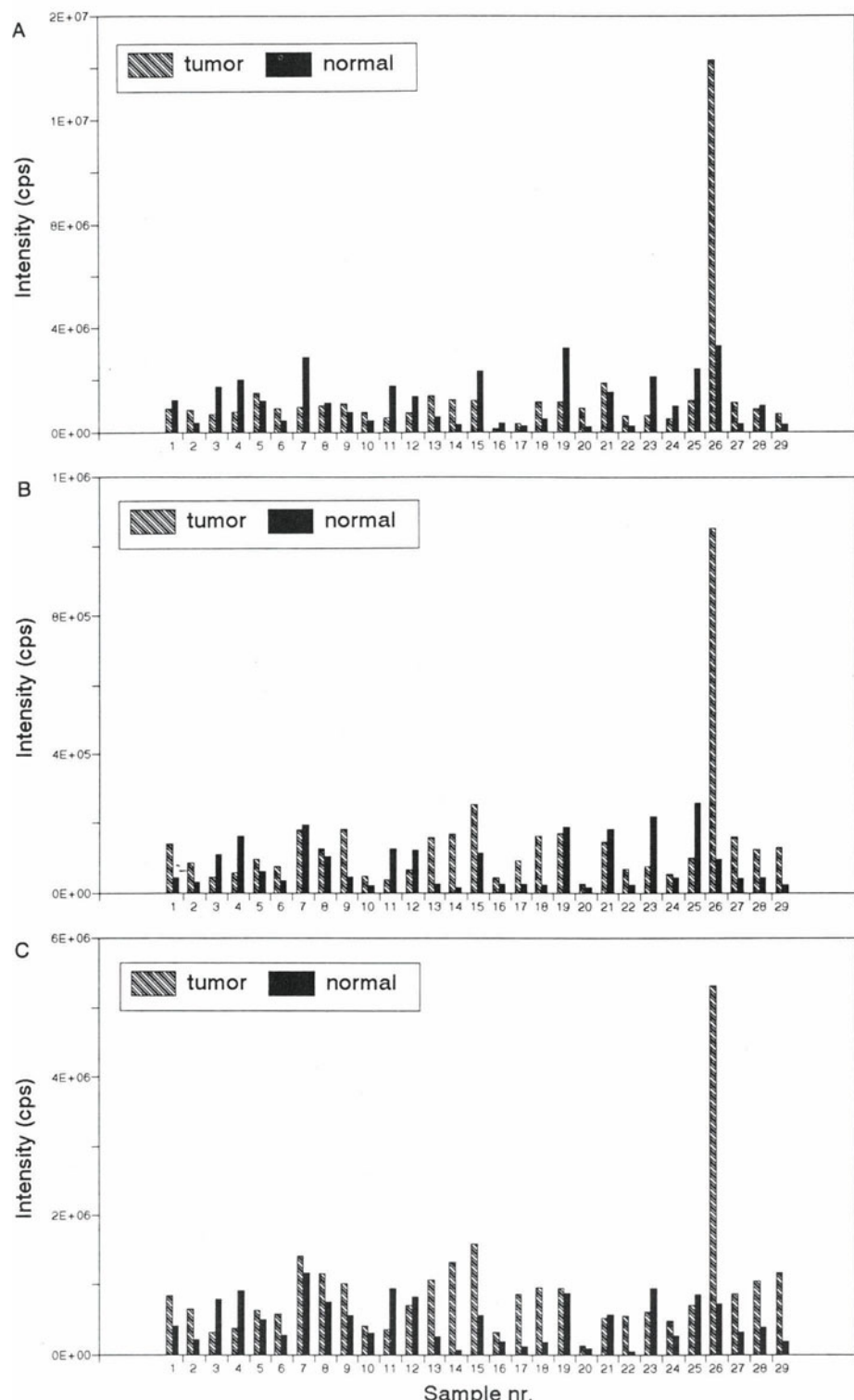


Figure 3. Fluorescence intensities of all the samples of group A, measured at the center of the emission bands: a) 340 nm, b) 400 nm, c) 470 nm. a) $\text{exc}=295\text{nm}/\text{emi}=340\text{nm}$, b) $\text{exc}=340\text{nm}/\text{emi}=400\text{nm}$, c) $\text{exc}=340\text{nm}/\text{emi}=470$.

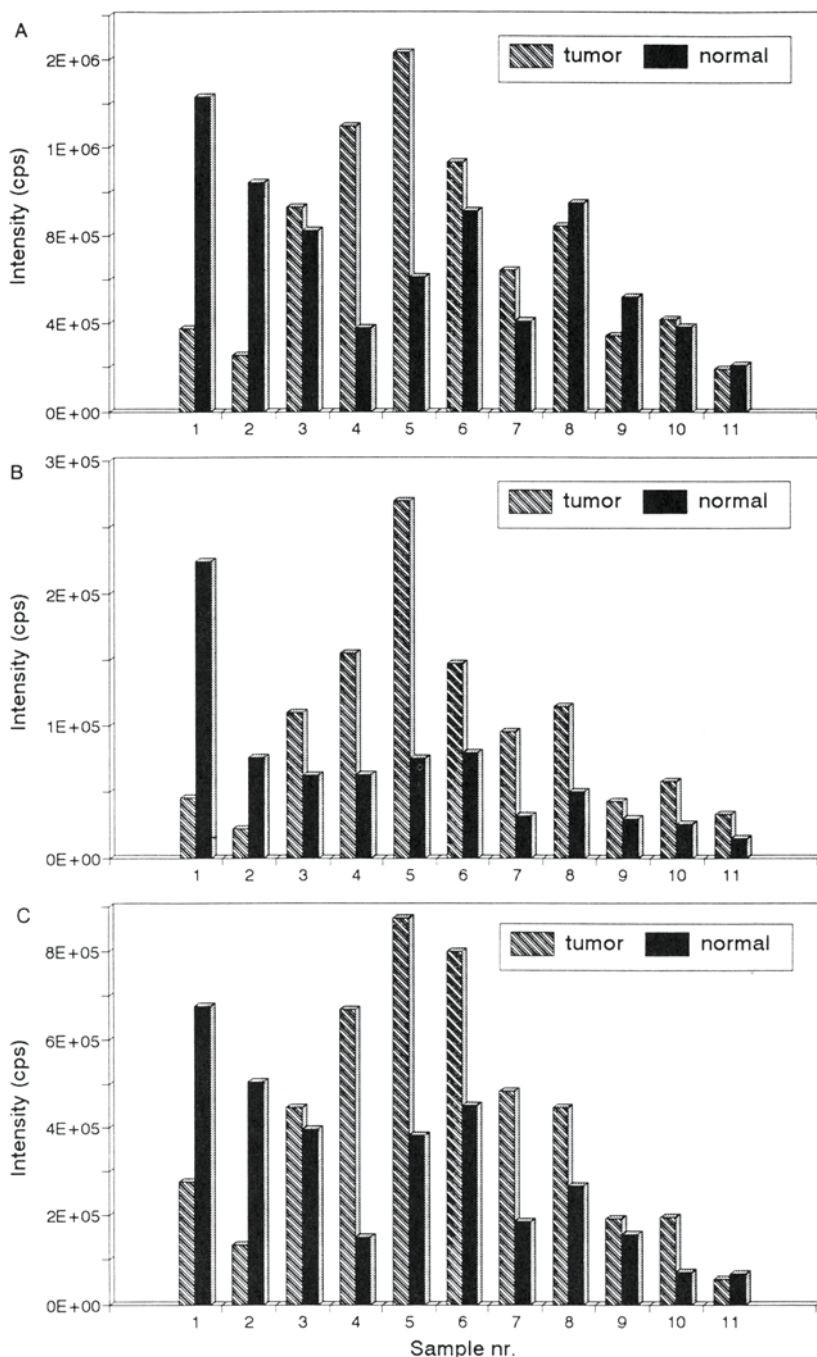


Figure 4. Fluorescence intensities of all the samples of group B, measured at the center of the emission bands: a) 340 nm, b) 400 nm, c) 470 nm. a) exc=295nm/emi=340nm, b) exc=340nm/emi=400nm, c) exc=340nm/emi=470.

samples presenting a standard emission spectrum at 340 nm excitation. Fig.3 presents the fluorescence intensities measured at the center of the emission bands at a) 340 nm, b) 400 nm and c) 470 nm, for group A. Fig.4 presents the fluorescence intensities measured at the center of the emission bands at a) 340 nm, b) 400 nm and c) 470 nm, for group B. Figs.5 and 6 show the intensity ratios of fluorescence emission for cancerous and normal tissues of group A and B respectively.

DISCUSSION

Comparing the results we have obtained for the human stomach tissues, see Fig 7 and Fig. 8, with the results of this work with mouse tissues, we see similarities in the behaviour of the emission bands. However there are some shifts of the band centers.

The band centered at 380 nm for the human tissue is centered at about 400 nm for the rat tissues and is much less intense.

The similarities between the results of samples of group A and group B are evident from the figures, revealing however that the results obtained from group B (spontaneous tumor induced by ionizing radiation) have a better statistic, 82% against 69% of group A.

In general the cancerous tissues exhibit a fluorescence intensity higher than for the normal tissue. We are led to think that the fluorescence observed in these tissues, seems to be related with the fluorescence of the amino acid tryptophan. So, in order to understand the presence of the bands centered at 380 nm and 400 nm we decided to investigate more about this amino acid.

As it is known, the amino acid tryptophan dominates the near ultraviolet absorption and fluorescence of many proteins^{9, 10}.

Until recently, molecules of biological interest have been studied almost exclusively in solution. Many of these studies have examined the effects of conformation and solvent on the time and wavelength resolved fluorescence of amino acid residues, so that the spectra of the aromatic amino acid could be used as optical probes of protein structure and dynamics^{11, 12, 13}. However, poor spectral resolution in solution makes it impossible to resolve spectral features of individual conformers and study their properties. To more completely understand the role of the solvent in the spectroscopy and dynamics of amino acids in solution, investigations of these molecules in supersonic jets were initiated. The cooling resulting from the supersonic expansion greatly reduces spectral congestion and facilitates the assignment of the remaining sharp structure. The cold isolated environment of a molecular beam allows the study of dynamical processes intrinsic to the molecule of interest, in the absence of solvent¹⁴. The amino acid tryptophan has been studied in detail. These studies have revealed the presence of six noninterconverting conformers, one of which exhibits a nearly harmonic 26 cm⁻¹ vibrational progression which did not appear in the spectra of other indole derivatives¹⁵.

Analysis of the dispersed emission spectrum of this conformer revealed broad red-shifted fluorescence produced by the formation of an intramolecular exciplex¹⁴. In the same study were measured some of the electronic properties of the individual conformers of cold, isolated tryptophan in its excited electronic state. They conclude that the excited state of the conformers of tryptophan do not interconvert during the fluorescence lifetime, so that the fluorescence emission from each conformer may be different.

Also, it is known that tryptophan is the only amino acid containing an indole ring. It is also an essential amino acid. Its metabolism is complex, involving a number of alternative routes. Enzymes have not yet been designated for each step of all these routes.

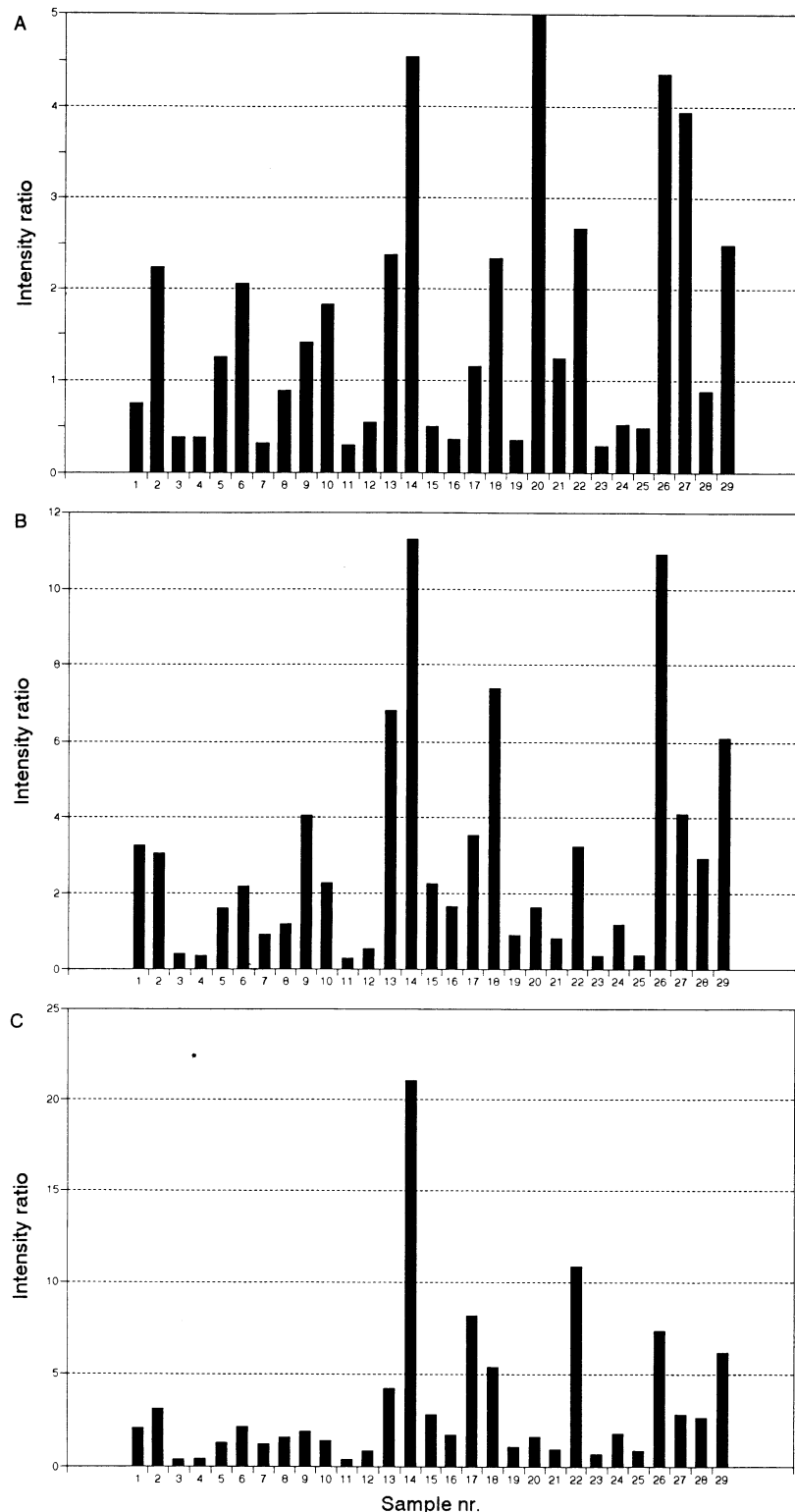


Figure 5. Intensity ratios of fluorescence emission for cancerous and normal tissue of group A at the center of bands: a) 340 nm, b) 400 nm, c) 470 nm. a) exc=295nm/emi=340nm, b) exc=340nm/emi=400nm, c) exc=340nm/emi=470.

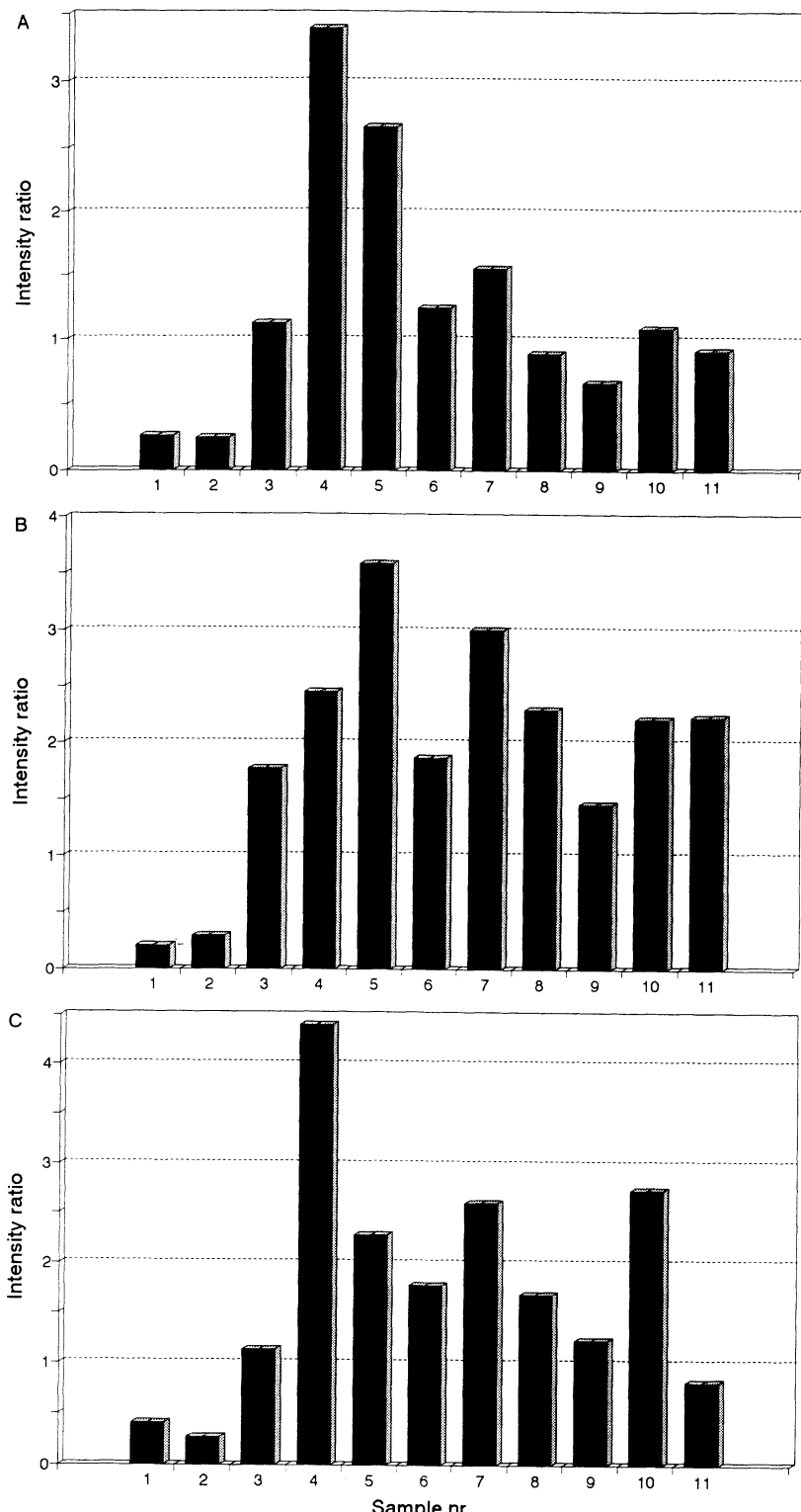


Figure 6. Intensity ratios of fluorescence emission for cancerous and normal tissue of group B at the center of bands: a) 340 nm, b) 400 nm, c) 470 nm. a) exc=295nm/emi=340nm, b) exc=340nm/emi=400nm, c) exc=340nm/emi=470.

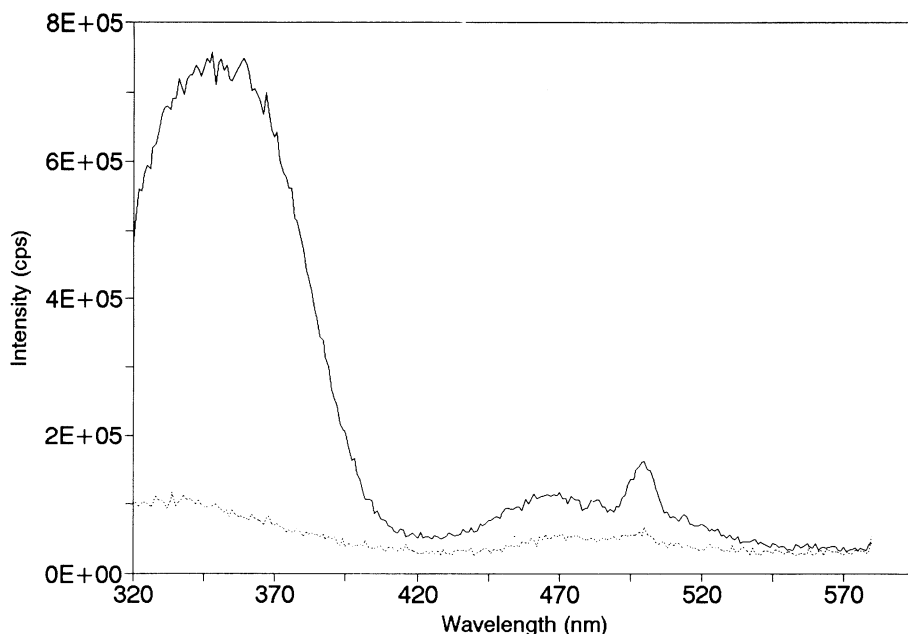


Figure 7. Fluorescence spectra of normal (.....) and tumor (—) stomach tissue, excited at 295 nm.

The conversion of tryptophan to 5-hydroxyindolacetate is one of these alternative pathways of tryptophan metabolism¹⁶, but in the normal way is of little quantitative significance, as only about one per cent of the total tryptophan is metabolized by this route.

In the carcinoid syndrome; small tumors in the small intestine, appendix, stomach or colon will metabolize tryptophan by this route. This is a serious condition which results in

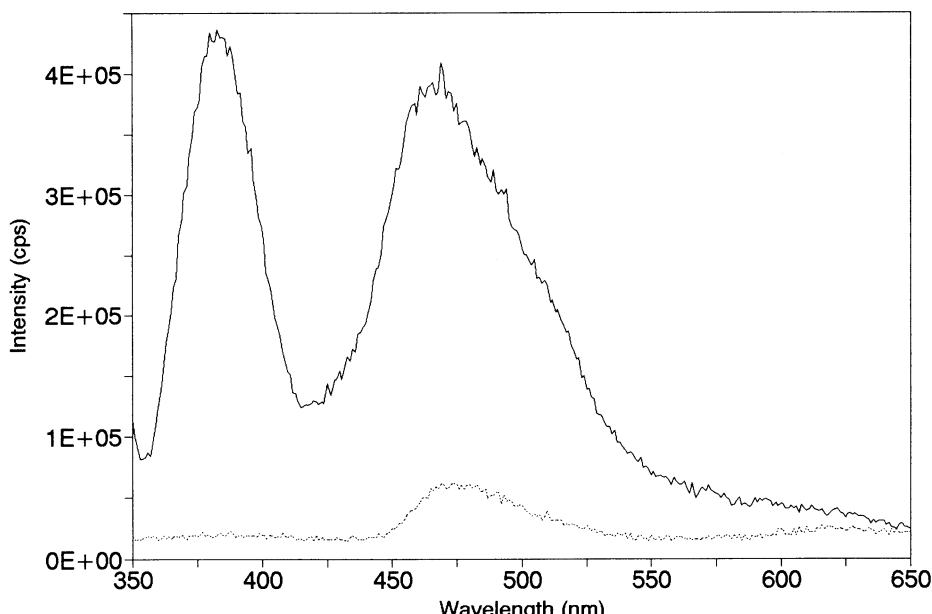


Figure 8. Fluorescence spectra of normal (.....) and tumor (—) stomach tissue, excited at 340 nm.

diarrhea, asthma, pulmonary regurgitation and tricuspid valve stenosis. In these cases about 60 per cent of the total tryptophan is metabolized by the 5-hydroxyindolacetate route¹⁶.

The conversion of tryptophan to the 5-hydroxyindolacetate¹⁶ follows the pathway indicated below:

L- tryptophan → 5-hydroxytryptophan → 5-hydroxytryptamine → 5-hydroxyindolacetate.

Some steps of this route have been detected by chemical ionization mass spectrometry¹⁷.

In Fig.9 we present the fluorescence emission spectra of the products of the above degradation pathway of tryptophan¹⁸, excited at 340 nm and obtained under the same conditions as the tissue spectra.

Comparing the spectra on Fig.9 with the spectra from the tissue, excited at 340 nm, we are inclined to think that the compound most probably responsible for the band at 400 nm in the cancerous mouse tissues is the 5-hydroxytryptamine. However we can not exclude the contribution of all three compounds.

Trying to understand the band centered at 380 nm for the cancerous human stomach tissue, we are led to the conclusion that in this case the substance most probably responsible for this band is the 5-hydroxyindolacetate. This situation can be related to more or less advanced degradation on the tryptophan metabolism. We do not explain yet why the other bands centered at 340 nm and 470 nm exhibit in general higher intensity for the cancerous tissue than for the normal one. These bands are related also to the fluorescence and phosphorescence of tryptophan emission from proteins¹⁹. At this stage more investigation needs to be carried out, specially in order to determine the exact cell population of normal vs. malignant samples being compared. Until then, no final interpretation of the results can be made.

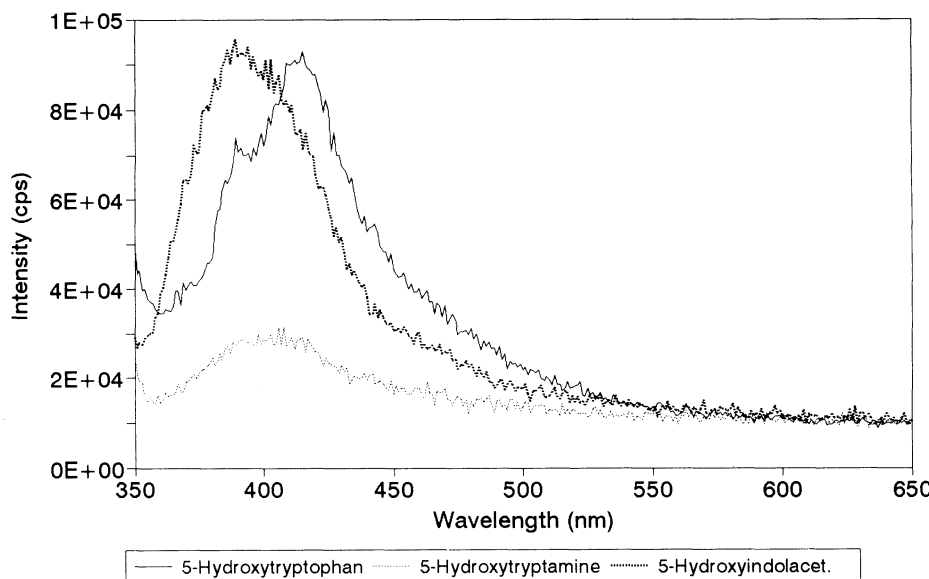


Figure 9. Fluorescence emission spectra of the 5-hydroxytryptophan, 5-hydroxytryptamine and 5-hydroxyindolacetate, excited at 340 nm. All these samples are powder supplied by Sigma-Aldrich Quimica, SA (Alcobendas, Madrid, Spain) and have been used without any treatment.

REFERENCES

1. G. M. Barenboim, A. N. Domanskii and K. K. Turoverov, "Luminescence of Biopolymers and Cells", Plenum Press, New York, NY, London (1969)
2. G. G. Guilbault, "Practical Fluorescence: Theory, Methods and Techniques", Marcel Dekker Inc., New York NY (1973)
3. R. R. Alfano, D. B. Tata, J. Cordero, P. Tomashetsky, F. W. Longo and M. A. Alfano, Laser Fluorescence Spectroscopy from Native Cancerous and Normal Tissues", *IEEE Journal of Quantum Electronics*, vol. QE-20, nº.12(1984)
4. S. Anderson-Engels and B. C. Wilson, *In vivo* Fluorescence in Clinical Oncology: Fundamental and Pratical Issues, *J. Cell Pharmacology*, 3:66-79 (1992)
5. R. R. Alfano, G. C. Tang, A. Pradhan, W. Lam, D. S. J. Choy and E. Opher, Fluorescence Spectra from Cancerous and Normal Human Breast and Lung Tissues", *IEEE Journal of Quantum Electronics*, vol. QE-23, nº.10,1806-1811 (1987)
6. Yuanlog Yang, G. C. Tang, M. Bessler, R. R. Alfano, Optical Spectroscopy Methods to Detect Colon Cancer, *SPIE*, 2135:36-39 (1994)
7. Z. Z. Huang, w. L. Glassman, G. C. Tang, S. Lubicz, R. R. Alfano, Fluorescence Diagnosis of Gynecological Cancerous and Normal Tissues, *SPIE*, 2135:42-45 (1994)
8. M. L. Fraser Monteiro, T. Rézio, Jorge Soares, J. M. G. Martinho, D. Liang, L. Fraser Monteiro, Fluorescence Spectroscopy of Normal and Cancerous Human Stomach Tissue, *SPIE*, 2081:230-236 (1993)
9. I. Weinryb and R. F. Steiner, in "Excitated States of Proteins and Nucleic Acids", Ed. R. Steiner and I. Weinryb, Plenum, New York (1971)
10. D. Creed, the Photophysics and Photochemistry of the Near-UV Absorbing Amino Acids I. Tryptophan and its Simple Derivatives. *Photochem. Photobiology*, 39:537-575 (1984)
11. I. Munro, I. Pecht and L. Stryer, Subnanosecond motion of tryptophan residues in proteins. *Proc. Natl. Acad. Sci. U.S.A.*, 76:56-60 (1979)
12. M. R. Eftink and C. A. Ghiron, Exposure of Tryptophanyl Residues in Proteins. Quantitive Determination by Fluorecence Quenching Studies. *Biochemistry*, 15:672-680 (1976)
13. J. B. A. Ross, K. W. Rousslang and L. Brand, Time-Resolved Fluorecence and Anisotropy Decay of the Tryptophan in Adrenocorticotropin- (1-24). *Biochemistry*, 20:4361-4369 (1981)
14. T. R. Rizzo, Y. D. Park and D. H. Levy, Dispersed Fluorescence of Jet-Cooled Tryptophan: Excited State Conformers and Intramolecular Exciplex Formation, *J. Chem. Physics*, 85:12, 6945-6951 (1986)
15. T. R. Rizzo, Y. D. Park, L. A. Peteanu and D. H. Levy, *J. Chem. Physics*, 84:5, 2534-2541 (1986)
16. H. G. J. Worth and D. H. Curnow, "Metabolic Pathways in Medicine", Ed. E. Arnold, London (1980)
17. M. F. N. Duarte, D. W. Hutchinson and K. R. Jeannings, Chemical Ionization Mass Spectrometry of Derivatives of L-Dopa and L-Tryptophan and their Detection in Tumor Samples, *Org. Mass Spectrometry*, 20:7, 476-478 (1985)
18. Samples obtained from Sigma-Aldrich: 5-hydroxytryptophan cat. nº.H9772; 5-hydroxytryptamine cat. nº. H7752; 5-hydroxyindole-3-acetic acid. cat. nº. H32006
19. Jane M. Vanderkooi, in "Topics in Fluorescence Spectroscopy", vol. 3, Biochemical Applications, Ed. Joseph R. Lakowicz, Plenum, New York (1992)

SOLVENT-DEPENDENT EXCITED STATE PROPERTIES OF PSORALENS

A Model to Their Antiproliferative Action

T. Sa e Melo and C. Sousa

Centro de Quimica Fisica Molecular
Instituto Superior Técnico
1096 Lisboa Codex, Portugal

1. ABSTRACT

The singlet and the triplet excited states parameters of psoralen and derivatives, 4,6,4'-trimethylangelicin and 4,5',8-trimethylpsoralen, show an extreme sensitivity to solvent polarity in dioxane/water mixtures. The internal conversion rate constant is the non-radiative deactivation path dominating their photophysical behaviour. The minimum values of this radiationless rate constant correspond to a more allowed radiative transition and to a longer fluorescence wavelength. Thus, the singlet-triplet energy gap decreases and intersystem crossing is promoted. This work shows that dioxane/water mixtures can display the same solvent-induced changes in the electronic structure of psoralens during solvation as those induced by the biological microenvironment sensed by the drug localization in serum lipoproteins.

2. INTRODUCTION

Psoralen derivatives used in PUVA therapy are potent phototoxic drugs to mammalian cells in culture. Their antiproliferative action is based on the photochemical reactions from their triplet excited states within the microenvironment of the biological medium. The first attempt to correlate the primary photophysical processes with *in vivo* photobiological activity has been made by using the triplet formation quantum yields¹ and the oxygen singlet yields² of psoralens in homogeneous solutions. In the light of our recent studies^{3,4,5}, some of the above correlations are re-examined. The extreme sensitivity to solvation of the singlet and triplet excited state parameters of psoralen and derivatives preclude the validity of a comparative method based on a single solvent determination. In our work, the dioxane/water mixtures have been chosen in order to average the multiple microenvironment of the biological medium^{3,4}. These mixtures have solvent composition properties which are the best

known models of the cell situation. Recently we have shown that psoralen location in the above solvent mixtures determines the amount of their triplet reactive state and thus the photoreactions occurring at cell membrane or proteins^{3,4}.

3. RESULTS

Figure 1 shows the fluorescence quantum yields (Φ_f) the fluorescence lifetimes (τ_f) and the triplet formation quantum yields (Φ_T) observed in dioxane/water mixtures for psoralen (PSO), 4,5',8-trimethylpsoralen (TMP) and 4,6,4'-trimethylangelicin (TMA).

These photophysical parameters were found to be simultaneously comparable to those observed in pure organic solvents (Fig. 1). In fact, the fluorescence lifetimes of the above three compounds are exponentially correlated to an empirical polarity scale E_T ⁵, as shown in Figure 2.

This solvent polarity scale was determined using the triplet yields of PSO in 17 pure organic solvents and in solvent mixtures⁵. This empirical scale is much better correlated with our experimental data Φ_f , τ_f and Φ_T for all analogs and derivatives of psoralens (furocoumarins), than the commonly used $E_T(30)$ of betaine, from Dimroth/Reichardt/Taft⁶.

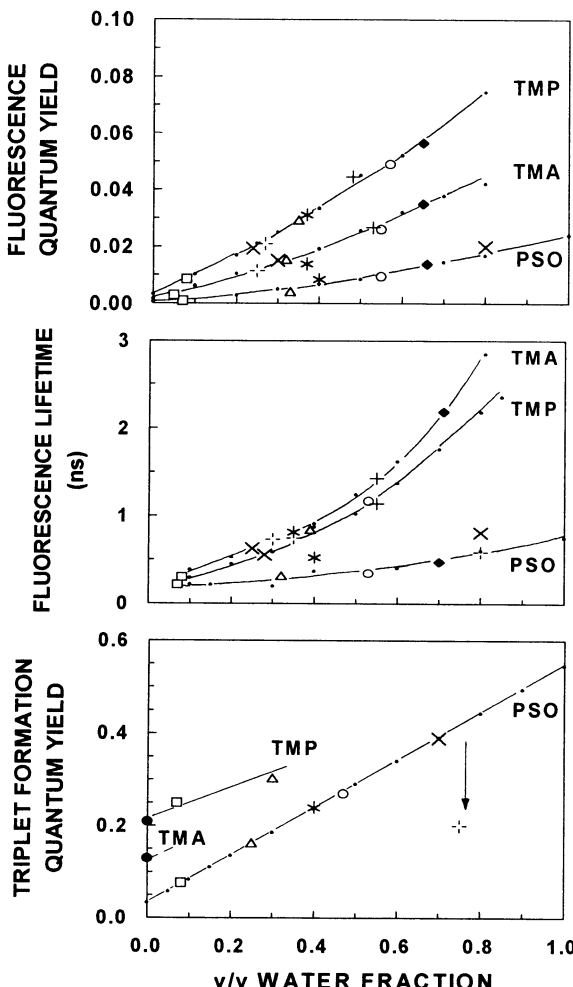


Figure 1. Photophysical parameters (Φ_f , τ_f and Φ_T) of PSO, TMP and TMA in dioxane/water mixtures (—), in pure solvents, (●) benzene, (□) acetonitrile, (Δ) methanol, (○) formamide and (◆) in 50% v/v water in methanol. These photophysical parameters in biological model systems such as (*) dodecyltrimethyl ammonium chloride (DTAC) and (+) sodium dodecyl sulfate (SDS) micelles, (x) dodecyl trimethyl ammonium chloride (DPPC) liposomes and (+) human serum low density lipoproteins are also shown. The lower Φ_T value observed for PSO in LDL as compared to DPPC liposomes, will be attributed to photoreaction inside the LDL particle.

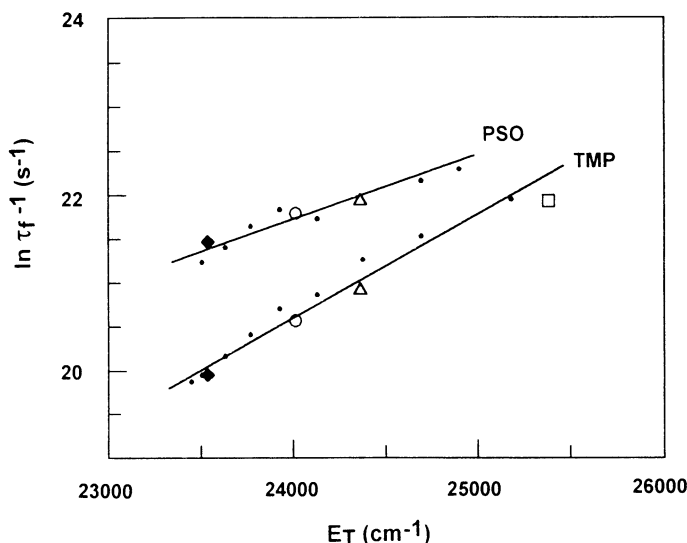


Figure 2. The logarithm of the inverse of the fluorescence lifetimes (sum of radiative and non radiative rate constants) of PSO and TMP in function of the empirical polarity scale E_T of psoralen. Symbols are the same as in Fig.1.

The internal conversion rate constant, k_{ic} , is the nonradiative deactivation path dominating the photophysical behaviour of psoralen's derivatives³. The psoralen (PSO) and derivatives (TMP, TMA) present high k_{ic} values in nonpolar solvents, as determined by the expressions:

$$\text{"Eq." } \Phi_f = k_f \times \tau_f ;$$

$$\text{"Eq." } \Phi_T = k_{isc} \times \tau_f ;$$

$$\text{"Eq." } k_{ic} = \tau_f^{-1} - (k_f + k_{isc})$$

The k_{ic} decrease with increase solvent polarity from dioxane (or benzene) to acetonitrile (or in 7% v/v water in dioxane) and from methanol (or 30% v/v water in dioxane) to 70% v/v water in dioxane (or 50% v/v water in methanol), as shown in Table 1.

The k_{ic} rate constant for 8-methoxysoralen (8MOP) presents the higher value of all derivatives, $10 \times 10^9 \text{ s}^{-1}$ in non polar solvents. The solvents, acetonitrile, methanol and 70% v/v water in dioxane, shown in Table 1, were chosen to describe the present results because they have the specific dielectric properties of the medium where psoralen derivatives are located when incorporated in biological model systems. Fig.1 shows the photophysical parameters (Φ_f , τ_f and Φ_T) of PSO, TMP and TMA in SDS and DTAC micelles, in DPPC liposomes and in human serum low density lipoproteins, LDL. It can be observed that TMP and TMA are incorporated in a nonpolar lipophylic region of LDL particles, in contrast to PSO which is located in a water rich region at the membrane interface of the LDL particles (Fig. 1). As expected, the same dielectric localization was found in DPPC liposomes, i.e., 25% v/v water in dioxane for TMP and TMA, and 80% v/v water in dioxane for PSO (Fig.1). In DTAC cationic micelles, all derivatives are located in a dielectric medium analog to 40% v/v water in dioxane (Fig.1). In SDS anionic micelles, the TMP and TMA derivatives are in a medium-like 55% v/v water in dioxane. The same location in SDS micelles has already been found for 5-methoxysoralen (5MOP)³.

Table 1. The internal conversion rate constants (s^{-1}) of psoralen and derivatives

	TMA	TMP	PSO
Dioxan	3.7×10^9 (a)	6.8×10^9 (c)	8.4×10^9
Acetonitrile	2.4×10^9 (b)	2.7×10^9 (c)	4.3×10^9
Methanol	nd	0.9×10^9 (d)	2.8×10^9
70% v/v H ₂ O:Dx	nd	nd	1.2×10^9

(a) Assuming the same value of $\Phi_T = 0.13$ in dioxane and in benzene (Knox et al. 1988⁷), as experimentally observed for psoralen, in both solvents⁵.

(b) For an estimated value of $\Phi_T = 0.15$ in acetonitrile (see Fig.1).

(c) Using the relative Φ_T values from Lim et al. 1982⁸ and assuming the same value of $\Phi_T = 0.21$ in dioxane as in benzene¹¹.

(d) Assuming $\varepsilon_T = 10500 M^{-1}cm^{-1}$ and thus a $\Phi_T = 0.30$ in methanol, a greater value than the previously reported by Beumont et al. 1979⁹.

4. DISCUSSION

The high radiationless transition between S_1 and the ground state S_0 , and its great dependence on solvent composition, is due to the relative position of the two first singlet excited states (S_1 and S_2) in these carbonyl compounds (Table 1). In non-polar solvents, the $S_1(\Pi\Pi^*)$ and the $S_2(n\Pi^*)$ are isoenergetics showing the maximum value for the k_{ic} rate constants and the minimum, Φ_f and Φ_T , quantum yields. An increase in the solvent polarity corresponds to longer fluorescence wavelengths and thus to a decrease in the $\Delta E(S_1-S_0)$ energy gap. An increase Φ_f and Φ_T quantum yields due to the decreasing values of the k_{ic} rate constants is observed (Table 1). At long emission wavelength and high solvent polarity, the singlet-triplet energy gap, $\Delta E(S_1-T_n)$, decreases, and the intersystem crossing is promoted. Since the fluorescence quantum yields for all derivatives are very low, both in polar and non-polar solvents (see Fig.1), the minimum and the maximum solvent dependent values of k_{ic} rate constants determine respectively the maximum and the minimum values of the triplet reactive state amounts. Since the photophysical parameters present the same behaviour in the above solvent mixtures, they can be used to model the molecular mechanisms of photoreactions from the triplet state. Indeed, in the absence of any physical and chemical quenching, the fluorescence lifetimes and the triplet formation quantum yields of psoralens must behave in the same way, i.e., showing the same shape as the fluorescence quantum yields in dioxane/water mixtures (see Fig.1). In contrast with the observed monotonic increase of Φ_f , τ_f and Φ_T values for PSO, TMP and TMA (Fig.1), the 5MOP shows a bell-shaped curve for the above three photophysical parameters in dioxane/water mixtures³. However, 5MOP as TMP and TMA are found to be located in the same non-polar lipophylic region of the LDL particle. On the contrary, PSO is located in a water rich region of the LDL interface, analogous to a dielectric medium like 80% v/v water in dioxane. These results have important consequences in the molecular mechanism of the antiproliferative action of psoralens.

5. CONCLUSIONS

Dioxane/water mixtures can display the same solvent-induced changes in the electronic structure of psoralens during solvation as those induced by the incorporated drug in biological media. Since the photophysical parameters, Φ_f , τ_f and Φ_T , present the same behaviour in these solvent mixtures, they can be used to model the molecular mechanisms of photoreactions from the triplet state. We believe that this phenomenon is not particular to

psoralens but rather more general and not dependent on the specific hydrogen bonding or other special interactions. The importance of the hydrophobic environment is underlined by the kinetic results in the presence of micelles, liposomes and human serum low density lipoproteins (Fig. 1 and Table 1). With the present results we conclude that PSO is able to photoreact in the interface of the cell membranes by an oxygen dependent photodynamic mechanism (type II). In fact, PSO have already been described to be more erythemogenic than the other derivatives. In contrast, 5MOP, TMP and TMA, are able to induce oxygen independent photoreactions producing photoadducts inside the cytoplasmic organelles of the cell, as observed *in vivo*¹⁰.

6. ACKNOWLEDGMENTS

This work was supported by JNICT, with a PhD grant (nº 857/94) for the graduate student (CS) and by the Instituto Superior Técnico (CQFM) funds.

This work is a long term cooperative study between the author (TSM) and INSERM unit 312 in Paris. We are grateful to Dr. R. Santus and M. Bazin for the flash photolysis facilities and valuable scientific discussions. Thanks are due to Dr. Maçanita for his interest and discussions about the accuracy of the SPC measurements. Moreover, we wish to thank Dra. A.T. Reis e Sousa and Dr. J.M.G. Martinho for technical assistance, scientific advice and facilities for the SPC equipment. Trimethylangelicin was kindly supplied by Dr. Dall'Acqua.

7. REFERENCES

1. T.Sá e Melo, D.Averbeck, R.Bensasson, E.Land and C.Salet (1979) Some furocoumarins and analogs:comparison of triplet properties in solution with photobiological activities in yeast. Photochem.Photobiol. 30:645-651.
2. P.Joshi and M.Pathak (1983) Production of singlet oxygen and superoxide radicals by psoralens and their biological significance, Biochem. Biophys. Research Comm. 638-646.
3. T.Sá e Melo, A.Maçanita, M.Prieto, M.Bazin, J.Ronfard-Haret and R.Santus (1988) Photophysical behaviour of 5-methoxysoralen in dioxan-water mixtures, Photochem.Photobiol. 48:429-437.
4. T.Sá e Melo, L.Ribeiro, A.Maçanita, M.Bazin, J.Ronfard-Haret and R.Santus (1990) Photochemical processes of psoralen and derivatives (8MOP and 5MOP) in biological systems, Int.Conf. on Luminescence.
5. T.Sá e Melo, M.Bazin, J.Ronfard-Haret and R.Santus (1993) Quantification of the solvent effects on the triplet quantum yield of psoralen by the linear solvation energy relationship, Photochem.Photobiol. 58:19-27.
6. C.Reichardt (1990) Solvents and solvent effects in Organic Chemistry, VCH Verlag, 2nd ed. Weinheim, Germany.
7. C.Knox, E.Land and T.Truscott (1988) Triplet state properties and triplet-state-oxygen interactions of some linear and angular furocoumarins, J.Photochem.Photobiol. 1:315-321.
8. T.Lai, B.Lim and E.Lim (1982) Photophysical properties of biologically important molecules related to proximity effects:Psoralens, J.Am.Chem.Soc. 104:7631-7635.
9. P.Beaumont, B.Parsons, G.Phillips and J.Allen (1979) A laser flash photo-lysis study of the reactivities of the triplet states of 8-methoxysoralen and 4,5',8-trimethylpsoralen with nucleic acid bases in solution, Biochem: Biophys. Acta 562: 214-221.
10. F.Bordin, C.Marzano, C.Gatto, F.Carlassare, F.Rodighiero, F.Baccichetti (1994) 4,6,4'-Trimethylangelicin induces interstrand cross-links in mammalian cell DNA, J.Photochem.Photobiol.B 26:197-201.
11. C.Knox, E.Land and T.Truscott (1986) Singlet oxygen generation by furocoumarin triplet states. Linear furocoumarins (psoralens), Photochem.Photobiol. 43, 359-363.

FLUORESCENT PROBES IN BREAST TUMOR

Ayse Zehra Aroguz and Nezih Hekim

Istanbul University
Faculty of Engineering
Chemistry Department
Avciilar Campus
Istanbul 34850
Turkey

SUMMARY

In our study, we developed a new method for fluorescence probes which is novel, inexpensive and renders useful information for prognosis on tumor tissues. It could be used in place of the receptors analysis. Comparative studies applying fluorescence probe techniques to the determination of Intracytoplasmic Immunoglobulin (Ic-IgG) have shown to generally provide more precise results and to be time saving as compared to receptors and DNA analysis. The use of fluorescence probe techniques for the measuring of Intra cytoplasmic Immunoglobulin (Ic-IgG) is well established for breast tumors. Ic-IgG has been determined in mammary tumor cells with fluorescein isothiocyanate (FTIC)labeled anti human IgG using the flow cytometer. Ic-IgG content provides additional prognostic information within both the estrogen receptor (ER) positive patient or estrogen receptor (ER) negative patient groups. There is a correlation between (ER) positive or (ER) negative patients and diploid or aneuploid patients.

INTRODUCTION

Breast cancer is the most common malignant disease in women. During recent years, flow cytometry studies of DNA and receptors have frequently been used to characterize cell kinetics in breast cancer in relation to clinical and histopathologic parameters. However, the relation to therapeutic response and prognosis has been studied to a lesser extent.

Nonspecific interactions of immunoglobulins (IgG) with estrogen receptors have been reported¹. It has been investigated whether high levels of (IgG) in the cytosol truly represent negative hormone receptor values and whether the (IgG) level can be correlated with response to therapy². It has also been shown that (IgG) binding to estrogen receptors prevents estrogen binding to the receptors³.

METHODS

Preparation of the Sample

The samples were prepared for Ic-IgG analysis as follows:

Measurements of Ic-IgG in the cell were made from fresh tissue. Tumor tissues were stored 20°C until analysis and IgG flow cytometer studies were performed. The tissue was brought to room temperature and minced in trypsin solution containing phosphate buffer solution (PBS) by mechanical means. The samples were incubated for 25 minutes at 37°C. Then, they were centrifuged at 1500 rpm for 10 minutes and the supernatant fluid was removed. The samples were washed three times, using lysing buffer solution with vigorous vortexing every time. They were aspirated and the supernatant solution was discarded. Finally, the suspension was filtered through a nylon wool and charcoal with goat anti serum to human IgG and again incubated for 15 minutes at 25°C. The samples were analyzed using a Coulter Profile II flow cytometer with a 488nm argon laser for excitation.

RESULTS AND DISCUSSION

The aim of the present investigation is Ic-IgG analysis by means of flow cytometry and it has been used to predict the progression of solid tumors, including breast cancer. This technique does not require specialized technology or processing. It gives rapid results and may give useful information on tumor tissue.

Flow cytometry is a modern method of studying cells. The measurement in DNA analysis is based on the ability of certain fluorescent dyes to bind specifically to DNA under appropriate conditions. This technique has shown that the cancer cells often have abnormal DNA content (DNA "aneuploidy") in comparison to normal (diploid) cells. Aneuploidy is believed to reflect the numerical or structural chromosomal aberrations present in neoplastic cells. Flow cytometry has the potential to play an important role in the study of breast tumors. From the current data, it is clear that the determination of Ic-IgG content provides additional prognostic information within both the ER+ and ER- patient groups. Besides that, this technique has been used successfully for simultaneous measurement of DNA and Ic-IgG.

Fluorescence is measured by using fluorochromes. To measure DNA content propidium iodide (PI) is used; it gives the red fluorescence. The flow cytometer has different filters. Filter blocks are used to separate the various colors for measurements. One of the filter blocks is used to separate the fluorescent light from two different dyes and direct the light to the fluorescence 1 (FL1) and Oluorescence 2 (FL2) units for measurements. To measure the red fluorescence, the red fluorescence 3 (FL3) unit is used.

The results are shown in Figures 1,2,3 for aneuploid patients and in Figures 4,5,6 for diploid patients. On the other hand, significant correlation was found between Ic-IgG level and the patients being diploid or aneuploid.

Figure 1a is a plot of the red fluorescence peak (i.e. highest level) values (FL3P) in the ordinate, against the red fluorescence (FL3) expressed as a percentage of the overall red fluorescence in the abscissa. In this figure, the bitmap show the population of the cells colored with Piopidium iodide (PI).

Fluorescence can be measured in two ways. These are linear fluorescence and logarithmic fluorescence. For surface markers the use of logarithmic fluorescence is preferred since the fluorescence of the cells is quite variable. Linear fluorescence is measured with 256 fluorescent channels while logarithmic fluorescence is measured with 1023 channels.

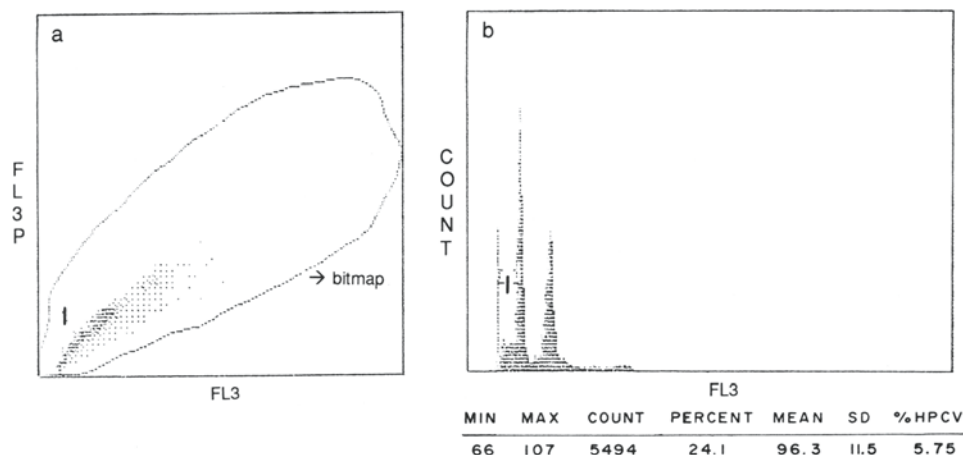


Figure 1. The measure of red fluorescence of the cells for the aneuploid patient.

Figure 1b: The relationship between the number of the counted cells and the measure of the red fluorescence 3(FL3) for the aneuploid patients. The values at the bottom of Figure 1b show statistical variation.

Minimum (min) : Number of the channel where the marker begins.

Maximum (max) : Number of the channel where the markers ends.

Count : Number of the cells or particles counted in the markers.

Percentage : Percentage of the cells counted in the marker compared to the total number of the cells.

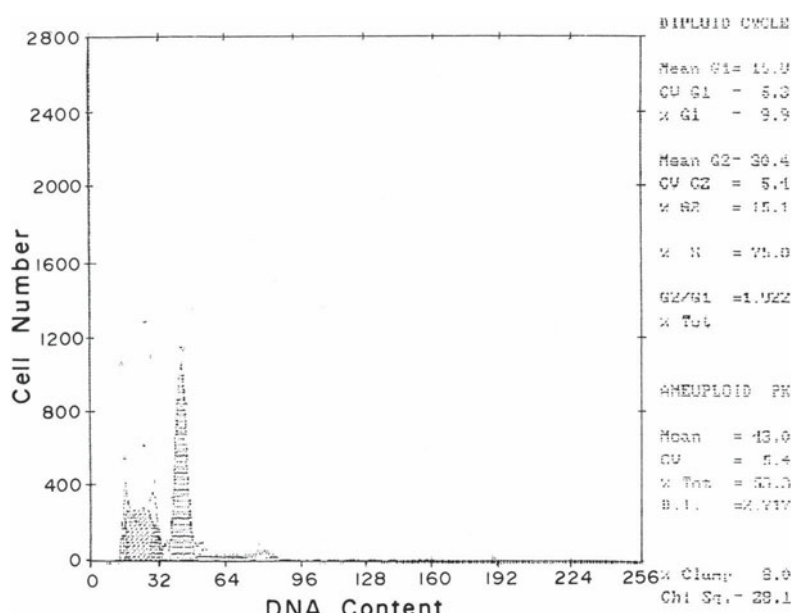


Figure 2. DNA histogram from the aneuploid patient related to the cell number.

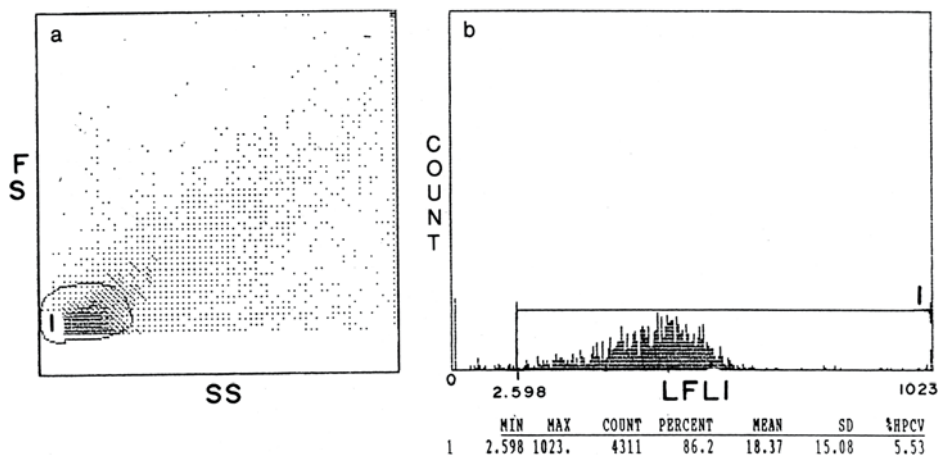


Figure 3. a: The relationship between the forward scatter (FS) and the side scatter (SS), to evaluate the size and granularity of the cell for the aneuploid patient. b: The histogram of the counted cells on the logarithmic scale for the aneuploid patients.

Mean : Mean channel number of histogram.

SD = Standard deviation

$$CV = \frac{\text{Standard deviation}}{\text{Mean channel number}} \times 100$$

Mean Channel number

%HPCV = CV calculated according to SD and mean channel number at mid height.

Figure 2 shows DNA content with respect to the cell number. Flow cytometric DNA histograms from the patients with breast cancer are shown in this figure. Figure 5 shows the DNA content with the normal (diploid) cells related to the cell number. Among the malignant

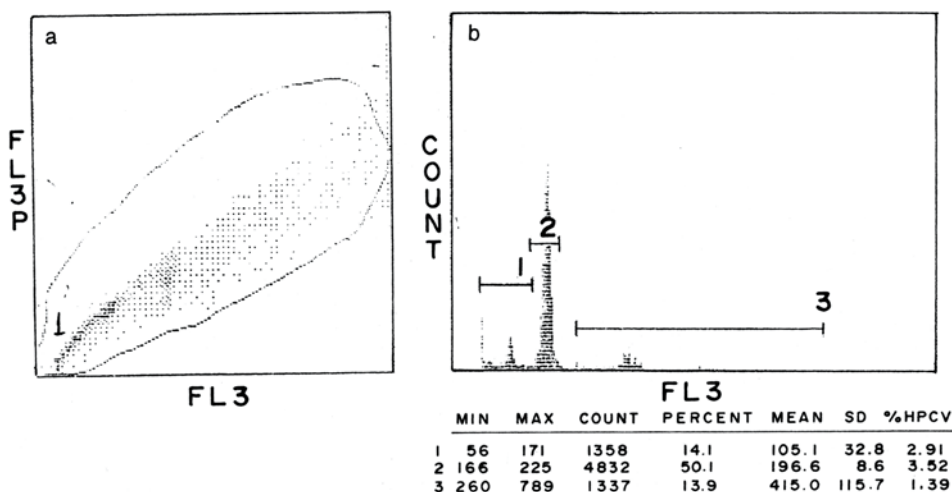


Figure 4. a: The measure of the red fluorescence of the cells for the diploid patient. b: The relationship between the number of the counted cells and the measure of the red fluorescence for the diploid patients.

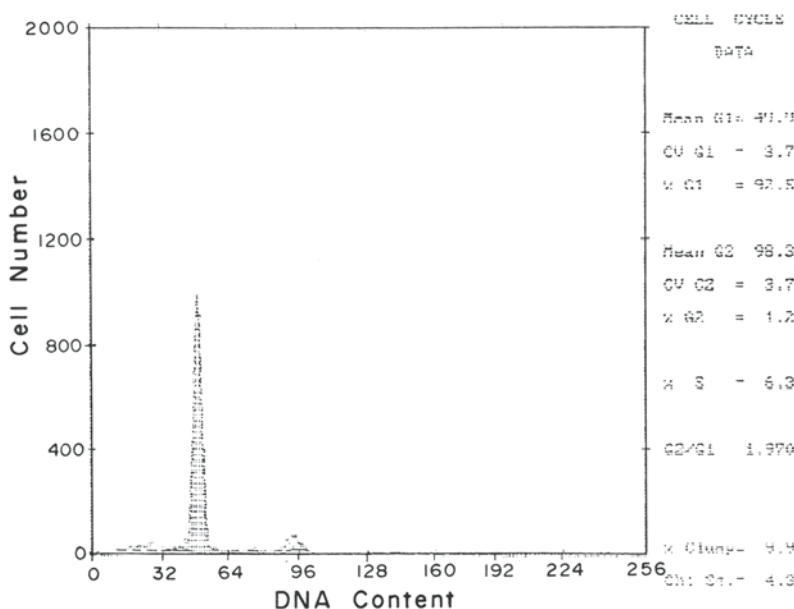


Figure 5. DNA histogram from the diploid related to the cel number.

breast tumors a good correlation has been observed between relative DNA content (diploid versus aneuploid) and the grade of differentiation. Abnormal DNA content (aneuploidy) is characteristic of the majority of breast carcinomas.

There is a correlation of breast tumor estrogen receptor (ER) positivity with normal DNA content and low proliferative activity and of estrogen receptor (ER) negativity with aneuploidy and increased proliferative activity.

To plot the Forward Scatter (FS) and Side Scatter (SS) on the same cytogram enables us to see the cells or particles in groups on the screen. Cells or particles small in size and granularity fall to the lower left part of cytogram, bigger and more granular particles or cells are seen higher and further to the right part of the cytogram, respectively.

Figure 3a shows the relationship between FS and SS for the aneuploid patient and Figure 6a shows this relationship for the diploid patient. The histogram of the counted cells on a logarithmic scale is seen in Figure 3b for the aneuploid and Figure 6b for diploid patients. The minimum value of the x axis is 2.598 and the maximum value is 1023. The number of cells counted in the markers is 4311 for aneuploid and 804 for diploid patients. The percentage of the cells counted in the marker to the total number of the cells is 86.2% for aneuploid and 47.2% for diploid patients. The mean channel number of histogram for aneuploid and diploid patient is 18.37 and 14.72, respectively.

Figure 4a and 4b show similar results to the Figure 1a and 1 b of the diploid patient.

By the use of Ic-IgG analysis, as shown from the figures it is possible to correlate to ER+ and ER- patients. In aneuploid patients, the Ic-IgG levels are greater than 86% and in diploid patients Ic-IgG levels were approximately obtained between 47%-63%.

We showed that negative values of intracytoplasmic IgG can reflect positive values of estrogen receptor level and the positive values of Ic-IgG shows usually negative value of ER.

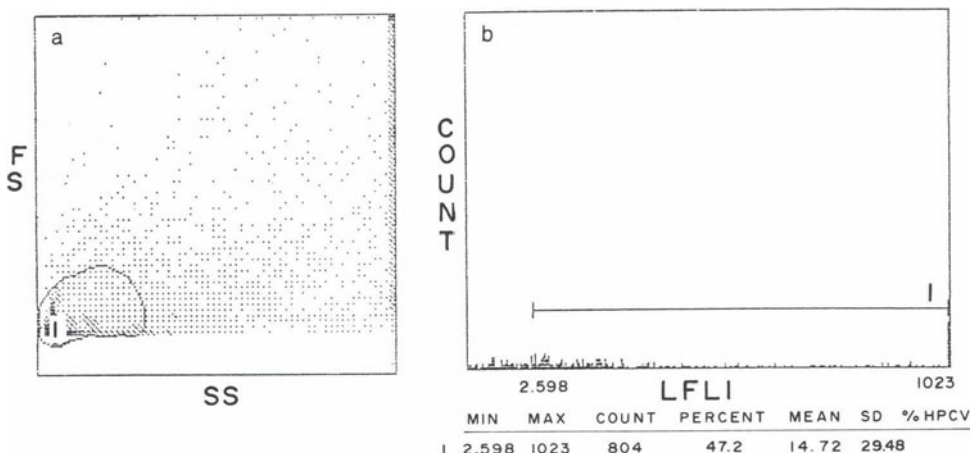


Figure 6. a: The relationship between the forward scatter (FS) and the side scatter (SS) to see the size and granularity of the cell of the diploid patient. b: the histogram of the counted cells on the logarithmic scale for the diploid patient.

This investigation shows fluorescence probes which are new, inexpensive and give information to be used in the place of the receptors. Receptors are more expensive than fluorescence probes and the experiments with receptors take more time than this method.

Comparative studies applying both Immunoassay techniques to the determination of IgG have generally shown to provide more precise results than techniques measuring estrogen receptors. This technique has been used successfully for simultaneous measurement IgG and tumor associated antigens.

This investigation is in a preliminary stage. We hope that fluorescence probes using the flow cytometer technique will be a convenient method in an increasing number of cases.

The following list summarizes the signals available to the operator and symbols used in referring to that signal.

FS : Forward angle light scatter.

SS : Side scatter

FL1 : Fluorescence 1

FL2 : Fluorescence 2

FL3 : Fluorescence 3

LFL1 : Log fluorescence 1

LFL2 : Log fluorescence 2

FL3P : Peak fluorescence 3

REFERENCES

1. N. Hekim and P.W. Jungblut; Z. Physiol. Chem. 607-611, May 1983.
2. S. Winstein, J. Tabachnic and I. Young; A.J.C.P 364-366, 83, 3, 1985
3. N. Hekim and P.W. Jungblut; Z. Physiol. Chem. 769-755, June 1983.

APPENDIX FOR CLARIFICATION OF FIGURES

FL3 is a parameter to measure the red fluorescence emitted between 575-610 nm, as the cell passes through the argon laser beam. FL3P (FL3P) represents the peak values at maximum level of FL3. Fig 1a is a plot of FL3P (ordinate) against FL3 (Abscissa). If it is considered that the plots are three-dimensional, then there are a number of nuclei at the same fluorescence level behind each point of the plot. The histogram of the FL3P against the FL3 parameters in DNA analysis prevents the confusion between the data from the individual nuclei and those from the nuclei that are stuck to each other forming aggregates.

USE OF FLUORESCENCE *IN SITU* HYBRIDIZATION FOR MAPPING AND ORDERING YAC CLONES FROM CHROMOSOMAL REGIONS WITH SUSPECTED TUMOR-SUPPRESSOR ACTIVITY

V. Macheraki,^{1,2} V. Orphanos,¹ S. Kamakari,³ M. Kokkinaki,³ G. Stephanou,² N. Demopoulos,² G. M. Maniatis,¹ N. Moschonas,³ and D. H. Spathas¹

¹ Laboratory of General Biology
Medical School

² Department of Biology
University of Patras, Greece

³ Institute of Molecular Biology and Biotechnology
Foundation for Research and Technology
Crete, Greece

INTRODUCTION

Deletions or loss of heterozygosity in certain regions of the long arms of human chromosomes 6 and 10 have been reported over the last few years in several types of malignancies; more specifically, region 6q16.3-q21 is frequently deleted in patients with acute lymphoblastic leukemia¹ (ALL) and the same region, as well as 6q25-qter are often deleted in patients with Non-Hodgkins lymphoma¹; loss of heterozygosity in both these regions has also, been documented in breast² and ovarian³ cancer. In addition, loss of heterozygosity within the 10q23-24 region has been reported in patients with prostate cancer⁴ and patients with glioblastoma multiforme⁵. These observations suggest the presence of tumor-suppressor gene(s) in these regions and, therefore, detailed physical mapping may lead to the identification and subsequent isolation of such genes.

To this end, several YAC clones were isolated from the ICI library using STSs designed from the analysis of microsatellite markers for chromosomes 6q and 10q. Single and double colour fluorescence *in situ* hybridization (FISH) have been employed to map these clones to the corresponding chromosomal arms, as well as to define their relative order. Data are presented for 7 loci from 6q and 4 loci from 10q. Our study contributes to the

physical mapping of the selected regions and may eventually lead, in conjunction with other molecular studies, to the isolation of gene(s) with tumor-suppressor activity.

METHODS

YAC clones for 6q and 10q were isolated from the ICI library⁶ using STSs designed from the analysis of microsatellite markers, mapped to these regions. For mapping these clones, total yeast DNA or Alu PCR products were nick-translated using either biotin-dUTP or digoxigenin-dUTP. Hybridisation to human metaphase chromosomes was carried out with 100-150ng YAC DNA in 20pl hybridisation mixture (50% formamide, 4xSSC, 2mg/ml BSA, 20% dextran sulphate and 20-fold excess of cot 1 DNA) at 37°C for 16-18hrs. For single colour FISH, signals were visualised using avidin FITC and biotinylated goat anti-avidin and again avidin-FITC for biotinylated probes and anti-digoxigenin (in mouse), anti-mouse IgG-FITC (in rabbit) and anti-rabbit IgG-FITC (in goat) for digoxigenated probes. For double colour FISH, biotinylated or digoxigenated probes were visualized as described above with the addition of Texas Red as the alternative fluorochrome. Chromosomes were stained with DAPI that gives a Q-banding pattern and propidium iodide as a counterstain for FITC detection. Signals on metaphase chromosomes were viewed using either a Leitz Diaplan or a Zeiss Standard microscope, equipped with suitable filters for fluorescence and photographed with 400 ASA Kodak Gold film.

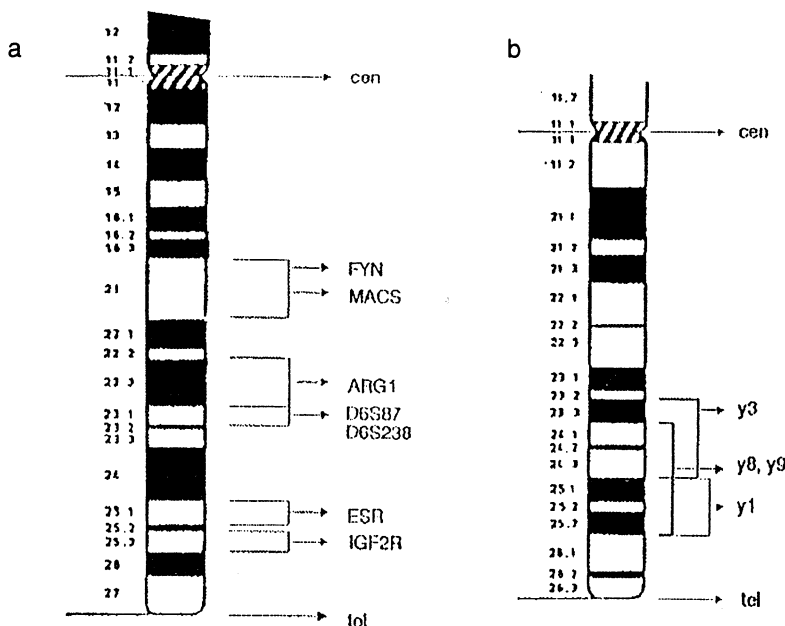


Figure 1. a: Ideogram of 6q with the relative order of the mapped loci by double colour FISH. b: Ideogram of 10q with the mapped loci by single colour FISH.

RESULTS AND DISCUSSION

Chromosome 6

Seven different YAC clones were mapped to 6q. From these, five clones, namely ARG1, FYN, MACS, ESR and IGF2R, include the corresponding genes, while the other two clones represent anonymous microsatellite markers. FYN and MACS map to 6q21, ARG1, D6S87 and D6S238 map to 6q22.3 - q23.1 and ESR and IGF2R map to 6q25. These results are in agreement with previous data^{7,8}. The relative order of these YACs, cen-FYN-MACS-ARG1-D6S87-D6S238-ESR-IGF2R-tel (fig. 1a) was determined by double colour FISH.

Chromosome 10

We developed novel chromosome-10 microsatellite genetic markers and used them to screen by PCR the ICI YAC library. Positive YACs are employed in FISH experiments on metaphase chromosome spreads. Presently, three sets of YACs, each one corresponding to a different marker, have been mapped to 10q. One set of four YACs, represented by y3, contains marker gata 1 and maps to 10q23.3-q24; Another set of three YACs represented by y8 and y9 contains marker gata 4 and maps to 10q24.-25, while the third set of five YACs, represented by y1, contains marker gata 2 and maps also to 10q24-25 (Fig. 1b).

Genetic mapping of the corresponding microsatellites for chromosome 6 has been performed as described elsewhere⁷ while for chromosome 10 the CRI-MAP software was used. The determined loci positions were in agreement with our cytogenetic data for both chromosomes. These results should be useful tools for the construction of an integrated physical and genetic map of the distal part of 6q and 10q. These maps will form a framework for the isolation, characterization and mapping of novel transcripts of genes in order to investigate their role in malignancy and tumour progression.

REFERENCES

1. Menasce L.P., Orphanos V. et al. (1994): Common region of deletion on the long arm of chrom.6 in Non-Hodgkins Lymphoma and ALL. *Genes, Chrom. Cancer* 10: 286-288.
2. Orphanos V. et al. (1995): Proximal 6q, a region showing allele loss in primary breast cancer. *Br.J.Cancer* 71: 290-293.
3. Orphanos V. et al (1995): Allelic imbalance of chromosome 6q in ovarian tumours. *Br.J.Cancer* 71: 66-669.
4. Arps S. et al. (1993): Cytogenetic survey of 32 cancers of the prostate. *Cancer Genet.Cytogenet.* 60: 93-99.
5. Fults D. and Pedone C. (1993): Deletion mapping of the long arm of chromosome 10 in glioblastoma multiforme. *Genes.Chromos. and Cancer* 7: 173-177.
6. Anand R. et al. (1990): A 3.5 genome equivalent multi-access YAC library: Construction, characterization, screening and storage. *Nucleic Acid Res.* 18: 1951-56.
7. Volz A. et al. (1994): Report of the Second International Workshop on Human Chromosome 6. *Genomics* 21: 464-472.
8. Menasce L.P. et al. (1993): Localization of the estrogen receptor locus (ESR) to chromosome 6q25.1 by FISH and a simple post-FISH banding technique. *Genomics*, 17: 263-265.

PHOTOCHEMICAL AND PHOTOPHYSICAL STUDIES OF AN ANTHOCYANIN

Fast Excited-State Proton Transfer from 4-Methyl 7-Hydroxyflavylium Chloride to Water

Isabel Abreu,¹ J. C. Lima,¹ M. Helena Santos,^{1,2} Raymond Brouillard,³ and António L. Maçanita^{1,4}

¹ Instituto de Technologia Química e Biológica
Apt. 127
2780 Oeiras, Portugal

² Departamento de Química
Facultade de Ciencias e Tecnologia
UNL, Quinta da Torre
2825 Monte de Caparica, Portugal

³ Laboratoire de Chimie des Polyphénols
associé au CNRS
Institut de Chimie
Université Louis Pasteur
Strasbourg, France

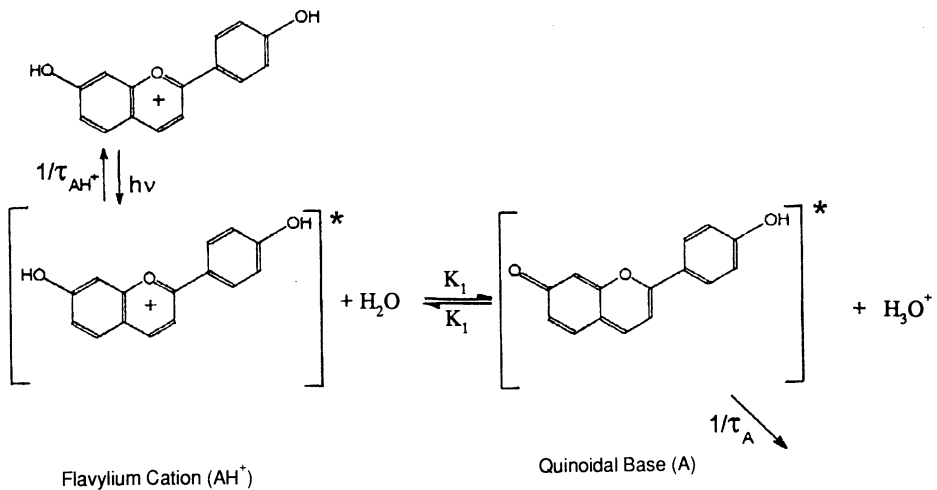
⁴ Instituto Superior Técnico
Av. Roviacos Pals
1096 Lisboa codex, Portugal

Anthocyanins are plant pigments which constitute the major source of colour in flowers and fruits. Their abundance permits us to consider them as the most important candidates to substitute for synthetic dyes as food additives. Namely, they are part of a normal human diet in the amount of ca. 1g per day. As they generally suppress active oxygen species and because many toxic injuries and diseases, including cancer, have been found in recent years to be linked with active oxygen-mediated disturbances, further investigations should be performed on the suppression of these injurious effects by natural anthocyanins encountered in normal diets.

Assuming that anthocyanins (fluorescent molecules) are antioxidants in the ground-state, pH dependence, and other molecular environment effects, and fluorescence (excited-state) were studied.

In this work, one and two-dimensional ¹H NMR techniques were employed to establish the ground-state equilibria of the synthetic anthocyanin, 4-methyl 7-hydroxy-

flavylium chloride, and fluorescence techniques (steady-state and time-resolved) were employed to follow the excited-state proton transfer reaction in this compound (scheme 1).



SELECTIVITY AND LOCALIZATION OF ANTHRACYCLINES IN CARDIAC-MUSCLE AND NON-MUSCLE CELLS RELEVANCE TO MULTIDRUG RESISTANCE

T. J. Lampidis, D. Kolonias, N. Savaraj,¹ M. Israel,² and W. Priebe³

Department of Cell Biol
University of Miami
Miami, Florida 33143

¹Hem/Onc.,VA
Miami, Florida

²Department of Pharmacol.
University of Tennessee
Memphis, Tennessee

³Clin. Invest.
University Texas M.D. Anderson Cancer Ctr.
Houston, Texas

Cardiac-muscle (CM) vs cardiac non-muscle (NM) cells (fibroblasts) have been shown to preferentially accumulate positively-charged anthracyclines (AT) (1), xanthene dyes (2), and other organic cations (3). It was not clear however, how the chemical charge and lipophilicity of AT affected uptake and intracellular localization in these cells which have been further characterized as being pgp multi-drug resistant negative (MDR -) for cardiac-muscle cells and MDR+for cardiac fibroblast.

DRUG ACCUMULATION AND LOCALIZATION

After 30 min incubation with a number of well-matched AT pairs in which either lipophilicity or positive charge at the amino site of the molecule has been altered (4,5), i.e. protonatable analogs in the order of increasing lipophilicity, ADR < AD 288 < AD198 and their respective non-protonatable analogs, WP 159, WP546 and WP549 we find that : (1) ADR accumulates preferentially in the nucleus of CM vs NM cells while WP159 distributes similarly but less selectively than ADR; (2) AD288 but not WP546, stains the nucleus of CM cells preferentially; (3) AD 198 and WP549 stain mitochondria as well as other parts of the

cytoplasm but not the nucleus; accumulation of WP549 is slightly favored in NM vs CM cells and equal for AD198 in these cell types.

DIFFERENTIAL CYTOTOXICITY IN MDR+VS MDR- CELL LINES

To further characterize MDR we used matched pairs of MDR+ and MDR- cell lines from murine (Friend leukemia cells) (6) and human (CEM) (7) sources to test for differential cytotoxicity of each of the above anthracycline analogs. We find that the resistance ratios for both pairs of MDR+ and MDR- cell lines are in the following order: ADR > AD288 > WP546 = AD198 = WP549.

Our conclusions, for these AT are: (I) the ability for the amino group to be protonated and thus become positively-charged appears to be a factor for selective accumulation and cytotoxicity in (MDR-) vs (MDR+) cells, (II) the degree of lipophilicity can reduce or completely overcome MDR selectivity and the nuclear localization of positively-charged AT. These results may have relevance for mechanisms responsible for AT cardiotoxicity as well as those involved with MDR recognition. Supported by NIH grant #CA37109 and a national VA grant.

REFERENCES

1. Lampidis, T.J., Johnson, L.V., and Israel, M. Effects of adriamycin on rat cells in culture. Increased accumulation and nucleoli fragmentation in cardiac muscle vs. non-muscle cells. *J. Mol. Cell. Cardiol.* 13: 913-924, 1981.
2. Summerhayes, I.C., Lampidis, T.J., Bernal, S.D., Shepherd, E.L., and Chen, L.B. Unusual retention of Rhodamine 123 by mitochondria in muscle and carcinoma cells. *Natl. Acad. Sci. USA* 79: 5292-5296, 1982.
3. Lampidis, T.J., Salet, C., Morcao, G., and Chen, L.B. Comparative effects of the mitochondrial probe Rhodamine 123 and related analogs of the function and viability of pulsating myocardial cells in culture. *Agents and Actions* 14: 751-757, 1984.
4. Israel, M., Seshadri, R., Koseki, Y., Sweatman, T.W., Idriss, O.M., Amelioration of adriamycin toxicity through modification of drug-DNA binding properties. *Cancer Treatment Reviews.* 14(3-4): 163-7, 1987 Dec.
5. Priebe, W. Anthracycline Antibiotics. Novel Analogues, Methods of Delivery and Mechanisms of Action. (1995) American Chemical Society, Washington D.C.
6. Tapiero, h., Munck, J.N., Benoun, M. Fourcade, A., and Lampidis, T.J. Cross resistance to rhodamine 123 in adriamycin and daupomycin resistant Friend leukemia cell variants. *Cancer Res.* 44: 5544-5549, 1984.
7. Kartner, N., Evernden-Porelle, D., Bradley, G., and Ling, V. Detection of P-glycoproteins in multidrug-resistant cell lines by monoclonal antibodies. *Nature* 316: 820-823. 1985.

INDEX

- Absorbance spectra, 43
chromophores, in strongly scattering media, 51, 78
shifts, 13
- Absorption coefficient, 42, 50
at every voxel, 47
map, 50
parameters, 47
simultaneous measurement with scattering coefficient, 44
of tissue, 31
two different values of, 48
- Acceptor
bleaching, 54
donor fluorescence quenching by, 54
photochemical destruction, 54
photodestruction, 54
release of the quenching by, 54
- Acetylcholine-like effects, 155
- Acridine orange (AO)
green fluorescence, 157
red fluorescence, 157
- Acidosis, intracellular, 110
- Acinar cells, 150
calcium application, intracellular 155
carcinoma, pancreatic, 151, 155
junctional coupling, 151, 155
heterogeneity, 153, 155
markers, 151
populations, 153
- Acoustic frequencies, 3
- Adenosine diphosphate state 4/3 transition, 26
- Adhesion
consensus sequence, 141
molecules, 147
- Adhesion stabilization
of blood-borne cancer cells, 8, 137
lag time (ASLT), 8, 141, 142, 143, 147
- Adolezesin, 165, 169
- Adriamycin (ADR), 12, 159, 170, 232
-treated (grown) cells, 233–238
- Aerobic oxidation system, deficient, 243
- Aggregation, 159
- ALA-induced PP, 114, 241, 367; *see also* Aminolevulinic acid, Protoporphyrin
- Alkaline phosphatase-antialkaline phosphatase (APAAP), PR revealed, 182, 183
- Alkanes
intrinsic fluorescence, 79
in liver, two-photon induced fluorescence, 79
vacuum ultraviolet (VUV) region excitation, 70
- Alkylating agents, 163
- Alkylator, 159
- Alpha-quartz phonon bands, 384
- Amiloride-sensitive Na^+ channel, 313
- 5-Aminolevulinic acid (ALA), 7, 21, 113, 241, 242, 367
- Amphiphilic peptide isolated from bovine haemoglobin, 363
highly improves solubility of hydrophobic compounds, 363
and hydrophobic protoporphyrin IX (PpIX chosen as a model), 363
- Amylase secretion, 151, 153, 155
effects of n-alcohols, 155
heterogeneity, 155
- Aneuploid cell population disappearance, 169
- Anisotropy techniques, 213
- Ankyrin
binding to
amiloride-sensitive Na^+ channel, 313
members of anion exchanger gene family, 313
 Na^+/K^+ -ATPase, 313
ryanodine receptors, 313
voltage-dependent Na^+ channel, 313
- binding to IP_3 receptors in brain and lymphoma, cells, 310
inhibits IP_3 binding and IP_3 -mediated internal Ca^{2+} release, 310
- binding to surface proteins and intracellular molecules, 310
- BK stimulation of its association to perinuclear structures and onset of DNA synthesis, 313
- drug effects on its rearrangement, 314

- Ankyrin (*cont.*)
 immunofluorescence staining techniques, 313
 in the linkage of erythrocyte band 3 to spectrin-fodrin microfilaments, 310
 reorganization after addition of BK followed by onset of DNA synthesis, 19, 309
- Ankyrin-associated microfilament system, 309
- Annexin V, fluorescein-labelled, 134
- Anoxic state of the eye, 11
- Anthocyanin, photochemical and photophysical studies, 423
- fast excited-state proton transfer from 4-methyl-7- ground state equilibria, 423
- hydroxyflavylum chloride to water, 423
- Anti-bleaching compounds, 267
- Antibody
 against α -tubulin, TU-4, 14
 AMCA-conjugated anti-rabbit, 14, 267
 chemically conjugated, 213
 domain-specific, β -tubulin, 14
 FITC-conjugated anti-mouse, 14, 258, 268, 332
 indocyanin-conjugated, 193, 258
 localization, γ -tubulin, TU-30, 14
 centrosomes, spindle poles, half-spindles, 14
 taxol-treated cells, 14
 monoclonal
 against acetylated α -tubulin (6–11B-1), 258
 against glial acidic protein, 332
 anti-vimentin, 15, 332
 against glutamylated α,β tubulin, 258
 against NF-H, 332
 mouse-antivimentin, 14, 332
 panel of, 14
 with rhodamine B sulphonylchloride, 258
 against tubulin subunits, 258
 against tyrosinated form of α -tubulin (YL 1/2), 258
 for multiple labelling, 267
 rabbit-antitubulin, 14
 rhodamine-conjugated anti-tubulin, 266, 268
 rhodamine-conjugated anti-vimentin, 266, 268
 polyclonal, 54
 antibulin-antibody decorated microtubules, 267
 primary, 213
 secondary, 213
 biotinylated, detected with fluorophore conjugated streptavidin, 267
- Antibromodeoxyuridine fluorescein conjugate, 9
- Anti-carcinoembryonic antigen (CEA) monoclonal Antibodies (MAb), 194
 coupled to fluorescein, 189
- Anti-CEA indocyanin Mab, 194, 198
 chimeric, 199
- Anti-CEA Mab fluorescein conjugates, 200, 202
- Anti-CEA Mab indocyanin conjugates. 200, 201, 202
- Antidigoxigenin-FITC or TRITC, 182
- “Antifading” medium, 182
- Antigen
 -antibody interaction, 213
 Ki-67 staining, 182
 antibody followed by FITC conjugated goat antimouse antibody, 182
 microtubule associated MA-01, 14
- Antihistaminic drug, 193
- Antimetabolite, 159
- Antineoplastic drugs, 113
- Anti-squamous cell carcinoma Mabs, 189
- Anti-tubulin monoclonal antibody, 174
- Anti-tumor drug
 efflux from cells, 284
 evidence for an active drug efflux pump in plasma membrane *vs* drug in the plasma membrane and drug vesicles, 284
 fluorescence, 284
 non-invasive method for measuring drug transport, 284
- Antracyclines, localization in cardiac-muscle and non-muscle cells, 425
- relevance to mechanisms responsible for cardio-toxicity, 426
- relevance to multidrug resistance, 425
 selective accumulation and cytotoxicity in (MDR-) *vs* (MDR+) cells, 426
- Apo B/E surface cell receptor, 115
- Apolipoprotein B/E
 cell surface receptor, 7
 receptor-mediated endocytosis, 18, 302
 not required for trafficking of polar LR or SR sphingolipids to lysosomes, 392
 trafficking of liposomes containing fluorescent sphingolipid to lysosomes, 302
- Apoptosis, 7, 129
 with anticancer drugs, 135
 cell cycle analysis, 135
 cisplatin induced, 135, 158
 of interleukin-3-dependent haemopoietic cells, 135
 of thymocytes, 135
- Apoptotic cells 8, 129, 133, 173
- Argon ion pumped Ti:sapphire laser, 2, 13, 18, 21, 35, 131
- Astrocytoma
 anaplastic stained for vimentin only, 14
 well differentiated with co-expression of GFAP and vimentin, 14
- Asynchrony in the function of individual cells, 153
- ATP bioluminescence cell viability assay, 162, 165, 168, 169, 171
- Autocrine growth factors, 148
- Autofluorescence, 4, 244
 of endogenous chromophores, 242
 of epidermoid carcinoma G1 cell, 243
 heterogeneity, 173

- Autofluorescence (cont.)
 laser-induced, 13
 prompt, off-gating of, 65, 66
 of single normal urothelial cell, 242, 243
 of tumor urothelial cell, 243
of NADH, in normal bladder mucosa, inflammatory bladder mucosa, and bladder tumor including CIS, 244
ratio imaging, prototype, 13, 246
of tissue, 189, 195
urothelial tissue, 242
- Autoradiography, 161
 of indocyanin-¹²⁵I-Mab E48 conjugate, 105
- Avalanche photodiode in SNOM, 19, 318
- Avian cell centrosomes and TU-3O antibody, 14
- Babesia divergens, 121
- Babesiosis, effect of the photosensitizer pheophorbide butanol on, 306
- Bacterial phosphotransferase system (PTS), 283, 284
- Bacteriopheophorbide photosensitization for eradication of solid tumors in animals, killing of parasites and viruses in blood, 301, 305, 306
- Beer-Lambert law, 41, 47, 357
- Bellnier experiment, 126
- Benzoporphyrins, 199
- Benzo[a]pyrene 7,8-diol-9,10-epoxid, 16
- β (Beta) cells, 8, 150
 coupling and electrophysiological evidence, 153, 155
 heterogeneity in glucose sensitivity, 153–155
 glucose stimulation of, 155
 islet cell interactions with, 156
 recruitment of proinsulin synthesis, 156
- Beta(β)-to-β-cell contact and exchange, 150
- Bilayer model system, 253
- Biodistribution of 125-indocyanin, 195
- Biokinetic results, 199
- Biomathematical modelling and fluorescence methods, 290
- Biomolecules, fluorescence-tagged, 53
- Biotin-dUTP, 131
- Bisbenzimidazol (Hoechst-Behringer 33342), 182
- Bladder, normal and tumoral, 13, 242–247
- Blood-brain barrier, 284
- Boltzmann transport equation, 42
- Bleomycin, 159
- Bradykinin (BK) binding to receptor on cultured bovine endothelial cells, 309
 effect on ankyrin network, Ca²⁺ mobilization, cytoskeleton rearrangement, DNA synthesis and proliferation, 18, 312
- Brain
 effect of hyperventilation on cortex of piglets, 96
 tumor metastasis to, 148
- BrdUrd-linked fluorescence, 160
- Breast cancer
 aneuploid, 160
 angiogenesis, 2
 clone MCF-7, 181
 correlation between ER positivity and low proliferative activity, 415
 detection, VI, 1, 25–30
 double FISH, 181
 PR gene deletion, 184, 185
 PR-negative, 10
 PR-positive, 10
 fluorescent probes, 411
 aneuploid and diploid patients, 412
 DNA analysis with propidium iodide (PI), in prognostic value of intracytoplasmic immunoglobulin (Ic-IgG) vs receptor and DNA analysis, 411, 412
 fluorescence spectroscopy of mice inoculated with breast cancer cells, 22
 injection of indocyanin green in, 28
 Near Infrared Raman-Fourier Transform spectroscopy, 382
 postmastectomy recurrence, 7
 detection with Photofrin of small nests (100–1,000 cells), 7
 subclones, 181, 182
- Bromoconduritol B-epoxide (Br-CBE), 305
- Bromodeoxyuridine (BrdUrd), 160
 staining with antibody followed by second FITC conjugated antibody, 182
- t-Butylhydroperoxide, 111
- “Bystander correction” following autologous transplantation of retrovirally-transduced NPD cells into patients, 305
- Ca²⁺
 channels, 153
 cytosolic potential of, 103
 free cytosolic, 108
 glucose-induced oscillations of, 156
 intracellular free, 153
 intercellular exchanges of, 153
 receptor-activated spikes of cytoplasmic, 156
 signaling, 309
 cytoskeleton reorganization, 309
 endothelial cells stimulated by bradykinin, 18, 309
 synchronization of oscillations of free, 150, 153
 temporally and spatially coordinated changes in level of, 153
- Ca²⁺/calmodulin-dependent microfilament system, 314
- Cadherins, 8, 138
- Caenorhabditis elegans, 129
- Caffeine, 163, 167
- Calcein, 6, 8, 100, 101, 103, 105, 109

- Calcium
 probe, 101, 108, 118, 119
 fura-2, 12 fluorescence excited at 340 nm/ excited
 indo-1 ratio imaging, 4, 109
 new generation of, 79, 110
 at 380 nm, 18
 transients, 109, 111, 148
- Calmodulin, 309
- cAMP
 -dependent control, 150
 glucocorticoid-mediated inhibition of insulin gene expression prevented by, 156
- Cancer
 bladder, 169
 cells resistant to estramustine, 339
 cervical, 169
 detection by fluorescence spectroscopy, 82
 endometrial, 169
- Carbocyanine dyes, 101, 103
- Carbogen, 1, 29
- Carboplatin, 162
- Carcinoid syndrome, 402
- Cardiac myocytes, 206
- Cation and anion antiport, 228
- Cationic dyes, 101
- CCD detector, 294
 cooled CCD camera for high resolution multi-mode digital microscope system, 350
- Cell
 adhesion molecules, 149
 aging, 118
 compartments(negatively charged), 101
 culture
 endothelial, 139, 147
 melanoma MeWo parental cells, 139
 cycle
 chemotherapy-induced perturbations, 9, 158, 159, 168
 flow cytometry of, 157
 phase and synthesis of non-histone proteins, 170
 position and nuclear protein content, 170
 resolution in six components, 158
 stage most sensitive to specific agents, 9
 hypoxia, 207
 kinetic responses, 170
 metabolism
 combined Fabry-Perot/Michelson interferometry for excitation microscopy, 295
 fluorescence excitation spectra, 20
 monitoring in optical tissue by two-photon non-invasive optical monitoring, 11, 295
 real time study, 293-298
 population heterogeneity, 12, 173
 spreading, 146
 suicide, 135
- Cell (*cont.*)
 surface
 glycoproteins, 147
 receptors, 138
 types
 apoptotic, 10
 drug-resistant, 15
 living (metabolic control mechanisms), 17
 microvessel endothelial, 138
 necrotic, 10, 173
 reactive, 10
 stromal, 9
 survival curves according to, 113, 114
 tumor, 10, 173
 wild type, 15
 viability probe, 100, 110
 volume, 12, 105, 106, 110, 157
- Cell-to-cell
 communication direct, indirect, 8, 149
 contact, 8, 153
 diffusional exchange, 8, 149
 signaling by
 direct interactions between adjacent cells, 154
 intrinsic and extrinsic neural inputs, 154
 local and circulating hormones, 154
 nutrients, 154
- Cerebral tumors, 13
- Centrosomes (immunofluorescence detection), 261
- Channels, 149
 Ca²⁺, 153
 Ca-activated K⁺, 155
 ion, 249
 K⁺, 153
 L-type in neurites and somata, 251
 regional, variation in function of, 249, 251
 voltage-gated, 249
- Charge delocalization, 214
- Chemiosmotic hypothesis, 105
- Chemopotentiation, 113
- Chemosensitivity, 113, 160
- Chemotherapeutic agents, 9, 166
 specific, preselection, 169
- Chemotherapy
 combination therapy of ovarian cancer, small cell lung cancer, advanced breast cancer, 231
 drug resistance, intrinsic or acquired, 231
- Chimeric anti-CEA coupled to indocyanin, 189
- Chinese hamster lung fibroblast V79, 16
 zero cytochrome P450 background, 16
- Chlorins, 6, 113, 199
- Cholera toxin and intracellular trafficking, 57
- Cholesterol
 mole fraction in phosphatidyl choline liposomes, 253
 /phospholipid ratio's link to intramembrane electric field, 14, 243
- Cholinergic expression, 151

- Chromophore, 242
absorption, 31
fluorescein, 110
potentially diffusible, 213
scattering and non-remitting, 31
- Chromosome centromere's four to six copies, 10
- Circular dichroism (CD) of PpIX-peptide, 365
- Cis dichlorodiamineplatinum (II), 9, 159–163, 166, 170, 171 Clonogenic bioassay, 159
- Colchicine effect on microtubule disassembly, 310
- Collagen, 5
autofluorescence, 13
Type I, 6, 100
- Collisional quenchers, 76, 77
- Colon
adenocarcinoma HT29–18 cells' lysosomes
stained with a methyl pheophorbide derivative, 7
carcinoma's immunophotodetection and first *ex vivo*, 11, 193, 202
- carcinoma T380 (human), 11
HT29 cells (human), 114
normal vs. malignant, 5
penetration of PPIX-peptide complex, 21
- Communication territories, 9, 150
- Computerized imaging techniques, 8
- Concanavalin A conjugated to Ru-complex, anisotropy decay, 66
- Confocal computerized fluorescence microscopy, 6, 19, 302, 348
antimicrotubule drugs, 339
cytoskeletal elements in wild type and drug-resistant cells, 339
images, 111
with calcein, 15
serial, 105
TMRM fluorescence, 102
laser scanning, 97
sections, 99, 102
structural, morphological and drug efflux studies, 339
three-dimensional, *in vivo*, 11, 330
- Confocal microscope, 54, 98
optical system for z-axis localization, 294
scanning (zoom feature), 98
ultraviolet, 108
- Conjugated ring system, highly, 214
- Connexin (Cx43 protein)
gap junctions made of, 151
gene coding for, 151
-mediated coupling of gland cells, 149, 154, 156
mRNA, 151
- Continuous wave (CW) measurements, 31
- Critical micelle concentration (CRC), 22
- Cotransfected neomycin marker gene, 305
- Coulombic interactions, 115
- Coulter-counted cells, 233
- Coumestrol, 11, 213, 216
/ER complex, 11, 215
- Cryosections, 260
- CT scan, V
- Cy3PKC β 1 (C β 1) and Cy5C16 (Cy3), 54, 55
- Cy5-labeled IgE, 319
- Cy5 N-hydroxysuccinimide ester, 319
- Cyclophosphamide, 159, 161
- Cytocalasine D inhibitor of microfilament function 310
- and in platelets inhibitor of IP₃ IP₃-induced Ca²⁺ release, 309, 310
- Cytochrome P450, 16
ancestral gene, 16, 273
cDNAs for heterologous expression in bacteria, yeast, insect and mammalian cells, 274
isoforms, cloned cDNA and purified enzyme, 16, 273
mass production of purified, 274
metabolic activation of cytostatic drugs (cyclophosphamide, ifosfamide) by, 274, 279
- V79 cells transfected with cytochrome P450 1A1, 1 273
(from human origin) preferential oxidation of benzo-(a)pyrene in the 7, 8-position (pre-bay region), 278
(from rat origin) preferential oxidation in the 4,5-position (K-region), 278
zero cytochrome P450 background, 275
- Cytofluorometry, 135
analysis of steroid receptors by, 213
- Cytogram, 134
- Cytokeratin (CK) antibodies, 10, 173
- Cytokines, 146, 148
- Cytomorphologic findings, 159
- Cytosine arabinoside, 16
- Cytoskeleton
detergent-extracted, 259, 266
double-label immunofluorescence, 266
immunofluorescence microscopy with microinjection of affinity purified polyclonal antibodies, multiple monoclonal antibodies and secondary antibodies coupled with new fluorophores, 265
- filaments
actin microfilaments, 265
interaction of filaments with each other, 265
intermediate filaments, 265
tubulin microtubules, 265
- microinjection of antibodies to, 266
- protein inhibitors of, 309
- reactivity of antibodies and phalloidin with, 267
- rearrangement, 18
- role in cell motility, segregation of chromosomes and signal transduction, 18, 149, 265
- Cytotoxicity, 163
cell or nucleus sizes, 231
DNA or mitochondria labelling, 232
growth inhibition of cell cultures, 231
intracellular ionic concentrations, 232

- DAPI, 173, 174
 collected in FITC channel, 175
 image of spindle, 16
- Daunorubicin, 17
 active extrusion mechanism by efflux against its concentration gradient, 285
 association to and dissociation from DNA, 284
 binding constant, 284
 fluorescence quenching when bound to DNA, 284, 286
 net influx affected by addition of verapamil and depletion of ATP, 285
 passive permeation coefficient, 286
 pumping by P-glycoprotein, 284
 transport assay, 286
 uptake into vesicles, 286
- Demodulation, AC and DC components, 2
- Deoxyhemoglobin, 44
- Deoxynucleotyldyl transferase (Tdt), 8
- Depth profile spectra
 of chromophores, Fourier analysis V, 62, 63
 of sunscreen, UV absorbing chromophores, 62
- Detection of
 breast tumors
 absorption and fluorescence of photon diffusive waves, 1
 microscopic recurrences, VI, 7, 123, 125
 urothelial tumors, VI, 13
- Dexamethasone, 151, 152
- Dextran polymer, 199
- Diacyl-glycerol (DG), unsaturated, possible messenger for activation of protein kinase, 57
- Diagnosis
 aerodigestive, 5, 82
 breast, 5, 82
 digestive tumors, V, 5
 genetic disease, 18
 gynecological tumors, V, 5, 82
 respiratory tumors, V
 in vivo tumor, 189
- Dichlorofluorescein, 101
- Di-8-ANEPPS, sensor portion, 13, 240–251
- Diethylthiotriocarbocyanine iodide (DTTCI), 2, 35
- Differential interference contrast (DIC) optics, 349
 digitally enhanced images of dividing yeast *Saccharomyces cerevisiae* 352
- Differentiating NIE-115 cells, di-8-ANEPPS, 250
- Diffusion equation when multiple light scattering occurs, 34
- Digoxygenin-dUTP, 132
- Dihydroethidium, 101
- Dihydronordaridine 123, 101
- DNA
 -binding fluorescent dyes, 157, 349
 binding of propidium iodide (PI) to double stranded, 157
 content analysis, 173–174
 degradation at linkers, 130
- DNA (*cont.*)
 histogram, 160
 apoptotic cells, 8, 131
 ovarian carcinoma, 163
 simultaneous measurement with RNA, 157
 staining
 DAPI, 9, 10, 173
 Hoechst-Behringer 33342, 10, 12, 181
 strand breaks, 132
 synthesis, 9, 160
 following ankyrin reorganization, 309
 and cytoskeleton, 18
- DnsEM emission, 15
- Donor
 fluorescence image, 55
 fluorophore, 54
 quantum yield quenching, 54
- Double interferometry, 20
 Fabry-Perot and Michelson, 20
- Doxoreubicin cross resistance, 15, 159, 160, 161
- Drug-
 efflux pump, arithmetic model, 17
 resistance in cultured cells, 339
 failure of prodrug activation because of low cytochrome P450, 278
 with vinblastine, taxol and estramustine, 339
- Dual wavelength
 di-8-ANEPPS fluorescence ratios (R), 250
 effects of 6-KC and phloretin, 253
 image pairs (excitation; emission), 250
 multidistance method, 50
 ratiometric imaging, 249
 sensitivity to transmembrane potential, 253
- Dynamic adhesive potential of tumor cells, 8
- Efflux-blocker and efflux pumping, 17
- Elastic scattering, 82
- Elastin, 5, 82
- Electrical coupling, 8, 150
- Electrical potential probe, 6, 110
- Electrochemical concentrations, 151
- Electrochromic mechanism, 13, 21
- Electrochromism, 372
- Electron donor/acceptor pairs, 214
- Endocytosis, 7, 115
 receptor-mediated via the LDL receptor, 18
 trafficking of sphingomyelin-loaded liposomes to lysosomes, 18
- Endoplasmic reticulum probe, 101
- Endosomes' probe, 101
- Endothelial cells, 309, 310
 BK-stimulated proliferation, 310
 bovine, 309
 free calcium concentration, 79
 intracellular Ca^{2+} mobilization, 309
 hydrolysis of PIP_2 to diacylglycerol and IP_3 , 309
 loaded with Fura-2/AM, 310
- monolayers, 141

- Endothelial cells (*cont.*)
permeabilized, 309
pretreated with cytochalasin D, 3
stained with FITC-conjugated monoclonal mouse anti-ankyrin antibody (ANK 016), 311
- Endothelial leucocyte adhesion molecule, 148
- Enzyme-linked immunosorbent assay (ELISA), 259
- Epidermal growth factor receptor (EGFR) isomerization, time-resolved fluorescence imaging microscopy, 57
- Epifluorescence microscope, 216
- Epithelial mucin antigen (MC5), 10, 173
- Equilibrium binding constant (K_d) for ER high affinity binding sites, 11
- Escherichia coli* polymerase, 132
- E-selectin, 148
- Esterases, cytosolic, endogenous, 106
- Estradiol, 15
17 β -, 214, 205
linked to nor-nitrogen mustard through a carbamate bond, 15
- Estramustine (EM), 15, 339
antimicrotubule agent, 339
cancer cell resistance to, 339
cells blocked in G2/M, 340
colony-forming assays, 341
confocal studies, optical sectioning using Differential Interference Contrast (DIC) 342
depolymerization of microtubule spindle fibres, 340
dansylated (Dns-EM), 15, 341
efflux studies, 341
in hormone-refractory prostate cancer, 339
increased sensitivity to cytochalasin B, 344
localization in tissue having estrogen receptors, 340
- microtubules
cells immunofluorescently-labeled for β -tubulin and stained with propidium iodide, 344
non-covalent binding to tubulin and microtubule-associated proteins (MAPS), 340
- resistant cells
absence of upregulated p-glycoprotein mRNA and clonally-selected, 340
glutathione-S-transferase activity, 340
efficacy in combination treatment not mediated by lack of cross-resistance to doxorubicin, taxol and vinblastine, 340
- microfilament organization using rhodamine-phalloidin conjugate, 344
- the multi-drug resistance phenotype, 340
- ovarian carcinoma, 340
- and wild type cells grown on coverslips, 341
fluorescence excitation-emission spectra, 341
- phase images superimposed with corresponding fluorescence images, 341
- Estramustine (EM) (*cont.*)
three-dimensional volume rendering software for comparison between wild type and resistant cells, 342
calcein-acetomethyl ester (calcein-AM), 342
- Estrogens
nonfluorescent, 215
17 β -estradiol, diethylstilbestrol, 218
fluorescent conjugates, 214
conjugation of steroid nucleus, 214
heterogeneity of expression, 214
imaging techniques, 214, 215
fluorescent ligands, 213, 214, 215
absorbance and fluorescence emission maxima, 215
nonsteroidal compounds, 214
relative binding ability (RBA), 215
plant estrogen coumestrol, 213, 216
target specific probes, 216
tetrahydrochrysens (THCs), 215, 216
- non fluorescent ligands, 214
- nuclear fluorescence in cultures that express ER, 216
- receptors (ER), 11, 213
analysis of expression as a function of the cell cycle, 214
- Cos-7 cells transfected with pCMV-ER, 217
dynamics of real-time motion, 214
equilibrium binding constant (K_d), 11
expression plasmid pCMV-ER, 11, 216
expression vector alone, 217
-responsive tissue, 215
visualization in Cos7 cells transfected with pCMV-ER, 216, 217
wild type human ER cDNA, 216
- Ethidium bromide (EB), 101, 157
- Excimer laser, 13
- Excitation-contraction coupling, 111
- Excitation photon density wave, 34
- Excited state
anisotropy and polarization, 74
control, 65
population control, V
- Exocrine pancreas, 8
- Extracellular chloride concentration, 227
- Extracellular matrix (ECM) protein, 141, 144
- Extracellular matrix invasion, NGF-stimulated, 147
- Fabry-Perot interferometer, 20, 296, 297
“comb spectrum,” 297
flat parallel partially-reflecting mirrors, 297
- Fabry-Perot and Michelson interferometry (combined)
metabolic studies in living cells, 20
- FALS, 134
- Ferrodoxin reductase, 273
- Fiber optics, 81

- Fibroblasts
 human, 114, 116
 lysosomes
 colocalization of methyl pheophorbide derivative (MPH) and lucifer yellow (LH), 7
 Niemann-Pick, 18, 305
 retroviral ASM vector, 18
- 3T3
 double-label immunofluorescence staining of cytoskeleton, 270
 mouse embryonic, 259
 simultaneous shear-force and bright field reflection images, 319, 320
 SNOM images, 19
- Fibronectin (FN), 8, 144
- Fine needle aspiration (FNA), 162
- Flavin, 5, 82, 243
 endogenous, 244
 oxidized, 244
- Flavoproteins
 fluorescence as intrinsic probe of cellular metabolism, 210
 mitochondrial, 11
 oxidized, 243
 corneal tissue, 206
 redox scanning, 29
- FLIM, *see also* Fluorescence lifetime imaging microscopy
 of calcium in COS cells using Quin 2, 78
 of MLC probes
 with CCD detector and phase sensitive images without an image intensifier, 4, 69
 instrumentation using LED light source and photostable MLC, 69
 pixel-by-pixel analysis, 57
 spatial resolution of microstructures on nanosecond time scale, 57
- Flow cytometry, V, 10, 161, 164
 analysis of clinical specimens
 effects of tumor heterogeneity, 173
 apoptotic cells, 129, 135
 arrest of murine leukemia cells in G2, 158
 cells treated with taxol, 9
 cells treated with X-irradiation, 9
 cellular heterogeneity, 9
 simultaneous measurements of DNA and nuclear protein, 170
 two-parameter, 9, 158
- Flow microfluorometric analysis, 170
- Fluo-3, 100, 101, 106, 107, 108
- Fluorescein, 10
 green fluorescence, 190
- Fluorescein-anti-digoxygenin, 132
- Fluorescein-deoxyuridine triphosphate (dUTP) 8, 132
- Fluorescein diacetate, 101
- Fluorescein diacetate-propidium iodide, 110
- Fluorescein isothiocyanate (FITC), 9, 158, 160, 163
 conjugated anti-BrdUrd, monoclonal, 160, 164
- Fluorescein-streptavidin, 132
- Fluorescence
 Activated Cell Sorter (FACS), 302, 395
 anisotropy, small changes, V
 digital image analysis, 156
 excitation spectroscopy
 metabolic control, VI, 293
 excitation spectrum
 double interferometry with Fabry–Perot and Michelson interferometers, 20, 298
 limiting factor in the amount of exciting radiation for measurements in living cell, 28, 295
 population of vibrational levels, 295
 sequential method in the recording of, 295
 simultaneous spectral encoding (SSE), 295
 two-photon, V
 three-photon, V
- and gene expression, 16
- imaging, V
 analysis of fluorescence of intact cells, 302
 estrogen, VI
 and immunofluorescence of progesterone receptors, 10
 membrane potential components, 249
 progesterone, VI
 receptors, 10
 three-dimensional, VI
- intensity
 linear combination of each component at the same spectroscopy, 31, 32
 small changes, V
 wavelength, 12
- lifetime
 amplitude demodulation, 2
 frequency domain method of lifetime determination, 2, 32, 41
 imaging microscopy (FLIM), 4, 53, 57, 78
 measurement from phase-shift and amplitude demodulation, 32
 metal-ligand probes, V, VI, 37
 phase-shifts in scattering media, 2, 38
 sensing in random media of photon migration in tissues, 31
 spectroscopy in scattering media, 31, 34
 time domain method of lifetime determination, 41
 tissue spectroscopy, 31
- polarization
 analysis of receptor mobility, 214
 immunoassay of high-molecular weight antigen based on a long-lifetime Ru-ligand complex, 78
- quenching
 Pd-porphyrin fluorescence, V
 stacking-induced, in lysosomes, 118
- Raman spectroscopy, V

- Fluorescence (*cont.*)
ratio measurement, 108, 250
resonance energy transfer, V
domain-to-domain motions in proteins, 69
dynamics of zinc finger peptide, 78
Fret efficiency, 3
imaging the molecular state of proteins in cells, 57
microscopy (FRET), 3, 53, 57, 69, 215
spectrum, calculated, complex, experimental, 12
in situ hybridization (FISH) 10
double color FISH in chromosome 11 centromere and PR gene in breast cancer MCF subclones, 184, 185
mapping of tumor suppressor genes, 23, 419
mapping of YAC clones from chromosomal regions with tumor-suppressor activity, 419
single and double color FISH, 23, 419
spectral shifts, 12, 13
spectrophotometer, 310
fura-2 loaded endothelial cells, 310
spectroscopy
cancerous and normal human stomach tissues, 393
diagnosis of cancerous tissue, 22, 393
emission band for the cancerous tissue, 395
fluorescence emission spectra of the 5-hydroxytryptophan, 5-hydroxytriptamine and 5-hydroxyindolacetate excited at 340 nm, 403
fluorescence spectra of normal and tumor mouse tissue, 396
fluorescence spectra of normal and tumor stomach tissue, 402
intensity ratios of fluorescence emission for cancerous and normal tissue, 400, 401
of Ph2-NH₂, Ph4-OH, recent developments, 96, 117
videocinematography, 11, 214
- Fluorescent analog cytochemistry, 349
- Fluorescent antibodies, 53; *see also* Antibody
- Fluorescent derivatives, 299
diagnosis of genetic diseases, 18, 299, 304
polar probes which contain a negatively-charged sulfonate and two positively-charged amines, 300
pyrene, a non-polar polycyclic hydrocarbon, 300
selection of gene-corrected cells, 18, 300
- Fluorescent donor, 53
- Fluorescent dyes
DNA, 157
mitochondria, 157
nuclear proteins, 157
single stranded nucleic acids, 157
- Fluorescent lipids
phosphatidylcholine liposomes, 302
sphingolipids directed to lysosomal compartment, 302
- Fluorescent-phosphorescent dyes
excitation and reemission in the NIR, 31
- Fluorescent photon density wave, 34
- Fluorescent probes
biotinylated goat antiavidin-avidin-FITC, 23
breast tumor, fluorescein isothiocyanate labeled anti human IgG, 411
cations, V, 222
connexin channels, 8
cytoskeleton, V, 14
digoxigenated probe, 23
drug resistance, 15
endogenous and exogenous, 31
enzymes, V
FITC-labeled anti human IgG, 411
membrane potential, 6
metabolic control, V
nucleic acids, dynamic probes, V
pH sensitive, 222
organelles, V
sphingolipoid lissamine-rhodamine (LR), 18
vascular volume, 28
- Fluorescing laser dyes, 37
- Fluorometric method of RNA and DNA determination, 170
- Fluorophore, 31, 97, 101, 106
ion-indicating, 106
lifetime exceeding (or comparable to) typical “times-of-flight” associated with photon scatter, 32
lipophilic cationic, 6, 32
- 5-Fluorouracil, 160, 165
- Flux control coefficients, 284
- Four-dimensional image, 16
- Förster’s donor-acceptor sequential photobleaching mechanism, 53, 57
- Fourier transform
analysis, 3, 5, 31, 61
infrared and Raman spectroscopy, 22
infrared spectrometer, 384
- Freeze trapped redox state system, 1, 28–30
- Frequency-domain, 50
decay of tetradecane, 71
definition of light propagation, 42
diffuse-photon tomography, V, 2, 50, 51
near-infrared optical imaging system, 51
optical tomography, 51
resolution of complex intensity and anisotropy decays, 65
spectroscopy, 2, 42, 50
- FRET, efficiency maps and microscopy, 53, 54, 56; *see also* Fluorescence resonance energy transfer
- Full three-dimensional images of thick tissue, 205
- Fura-2, 222; *see also* Ca²⁺ probes
endothelial cells, 310
ratio 340/380 excited fluorescence, 311, 312

- Gamma scales, 102
 Gap junctions, 8, 149, 150, 155; *see also Connexins*
 Ca²⁺-, pH- and PKC-independent gating, 152
 drugs blocking, 151
 -mediated modulation of pancreatic functions, 154
 molecular biology and genetics, 155
 transfer of second messengers, 154
- Gating
 of DAPI, tubulin, CK, MC5, 175
 of PCNA expression targeted live breast tumor cells, 175, 177
 of tetraploid cycle (live breast tumor cells, 177
- Glial fiber associated protein (GFAP), immunolocalization in glial cells, 15, 333
- Glioblastoma
 positive for vimentin only, 15
 multiforme, FISH for deletion of heterozygosity, 23
- Glucocorticoid-induced
 thymocyte apoptosis, 135
 expression of insulin gene, 156
- Glucosylceramide, fluorescent, 305
- Glutathione, 101
 S-transferase activity, 15
- Glycoproteins of the cell's surface, 149
- Glycosidase and glycosidation, 144, 299
- Golgi
 LR- or SR-ceramide translocated from across the lysosomal membrane into, 304
 probe, 101, 103, 111
- G1 phase, 159, 169, 163, 166
 sensitivity to cisplatin, 160
- Green fluorescent protein (GFP), photoactivated, 16
- Green's function, 34
- Growth cones, 249
- Growth factors, 148
- G2 phase, 158, 159, 160, 162, 163, 165
 arrest, murine leukemia cells, 158, 163
 biphasic block, 165
 cisplatin-induced block, 160, 162
 reverse-dose dependent block, 165
- G2M phase, 159, 160, 160, 161, 164
 accumulation, 159, 160, 168
 VLB-treated cells, 234, 236, 238
- Gynecologic cancer cell lines, 165
 effect of doxorubicin, pirarubicin, 169
- Gynecologic malignancies, 9, 161
 squamous cell carcinoma, 170
- Haemodynamic shear stress, 148
- HDL, 115, 117
- Hematoporphyrin, 199
 derivative (HPD), 124, 241
- Hemoglobin, 44
- Hemoproteins, 273
- Hepatic sinusoidal cells (HES), 8, 139, 144
- Hepatocytes, 103, 104, 103, 110, 111
- Heterogeneity for integrin expression, 148
- Hexyl ether of pyropheophorbide (HMP), 114
- Histogram
 dual parameter, PAA + PI, 161, 177
 gated on blue (+) and red (-) fluorescence, 133
 single parameter, 157, 161
- Hoechst 33342, 132–134, 136, 232, 234–237
 quenching of fluorescence, 160
 /PI method, 133
- Hormones, 8, 149, 154
- Human acute promyelocytic cell leukemia line (HL-60), 383
 differentiated to granulocytes or macrophages, 303
 pyrene dodecanoic acid fluorescence in HL-60
- Human cervical adenocarcinoma HeLa S3, 259
- Human colon cancer, 189, 190
 cell line (Lo Vo), 159
- HT29 cells incubated with ALA, 364, 367
- HT29 cells incubated with [PpIX-peptide], 365, 367
- T380 serially transplanted subcutaneously into nude mice, 192
- Human leukemic cell line (CCRF-CEM) 223, 227, 232
 drug resistant derivative lines, 232, 234, 235, 237, 238
- Human lymphoblastoid cells, 130
 lymphoma cell line, 159
- Human malignant melanoma cells, 141, 148
 metastatic melanoma, 137
- Human neuroblastic and glial neoplasms, 332
 immunofluorescence microscopy with monoclonal antibodies, 332
- Human ovarian carcinoma cell line, 135
 tumor stem cells, 170
 tumor xenografts, 193
- Human skin, membrane permeability PAS, 3
- Hybridomas, 259
- 4-Hydroperoxycyclophosphamide, 155
- Hyperthermia, 115
- Hypoxia, chemical, 1, 110, 111
- ICAM-1 (natural adherence molecule), 148
- Imaging
 autofluorescence ratio, 13
 cell and mitochondrial membrane potential, simultaneous, 110
 cell surface topography and volume, 105
 computerized, 8
 monochromatic, 7
 ratio, 106
 spectrographic, 7
- Immunocytochemistry, PR and chromosome 11 FISH, 182, 184
- Immunofluorescence analysis
 blue, green and red combination, 14
 cytoskeleton, double- and triple-label, V, 14, 259, 266, 268

- Immunofluorescence analysis (*cont.*)
intermediate filament expression, 15
with multiple labelling techniques, 267
under normal and pathological conditions, 331
of progesterone receptor (PR), 10
quadruple labelling: microtubules, vimentin filaments, mitochondria and endoplasmic reticulum, 268
triple-labelling with AMCA, FITC and rhodamine as fluorophores, 268
of microtubules, vimentin filaments and microfilaments, 268
- Immunoglobulin-supergene family, 138
- Immunophotodetection of, VI
cancer, 10, 189
colon carcinoma, 11, 197
SCC, 197
tumors, 194
and radioactivity counting, 194
- Indo-1, 66, 101, 106, 222
emission spectra for one- and three-photon excitation, 4, 73, 79
ratio-imaging, 10, 194
- Indocyanin antibody conjugates, 194
anti-CEA antibody coupled to, 189, 194
anti-SCC conjugated to, 190
coupled with ^{125}I -MAb E48, 192, 193, 194, 199
LOVO-D1 Mab, 199
 $/$ MAb ratios (in) nude mice xenografts, 191, 193
green, 11
- Indopentomethincyanin N-hydroxy-succinimydil ester (CY5.18), 10, 191
- Inducible cell adhesion molecule (INCAM-110), 148
- Infrared absorption imaging, 51
- Infrared spectroscopy, 384
biological and biomedical studies, 389
carcinogen-induced exfoliated cells, 389
pair of normal and malignant cervical tissues, 389
pair of normal and malignant colon tissues, 389
carbon-hydrogen stretching vibrations, 385
DOPC bilayers and discontinuities, 386
high pressure infrared spectroscopy, 383, 386
infrared red and Raman spectra, 386
model biomembranes, 389
modes of the methylene and methyl groups, 390
- Inhomogeneity(ies) in real tissue, 46, 48
- Insulin, 182
gene, basal expression, 150
-producing tumoral, transformed β cells, 9
release, 9, 153
- Insulinoma, 151
- Integrins, 8, 136, 137, 136, 139, 144, 146, 147
heterogeneity for expression, 148
- Intercellular coordination, 154
- Interferon- γ , 148
- Interleukin 1, 148
- Interleukin-3, 130, 136
- Intermediate filaments
differential expression in normal human developing neural tissue, neuroblastic and glial neoplasms
changes in the expression of vimentin, GFAP and NF-H, 336
timing of expression in ontogenesis, 332
immunofluorescence microscopy, 331, 332
immunostaining, 332
markers of tumor cell origin in metastases, 331
in round-cell carcinoma of lung, 332
- Internucleosomal degradation, 126
- Intracellular detection of cations
calcium, magnesium, proton, sodium, 222
- Intracellular ion concentrations, 221, 228
bicarbonate, chloride, 222
 $\text{Mg}^{++}, \text{Na}^+$, pH, 12
- Intracellular ionic balance, 222
- Intracellular transfer of information, 221
- Intralipid solution, 2, 37, 43, 45, 48, 49, 50
- Intramembrane electric field, 250
components
dipole potentials dependent on cholesterol/phospholipid, 251–253, 254
surface potentials different between neurites and somata, 251, 252
transmembrane potentials and influence of KCl, valinomycin, 250, 252
- mapping, 249
mean local, associated with the neurites or the somata, 13, 249, 250
regional variation, 13, 249
- Invertebrate axons, 249
- Iodoacetate, 104
- Ion
channel distribution, intrinsic heterogeneities, 252
conductance, uneven, 252
currents, 253
transport, 12
- Ionic fluxes, 153
- Ionic gradients, 151
- Ionophore for potassium, 13
- Irradiation modulators, 169
- Islets of Langerhans, 150, 153
electrical coupling between cells, 155
topography of electrical synchrony among B-cells, 155
- I-sulfosuccinimydil-3(4-hydroxyphenyl)-propionate, 141
- Junctional channels, 140
communication and coupling, 8, 150, 151, 153
- K^+ probe, 191
- Karyolysis, 166
- Kaschke's group, 46

- Keratinocytes, 7, 114, 121
 6-Ketocholestanol (6-KC), 13, 250, 253
 Keyhole limpet hemocyanin (KLH), 258
- Lamellipodium, 249
 Laminin, 100
 Lanthanide-substituted nucleotides, VI
 Laser
 argon-ion, 206, 242, 243
 argon-krypton, 100
 coumarin dye, 242
 excimer (XeCl), 242
 fs, 65
 helium-neon, 100
 multi-line, 103
 multiple system, 54
 Nd:YAG pumped Satori dye, 206
 nitrogen, 242
 ps, 65
 scanning confocal microscope, 97, 100, 110,
 111, 286, 287
 Ar/Kr, 311
 Ti:sapphire, 206
 Laser-induced autofluorescence spectroscopy (LIAFS), 13, 242
 demarcation of lung, colon and cerebral tumors, 13
- Laser-induced fluorescence spectroscopy, 241
 of chlorin and hematoporphyrin derivatives (HpD), 241
 of Photofrin, 241
- LDL-bound photosensitizer, 7, 115, 117, 118
 LDL-LDL-bound methyl pheophorbide derivative (MPH), 116, 117
- LDL-receptor mediated endocytosis, 302
 apolipoprotein E, 302
 small unilamellar liposomes (SUV), 302
- Lecithin (phosphatidylcholine), 302
- Leiden culture batb, 329
 intracellular PO_2 measurements in single macrophages, 329
 pathophysiology of ischemia-reperfusion, 328
 Pd-porphine quenching of phosphorescence, 328, 329
- Leukemia cells, 159; *see also* Human leukemia
 Lifetimes of intermediates in photosynthesis, V
 Light induced fluorescence (LIF), 193; *see also* Fluorescence
 Light quenching (LQ), 74
 access to dyes intercalated in DNA, 76
 access to tryptophan residues in protein, 76
 control of excited state population 74
 effects on the intensity and anisotropy decays of fluorescence, 75
 time-dependent, 78
 two classes of LQ experiments
 excitation and quenching by same pulse, 74
 quenching pulse delayed relative to excitation pulse, 74
- Lipid, 5
 ester groups of water molecules, 13
 traffic, 115
- Lipodiosis, 304
- Lipophilic cationic fluorophores, 101
 Lipoproteins, 113, 115, 121
 Liposomal dye, 250
 Liposomes, 250
 incorporation of sphingolipids with the hydrophobic probe pyrene, 253
 unilamellar, coated with apolipoprotein E, 303
- Liquid nitrogen microtome, 1
- Lissamine (or sulfo) rhodamine dodecanoic acid, 300
- Lissamine-rhodamine (LR) fluorescent derivatives, 300, 301
- Liver peripheral blood mononuclear cells (PBMCs), 10
- LOVO-DI Mab, 194
- LRdodecanoylsphingomyelinase choline (LR-SPM), 18
 labelling of sphingomyelinase, 18
- Lucifer Yellow (LY), 7, 114, 116, 118
- Lung tumors
 adenocarcinoma cell line (A549), 160
 bronchogenic cancer *in situ*, 127, 128
 small cell cancer, 159, 170
- Lymphoblastic cells
 lymphoblastoid line CCRF-CEM, 10, 12, 173
- Lymphocytes
 elevation of $[\text{Ca}^{2+}]$, before cytoskeleton-mediated receptor patching/capping, 313
- Lymphoma
 adhesion to FN or VN coated surfaces, 8
 large-cell, 139
- Lysosomes, 103
 dextran conjugates of rhodamines, 103, 104
 hydrolases, 115, 304
 α - and β -N-acetylhexosaminidase, arylsulfatases, ceramidase, β -glucosidase, α - and β -galactosidases and sphingomyelinases probes, 101, 114
 photochemotherapeutic applications, 121
 stacking-induced fluorescence quenching, 118
 stained with a methyl pheophorbide derivative, 7
- Lysosomotropic detergent, 7, 118, 121
- Lysosomotropic substance, 117
- Lysosphingolipids, 300
- Mag-Indo, 101
- Mammomatotropic tumor, 156
- Mass spectrometry
 of amphiphilic sequence of peptide in [PpIX]-peptide complex, 364
- Maxwell's equation, 317
- Mdr1a* gene product involved in transport of substances across blood-brain barrier, 284
- MDR phenotype, 12

- Medical Optical Tomography, 51
Medium
 homogenous or heterogenous, 44
 infinite, 47
 scattering and absorbing, 47
 semi-infinite, 47
 uniform, 47
Melanin, ocular (PAS), 63
Melanocytic progression, 147
Melanoma cells, 137, 146; *see also* Human melanoma
 adherence to FN or VN coated surfaces, 8
 adhesion
 to extracellular matrix proteins, 148
 under laminar flow, 147
 basal adhesion potential of, 146
 brain-colonizing, 146
 expression of integrin receptors, 146
 mutants, wheat-germ agglutinin-resistant, 147
Melfalan, 159
Membrane potential, 6; *see also* Intramembrane potential
 converted to intramembrane electric field, 250
 of mitochondrial membrane, 6, 101
 of neurites, 13
 resting, 153
 of somites, 13
Membrane probe
 Nile Red (NR), 12
Membrane soluble
 fluorescent compound 1-(4-trimethylammonium-phenyl)-6- phenyl-1,3,5-hexatriene (TMA-DPH), 289
 potential-sensitive fluorescent dye, 249
Methotrexate, 158, 166
Mitomycin, 166
Michelson interferometer, 297
Mitotic index, 158
Mercury cadmium telluride detector, 384
Merocyanine 540 (MC-540)
 amphiphilic, 371
 physical and chemical properties dependent on polarity of solvent, 372
 in aqueous solutions
 micelles at high concentrations, 371
 stacked aggregates (dimers, trimers) at low concentrations, 371
 behavior of classical surfactant above and below Critical Micelle Concentration (CMC), 380
 biological probe
 of the multidrug resistance phenotype, 372
 for membrane system studies, 372
 dipole moments
 in aliphatic nitrile solvents, 372, 373
 in a mixed solvent (dioxane-dimethylformamide, 15 : 1, v/v), 372
 in water, 372
Merocyanine 540 (MC-540) (*cont.*)
 electrochromism, 372
 electronic absorption spectra, 371
 blue shift trend with increasing dielectric constant of the solvent, 373
 concentration effects in ethanol and water, 377
 solvent effects, 373
 excited state lifetimes, 372
 fluorescence emission spectra, 371
 decrease of the 534 nm band with increased self-stacking of MC-540 in dimers, trimers, tetramers, 377
 fluorescence excitation spectrum homothetic to its absorption spectrum, 375
 optical probe for transmembrane potentials, 372
 oscillator strength, 372
 phosphorescence spectra, 371
 photodynamic purging of neoplastic cells in bone marrow explants, 372
 photosensitizer, 371
 sterilization of blood and blood products, 372
 phototreatment of leukemia, lymphomas and metastatic neuroblastomas, malaria, *Herpes simplex*, HIV, 371, 372
 polarity
 of first excited singlet state, 371
 solid state density
 Onsager cavity radius determined pycnometrically, 373
 solubilities in different solvents, 371
 solvatochromic method
 calculated value of the ground- and first excited state dipole moments (McRae, Suppan, Bakshhiev, Kawski-Chammah-Viallet, 372, 373, 377)
 solvatochromic shift, 372
 solvent effects, 372
 with dimer-monomer change, 372
 statistical treatment of, 376
 Mesothelia, 137
Metabolic control
 analysis (MCA), 17, 286
 and non-ideality, 289
 response and control coefficients, 287
 sum of control coefficients for methyl- α -glucoside (α -MG), 290
 sum of control coefficients with respect to flux of phosphoryl through PTS pathway, 290
mechanisms
 emission fluorescence spectra of living cells, 17, 293
 excitation fluorescence spectra 293
 real-time parameter interactive experimental control (RIPEC) to study, 293

- Metabolic coupling, 150, 155
 Metabolic states
 in brain, liver, heart, kidney and *ex vivo* human ocular lens, 207
 5-4-3-2, 25
 skeletal muscle, 25
 state3/state 5 transition, 25
 in *ex vivo* rabbit eye, 207
 Metabolism
 of endogenous chemicals (steroids), 273
 of exogenous chemicals (drugs and pollutants), 273
 phosphotransferase system (PTS), 290
 catabolite repression-linked signal transduction, 290
 in vivo non-ideal, 290
 Metabolite formation (study in real time), 281
 Metal-ligand complexes (MLC)
 anisotropy, 96
 conjugated, 66
 decay times, 4
 FLIM and FRET measurements, 69
 photostability, 69
 protein hydrodynamics, 78
 ruthenium, 96
 output of LED well matched to absorption spectra of complexes, 69
 Stokes shift, 70
 Metal-ligand probes
 for Ca^{2+} , FLIM, Mg^{2+} , pH, 70
 considerable fluorescence lifetime, VI, 65
 Metalloporphyrin, 21
 Metastatic cells, 137
 Metastatic colonization, 146
 Metastatic variants, 144
 Methemoglobin, 43
 Methyl pheophorbide derivative (MPH)
 stacking, unstacking, 7, 118
 Methylene blue, 43
 Methylxanthines, 165
 Mg^{2+} probe, 101
 Michelson interferometer (fringe maxima), 20
 Microcirculation
 adhesion stabilization of blood-borne cells, 8
 Microfilament stress fibers, 269
 Microfluorometry, 170
 intercellular communication, 155
 multiwavelength and numerical image analysis, 12, 231, 238
 penetration of PpIX-peptide within human colorectal adenocarcinoma (HT29) cells, 364, 369
 Microinjection, 53
 Microspectrofluorometer, 242
 custom-built long range phase condenser for, 294
 dedicated computer affording real-time visualization, 294
 with micromanipulators, 294
 Microspectrofluorometer (*cont.*)
 model multi-option with real-time interactive parameter experimental control (RIPEC), 294
 “brain control” for interactive control of experiments, 294
 piezoelectric positioners for interactive study, 294
 Microspectrofluorometry, V, 114, 115, 121, 223, 242
 analysis of
 complete fluorescence spectrum of C-SNARF1-loaded cells, 226
 fluorescence of intact cells, 302
 PDT-photosensitizers (second generation), 6
 pharmacokinetic data for fluorescent drugs (with or without carrier), 369
 Microspheres
 cells grown as, 126
 monodisperse polystyrene, 35
 Microtubule-associated MA-01 antigen, 14
 Microtubule-asters, 261, 262
 Microtubules, 14, 121
 anchorage, 257
 bright staining after injection of antibodies, 257
 depolymerization by exposure to EM, 15, 259, 269
 double-label immunofluorescence with anti-tubulin and anti-vimentin antibody, 269, 270
 at interphase, 261
 labeling by antibodies with epitopes located on the C-terminal domains, 260
 immunofluorescence microscopy, 257, 260
 with monoclonal antibodies, 257, 260
 nucleation and organizing center probes of, 257
 stabilizing buffer, 259
 triple-label staining with anti-a-tubulin, TU-30 and DNA-binding dye, 262
 Microvascular wall adhesion thresholds, VI
 for cells with high metastatic potential, VI
 for cells with low metastatic potential, VI
 Mini-column chromatography, 301
 Mitochondria, *see also* Rhodamine 123
 electrical potential, 110
 membrane potential, 6, 101
 probe (TMRM), 6
 of myocyte sarcomere, 6
 R110 treated cells, 237
 R123 staining energetic state, 237
 transmembrane potential probe, 110
 Mitochondrial damage induced by traces of PP, 119
 Mitochondrial F_1F_0 -ATPase
 oligomycin-sensitive, 102
 Mitochondrial flavoproteins, 11
 Mitochondrial free Ca^{2+} , 107, 108, 111
 Mitochondrial matrix probed with rhodamine 123, 102
 Mitochondrial matrix space NADH, 26

- Mitochondrial membrane
 fluorescence emission, 26
 high conductance pore, 103
 NADH, 25
 potential probed by fluorescence microscopy,
 110
- Mitochondrial PP measured at two sites, 120
- Mitochondrial permeability transition, 103
- Mitogen, 139
- Modulators of chemotherapeutic response, 163, 166
- Molecular gradients, 151
- Monochlorobimane, 101
- Monochromatic image, 7
- Monte Carlo analysis, 34
- MPAS, 3
- MRI scan, V
- Multicellular Spheroids (MSC)
 retinoid-treated *vs.* untreated, 5
- Multidrug pumps
 “vacuum cleaning” and “non vacuum cleaning”
 models, 283
- Multidrug resistance (MDR), 12, 15, 17
 arithmetic model, 285
 concept of ideal metabolism, 288
 non-ideal behaviour, 288
 associated protein (MRP), 284
 direct transfer of control, 17, 283
 drug-efflux pumps, 285, 286
 control of intracellular drug concentration,
 287
 fundamental rate equations, 285
- MDR
 genes and overexpression of MDR genes, 285
 P-glycoprotein, 284
 phenotype, 12, 231
- Multifrequency phase fluorometer, 51
- Multimode digital fluorescence microscopy, 349
 for cell cycle control of chromosome segregat-
 ion with cooled CCD camera, 349-350
 chromosome movement detected with differ-
 ential interference contrast (DIC) op-
 tics, 349
- DAPI fluorescence image stacks for recording
 of chromosome movement, 353
- reconstitution of mitosis from sperm nuclei and
 cytoplasmic extracts of *Xenopus* eggs,
 353
- Multimode imaging, 349
 DAPI and rhodamine images of the same spin-
 dle in time lapse, 352, 353
 dynamics of kinetochore fiber microtubules, 354
 GFP-histones expressed, 353
 mitosis *in vivo* and *in vitro*, 16
 multi-color overlays of different image stacks,
 353
 stereo pair images of DAPI stained chromo-
 somes, 352
 X-rhodamine-tubulin labeled spindle and aster
 microtubules, 352
- Multi-option fluorescence microscope, 298
- Multiparameter digitized confocal microscopy, 110
- Multi-photon excitation, 65
- Multi-pulse experiments, V, 4, 5
- Multi-recognition capability, 148
- Multispecific organic anion transporter, 284
- Multiwavelength microfluorometry, 12
- Multi-well fluorescence scanner, 111
- Murine erythroleukemia (MEL cells), 303
 differentiation of MEL with hexamethylene
 bis acetamide (HMBA), 303
 pyrene dodecanoic acid fluorescence in dif-
 ferentiated normoblasts and undifferen-
 tiated MEL-60, 303
- Murine haemopoietic cell line, BAF3, 130, 131,
 133, 134
- Murine large-cell lymphoma, 137, 139, 141, 145,
 146, 148
- Murine leukemia cells (L1210/0), 158
- Murine mammary tumor cell line, 114
- Murine monoclonal antibody Ki-67, 10
- Muscarinic receptors, 152
- Muscle oxygenation, 44
- Myocyte
 calcein-labeled, 104
 cardiac, cultured, 102, 107, 110
 rabbit, Ca²⁺ transients, 111
 reconstruction, 6
- N-(2-aminoethyl) pheophorbamide α (Ph2-NH2),
 114
- N-(4-butanol)pheophorbamide α (Ph4-OH), 114
- Na⁺
 channel, 249
 probe, 101
(Na⁺/H⁺) antiport, 226
 activation by growth factors, 228
- NADH, 1, 82
 bladder tumors, 244, 246
 cytosolic, 25
 /flavin ratio, 1
 fluorescence, 25, 30
 in aerobiosis-anaerobiosis, 27
 in exposed cortex of the rat brain, 27
 under nitrogen breathing, 27
 redox scanning, 29
 technology, 25
 in vivo, 25
 in mitochondrial matrix, 25
 videofluorometry, VI, 5
- NAD(P)H
 fluorescence image
 ex vivo rabbit cornea, 208, 209
 two-photon excitation microscopy, 206
 corneal endothelial cells, 207
- N-Dodecylimidazole, 7, 115
- Natural tissue fluorescence, 1
- Near Infrared Fourier Transform and Raman spec-
 troscopy, 5, 82

- Near Infrared Fourier transform spectroscopy (NIR-FT), 5
- Near Infra-Red (NIR) spectroscopy, 1
cerebral and muscle oxygen saturation, 51
imaging multi-wavelength optical spectrometer, 51
- Near IR CCD systems, 82
- Nebenkern, 25
- NF-H
immunolocation in dorsal root ganglia and spinal cord of human embryos and foetuses, 333
- Neoplastic urothelial lesions, 241
- Nernst equation, 101, 102
- Nernstian distribution of cationic dyes, 110
- Neurite, 13, 249; *see also* Intramembrane potential
- Neuroblastic and glial neoplasms
cells positive for vimentin, negative for GFAP, 335
co-expression of NF-H and vimentin in neuroblastomas and ganglioneuromas, 336
co-expression of vimentin with GFAP in astrocytomas and glioblastomas, 335
double-label immunofluorescence, 336
- Neuroblastoma, 13, 251, 258, 259
- Neuroepithelium, 137
- Neurohormonal control, 156
- Neuromediators, 8, 149
- Neuron
crustacean peptidergic, 249
different regions, 248
- Neuronal plasmalemma, 251
- Neurotrophins receptor, 147, 148
- Neutral Red (NR), 7, 114
- Nicotiana tabacum*, 14
- Nicotinamide adenine dinucleotide, 5; *see also* NAD(P)H
functional metabolic monitoring with two-photon excitation microscopy, 205
three-dimensional metabolic imaging, 205
- Nick translation for plasmid labeling with digoxigenin 11-dUTP, 182
- Niemann-Pick disease (NPD), 305
cell population labelled with a fluorescent sphingomyelin, 305
grown together gene-corrected and original NPD cells, 305
isolation of “normalized” cells, 305
retroviral vectors expressing normal lysosomal (acid) sphingomyelinase (ASM), 395
transfer of acid sphingomyelinase from the gene-corrected to the NBD cell, 305
- Nigericin, 223
- Nile red, 232, 233
-stained plasma membrane fluorescence, 233
- NIR window, 28
tissue images of antigen/antibody reactions deep within human tumor, 2
- NMR contrast agents, 28
- N-nitrosamine benzyl amine (NMBA), 5
aerodigestive tumors, 5
- Nocadazole, 121
- Non-glycosylated proteins, 8
- Non-invasive measurement of tissue optical properties, 52, 210
tissue spectroscopy and oximetry, 50, 51
- Normal urothelial cell (NU), 242
- Normoxic state of the eye, 1, 11
- Nucleic acid probes, state-of-the-art, VI Nucleosomal linkage, 131
- Nude mouse, 9, 11
biodistribution of PpIX-peptide in mice grafted with human adenocarcinoma, 364
fluorescence emission, 366
fluorescence intensity of organs, 369
xenografts, 193
- Object
fully absorbing, 47
weakly scattering, 50
- Optical absorption coefficient, 59
- Optical biopsy, 81
- Optical diffusion tomography, 51
- Optical fiber
for re-emitted light, 35
for reflected optical pulse train, 35
for unreflected optical pulse train, 35
- Optical fiber bundle, bifurcated, 20
- Optical filter fluorometer, 13, 242
- Optical multichannel analyzer (OMA), 193
spectrometer coupled, 242
- Optical parameter map, 45
- Optical sectioning, 11, 205, 207
- Optical tomography, 51
- Opto-thermal spectro-radiometry, 64
- Organelle visualization, 102
- Osmotic pressure, ion transport related, 12
- Ovarian cancer
aneuploid populations, 161
cell line, 135, 162, 164
platinum-resistant, 161
xenograft (from primary, recurrent), 164
- Oxidative phosphorylation, 110
- 12-Oxo-9(11)-dehydroestradiol, 214
- Oxygenation of tissue *in vivo*
P-porphyrin phosphorescence quenching, 5, 96
- Oxygen radicals, 101
- Oxygen transport, *in vivo* visualization of microvascular network, 96
- Oxyhemoglobin, 44
- Pancarcinoma antigen, 191
- Pancreas
dysfunctions, pathogenesis, 154
endocrine, 8, 149
electrophysiology, 156
exocrine acinus, 8, 9, 149
pulsatile secretion, 156

- Panel of probes, 10
Paracrine growth factors, 148
Paraformaldehyde fixation, DNA crosslinks, 131
PBF1, 101
Pd *meso*-tetra carboxyphenyl porphine, 5
Pd-porphine, 19, 96
Pd-porphyrin phosphorescence quenching, 5, 96
PDT, 113, 121
 chemotherapeutic agents, 113
 in early stage lung cancer, 126
 on human tumor spheroids with Photofrin, 124
photosensitizers, second generation, 6, 113
 chlorins, pheophorbides, phtalocyanins, purins, 6
 role in vascular damage *vs.* direct tumor cell kill, 127
 targets, 6, 113
Pentoxifylline, 9, 163, 164, 166
Perinuclear cap, 14
Peripheral blood mononuclear cells (PBMCs), 173, 174
Perturbation approach in optical diffusion tomography, 51
P-glycoprotein (Pgp), 17, 232, 284
 in mediated efflux of daunorubicin, 284
 positive co-operativity, 286
 in pumping of hydrophobic drugs, 288
 mathematical model of function, 283
 monitored in intact cells by daunorubicin fluorescence, 283
 pumping rate, 283
 cooperativity in terms of daunorubicin concentration, 283
 fluorescence quenching of daunorubicin, 283
 saturability, 286
pH probe, 101, 106
pHi equilibration, kinetics, 221
PH2-NH₂, 117
PH4-OH, 109, 110, 117
Phalloidin, 14
Pharmacology, VI
 application of photodiode array fluorescence and spectroscopy in, 20
Phase modulation spectroscopy, 51
Pheophorbide, 6, 114, 121, 300
 alcohols, amines, ethane, ethyl sulphydryl, ethyl sulfonate, ethyl trimethyl amine, fatty acids, hexylphosphate, 301
 from bacteriochlorophyll of *Rhodobacter*, 300
 cancer cells, 300
 from chlorophyll of *Spirulina*, 300
 photosensitization by, 35, 306
 used for cleanup of blood infected with parasites or viruses and eradication of solid tumors, killing of
Pheophorbine ring, 117
Phlolein, 13, 250, 253
Phorbol esters, 57
Phorbol myristate acetate (PMA), 54, 55
Phosphatidyl-choline liposomes
 fluorescent sphingolipoid loaded, 18, 302
Phospholipid
 sphingomyelin, 299
Phosphorescence
 PD-porphyrin, 5, 32
Phosphorimeter
 analysis of exponential decay profiles by real time monitoring, 96
Phosphosphingolipids, 299
Photoacoustic effects, 64
Photoacoustic spectroscopy (PAS), 59, 60, 63
 acoustic response, 59
 applications to
 charge transfer state states in vision, 59
 depth profile, density of chromophores in the material, 59, 63
 diffusion of chromophores, 64
 human skin, 59
 penetration of sunscreens, 62, 64
 thylakoid membranes, 64
 in dermatology research, 63
and in-depth characterization of homogenous or heterogenous non transparent materials, 59
with Fourier transform analysis, 63
and the heat response signal, 59
of human stratum corneum, 63
of leaves (photosynthesis), 59, 61
modulated (MPAS), V, 59, 60, 61
 chemical storage energy in photosynthetic activity, 61
 photosynthetic energy storage and transduction, 61
 photosystems I and II inside plants, 61
 separation of thermal from oxygen emission, 61
pulsed (PPAS), V, 59, 60
 of condensed matter, 64
 of intermediate state lifetimes, 61
 of radiationless deactivation processes in biological materials, 54
 with simultaneous recording of the response at all acoustic frequencies, 60
Photoacoustic transients
 in dark-adapted intact leaves, 63
Photoactive drugs, 199
Photobleaching, 98, 99, 106, 205, 206
Photobleaching digital imaging microscopy (phDIM), 53
Photochemical destruction of energy acceptor, 54
Photochemistry, V, 114
Photochemotherapy, V, 22, 98
Photodestruction of Cy5, by 633 nm illumination, 54, 56
Photodiagnosis of early bronchial carcinoma, gastrointestinal cancer, ocular cancer, respiratory cancer, skin cancer, urogenital cancer, 190

- Photodiode array fluorescence spectroscopy, 20, 357, 359, 360, 361, 362
of chromophores responsible for naturally occurring fluorescence in rodent skin, 359
localization and pharmacokinetic behavior in diseased tissues of porphyrins, chlorins, phtalocyanines by, 361
(PP) determined by, 360
a quantitative optical biopsy system, 361
rate of formation and clearance of 5-aminolevulinic acid (ALA) induced protoporphyrin, IX
in surface detected fluorescence spectroscopy, 360
tissue pH determination with bis-carboxyethyl-carboxyfluorescein by, 361
Photofrin IITM uptake as a function of tumor size, 5, 7, 123, 241
Photodynamic agent, 31
Photodynamic therapy (PDT) with, 363
formation of singlet oxygen ($1O_2$), 363
HpD, Photofrin, 363
second generation sensitizers, 363
chlorin, benzoporphyrin derivatives, 363
Photograph of
indocyanin E48 Mab conjugate labeled human colon carcinoma, 198
Photon diffusive wave
absorption, emission, migration and imaging in random media and tissues, V, 1, 51
density, diffraction, refraction, scattering, 42, 45, 46, 51
measurement, 2, 31
Photonic pathology, 5, 81
Photophysical parameters of psoralens, 22
Photoreactions of psoralens at cell membranes or proteins, 22
Photosensitization, 303
by ALA-induced PP, 118
cell death using vital stains, 303
Photosensitizer
delivery system to tissue by chromophores, liposomes, microspheres, nanoparticles, lipoproteins, PpIX
hydrophobic, 21, 115, 363
lipophilic, 113
-peptide, 21, 363, 364
second generation, 113
Photosynthesis studied by PAS, 3
Photosynthetic activity of leaves studied by MPAS, 61
Photothermal phenomena, 63
Phototoxicity, 99, 114
Phtalocyanins, 6, 113
Phylogenetically preserved c-peptide, 14
Physiopathology of tissue, VI
Phytoestrogen, 11, 214
Piezo-driven vibration for SNOM, 19
Pigment/chromophore penetration studies, 4
Pirarubicin, 165
Plasma membrane potential, 102
Pixel-by-pixel imaging of heterogeneity, 186, 223
Plasmids
ER expression plasmid pCMV-ER, 11
pRB₂ and pSG₅, 182
Plasmalemmal membrane, 109
Plasmodium falciparum, 121
Platinum derivative, 254S, 162
Pleitropic cell responses, 53
Polarization by light quenching, 76
Polyclonal antibody
FN receptor (FNR), 144
serine/threonine protein kinase, 3
vimentin (VN) receptor, 144
Polychromator emission, 20
Polycyclic hydrocarbon (pyrene), 300
Polylysine, 6
Polymerase chain reaction (PCR), 144
Polyvinyl alcohol intermediates, 199
Porphyrin, 5, 82
fluorescence, 124
polyethers, 123
tumor localizing, 124
Post-stabilization adhesion phase, 8
PPAS, 3
Prednisolone, 193
Pressure tuning infrared spectroscopy, 383
discontinuities in the pressure dependencies of various infrared spectra parameters, 383
intermolecular interactions in DOPC and DPPC, 383, 384
spectra of the high pressure phases, 383
structural and dynamic changes the molecular level in the model lipid, 383
PRO probes, 100
Probability of fluorescent photon generation, 34
Probe microenvironment, 12
Progesterone (PR) gene, 10
number of copies, 10
Progesterone (PR) receptors, 10, 181
expression and cell kinetics, 186
gene on chromosome 11, 181, 187
number of copies, 181
FISH, 182–185, 187
double FISH on chromosome 11 centromere and PR gene, 185
heterogeneity of number of chromosome 11 and PR expression, 185
immunostaining, 181
triple (PR, Ki-67 antigen, DNA), 181–183
negative cell line HECIA, 166
positive tumors
heterogenous staining, 181
MCF-7 breast tumor cell line and subclones, 181
videomicrofluorometry, 181, 186

- Prognostic parameters, VI, 9
Progression-related differences in integrin expression, 144
Proinsulin biosynthesis, 156
Proliferating cell nuclear antigen (PCNA), 10, 173, 177
Proliferation-associated antigens (PAAs), 10, 176
Propidium-iodide (PI), 9, 100, 133, 136, 158, 163, 166, 174, 177
selective binding to double stranded DNA, 157
Prostate cancer, 169; *see also* Estramustine
Dunning carcinomas (R3327-AT) grown subcutaneously on the flanks of rats, 386
pheophorbide derivatives injected, 306
DU145 cells, 340
Estramustine-resistant cell lines, 340
cell volume studies, 342
clonally selected, 340
cytoskeletal studies, 344
drug localization and efflux, 341
mitotic spindles 25% smaller in resistant cells than parental lines, 345
optical sectioning with DIC, 342
FISH for deletion of heterozygosity, 23
Protein
biosynthesis, 150
domain-to-domain motion, 69
FITC staining, 9
fluorescently labeled, 53
hydrodynamics on microsecond timescale, 65
Proteinase K, 182
Protein kinase
calcium-activated, 57
catalytic domain detected by Cy5 fluorescence, 54, 56
cyclic AMP-dependent and independent, 57, 156
down-regulation, differential, 57
fluorescent, 54
intracellular processing, 57
lipid binding, 57
multifunctional, 57
phospholipid-dependent, 57
(in) platelets, 148
proenzyme in mammalian tissue, 57
proteolytic processing, 56
(in) rat brain single cells, fluorescent labeled, 57
regulatory domain detected by Cy3 fluorescence, 54, 56
serine/threonine, 54
Protoporphyrin (PP), 113, 119, 212
ALA-induced, 7, 21, 241
from bovine haemoglobin, 363
highly improved solubility, 363
hydrophobic, chosen as a model of non-covalent association with amphiphilic peptide isolated
Protoporphyrin (PP) (*cont.*)
-peptide (PpIX-peptide), 363
circular dichroism (CD), 365
fluorescence quantum yield of, 365
fluorescence spectrum of aqueous solution, 367
penetration of, 21, 367
photodegradation of, 367
uptake by HT 29 cells as determined from 636 nm fluorescence intensity, 358
in vivo fluorescence spectra in nude mice grafted with HT29 cells, 364
Provera a progesterone compound, 166
Pseudocoloring, 103
Psoralens and derivatives
antiproliferative action based on photochemical reactions from the triplet state, 405
fluorescence lifetimes (τ_f) and fluorescence quantum yields (Φ_f) of PSO, TMP and TMA, 406
primary photophysical processes correlated with *in vivo* photobiological activity
triplet quantum yields and singlet oxygen yields in homogenous solutions, 485
PSO in water rich region at the membrane interface of LDL liposomes, 407
PUVA therapy, 405
sensitivity to solvation of the singlet and triplet excited state parameters, 405
singlet-triplet energy gap decrease at high solvent polarity, 408
triplet formation quantum yield of PSO, TMP and TMA in dioxan-water mixtures, 406
LDL liposomes
“Pulse and chase” of fluorescent sphingolipid, 302
Pulse cytophotometric analysis, 170
Purkinje cells, 249
Purpurins, 6, 113
Pyrene
fluorescent derivatives, 301
illumination with UVA, 300
selective killing of cells derived from patients with lipid storage disorders and leukemic cells, 300
Pyrene dodecanoic acid (P12), 300
activated to form P12 coenzyme A ester, 303
fluorescence of leukemic cells, 303
taken up by cells and metabolized, 303
Pyrene sulfonylamidoundecanoic acid (PSA-11), 300
Pyridine nucleotides cytosolic, 11
Pyropheophorbide, 114
Quadruple fluorescence labelling of microtubules, vimentin, mitochondria and endoplasmic reticulum, 14
Quantitative optical biopsy system, 21
Quantum yield of fluorescence, 190
Q-switched laser source, 78

- RALS, 134
 Raman spectroscopy, V, 81, 389
 Ratio of fluorescence intensity at two wavelengths and ratio images, 5, 106, 108
Receptor
 for apolipoprotein B/E, 7
 cognate, 154
 distribution, 213
 expression, 213
 imaging, 214, 215
 recruitment, 8
Reconstruction, 3D, 2, 43, 49, 50, 51, 105
Red fluorescing dyes, 100
Redox scanning, 1, 19, 29
Re-emitted excitation light and fluorescence, 2, 35
Relative binding activities (RBAs)
 of fluorescent ligands to ER, 215
Retinoid, 5
Rhenium(1) complexes as probes of intra- and intermolecular excited state interactions, 78
Rhodamine 110 (R110), 232, 233, 237
 -grown CEM-WT cells
 R123 versus Hoechst fluorescence intensities in, 237
Rhodamine 123, 6, 7, 12, 100, 101, 109, 110, 121, 232–237
 co-localization with LY or NR, 11
 decrease of mitochondrial staining in cells treated by R110, 233
 correlated to reduction of energetic level of mitochondria, 233
 heterogenous fluorescence, 233
 relocalization kinetics, 129
Rhodamine-conjugated phalloidin, 267
Rhodamine-dextran, 101
Rhodamine dyes, 99
Rhodamine microspheres, 101
Rhod-2, 101, 106
Riboflavin, 243
Rotational correlation time, 67
Rotational diffusion, 5, 67
[Ru(bpy)₂(dcbpy)]
 absorption spectra, 67
 conjugated to Con-A, 69
 to ferritin, 68
 excitation anisotropy spectra, 67
Ru complex conjugated to
 concanavalin, 67
 ferritin, 67
S phase
 arrest, 164, 165
 biphasic, 165
 block, 158, 162
 BrdUrd incorporation during, 160
 delayed transit, 160
 dose-related accumulation, 159, 161
 percentage of cells in (%SPF), 160, 175
S phase (cont.)
 population, 166
 transit through, 158
Sarcolemma, 103
Sarcomeres, 105
Saturated hydrocarbons, 78
SBF1, 101
Scanning force microscope (SFM), 317
Scanning near-field optical microscopy (SNOM), 19, 317
 amplitude of tip vibration determined from the motion of a diffraction pattern of a laser diode, 318
 fluorescence focused onto a single-photon counting avalanche diode head, 318
 IgE-receptors distributed in discrete arrangements as seen by, 321
 resolution not diffraction limited, 317
 simultaneous shear force topographic and fluorescence images of basophilic rat leukemia cells, 19
Scanning tunneling microscope (STF), 317
Scattering tissue and parameters, 31, 33, 47
Scattering coefficient map at every voxel, 2, 31, 33, 42, 43, 47, 50
Scintillation counter, 194
Second generation sensitizers, 241
Secretagogues, 159, 151
Selectins, 8, 138
Sequential tumor fluorescence measurements, 193
Serine-threonine protein kinase, 3
Sialidase, 148
Signal transduction cascade in living cells, V studied by FRET, 3, 53
Single living cells study techniques
 confocal observations, 325
 with caged compounds, 325
 with intracellular injections of DNA, 325
 With vital fluorescent or phosphorescent probes, 325
 Singlet oxygen, 124
Sinusoidally modulated light, 32, 42
In situ End Labeling (ISEL) of strand breaks, 8, 132
In situ fluorescence based diagnosis, 305
In situ fluorescence microscopy, 213
Skin cancer, 169
SNARF-1, 101, 106, 109, 221, 222, 223, 225
 experimental cell fluorescence spectrum, 223
 resolution of complex spectra, 224
 participation coefficients of components, 224
SNOM: *see* Scanning near-field optical microscopy
Solvation change associated with receptor binding, 214
Solvatochromism, 21; *see also* Psoralen
Somites, 13; *see also* Intramembrane potential
Soret band hypochromicity of PpIX-peptide, 365
Spectrographic image, 7, 115
Spectrophotometer, 43
Spectrophotometric cell sorter, 170

- Spectroscopy
of tissues in the frequency-domain, 41
in vivo, 1
- Spheroids, human tumor, 128
- Sphingolipid, *see also* Nieman–Pick disease
fluorescent probe degraded in lysosome to LR- or SR ceramide, 303
converted in Golgi to LR- or SR-sphingomyelin, 303
- Sphingolipid precursor, 111
- Sphingolipid storage disorders, 18, 299
- Sphingomyelin, 299
fluorescent form
lissamine rhodamine dodecanoylsphingosyl-phosphocholine (LR-SPM), 305
- Sphingomyelinase, lysosomal, acid (ASM), 305
“normalized” cells expressing ASM, 305
retroviral vector expressing normal lysosomal (ASM), 18, 305
- Spindle, *see also* Estramustin, Microtubules, Taxol, Tubulin
assembly dynamics measured by photoactivatable fluorophores, 349
4-D (3-D time lapse) image, 349–350
organization in living cells and *in vitro* systems, 349
photodamage and phototoxicity of, 350
proteins conjugated to green fluorescent proteins (GFP) and expressed *in vivo*, 349
X-rhodamine labeled tubulin subunits, 349
- Spin quantum number, 124
- Spirulina*, 300, 301; *see also* Pheophorbides
- Squamous cell carcinoma (SCC), primary, human, 11, 189, 193, 194
- Stacking-induced fluorescence quenching, 118
- Stern–Volmer relationship, 2, 6, 32
- Steroidal estrogens, 214; *see also* Estrogens
- Steroid fluorescent derivatives and receptors, 213
- Stimulated emission, 3
- Stokes shift of emission spectra, 214
- Sulfoindocyanine succinimide ester, 3, 54
- Sunscreen chromophore depth profile, 3
- Surface-biotinylated tumor cell lysates, 140
- Synchronization of free Ca^{2+} oscillations and electrical activity, 8, 150
- Syncytial unit of exocrine pancreas acinar cells, 9, 150
- Syngeneic mice, 139
- Synthetic tetrahydrochrysene (THC) estrogens, 213, 214
- Taxol, 9, 168, 261; *see also* Microtubules, Spindle, Tubulin
cross-resistance to, 15
(and) radiation, 168
spindle disruption and assembly of new microtubule asters in mitosis, 261
- Teniposide (VM1), 12, 232
- Tetrahydrochrysenes, 215
- Tetramethylrhodamine ethyl ester, 102
- Tetramethylrhodamine isothiocyanate (TRICTC), 10
- Tetramethyl rhodamine methyl ester (TMRM), 6, 100, 101, 102, 103, 107, 108, 109
- Texas Red, 23, 99, 101
- Thermal conductivity, 59
- Thin layer chromatography (TLC), 301
- Thiols, 100, 101
- Thiotepa, 160
- Thyroid blocked by Lugol, 193
- Three-dimensional confocal microscopy, *in vivo*, V
- Three-dimensional imaging of calcium-loaded myocytes, VI, 105
- Three-dimensional metabolic imaging of NAD(P)H and flavoproteins, 205
- Three-dimensional optical imaging with two-photon excitation laser microscopy, 205
- Three-photon excitation of calcium probe indo-1, 79
UV absorbing fluorophores, 74
- Thresholding and contour smoothing, 233
- Time-correlated single photon counting (TCSPC), 67
- Time-of-flight associated with photon scatter, 32
- Time-resolved fluorescence energy transfer, 78
- Time-resolved reflectance and transmittance, 52
- Time-resolved spectra of visual pigments, V
- Tissue
diffusion of light, 45
model for reconstruction, 45
optical properties, 45
oxygenation measurement, VI
scatter, 33
- Tomography of tissues in the frequency domain, 2, 41
- Topoisomerase II-reactive chemotherapeutic drugs, 135
- Total internal reflection microscopy, 20
- Transferrin, human, 259
- Transglutaminase, 147
- Transillumination geometry, 2
- Transition metal complexes, highly luminescent, 78
- Transporters, 149
- Triple-label staining of actin, tubulin and vimentin, 14
- Trophic factors, 148
- Trypan blue exclusion test, 100, 233
- Tryptophan, 5
autofluorescence, 13
metabolism, 393
metabolite, 22
photophysics, 393
- 3T3 cells, 14; *see also* Fibroblasts
SNOM images, 19
- Tubulin, 173
of brain, 257
caged-fluorescein labeled-, 16
charged variants (isotubulins), 257

- Tubulin (*cont.*)
 C-domain exposed on the surface of microtubules, 260
 C-terminal variable domain of, 257
 epitopes, 260
 immunofluorescence microscopy, 257
 isotype expression, 257
 multiple genes, 257
 N-terminal structural domains with unexposed or masked epitopes, 260
 vinblastin binding, 12
 x-rhodamine labeled, 16
- Tumor
 aneuploid, diploid, 16, 169
 cell populations, resistant, 166, 204
 heterogeneity, 9, 165
 effects on flow cytometry of clinical specimens, 173
 Tunable source of light pulses, continuous, 3
- Two-photon excitation (TPE), 3, 70
 avoidance of out-of-focus signal, 74
- Two-photon excitation laser microscopy, 205, 207, 208, 209
 with intrinsic functional metabolic probes, 209
- Two-wavelength ratio method, 221
- Tyrosine kinase
 receptor activation, stereochemical model, 57
- Ultimate carcinogenic metabolite
 benzo[a]pyrene 7,8-diol-9,10-epoxide, 278
- Ultraviolet laser scanning confocal microscope, 97
- Urothelial carcinoma *in situ* (CIS), 241
 cancer progression, 241
 tumor recurrence, 241
- Urothelial cell, 13, 243, 245
- Uterine cancer lines, 188
- UV-excited fluorophores, 97
- Van der Waals interactions, 115
 "vacuum cleaner" model of asymmetrical and
 asymmetrical membrane with three compartment system, 288, 289
- Valinomycin, 14
 -mediated K⁺ diffusion potentials, 250
- Vascular adhesion molecule-1, 148
- VDL bound molecules, 7
- Verapamil, 17, 284
- Vibronectin (VN), 8
- Video-imaging system
 combined with chromophore carrying substrates, 281
 for study of single cell metabolism in *real time*, 16
- Video-microfluorometry
 of cation and anion antiport mechanisms, 227
 digitized microscope for, 223
 of estrogen receptor (ER), 11
 of gene probes, 10
 of intracellular ionic concentrations, 12, 221, 223, 225–227
 of progesterone receptors (PR), 10, 181
- Vimentin, 15
 antibody VI-01 against, 266
 co-expression with GFAP positive cells, double-label experiments, 332
 immunolocation in ependymal cells, mesenchymal derivatives, neural tube and spinal cord, 333
 receptor antibody, 144
- Vinblastine (VLB), 12, 232
 cross-resistance to, 15
 -grown cells, 232–238
- Vincristine, 158
- Vision, PAS, 3
- Vital fluorescent and phosphorescent dyes, 19
- In vitro* autofluorescence, 242
- In vitro* fertilization (IVF), 305
- In vivo* autofluorescence, 242
- In vivo* imaging highly scattering tissues, 209
- In vivo* kinetics of the biodistribution of ¹²⁵I-indocyanin, 196
- In vivo* optical fiber spectrofluorometry, 364, 367, 369
- In vivo* tumor fluorescence measurements, 193, 195
- VLDL, 117
- Von Willebrand factor, 148
- Voxel view Ultra Volume Rendering software 343
 volume of estramustine-resistant lines, 343
- V79 cells constructed for expression of rat and human cytochrome P450, 275, 278; *see also* Cytochrome P450
- Wall shear
 adhesion threshold (WSAT), 8, 141, 142
 stress (WSS), 140, 141, 142
- Wave vector complex, 46
- Wheat germ agglutinin (WGA), 139
- Wide-field fluorescence microscopy, 97
- Wood's light, 127
- W-7 (a calmodulin antagonist), 309
- Xenograft in nude mouse of primary and recurrent ovarian cancer, 9
- X-ray computed tomography, 3
- YOPRO-1, 134